PROJECT ADVISORY COMMITTEE

Subcommittee on

Engineering

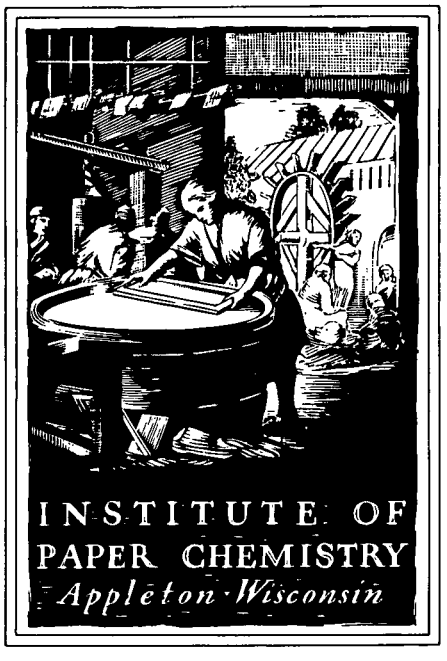

IPC STAFF STATUS REPORTS

This information represents a review of on-going research for use by the Project Advisory Subcommittees. The information is not intended to be a definitive progress report on any of the projects and should not be cited or referenced in any paper or correspondence external to your company.

Your advice and suggestions on any of the projects will be most welcome.

FOR MEMBER COMPANIES ONLY

NOTICE & DISCLAIMER

The Institute of Paper Chemistry (IPC) has provided a high standard of professional service and has exerted its best efforts within the time and funds available for this project. The information and conclusions are advisory and are intended only for the internal use by any company who may receive this report. Each company must decide for itself the best approach to solving any problems it may have and how, or whether, this reported information should be considered in its approach.

IPC does not recommend particular products, procedures, materials, or services. These are included only in the interest of completeness within a laboratory context and budgetary constraint. Actual products, procedures, materials, and services used may differ and are peculiar to the operations of each company.

In no event shall IPC or its employees and agents have any obligation or liability for damages, including, but not limited to, consequential damages, arising out of or in connection with any company's use of, or inability to use, the reported information. IPC provides no warranty or guaranty of results.

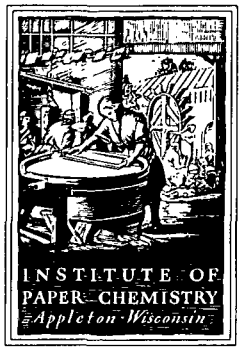

THE INSTITUTE OF PAPER CHEMISTRY
Post Office Box 1039
Appleton, Wisconsin 54912
Phone: 414/734-9251
Telex: 469289

September 30, 1985

TO: Members of the Engineering Project Advisory Committee

Enclosed is advance reading material for the October 23-24 meeting of the Engineering Project Advisory Committee. Included are status reports for active projects, an agenda, and a current committee membership list.

Rooms have been reserved in the Continuing Education Center, and meals will be provided as stated on the agenda. If you haven't already indicated your attendance, please do so at your earliest convenience by calling Barbara Bisby at (414) 738-3328.

For the fall series of Project Advisory Committee meetings, the Institute invites its member companies to send one or more representatives to attend the review sessions (first day) of any or all of the meetings. These invitations were mailed in early August. PAC members from member companies are also welcome to attend these other meetings, and may stay in the CEC and attend meetings and meals of their choice at no cost. If you wish to attend any of these other meetings but haven't registered, please call Barbara Bisby to do so. A meeting schedule is enclosed for your information.

We look forward to meeting with you on October 23-24.

Sincerely,

Clyde H. Sprague

Clyde H. Sprague, Director
Engineering Division

CHS/el
Enclosures

TABLE OF CONTENTS

* * * AGENDA * * *

ENGINEERING
PROJECT ADVISORY COMMITTEE

October 23-24, 1985

Continuing Education Center (CEC)
The Institute of Paper Chemistry
Appleton, Wisconsin

Wednesday, October 23, 1985

10:00am --	INTRODUCTION	Sprague/White
	PROJECT REVIEWS	
	- Fundamentals of Kraft Liquor Corrosivity	Crowe
	- Fundamentals of Corrosion Control in Paper Mills	Yeske
12:00pm --	LUNCH	
1:00pm --	PROJECT REVIEWS - continued	
	- Refining of Chemical Pulps	Staff
	- Process Fundamentals of Wet Pressing	Sprague
3:00pm --	BREAK	
3:15pm --	PROJECT REVIEWS - continued	
	- Higher Consistency Processing	Sprague/Farrington
	- Fundamentals of Drying	Sprague/Lavery
5:30pm --	COCKTAILS	
6:00pm --	DINNER - CEC Dining Room	
7:15pm --	Process Demonstrations	

Thursday, October 24, 1985

7:15am --	BREAKFAST -- CEC Dining Room	
8:00am --	Discussion of Projects	Committee & Research Staff
9:30am --	BREAK	
9:45am --	Continued Discussion of Projects	
10:30am --	Report Preparation	Committee
11:30am --	Adjourn	
--	LUNCH - CEC Dining Room	

NOTE: The spring Engineering PAC Meeting is scheduled for April 2-3, 1986.

ENGINEERING

Project Advisory Committee

Mr. David E. White (Chairman) 6/87*
Group Leader
Research & Development
Union Camp Corporation
P. O. Box 3301
Princeton, NJ 08540-0148
(609) 896-1200

Mr. LeRoy H. Busker - 6/88
Director, Research & Planning
Beloit Corporation
Rockton R & D Center
1165 Prairie Hill Road
Rockton, IL 61072
(608) 364-7961

Mr. Gerard P. Closset - 6/88
Director, Papermaking and
Coating Technology
Champion International
Technical Center
West Nyack Road
West Nyack, NY 10994
(914) 578-7142

Mr. John W. Glomb - 6/88
Corporate Research Director
Research Department
Westvaco Corporation
299 Park Avenue
New York, NY 10171
(212) 688-5000

Dr. Sam Lin - 6/86
Senior Process Engineer
Owens-Illinois, Inc.
One SeaGate
Toledo, OH 43666
(419) 247-5688

Mr. Max D. Moskal - 6/88
Metallurgical Engineer
Stone Container Corporation
616 Executive Drive
Willowbrook, IL 60521
(312) 655-6949

*date of retirement
10/23-24/85

Mr. Robert Murphy - 6/87
Vice President, Pulp & Paper Technology
James River Corporation
P.O. Box 6000
River Park 34A
Norwalk, CT 06856
(203) 854-2374

Mr. M. Thomas Neill - 6/88
Vice President R&D
Abitibi-Price, Inc.
Research Centre
Sheridan Park
Mississauga, Ontario L5K 1A9
CANADA
(416) 822-4770

Mr. Amar Neogi - 6/87
Senior Scientific Specialist
Weyerhaeuser Company
Tacoma, WA 98477
(206) 924-6722

Mr. James Rugowski - 6/88
Engineering Consultant
Kimberly-Clark Corporation
2100 Winchester Road
Neenah, WI 54956
(414) 721-2000

Mr. David South - 6/86
Technical Director
Chesapeake Corporation
P. O. Box 311
West Point, VA 23181
(804) 843-5252

Mr. Ronald Swanson - 6/88
Manager, Process Research
Hammermill Paper Company
P.O. Box 10050
Erie, PA 16533
(814) 456-8811

Dr. Donald Wensley - 6/86
Engineering Associate
MacMillan Bloedel
3350 East Broadway
Vancouver, British Columbia V5M 4E6
CANADA
(604) 254-5151

THE INSTITUTE OF PAPER CHEMISTRY

Appleton, Wisconsin

Status Report

to the

ENGINEERING PROJECT ADVISORY COMMITTEE

Project 3556

FUNDAMENTALS OF KRAFT LIQUOR CORROSIVITY

September 11, 1985

PROJECT SUMMARY FORM

DATE: September 11, 1985

PROJECT NO.: 3556 - Fundamentals of Kraft Liquor Corrosivity

PROJECT LEADER: D. C. Crowe

IPC GOAL:

Increase the useful life of equipment by proper selection of materials of construction, and by identifying suitable process conditions.

OBJECTIVE:

Use electrochemical methods to understand the corrosion processes occurring in kraft process streams as the basis for timely detection and elimination of corrosion and corrosion-assisted cracking in the kraft pulp mill.

CURRENT FISCAL BUDGET: $130,000

SUMMARY OF RESULTS SINCE LAST REPORT: (April, 1985 - September, 1985)

Corrosion testing in the laboratory using weight loss coupons continues in an effort to establish the effects of white liquor constituents on corrosivity. A test matrix of liquors with NaOH + Na_2S + $Na_2S_2O_3$ was completed. The thiosulfate ($Na_2S_2O_3$) was found to accelerate corrosion at all concentrations by placing the corrosion potential at the active-passive transition, where iron dissolution is greatest. Thiosulfate also impaired passivation. A test program involving liquors with NaOH + Na_2S + Na_2SO_3 (sulfite) has been initiated.

Equipment for performing rotating cylinder electrode tests has been procured, and assembly is underway. The equipment will permit tests to be performed at well controlled rotation rates. The results will be related to behavior at corresponding flow rates in white liquor circuits.

The field testing program has continued, with measurements of corrosion rates being completed at two additional mills. The work was troubled by continuing difficulties with instruments. Results showed a wide variation in corrosivity of liquors from mill to mill, related to liquor composition. The steels being tested were ranked in order of decreasing corrosion rate: 1018, A285C, A283 and A285-SPECIAL.

New instrumentation was obtained and is being assembled and programmed to collect linear polarization resistance data in the field and store it on computer disc for remote retrieval by telephone. This system will be utilized at the next test mill.

THE INSTITUTE OF PAPER CHEMISTRY

Appleton, Wisconsin

LIQUOR COMPOSITION EFFECTS ON CORROSION RATES IN KRAFT WHITE LIQUOR

Project 3556

PRELIMINARY

Report Three

A Progress Report

to

MEMBERS OF THE INSTITUTE OF PAPER CHEMISTRY

September 11, 1985

TABLE OF CONTENTS

THE INSTITUTE OF PAPER CHEMISTRY

Appleton, Wisconsin

LIQUOR COMPOSITION EFFECTS ON CORROSION RATES IN KRAFT WHITE LIQUOR

ABSTRACT

The effects of additions of elemental sulfur and sodium thiosulfate on corrosion rates of 1018 carbon steel in alkaline sulfide solutions have been determined by long term weight loss tests. The polarization behavior of 1018 steel and gold in the solutions was investigated.

Elemental sulfur, which forms polysulfide, had a transient effect at low concentration, increasing corrosion rate initially. After further exposure the corrosion potential increased, the electrode passivated, and corrosion rate decreased. At higher concentrations, passivation was immediate.

Thiosulfate increased corrosion rates dramatically by placing the corrosion potential at the active-passive transition, where iron dissolution is greatest. Passivation was impaired by thiosulfate.

SUMMARY FOR THE NONSPECIALIST

Corrosion of carbon steel in kraft white liquors reduces the service life of equipment and causes unexpected failures to occur. There is a need to understand the fundamental causes of this corrosion as a first step in reducing corrosion costs. This work addresses that need by providing information on the effects of variation in liquor chemistry.

In general, corrosion rates depend on the concentrations of corrosive species in the solution. This is true of kraft pulping liquors. Changes in concentration of corrosive species will influence the rate of corrosion. The magnitude of this effect will depend on the role a particular species plays in the corrosion process. If the effect on corrosion rate for a range of anticipated concentrations of various corrosive species is known, it should be possible to predict the effect of changes in process chemistry on corrosion rates in the mill. The objective of this work has been to measure the effects on corrosion rates of varying the concentration of important corrosive species in solution.

Specimens were exposed in NaOH + Na_2S aqueous solutions containing polysulfide or thiosulfate, both known to influence corrosion rate. Polysulfide and thiosulfate are common white liquor contaminants resulting from incomplete reduction in the recovery boiler or from air oxidation. Weight losses were measured after 2, 4, 6, and 8 weeks, and corrosion rates were calculated. In the solutions containing low concentrations of polysulfides, there was a high rate of corrosion initially, but the rate decreased to a very low level after a period of exposure, apparently because the electrode formed a passivating oxide film. Dramatic increases in corrosion rate were observed in solutions containing thiosulfate, with the increase in proportion to the thiosulfate concentration.

When steel is exposed in white liquor it develops an electrochemical potential due to the corrosion reactions occurring on its surface. This corrosion potential will depend on the concentration of corrosive species and temperature and therefore will vary depending on the conditions where the steel is exposed. It is possible to obtain information on expected behavior in a variety of conditions by varying this electrochemical potential and observing the behavior. At low potential, the steel actively corrodes; this is the 'active' region. At higher (more noble) potential, the surface becomes partially protected by the formation of an oxide film. Iron sulfides interfere with proper formation of the passive oxide film and dissolution of the steel continues through the poorly formed film. At still higher potential, a protective or 'passive' oxide film forms and the corrosion rate is very low. Depending on the corrosion potential, dissolution or passivation of the steel occurs. This can account for some of the variation of corrosion rates that may be observed in white liquors. The effects of varying concentrations of polysulfide and thiosulfate on this behavior has been investigated to provide better information on how chemistry can be manipulated to cause passivation of steel in kraft white liquor.

INTRODUCTION

The seriousness of corrosion and stress corrosion cracking in white liquor streams in the kraft pulp mills has been recognized and received considerable attention in efforts to reduce the costs of corrosion. Nevertheless, no thorough investigation of the effects of liquor composition on corrosion rate has been published.

As early as 1951, corrosion in kraft mills was investigated in Sweden. Ruus and Stockman[1] found that increasing concentrations of sodium sulfide (Na_2S), sodium hydroxide (NaOH), sodium thiosulfate ($Na_2S_2O_3$), and sodium polysulfide (Na_2S_x) stimulated corrosion. Corrosion was also related to the amount of oxygen present in the (batch) digester.[2]

An account of a U.S. study indicated that poor reproducibility of weight loss test results that had been observed could be related to whether or not the steel was passivated by a protective oxide film.[3]

Haegland and Roald[4] suggested that corrosion rates were controlled by the rate of diffusion of polysulfide to the surface, where it was cathodically reduced while anodic dissolution of the steel occurred. Thiosulfate increased polysulfide concentration and sulfite decreased it, apparently by equilibration. Roald[5] developed an equation relating corrosion rate to the rate of diffusion of polysulfide to the surface. Corrosivity was a function of NaOH, Na_2S, Na_2SO_3, and Na_2SO_3 (sodium sulfite) concentrations.

Mueller[6] utilized anodic polarization curves to determine the active-passive nature of steel in white liquor. A large active-passive peak was observed between the active and the passive potential ranges as illustrated in Fig. 1. Higher concentrations of oxidizing species could shift the potential

into the passive range where corrosion rates were lower. The surface is 'passivated' by formation of a thin oxide layer which protects the surface from dissolution. Thus corrosion rates would depend on whether the electrode was passivated or not and this could account for some of the great variation between mill and laboratory. In a subsequent publication, Mueller[7] stated that stirring doubled the size of the active-passive peak.

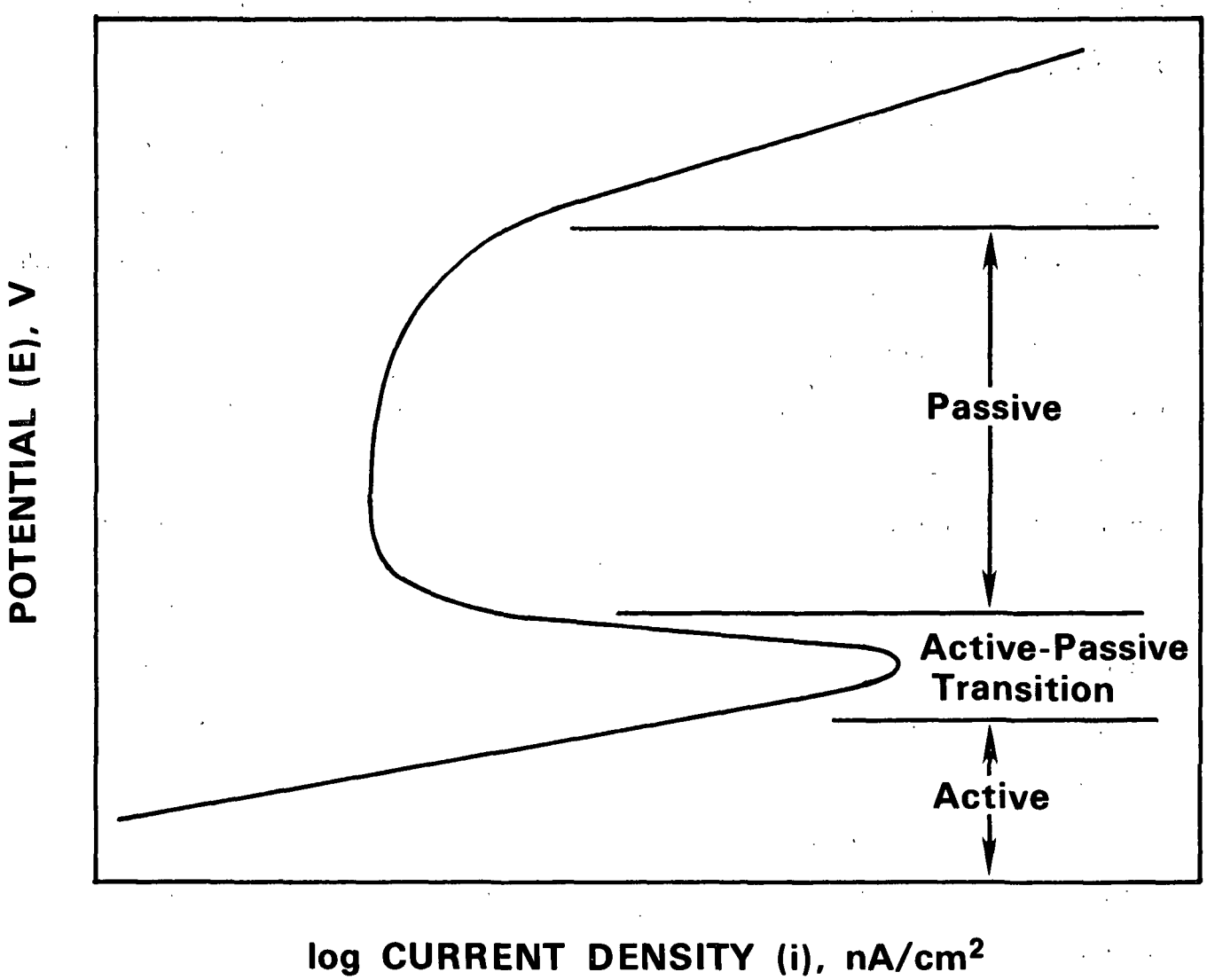

Figure 1. Schematic anodic polarization curve of steel.

At The Institute of Paper Chemistry, Kesler and Bakken[8] determined that carbonate (Na_2CO_3), chloride (NaCl), and sulfate (Na_2SO_4) slightly depressed the

maximum anodic current density at the active-passive peak. Corrosion was increased only if Na_2SO_3 concentration was < 1 g/L. The additives had a negligible or slightly inhibitive effect when sulfite content was higher. These peak currents could have been influenced by the value of the corrosion potential, with a high cathodic current masking an increase in anodic currents associated with higher actual corrosion rates. They performed weight loss tests and found that corrosion rate correlated with Roald's equation only when liquors contained > 1 g/L Na_2SO_3.

Landmark and Roald[9] determined that increasing concentrations of polysulfides decreased the size of the active-passive peak, making passivation easier, and attributed this decrease to the simultaneous cathodic reduction of polysulfide.

The polarization behavior of steel in white liquors was studied by Wensley and Charlton[10] in an effort to determine the effect of various species. Sulfide and thiosulfate impaired passivation. Sulfate and sulfite had no effect. The corrosion potential was controlled by polysulfide concentration.

Tromans[11] investigated the polarization behavior of carbon steel in NaOH + Na_2S solutions in an effort to better understand the processes causing corrosion. Passivation was found to be inhibited by the incorporation of sulfide into the passivating Fe_3O_4 film. This effort was extended by Crowe,[12] in a study at high temperature. Passivation required the formation of an Fe_2O_3 film, and sulfide impaired the formation of this film. The formation of a soluble iron sulfide species was associated with the active-passive peak.

In the research of stress corrosion cracking in kraft white liquor, Singbeil and Garner[31] found that inorganic constituents present in spent liquor inhibited cracking. Their result suggests that inorganics may influence corrosion rates.

IPC has undertaken the task of obtaining information on the effect of liquor composition on corrosion rate. Some of these results for NaOH + Na_2S solutions have been described in a previous progress report.[14] At higher NaOH concentration, passivation in sulfide solutions was slower, or did not occur thus resulting in higher corrosion rates. The corrosion rates after 8 week exposures are summarized in the iso-corrosion plot in Fig. 2. Active corrosion was balanced by hydrogen reduction. Corrosion potential in the passive region corresponded to the S^{2-}/S_2^{2-} redox potential. Intermediate polysulfide concentrations (0.5-2.0 g/L S) increased corrosion rate, but higher concentrations did not. Thiosulfate additions increased the corrosion rate substantially, and copious $NaFeS_2$ formed on the electrode.

The objective of the present work has been to determine the effect of a range of concentrations of the oxidized sulfur species S_x^{2-} and $S_2O_3^{2-}$ on long-term corrosion rate and to investigate the effects on the polarization behavior. The polarization behavior of gold was investigated to determine which features of the polarization curve of steel are due to reduction and oxidation reactions of sulfides in solution; the gold itself is inert.

The chemistry of alkaline sulfide solutions is complicated by the number of oxidized sulfur species which form, including S_x--, $S_2O_3^{2-}$, SO_3^{2-} and SO_4^{2-}. Polysulfide can be formed by addition of elemental sulfur to sulfide solution where it will combine with sulfide. This polysulfide is present in a range of sizes: S_2^{2-}, S_3^{2-}, S_4^{2-}, and S_5^{2-}, in equilibrium with each other. Sulfide in its most reduced form is present in alkaline solutions as HS- or S^{2-}. The bisulfide ion, HS-, is considered to be the predominant form of reduced sulfide at the pH of white liquor[12,15,16] and for this reason electrochemical equilibria have been written in terms of HS- in the present work.

The accuracy of experimental methods used in the work was appraised as summarized in Appendix I.

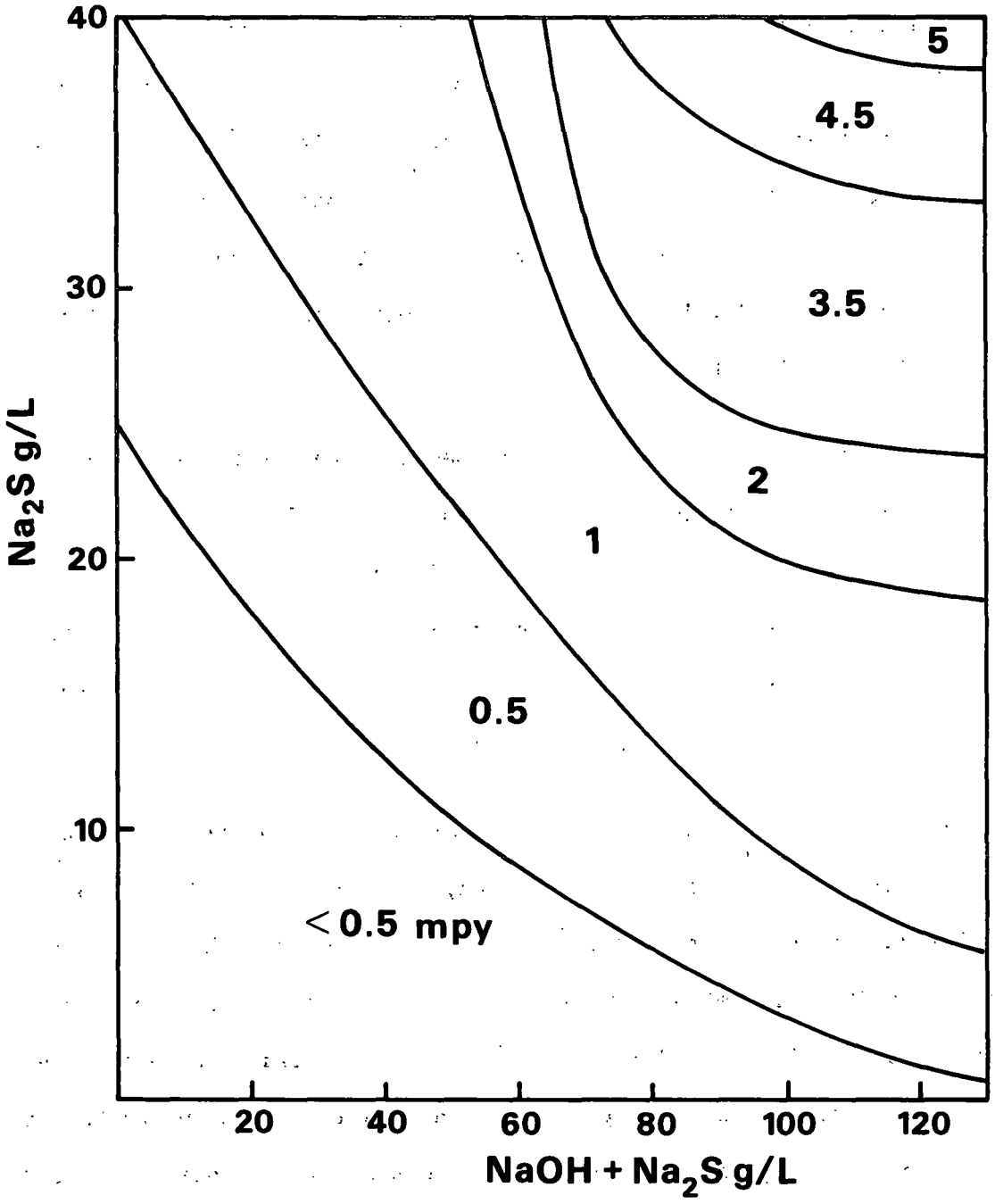

Figure 2. Iso-corrosion plot for NaOH + Na_2S solutions.

EXPERIMENTAL PROCEDURES

Corrosion rates were investigated in the present work by exposing 1018 steel weight loss coupons to liquors at 90 C containing NaOH (60-120 g/L), Na_2S (10-40 g/L), S (0-10 g/L), and $Na_2S_2O_3$ (0-50 g/L) for 2, 4, 6, and 8 weeks.

Experiments were performed in 180 mL Teflon™ beakers with screw-top lids as described in a previous report.[14] The cylindrical electrodes were 3/8-inch in diameter with a surface area of 9 cm^2, tapped at one end and polished to 120 grit and degreased. The composition of the 1018 steel has been listed previously.[14] The electrode holders were constructed of Teflon™. The electrode was isolated from the holder by a Hypalon™ gasket. Each cell contained four electrodes to be removed at two week intervals and a silver-silver sulfide reference electrode. After the test the electrodes were carefully blasted clean before weighing. The experimental procedures and cleaning methods were evaluated as described in Appendix I.

Polysulfide solutions were prepared in a purged flask using analytical reagents and distilled water. Thiosulfate solutions were purged after make-up. In the series using elemental sulfur to form S_x^{2-}, solutions were changed every three days to ensure that polysulfide concentrations were not decreased by oxidation. Solutions containing thiosulfate, considered more stable, were changed at two week intervals. The solutions were changed in a glove bag under a nitrogen atmosphere to prevent oxidation by air. Solutions were maintained at 90 C throughout the test. The open circuit or corrosion potentials of the specimens were recorded daily and plotted.

Anodic and cathodic polarization curves were obtained for steel and gold in each liquor composition at 90 C. Potential was scanned at 1 mV/s using a

Princeton Applied Research Model 350 corrosion measurement system. All measured potentials have been quoted with respect to the silver-silver sulfide electrode, V(SSSE), or have been converted to the standard hydrogen scale, V(SHE). These potentials may be related by the equation:

$$V(SHE) = V(SSSE) - 0.7125 - 0.039 \log ([Na_2S]/858) \quad (1)$$

where $[Na_2S]$ is the sodium sulfide concentration in g/L, as described previously.[17]

RESULTS

POLYSULFIDE

Elemental sulfur was added to sulfide solutions to form polysulfide via:

$$S + HS^- + OH^- \rightleftharpoons S_2^{2-} + H_2O \quad (2)$$

The effect of S_x^{2-} on corrosion weight loss is summarized in Table 1. Low concentrations of polysulfide (0.5-2.0 g/L S) caused a substantial increase in corrosion initially, but the rate declined after some exposure time, presumably due to passivation of the surface. This effect was more pronounced at high HS- concentrations and to a lesser extent at high OH- concentrations. After eight weeks exposure, the differences were reduced apparently because the electrodes spent most of their exposure in the passive condition. Figures 3 and 4 illustrate the 5 mpy isocorrosion surface in the NaOH + Na2S + S solutions after 2 and 8 weeks, respectively. Corrosion rates in solutions of compositions located inside the isocorrosion surface exceeded 5 mpy. Solutions with compositions located on the surface caused corrosion rates of 5 mpy. The figures illustrate that the average corrosion rate is above 5 mpy for a smaller range of solutions after 8 weeks exposure and the range corresponds to the range of much higher rates measured after the 2 week test.

The effect of S additions on corrosion rate (after 2 weeks exposure) is shown dramatically in Fig. 5 for 120 g/L NaOH solution with a range of Na_2S concentrations.

The variation of the corrosion potential of the electrodes with time is plotted in Fig. 6 for the range of S_x^{2-} concentrations in 100 g/L NaOH + 30 g/L Na_2S. The plot indicates that the potential became more noble after a period of

Table 1. White liquor studies - polysulfide weight loss results.

NaOH, g/L	Na_2S, g/L	S as elemental sulfur, g/L						
		0	0.5	1.0	1.5	2.0	5.0	10.0
		2 Weeks, mpy						
60	10	2.3	5.0	3.6	0.6	0.9	0.5	0.8
	20	2.1	6.1	9.5	0.8	18.2	3.3	3.8
	30	4.3	17.7	15.4	13.3	18.9	3.8	3.3
	40	5.2	21.8	19.7	14.4	15.4	6.4	1.1
80	10	2.2	5.3	0.5	0.7	1.1	0.4	0.6
	20	2.9	7.6	8.8	12.4	20.4	1.7	2.2
	30	3.4	21.7	13.9	19.1	18.6	2.0	2.4
	40	4.5	15.7	14.2	17.1	22.0	4.8	2.4
100	10	3.4	7.7	10.8	1.7	7.7	1.2	1.2
	20	2.7	10.2	15.9	22.5	17.9	1.1	1.2
	30	4.3	9.0	24.7	19.0	20.3	11.8	2.6
	40	4.1	20.9	35.0	51.3	62.4	9.4	2.1
120	10	5.1	7.2	10.4	14.3	9.7	2.0	2.0
	20	5.1	15.6	9.5	14.0	19.4	5.9	3.8
	30	6.5	21.2	38.9	19.4	19.9	12.8	7.2
	40	5.5	19.9	39.0	16.8	20.8	16.6	14.1
		4 Weeks, mpy						
60	10	0.6	2.6	0.8	1.0	0.5	0.6	0.5
	20	—	4.9	4.3	12.6	1.3	2.0	2.1
	30	3.6	8.7	6.0	6.0	1.6	1.8	1.9
	40	4.1	12.4	19.9	14.8	9.7	0.8	0.7
80	10	2.1	3.0	9.6	0.7	0.8	1.0	0.8
	20	2.6	4.0	4.5	6.7	8.5	2.1	1.5
	30	3.3	16.1	7.3	9.7	14.7	1.4	1.8
	40	5.4	18.0	7.1	10.2	11.9	6.7	2.1
100	10	4.4	4.9	6.3	1.9	1.4	1.2	1.2
	20	3.6	10.3	11.6	14.0	21.5	2.0	1.7
	30	3.6	8.2	14.0	10.2	11.0	3.4	1.7
	40	4.8	21.7	35.1	26.5	37.6	4.9	1.9
120	10	4.1	4.2	5.9	7.7	6.3	1.8	1.6
	20	5.9	10.8	4.9	7.3	13.5	5.1	2.2
	30	5.4	20.2	34.1	10.4	25.8	7.4	8.8
	40	5.1	19.3	34.6	8.6	10.5	6.6	7.0

Table 1 (Continued). White liquor studies - polysulfide weight loss results.

NaOH, g/L	Na_2S,g/L	S as elemental sulfur, g/L						
		0	0.5	1.0	1.5	2.0	5.0	10.0
		6 weeks, mpy						
60	10	0.6	1.6	0.7	0.6	0.5	0.6	3.4
	20	2.1	2.5	2.8	0.6	1.2	0.9	0.9
	30	2.7	5.0	3.6	3.6	6.5	0.6	0.4
	40	3.1	15.7	6.4	10.8	5.3	0.7	0.6
80	10	2.0	2.1	6.6	0.8	0.9	0.6	0.9
	20	2.4	3.0	3.6	4.3	7.0	2.0	1.3
	30	4.0	17.8	5.7	7.4	3.6	0.9	1.0
	40	4.1	13.6	4.4	6.8	8.7	4.6	1.1
100	10	2.8	2.6	4.1	4.9	3.0	0.6	0.8
	20	2.8	11.1	10.9	11.6	9.5	1.5	1.5
	30	3.5	5.5	9.3	14.6	7.4	1.3	1.3
	40	5.6	19.4	37.6	14.8	23.4	3.4	0.9
120	10	3.9	2.8	4.0	5.0	4.1	1.1	0
	20	13.6	8.0	3.4	4.7	7.5	6.6	1.5
	30	5.5	20.8	36.4	6.3	6.5	4.4	6.2
	40	5.5	24.5	31.8	5.0	6.6	3.0	4.1
		8 Weeks, mpy						
60	10	0.9	1.5	0.6	0.7	0.7	0.8	0.6
	20	2.0	—	2.4	5.5	1.0	0.9	0.8
	30	2.7	3.4	2.5	3.1	5.3	1.7	0.5
	40	3.7	4.2	2.5	4.8	4.7	0.7	0.6
80	10	1.6	1.9	0.8	0.7	0.6	0.5	0.7
	20	3.1	2.2	2.6	3.9	4.6	1.4	1.3
	30	4.1	15.3	4.6	5.5	6.6	2.5	0.7
	40	4.8	10.6	3.7	6.2	6.3	3.2	0.8
100	10	1.9	2.0	3.0	0.9	1.0	0.8	1.1
	20	2.8	8.6	8.1	9.0	9.1	1.5	1.3
	30	4.7	4.0	6.6	10.6	4.3	1.1	1.1
	40	5.3	19.5	33.8	14.4	22.2	3.0	0.7
120	10	2.9	2.5	3.5	4.2	3.3	1.3	1.9
	20	6.9	6.9	3.0	4.0	6.3	4.5	1.3
	30	5.3	21.1	40.4	5.0	3.8	3.6	3.7
	40	5.8	11.1	34.2	3.8	4.8	3.5	3.1

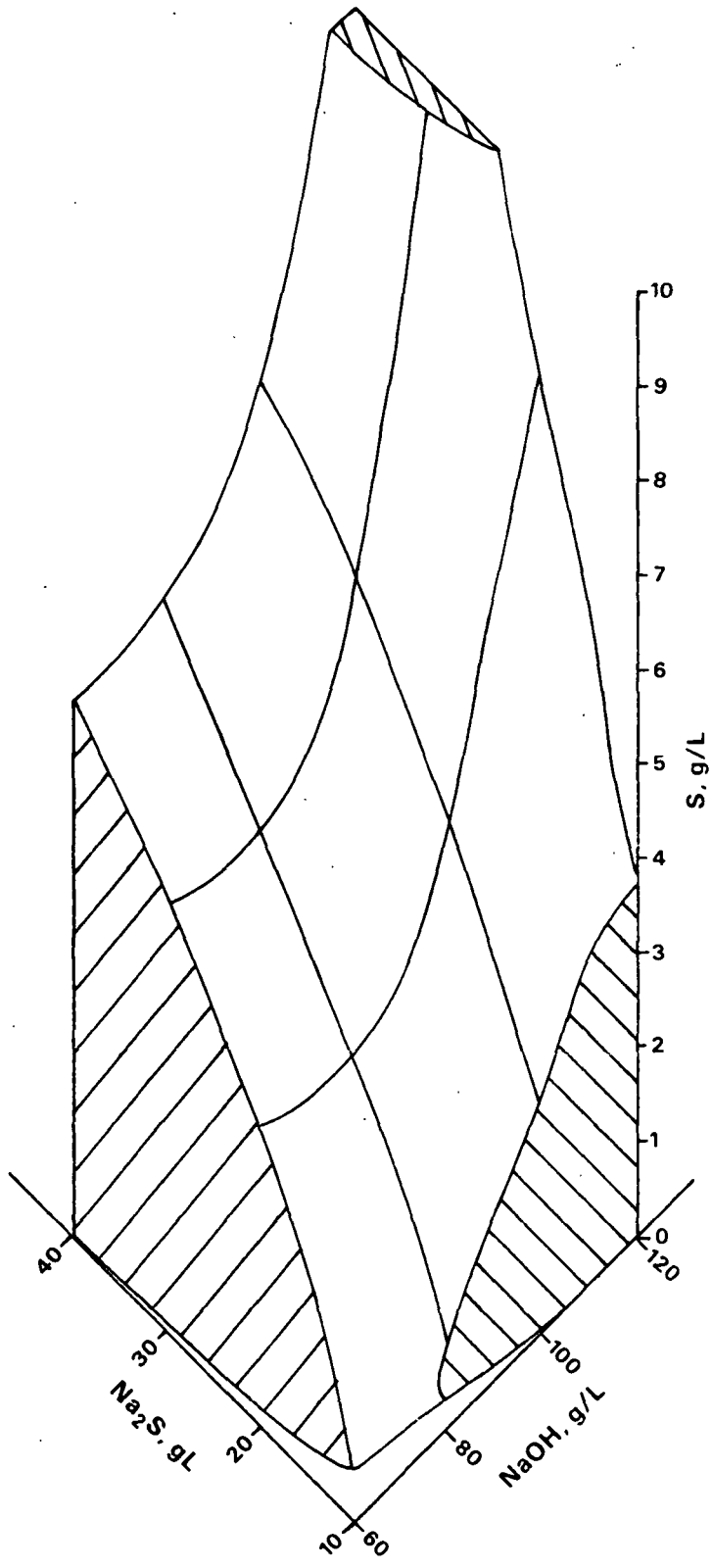

Figure 3. Isocorrosion surface 5 mpy in NaOH + Na_2S + S solution after 2 weeks exposure.

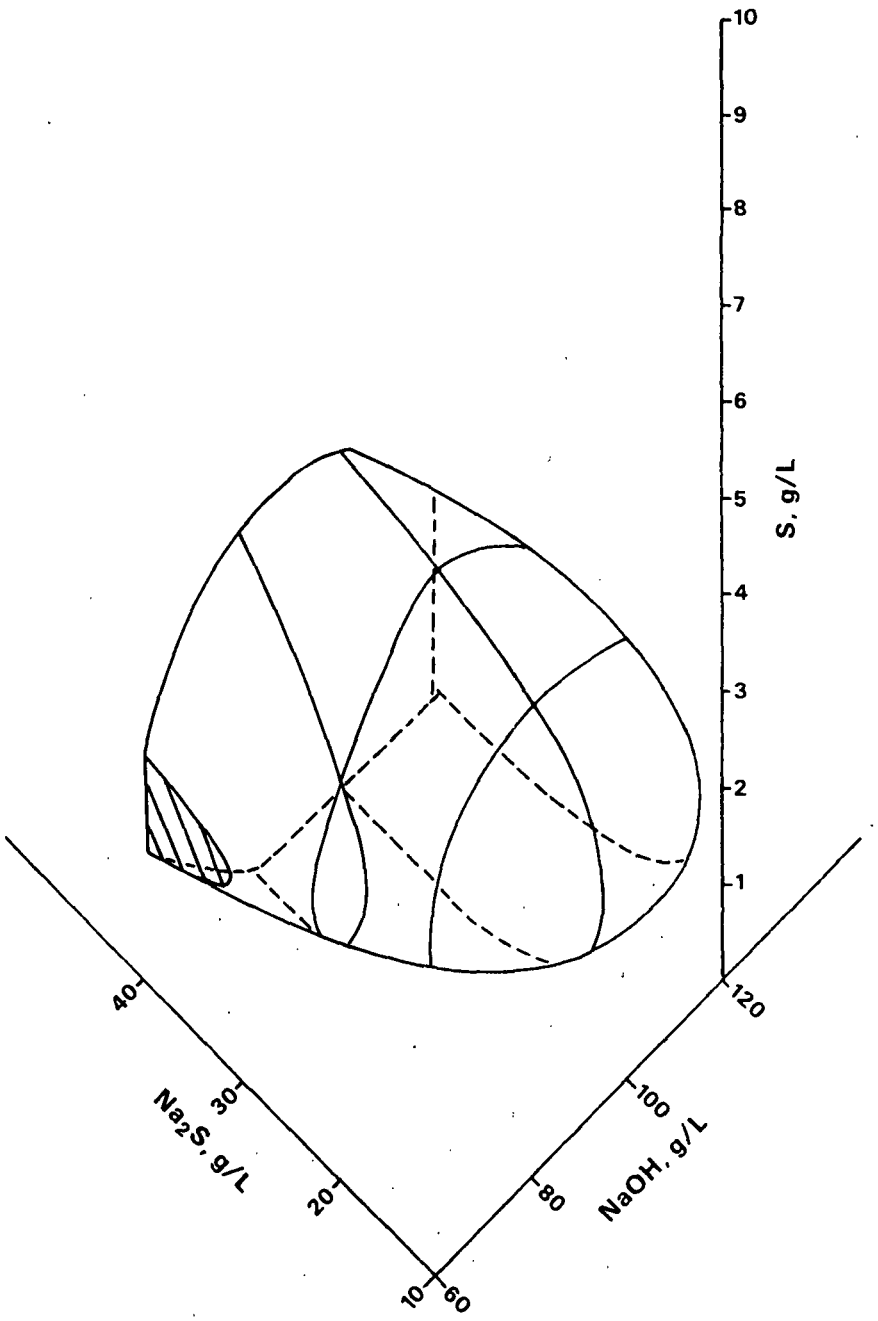

Figure 4. Isocorrosion surface 5 mpy in NaOH + Na_2S + S solution after 8 weeks exposure.

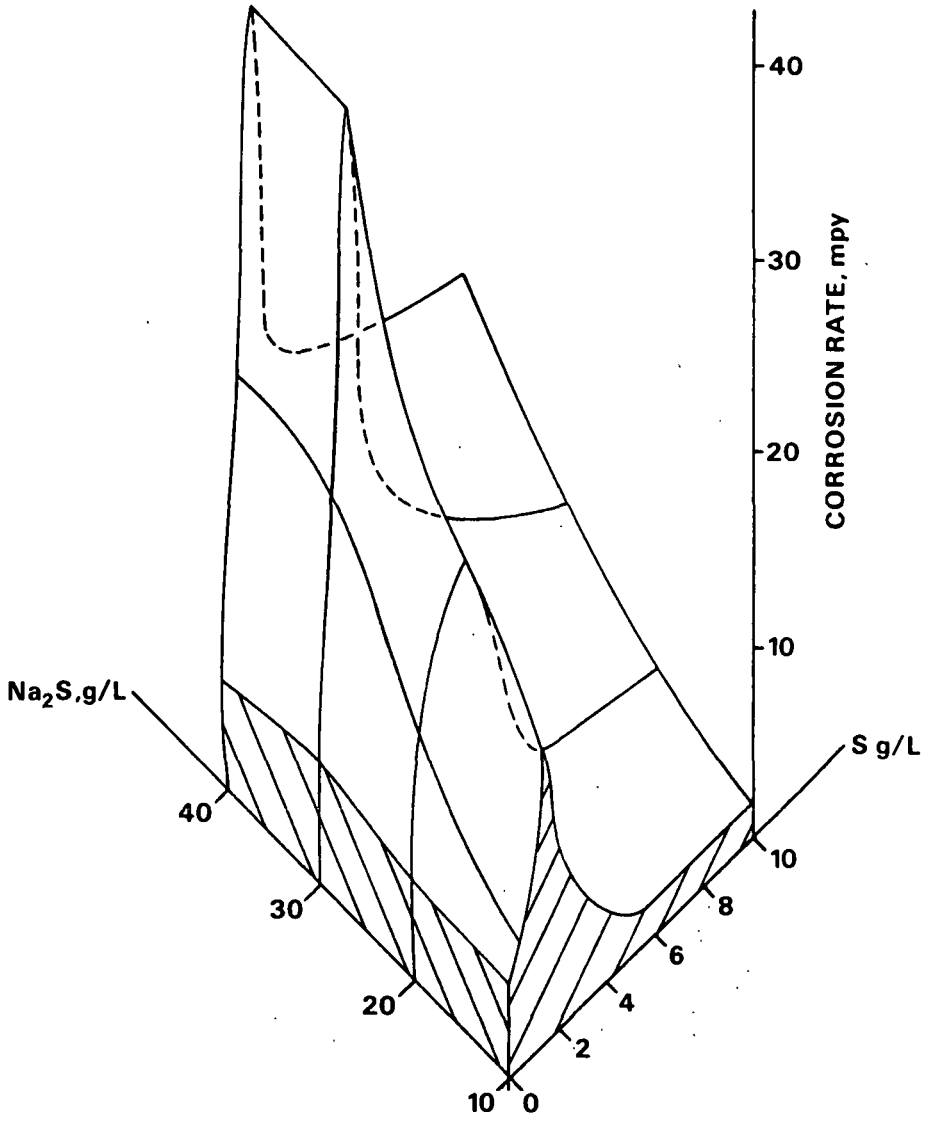

Figure 5. Corrosion rates in Na_2S + S + 120 g/L NaOH solution after 2 week exposure.

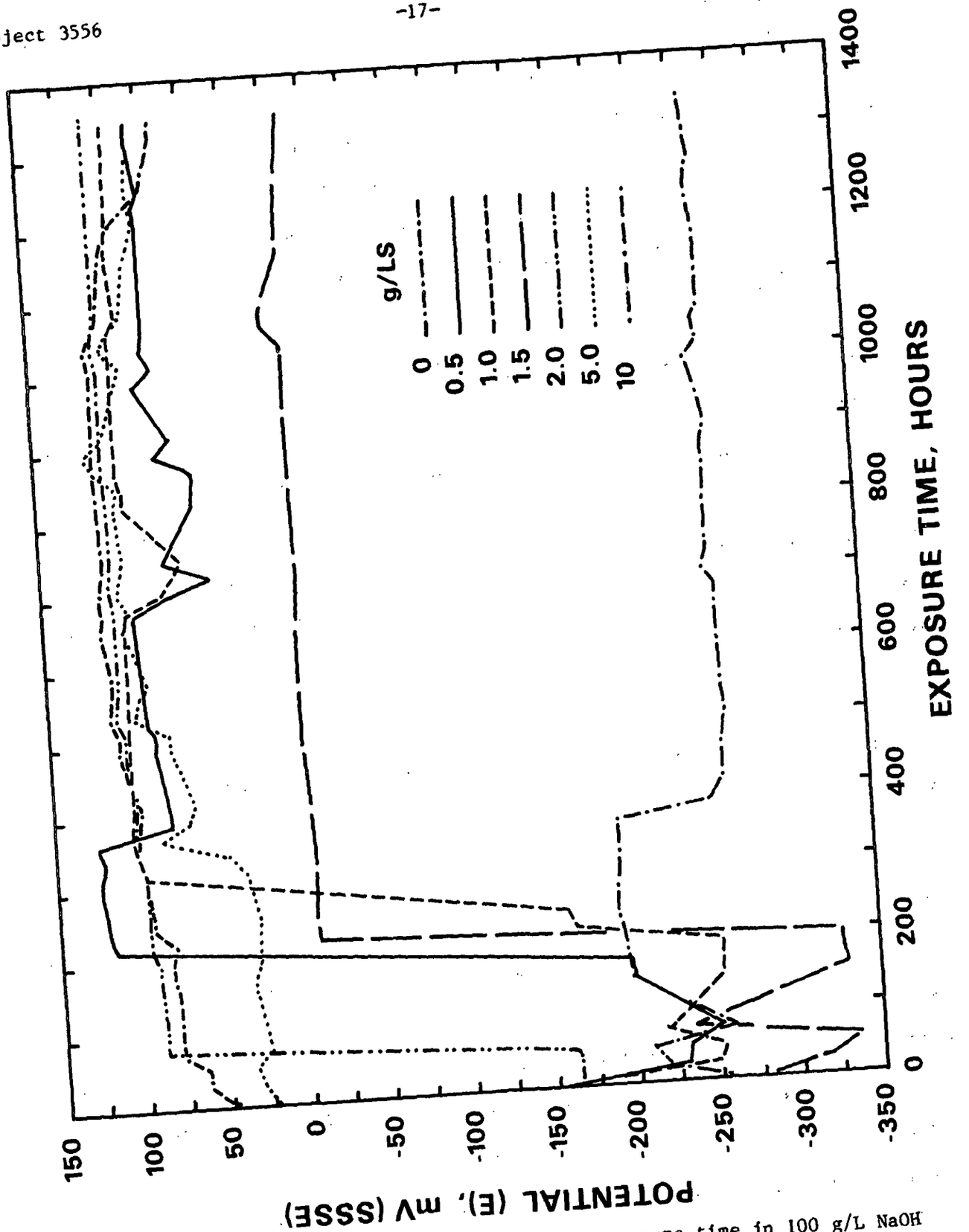

Figure 6. Corrosion potential as a function of exposure time in 100 g/L NaOH + 30 g/L Na_2S + 0-10 g/L S.

time in the polysulfide solutions, corresponding with passivation of the electrode. The time to achieve passivation depended on the polysulfide concentration. As seen in Fig. 6, if no S was added, the electrode remained active. Fluctuations of potential were especially noticeable as the electrode moved from the active to the passive condition. Representative plots for all solution compositions are contained in Appendix II.

As the OH- and HS- concentration increased, the amount of S_x^{2-} needed to cause immediate passivation was increased. In the solution 100 g/L NaOH + 30 g/L Na_2S, passivation was immediate in a solution containing 5 g/L S. In lower concentration 60 g/L NaOH + 10 g/L Na_2S solution, only 1 g/L S was necessary to cause immediate passivation, but in 120 g/L NaOH + 10 g/L Na_2S, 5 g/L S was required to cause immediate passivation. When no sulfur was added, the electrode remained active.

Electrodes which experienced a high corrosion rate spent a significant portion of their life at corrosion potentials ranging from -200 to -150 mV(SSSE).

Polarization behavior of steel was investigated in each solution composition. Data from the polarization curves are summarized in Appendix III. The corrosion potentials on steel were clustered around four values as shown in Fig. 7. The value of corrosion potential was more noble for higher S concentrations. Representative anodic and cathodic polarization curves for steel are presented in Fig. 8. Three major current peaks were observed repeatedly, although the peaks shifted slightly as the solution composition was varied. Typically, the peaks were located at 70, -40 and -150 mV(SSSE), although the peaks at -150 mV were somewhat indistinct. These peaks are associated with oxidation reactions: dissolution or formation of solid products such as oxide films.

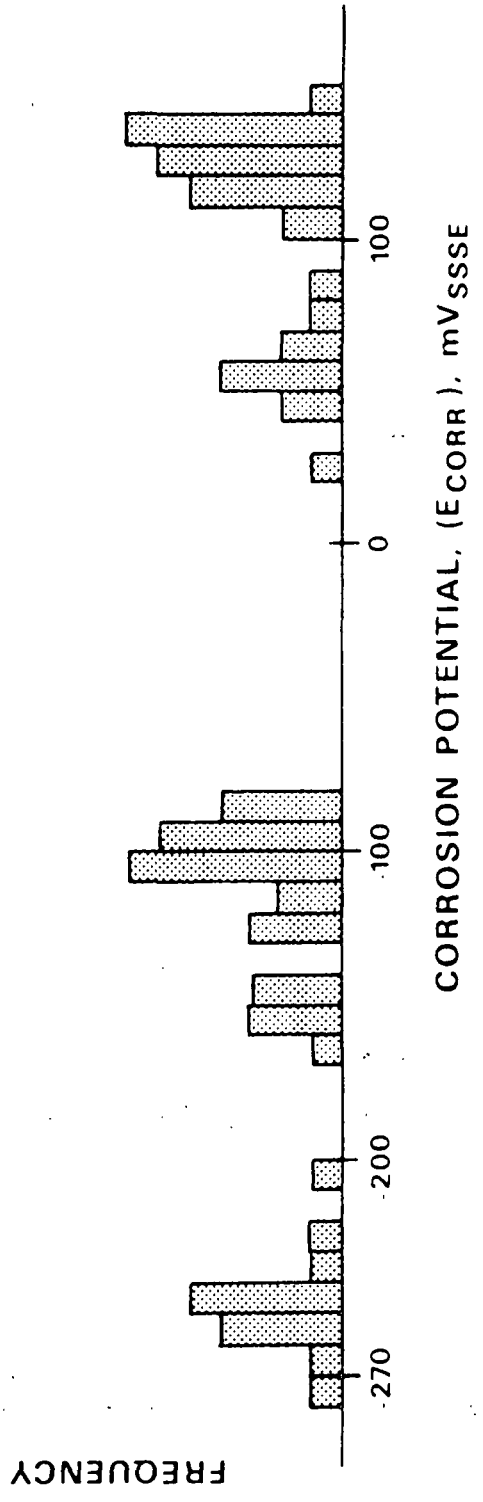

Figure 7. Frequency of different corrosion potentials on steel in all solutions prior to polarization.

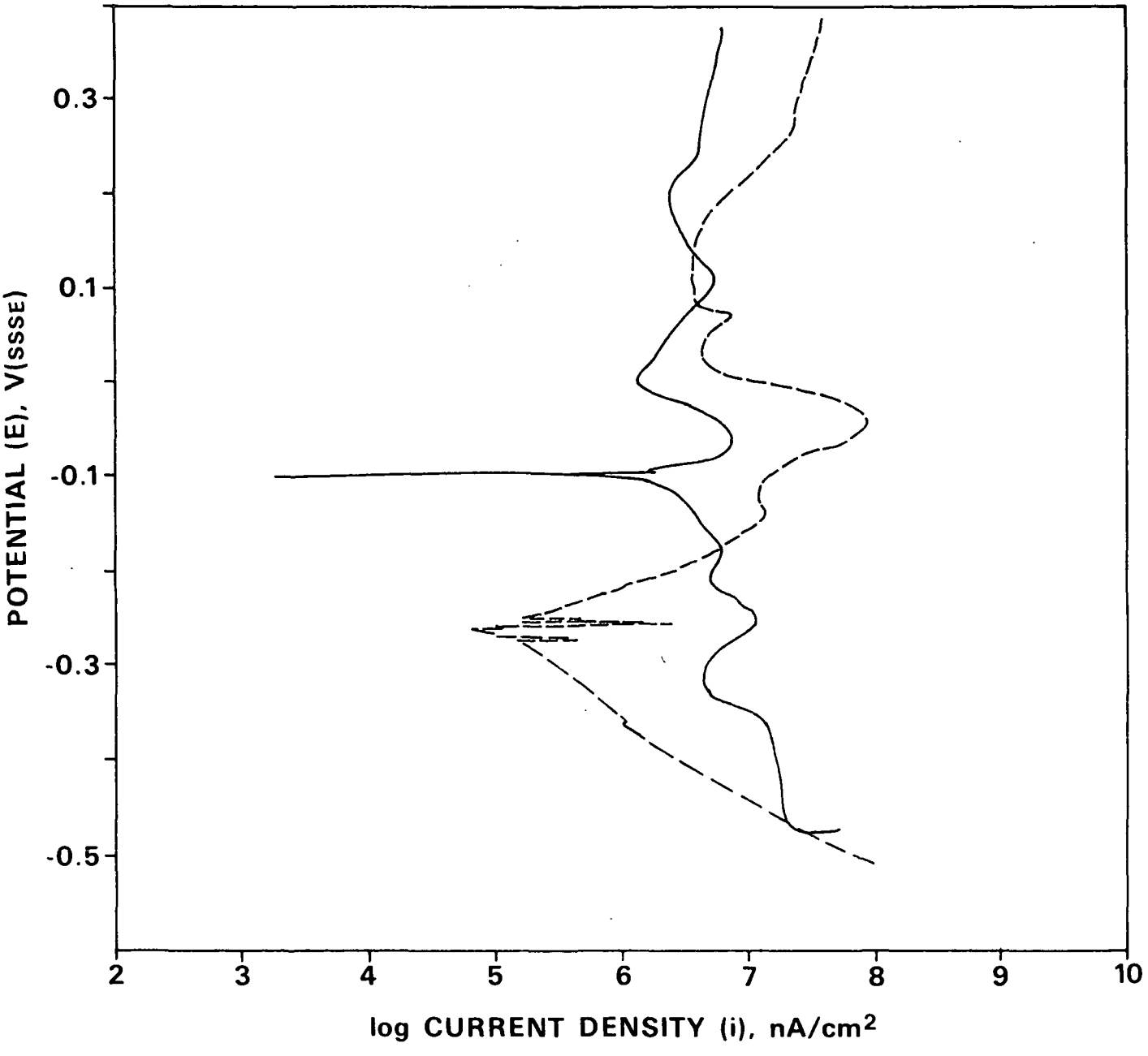

Figure 8. Polarization curves for 1018 steel, 90 C, 1 mV/s in 100 g/L NaOH + 20 g/L Na_2S with (___) and without (---) added S.

The polysulfide obscured the features of the anodic polarization curve of steel compared to plain NaOH + Na_2S solutions. At high S concentrations, E_{corr} was very high and anodic peaks were located below E_{corr}. The slope of the polarization curve, in mV/logarithmic unit of current, is related to the charge passed during the electrochemical reaction or reactions occurring at that potential, and therefore can provide some information on the corrosion process, useful in understanding the fundamental causes of the corrosion. The anodic Tafel slope, β_A, on steel was 64 mV (av. 26 values, s = 34 where s is the standard deviation). The cathodic Tafel slope, β_C, was 128 mV (av. of 18 values, s = 47).

The polarization behavior of gold was similar in all solutions. Data from the polarization curves is summarized in Appendix III. The cathodic polarization curves had two or more sections as seen in Fig. 9, indicating that a number of reduction steps occur for the sulfides in solution. At higher S_x^{2-} concentrations, the current densities were increased and the current density reached a plateau, suggesting concentration polarization. The anodic Tafel slope, β_A, was 78 mV (av. of 56 values, s = 18), with a trend to slightly lower values at high S_x^{2-} concentrations. The cathodic Tafel slope, β_C, was 125 mV (av. of 70 values, s = 34), with a general decrease with decreasing OH- and HS- concentration. This is the opposite trend to the anodic Tafel slopes on gold. The lower section of the gold cathodic polarization curve had a slope of 38 mV (av. of 11 values, s = 4.5). At these potentials gas evolution was observed at the electrodes.

THIOSULFATE

Additions of thiosulfate increased the corrosion rate significantly as summarized in Table 2. This effect was more pronounced at higher OH- and HS-

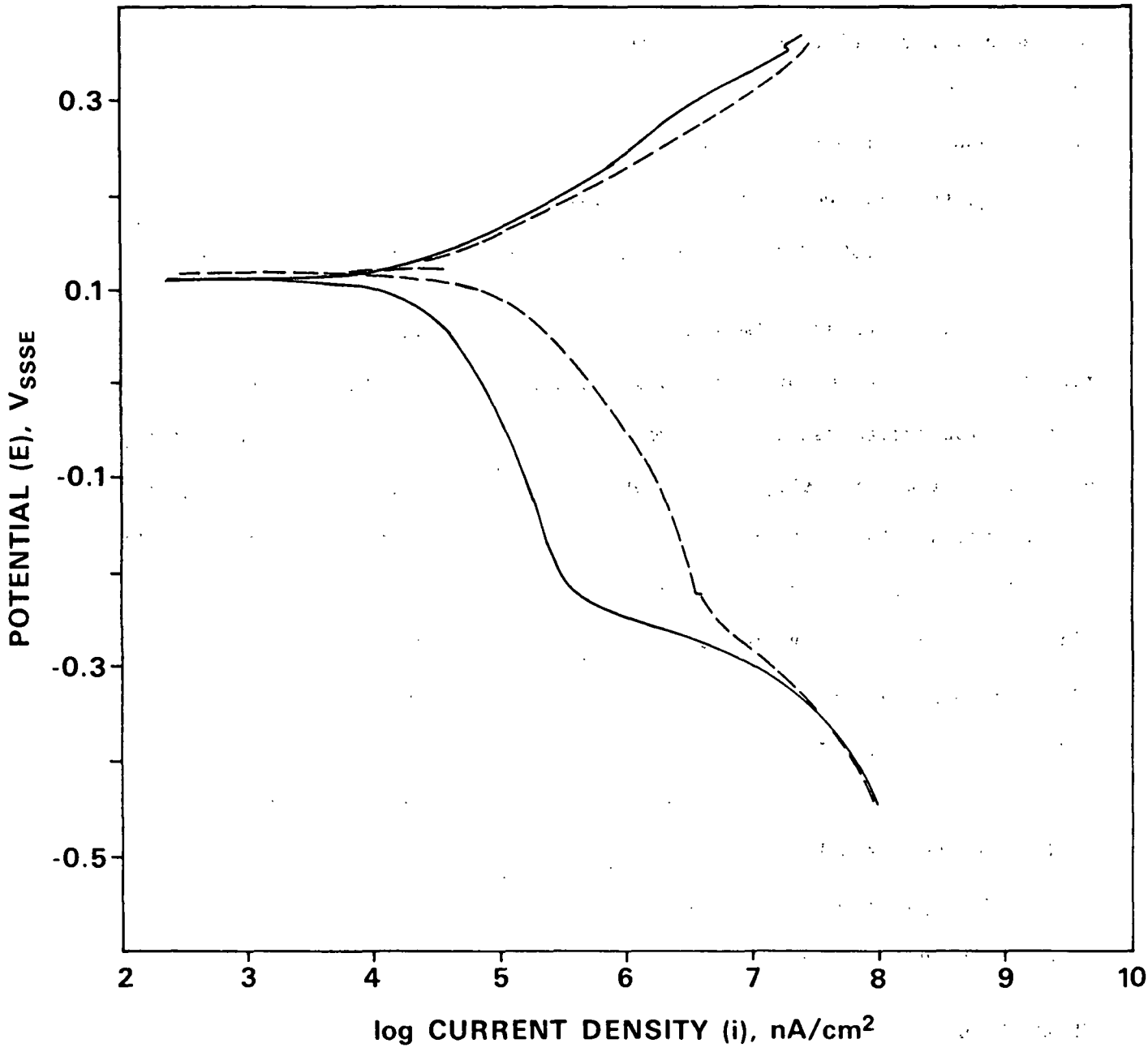

Figure 9. Polarization curve for gold, 90 C, 1 mV/s in 100 g/L NaOH + 30 g/L Na_2S with 0.5 g/L S (___) and 1.5 g/L S (---) additions.

concentrations. Thiosulfate increased the corrosion rate more than did polysulfide. At higher HS- concentration the corrosion rate did not fall with time, suggesting that passivation never occurred. Weight loss was much greater than in polysulfide, especially after long exposure times. This is illustrated schematically in Fig. 10 and 11 for 2 and 8 weeks exposure respectively which show the 15 mpy isocorrosion surface. This region, enclosing higher corrosion rates than the 5 mpy isocorrosion surface drawn for the polysulfide solutions, covers a large range of solution compositions and within that area corrosion rates are as high as 60-80 mpy.

Table 2. White liquor studies - thiosulfate weight loss results.

NaOH,g/L	Na_2S,g/L	$S_2O_3^{--}$, g/L					
		0	2.5	5.0	10.0	25.0	50.0
		2 Weeks, mpy					
60	10	3.1	2.7	4.4	9.1	9.9	15.9
	20	3.9	3.3	4.6	8.6	14.5	30.3
	30	8.6	6.6	5.6	9.3	20.6	41.6
	40	8.3	9.1	7.1	9.9	29.2	44.6
80	10	5.0	11.4	16.9	10.1	10.5	12.0
	20	5.5	10.5	14.7	6.3	22.6	39.6
	30	--	10.5	16.8	15.5	21.7	45.0
	40	--	11.9	20.9	14.3	27.8	50.6
100	10	--	13.4	14.1	24.8	6.6	12.4
	20	--	10.0	18.8	32.6	30.1	58.8
	30	--	22.0	33.0	33.5	23.7	58.1
	40	--	13.9	22.7	30.1	36.	62.6
120	10	--	13.8	16.2	28.6	8.7	15.0
	20	--	15.0	24.7	40.4	38.9	69.5
	30	--	--	--	--	--	--
	40	--	16.0	45.5	34.6	43.8	76.9

Table 2 (Continued). White liquor studies - thiosulfate weight loss results.

NaOH, g/L	Na_2S, g/L	$S_2O_3^{--}$, g/L 0	2.5	5.0	10.0	25.0	50.0
		4 Weeks, mpy					
60	10	1.4	1.9	2.2	4.4	5.4	7.6
	20	2.2	3.1	4.4	8.4	17.1	35.3
	30	4.1	4.2	4.2	8.8	23.4	47.5
	40	3.9	6.0	6.8	9.8	29.3	53.4
80	10	3.1	5.0	10.1	6.1	5.4	6.8
	20	3.6	11.6	8.5	9.8	24.6	42.4
	30	—	12.8	8.9	18.4	26.1	49.8
	40	—	13.4	16.5	19.1	30.6	61.8
100	10	—	6.7	7.6	12.6	4.0	7.0
	20	—	12.3	23.6	16.8	34.9	63.5
	30	—	13.0	32.4	19.9	27.2	66.3
	40	—	14.0	22.0	25.5	36.1	67.2
120	10	—	7.7	9.9	13.1	3.8	7.9
	20	—	11.8	13.8	21.9	46.6	39.0
	30	—	—	—	—	—	—
	40	—	14.4	37.9	31.7	41.5	52.9
		6 Weeks, mpy					
60	10	4.3	2.7	4.7	3.2	4.2	5.3
	20	2.2	3.1	4.6	8.5	23.0	39.8
	30	2.9	3.6	3.9	9.8	24.5	52.4
	40	3.0	5.2	6.5	9.9	31.5	61.8
80	10	2.7	4.5	7.8	4.5	4.3	5.0
	20	6.0	8.6	7.0	10.3	26.6	49.5
	30	—	8.6	7.0	12.7	16.9	33.9
	40	—	17.1	11.8	18.3	36.0	74.6
100	10	—	6.8	5.3	13.7	3.2	5.3
	20	—	12.6	6.4	17.0	43.7	72.0
	30	—	13.5	34.5	20.4	33.9	72.5
	40	—	9.6	14.2	26.4	39.7	78.9
120	10	—	6.8	6.4	9.1	3.6	6.7
	20	—	9.0	12.3	13.7	54.7	29.1
	30	—	—	—	—	—	—
	40	—	23.4	40.3	29.1	40.4	30.2

Table 2 (Continued). White liquor studies - thiosulfate weight loss results.

NaOH,g/L	Na_2S,g/L	$S_2O_3^{--}$, g/L					
		0	2.5	5.0	10.0	25.0	50.0
		8 Weeks, mpy					
60	10	0.6	2.3	3.5	2.2	2.3	3.5
	20	1.9	2.5	5.7	9.2	24.6	38.1
	30	4.4	3.4	4.1	10.4	26.3	57.6
	40	3.6	5.1	7.0	11.3	35.6	65.1
80	10	1.9	3.5	5.7	2.2	3.0	3.3
	20	6.5	7.1	7.0	10.5	27.8	52.5
	30	--	6.4	5.0	9.6	36.1	26.8
	40	--	5.5	19.6	20.8	43.2	86.5
100	10	--	7.1	4.0	9.4	2.1	4.2
	20	--	15.1	12.5	22.8	52.6	79.0
	30	--	19.3	20.3	21.5	43.1	81.9
	40	--	7.4	11.3	26.0	45.2	70.3
120	10	--	4.2	4.7	6.6	2.4	5.8
	20	--	7.5	17.1	10.7	61.5	19.0
	30	--	--	--	--	--	--
	40	--	26.4	44.0	27.4	35.0	25.4

Corrosion potential, E_{corr}, of the electrodes was monitored throughout the exposure and is plotted in Fig. 12 for a range of $S_2O_3^{2-}$ concentrations in 80 g/L NaOH + 40 g/L Na_2S. Representative plots of corrosion potential *vs.* time are shown in Appendix II. Shifts of E_{corr} occurred in conjunction with change of electrodes, perhaps due to the momentary loss of temperature or the agitation associated with specimen removal[14] or because of some drying of the electrode as it was transfered to the fresh solution.

Polarization curves for steel were obtained for each liquor composition. A representative curve is shown in Fig. 13. Data for the polarization curves is summarized in Appendix III. Generally, as the thiosulfate concentration was increased, the corrosion potential increased from -240 to approximately -140 mV. The E_{corr} was slightly more noble in lower HS- concentrations. This range of

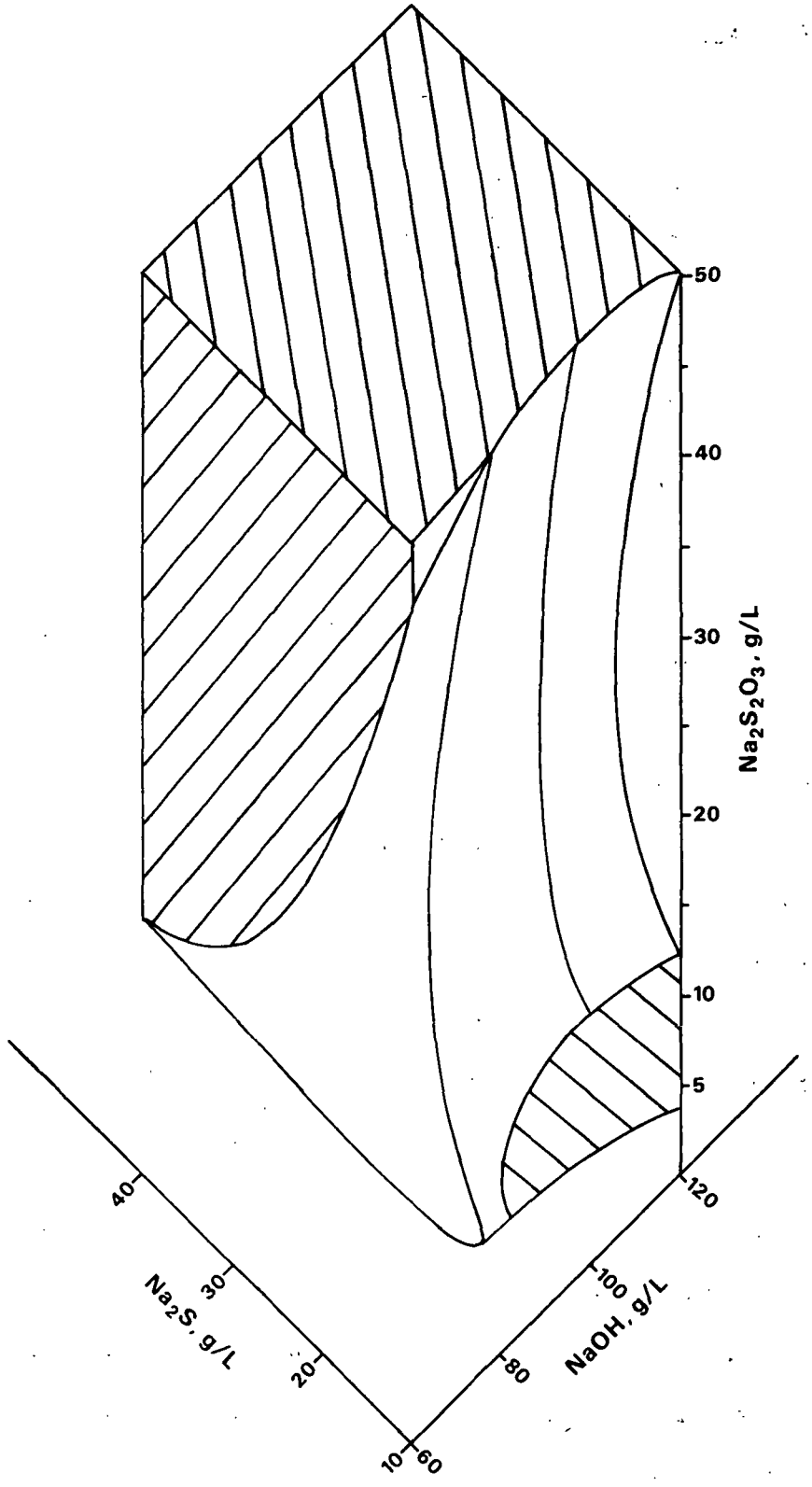

Figure 10. Isocorrosion plot of 15 mpy surface in NaOH + Na_2S + $Na_2S_2O_3$ solutions after 2 weeks exposure.

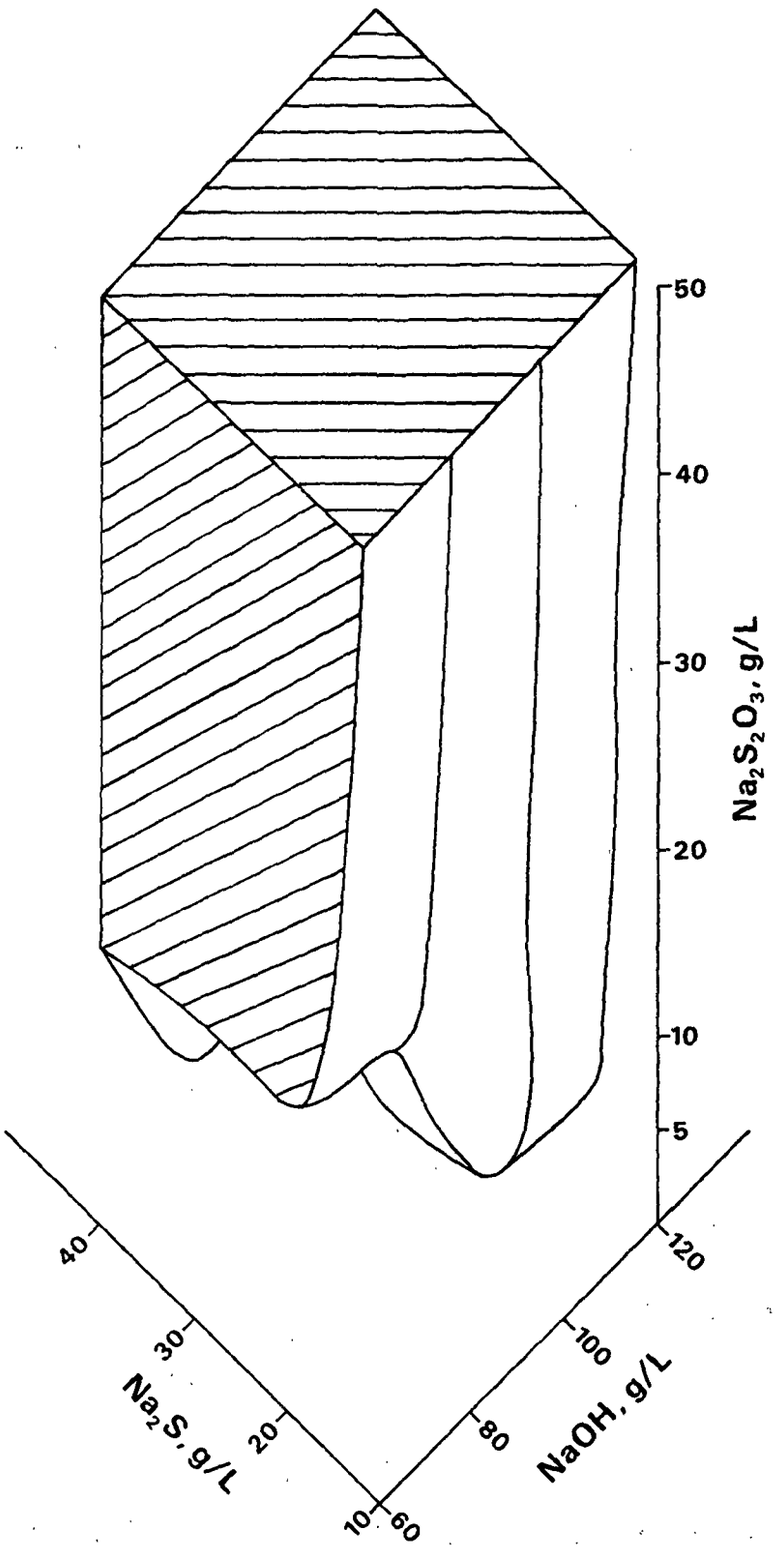

Figure 11. Isocorrosion plot of 15 mpy surface in NaOH + Na_2S + $Na_2S_2O_3$ solutions after 8 weeks exposure.

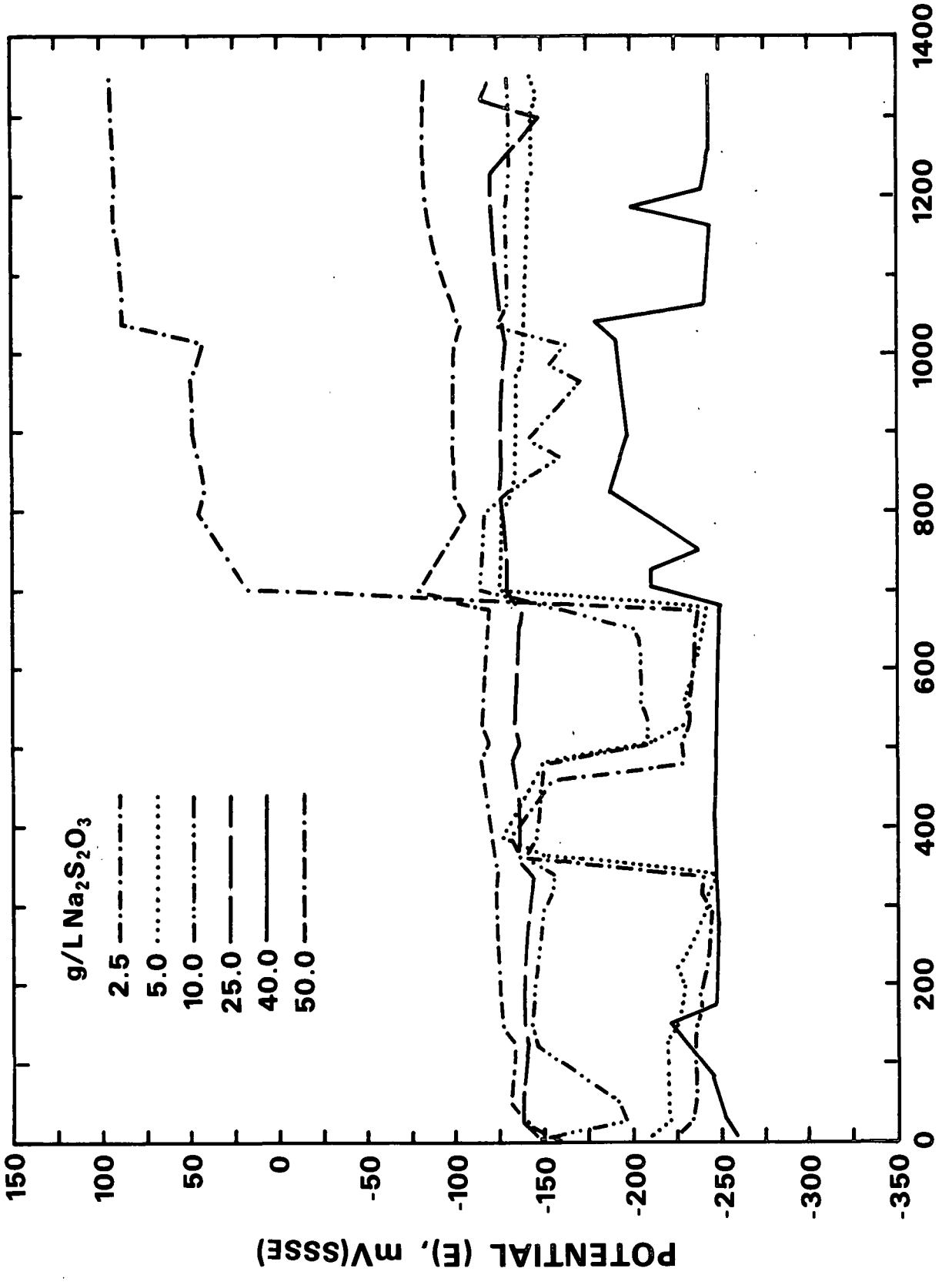

Figure 12. Corrosion potential during exposure in 80 g/L NaOH + 40 g/L Na_2S + 0-50 g/L $Na_2S_2O_3$.

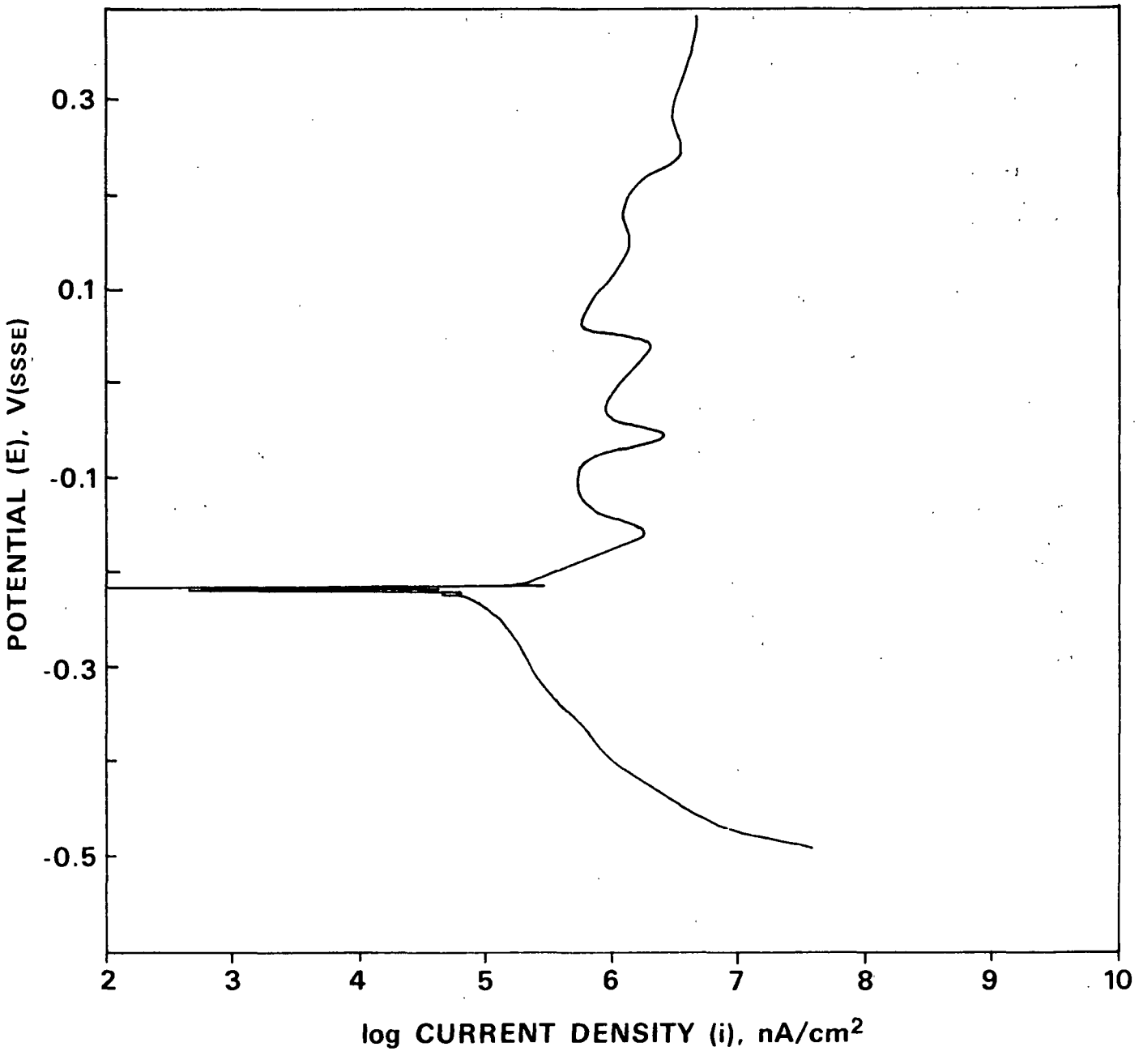

Figure 13. Polarization curve of steel in 100 g/L NaOH + 10 g/L Na_2S + 10 g/L $Na_2S_2O_3$, 90°C, 1 mV/S.

potential was in the active-passive transition, very close to one of the peaks where dissolution rates where high. There was no trend in either the anodic or cathodic Tafel slopes and they varied from test to test. In solutions containing no thiosulfate, the anodic Tafel slope was approximately the same as in polysulfide solution. Otherwise, there was no consistency in either the anodic or cathodic Tafel slopes on steel. At -240 mV(SSSE), a peak was generally observed in the cathodic scan. Anodic peaks were located at approximately -150, -50, 75 and 165 mV(SSSE).

Corrosion potential on gold was comparable to Sx-- solutions. It was comparatively unaffected by $S_2O_3^{2-}$, but declined at higher HS- concentration. Data from the polarization curves is summarized in Appendix III. The anodic Tafel slope, β_A, on gold was 59 mV (av. of 66 values, s = 9). At higher potential, the Tafel slope was 263 mV (av. of 55 values, s = 91); these values varied widely. The cathodic Tafel slope was 51 mV (av. of 72 values, s = 10). A representative polarization curve for gold in NaOH + Na_2S + $Na_2S_2O_3$ solution is illustrated in Fig. 14.

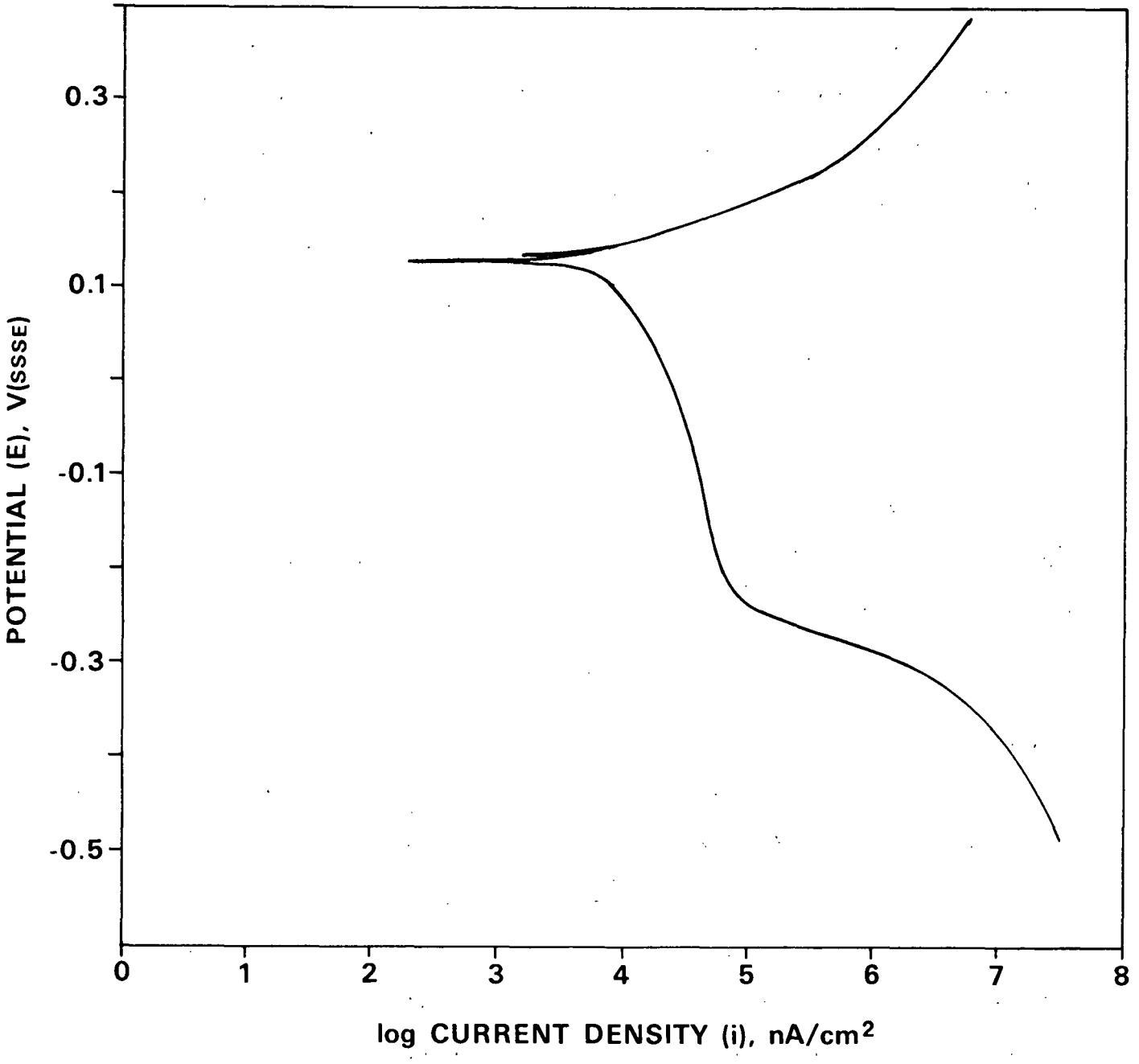

Figure 14. Polarization curve of gold in 100 g/L NaOH + 10 g/L Na_2S + 10 g/L $Na_2S_2O_3$ solution.

DISCUSSION

POLYSULFIDE

High initial corrosion rates were a transient effect in low concentration polysulfide solutions (0.5-2.0 g/L S), and rates decreased dramatically when passivation occurred as seen by comparing Fig. 3 and 4. The isocorrosion surface encloses fewer solutions after 8 weeks than after 2 weeks and these are mostly solutions in which very much higher corrosion rates were observed after the two week exposure test. Figure 5 shows how corrosion rates were much higher in solutions with low concentrations of S. The passivation process is well illustrated by the plot of the rest potential, E_{corr}, vs. exposure time (Fig. 6) where it can be seen that the potential moves from the active region, -240 mV(SSSE), to the passive region, 100 mV(SSSE), after a period of time. After the steel became passivated, the corrosion rate was decreased to 2.5 mpy. At high polysulfide concentrations (5-10 g/L S), immediate passivation occurred and no period of high corrosion rate was observed.

The increase of corrosion rate at higher sulfide concentration may be attributed to increased difficulty of passivation in these solutions. This increased difficulty of passivation can be rationalized by consideration of the polarization curve. Anodic peak heights are larger in higher sulfide concentration solutions.[10,12] As the electrodes passivate, the potential must increase through the range of potentials of this peak where the increased currents are associated with increased dissolution. The peak current is known as the critical current for passivation, $i_{(crit)}$. More corrosion occurs before passivation is complete, that is, $i_{(crit)}$ is larger for higher sulfide concentrations. Indeed, electrodes which experienced high corrosion rates spent considerable time in the peak potential range from -150 to -200 mV(SSSE), before passivating.

At high sulfide concentrations, more polysulfide was required to passivate the electrode within a given period. In combinations of high OH- and HS- (120 g/L NaOH + 40 g/L Na_2S, 100 g/L NaOH + 40 g/L Na_2S), corrosion rates were high even after 8 weeks due to the difficulty of passivation.

Polysulfides stimulate passivation by their oxidizing nature. The redox potential for the half-cell:

$$S_{x+1}^{2-} + H^+ + 2\ e^- \rightleftharpoons S_x^{2-} + HS^- \qquad (3)$$

is located at a noble potential. For example, for:

$$S_3^{2-} + 3\ H^+ + 4\ e^- \rightleftharpoons 3\ HS^- \qquad (4)$$

the reversible potential at 90 C in 100 g/L NaOH + 30 g/L Na_2S is 136 mV(SSSE). This reaction and similar reactions for other polysulfides form a mixed potential. On an inert electrode, it has been shown[12] that these polysulfides also form a mixed potential with thiosulfate in solution and that this mixed potential of polysulfides and thiosulfate is located at a potential slightly below the mixed potential for the polysulfides alone. At higher temperature, this potential moves closer to the thiosulfate equilibrium. The mixed potential of polysulfides and thiosulfate in sulfide solution has been described in more detail elsewhere.[12] At the mixed potential, polysulfides are reduced. The reduction of polysulfides comes to electrochemical equilibrium with oxidation of iron at the corrosion potential, E_{corr}, in the solution. Apparently sufficient current to maintain the passive oxide film on steel can be supplied by S_x^{2-} reduction. If large quantities of polysulfide are available, their reduction can provide current to passivate the surface immediately, as was observed in high polysulfide solutions. Thus the polysulfide reduction supplies current just as an anodic protection system would.

The change of E_{corr} with time of exposure is not related to changes in the solution composition due to oxidation of the polysulfide; solutions were changed frequently to ensure that polysulfide concentrations were maintained. Passivation may take longer in some cases because some transformation of the film must occur to make it protective. New films may contain significant sulfide, making them nonprotective. Some period may be required to convert this film to a protective one by replacing the sulfide with protective oxide. This is supported by the observation that the film is more adherent after a long exposure than newly formed film.

The corrosion potentials of electrodes prior to polarization were observed to attain values distributed around -250, -100, 60 and 130 mV(SSSE), (Fig. 7). The lowest value coincides with reduction of hydrogen. At this mixed rest potential (-250), the anodic dissolution of the steel is balanced by the hydrogen evolution reaction:[14]

$$2\ H_2O + 2\ e^- \leftrightharpoons H_2 + 2\ OH^- \qquad (5)$$

as illustrated schematically in Fig. 15. The mixed potential is in the active region of steel. The theoretical potential for hydrogen evolution may be calculated using the Nernst equation:

$$E = Eo - (2.303RT/2F)\ \log(a_{H_2}) - (2.303\ RT/F)pH \qquad (6)$$

The pH is approximately 12.9 in these solutions at 90 C.[18] The potential for hydrogen evolution at 90 C is calculated to be -929 mV(SHE) or -279 mV(SSSE) which is in fairly good agreement considering that hydrogen activity was unknown and errors due to liquid junction potential were neglected.

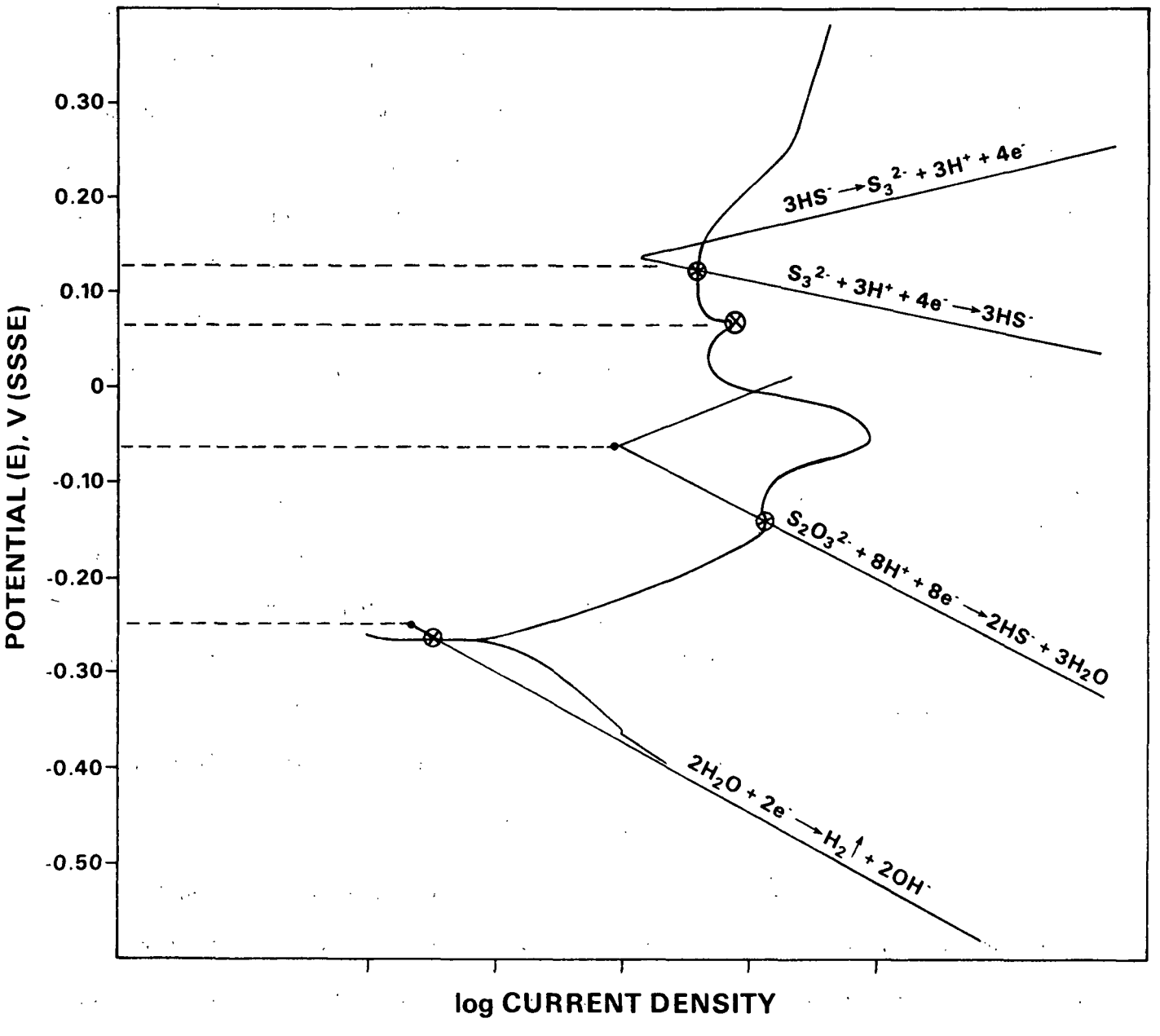

Figure 15. Schematic diagram illustrating the reactions which may control the corrosion potential.

The E_{corr} at -100 mV(SSSE) corresponds closely with the active-passive peak. This corrosion potential also coincides with the half-cell:

$$S_2O_3^{2-} + 8\ H^+ + 8\ e- \leftrightharpoons 2\ HS- + 3\ H_2O \qquad (7)$$

The reversible potential of this reaction is calculated to be -699 mV(SHE) at 90 C or -55 mV(SSSE) in 100 g/L NaOH + 30 g/L Na_2S solution with an impurity level of 0.001 g/L $Na_2S_2O_3$. The mixed potential with steel would be expected at a lower potential as was observed (-100) because the thiosulfate would be reduced as the iron oxidizes. Thus the corrosion potential in this range results from a balance of oxidation reactions of the steel and the reduction of thiosulfate as illustrated in Fig. 15. Electrodes which attained a rest potential in this region experienced a high corrosion rate because this also corresponded to the active-passive peak of the steel.

The highest values of E_{corr} (60, 130) were close to the polysulfide equilibrium, [Eq. (3)]. The highest potential, 130 mV, is close to the reversible potential for reaction 4. The lower potential, 60 mV, may result from mixed potential of reaction 4 with reaction 7. In this case, iron oxidation is apparently balanced by reduction of polysulfide as shown in Fig. 15. At high concentrations of polysulfide, the corrosion potential attained noble values, close to the polysulfide equilibrium, as would be expected.

The polarization curves for steel were significantly affected by additions of polysulfide. As illustrated in Fig. 8, the current density of the peaks was decreased in polysulfide solutions. The applied current of a polarization curve is the difference between spontaneous oxidation and reduction currents. A decrease in current may result from a decrease in the oxidation current or an increase in the reduction current. The current for the oxidation

of steel (due to film formation or dissolution) may have the same value as in polysulfide-free solution but when summed with the reduction current for the polysulfide which is of opposite sign, the total current is decreased. Thus the critical current for passivation is decreased by reduction of polysulfide.

The anodic peaks have been discussed by Crowe,[12] and can be identified with reasonable confidence. The peak at -150 mV(SSSE) was close to the potential for formation of Fe_3O_4 and some of the current may result from dissolution to $Fe(OH)_3^-$. The peak at -40 mV(SSSE) corresponded with FeS_2 formation from FeS. The peak at 70 mV(SSSE) was consistent with the formation of Fe_2O_3 or FeOOH, which forms a protective passive surface film. These reactions may be seen by reference to an E-pH diagram for the Fe-S-H_2O system at 100 C,[12] Fig. 16. This diagram illustrates the stability regions of species satisfactorily at 90 C. In these solutions, at 100 C the pH is approximately 13.[18] At this pH, indicated by the vertical arrows, iron is stable as a number of forms depending on the potential. As the potential increases the species stable at that potential forms: first, soluble $Fe(OH)_3^-$, then oxide Fe_3O_4, and finally Fe_2O_3 which is a passive layer. Note that the FeS_2 region is nearby and may extend to higher pH in the potential range of the peak if the activities of the species are different than assumed in constructing the diagram. The FeS_2 may prevent the formation of the protective passive film.

The anodic Tafel slope of 64 mV indicated that the rate determining step for oxidation involves the passage of a doubly charged species away from the surface. This may be for oxidation of the steel or the sulfides in solution. The cathodic reaction may be limited by a step involving a singly charged species as evidenced by the larger Tafel slope (128 mV).

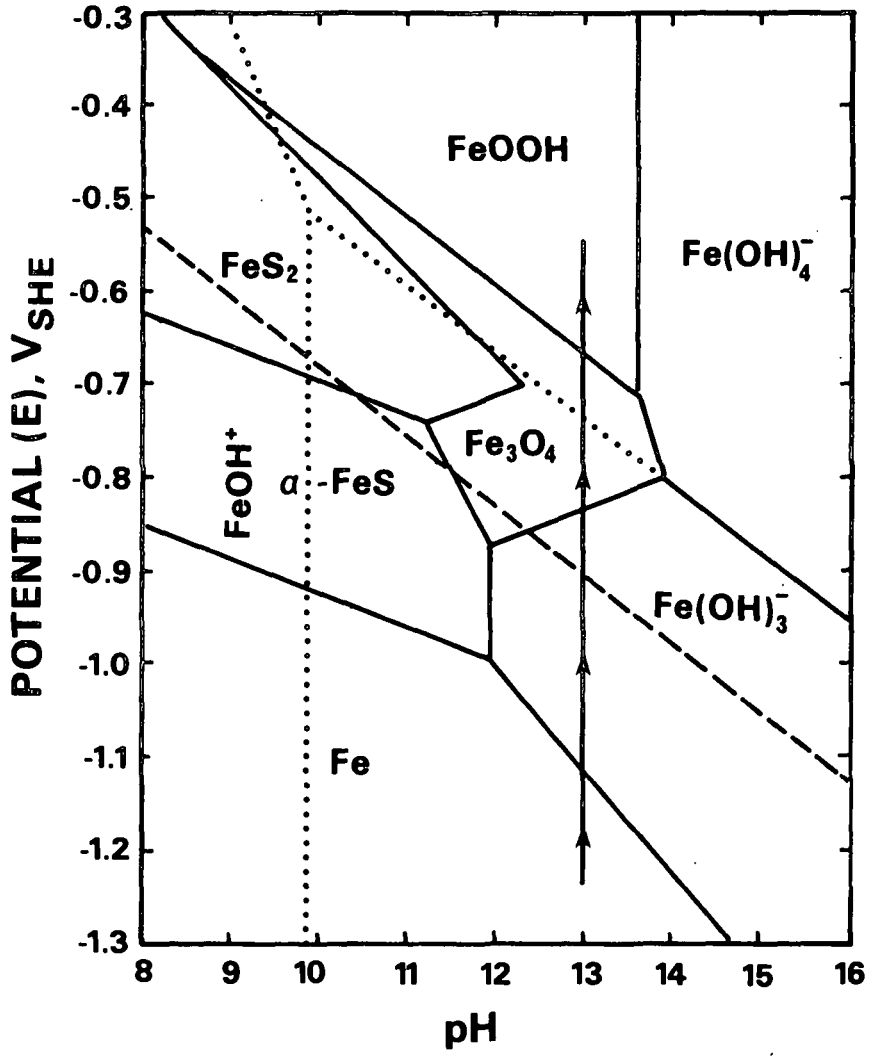

Figure 16. E-pH diagram for the Fe-S-H_2O system at 100 C.[12]

The polarization behavior of gold results from the oxidation and reduction reactions of the constituents of the solution only because the gold itself is inert and does not participate. The cathodic polarization curve had two sections indicating that at least two reduction reactions were taking place when the electrode was polarized. The lower section was consistent with H+ reduction[14] and was confirmed by visual observation. The Tafel slope was 38 mV which was fairly consistent with a mechanism for hydrogen evolution described by O'Brien and Seto.[19] The upper section of the cathodic polarization curve is consistent

with reduction of S_x^{2-} to HS- as described by Yeske.[14] There may also be some reduction of $S_2O_3^{2-}$ at lower potentials. The large cathodic Tafel slope in this range was suggestive of concentration polarization. The linear portions observed in this range would result from the various sulfide species present in the solution which could be oxidized. This was supported by the observation of an increase in current with increasing S concentration seen in Fig. 9.

The anodic Tafel slope on gold (~78) was close to 75, indicating that a doubly charged species was moving through the double layer, which would be consistent with oxidation of HS- to S_x^{2-}.[12] Thus the high currents at these potentials are principally due to oxidation of sulfide to form polysulfide. The cathodic Tafel slope was higher (125 mV) indicating that movement of single charged species (perhaps HS-) was involved in the rate determining step.

Polysulfides exert a strong influence on the corrosion potential as observed by others.[10,20] Low concentrations of polysulfides accelerate corrosion by shifting the corrosion potential into the active-passive region and high concentrations cause spontaneous passivation. The present study has shown that passivation eventually occurs even with low concentrations. Ahlers[21] found that low concentrations of polysulfide increased the corrosion rate in batch cooks. The surface would be exposed to the air between cooks and the passive layer would be damaged. Thus, the transient effect would be repeated in each cook cycle resulting in a much higher corrosion rate than would be expected for a continuous exposure. Polysulfide may also be very important when upsets occur frequently or where the surface passive film is repeatedly damaged. Frequent damage to the film would occur due to high flow rate or mechanical abrasion. The transient effect of S_x^{2-} on corrosion rate is of importance to the problem

of stress corrosion, too. In polysulfide solutions of low concentration, dissolution rates may be very high at the tips of stress corrosion cracks where deformation repeatedly breaks the passive film. Competing repassivation processes may be slow, as indicated by the long period for passivation to occur in weight loss tests. The effect of polysulfide on long-term exposure is to passivate the electrode, thereby decreasing corrosion rate.

THIOSULFATE

Thiosulfate increased the corrosion rate significantly throughout the period of the exposure in proportion to the amount of thiosulfate in solution. The isocorrosion surface, 15 mpy, illustrated the large number of solution compositions in which the corrosion rate exceeds 15 mpy. This effect was again increased by higher HS- concentrations probably due to increased dissolution currents at the active/passive peak as were observed by Wensley.[10] More corrosion would occur while the electrode was in the peak potential range.

The redox potential for the equilibrium 7 ($HS^-/S_2O_3^{2-}$) has a value of -699 mV(SHE) or -45 mV(SSSE) in 100 g/L NaOH + 30 g/L Na_2S + 5 g/L $Na_2S_2O_3$ which is very close to the active-passive peak potential of -50 mV(SSSE). The corrosion potential of the steel would rest in this potential range due to the thiosulfate equilibrium and increased corrosion would take place. The active-passive peak is consistent with formation of FeS_2.[12] At higher potentials, passivation with an oxide film prevents dissolution. Thus thiosulfate stimulates corrosion by increasing the active/passive peak heights and by placing the corrosion potential into the active/passive range. Thiosulfate must delay the point of onset of passivation and thus stimulate larger active/passive peaks. Figures 10 and 11 illustrate that high corrosion rates were experienced for almost all solutions containing thiosulfate.

In low concentration of thiosulfate (2.5-5.0 g/L) or sulfide (10 g/L) corrosion rate decreased with time because the electrode became passive as can be seen in Fig. 12 for 2.5 g/L $Na_2S_2O_3$. It is possible that some of the thiosulfate is converted to polysulfide via the equilibrium:

$$S_2O_3^{2-} + HS^- \rightleftharpoons S_2^{2-} + SO_3^{2-} + H^+ \quad (8)$$

The polysulfide thus formed may assist the electrode to passivate during a sufficient period of exposure. The passivation is presumably easier in low sulfide solution due to the smaller size of the active-passive transition in these solutions as described previously.

The polarization behavior on steel was almost the same as in polysulfide solution. Peaks were probably identified with the same reactions. The peak at 165 mV(SSSE) could not be identified due to the large number of reactions which may occur in this range. No conclusions could be drawn from the Tafel slopes observed on steel; presumably a number of reactions are occurring to cause the scatter in values.

Polarization behavior on gold was similar to that in polysulfide solutions, too. Nothing conclusive could be stated about the Tafel slopes. The high anodic Tafel slope was consistent with diffusion control.

Thiosulfate does not increase corrosion rate by generating low concentrations of polysulfide. If this were true, then very high concentrations of thiosulfate would generate a large amount of polysulfide and passivation should occur after a period of exposure. This was not observed.

The results obtained here are significant because they indicate that the corrosion rate will be high where thiosulfate is formed by oxidation of

sulfide, for example at the liquid-vapor line in pipes and tanks or where it is present as the result of poor reduction in the recovery boiler. Furthermore, thiosulfate impairs passivation and a high corrosion rate is maintained.

IMPLICATIONS FOR PULP MILL OPERATIONS

The results of the studies of liquor composition effects on corrosion rates in kraft white liquor have some practical implications for operations. These mostly concern the process chemistry.

The oxidized sulfide species have a considerable influence on corrosion rate. Therefore high reduction efficiency in recovery boilers is important to minimize concentrations of polysulfide and thiosulfate. Also, air should be excluded from the process to prevent formation of thiosulfate. The effect of air oxidation is especially noticeable in the wet/dry zone of tanks where corrosion rate underneath moisture films is high. Splashing should be minimized in the process to reduce the amount of contact with air.

Polysulfide, in sufficient quantities, may reduce corrosion rates. This confirms that polysulfide pulping may be beneficial in reducing corrosion. The addition of smaller amounts of emulsified sulfur make-up in the recausticizing area may place the polysulfide concentration at a low level, and a high transient corrosion rate will be experienced following the addition. This effect could extend for significant distances from the addition point, as the liquor is diluted. To avoid this problem, emulsified sulfur should be added in the black liquor area prior to reduction in the recovery boiler.

CONCLUSIONS

1) Low concentrations of polysulfide increase corrosion rates only initially, but assist passivation, thus decreasing corrosion rate in the long run. Their effect would be most pronounced when the steel surface is continuously exposed by abrasion, deformation or changing solution level.

2) Thiosulfate increases the corrosion rate throughout the exposure except at very low Na_2S and NaOH concentrations. Rest potential is controlled at the potential of the half cell reaction between HS- and $S_2O_3^{2-}$ which is close to the potential of the active-passive transition peak.

3) Time of exposure has an influence on the corrosion rate. A protective passive layer is formed after a period of exposure which depends on the polysulfide and thiosulfate concentrations.

ACKNOWLEDGMENTS

The authors wish to acknowledge the diligence of Mr. Mike Heath in obtaining the experimental results and Mr. Craig Thompson for the appraisal of experimental procedures described in Appendix I.

REFERENCES

1. Ruus, L.; Stockman, Svensk Papperstid. 56:857(1953).
2. Stockman, L.; Ruus, L., Svensk Papperstid. 57:831(1954).
3. Hassler, J. W., Tappi 38:265-74(1955).
4. Haegland, B.; Roald, B., Norsk Skogind. 9:351-64(1955).
5. Roald, B., Norsk Skogind. 10:285-9(1956).
6. Mueller, W. A., Can. J. Tech. 34:162-81(1956).
7. Mueller, W. A., Tappi 40:129-40(1957).
8. Kesler, R. B.; Bakken, J. F., Tappi 41:97-102(1958).
9. Landmark, P.; Roald, B., Norsk Skogind. 15:342-7(1961).
10. Wensley, D. A.; Charlton, R. S., Corrosion 36:385-8(1980).
11. Tromans, D., J. Electrochem. Soc. 127:1253-6(1980).
12. Crowe, D. Ph.D. Thesis, The University of British Columbia, 1985.
13. Singbeil, D.; Garner, A. Final Semiannual Progress Report of the Research Program to Investigate Cracking of Continuous Digesters, Pulp and Paper Research Institute of Canada, Contract Report 6294, 1984.
14. Yeske, R. Corrosion rate measurements in kraft white liquor, Project 3556 Progress Report Two, The Institute of Paper Chemistry, May 21, 1984.
15. Ellis, A. J.; Giggenbach, W. Geochim. et Cosmochim Acta 35:247-60(1971).
16. Giggenbach, W., Inorg. Chem. 10:1333-8(1971).
17. Yeske, R. The silver/silver sulfide reference electrode for use in corrosion studies in kraft white liquor, Project 3556 Progress Report, The Institute of Paper Chemistry, February 15, 1984.
18. Macdonald, D. D.; McKubre, M. C. H. Temperature limitations of alkaline battery electrodes. Part II. The thermodynamic properties of iron, nickel and zinc in concentrated sodium hydroxide solutions, SRI International Project 7775. Final Report to DOE Contract EM-78C-01-5159, Menlo Park, California, 1979.
19. O'Brien, R. N.; Seto, P., J. Electrochem. Soc. 117:32-4(1970).
20. Singbeil, D.; Tromans, D. In: Pulp and Paper Industry Corrosion Problems, vol. 3, pp. 40-46, N.A.C.E., Houston, 1982.
21. Ahlers, P. E. In: Pulp and Paper Industry Corrosion Problems, vol. 4, pp. 53-55, N.A.C.E., Houston, 1983.

THE INSTITUTE OF PAPER CHEMISTRY

David C. Crowe
Research Fellow
Corrosion & Materials Engineering Section
Engineering Division

Ronald A. Yeske
Section Leader
Corrosion & Materials Engineering Section
Engineering Division

Clyde H. Sprague
Director
Engineering Division

APPENDIX I

EVALUATION OF EXPERIMENTAL PROCEDURES

The purpose of these studies was to determine possible sources of error in white liquor studies. The effects on weight loss of 1) removal of corrosion products by blasting versus abrasion methods, 2) initial surface condition, 3) liquor volume, 4) material of test container and 5) removal of corrosion products were studied. Surfaces were examined after blasting and chemical cleaning to determine if cleaning introduced impurities. A procedure for removal of corrosion products was adopted, as described below.

Electrodes were blasted with spherical silica glass beads at 20-30 psi in a Cyclo-blaster to remove the corrosion products. The rate of material loss from a bare specimen averaged about 100 mg/min of blast time. The rate of loss was somewhat higher if the initial surface was blasted rather than abraded. Abrasion of an electrode to remove a mark made by a felt marker pen resulted in roughly twice the weight loss from removal of the mark by blasting.

Initial surface condition influenced subsequent rate of weight loss, as illustrated in Fig. AI-1. Rate of weight loss in 100 g/L NaOH + 33 g/L Na_2S solution was higher for more coarsely abraded specimens. The blast-cleaned specimen lost weight at approximately the same rate as the specimen abraded to 120 grit.

A 120 grit finish has been established as the standard finish for the threaded, cylindrical type specimens. This finish is easily obtained by abrading the surface to 120 grit with silicon carbide paper while rotating the specimen via an electric motor. Periodic cooling with water will prevent metallurgical changes to the surface due to heat. After abrasion, the specimens

should be rinsed thoroughly with water and acetone. Air blasting will assist drying. Tissues or tweezers should be used to handle the specimens after this point to keep the samples clean. The specimens should be left for one hour to come to equilibrium with the room temperature and humidity level. Prior to weighing with the analytical balance, the specimens may be placed in snap cap vials and labeled.

Figure AI-2 shows that the volume of liquor in the test container had a significant effect on corrosion rate. This effect suggests that some corrosive reactant is depleted or corrosion products are accumulated, slowing the corrosion rate.

The material of construction of the test container (stainless steel or Teflon) may affect the corrosion rate, but the effect was not determined conclusively.

Corrosion products were removed with a paper towel or by blasting, but subsequent corrosion rate was essentially the same as for untouched specimens.

Analysis of surface composition by EDS/SEM showed no significant concentration of unusual or heavy elements. Some of the Si detected may have been due to deposition of glass (from the blasting beads) on the surface, and some due to background.

Cleaning in Clarke's solution (10 g Sb_2O_3 + 25 g $SnCl_2$ + 500 mL HCl(sp. gr. 1.19)) generally resulted in surface staining. Surface analysis by EDS detected no Sn, and Sb and Cl were 0.5 and 1 % above background level, respectively. These low levels probably do not affect the corrosion rate significantly.

PROCEDURE FOR REMOVAL OF CORROSION PRODUCTS FROM CARBON STEEL WEIGHT LOSS SPECIMENS

Careful removal of corrosion products is critical in obtaining accurate, reproducible weight loss data. The following cleaning and handling techniques will aid in minimizing errors.

Corrosion products may be removed by blasting with a Cyclo-blast dry honer using glass beads. It is desirable that the specimens are hand-held and individually blasted at the lowest blast velocity that effectively removes the corrosion products from the surface. Careful attention is required to ensure that surfaces are not blasted any more than is necessary to remove visible deposits. Following blasting, the specimens are flushed with air. They are then rinsed in water and the threaded hole is rinsed and cleaned with a pipe cleaner. The hole is then blasted with air to remove any water and pipe cleaner fibers. The entire specimen is then rinsed with acetone, air blasted dry and allowed to sit for one hour before weighing.

Alternatively, corrosion deposits may be removed by a chemical cleaning method. Clarke's solution is prepared as noted above. The addition of an aldehyde such as formaldehyde, acetaldehyde, benzaldehyde, or glyoxal may prevent the evolution of toxic hydrogen sulfide gas from sulfide corrosion products. As a further precaution, preparation of the cleaning solution and the cleaning procedure should always be performed in a fume hood. The specimens may be supported by a perforated Teflon jar lid in the bottom of a beaker of cleaning solution at room temperature. The solution is vigorously stirred by means of a magnetic stir bar located underneath the perforated Teflon lid. The specimens are placed in the solution for about 15 minutes, then removed with tongs, rinsed in distilled water and lightly brushed with an acid resistant brush. Specimens

are then placed back into solution for an additional 10 minutes. Finally, the electrodes are rinsed in water, cleaned with a pipe cleaner, rinsed in acetone, air blasted dry and left to sit until weighing.

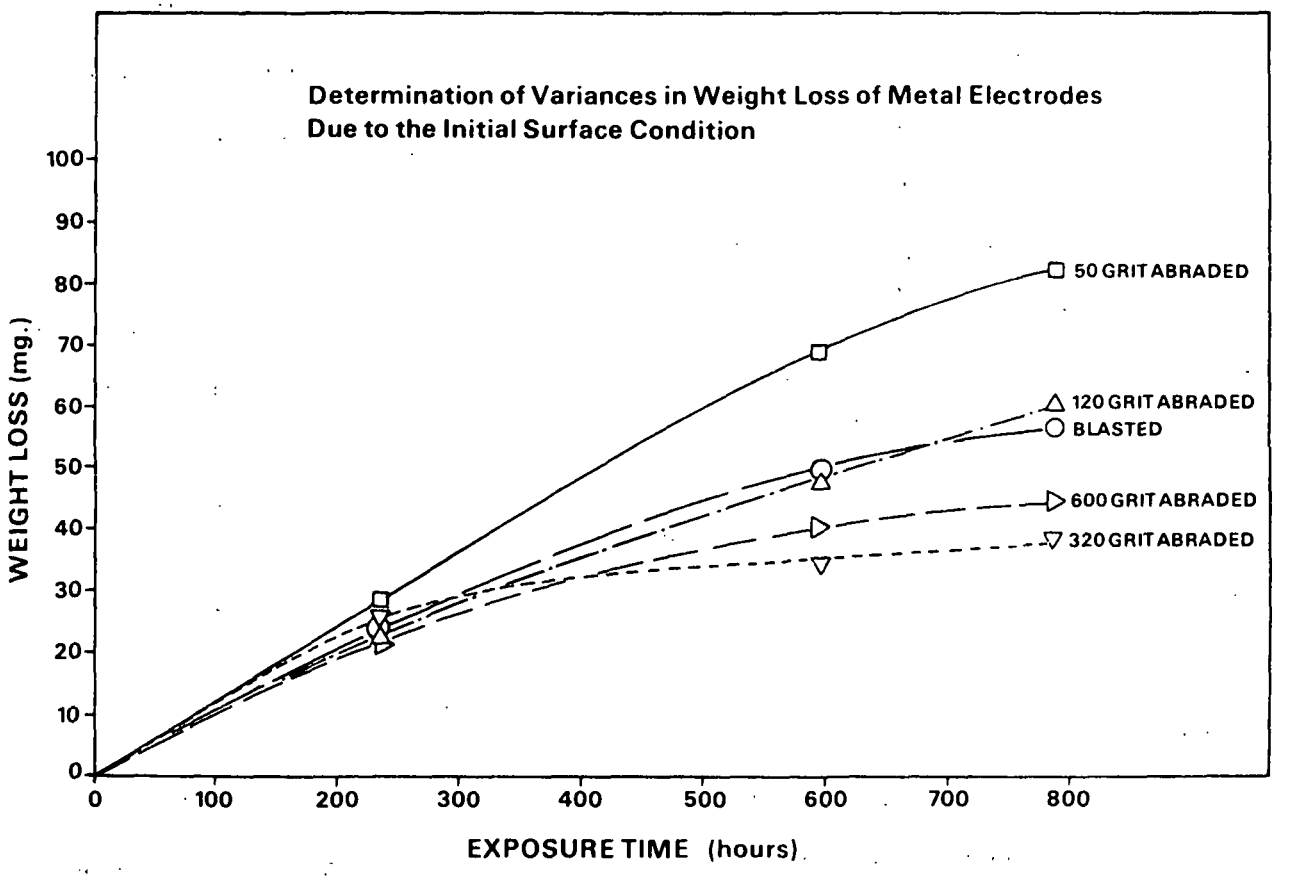

Figure AI-1. Determination of variances in weight loss of metal electrodes due to the initial surface condition.

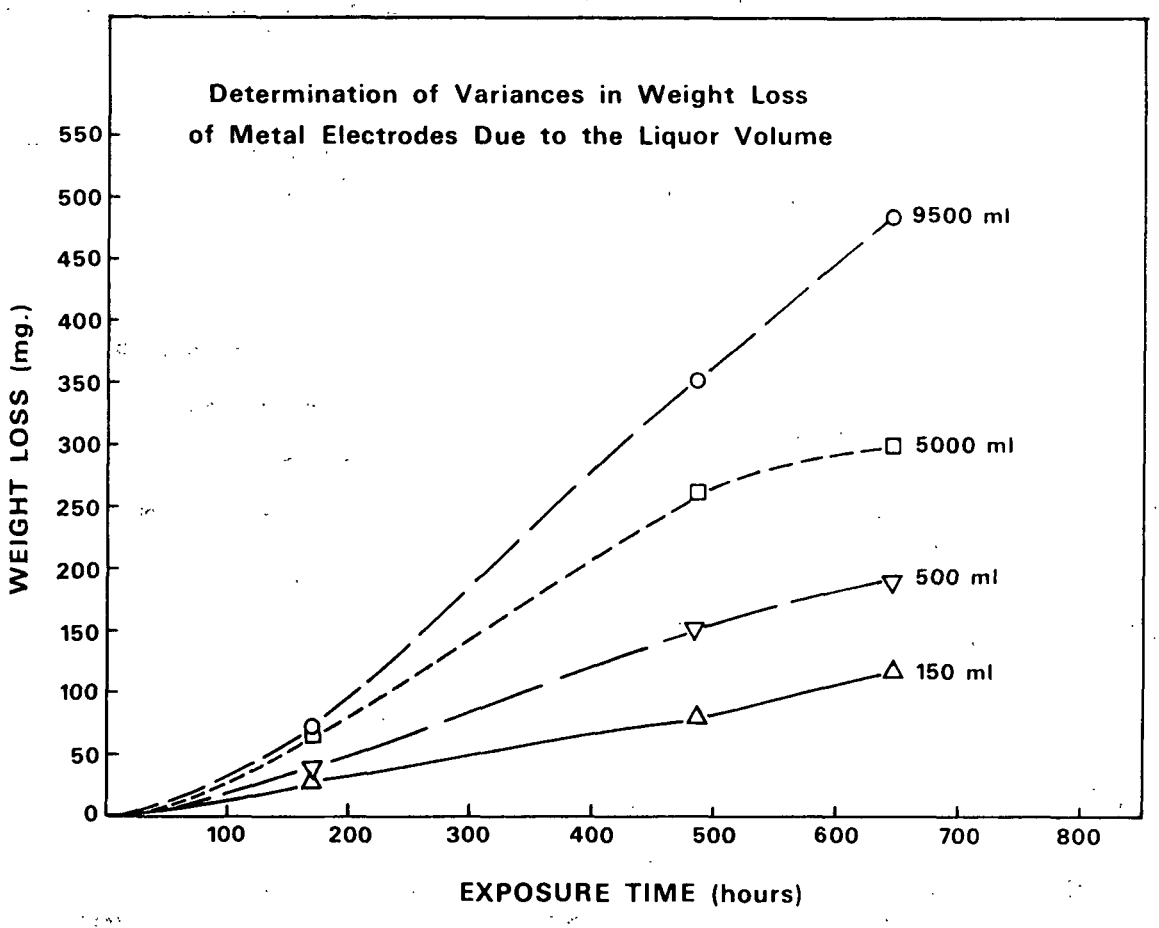

Figure AI-2. Determination of variances in weight loss of metal electrodes due to the liquor volume.

APPENDIX II

CORROSION POTENTIAL DURING WEIGHT LOSS TESTS

SOLUTIONS CONTAINING SULFUR ADDITIONS

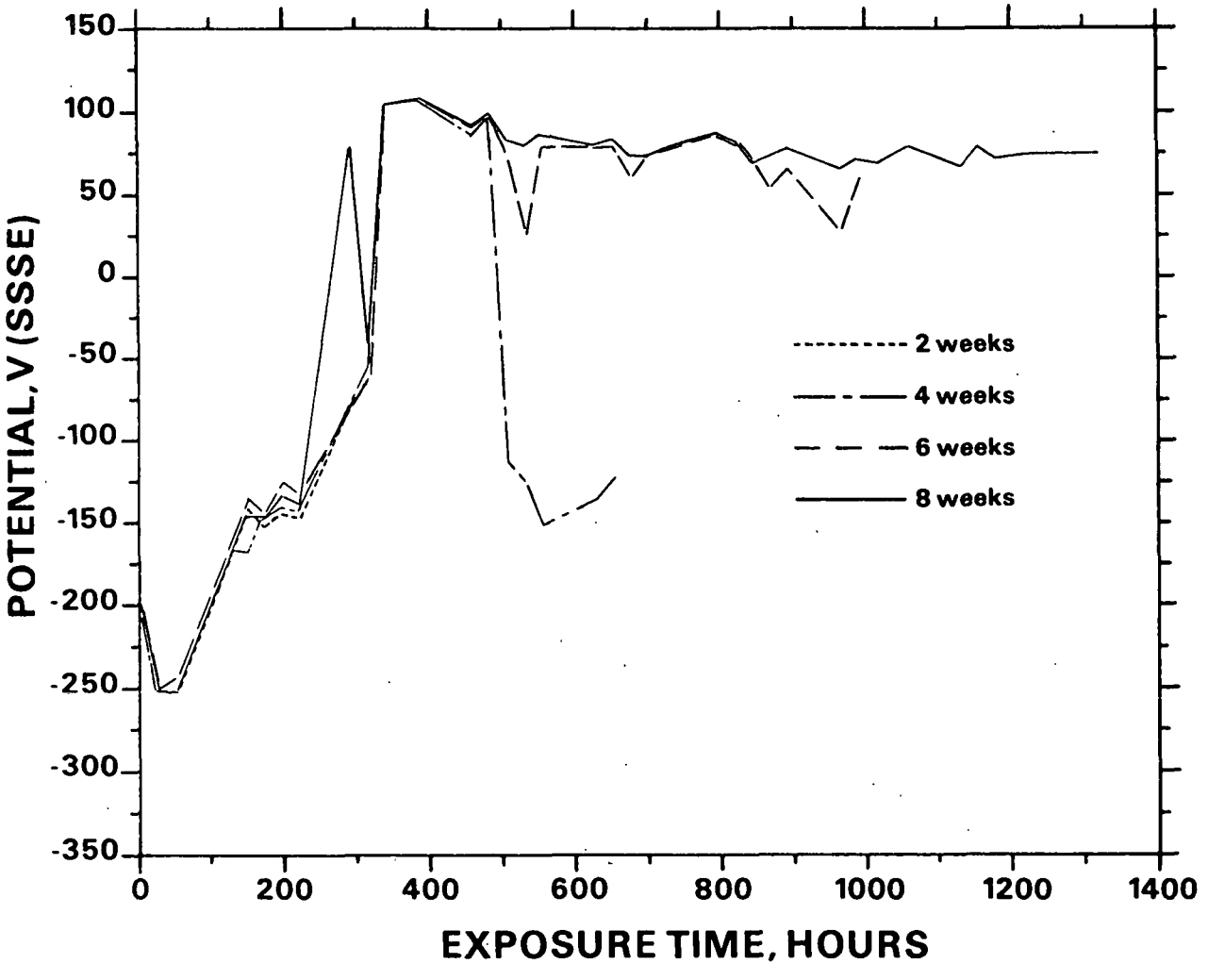

Figure AII-1. Corrosion potential in 60 g/L NaOH + 10 g/L Na_2S.

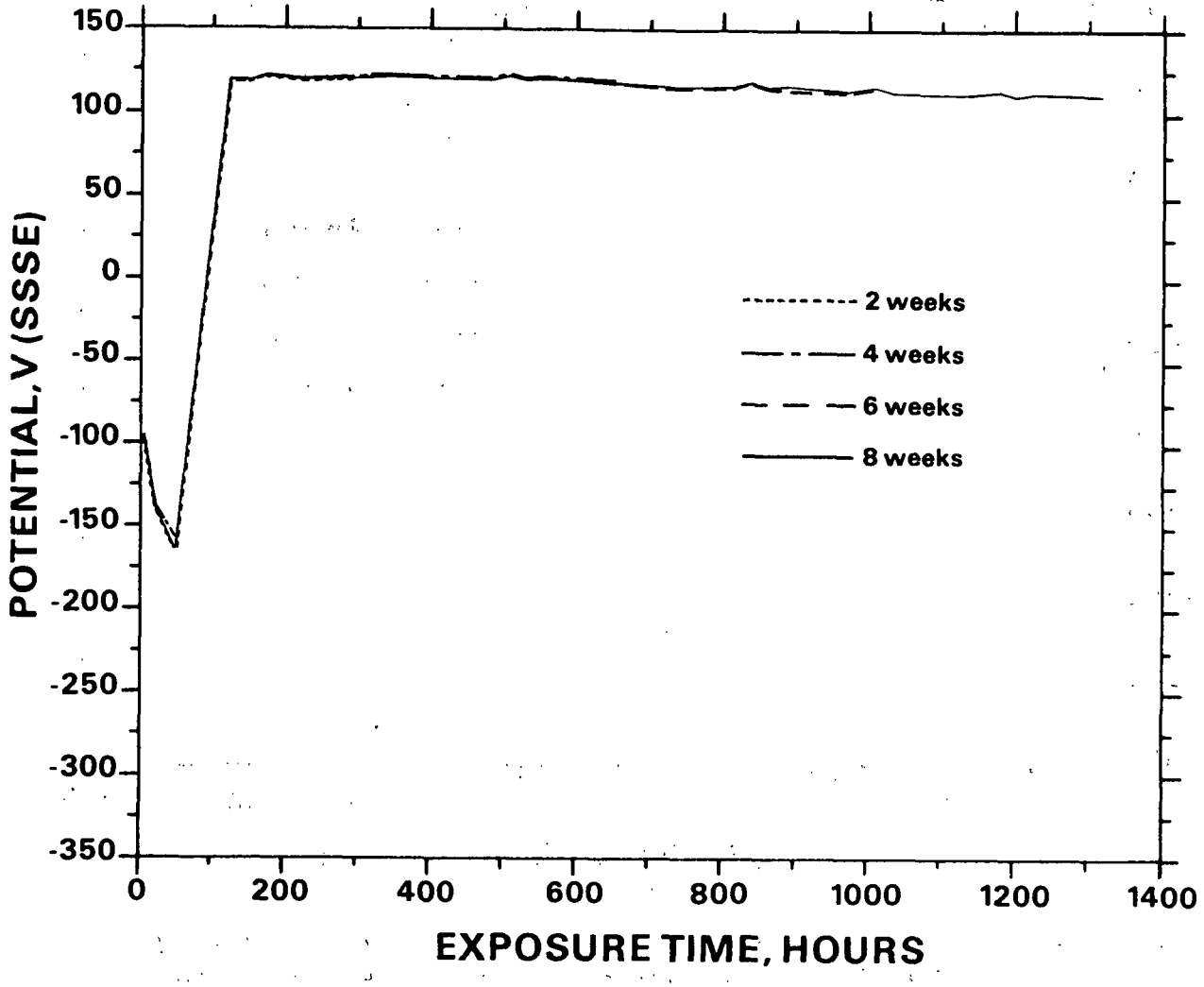

Figure AII-2. Corrosion potential in 60 g/L NaOH + 10 g/L Na_2S + 0.5 g/L S. Similar behavior was observed in the solutions of the following compositions:

NaOH, g/L	Na_2S, g/L	S, g/L
60	20	1.5
60	20	1
60	30	1.5
60	30	2
60	40	1.5
60	40	2
80	30	2
100	40	5
120	10	2

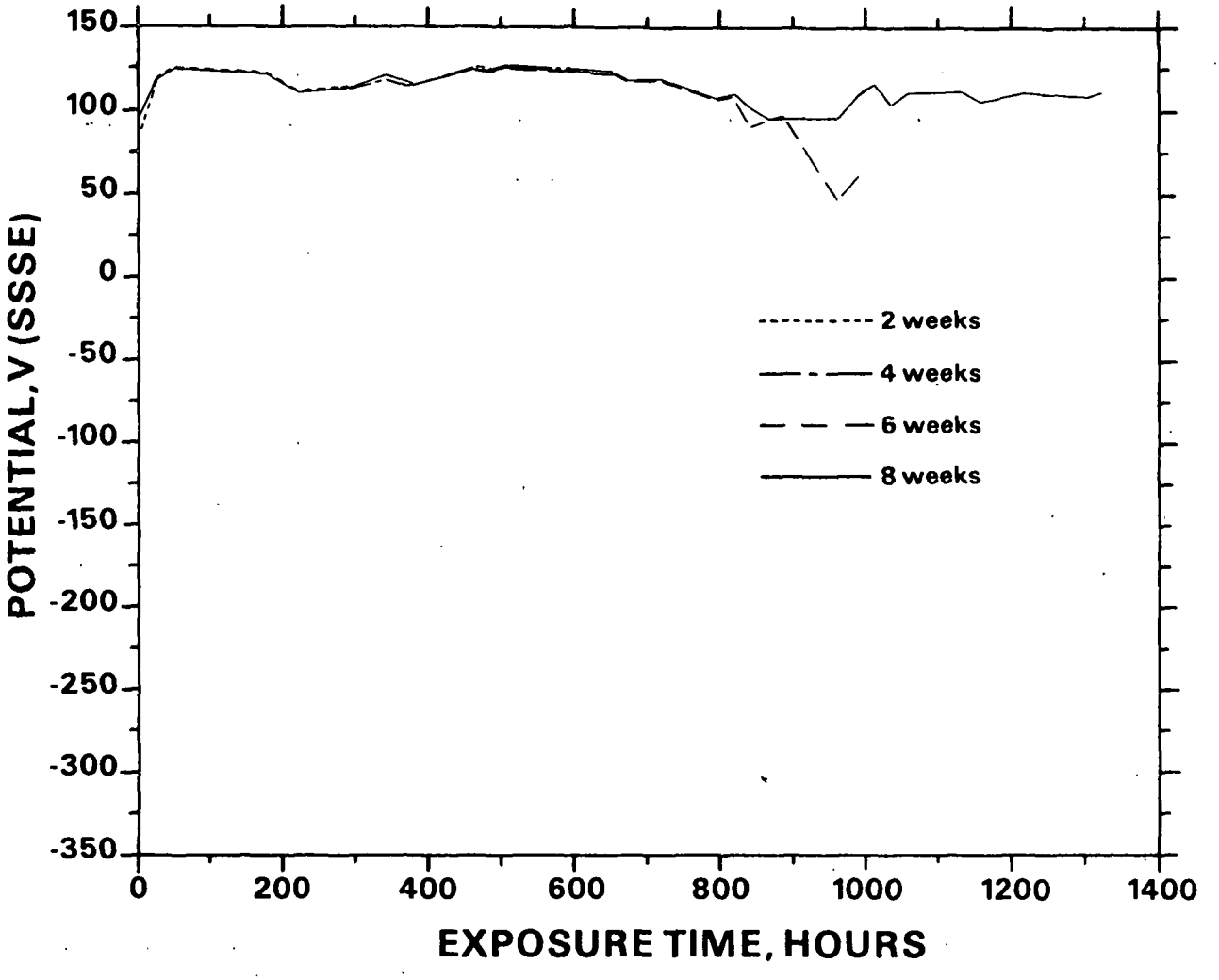

Figure AII-3. Corrosion potential in 60 g/L NaOH + 10 g/L Na_2S + 1 g/L S. Similar behavior was observed in solutions of the following compositions:

NaOH, g/L	Na_2S, g/L	S, g/L
60	10	1.5
60	10	2
60	10	5
60	10	10
60	20	2
80	10	1.5
80	10	2
80	10	5
80	10	10
100	10	1.5
100	10	5
100	10	10
100	20	5
100	20	10
120	10	5
120	10	10
120	20	10
120	30	5

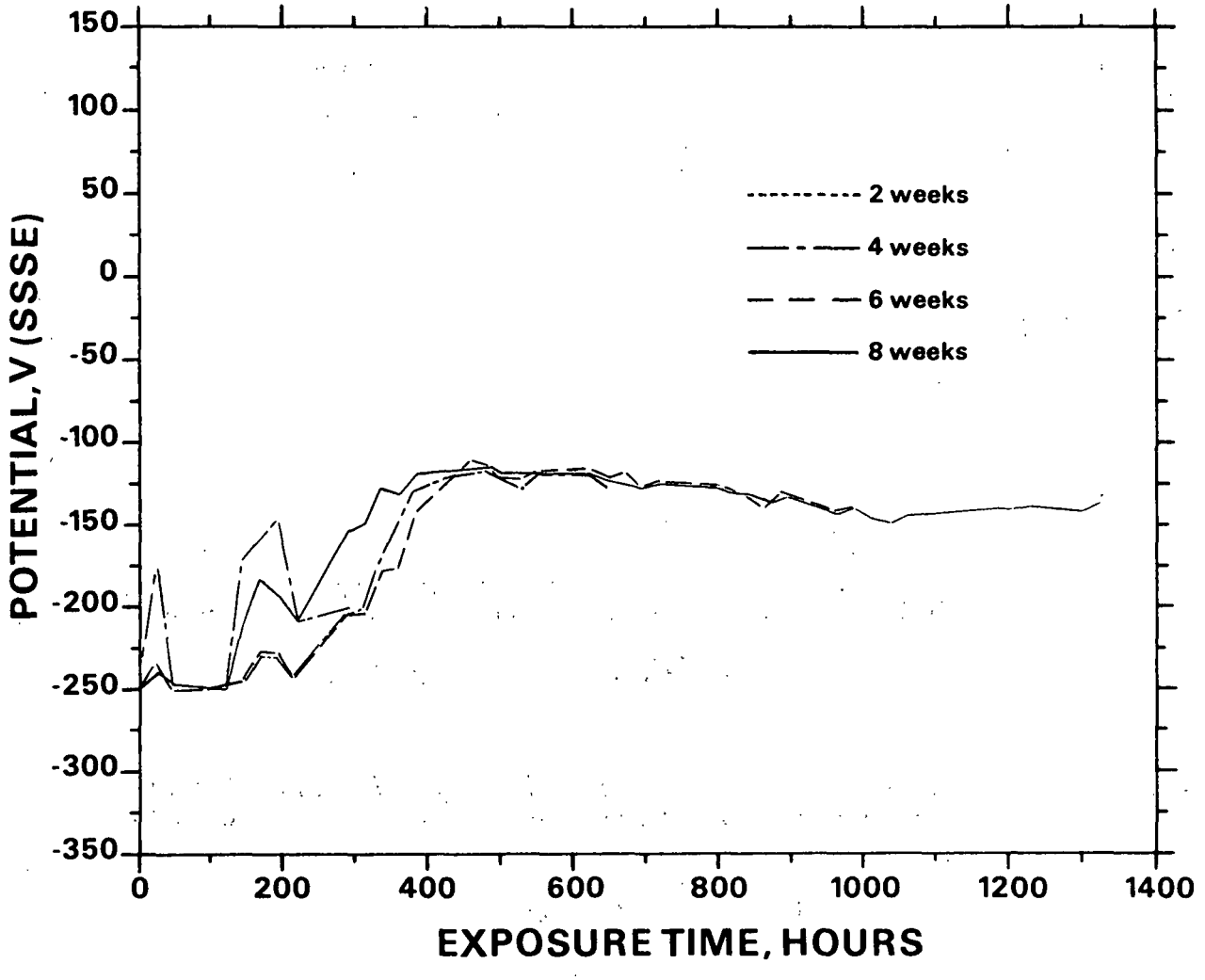

Figure AII-4. Corrosion potential in 60 g/L NaOH + 20 g/L Na_2S.

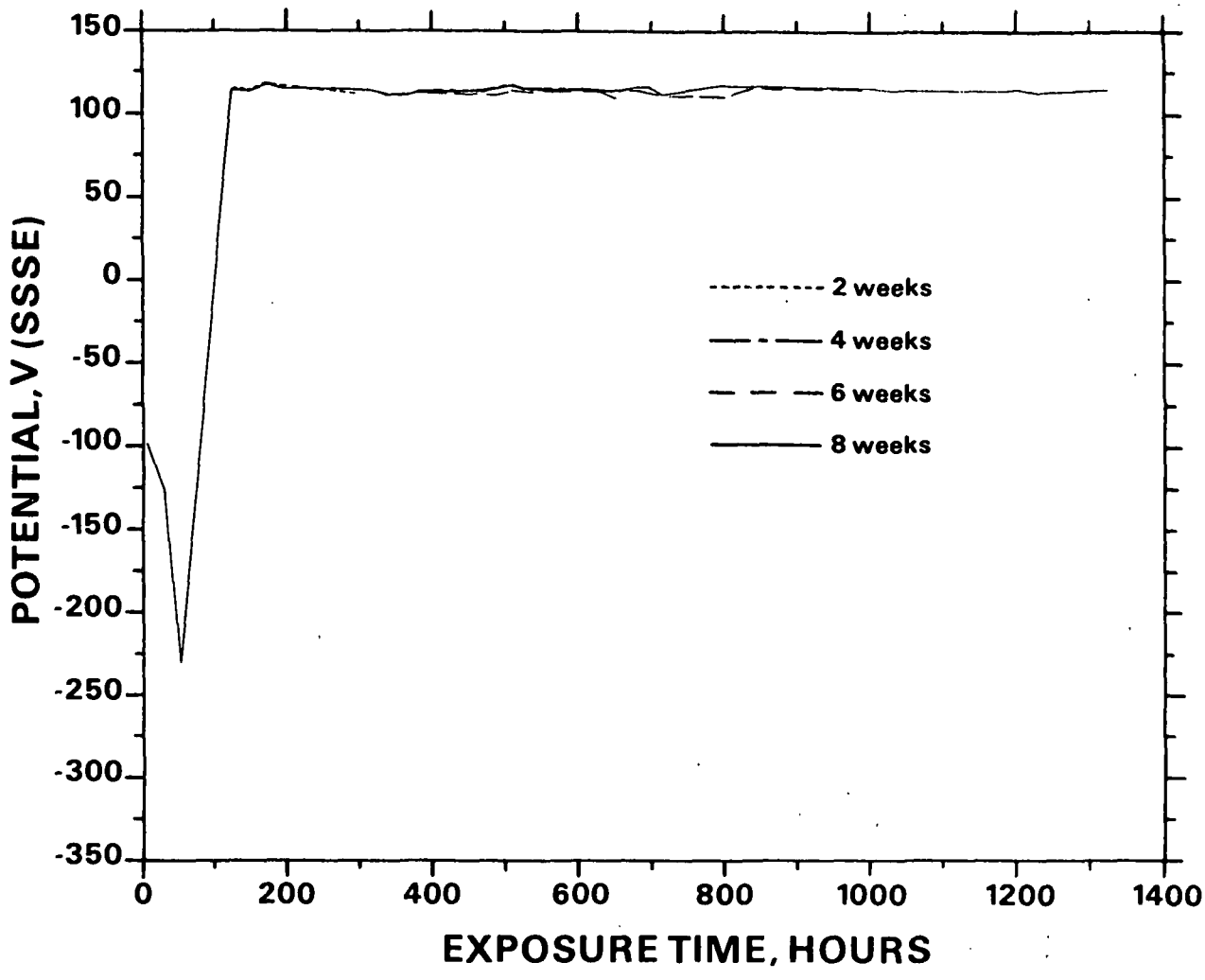

Figure AII-5. Corrosion potential in 60 g/L NaOH + 20 g/L Na_2S + 0.5 g/L S. Similar behavior was observed in solutions of the following compositions:

NaOH, g/L	Na_2S, g/L	S, g/L
60	30	1
60	40	1
80	30	1
80	40	1.5
80	40	2
100	10	0.5
120	10	0.5
120	20	1
120	20	1.5
120	20	2
120	30	1.5
120	30	2
120	40	1.5
120	40	2

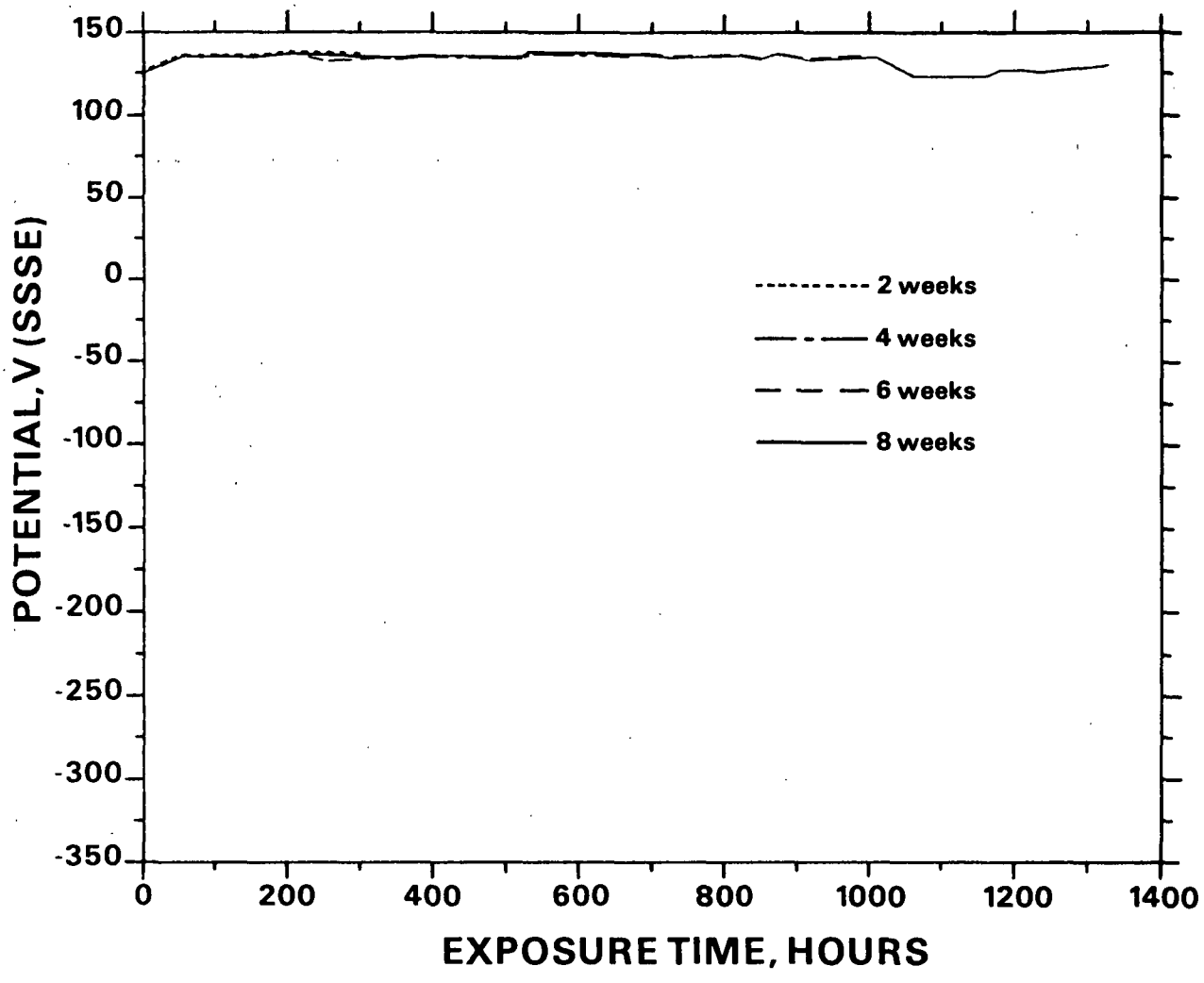

Figure AII-6. Corrosion potential in 60 g/L NaOH + 20 g/L Na_2S + 5 g/L S. Similar behavior was observed in solutions of the following compositions:

NaOH, g/L	Na_2S, g/L	S, g/L
60	20	10
60	30	5
60	30	10
60	40	5
60	40	10
80	40	5
80	40	10

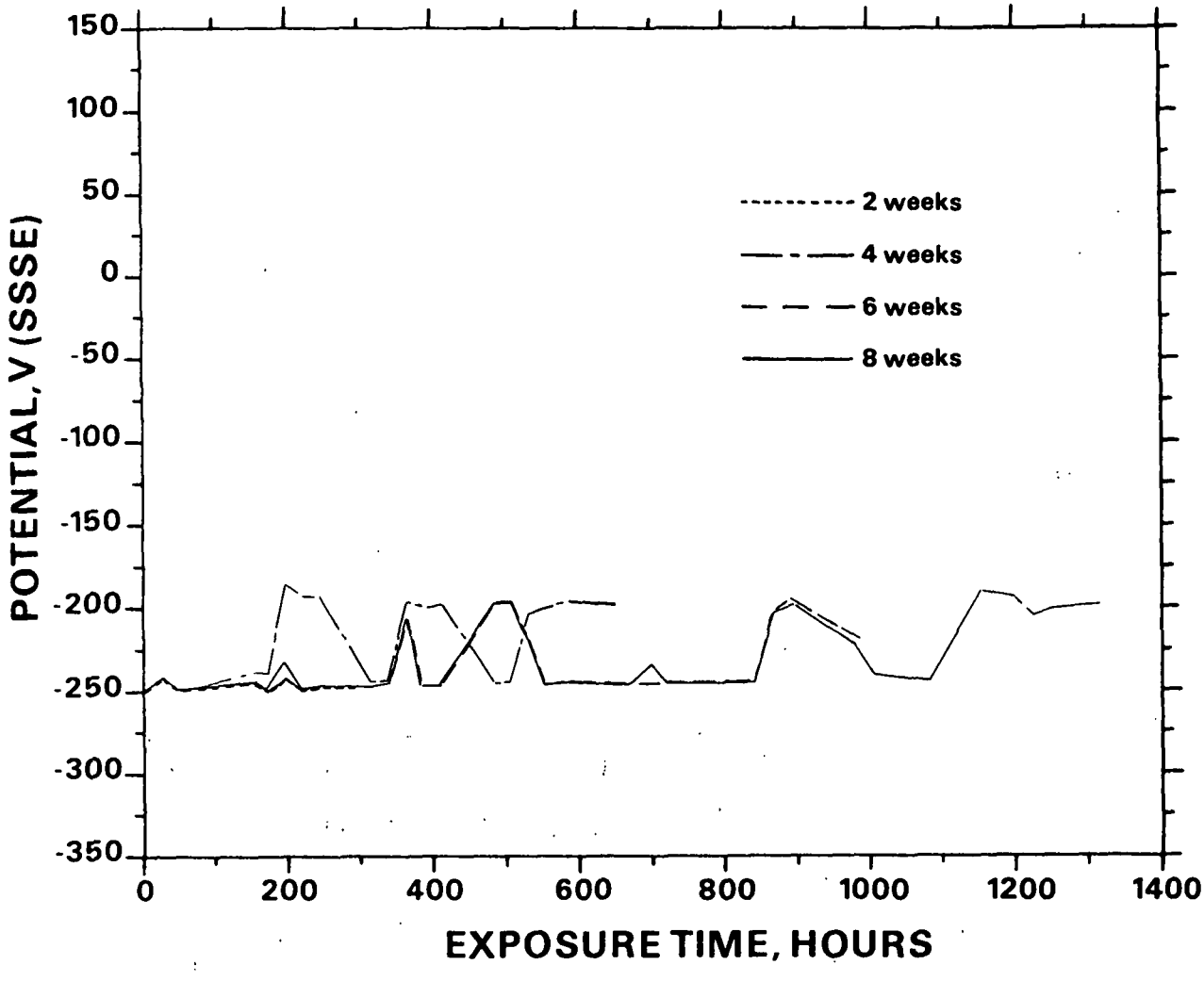

Figure AII-7. Corrosion potential in 60 g/L NaOH + 30 g/L Na_2S. Similar behavior was observed in solutions of the following compositions:

NaOH, g/L	Na_2S, g/L	S, g/L
60	40	
100	40	0.5
120	30	0.5

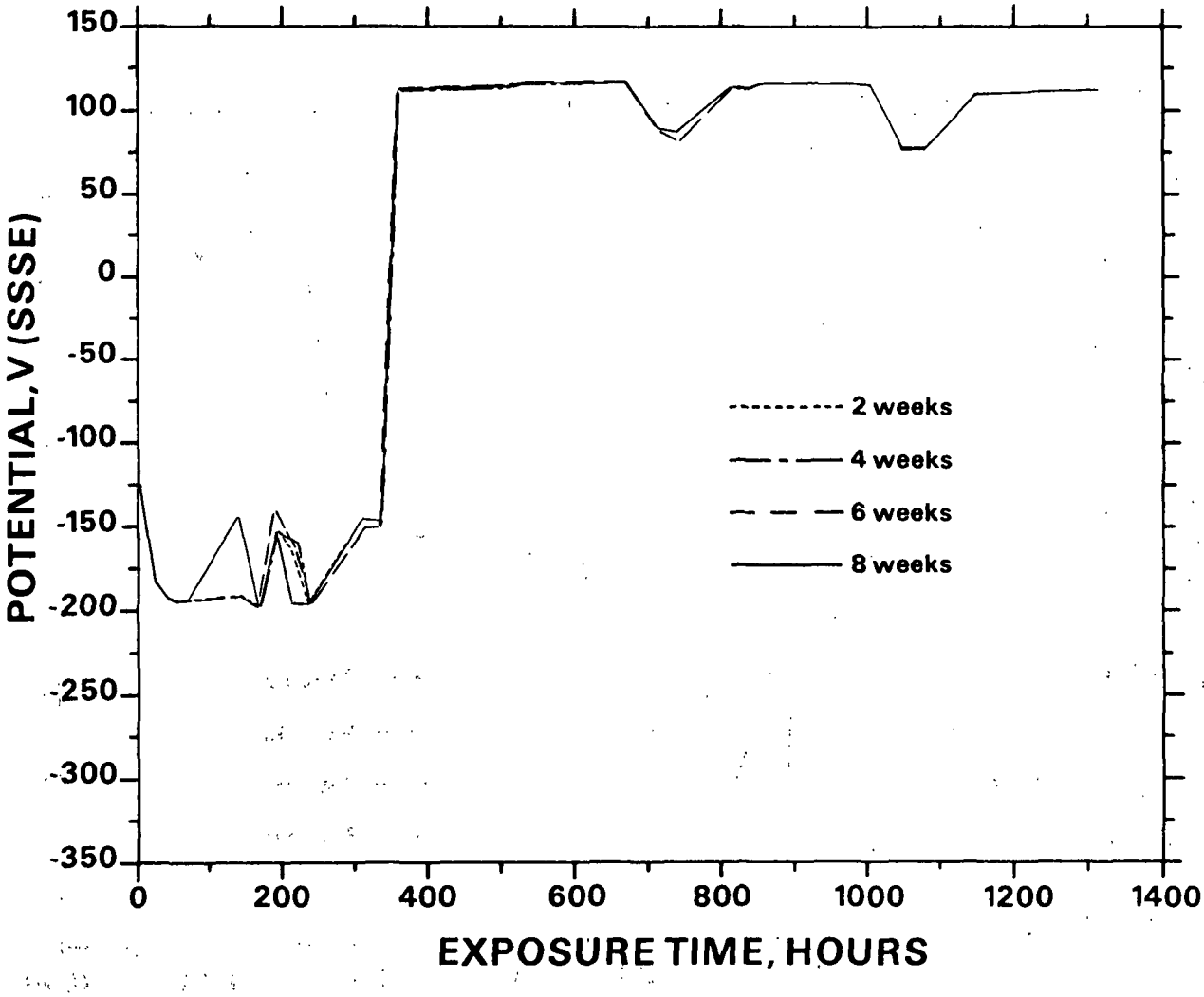

Figure AII-8. Corrosion potential in 60 g/L NaOH + 30 g/L Na_2S + 0.5 g/L S. Similar behavior was observed in solutions of the following compositions:

NaOH, g/L	Na_2S, g/L	S, g/L
60	40	0.5
100	40	1.5

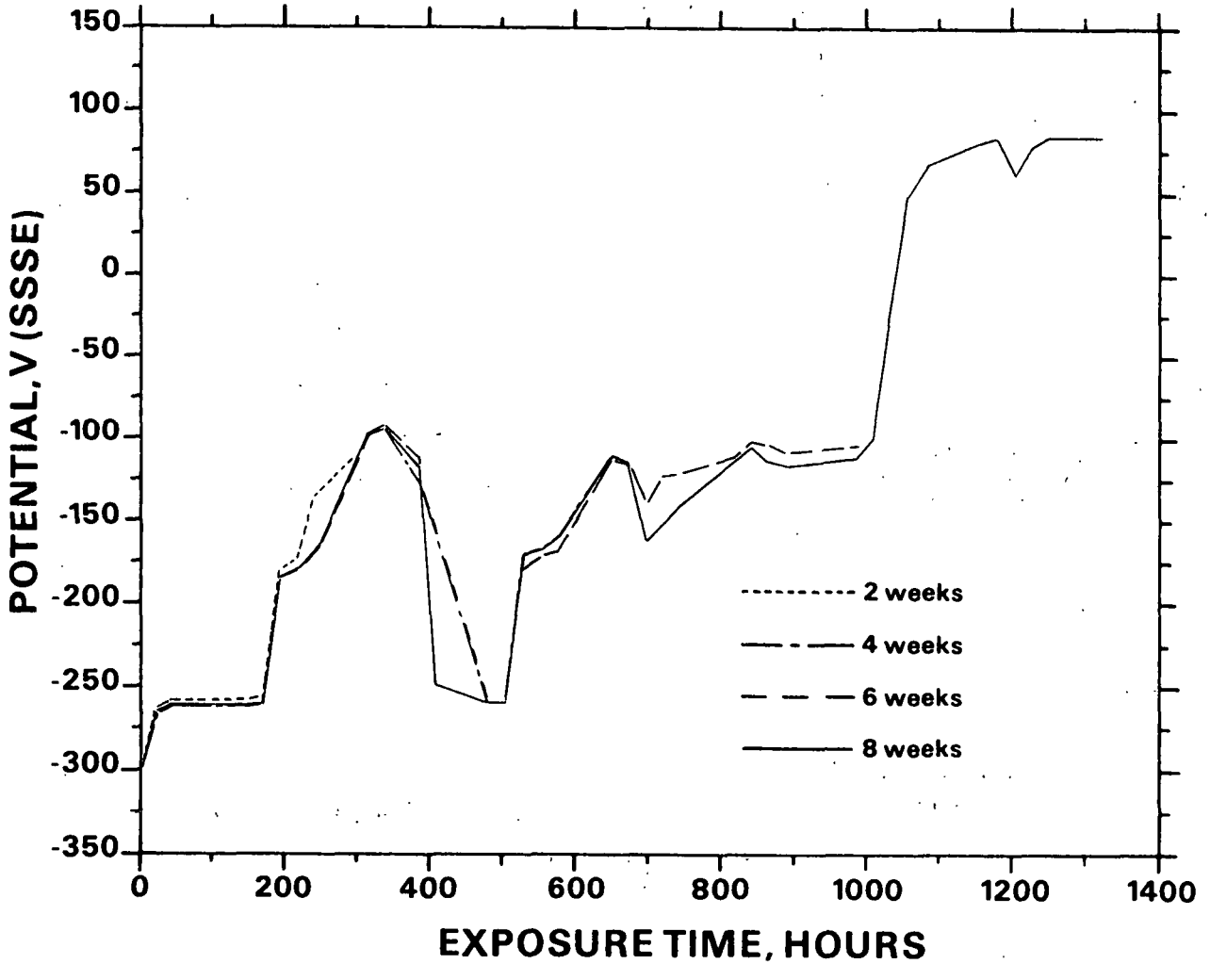

Figure AII-9. Corrosion potential in 80 g/L NaOH + 10 g/L Na_2S + 1 g/L S.

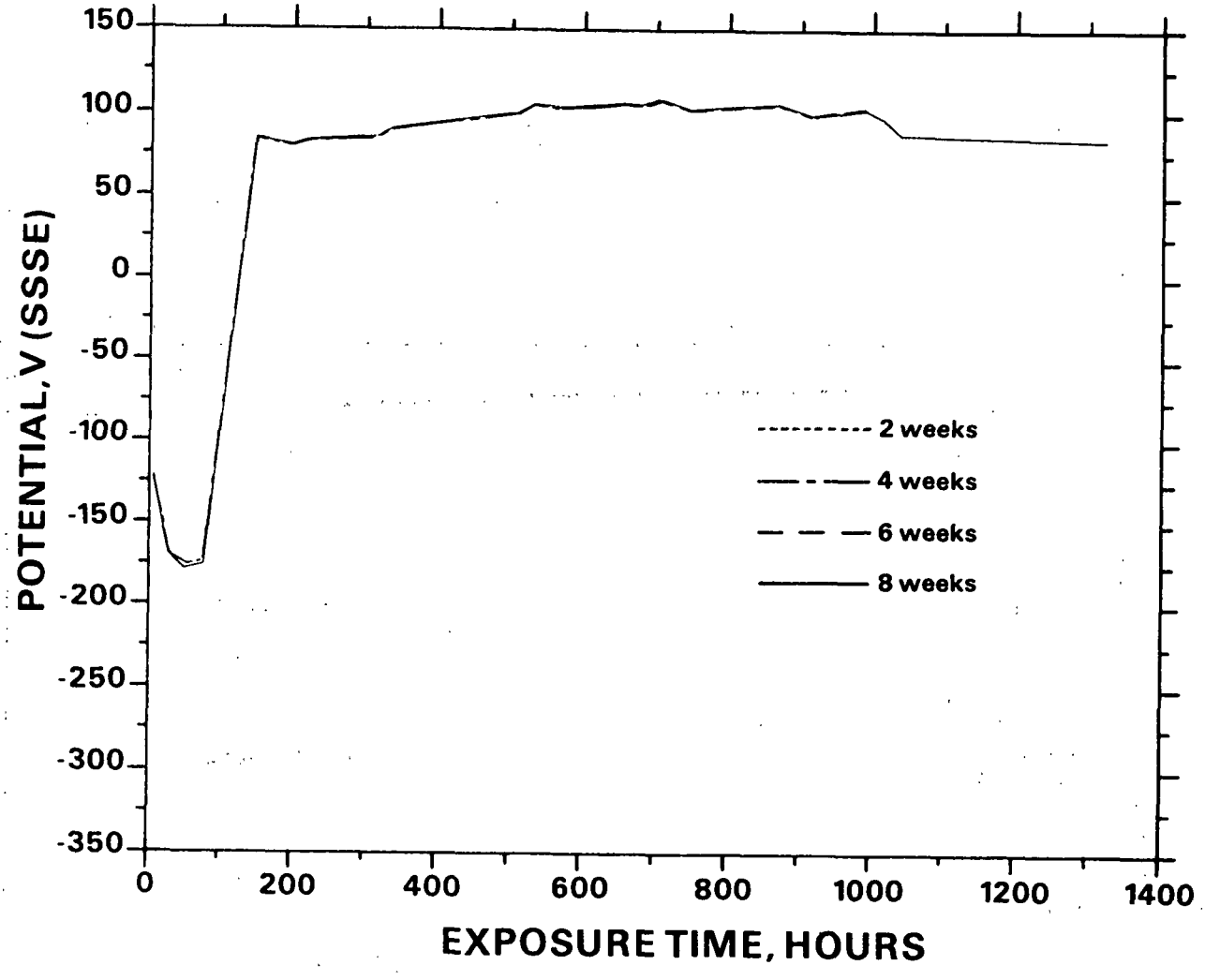

Figure AII-10. Corrosion potential in 80 g/L NaOH + 10 g/L Na_2S + 0.5 g/L S. Similar behavior was observed in solutions of the following compositions:

NaOH, g/L	Na_2S, g/L	S, g/L
80	20	0.5
80	20	2
100	10	1
120	10	1
120	10	1.5

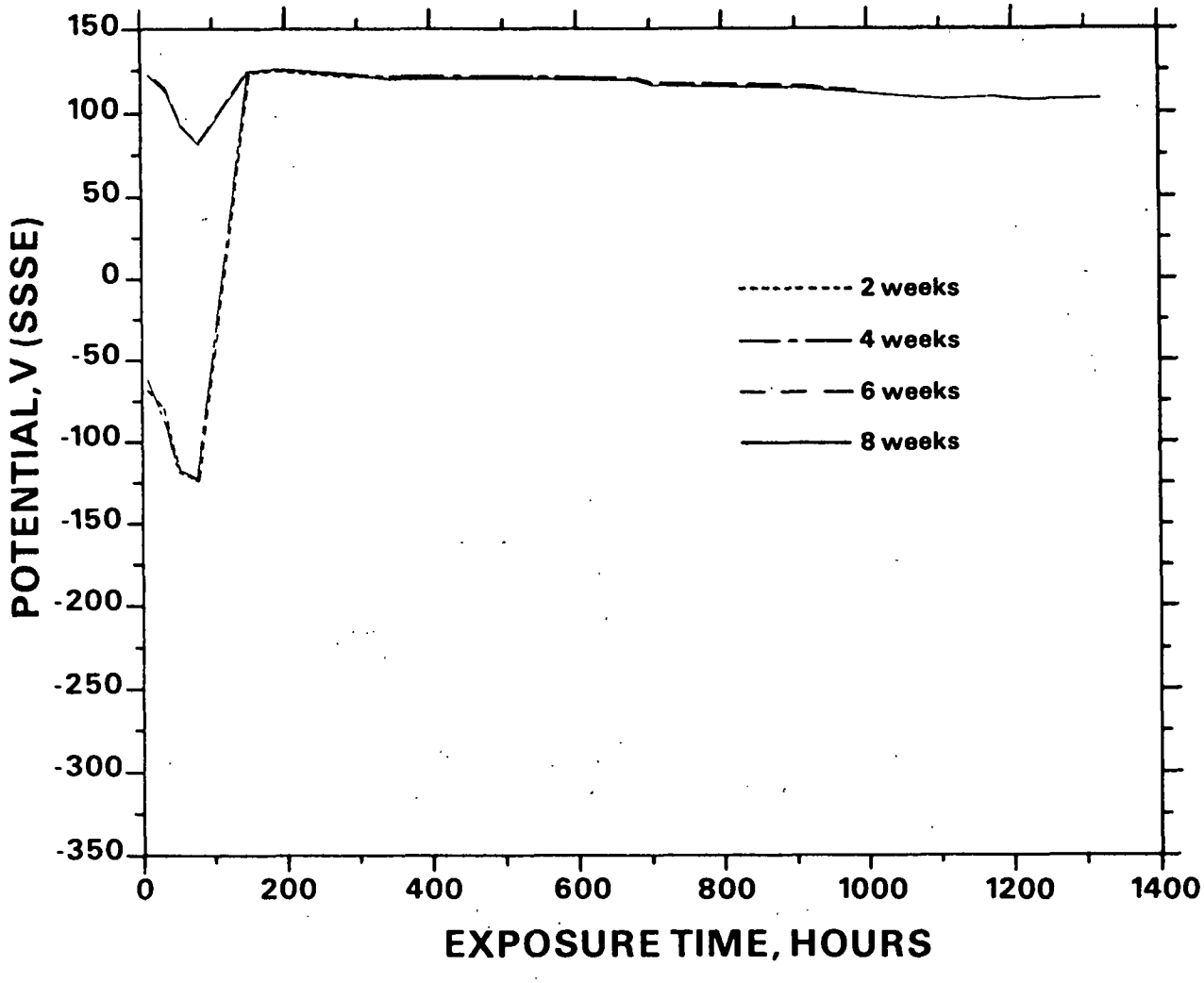

Figure AII-11. Corrosion potential in 80 g/L NaOH + 10 g/L Na_2S + 1 g/L S. Similar behavior was observed in solution containing 100 g/L NaOH + 10 g/L Na_2S.

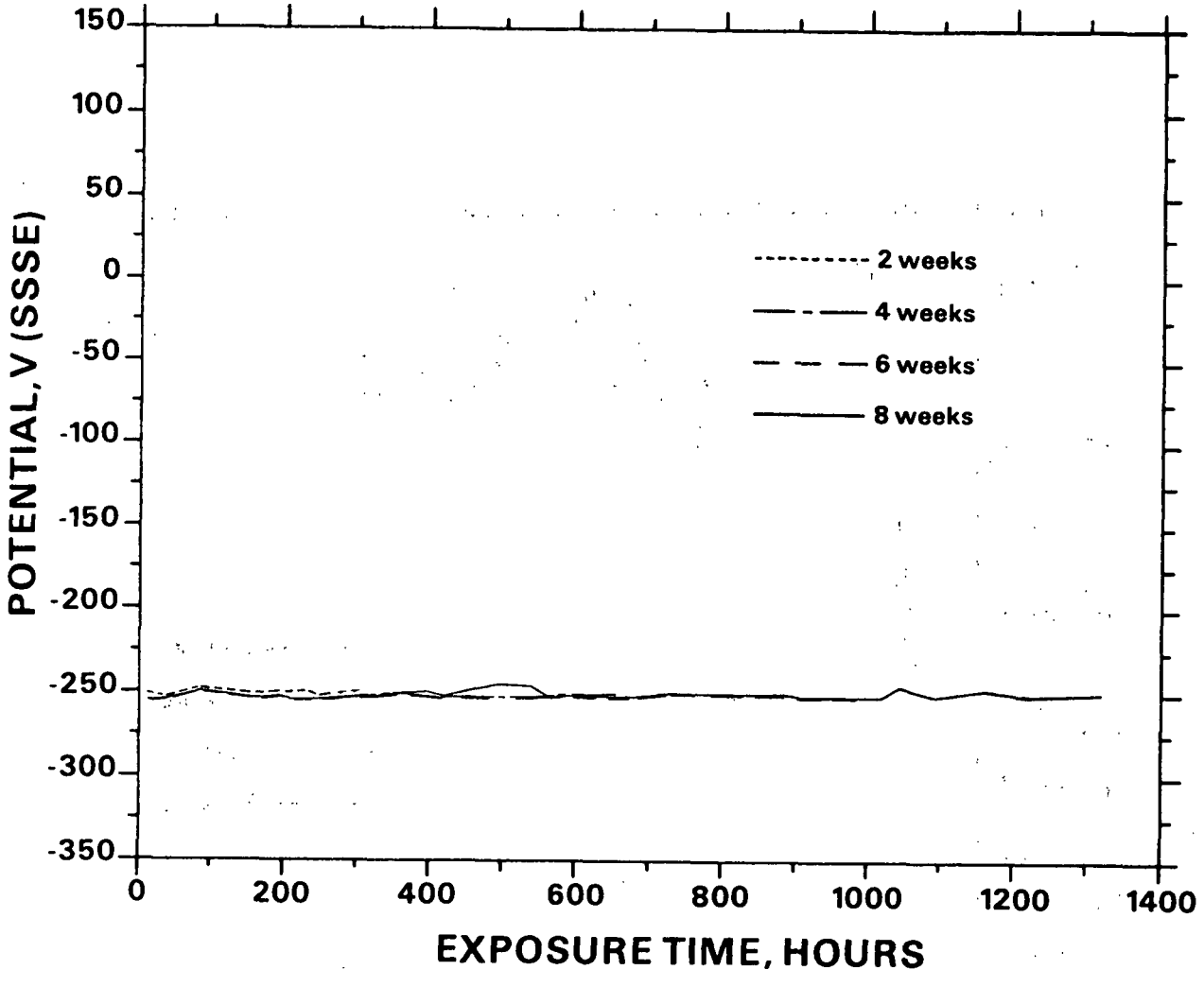

Figure AII-12. Corrosion potential in 80 g/L NaOH + 20 g/L Na_2S. Similar behavior was observed in solutions of the following compositions:

NaOH, g/L	Na_2S, g/L
80	30
100	40
120	20
120	30
120	40

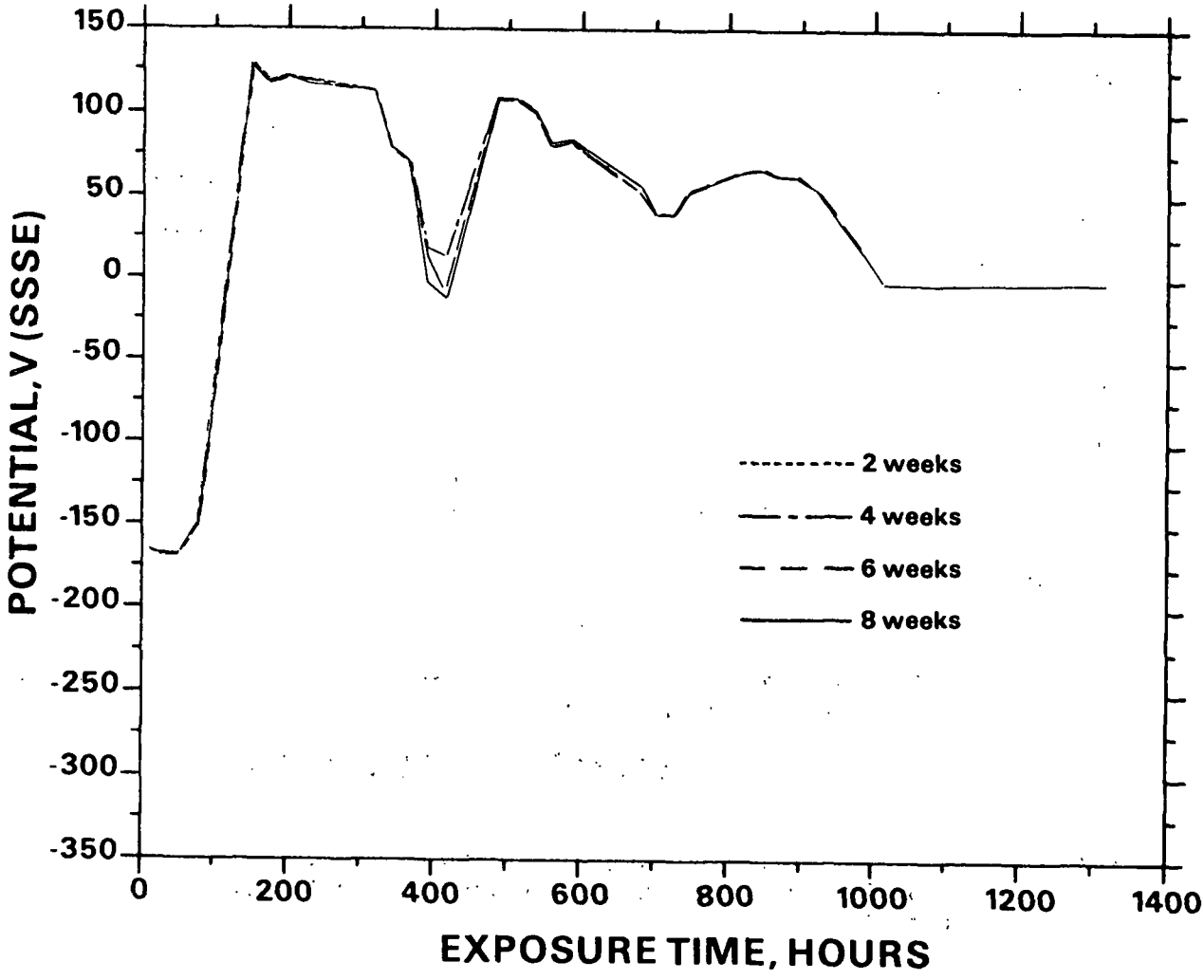

Figure AII-13. Corrosion potential in 80 g/L NaOH + 20 g/L Na_2S + 1 g/L S. Similar behavior was observed in solution containing 80 g/L NaOH + 20 g/L Na_2S + 1.5 g/L S.

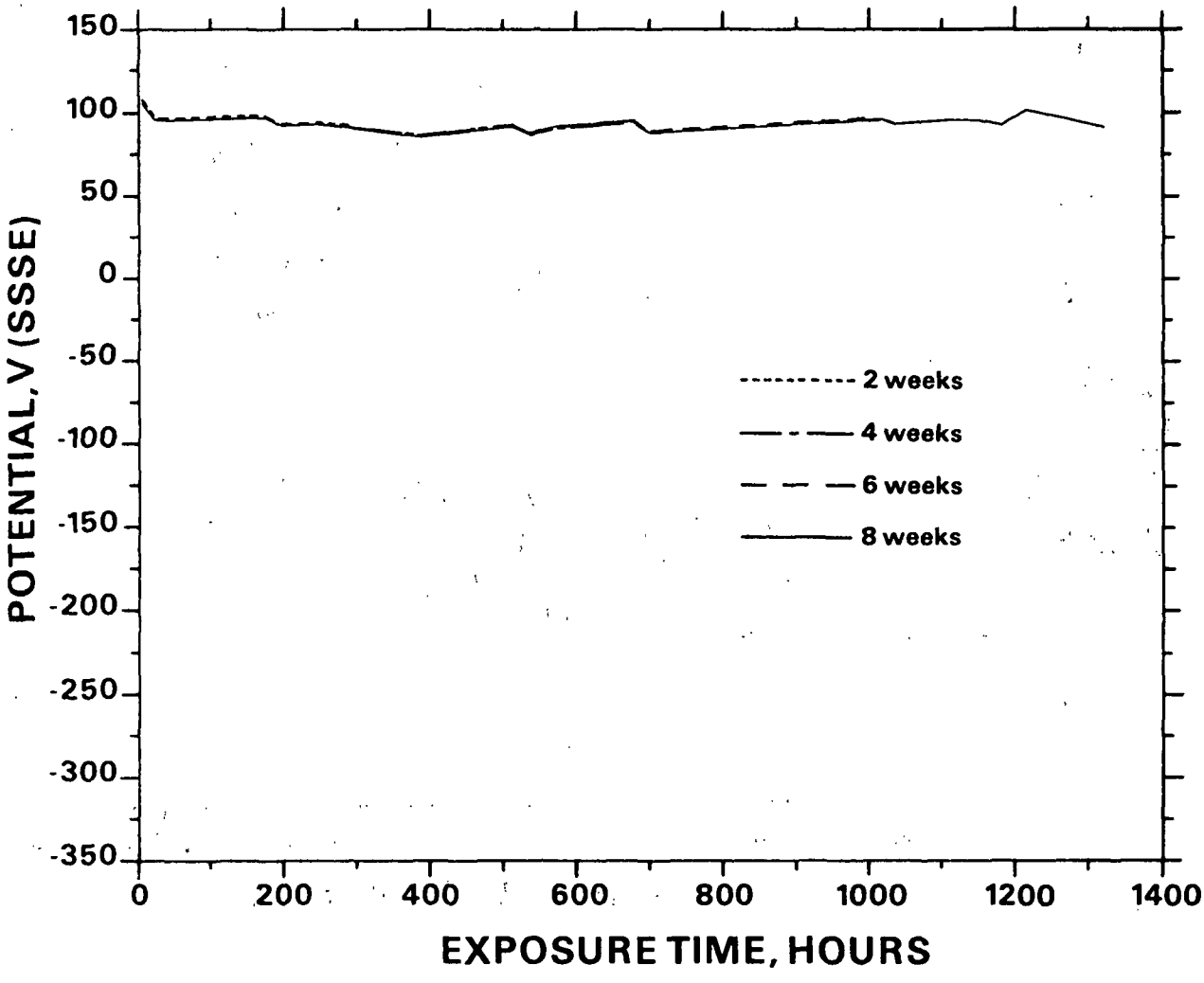

Figure AII-14. Corrosion potential in 80 g/L NaOH + 20 g/L Na_2S + 5 g/L S. Similar behavior was observed in solutions of the following compositions:

NaOH, g/L	Na_2S, g/L	S, g/L
80	20	10
80	30	5
80	30	10
100	40	10

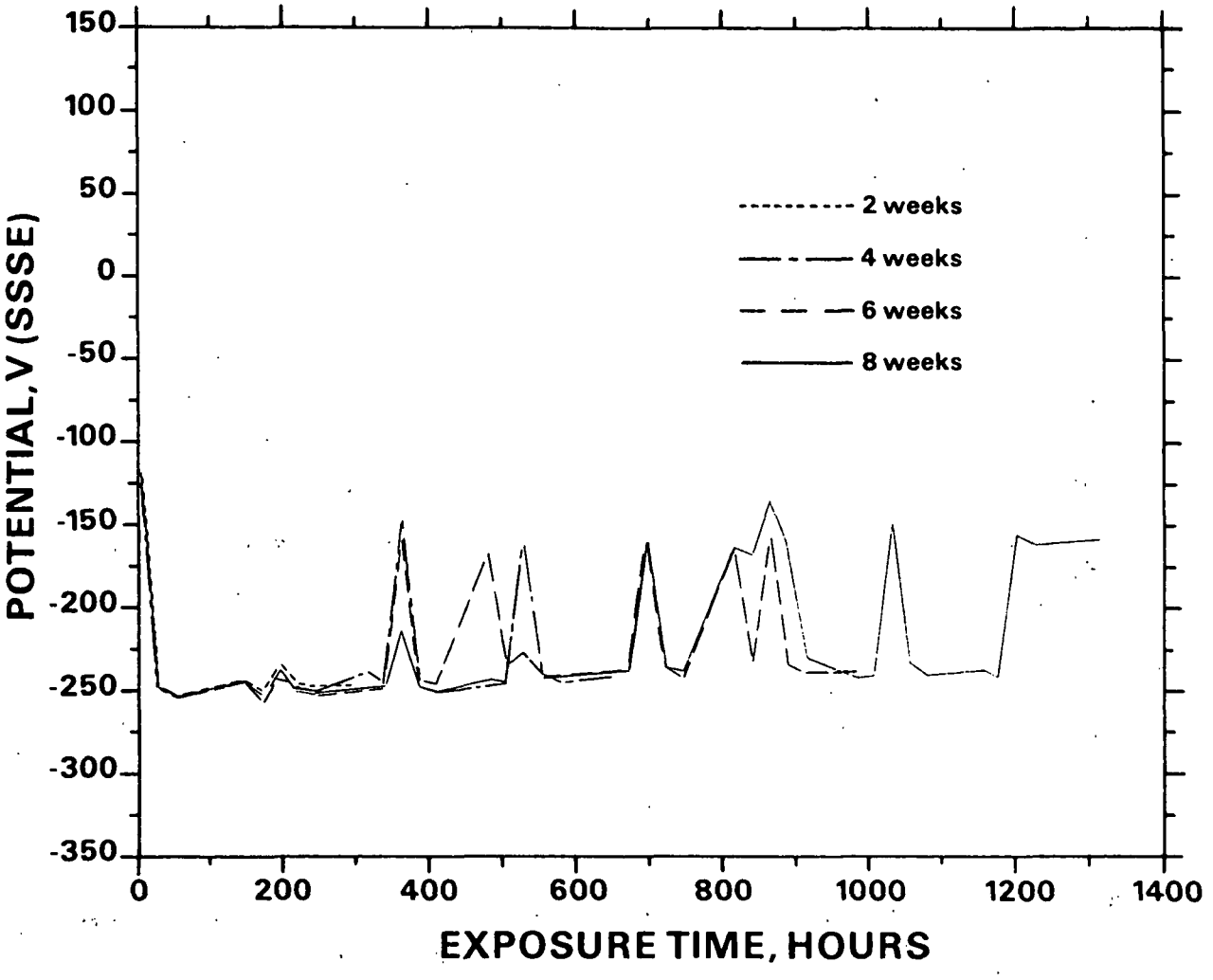

Figure AII-15. Corrosion potential in 80 g/L NaOH + 30 g/L Na_2S + 0.5 g/L S. Similar behavior was observed in solutions of the following compositions:

NaOH, g/L	Na_2S, g/L	S, g/L
100	20	0
100	40	1
120	30	1
120	40	1

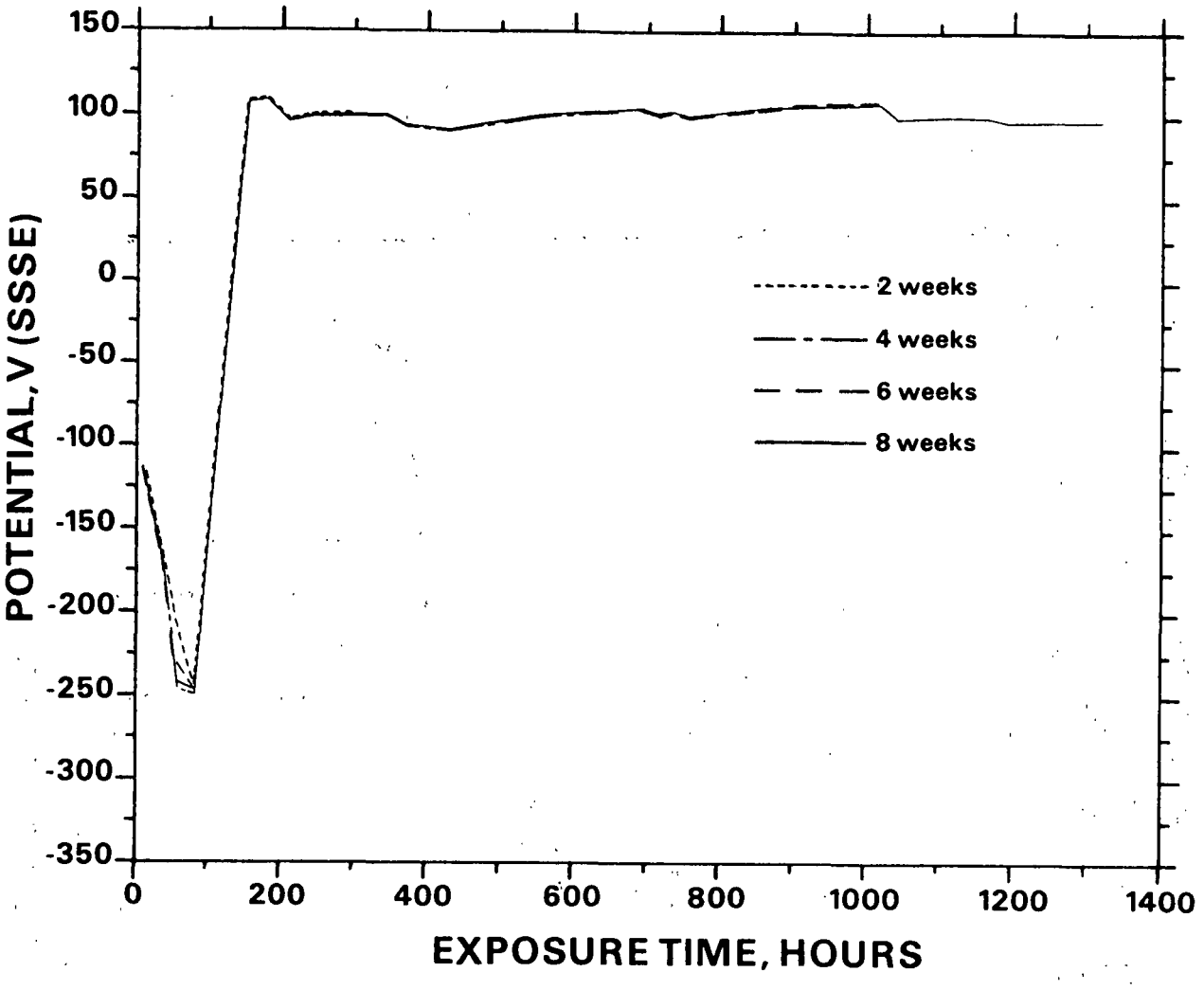

Figure AII-16. Corrosion potential in 80 g/L NaOH + 30 g/L Na_2S + 1.5 g/L S. Similar behavior was observed in solutions of the following compositions:

NaOH, g/L	Na_2S, g/L	S, g/L
80	40	1
100	20	1.5
100	20	2

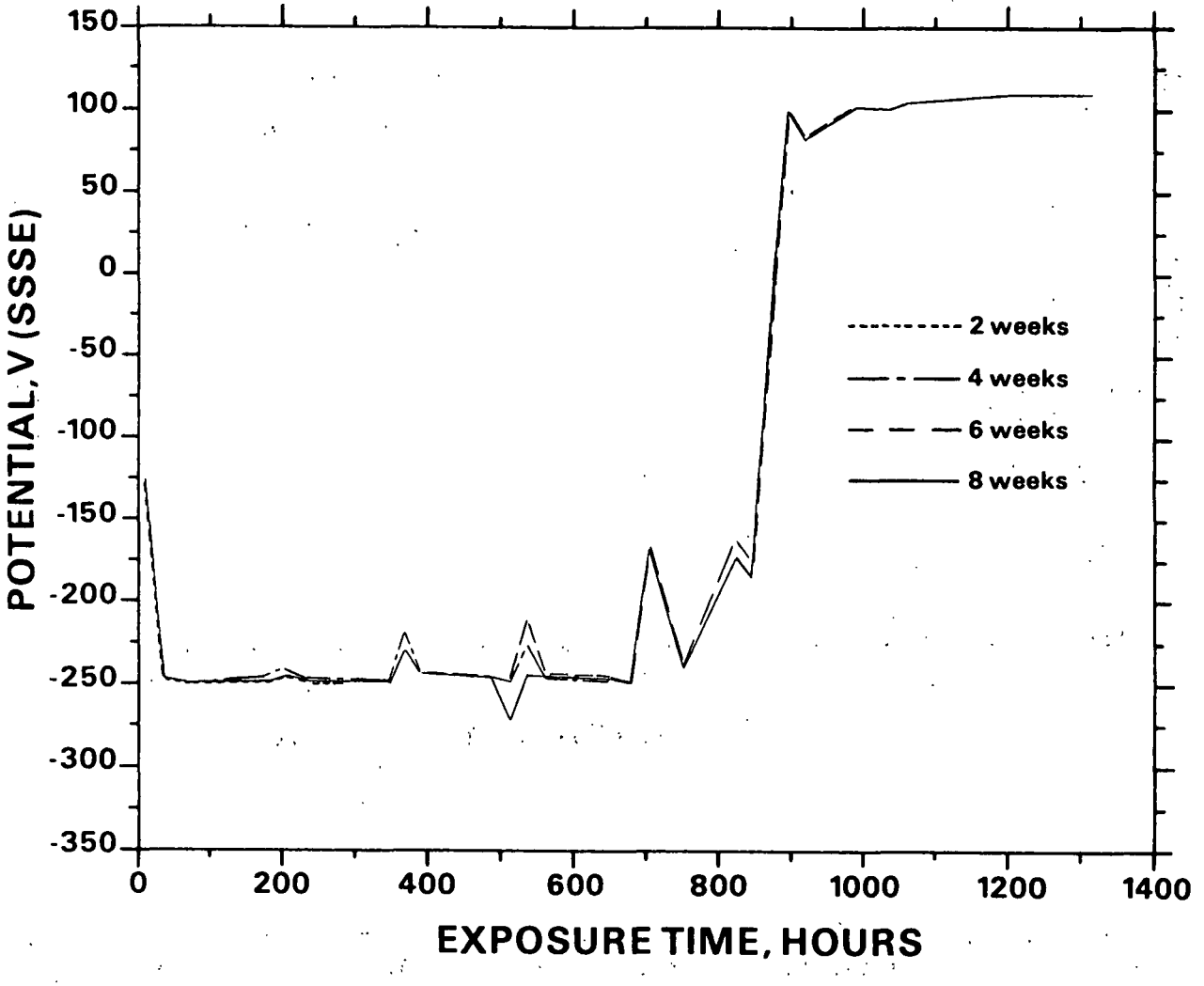

Figure AII-17. Corrosion potential in 80 g/L NaOH + 40 g/L Na_2S + 0.5 g/L S. Similar behavior was observed in 120 g/L NaOH + 40 g/L Na_2S + 0.5 g/L solution.

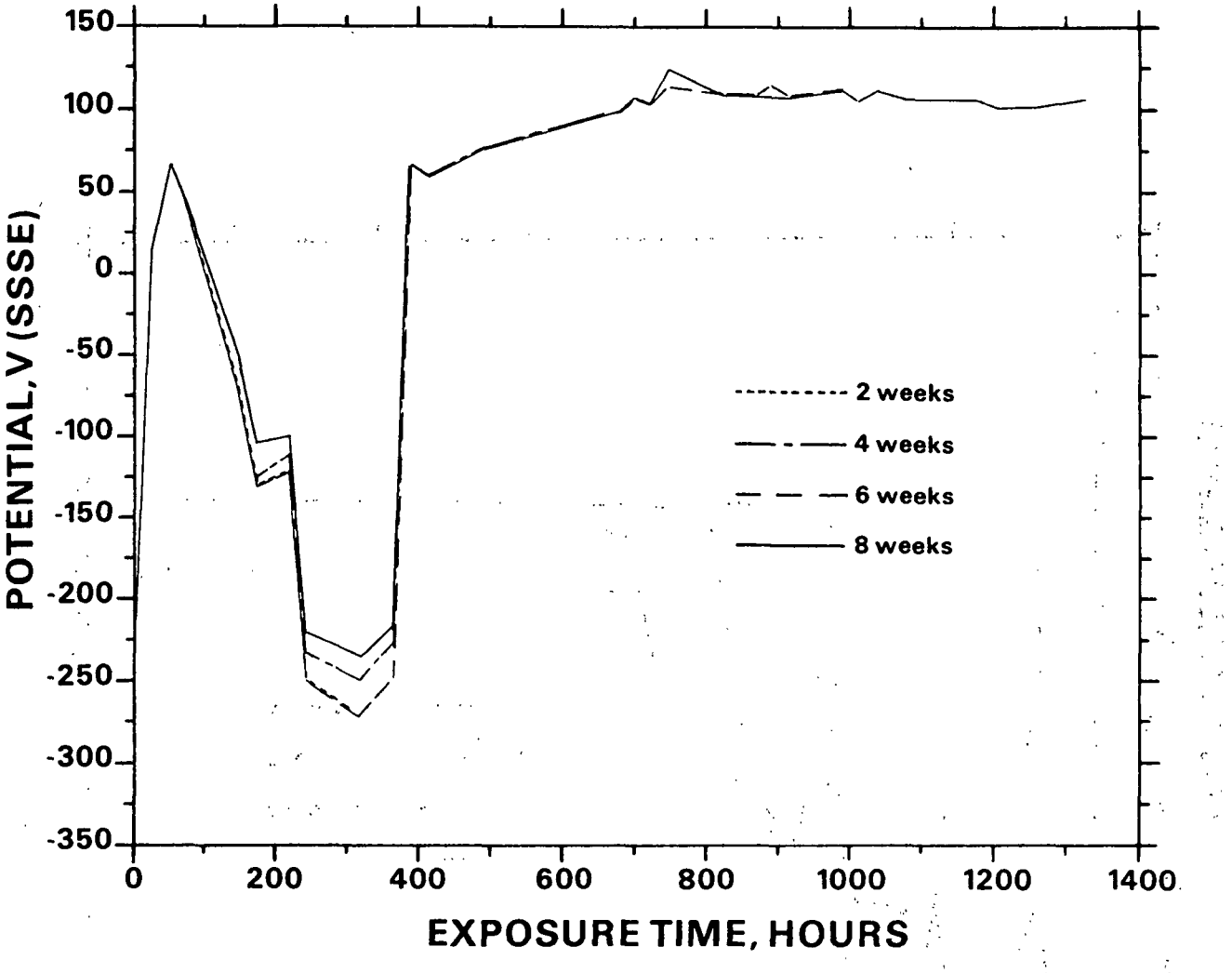

Figure AII-18. Corrosion potential in 100 g/L NaOH + 10 g/L Na_2S + 2 g/L S. Similar behavior was observed in solutions of the following compositions:

NaOH, g/L	Na_2S, g/L	S, g/L
100	20	0.5
100	20	1
120	20	0.5

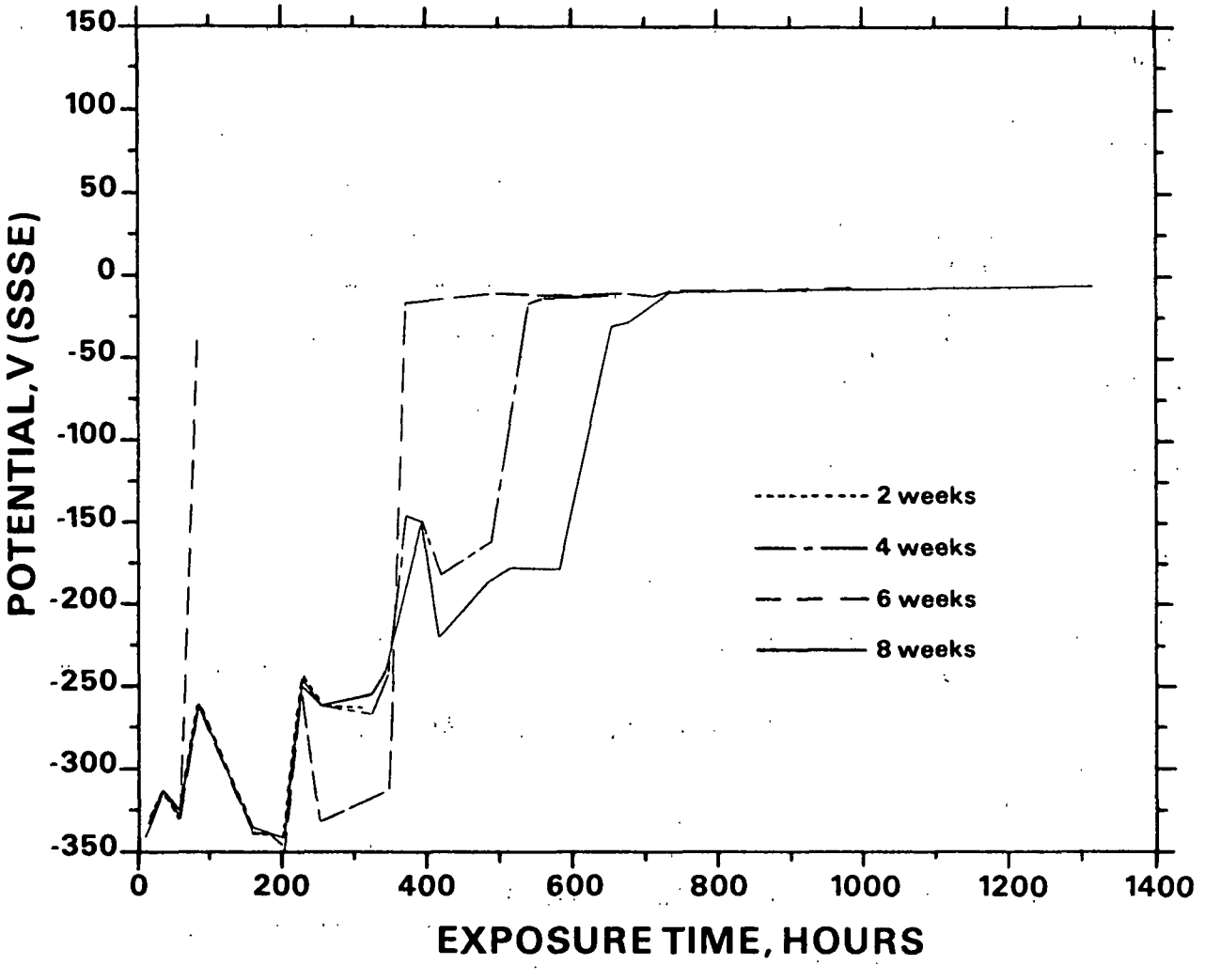

Figure AII-19. Corrosion potential in 100 g/L NaOH + 40 g/L Na_2S + 2 g/L S.

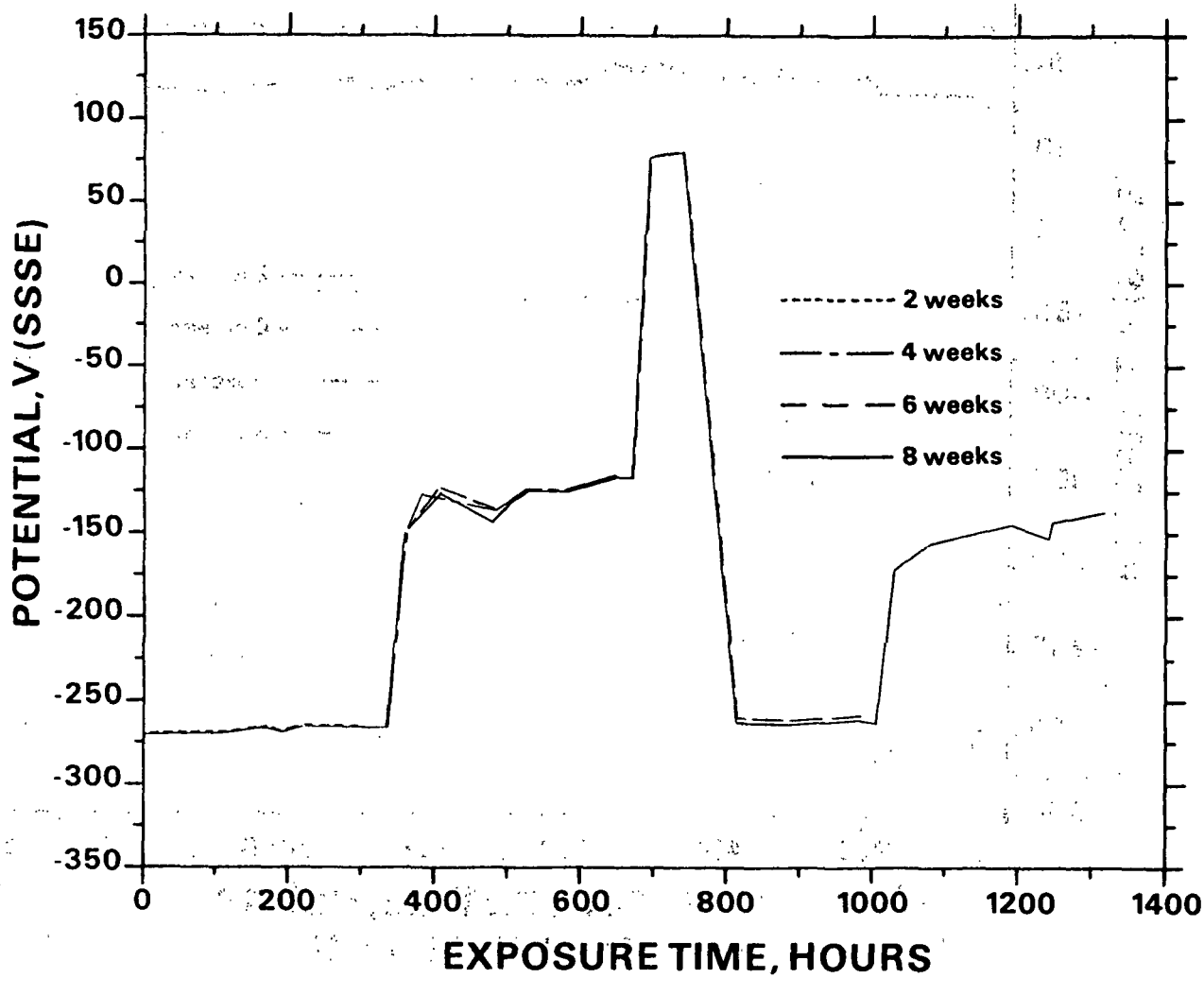

Figure AII-20. Corrosion potential in 120 g/L NaOH + 10 g/L Na_2S.

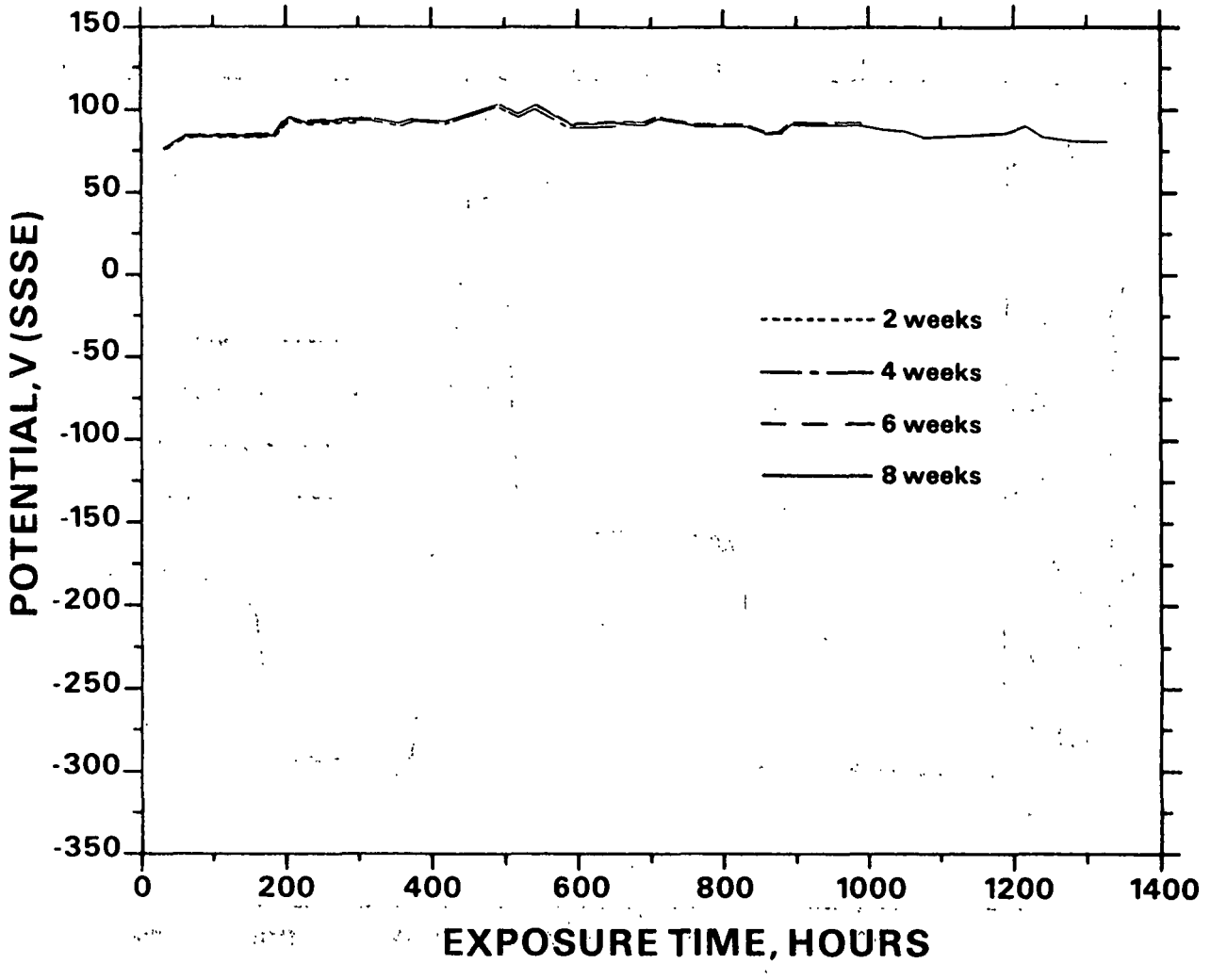

Figure AII-21. Corrosion potential in 120 g/L NaOH + 20 g/L Na_2S + 5 g/L S. Similar behavior was observed in 120 g/L NaOH + 30 g/L Na_2S + 10 g/L S.

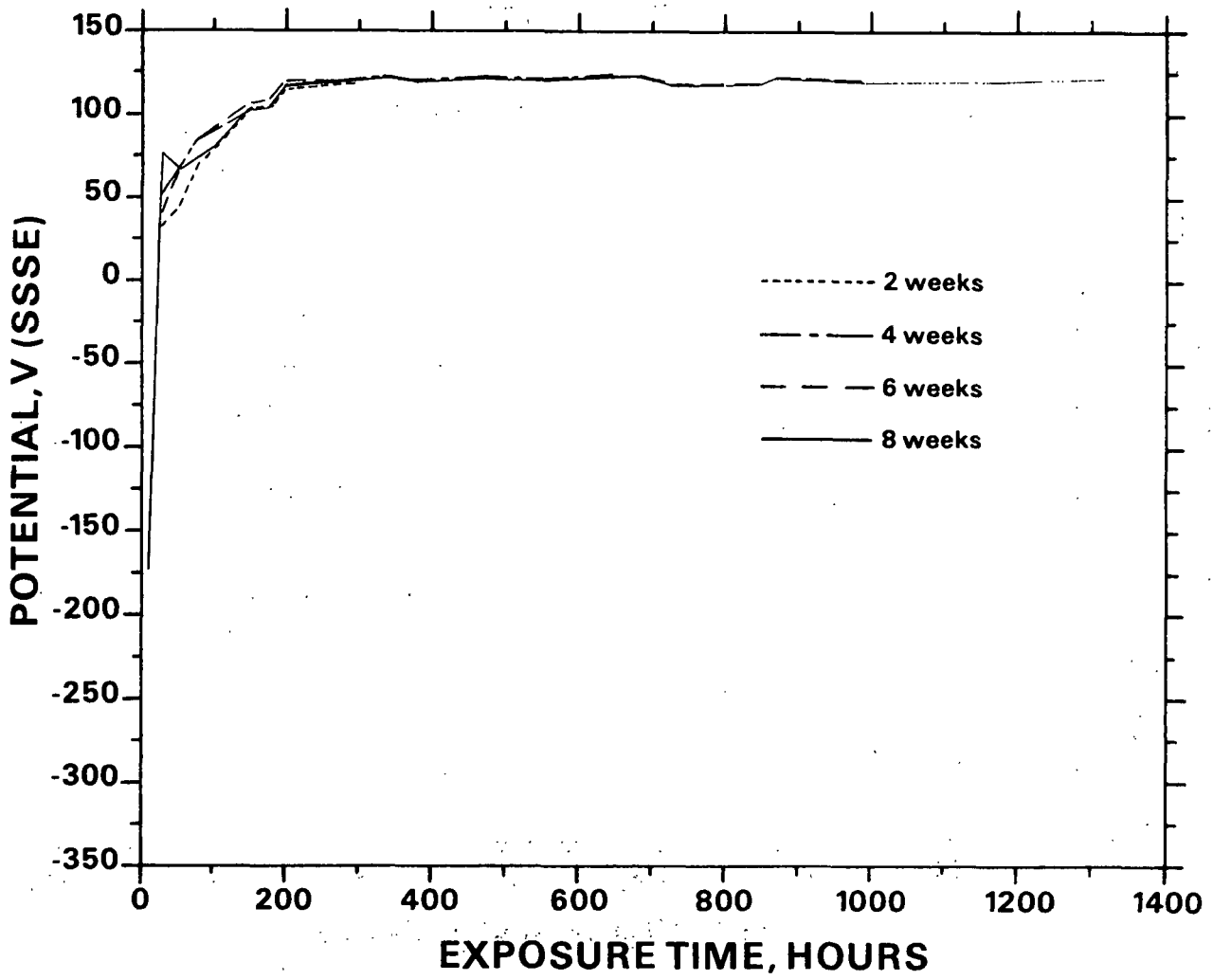

Figure AII-22. Corrosion potential in 120 g/L NaOH + 40 g/L Na_2S + 5 g/L S. Similar behavior was observed in 120 g/L NaOH + 40 g/L Na_2S + 10 g/L S.

SOLUTIONS CONTAINING THIOSULFATE ADDITIONS

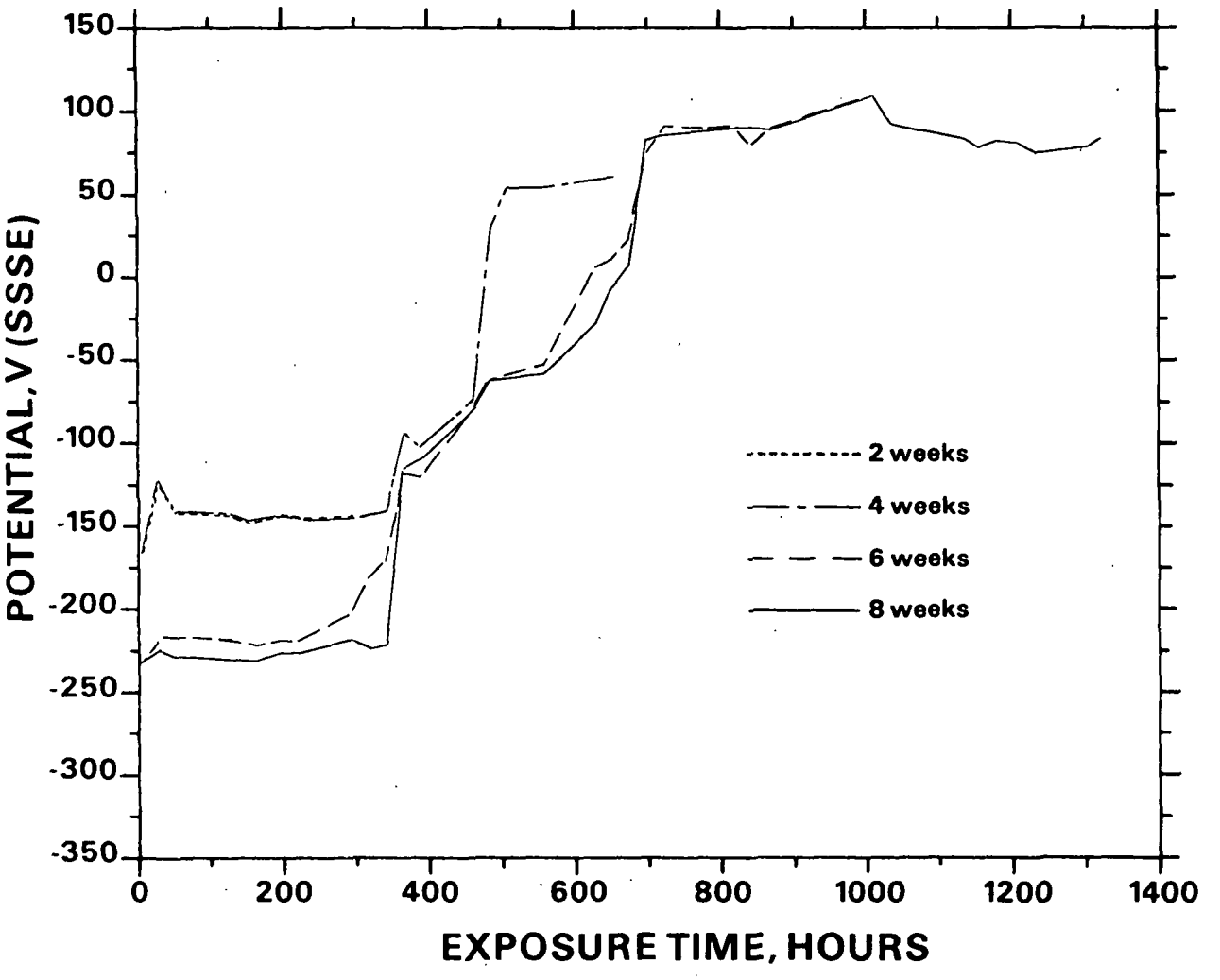

Figure AII-23. Corrosion potential in 60 g/L NaOH + 10 g/L Na_2S + 2.5 g/L $Na_2S_2O_3$. Similar behavior was observed in 80 g/L NaOH + 10 g/L Na_2S.

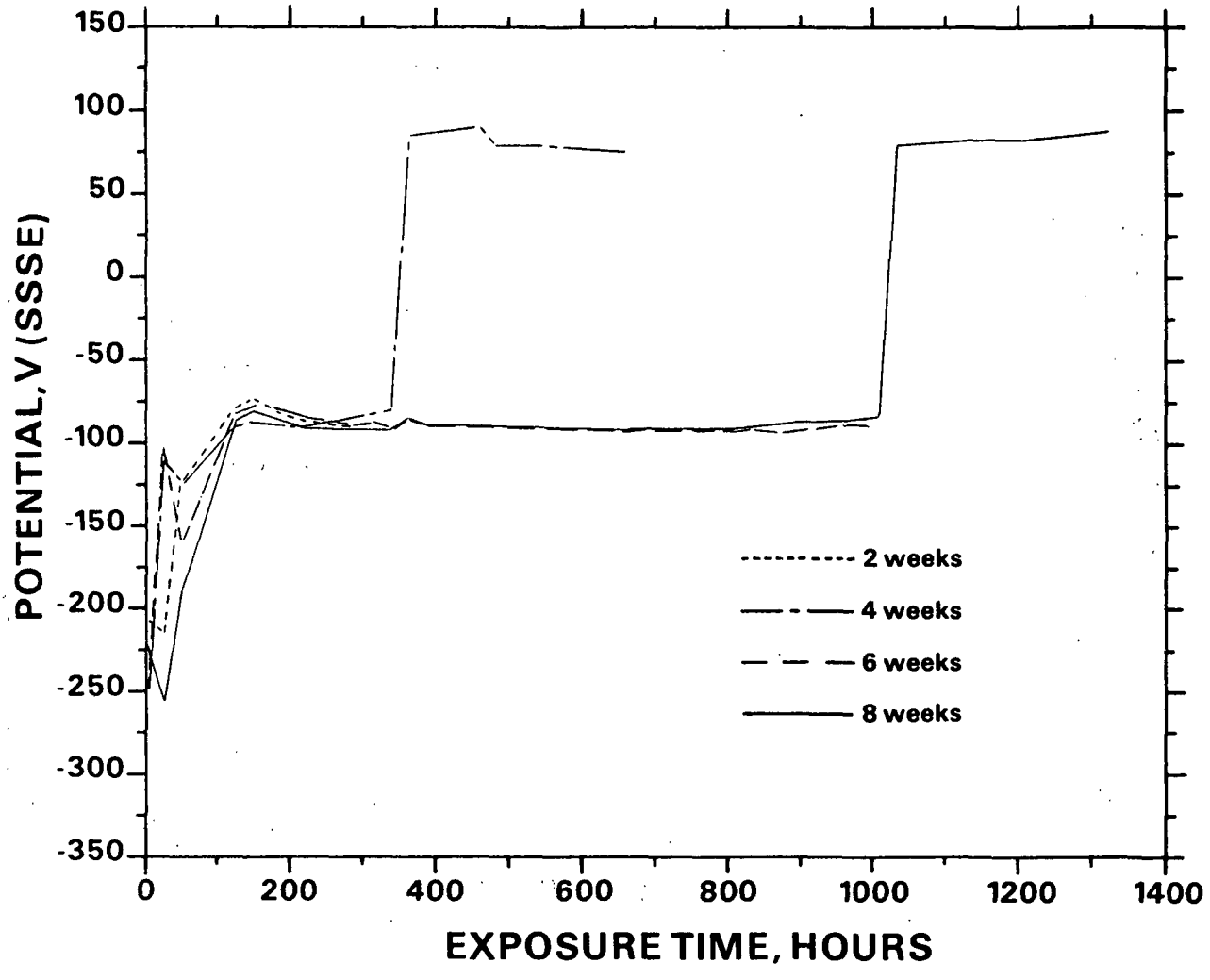

Figure AII-24. Corrosion potential in 60 g/L NaOH + 10 g/L Na_2S + 5 g/L $Na_2S_2O_3$. Similar behavior was observed in solutions of the following compositions:

NaOH, g/L	Na_2S, g/L	$Na_2S_2O_3$, g/L
60	10	10
60	10	25
80	10	2.5
100	10	10

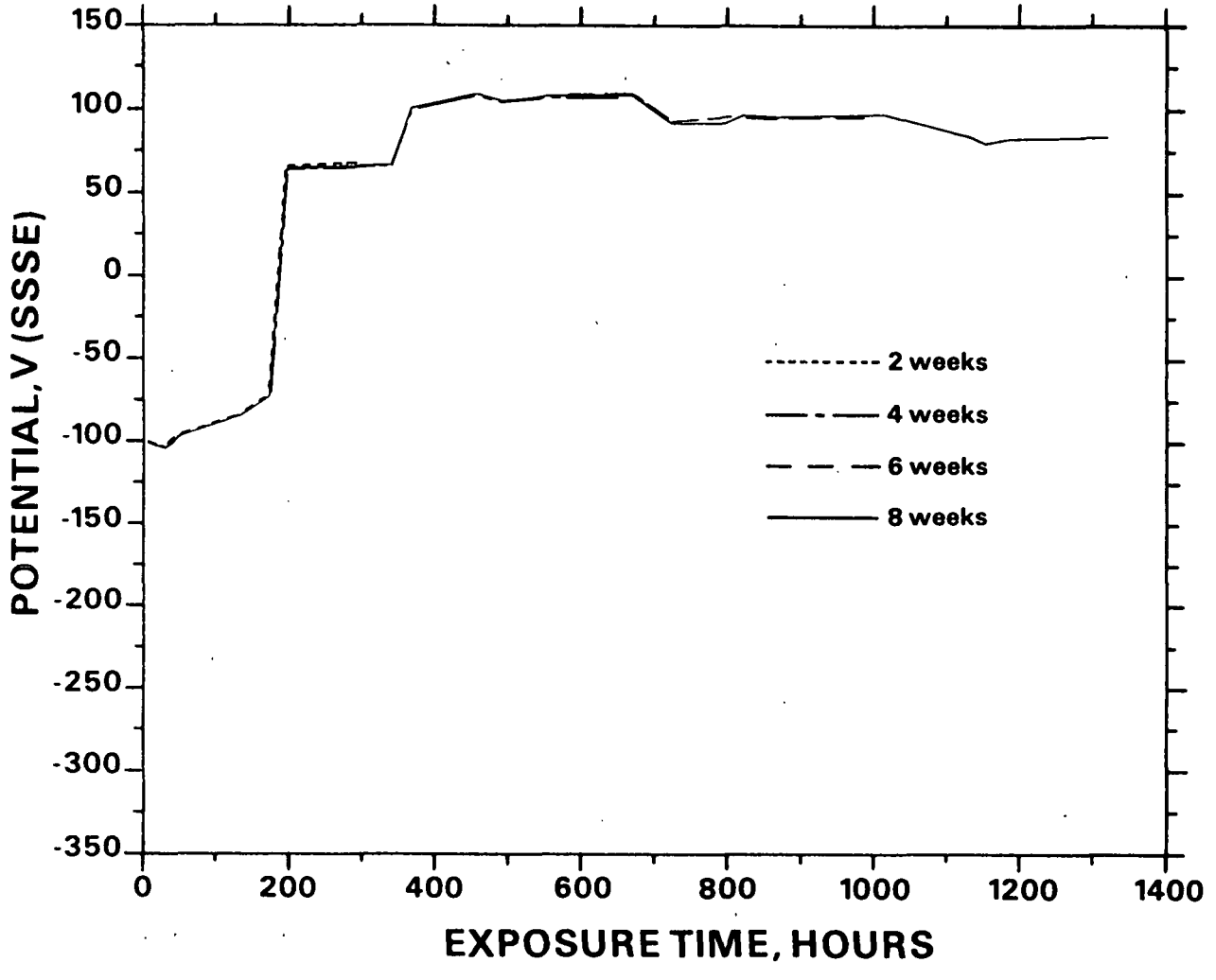

Figure AII-25. Corrosion potential in 60 g/L NaOH + 10 g/L Na_2S + 50 g/L $Na_2S_2O_3$. Similar behavior was observed in solutions of the following compositions:

NaOH, g/L	Na_2S, g/L	$Na_2S_2O_3$, g/L
80	10	25
80	10	50
100	10	25
100	10	50
120	10	25
120	10	50

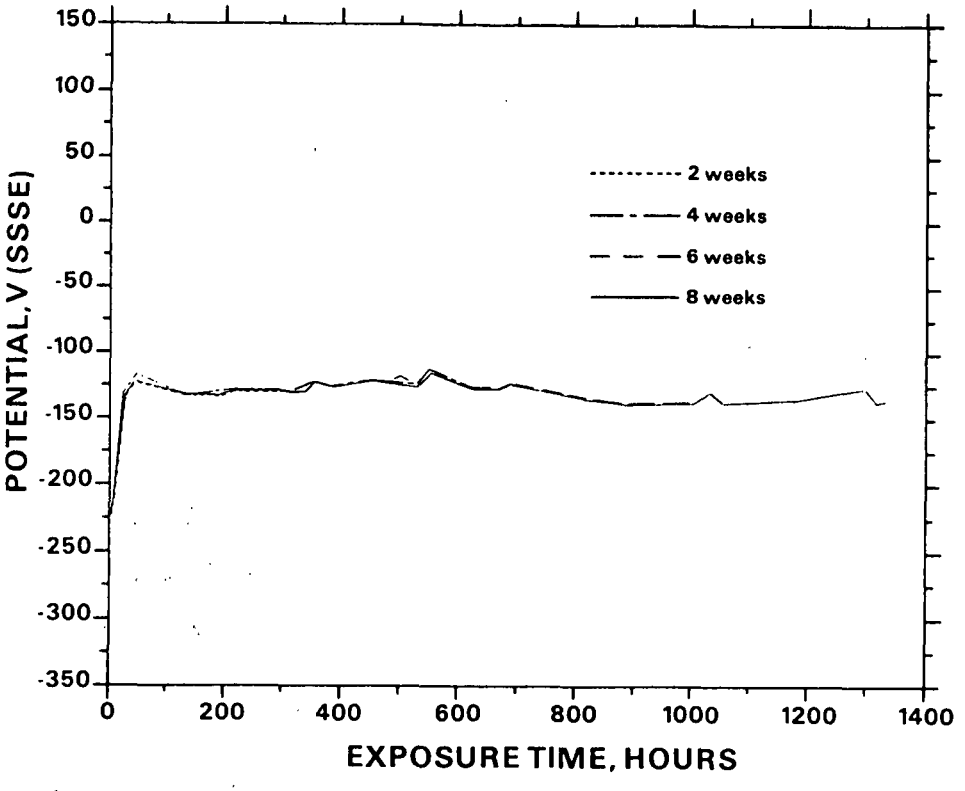

Figure AII-26. Corrosion potential in 60 g/L NaOH + 20 g/L Na_2S + 2.5 g/L $Na_2S_2O_3$. Similar behavior was observed in solutions of the following compositions:

NaOH, g/L	Na_2S, g/L	$Na_2S_2O_3$, g/L
60	20	5
60	20	10
60	20	25
60	20	50
60	30	2.5
60	30	5
60	30	10
60	30	50
60	40	25
60	40	50
80	20	10
80	20	25
80	20	50
80	30	25
80	40	25
80	40	50

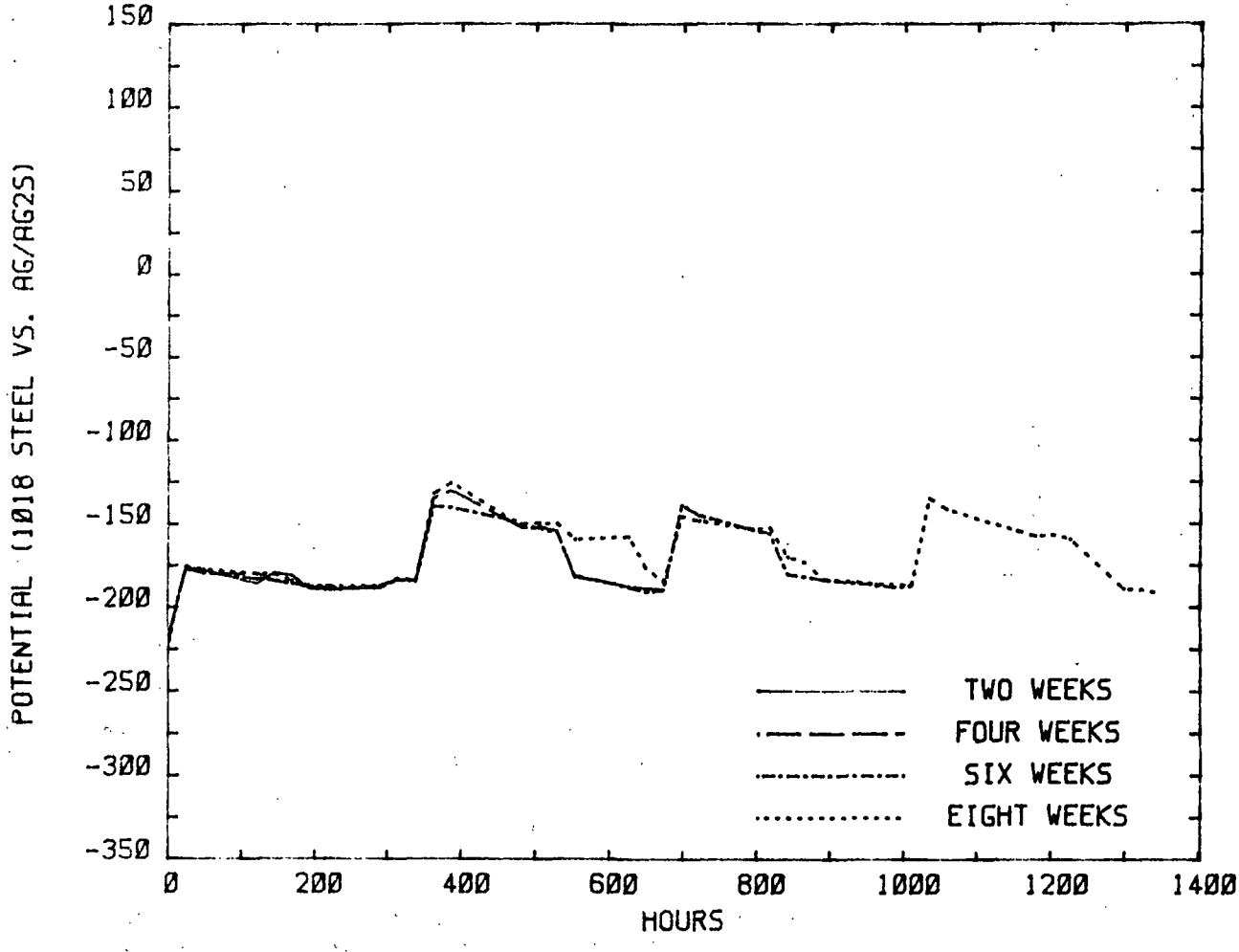

Figure AII-28. Corrosion potential in 60 g/L NaOH + 40 g/L Na_2S + 2.5 g/L $Na_2S_2O_3$. Similar behavior was observed in solutions of the following compositions:

NaOH, g/L	Na_2S, g/L	$Na_2S_2O_3$, g/L
60	40	5
60	40	10
80	40	10
100	20	2.5

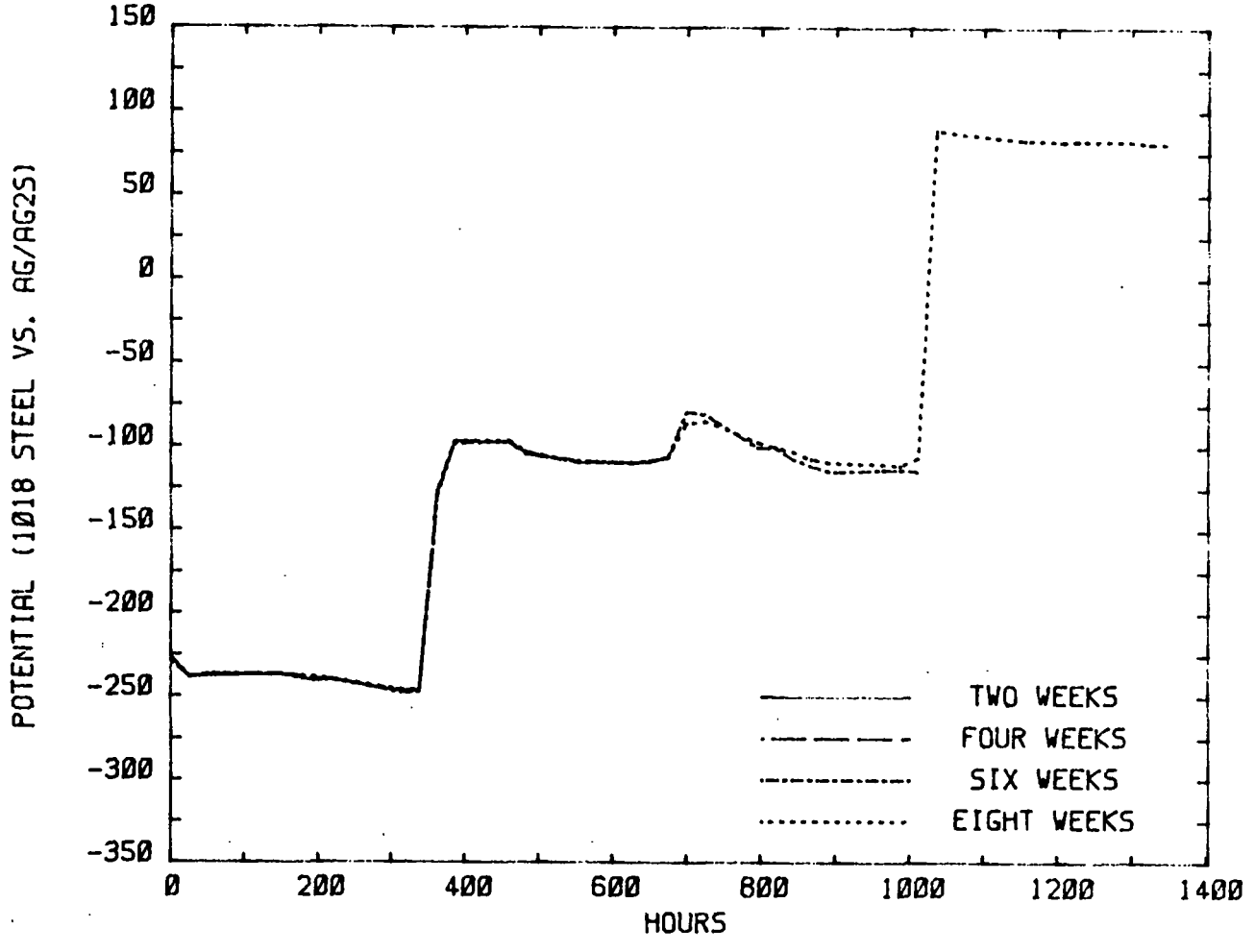

Figure AII-29. Corrosion potential in 80 g/L NaOH + 10 g/L Na_2S + 2.5 g/L $Na_2S_2O_3$. Similar behavior was observed in solutions of the following compositions:

NaOH, g/L	Na_2S, g/L	$Na_2S_2O_3$, g/L
80	10	5
80	10	10
80	30	5
80	40	5
100	10	2.5
100	10	5
100	20	5
100	10	10

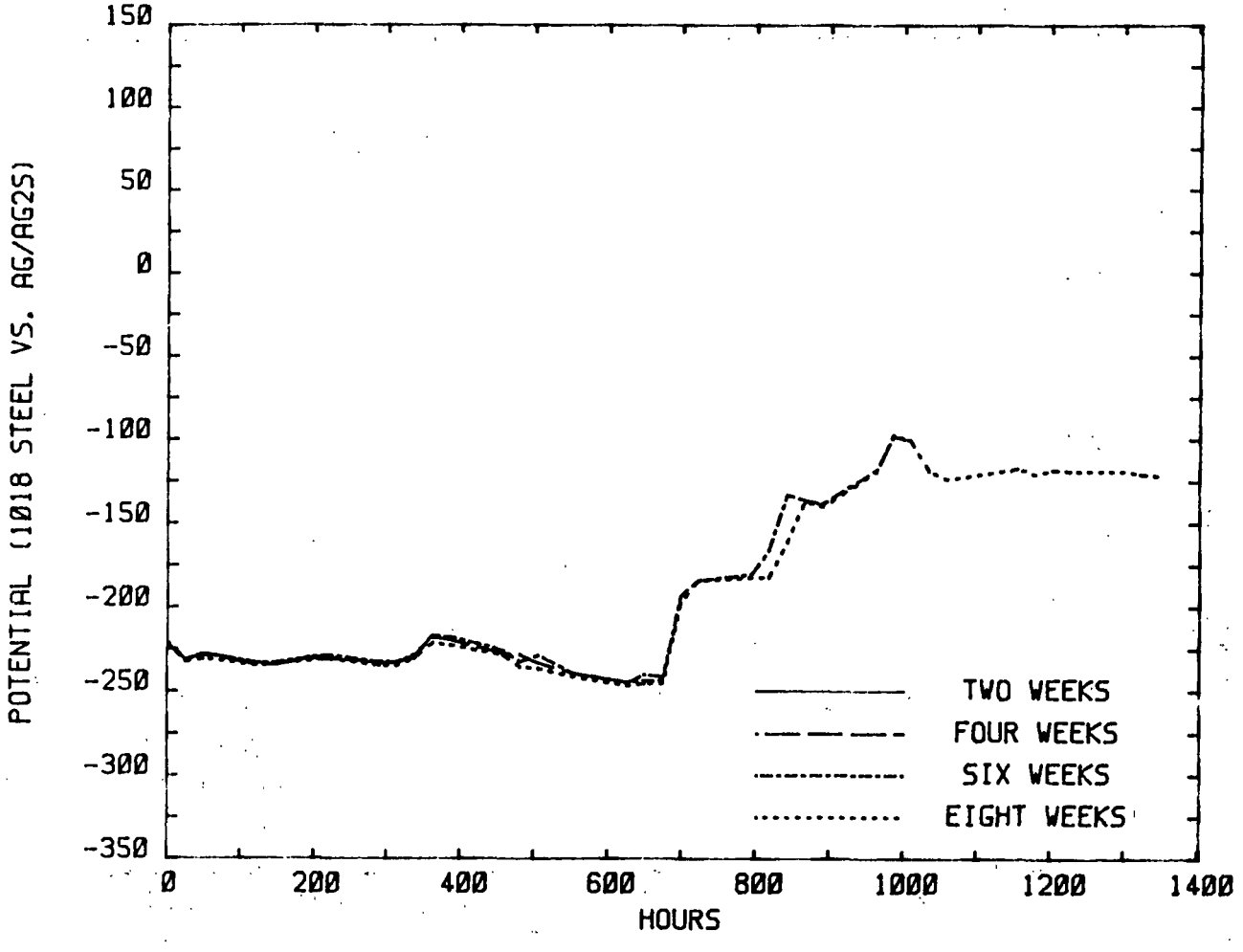

Figure AII-30. Corrosion potential in 80 g/L NaOH + 20 g/L Na_2S + 2.5 g/L $Na_2S_2O_3$. Similar behavior was observed in solutions of the following compositions:

NaOH, g/L	Na_2S, g/L	$Na_2S_2O_3$, g/L
80	20	5
100	10	2.5
100	30	5
100	40	10

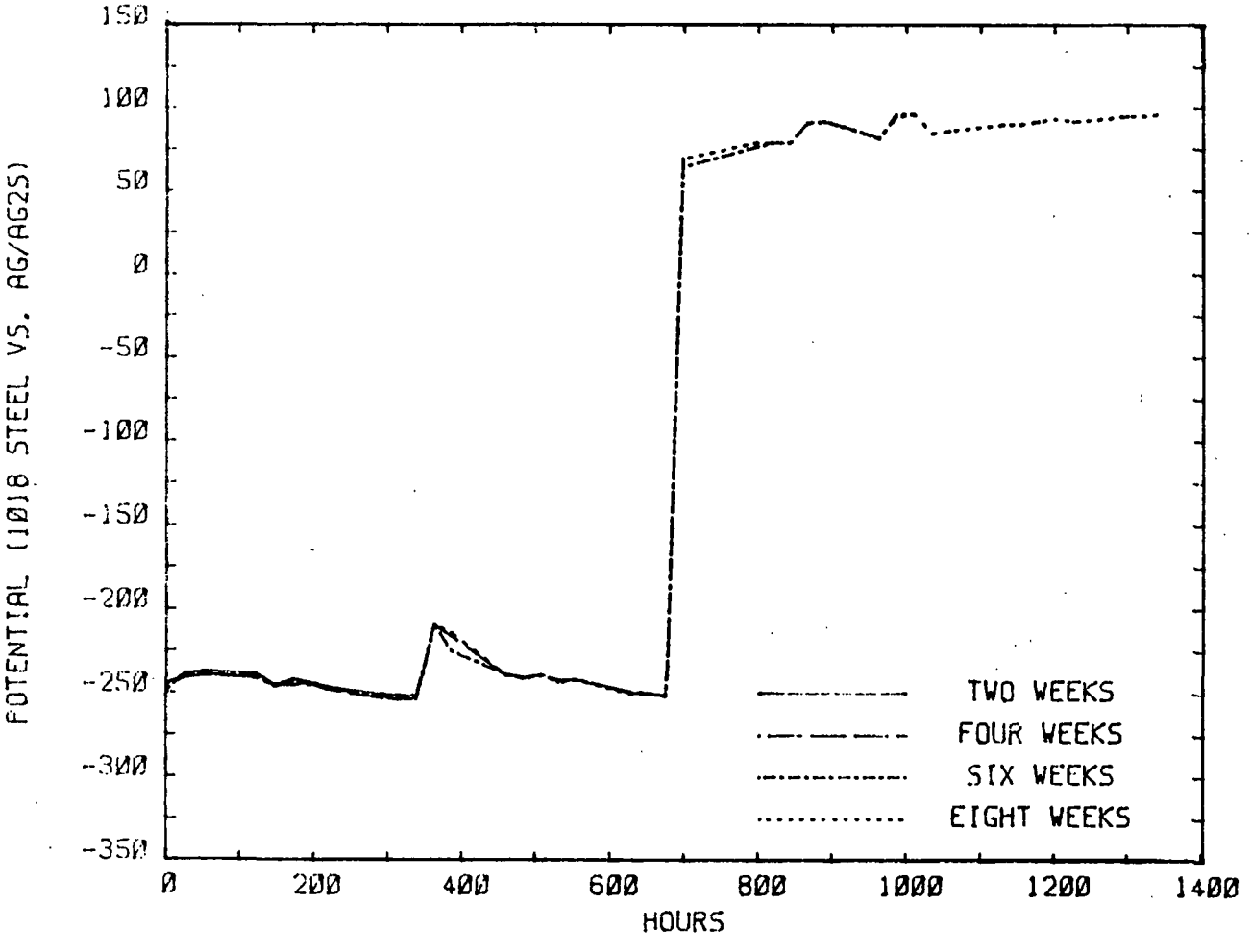

Figure AII-31. Corrosion potential in 80 g/L NaOH + 30 g/L Na_2S + 2.5 g/L $Na_2S_2O_3$. Similar behavior was observed in solutions of the following compositions:

NaOH, g/L	Na_2S, g/L	$Na_2S_2O_3$, g/L
80	40	2.5
100	40	2.5
100	40	5
120	20	2.5

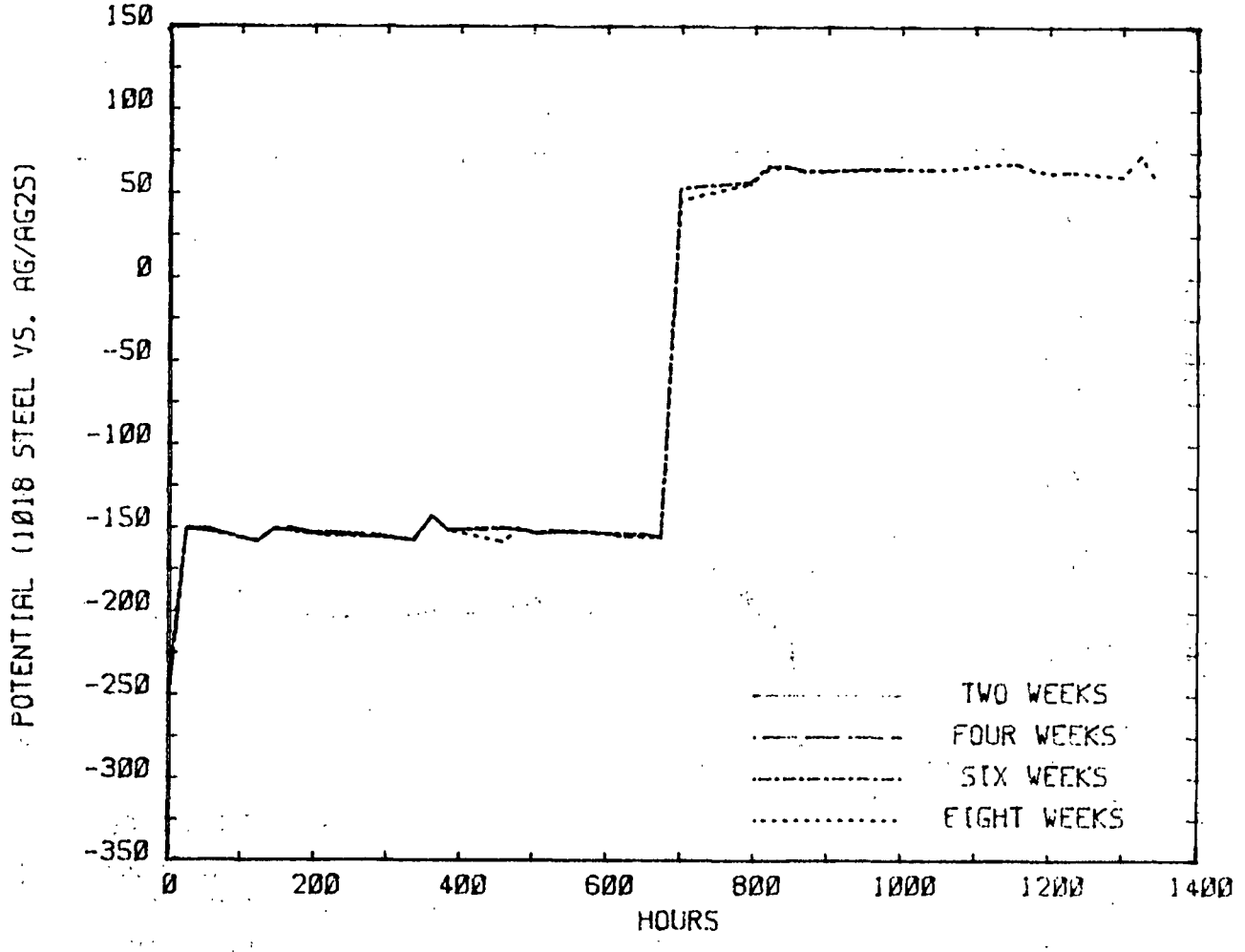

Figure AII-32. Corrosion potential in 80 g/L NaOH + 30 g/L Na_2S + 10 g/L $Na_2S_2O_3$. Similar behavior was observed in solutions of the following compositions:

NaOH, g/L	Na_2S, g/L	$Na_2S_2O_3$, g/L
80	30	25
80	30	50

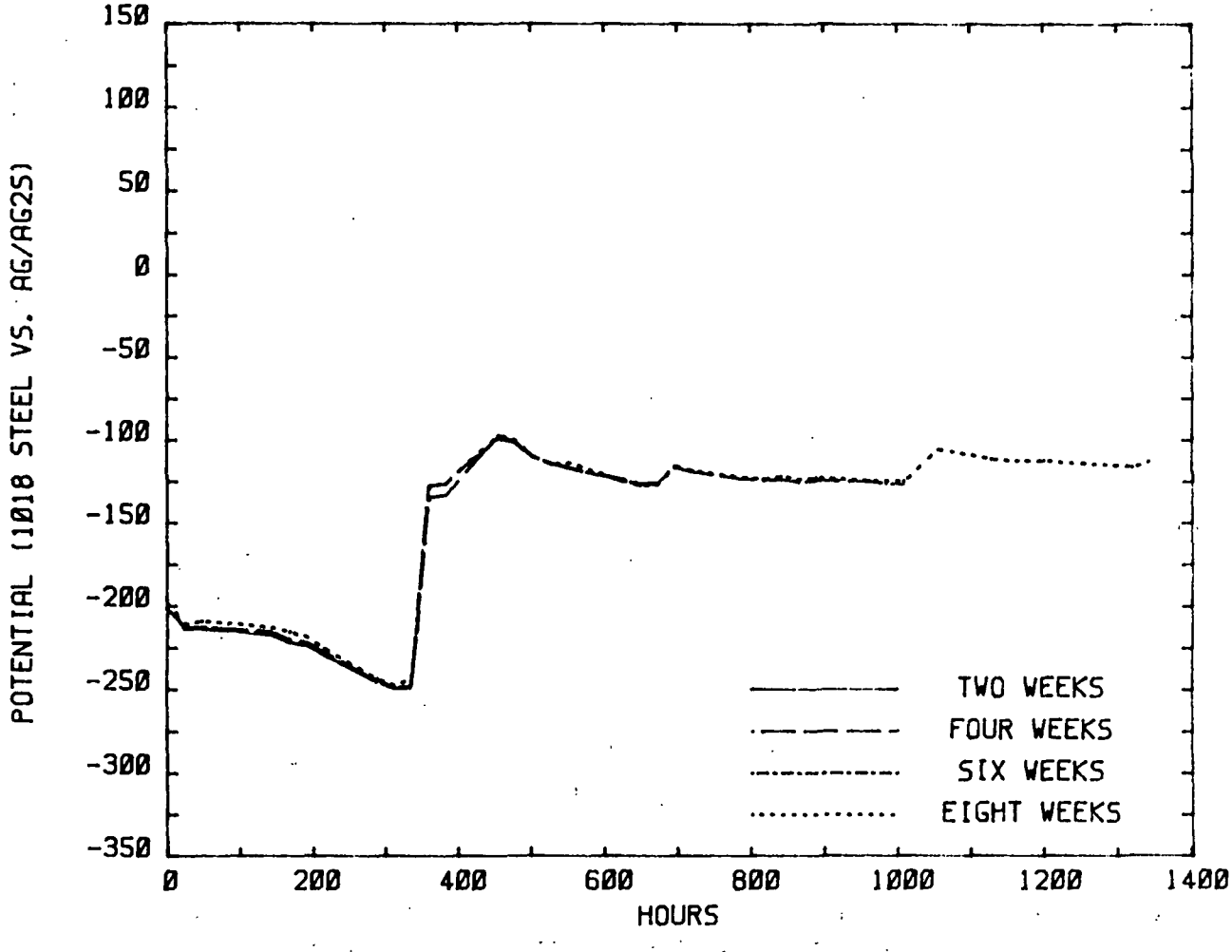

Figure AII-33. Corrosion potential in 100 g/L NaOH + 20 g/L Na_2S + 10 g/L $Na_2S_2O_3$.

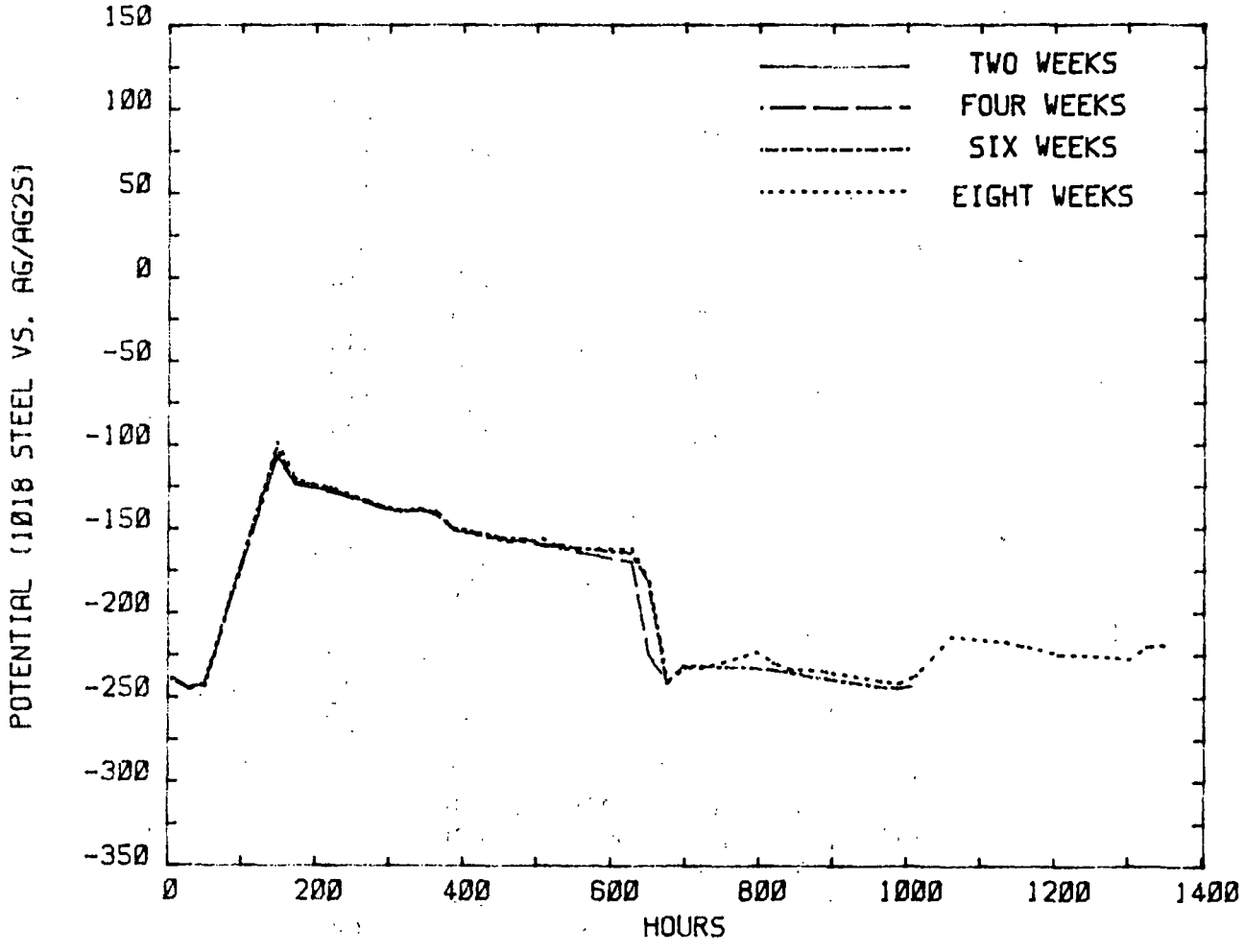

Figure AII-34. Corrosion potential in 100 g/L NaOH + 30 g/L Na_2S + 2.5 g/L $Na_2S_2O_3$. Similar behavior was observed in 100 g/L NaOH + 30 g/L Na_2S + 10 g/L $Na_2S_2O_3$.

APPENDIX III

DATA FROM POLARIZATION CURVES

SOLUTIONS WITH SULFUR ADDITIONS

Table AIII-1. Data from polarization curves. A. Solutions with sulfur additions; polarization curves on gold.

NaOH	Na_2S	S	Anodic E_{CORR}	β_A	Cathodic E_{CORR}	β_C	β_C	β_C
60	10	0	112		108	266		
		0.5	116		118	114		
		1	116		118	95		
		1.5	114		114	106		
		2	114		114	110		
		5	100		100	114		
		10	96		98	114		
60	20	0	104		108	311		
		0.5	116	104	118	110		
		1	118	97	118	108		
		1.5	114	90	116	114		
		2	118	86	120	120		
		5	116	69	114	140		
		10	112	81	112	133		
60	30	0	94		102			
		0.5	104	114	104	112		
		1	102	93	100	98		
		1.5	96		102			
		2	94	110	92	106		
		5	86	66	84	124		
		10	134	66	134	95		
60	40	0	100		62			
		0.5	109	106	108	91		
		1	110	100	110	91		
		1.5	96		104	110		
		2	102	106	104	104		
		5	106	66	106	130		
		10	92	66	80	104		
80	10	0	96	114	104	150		
		0.5	122	88	124	102		
		1	120	88	118	95		
		1.5	122	81	122	112		
		2	122	75	122	112		
		5	124		124	95		
		10	128		126	106		

Table AIII-1 (Continued). Data from polarization curves. A. Solutions with sulfur additions; polarization curves on gold.

NaOH	Na_2S	S	Anodic E_{CORR}	β_A	Cathodic E_{CORR}	β_C	β_C	β_C
80	20	0	90	118	96	193		36
		0.5	92	102	94	124		
		1	90	106	92	104		
		1.5	128	75	122	140		
		2	130	74	130	126		
		5	134	66	134	114		
		10	100	53	100	102		
80	30	0	82	135	94	250		34
		0.5	118	106	114		89	
		1	112	81	114	131		
		1.5	122	60	122	145	124	
		2	120	56	122	126	78	
		5	132	73	130	135	88	
		10	124	73	120	131	85	
80	40	0	86	122	84	225		36
		0.5	102	107	98		88	
		1	110	71	114	208		41
		1.5	116	70	118	135	89	
		2	126	71	124	142		
		5	118	57	120	124	78	
		10	132	73	130	135	91	
100	10	0	126	107	128			39
		0.5	112	—	114			34
		1	122	55	124	153		
		1.5	132	—	132	167		
		2	124	57	126	164		
		5	136	53	134	161		
		10	138	114	138			33
100	20	0	118		122	122		
		0.5	122	66	122	278		47
		1	126	69	126	217		
		1.5	124	78	124	134		
		2	126	66	126	165		
		5	126	60	126	135		
		10	128	56	128	174		
100	30	0	112	60/118	106			33
		0.5	112	75/114	114			44
		1	124	69	122	167		
		1.5	122	71	122	190	114	
		2	126	64	124	149		
		5	130	58	130	149		
		10	134	56	136	149		
100	40	0	88	85	110			39

Table AIII-2. Polarization curves of steel.

NaOH	Na_2S	S	Anodic E_{CORR}	β_A	Cathodic E_{CORR}	β_C	Anodic Peaks A	B	C	D	E	F
60	10	0	-254	45	-242	284	-137	-27		89	198	
		0.5	-82	—	-74	—		-50				
		1	116	—	116	—						
		1.5	114	—	114	—						
		2	112	—	114	—						
		5	100	—	102	—						
		10	96	—	116	—						
60	20	0	-244	45	-282	108	-140		20	80		
		0.5	-90	—	-90	—			0			
		1	-90	—	-86	—		-89	1	40		
		1.5	-90	34	-82	—		-29	7	130		344
		2	-84	57	-84	—		-30	5	129		346
		5	116	—	114	—						
		10	112	—	112	—						
60	30	0	-242	—	-192	—	-136	-21		98		
		0.5	-116	36	-98	—		-42		116		
		1	-104	28	-74	—		-48		106		
		1.5	-158	—	-142	—		-25				
		2	-126	28	-128	—		-53		112		
		5	86	—	84	—						
		10	136	150	136	—						
60	40	0	-238	59	-242	108	-133	-21				
		0.5	-100	19	-104	—	-99					
		1	-98	49	-100	—			17		137	
		1.5	-146	—	-144	—		-48				
		2	-108	—	-110	—		-57		119		
		5	58	—	42	—				103		
		10	86	—	84	—						
80	10	0	-248	65	-246	—	-143	-37		65	165	
		0.5	-80	—	-84	—		-48				
		1	120	83	120	—						
		1.5	122	—	120	—						311
		2	122	—	122	—						
		5	124	62	124	114						
		10	130	—	130	118						
80	20	0	-246	63	-248	122	-137		-9	73	167	
		0.5	-124	—	-124	—		-34		99		
		1	-290	—	-120	—	-169	-67	11	90	139	
		1.5	124	—	122	91						
		2	132	—	128	93						
		5	134	—	132	108						
		10	100	—	98	120						

Table AIII-2 (Continued). Polarization curves of steel.

NaOH	Na_2S	S	Anodic E_{CORR}	β_A	Cathodic E_{CORR}	β_C	Anodic Peaks A	B	C	D	E	F
80	30	0	-248	69	-182	131	-140		4	70		
		0.5	-102	—	-104	—		-20				
		1	28	—	0	—						
		1.5	58	—	60	—						
		2	60	—	66	—						
		5	52	—	52	—					143	
		10	48	—	46	—						
80	40	0	-224	66	-220	127						
		0.5	-124	—	-124	—			0			
		1	-166	98	-166	—		-34				334
		1.5	-152	—	-150	—	-93	-51		103		348
		2	-158	—	-164	—	-116			67		
		5	-116	—	-150	—				72		
		10	42	—	42	—						
100	10	0	-260	—	-260	—	-142	-41		76	222	
		0.5	-142	—	-144	—	-86				213	
		1	-144	—	-156	—	-125		28	79		
		1.5	84	—	-130	—						
		2	60	—	52	—						
		5	52	—	50	—						
		10	142	—	142	—						
100	20	0	-256	43	-258	114	-137	-43		69		
		0.5	-104	—	-104	—		-50		101		
		1	-94	—	-92	—		-57		105		
		1.5	-90	—	-92	170		-61		109		
		2	-84	49	-86	205		-54	24	132		277
		5	132	80	136	—						
		10	136	112	136	104						
100	30	0	-254	78	-254	94	-137	-42			191	
		0.5	-204	19	-202	—	-145	-41	50			260
		1	-108	—	-108	—	-97	-44		123		
		1.5	122	158	104	—						
		2	-100	—	-98	—		-69	-6	100		
		5	-90	—	-80	—		-54		106	180	325
		10	134	—	136	—						
100	40	0	-252	66	-254	95		-37				

Table AIII-3. Polarization curves on gold.

NaOH	Na_2S	$Na_2S_2O_3$	Anodic E_{CORR}	β_A	Cathodic E_{CORR}	β_C	β_C
60	10	0	128	36	118		40
		2.5	128	57	127		45
		5	128		132	370	50
		10	116		112	161	52
		25	138		120	167	60
		50	120	49	126	190	66
60	20	0	130	58	138		40
		2.5	118	55	122	393	42
		5	132	50	130	505	45
		10	118	52	112		48
		25	114	53	112	190	47
		50	114	50	116	163	58
60	30	0	118	61	116		40
		2.5	126	56	122		41
		5	112	56	116		44
		10	120	55	118		52
		25	114	58	110	173	50
		50	110	53	110	161	60
60	40	0	108	55	112		36
		2.5	116	57	112		44
		5	118	60	122		45
		10	110	57	112	208	49
		25	114	61	120	235	58
		50	114	58	114	170	69
80	10	0	138		136		37
		2.5	140	48	136		45
		5	126	45	134	310	48
		10	142	57	140	255	52
		25	130	58	132	255	60
		50	136	41	126	201	78
80	20	0	136	53	126		41
		2.5	122	56	120	417	43
		5	128	83	132	319	49
		10	114	75	124	250	56
		25	122	54	114		56
		50	112		118		67
80	30	2.5	152	57	124	352	41
		5	146	63	126	417	49
		10	128	60	108	505	44
		25	136	56	120	290	64
		50	104	61	118	183	61

Table AIII-3 (Continued). Polarization curves on gold.

NaOH	Na_2S	$Na_2S_2O_3$	Anodic E_{CORR}	β_A	Cathodic E_{CORR}	β_C	β_C
80	40	2.5	106	78	118	335	47
		5	112	74	110	278	45
		10	110	69	110	212	57
		25	102	66	110	170	56
		50	100	66	108	161	73
100	10	2.5	182	57	136	393	42
		5	142		126	250	48
		10	130	47	138		44
		25	114	48	128	235	57
		50	114	56	130	201	60
100	20	2.5	138	63	122	319	45
		5	126	60	116	230	28
		10	112	45	118	239	52
		25	110	57	124	216	56
		50	102	55	118	193	70
100	30	2.5	106	61	118	335	41
		5	110	66	116	250	53
		10	114	69	114	235	57
		25	104	66	118	201	69
		50	114	64	120	180	55
100	40	2.5	102	75	114	255	47
		5	92	72	106	235	44
		10	102	67	114	240	52
		25	110	69	116	255	63
		50	102	69	108	156	70
120	10	2.5	120	66	142	472	42
		5	116	60	136	393	44
		10		60		319	48
		25		55		208	57
		50		52		173	66
120	20	2.5		63		300	45

Table AIII-4. Polarization curves of steel.

NaOH	Na_2S	$Na_2S_2O_3$	Anodic E_{CORR}	β_A	Cathodic E_{CORR}	β_C	Anodic Peaks βA	B	C	D	E	F
60	10	0	-260	40	-262	94	-150	-44	82	175		
		2.5	-250	--	-252	78	-151	-42	77			
		5	-216	--	-214	--	-154	-44	62	179	261	
		10	-102	--	-98	--		-49	107	174		
		25	-92	--	-90	102		-54	97	143	282	
		50	-90	13	-88	--		-53	111	169	247	
60	20	0	-240	69	-250	126	-152	-45	72	182		
		2.5	-232	79	-230	--	-149	-50	72	180		
		5	-222	78	-224	--	-151	-47	67	175		
		10	-174	--	-108	--	-139	-46	118			
		25	-110	23	-112	50		-51				
		50	-114	20	-120	78		-53				
60	30	0	-238	66	-238	88	-144	-42				
		2.5	-232	74	-234	167	-146	-41	74			
		5	-230	77	-228	161	-146	-44	79			
		10	-122	--	-138	--		-47				
		25	-104	--	-128	--		-58	97			
		50	-128	--	-120	--		-56				
60	40	0	-242	69	-244	93		-36				
		2.5	-224	91	-228	170		-37				
		5	-170	--	-202	--		-38				
		10	-140	--	-114	72		-41				
		25	-132	--	-128	--		-39				
		50	-122	--	-120	--		-42				
80	10	0	-246	33	-246	83	-152	-49		159		
		2.5	-234	53	-232	--	-154	-54	55	155		
		5	-102	27	-100	98		-53		166	244	
		10	-206	53	-212	205	-154	-50	55	165	244	
		25	-100	34	-98	120		-52		170	247	
		50	-104	--	-110			-63	94	173	242	
80	20	0	-240	66	-242	170	-149	-51	63			
		2.5	-224	63	-232	176	-151	-53	65	168		
		5	-204	20	-202	--	-149	-51	55		261	
		10	-128	27	-194	335		-59			257	
		25	-118	20	-118	67		-59			255	
		50	-112	--	-110	88		-59			259	
80	30	2.5	-210	57	-216	255		-39				
		5	-186	37	-204	393	-145	-39			269	
		10	-190	--	-192	--	-165	-39	58		266	
		25	-126	--	-128	--		-56			263	
		50	-116	--	-114	57		-52	96		269	

Table AIII-4 (Continued). Polarization curves of steel.

NaOH	Na_2S	$Na_2S_2O_3$	Anodic E_{CORR}	β_A	Cathodic E_{CORR}	β_C	Anodic Peaks βA	B	C	D	E	F
80	40	2.5	-204	48	-216	335		-50				
		5	-200	49	-196	112					236	
		10	-166	--	-182	98	-146				271	
		25	-132	--	-132	78	-111	-41			269	
		50	-126	28	-132	94		-59		113	270	
100	10	2.5	-234	49	-234	--	-160	-59	45	145		
		5	-214	52	-208	34	-157	-57	48	159	246	
		10	-218	53	-216	230	-159	-56	40	155	251	
		25	-206	50	-204	190	-157	-54	43	159	241	
		50	-100	19	-106	118		-65				
100	20	2.5	-218	53	-218	--	-147	-47	49		257	
		5	-226	55	-224	--	-150	-53	48		259	
		10	-212	50	-210	255	-146	-49	46	190	255	
		25	-186	--	-186	78		-47	35		254	
		50	-118	--	-116	104		-60			264	
100	30	2.5	-232	54	-234	180	-146	-45	45	192		
		5	-202	49	-202	167	-143	-43			258	
		10	-194	--	-194	--	-146	-43	91		259	
		25	-128	--	-136	--		-47	91		263	
		50	-124	--	-120	44	-102	-52	100		265	
100	40	2.5	-206	55	-208	--		-40				
		5	-204	54	-204	142		-42			263	
		10	-180	86	-180	--		-41			261	
		25	-169	88	-166	116		-59	85		251	
		50	-138	36	-140	110		-50	83			
120	10	2.5	-246	42	-244	278	-162	-59	31			
		5	-232	--	-230	--	-162	-59	33	143		
		10		41		205						
		25		--		--						
		50		--		--						
120	20	2.5		47		--						

THE INSTITUTE OF PAPER CHEMISTRY

Appleton, Wisconsin

Status Report

to the

ENGINEERING PROJECT ADVISORY COMMITTEE

Project 3309

FUNDAMENTALS OF CORROSION CONTROL IN PAPER MILLS

September 11, 1985

PROJECT SUMMARY FORM

DATE: September 11, 1985

PROJECT NO. 3309 - Fundamentals of Corrosion Control in Paper Mills

IPC GOAL: Increase the useful life of equipment by proper selection of materials of construction and by identifying suitable process conditions

OBJECTIVE: Improve the life of paper machine suction rolls by corrosion and corrosion fatigue studies to establish failure mechanisms and to identify characteristics of improved materials.

CURRENT FISCAL BUDGET: $150,000

SUMMARY OF RESULTS SINCE LAST REPORT: (February, 1985 - August, 1985)

Measurements of fatigue crack growth rates have begun in an effort to determine if either the near-threshold or rapid growth regimes controls the service performance of suction roll alloys. Crack growth tests have been conducted on two commercial suction roll alloys which differ greatly in their resistance to crack growth in service. Tests have been performed using different simulated paper machine white waters. Two stress levels have been examined in an attempt to characterize the effects of residual stresses (in the suction roll) on corrosion fatigue resistance.

In a simulated white water containing 1000 ppm Cl-, Alloy 75 — a suction roll alloy with a good service record — exhibited a lower crack growth rate and a lower threshold stress than Alloy 63 — an alloy with an inferior service record. Thus, the crack growth rate continues to be a candidate indicator of relative resistance to corrosion-assisted cracking in the field.

Crack growth rates and threshold stress intensity values are not strongly affected by the composition of the simulated white waters examined thus far. The crack growth behavior in air and in white waters containing parts per million levels of chlorides, sulfates, and thiosulfates are nearly identical.

High mean stress levels increased the crack growth rate but did not affect threshold stress levels for crack propagation in Alloy 75 exposed to simulated white waters.

Efforts to compare different methods of S-N curve generation are continuing. Rotating bending and alternating bending methods are now available for corrosion fatigue testing of suction roll alloys.

SUMMARY OF RESULTS SINCE LAST REPORT: (Contd.)

Slow strain rate tests to examine stress corrosion resistance of suction roll alloys (as a predictor of service performance) have been initiated.

Testing to assess pitting corrosion resistance as a predictor of service performance has begun anew.

Five suction roll alloys have now been procured in quantities sufficient for mechanical testing, including three with relatively good service histories — Beloit/Sandusky Alloy 75, Valmet/Kubota Alloy 378, and Avesta 3RE60 — and two with numerous instances of cracking in service — Beloit/Sandusky Alloy 63 and Valmet/Kubota Alloy 171.

INTRODUCTION

Corrosion-assisted cracking of suction press rolls continues to be a costly problem in paper mills. Garner (1) has documented the large number of suction rolls that have failed in recent years. The mode of failure appears to be one of corrosion fatigue crack propagation from hole to hole in a circumferential direction. Fatigue stresses arise from the rotation of the roll under nip loading and other loading conditions. Residual stresses present in the rolls as a result of maunufacturing have also been implicated as contributing to the driving force for crack propagation.

A combination of events has contributed to the large number of suction roll failures resulting from corrosion-assisted initiation and growth of cracks. Paper machines are running faster, resulting in more fatigue cycles applied to a roll in a given time period. Faster running speeds have also led to higher nip pressures and multiple nip configurations, both of which tend to increase the magnitude of the cyclic stresses applied to suction rolls. Average paper machine widths are also increasing, and the greater distance between bearing points also increases the stress in the roll. Changes to polymeric fabrics — with the correponding need for extensive cleaning — and removal of zinc cations from hydrosulfite bleaches may also have had a detrimental effect on suction roll performance. Finally, increased closure of paper machines has led to more aggressive paper machine white waters in contact with the rolls. These events have led to a dramatic increase in suction roll failures in the preceding decade, although recent failures have declined to some extent.

While there may be other avenues for improving the lifetime of suction rolls in service, the most attractive remedy appears to be the development of roll alloys with improved resistance to corrosion-assisted cracking. Recent

development of suction roll alloys with a two phase metallurgical structure and low residual stresses has resulted in a marked improvement in the integrity of suction rolls. However, the higher cost of these new materials is an impediment to their widespread utilization.

Development of new generations of suction roll alloys with improved resistance to corrosion-assisted cracking is a high priority for the paper industry, but the path toward improved performance is not straightforward. It is clear that the martensitic stainless steels have higher resistance to corrosion-assisted cracking than the bronze, and the recently developed dual-phase steels have still higher corrosion fatigue resistance. However, these improved alloys were identified by a lengthy trial and error process that has not been guided by a fundamantal understanding of the reasons for roll failure. One reason for the uncertainty is the failure of the common laboratory tests to predict the performance of suction roll alloys in service.

LABORATORY TESTS OF SUCTION ROLL PERFORMANCE

Several different tests are used to screen potential suction roll alloys, in order to identify those that may offer improvements over current generations of alloys. These tests generally determine mechanical strength, corrosion resistance, and resistance to corrosion-assisted fatigue failure. Fatigue failure resistance may be examined by tests to characterize both crack initiation and crack growth under corrosive conditions. A detailed treatment of suction roll testing was presented in a recent progress report issued on this project (2).

Mechanical properties are usually determined by simple tensile tests to determine strength and ductility parameters such as yield strength, tensile

strength, elongation, and reduction in area. Tests may also be conducted to examine the toughness of the candidate alloy through impact testing or fracture mechanics testing. These mechanical properties are important because they affect the size of the roll for a desired loading configuration. Determination of the mechanical properties is reasonably straightforward.

Corrosion resistance is a another important parameter examined in considering a candidate suction roll alloy. An important reason for replacement of bronze suction rolls was the susceptibility of bronze to excessive corrosion of the hole surface at the outside diameter of the shell, as shown in Fig. 1. Corrosion resistance of suction roll alloys is usually examined by exposure tests, with samples of candidate alloys being exposed to simulated or actual paper machine white waters. Under these conditions, bronze alloys experience a high level of uniform attack, while stainless steels are more likely to experience a localized form of attack called pitting, as shown in Fig. 2. Tests to rank pitting resistance usually involve exposure to a white water, followed by visual examination to characterize the number, depth, and morphology of pits appearing on the specimen surface. The electrochemical potential may also be monitored as an indicator of the onset of pitting. Potentials will fall or will oscillate during pitting, whereas pit-resistant alloys will produce a slowly rising potential, as shown in Fig. 3. Resistance to pitting is important because fatigue cracks often initiate at pits as a result of the stress concentration and the agressive electrolytes that develop at pit sites.

A common method for evaluating corrosion fatigue resistance is generation of the S-N curve for the candidate alloy exposed to real or simulated white waters. In this test, a smooth or notched specimen is subjected to an alternating stress, S, in order to intitiate a fatigue crack that will eventually cause

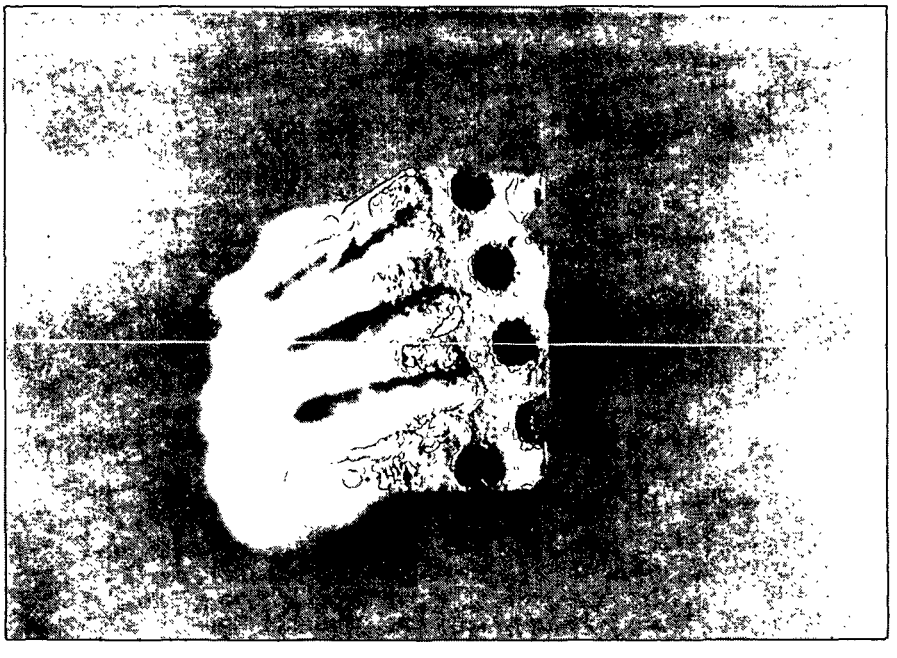

Figure 1. An example of loss of the ligament between adjacent holes in a bronze suction roll during service.

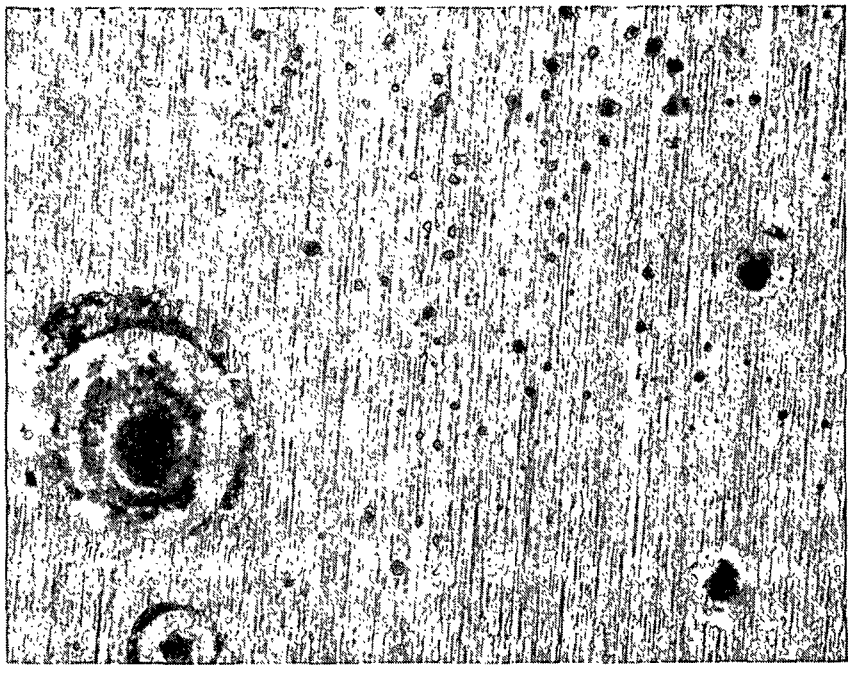

Figure 2. An example of pitting of a stainless steel suction roll alloy during exposure to a simulated paper machine white water.

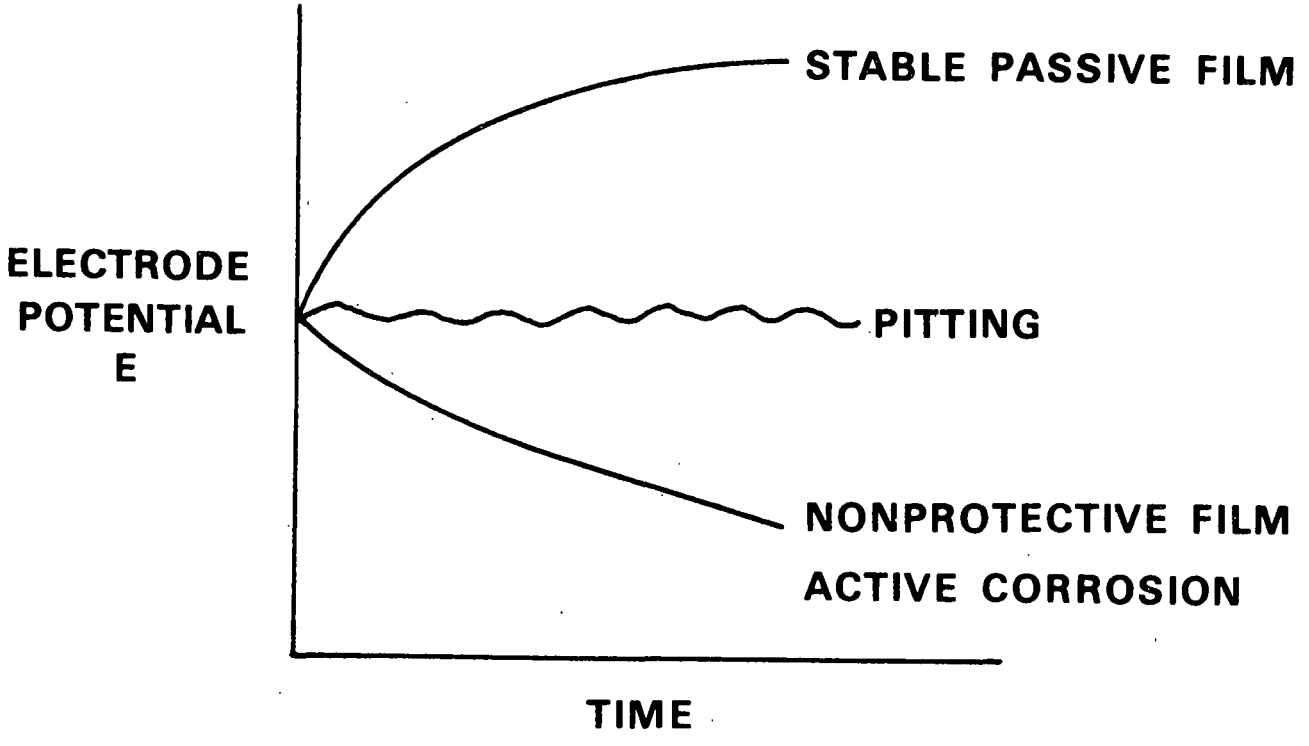

Figure 3. Variation in electrochemical potentials developed at the wetted surfaces of suction roll specimens exposed to a simulated white water.

failure of the specimen in a number of cycles of stress, N. As the magnitude of the alternating stress decreases, the number of cycles that must be applied to cause failure increases, as shown schematically in Fig. 4. The alternating stress that results in failure at some specified number of cycles (usually 10^7, 10^8, or 10^9 cycles to failure) is called the endurance limit at "x" cycles for the material. Cyclic stresses may be imposed in a variety of ways, such as rotating bending, alternating bending, and axial fatigue, as described in ref. 2. A high endurance limit at long lifetimes is thought to be a desirable characteristic in suction roll alloys since it implies that the suction roll fabricated from the alloy will withstand a large number of rotations in service without failure.

The S-N behavior of an alloy is affected by many variables associated with the test, including the mean stress superimposed on the alternating stress pattern, the environment used in the test, the frequency of the applied stress, the presence of multi-axial stress states, the surface finish at the site of failure, and the metallurgical composition and structure of the alloy. In practice, the test conditions used to generate S-N curves in the laboratory must differ from those experienced by actual suction rolls, in order to obtain results in reasonable timeframes. Usually, the frequency of the alternating stress is increased to impose many cycles in a reasonable period of time, but accelerated failure may also be induced by using notched specimens to raise the local stress, by making the test environment more aggressive, etc.

Many investigators have shown that most of the cycles in a long-lived fatigue test ($>10^7$ cycles) are expended in crack initiation. The changes that take place on the surface of a fatigue specimen develop slowly when the alternating stress is approximately equal to the endurance limit. On the other hand,

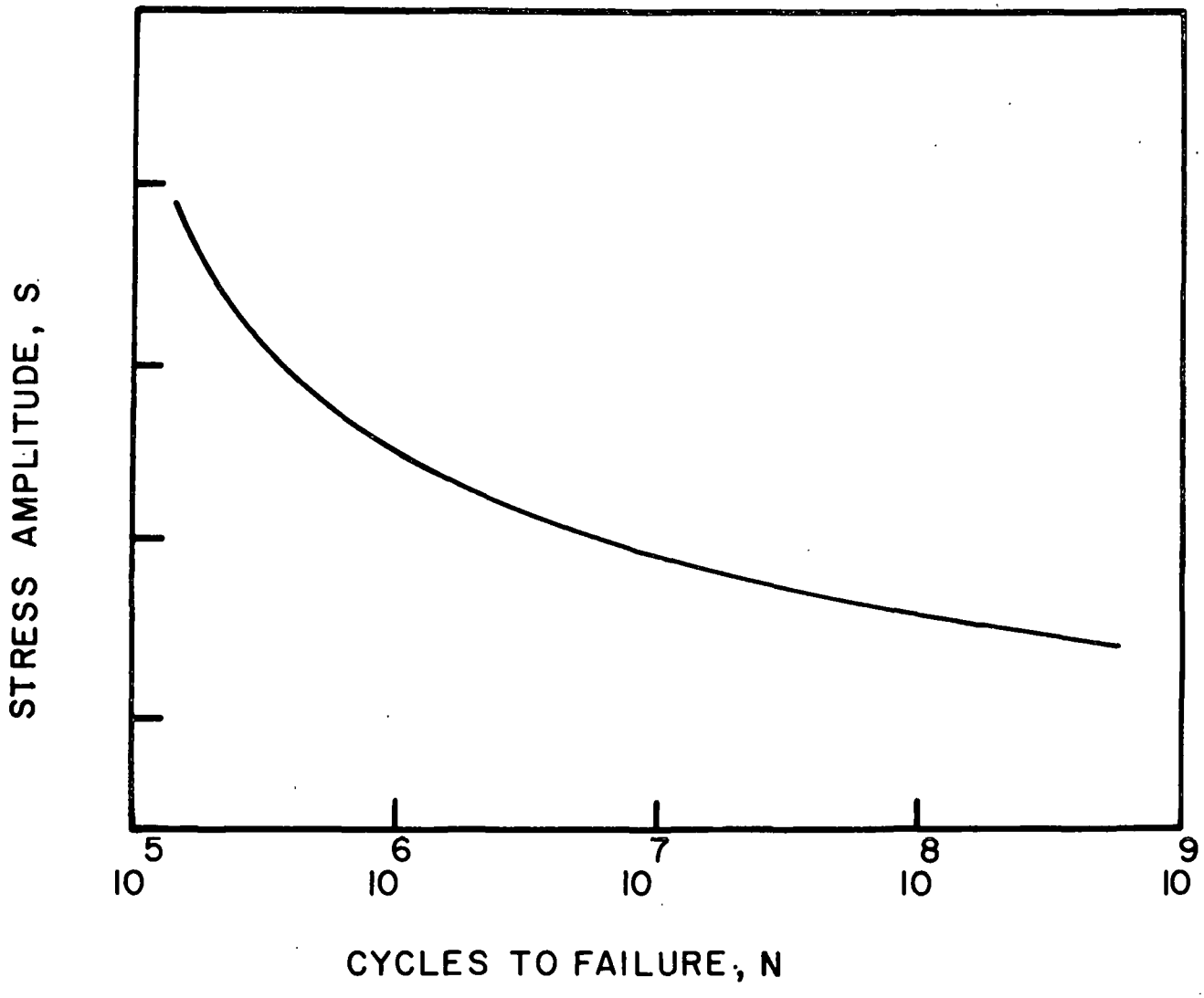

Figure 4. Schematic S-N curve depicting resistance to fatigue crack initiation.

once an initiated crack is visible on the surface of the fatigue specimen, relatively few cycles are expended in propagating the crack through the gage of the specimen to cause failure. Thus, the S-N curve is often considered a measure of the resistance of a material to fatigue crack initiation.

Resistance to fatigue crack propagation is studied directly in another type of fatigue test (3). In this test, the rate of growth of a crack is measured optically during imposition of a fluctuating load on a fracture mechanics type specimen. The rate of crack growth per cycle of applied stress is usually plotted as a function of the applied stress intensity — a measure of the driving force for crack growth. The stress intensity is a product of three terms, each of which affects the rate of crack growth. The first term is the nominal stress range (i.e., the difference between the maximum and minimum applied stress). The second term is the square root of the instantaneous crack length, reflecting the fact that the driving force at a given applied stress is greater if the specimen contains a long, deep crack. The third term in the stress intensity expression is a factor associated with the exact geometry of the test specimen. In practice, fatigue crack growth rate measurements are made on only a few types of specimens for which the stress intensity formulas are well known. The geometry of one such specimen — the compact tension specimen — is shown in Fig. 5, together with the formula for calculating the stress intensity. The stress intensity term is useful because it normalizes crack growth rate data obtained under a variety of load conditions, crack lengths, and specimen geometries.

The dependence of the crack growth rate on the applied cyclic stress intensity is shown schematically in Fig. 6. Note that both axes are logarithmic. Three stages of growth are commonly observed but the crack growth rates

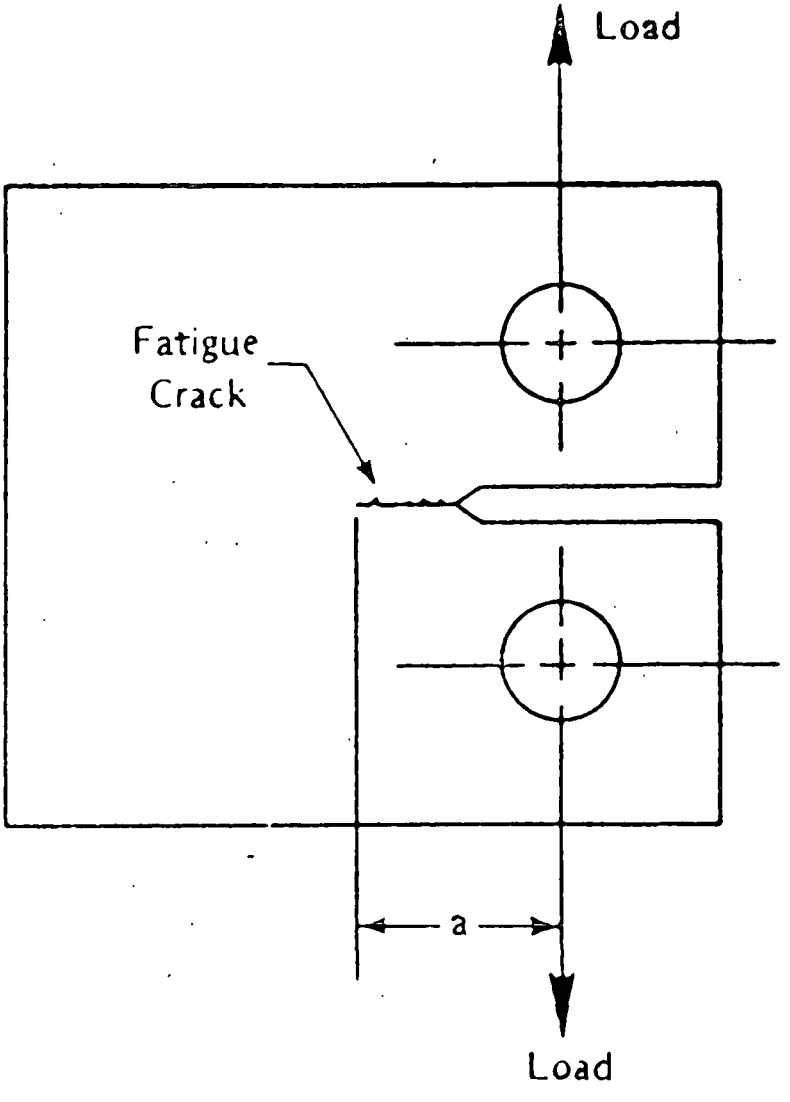

Figure 5. The geometry of a compact tension specimen for crack growth rate testing, together with the formula for calculating the cyclic stress intensity.

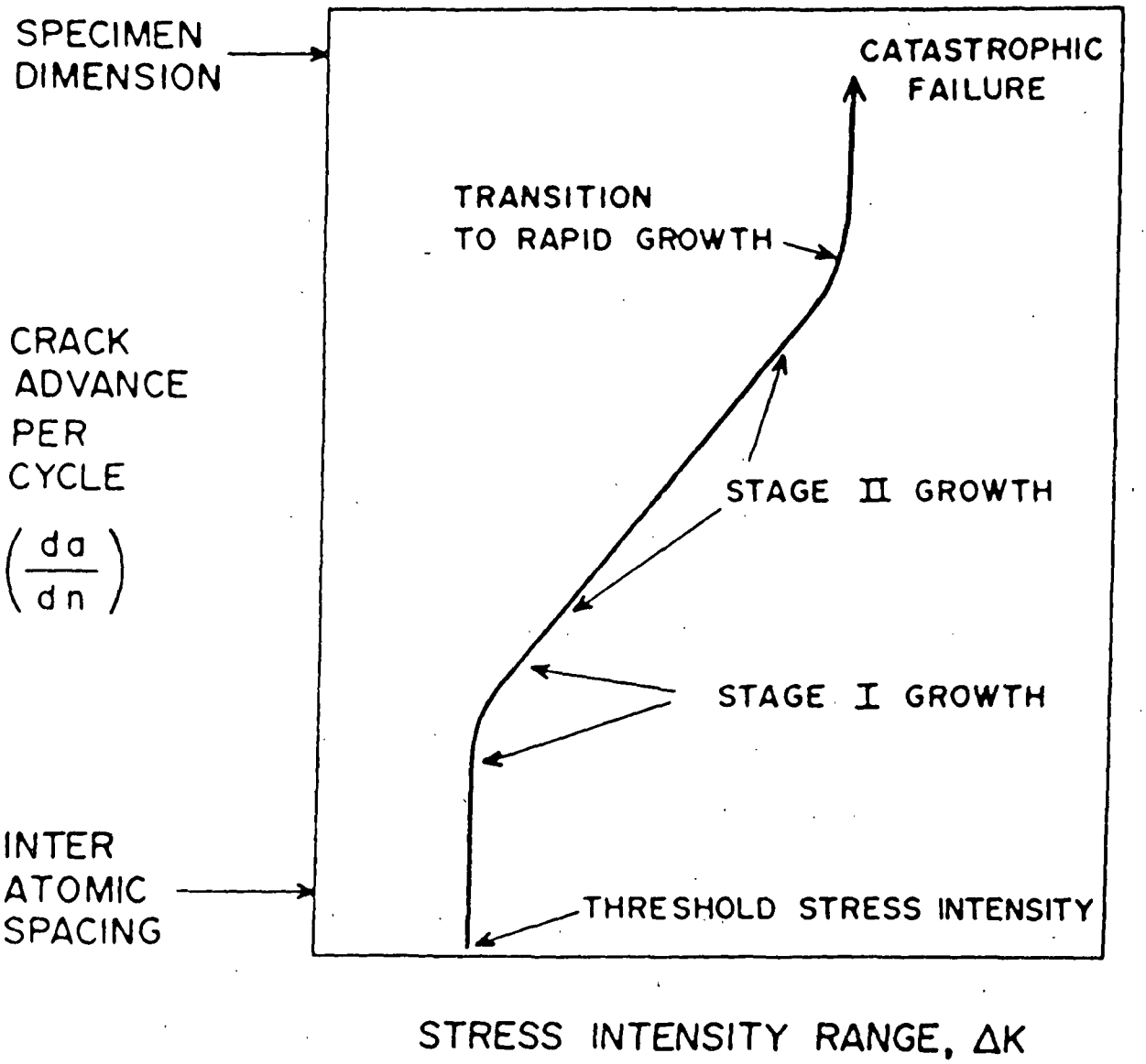

Figure 6. Schematic diagram showing the dependence of crack growth rates on the cyclic stress intensity.

are so high in the third stage that it has little engineering significance. Stage 1, which represents the transition from crack initiation to crack growth, is marked by low growth rates, a strong dependence on the cyclic stress intensity, and a threshold value of ΔK below which growth virtually ceases. Stage 1 cracks are often influenced strongly by the metallurgical composition of the test material, with crack propagation along microstructural features commonly observed. In contrast to Stage 1, Stage 2 growth is more rapid but is less dependent on the stress intensity range. Stage 2 cracks usually propagate at right angles to the direction of the applied load and normally follow paths that are not affected by the metallurgical structure. Both Stages 1 and 2 are affected by many of the variables that affect S-N curves. In particular, corrosive environments can lower the threshold stress and increase the crack growth rate dramatically.

Accurate determination of the threshold stress intensity for crack growth is a complicated matter because different thresholds are obtained depending on the test method. If the threshold is determined by gradually increasing the stress intensity range until crack initiation is detected, the threshold stress intensity will not be reproducible. Moreover, the threshold stresses determined in this fashion will be higher — and therefore not conservative — than those obtained by reducing the stress intensity range for a crack that has already been initiated. The preferred method to determine the threshold stress is the "load-shedding" approach, where the cyclic load is carefully removed in stages from a fracture mechanics specimen as the crack progresses. The load must be shed carefully, in stages, with crack growth stages following load shedding, to avoid the effects of compressive residual stresses introduced at the crack tip during load shedding. If precautionary measures are

not taken, these residual stresses can result in erroneously high values of threshold stress intensity for crack propagation.

Obviously, the preferred characteristics for suction roll alloys would be high threshold stress levels and low crack growth rates. However, there is relatively little to be gained from low crack growth rates in the Stage 2 regime. At typical rates of rotation, a suction roll will accumulate 10^8 stress cycles in one year. Even at growth rates as low as 10^{-8} inch/cycle — on the order of the lowest rates measurable — one inch of crack growth would be experienced in a year of suction roll operation at this stress intensity.

Relatively little attention has been paid to the stress corrosion cracking resistance of suction roll alloys, since it is widely held that corrosion fatigue is the responsible failure mode. However, since there is some evidence that tensile residual stresses degrade suction roll performance, it is plausible that stress corrosion cracking resistance could be important.

A common laboratory test for stress corrosion cracking is the slow strain rate test (SSRT). In this test, a slow tensile test is performed with the specimen immersed in the corrosive environment, to be compared with results of a similar test conducted in an innocuous environment. If the corrosive environment promotes stress corrosion cracking, the test in the corrosive environment will exhibit lost ductility and secondary cracking relative to the test in the inert environment.

LABORATORY PREDICTIONS OF SUCTION ROLL FIELD PERFORMANCE

Current roll alloys have been selected by roll suppliers who have conducted laboratory tests of the strength, corrosion resistance and corrosion-fatigue resistance of the alloys, followed by a trial period where prototype

rolls are tested in service. Although there have been broad correlations relating the results of laboratory tests with service performance of different classes of alloys, laboratory tests have not accurately identified those alloys in a given class with greater potential as candidate suction roll alloys. Consequently, greater reliance has been placed on the performance of prototype rolls installed on actual paper machines.

This reliance on service performance of prototype rolls is discouraging for several reasons. First, the time required for identification of an improved roll is unacceptably high, since a roll must prove itself for a number of years before being ranked as an acceptable roll material. Feedback about the performance of candidate rolls is thus delayed for a period of several years, which in turn limits the number of candidate rolls that can be examined. Second, identification of an acceptable roll by service performance records is undesirable because little is gained in terms of understanding that would help guide the developement of future generations of roll alloys with still better performance. If a roll performs well in service, it is unclear whether the improved performance is due to higher corrosion resistance, improved metallurgical structure, higher strength, or some other heretofore unknown factor. Laboratory tests are required to ascertain the reasons for improved performance, since laboratory test specimens can be dissected, examined and analyzed to reveal the reasons for improved performance. Successful rolls are never removed for scrutiny, even if they are successful in prototype situations. The lack of a good laboratory test that correlates with service performance of suction rolls is thus a significant impediment to early identification of new generations of suction rolls alloys with the properties needed for improved performance.

There is some evidence that the corrosion resistance of a suction roll alloy does not correlate well with the performance of that alloy in the field. For example, Beloit/Sandusky Alloy 63 has superior corrosion resistance compared to Alloy 75, yet Alloy 63 was withdrawn from the market with a poor service record while Alloy 75 has enjoyed widespread success as a suction roll alloy (Fig. 7).

Corrosion fatigue behavior in simulated white waters is likewise an uncertain predictor of the resistance of a suction roll alloy in the field. As shown in Fig. 8, the endurance limit for Alloy 75 is lower than that of Alloy 63, even though the Alloy 75 is a far better suction roll material based on performance (4).

Similarly, fatigue crack growth rate tests in the laboratory have failed to predict the performance of suction rolls in the field. There is very limited data on crack growth rates of suction roll alloys, and virtually no good data on the important near-threshold regime of crack growth. The crack growth data show that there is little influence of environments on crack propagation rates, in contrast to expected behavior for rolls.

It is apparent that the laboratory data gathered on candidate suction roll alloys — while providing some insight into overall performance — does not discriminate between improved and inferior alloys as determined by performance in the field. As a result, laboratory testing offers little guidance regarding the desired attributes of an improved suction roll materials. A fundamental improvement must be made in developing a relevant laboratory test if insight is to be gained into the desirable characteristics of suction roll alloys.

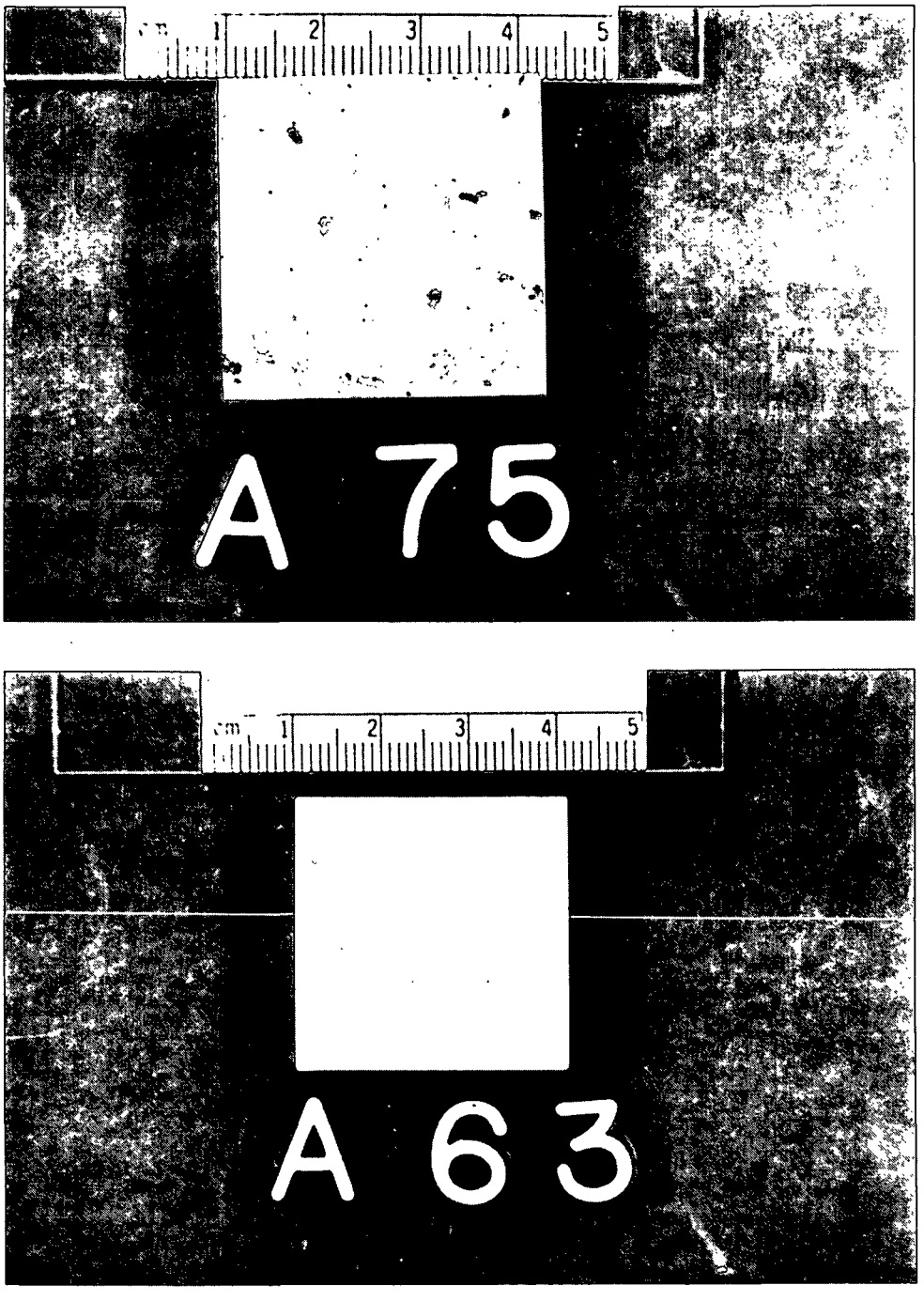

Figure 7. Examples of pitting corrosion resistance of Alloys 75 and 63 in simulated paper machine white waters. Alloy 75 has a superior service record.

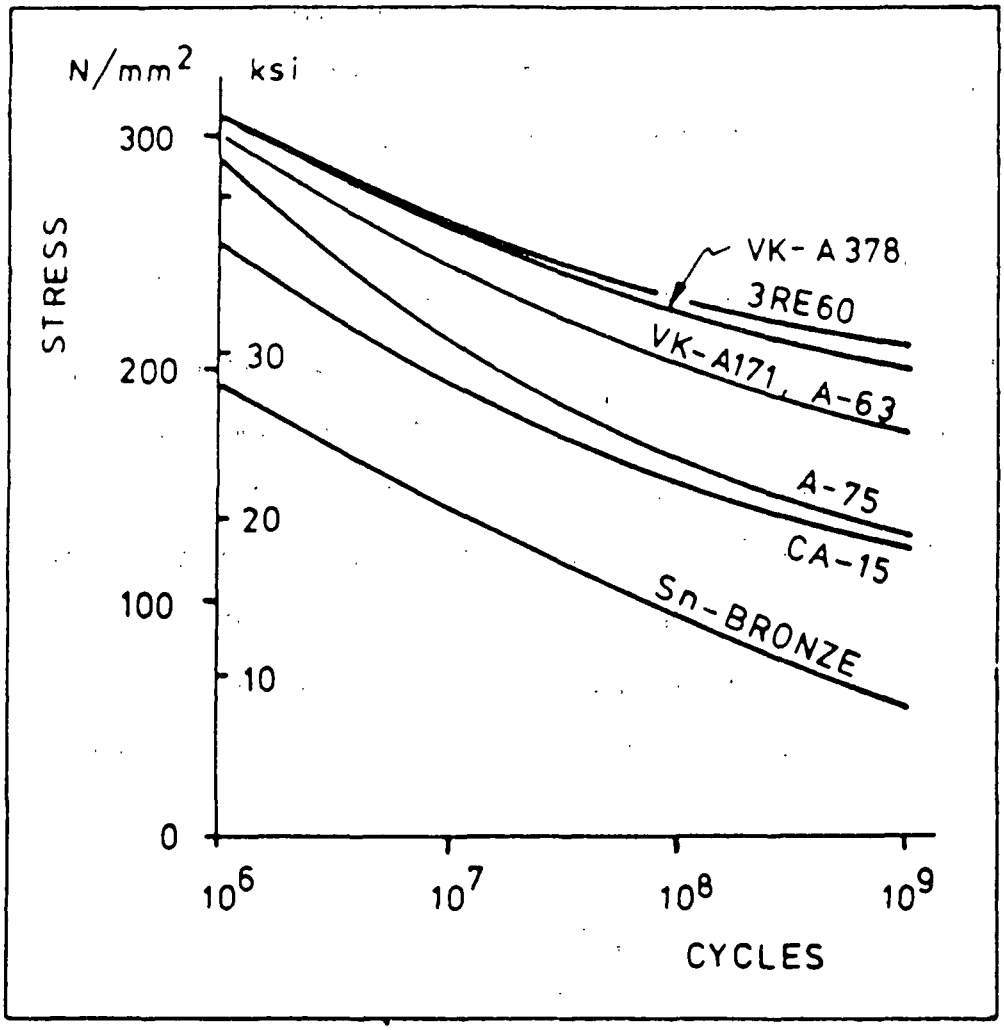

S-N curves for seven suction roll alloys in white water (pH 3.5, chloride 20-400 ppm, sulfate 250-1000 ppm) from rotating beam tests at 1500-1750 rpm

Figure 8. Although Alloy 75 is superior to Alloy 63 in service, the results of this S-N curve generated in the laboratory would indicate otherwise.

SHORT-TERM OBJECTIVES

Since the current laboratory tests offer little guidance concerning improved suction roll materials, the principal effort in this project has been focused on identifying a laboratory test that correlates with service performance of suction rolls. A variety of tests are being performed on alloys with either superior or inferior records in service in an attempt to identify a suitable laboratory test that reflects this service performance. Corrosion, stress corrosion, and corrosion fatigue tests are being conducted in this search for an improved laboratory test.

A related short-term objective is the normalization of different methods of generating S-N curves by different suction roll vendors. Although S-N curves are not perfect indicators of suction roll performance, they are used by suction roll vendors in marketing different alloys. Since different vendors use different methods to generate S-N curves, pulp and paper companies cannot readily evaluate conflicting claims about relative fatigue resistance. Consequently, the different test methods used by different suppliers will be used to generate S-N curves on a representative alloy to normalize the different methods of S-N curve generation.

PROGRESS

Near-Threshold Fatigue Crack Growth Testing

Near-threshold fatigue crack growth tests have been conducted on two suction roll alloys in the search for a laboratory test that correlates well with service experience. The two alloys investigated thus far include Alloy 75 and Alloy 63, both dual phase stainless steels, differing in their service histories as suction rolls in actual paper machines. Alloy 75 has an unblemished

record as a suction roll material with more than 100 installations without a significant failure, while Alloy 63 was withdrawn from the market after a short time because of a large proportion of cracked rolls.

Near-threshold crack growth tests are being conducted using compact tension fracture mechanics specimens as shown in Fig. 5, with careful load shedding techniques employed to determine the actual threshold stress intensity range for crack growth. In general, the procedures for crack growth rate measurements recommended in ASTM Standard E647 are being followed in this test program. In the typical test, a stable crack growth rate is established at a selected stress intensity range, followed by a small reduction in the stress intensity range. The R-ratio — the ratio of the maximum stress intensity imposed on a specimen in a load cycle to the minumum stress intensity in a cycle — is maintained constant during the load shedding procedure. Growth rate measurements are then suspended until the crack has grown beyond the zone of compressive residual stress introduced at the crack tip by the load reduction. Crack growth rates are measured by following the progress of the crack through a traveling microscope fitted with a filar eyepiece. Crack length measurements are made on both sides of the test specimen to insure propagation of a crack with a uniform crack length. Data are discarded if the crack length exceeds the recommendations of the ASTM Standard.

All testing has been conducted using the MTS electrohydraulic testing machine, as modified for fatigue testing in corrosive environments. The test stand is shown in Fig. 9. The specimens were loaded into the grips and load frame and then lowered into the test solution by lowering the entire upper crosshead assembly. Tests were conducted at a frequency of 25 Hz (i.e., 25 cycles per second). No compressive loads were imposed on specimens during

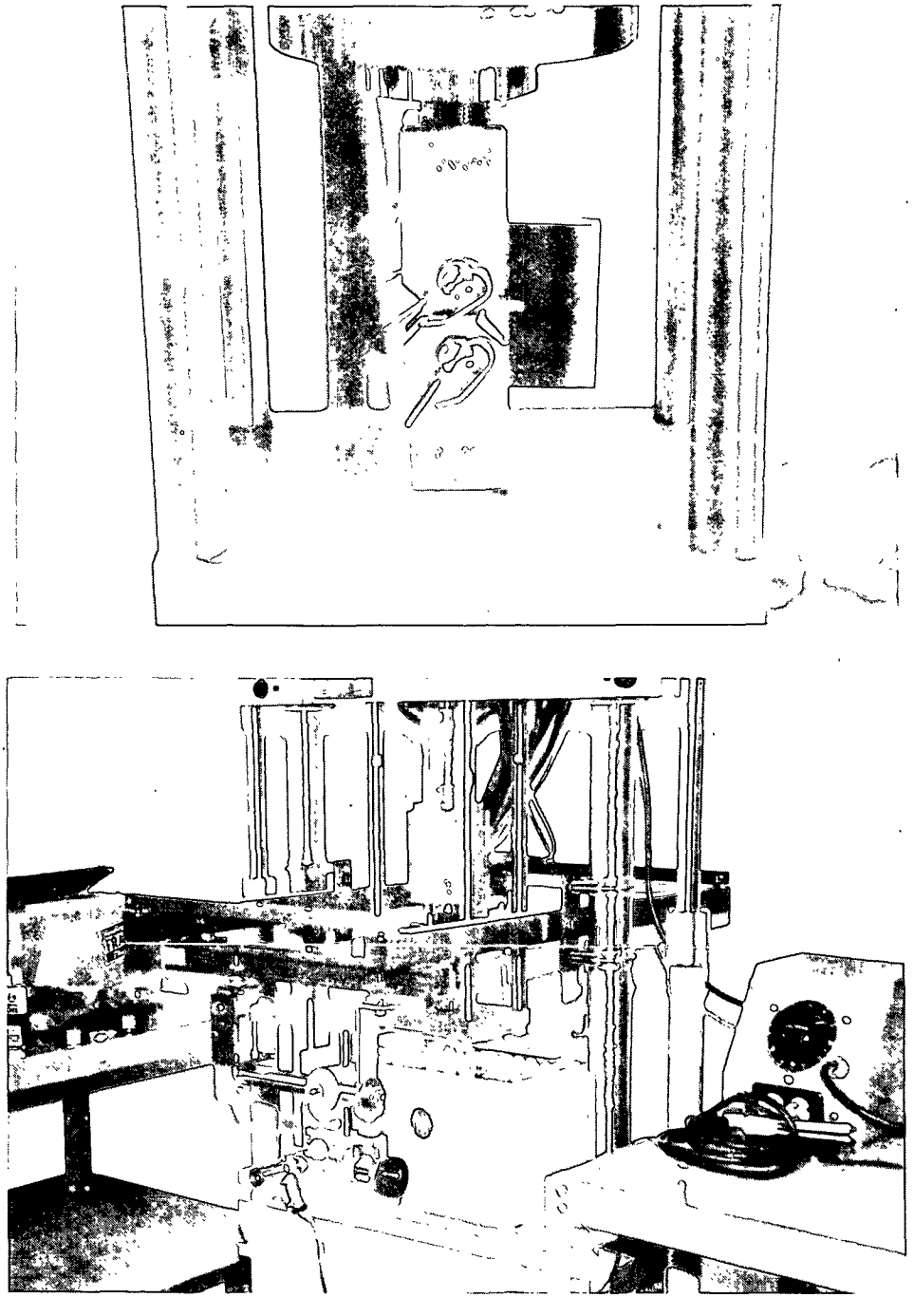

Figure 9. The MTS electrohydraulic testing machine equipped with modified test frame and environmental chamber for fatigue testing in simulated paper machine white waters.

testing, and R ratios were all greater than zero, since compressive loading of the compact tension specimen is experimentally difficult and there is considerable evidence that excursions into the compressive loading regime have virtually no effect on crack growth characteristics.

A test procedure had to be developed to accommodate the suspension of testing when there was no one present to monitor crack length visually. Allowing the cracks to progress unattended was considered to be an unnecessary consumption of expensive test specimens, since the crack would often cause speimen failure without data production under such conditions. However, suspension of the test and removal of the load during suspension led to artifacts in the crack growth rate data, apparently as a result of the introduction of compressive residual stresses at the crack tip during the unloading/reloading process. Nonpropagating cracks were a common occurrence after such a suspension in testing. Eventually, it was learned that tests could be suspended without introducing artifacts in the growth rate data if the peak load being imposed on the specimen during cyclic loading was also maintained during suspension of the fatigue test. This procedure was adopted to accommodate those periods when the laboratory was not staffed and crack lengths could not be monitored.

Crack growth rate tests have been conducted under controlled chemical and electrochemical conditions. Tests have been conducted in a variety of simulated white waters containing parts per million levels of chlorides, sulfates, and thiosulfates, as shown in Table 1. During fatigue testing, the specimen is electrically isolated from the titanium load frame by use of insulated pins consisting of a titanium alloy coated with a plasma sprayed layer of chromium oxide, ground to the desired diameter. Contact between the grips and the side of the specimen is prevented by the use of mica washers, as shown in Fig. 10. The

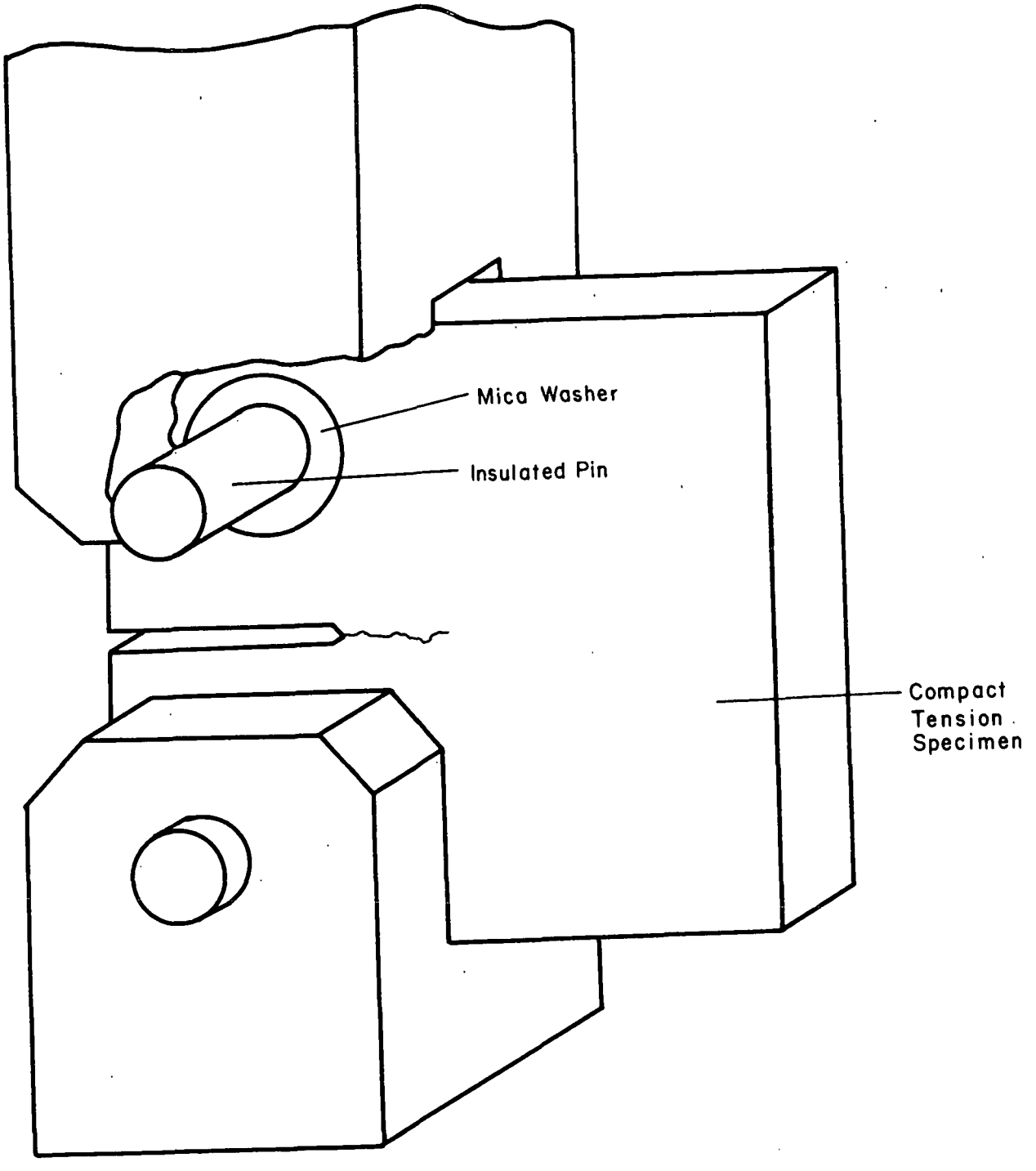

Figure 10. Cut-away view of the gripping arrangements used in near-threshold fatigue testing.

electrochemical potential of the test specimen is monitored using a calomel electrode immersed in the test bath. The potential is monitored using a digital voltmeter attached to the reference electrode and the test specimen. The simulated white water is maintained at 50°C by means of electrical heaters and a recirculation apparatus that also provided filtering necessary to prevent accumulation of corrosion products in the white water.

Table 1. Test environments.

Environment	Chloride, ppm	Sulfate, ppm	Thiosulfate, ppm	pH
A	1000	0	0	4.7
B	100	1000	0	3.6
C	1000	1000	0	3.5
D	200	500	50	4.1

Results of near-threshold measurements of fatigue crack growth rates are shown in Fig. 11-14. The reproducibility of the data is displayed in Fig. 11, which shows the results of two separate tests of Alloy 63 under identical onditions — R = 0.1, 50°C, 1000 ppm chloride and a pH in the range 4.7 to 4.9. The agreement between data from separate tests in the Stage 2 regime is evident. The effect of environment on the rate of fatigue crack growth in the near-threshold, Stage 1 and Stage 2 regimes is shown in Fig. 12, with crack growth rate data obtained in test in air included as a benchmark. There is little evidence of a significant environmental effect on crack growth rates in the near-threshold and Stage 1 regimes in any of the four simulated white waters tested thus far. The crack growth rates measured in the Stage 2 regime are higher than observed in air, but there appears to be little difference between growth rates in the different simulated white waters. The threshold stress intensity range for corrosion fatigue crack growth in Alloy 63 is 10 ksi$(in)^{1/2}$ in all of the simulated white waters and in laboratory air. The transition from Stage 1 to Stage 2 growth occurs at a stress intensity of approximately 15 ksi$(in)^{1/2}$ and a growth rate of approximately 2×10^{-7} in/cycle.

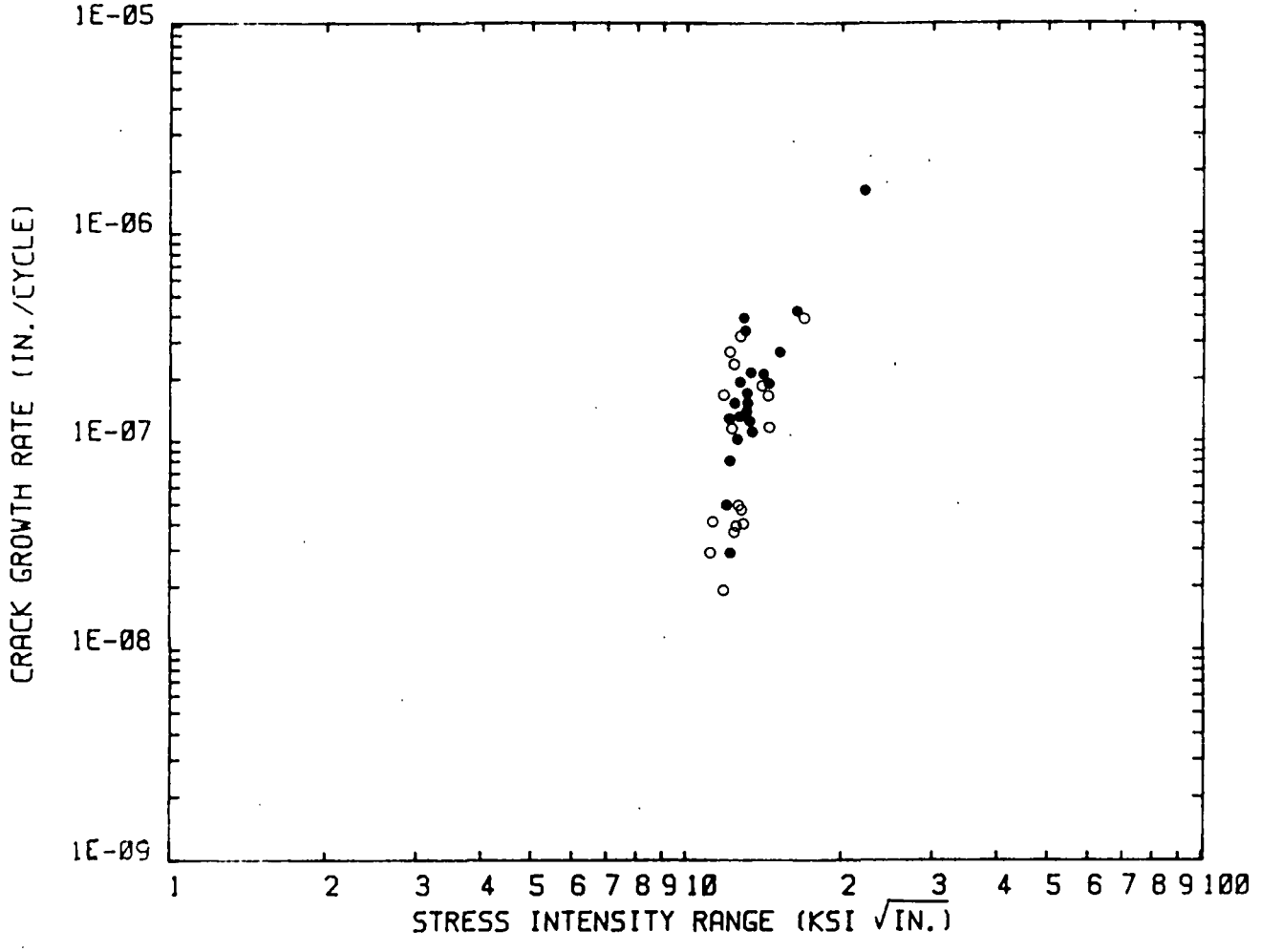

Figure 11. A comparison of fatigue crack growth rates measured in two separate tests on Alloy 63 in Environment A.

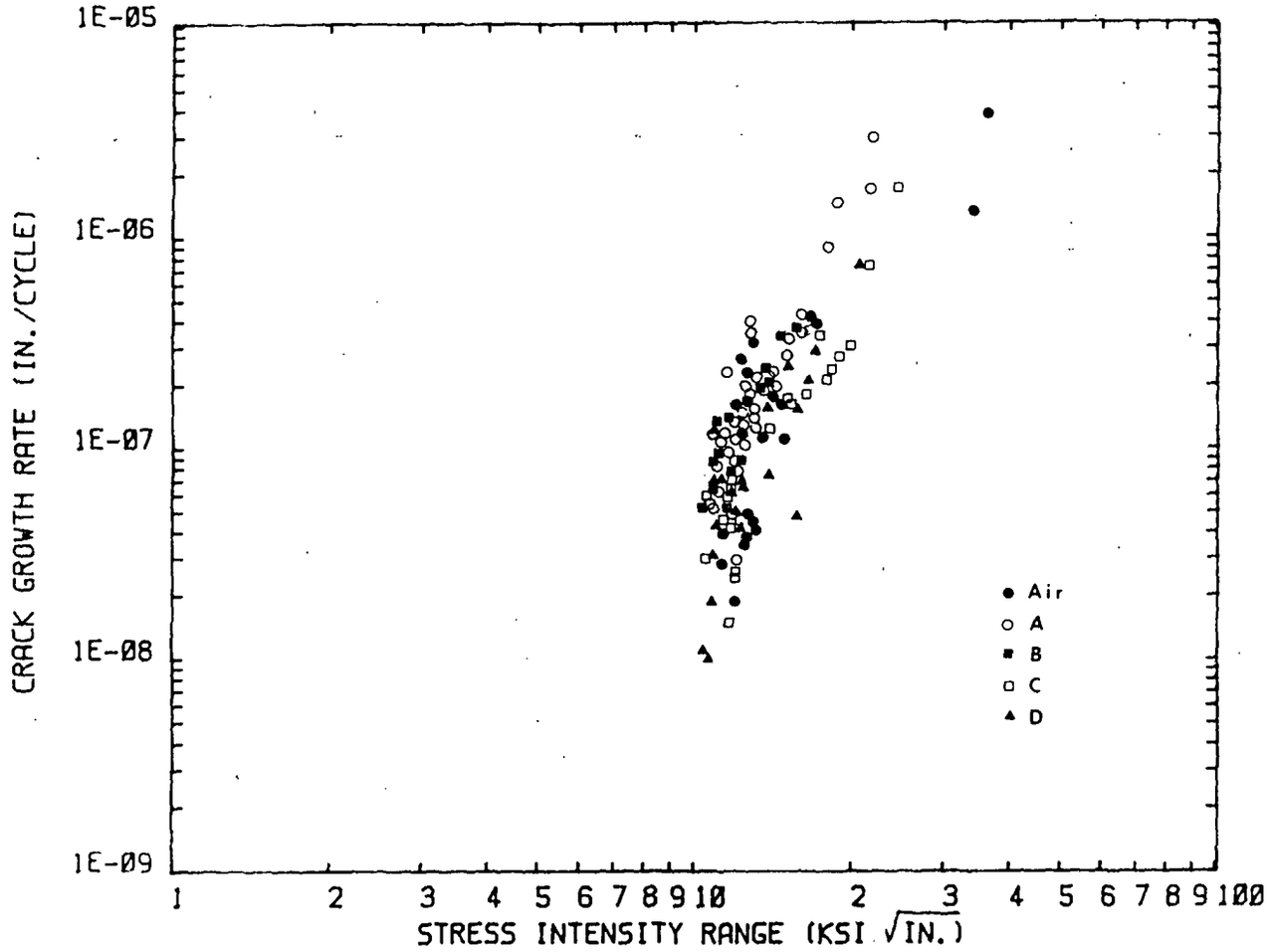

Figure 12. Comparison of the effects of test environment on fatigue crack growth in Alloy 63. R = 0.1, T = 50°C.

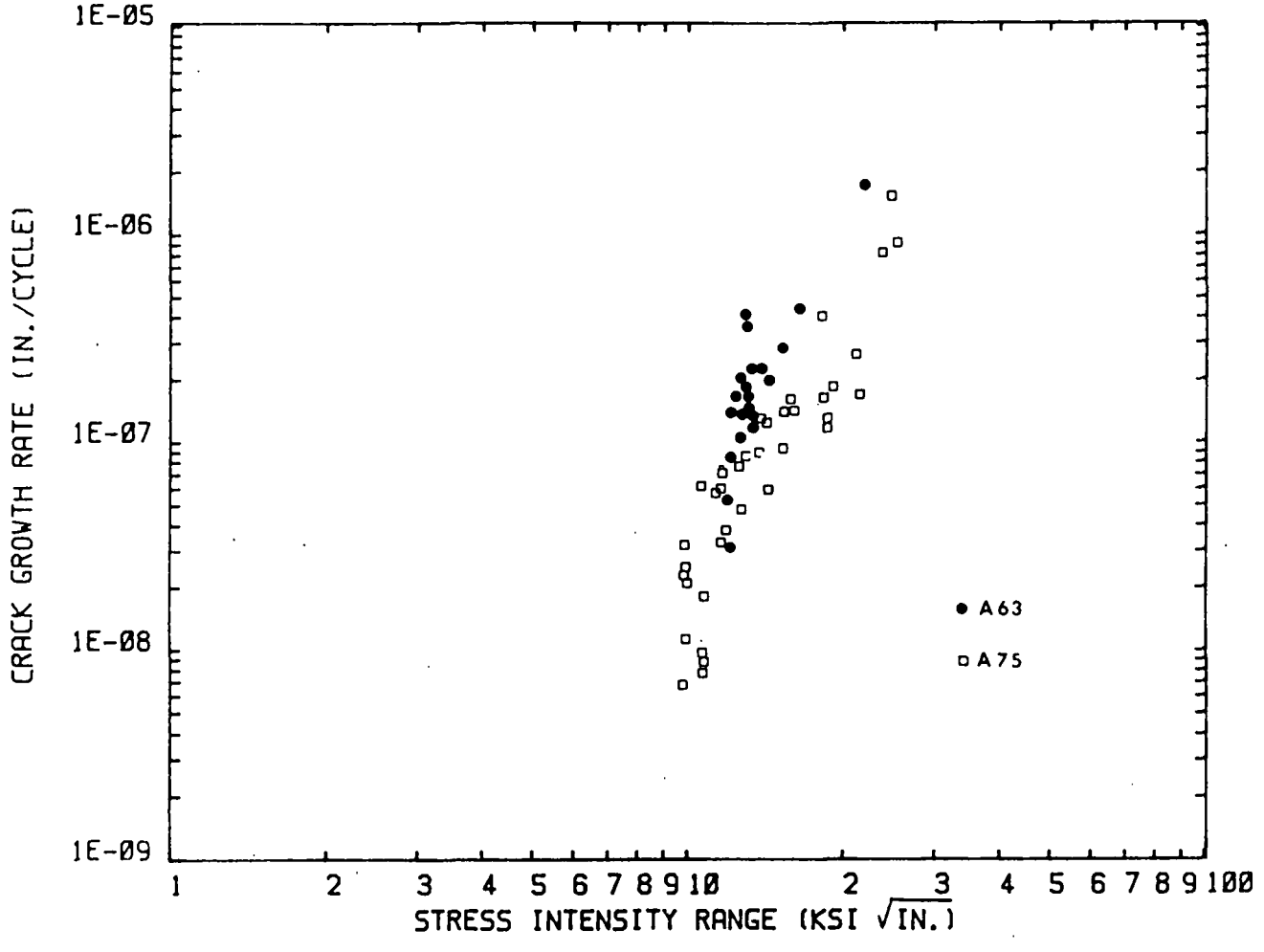

Figure 13. A comparison of the fatigue crack growth characteristics exhibited by Alloys 75 and 63 in a simulated white water containing 1000 ppm chloride.

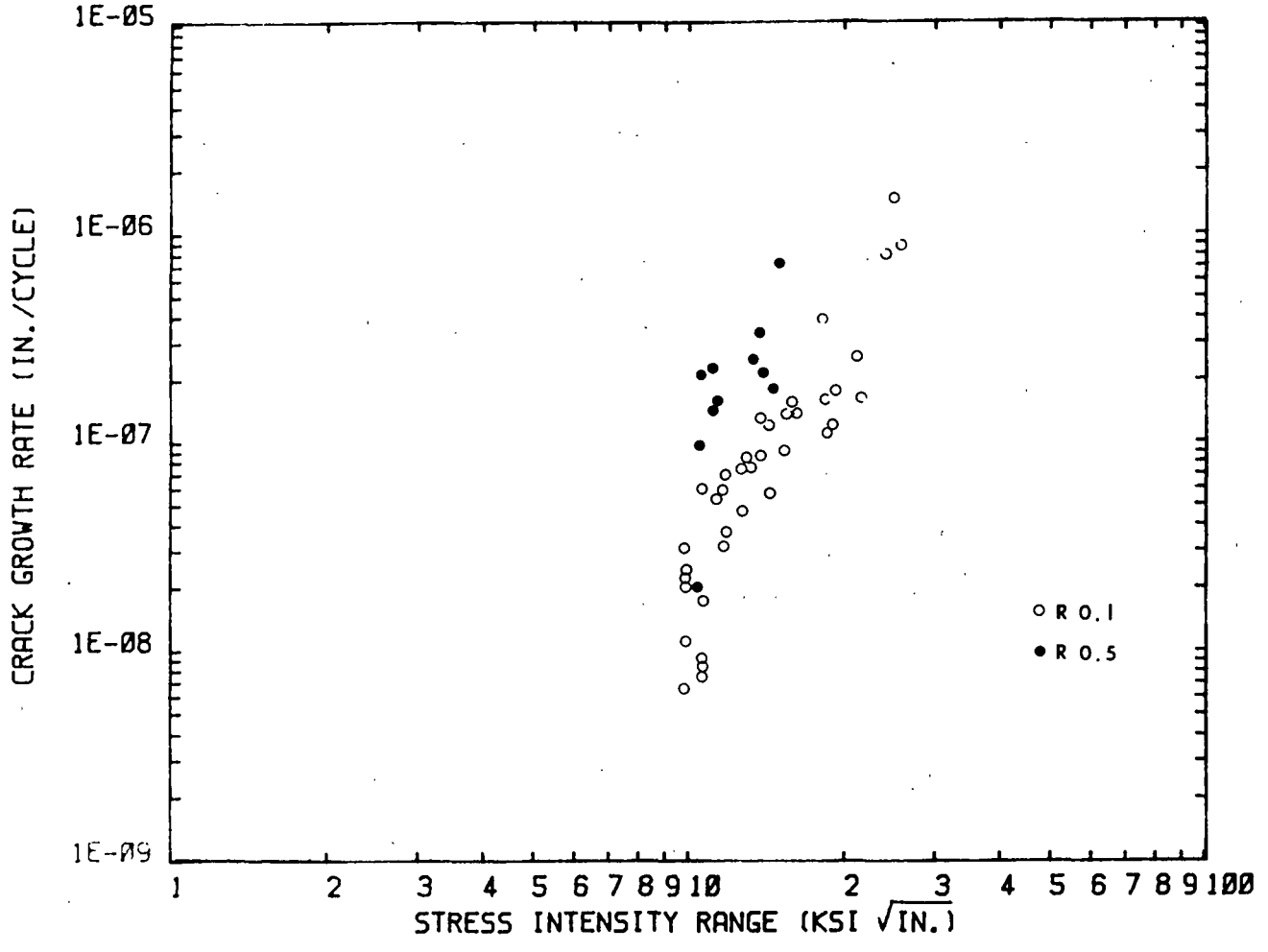

Figure 14. Crack growth rate data for Alloy 75 in a simulated paper machine white water showing the effects of mean stress on growth rate.

Crack growth rate data for Alloy 75 is less extensive, since this alloy was made available later in the testing program. The crack growth behavior in the 1000 ppm chloride environment is shown in Fig. 13, compared with the performance of Alloy 63 in the same simulated white water. It is apparent from this figure that the threshold stress for crack growth is lower for Alloy 75 than for Alloy 63, in contrast to expectations from the service history of these two alloys. However, the growth rate for Alloy 75 is about an order of magnitude lower than that exhibited in Stages 1 and 2 by Alloy 63 in this white water, in apparent agreement with their service histories. Based on this preliminary evidence, it appears that the threshold stress intensity range for corrosion fatigue crack growth does not qualify as a predictor of service performance, but crack growth rates in Stages 1 and 2 may indeed correlate with field experience. More testing is certainly required to reinforce this preliminary conclusion.

Tests have been conducted to examine the effects of a tensile mean stress on the crack growth characteristics of Alloy 75. Similar tests on Alloy 63 are scheduled in the next reporting period. The data shown in Fig. 14 for Alloy 75 indicate that the threshold stress intensity range is little affected by the imposition of a high mean stress during fatigue, but the crack growth rate in the Stage 2 regime is increased dramatically by mean stress. At the same stress intensity range, the crack growth rate is higher by nearly a factor of 10 when the mean stress is high (R ratio = 0.5), compared to the growth rate when mean stresses are low (R ratio = 0.1). This finding suggests that residual tensile stresses retained in suction rolls because of their fabrication could be influential in promoting failure by fatigue crack growth, as has been suggested in the literature. Whether mean stress sensitivity is a good predictor of suction roll performance will be determined upon further testing.

Limited fractography has been performed on the fracture surfaces of specimens tested in this program. A typical scanning electron fractograph is shown in Fig. 15, together with an optical metallographic picture of the typical Alloy 63 microstructure. As is clearly evident from comparison of the two pictures, the fractographic features are quite different for crack passage through the two microstructures. Fatigue cracks passing through the more ductile austenite phase results in ductile striation formation while crack passage through the ferrite phase results in "brittle" striation formation.

Near-threshold fatigue testing has just begun and much remains to be done. However, differences have been observed thus far which might be significant in the search for a laboratory test that correlates with the service lifetime of suction roll alloys. Continued testing is planned in the next reporting period.

STRESS CORROSION CRACKING TESTING

Although the primary mode of failure of suction rolls is thought to be corrosion fatigue, the apparent effect of tensile residual stress raises the possibility that stress corrosion cracking may be an important mode of failure itself, either independently or in conjunction with corrosion fatigue processes. To examine suction roll alloys for possible effects of stress corrosion cracking, slow strain rate tests are being performed on Alloys 75 and 63 exposed to simulated paper machine white waters. Strain rates of 5×10^{-7} in./in./s are being employed, and any changes in electrochemical potential are being monitored during the test. The first SSRT test has been completed with Alloy 63 in simulated paper machine white water A of Table 1, without detection of any evidence of stress corrosion cracking. Large elongations, high reduction in areas at fracture, and the absence of secondary cracking all indicate that SCC was not

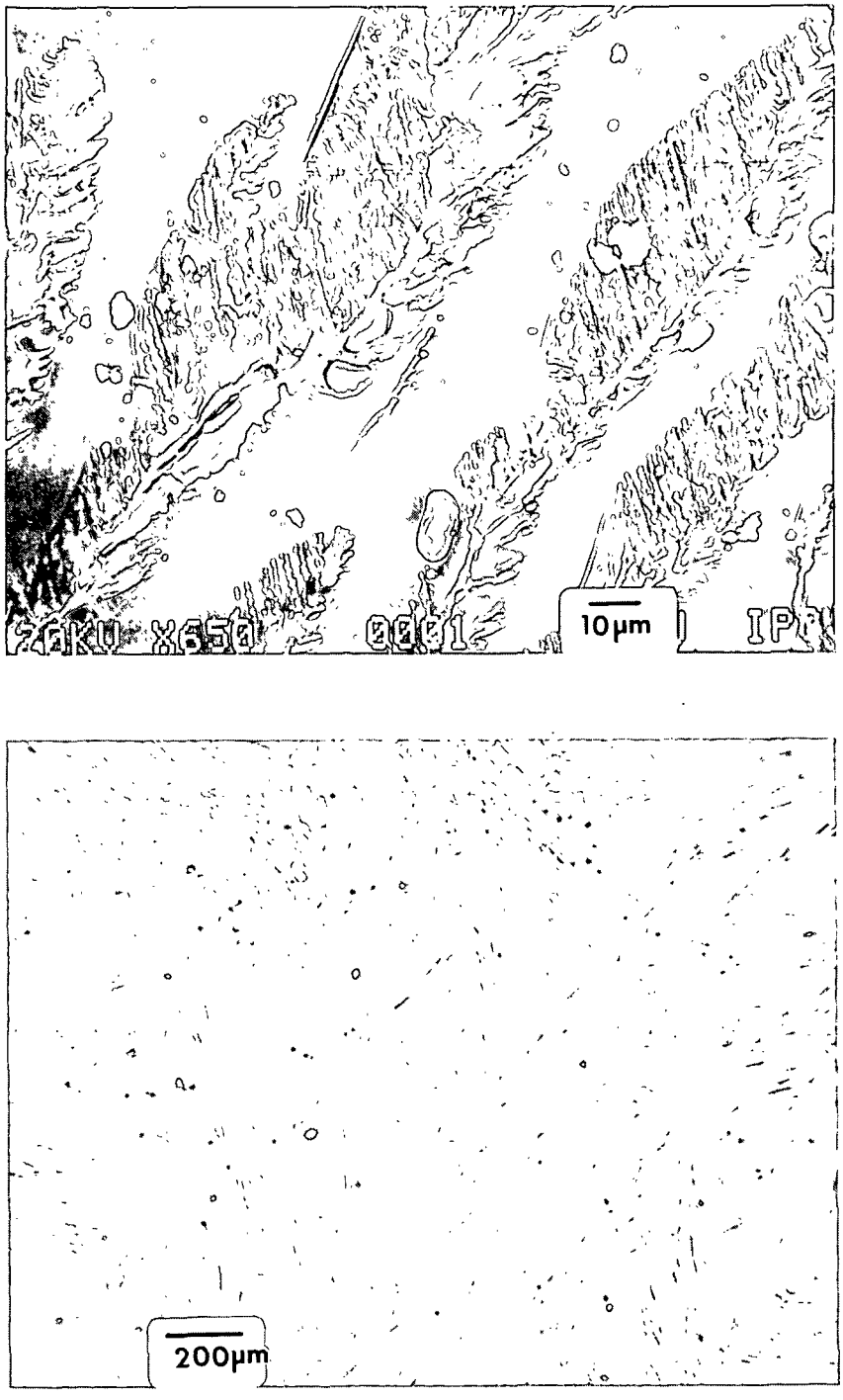

Figure 15. A typical scanning electron fractograph showing features on the fracture surface of an Alloy 63 specimen used in the fatigue crack growth studies.

occurring during the first SSRT test. Additional SSRT testing is scheduled on both Alloy 63 and 75.

CORROSION TESTING

The corrosion testing program initiated by Bowers (2) is being pursued to its originally scheduled conclusion. Corrosion tests are being conducted to determine if the corrosion resistance of suction roll alloys plays a pivotal role in the resistance to corrosion-assisted cracking of these alloys. These tests consist of coupon exposure to various simulated paper machine white waters while the electrochemical potential of the electrode is monitored to detect the onset of pitting and/or crevice corrosion. The presence of pitting or crevice corrosion is confirmed in visual inspections following the exposures.

Pitting corrosion tests have been completed in Environment #4 listed in Table 1, using various suction roll alloy materials. This test is a duplication and extension of tests reported in ref. 2 in a white water environment identified previously as WWI. This test was conducted first to insure continuity of testing methods during a change in research personnel, and to include alloys not considered in the previous study. Some difficulties were encountered in the computer-aided data acquisition of potential-vs.-time data, so complete plots of potential decay behavior are not available from this test. However, corrosion resistance was determined based on the visual examination and weight loss measurements following exposure.

The extent of localized corrosion due to an exposure test in White Water Environment #4 is summarized for several different alloys in Table 2. Although the corrosion was decidedly nonunifrom, the weight loss results are

normalized for exposed area and exposure time effects by presenting the data as an average weight loss over the exposed area. The corrosion resistance is divided into three categories. The 12 Cr alloys — CA15 and 1300 — exhibited the least resistance to corrosion in this simulated white water, as indicated by a high weight loss measurement. Intermediate corrosion resistance was exhibited by Alloy 75, 304L stainless steel, CF3M, 2505, and 1804 materials. This alloy group includes alloys with austenitic and austenitic/ferritic metallurgical structures. The highest corrosion resistance was found in Alloy 63, VK-A378, KA 171, 316L stainless steel, and 1811 forged alloy. It is interesting to note that the corrosion resistance of Alloy 63 is better than that of many of the austenitic/ferritic alloys, even though its service record as a suction roll is definitely inferior to these alloys. Thus, the corrosion behavior in this dilute white water environment does not correlate with suction roll service performance. Additional corrosion testing will be conducted to determine if the corrosion behavior in other environments is more representative, and to characterize the corrosion behavior in terms of fundamental understanding.

Table 2. Comparison of weight losses due to pitting of suction roll alloys.

Alloy	Corrosion Rate, mpy	Alloy	Corrosion Rate, mpy
A75	3.4	CF3M	1.0
CA15	12.1	1811	0.1
KA171	0.04	1804	0.5
2505	0.7	304L	3.0
KA171	0.08	VKA 378	0.06
A63	0.0	1300	14.3

CORROSION FATIGUE LIFETIME TESTING

Corrosion fatigue testing to determine fatigue lifetimes and S-N behavior is being examined as a possible laboratory test to correlate with service performance records, even though the published data is not encouraging in this

regard. A wider range of test conditions will be studied in the search for S-N behavior that predicts suction roll lifetimes. Testing is also being conducted to compare S-N data generated with the different test methods in current use, in order to normalize endurance limits for these different test methods.

Efforts to develop a suitable corrosion test chamber for rotating bending (i.e., R. R. Moore) fatigue testing have continued. Difficulties have been encountered in isolating the corrosive environment from contact with the lubricant in the bearing spindle assemblies at the ends of the fatigue specimen. Two different seal designs have been tested without success. A third design utilizing a throw plate and capture labyrinth without a mechanical seal is being evaluated. This design is shown in Fig. 16.

Two additional R. R. Moore testing machines have been ordered for use in this program, bringing the total number of test stands to three. Test stands, bearing supports, cycle counters, and related equipment have been designed and combined with purchased bearing spindle assemblies to constitute functional rotating bending testing machines.

An alternating bending fatigue machine has been obtained on loan for use in the effort to compare S-N data generated on different types of fatigue testing machines. This machine — called a Tatnall Krause machine — utilizes a plate specimen loaded in cantilever flexure by means of a motor driven crank arrangement as shown in Fig. 17. A hole is present in the plate to force the failure to take place at the stress concentration, rather than at the gripped edge. Corrosive solutions are maintained in contact with the hole by means of a wicking arrangement shown in Fig. 17.

Shakedown testing to develop test procedures has been conducted using plate specimens fabricated from 316L stainless steel — the wrought equivalent

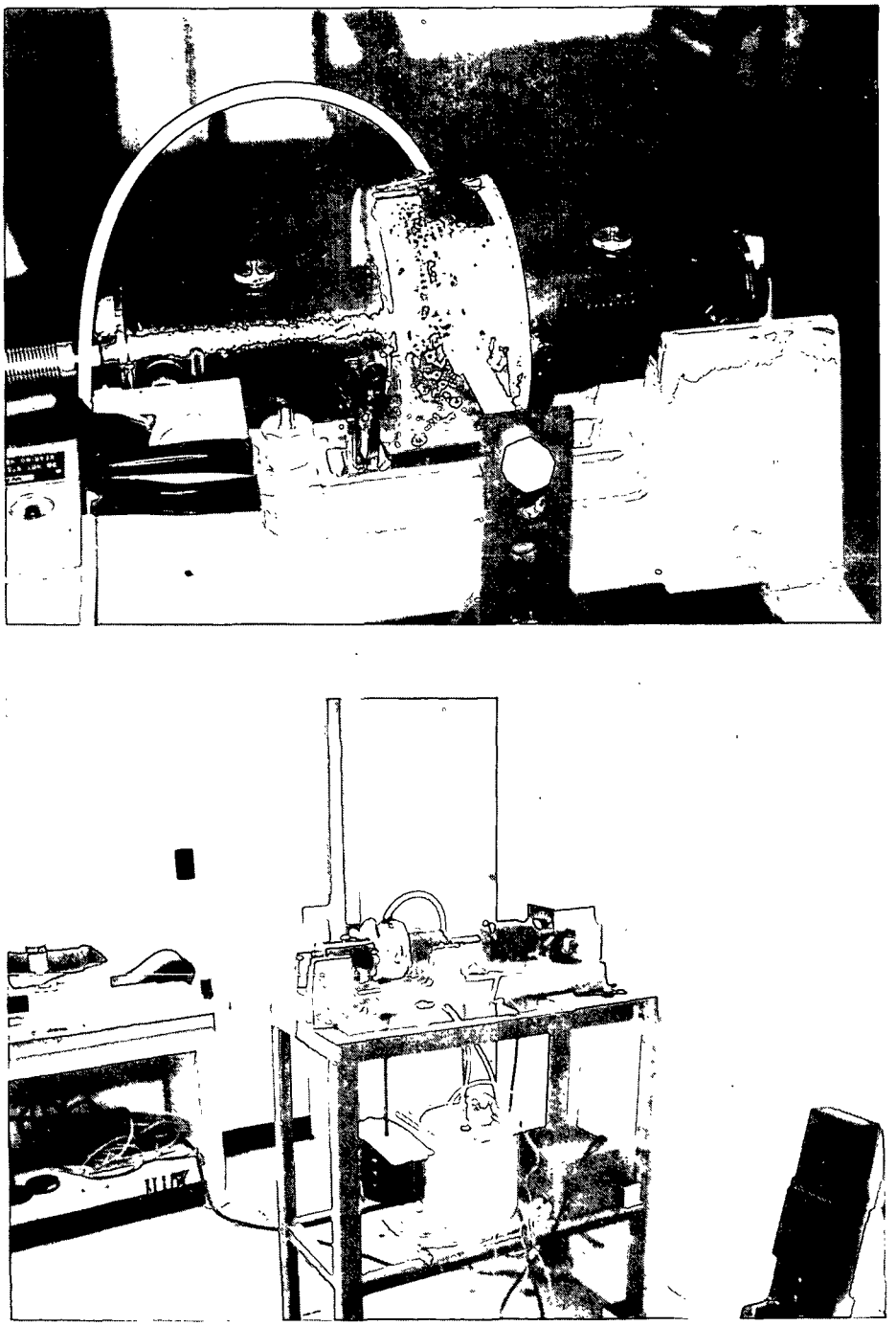

Figure 16. R. R. Moore rotating bending fatigue machine fitted with a recent version of a corrosion test chamber.

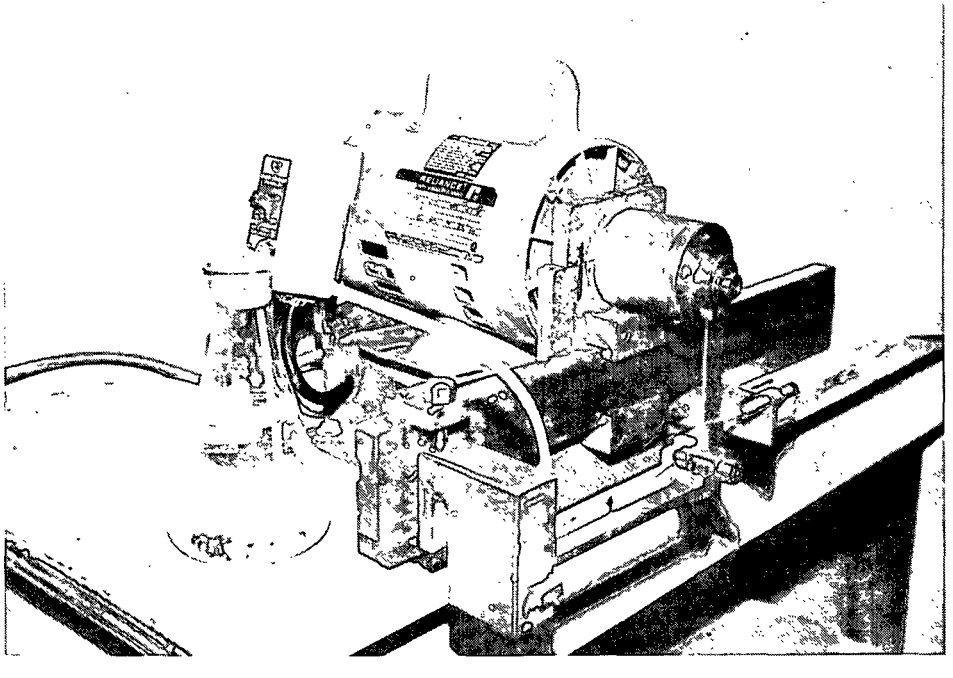

Figure 17. Tatnall Krause alternating bending fatigue machine fitted with a wick arrangement for delivery of corrosive solutions to a stress concentrating hole in the test plate.

of the CF3M suction roll alloy. The S-N curve for this alloy exposed to Environment #1 is shown in Fig. 18. The shape and reproducibility of the S-N data are acceptable, but a recurrent problem with failure at the grip rather than at the intended stress concentrator has been encountered. The current remedy involves isolation of the griped zone from contact with the corrosive solution by means of a caulking compound.

MATERIALS ACQUISITION

Additional suction roll materials have been acquired for use in this interesting program, thereby eliminating a previous obstacle to successful completion of the work. Valmet-Kubota Alloys 171 and 378 have been acquired through TVW, Inc. and 3RE60 have been obtained through Avesta. The 171 alloy has experienced repeated instances of cracking in the field, while the 3RE60 and 378 alloys have had a good service record. This acquisition complements the Beloit/Sandusky Alloys 63 and 75 previously obtained. The materials obtained represent two alloys with chronic cracking histories and three materials with relatively good service performance records. All materials have been provided in the heat treatment appropriate for actual suction roll alloys, although the exact heat treatment condition remains proprietary. All materials are available in sufficient quantity to meet the needs of this program for the foreseeable future.

FUTURE WORK

The search for a meaningful laboratory test that will accurately predict the resistance of suction roll alloys to corrosion-assisted cracking service has just begun. In the next reporting period, the testing effort will continue to focus on near-threshold fatigue crack growth rate measurements, S-N

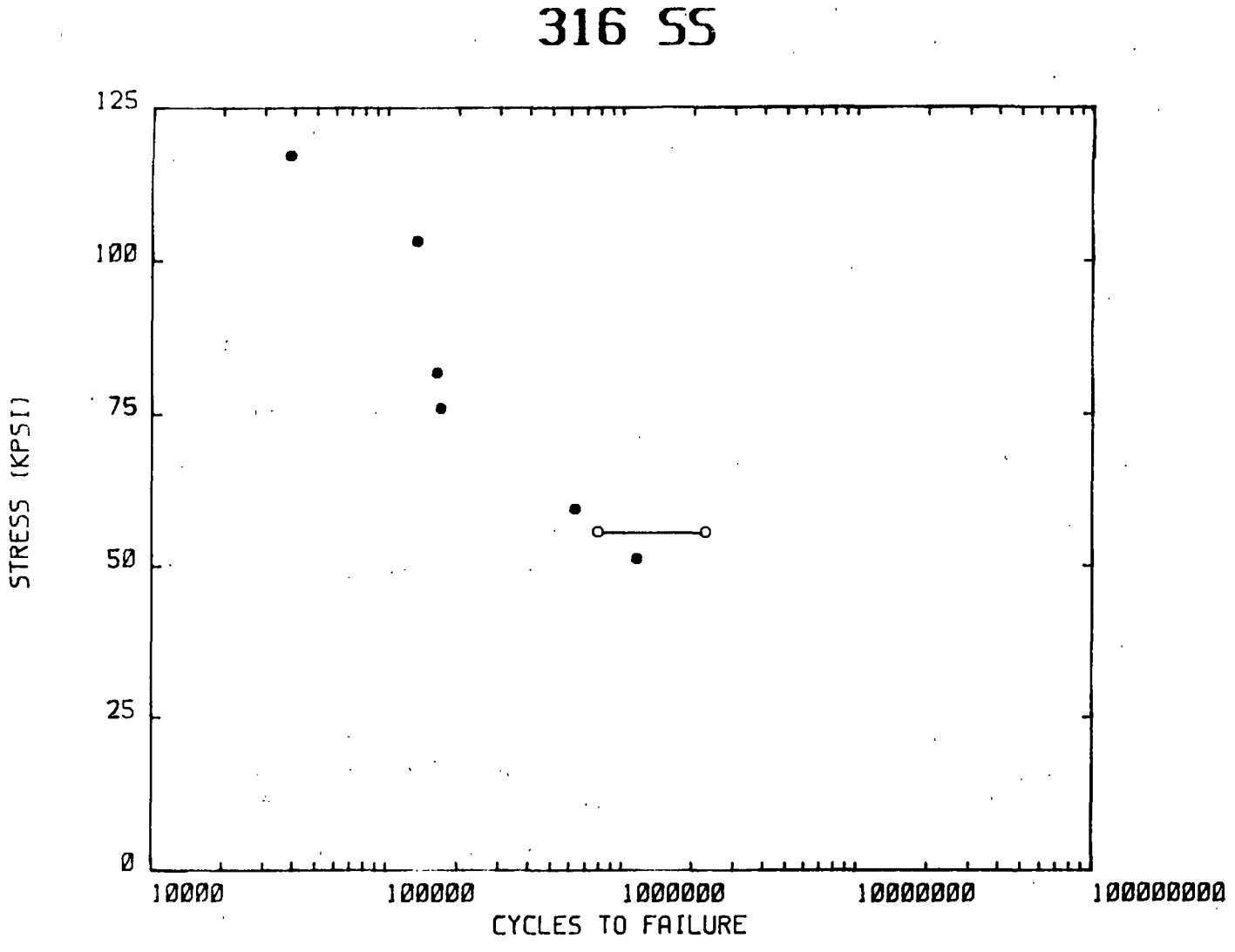

Figure 18. S-N curve for 316L stainless steel exposed to Environment #1 (1000 ppm chloride, pH 4.7), as generated with the Tatnall Krause alternating bending machine.

curve generation using various test methods, corrosion testing in different environments related to suction roll service, and slow strain rate testing to assess stress corrosion cracking resistance. Mean stress effects will continue to be addressed in fatigue testing, based on the importance of tensile residual stresses in suction roll performance. Tests with potential as indicators of suction roll performance will be extended to include the VKA 171 and 378 alloys, and the 3RE60 alloy, to determine the universality of the predictive method. Corrosion testing and metallographic studies will continue in an effort to obtain fundamental understanding of suction roll behavior.

SIGNIFICANCE TO THE INDUSTRY

Although the testing effort is in an embryonic stage, this program promises considerable insight into the causes of suction roll cracking and the development of new generations of alternative materials with increased resistance to corrosion-assisted cracking. Progress made in this area will help to reduce the costs of papermaking by removing a chronic source of failure in papermaking machinery.

REFERENCES

1. A. Garner, "Sunction Roll Failures in Canada:, Proc. 70th Annual Meeting of the Canadian Pulp and Paper Association, Paper A209 (1984).

2. D. Bowers, "Corrosion and Corrosion Fatigue of Paper Machine Sunction Roll Alloys", Report 2, Project 3309, December, 1984.

3. ASTM Tentative Test Method, E647. "Constant-Load-Amplitude Fatigue Crack Growth Rates Above 10^{-8}m/cycle.

4. J. Vestola, "European Alloy Development — New Suction Roll Steels" Proc. 1984 TAPPI Engineering Conference.

THE INSTITUTE OF PAPER CHEMISTRY

Appleton, Wisconsin

Status Report

to the

ENGINEERING PROJECT ADVISORY COMMITTEE

Project 3384

REFINING OF CHEMICAL PULPS

September 11, 1985

PROJECT SUMMARY FORM

DATE: September 11, 1985

PROJECT NO.: 3384 - Refining of Chemical Pulps for Improved Properties

PROJECT LEADER:

IPC GOAL:

Develop ways to measure and control manufacturing processes.

OBJECTIVE:

To identify or develop ways of measuring and controlling refining intensity, so that the operation can be carried out at the appropriate level of severity without detrimental fiber shortening and fines generation, as a function of fiber type (hardwood vs. softwood, e.g.) pulp end-use requirements, and refiner design and operation. Increased understanding of the factors which influence the stresses encountered by an individual fiber, and the fiber response, would assist us in maintaining stresses below levels which lead to undesirable fiber damage. Such knowledge may impact refiner design and operation, as well as our ability to utilize cheaper but more sensitive pulps, such as hardwoods.

CURRENT FISCAL BUDGET: $115,000

SUMMARY OF RESULTS SINCE LAST REPORT: (April, 1985 - September, 1985)

In previous reports, a model relating stress on a single fiber to fiber properties, refiner design and refiner operating parameters was developed. Normal pressure on a refiner bar segment, P_N, is a key factor in this model. A Valley beater has been instrumentd to permit measurements of P_N on a small segment as a basis for determining the distribution of P_N values experienced by a single fiber. Once proven, this measurement system will be transferred to a newly acquired 16" double-disk refiner, a gift from Beloit-Jones. To ease the instrumentation problem, it will also be operable as a single disk refiner.

Since the last meeting, a number of improvements have been made to the measurement and data acquisition system. Average pressure and pressure level distributions are now being measured for various fiber and operating conditions as a basis for verifying the model. The new double disk refiner is being installed.

INTRODUCTION

The refining of chemical pulp is a process involving mechanical action which renders the fibers more suitable for papermaking. It is carried out in machines of various designs. Typically, the fiber is abraded between bar-fitted surfaces which have a relative motion and are mechanically loaded against each other in the presence of water. At the consistencies normally used (2-6%), fibers receive impacts between the bars apparently while in the form of assemblages or flocs (1), which are nonuniform in time and space distribution in the machine.

Because of this nonuniformity and because of the heterogeneous nature of the fibers themselves, a broad spectrum of structural changes occurs in the pulp as a result of the refining action. As summarized by Ebeling (1), these effects include (1) the creation of new surfaces, such as by external and internal fibrillation, (2) the creation of new particles, such as fines of various types, or fiber fragments by cutting, and (3) structural damage and modification, such as that which weakens the cell wall to allow it to collapse upon drying. Certain of these effects are very desirable and necessary to the development of good fiber bonding and sheet characteristics. Other effects, however, are detrimental to pulp properties, especially in certain paper grades. Examples of the latter are fiber cutting which diminishes strength properties such as tear, and the generation of excessive amounts of fines which inhibit paper machine drainage but may not contribute much to sheet strength.

Unfortunately, our present knowledge and technology do not allow us predictive control of the type of fiber modification which will be brought about by refining. That is, we would like to be able to specify and control the

refining conditions (parameters like refiner speed, load, force levels, etc.) which would give optimum pulp properties, as a function of several considerations. One of these considerations, of course, is the set of papermaking and end-use properties desired. For example, if drainage rate (fines content?) is critical, or if tear strength (fiber length?) is very important, how do we change the refining to meet the requirements? Presently we can neither very well describe nor bring about the changes that ought to be made in refiner design or operation to meet such specifications.

Another of these considerations is fiber type. Southern pine, spruce, and hardwoods all require different refining treatment, but we are unable to quantify it or even establish with certainty which fiber properties make them different. The pulp history (recycled vs. virgin, e.g.) and pulping process are other variables which affect refining response. How do we control refining to get the desired pulp properties from kraft vs. sulfite vs. high-yield stocks? Or alternatively, could we, by proper refining control, utilize a lower cost fiber source?

When refining is carried out with more severe impacts, fiber cutting and fines generation tend to increase. Unfortunately, the available descriptions of refining severity account for only a few of the factors known to promote these (usually) undesirable fiber changes. In considering the control of fiber response to the type or intensity of refining, it seems necessary to first consider the stress encountered by an individual fiber. Knowledge of the factors which affect individual fiber stresses is needed to maintain those stresses at levels which produce desirable fiber modifications but below levels which lead to undesirable fiber damage.

The following section gives some background relative to factors and expressions which have been used to quantify refining severity, and some theoretical considerations pertaining to stresses on individual fibers.

BACKGROUND AND THEORY

In conventional disc refiners, the frequency at which fibers receive impacts by bar crossings may be up to 30 kHz. The refining may be quantified by two independent functions:

1. The amount of refining (the number of impacts per fiber) determines the extent of fiber modification. It is typically expressed as specific energy:

$$E_{net} = \frac{P}{qC}, \tag{1}$$

where P is net power consumed (exclusive of "no-load"),

q is volumetric flow rate, and

C is stock consistency.

2. The type or intensity of the impacts determines the character of the refining action on the fibers. That is, it affects the relative amounts of external fibrillation, internal delamination, fiber cutting, fines generation, etc. Refining severity has been quantitatively expressed in terms of specific edge load (2, 3):

$$SEL = \frac{P}{\Omega Z_r Z_s L}, \tag{2}$$

where Ω is the relative rotational speed of the discs,

Z_r and Z_s are the numbers of bars on the two discs, and

L is the average bar length.

THE UTILITY OF SPECIFIC EDGE LOAD

Presumably, the difference between gentle and severe refining relates to the plastic vs. elastic nature of the deformations. As a viscoelastic material, the pulp may respond to gentle impacts by absorbing much energy elastically, with little bond breakage per impact. This would maximize the "desirable" refining outcomes - internal delamination, external fibrillation, etc. - albeit with high elastic energy absorption. Very severe impacts, on the other hand, may tend to shatter the fiber, eliciting much cutting and fines formation. Indeed, the fact that various pulps respond differently to different levels of severity, or SEL, has long been recognized. Levlin (4) reported that pine kraft requires much less energy to attain a given tensile strength when refined at high SEL, with some loss in tear strength. Birch kraft, on the other hand, exhibited different effects at high SEL: higher energy and much lower tear at a given tensile. A similar comparison with spruce sulfite (5) revealed only small effects on energy efficiency over the same SEL range, however. Nevertheless, a substantial deficiency in tear-tensile relationships did result from the more severe refining. Canon and DeFoe (6) have substantiated significant advantages in very low intensity refining (SEL below 1 Ws/m) with bleached hardwood pulps. They confirm both the energy savings and property improvement trends noted previously with Scandinavian birch at low SEL. Since such energy and property advantages can be obtained by operating at an optimum SEL level for a given furnish, some have advocated the use of variable speed drives to control SEL independently of specific energy (7). Given the fact that fiber characteristics so greatly affect the pulp response to different levels of refining severity, there is a clear need for greater understanding of the factors which affect severity - their mechanism of action, their measurement and control.

Such knowledge is essential to obtain maximum benefit from such sensitive pulps as hardwoods, for example.

LIMITATIONS OF SEL

The specific edge load concept has proved very useful, both in clarifying the effects of certain design parameters of bar-filled refiners, and in providing guidelines for refiner control. However, it is not a comprehensive theory for characterizing refining and predicting the results. For instance, experience has shown that all the following parameters not considered in SEL, can influence refining intensity: bar angle, bar material, bar sharpness, groove depth, and consistency. The SEL concept has also been criticized for putting so much emphasis on the impact phenomenon of bar crossings: several refiner designs operate efficiently without edge-load type impacts. Included among these are basalt tackle refiners, and the Vargo refiner (8). In addition to these shortcomings, of course, is the lack of consideration of fiber characteristics. Specific edge load theory offers no explanation for the different responses of longer fibers or hardwood/softwood differences.

Several workers have attempted to develop more comprehensive refining severity models, notably by deriving expressions for energy per impact. Among the more recent of these is that of Leider and Nissan (9), who expressed energy per impact in the form

$$E = \frac{(E_{net}\ \frac{\text{energy}}{\text{kg}})(M\ \frac{\text{kg}}{\text{fiber}})}{(\text{impacts/fiber})}. \qquad (3)$$

They derived an expression for the denominator which could be written:

$$2\left(\frac{\pi\ D_m}{w_b + w_g}\right)^3 L\ \frac{\Omega}{q}\ \bar{\ell}\ \bar{d},$$

where D_m = mean diameter of refining zone,

w_b = bar width,

w_g = groove width,

$\overline{\ell}$ = average fiber length, and

$\overline{d}$ = average fiber diameter.

Substituting this and Eq. 1 into Eq. 3 yields an "energy per impact" expression:

$$E = \frac{PM}{2CL\Omega\overline{\ell d}} \left(\frac{w_b + w_g}{\pi D_m}\right)^3. \qquad (4)$$

This says that refining is more severe with coarser and denser fibers ($M/\overline{\ell d}$), and at lower consistencies, if everything else remains the same.

STRESS ON A SINGLE FIBER

Even if we assume that such additions to the SEL concept as those of Leider and Nissan do correctly model other effects, much is still lacking. The influences of many of the parameters which affect refining intensity have not been described. Moreover, the mechanism of fiber shortening, or of low-energy fines generation by shattering impacts, are not directly addressed in any of the previous models. Hence, the ability to predict the prevalence of those phenomena depends on empirical correlations, with conclusions not applicable in a very general sense. It is needful to express refining severity in terms of the stress experienced by individual fibers. Then, depending on the pulp's viscoelastic properties, this would directly relate to the strain - the fiber response. Controlling fiber stress levels in a refiner implies the ability to control fiber shortening, and the amount (and perhaps type) of fines generated from it vs. internal and external fibrillation, etc.

A knowledge of factors which affect average fiber stress, and the maximum stress levels encountered, are both necessary. During its course through a refiner, a fiber endures many impacts with a distribution of stress levels. The probability of its suffering undesirable damage depends not only on the average stress level over the whole refiner, but also on the frequency of encountering impacts with stress above a critical level. An objective of this effort would be to gain the capability of measuring and controlling stress levels within the desirable window - to maintain stress distributions with an average level high enough to economically effect useful fiber modification, while minimizing the frequency of damaging levels. This could lead to improved refining control strategies tailored to the raw material (hardwood vs. softwood, etc.) and the end-use requirements. In addition, there may be implications concerning the level of refiner precision, tram, and other operating conditions needed to maintain narrow stress distributions for sensitive pulps.

NORMAL STRESS

The work of Goncharov (10), in measuring the pressure on individual bars during refining, has provided evidence that the work of refining occurs only on the leading portion of the bar width, up to a distance less than or equal to the average fiber length $\bar{\ell}$. He reported normal pressures near the bar leading edge as high as 3500 kPa (ca. 500 psi). This was more than an order of magnitude higher than the measured thrust divided by bar contact area. Trailing portions of the bar generally experienced pressures of 10-15% of the maximum normal pressure P_N. The pressure profile during the bar crossing was almost a step function: it was maintained at a nearly constant P_N value from distance 0 to about 2.5-3.0 mm across the bar, then quickly dropped to a much lower value across the rest of the bar width.

The occurrence of stapled fibrages covering the leading portion of refiner bars had been reported by Banks (11). Using high-speed cinematography in a transparent disc refiner, he observed stapled fibers to cover 50-70% of the land area, on the stator bars only. A later study by Fox et al. (12) also showed stapling to occur on only one disc, but in this case mainly on the rotor side.

Referring to Fig. 1, let us assume a stapled fibrage on only one disc, of length $\overline{\ell}$. Then the thrust T between the plates is totally supported by the sum of active loaded area at all bar crossings: parallelograms of long side b and height h. If the opposing plates are of identical pattern, with bar width w_b and bar angle (from the radius) θ, then

$$\frac{w_b}{b} = \cos(90° - 2\theta) = 2 \sin \theta \cos \theta. \qquad (5)$$

Since $h = \overline{\ell} \cos \theta$, then the active area per bar crossing:

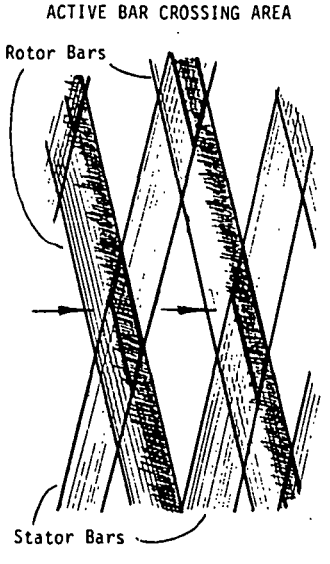

Figure 1. Conceptual depiction of active thrust-bearing areas-parallelograms wherein stapled fibrages are abraded between opposing bars.

$$bh = \frac{w_b \bar{\ell}}{2 \sin \theta} \tag{6}$$

Given groove width w_g, then $(w_b + w_g) = \pi D_m \cos \theta / Z$. Since $(w_b + w_g)/y = \cos(90° - 2\theta) = 2 \sin \theta \cos \theta$, then $y = \pi D_m / 2Z \sin \theta$. Therefore, the number of bar crossings per stator bar is

$$\frac{L}{y} = \frac{2ZL \sin \theta}{\pi D_m} \tag{7}$$

If $\overline{P}_N$ is the average normal pressure or stress experienced by fibers stapled in an active bar crossing, then the total thrust T is equal to the product of: $\overline{P}_N$, the active area per bar crossing, the number of bar crossings per stator bar, and the number of stator bars. From Eq. 6 and 7 above, then,

$$\overline{P}_N = \frac{\pi D_m T}{w_b \bar{\ell} Z^2 L} \tag{8}$$

This can be expressed in terms of power P rather than thrust by employing an overall friction coefficient μ: $2P/D_m\Omega = \mu T$. Substituting:

$$\overline{P}_N = \frac{2\pi P}{\mu w_b \bar{\ell} \Omega Z^2 L} \tag{9}$$

Bar sharpness (plate wear) and material probably influence the value of μ.

We might assume that the stapled fibers are squeezed together in that leading-edge work zone, such that there is a continuum of pressure being experienced by the fibers in the stapled mat. Then the normal pressure on a fiber increment $d\ell$ equals P_N, the compressive stress on the fiber. Hence, the normal force being experienced by a fiber increment of width w_f and length $d\ell$ is

$$dF_{Nf} = P_N w_f d\ell = \frac{2\pi P w_f d\ell}{\mu w_b \bar{\ell} \Omega Z^2 L} \tag{10}$$

FIBER STRESS IN OTHER DIRECTIONS

The work of Hartman (13) has demonstrated that compressive stresses applied to fiber mats can produce desirable internal delaminations, and impart fiber flexibility, when applied at fairly uniform levels of about 500 psi. This compares well with the compressive stress levels recorded in refiners by Goncharov (10), as mentioned above. However, Hartman's compressive forces produced very little fines or external fibrillation. When applied at levels of about 1500 psi (10,000 kPa), excessive fiber damage and cutting resulted.

These and other observations lead us to put forth the following postulates concerning "undesirable" refining outcomes:

- Fiber cutting can directly result from excessive normal or compressive stresses, perhaps at a level near 10,000 kPa for softwoods.
- The majority of fiber shortening, however, is a result of failure of the fiber in tension, within the stapled mat in the compression zone.
- The generation of excessive and choppy fines at low energy levels arises from high shear stress levels in the stapled mat.

Corollaries to these postulates may be stated in connection with "desirable" refining outcomes: reasonable levels of compressive stress promote kneading and internal delaminating, and reasonable levels of shear stress promote external fibrillation. In order to minimize the negative results, however, we must more closely examine shear and tensile stresses on the fiber level.

SHEAR STRESS

Considering our fiber increment of length $d\ell$ and width w_f, the force in the tangential direction is

$$dF_{Sf} = \mu_f dF_{Nf} = \mu_f P_N w_f d\ell, \qquad (11)$$

where μ_f is the local interfiber friction coefficient (perhaps different from the overall coefficient μ). Then the shear stress is

$$\tau_f = \frac{dF_{Sf}}{w_f d\ell} = \mu_f P_N. \tag{12}$$

Substituting Eq. 9:

$$\overline{\tau}_f = \frac{2\pi(\mu_f/\mu)P}{w_b \overline{\ell} \Omega Z^2 L} \tag{13}$$

Equation 13 states that pulps with shorter average fiber length (hardwoods, e.g.?) experience higher average shear stress at a given level of power or thrust. It also contains the specific edge load terms (Eq. 2), predicting effects identical to classical theory. If the postulates above are correct, then the primary effect of this higher shear stress would be seen in fines and debris production, rapid freeness drop, etc.

FIBER TENSILE STRESS

If the compressed thickness of our fiber segment is t_f, then the tensile stress in the segment is

$$d\sigma_f = \frac{dF_{Sf}}{w_f t_f} = \frac{\mu_f P_N \, d\ell}{t_f}. \tag{14}$$

Assuming that neither μ_f nor t_f change much with the amount of compression, then we can substitute Eq. 9 and integrate:

$$\overline{\sigma}_f = \frac{2\pi(\mu_f/\mu)P\ell_f}{w_b \overline{\ell} \Omega Z^2 L t_f} \tag{15}$$

If this expression is a reasonably valid representation of the average tensile stress experience by a fiber f in refining, then it should relate to the shortening rate of that fiber, such as described by Corte and Agg (14). They reported the shortening rate to be a linear function of fiber length in a refiner - longer fibers are more likely to be cut than shorter fibers. Equation

15 is consistent with this, indicating that fibers longer than the average ($\ell_f/\overline{\ell}$), and slender fibers (ℓ_f/t_f), will experience higher tensile stress. Hence, long softwood fibers would be more likely to be cut when refined at high severity along with large amounts of hardwood, than if they were refined separately under identical conditions of power, etc. In addition, the expression indicates a tendency toward less fiber cutting of more slippery fibers (pH effects on μ_f, e.g.). Equation 15 is also in agreement with classical SEL theory, predicting more cutting at higher power levels, lower disc speed, and with fewer bars at the same bar width w_f. However, the expression indicates that narrower bars would produce more cutting if the groove width were increased to maintain the same number of bars per disc Z. Implicit in this are the assumptions that w_b is greater than the width of stapled fibrage, and any changes in flow caused by different groove dimensions do not influence severity at a given power.

In light of the above, it appears that a greater fundamental understanding of fiber damage in refining, and its control, could be had by testing certain aspects of this model. The following discussion delineates specific objectives of the work, and the experimental approach and apparatus employed to accomplish those ends.

EXPERIMENTAL

OBJECTIVES

Specific objectives of the experimental program include:

1. Developing the capability of measuring P_N in a refining machine. The values obtained could be compared with the work of Goncharov (10) and Hartman (13).
2. Testing Eq. 9 with respect to factors which affect the magnitude of $\overline{P_N}$.

3. Establishing the variation or distribution of P_N, and factors which affect its distribution. This would be useful in testing the theory of Ebeling (1), who suggests that fibrages are stapled very nonuniformly along bar edges, as flocs. It would also involve testing the theory that the effect which consistency exerts on refining is due to changes in flocculation behavior and, therefore, to P_N distribution.
4. Correlating the average and the distribution of P_N with property development and especially the rates of cutting and fines generation.
5. Testing Eq. 13 and 15 with respect to the influence of fiber parameters (such as ℓ_f, t_f, μ_f, and $\overline{\ell}$) on the rates of cutting and fines generation.

APPARATUS

In considering alternative ways of measuring P_N in refining machines, it was decided to develop the instrumentation first for a Valley beater. It was felt that the geometry and the less severe environment in the beater refining zone would make the task easier, and the smaller-scale work prior to instrumenting a disc refiner should provide useful data. Hence, a stainless steel TAPPI Standard (T200-os 70) Valley beater was installed, and the rotor shaft was modified to accommodate a torque sensor (Fig. 2). Torque readings can be used to calculate overall friction coefficient μ, as well as SEL and specific energy in beating. In addition, the end of the shaft was equipped with a magnetic rotor and Hall cell effect switch for monitoring rpm.

The geometry of the rotor and stator bars in the beater is such that two rotor bars are in contact with the bedplate at all times (Fig. 3). Given this and other geometrical factors, it can be shown that the area of stapled

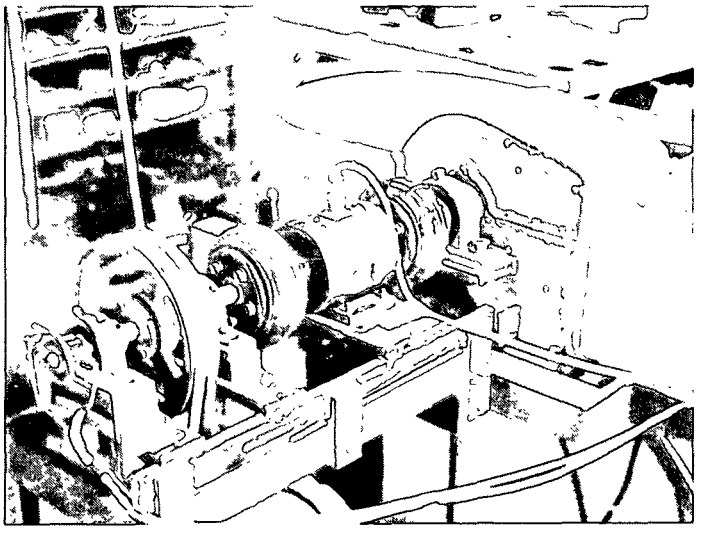

Figure 2. Valley beater with rotor shaft modification to accommodate torque sensor.

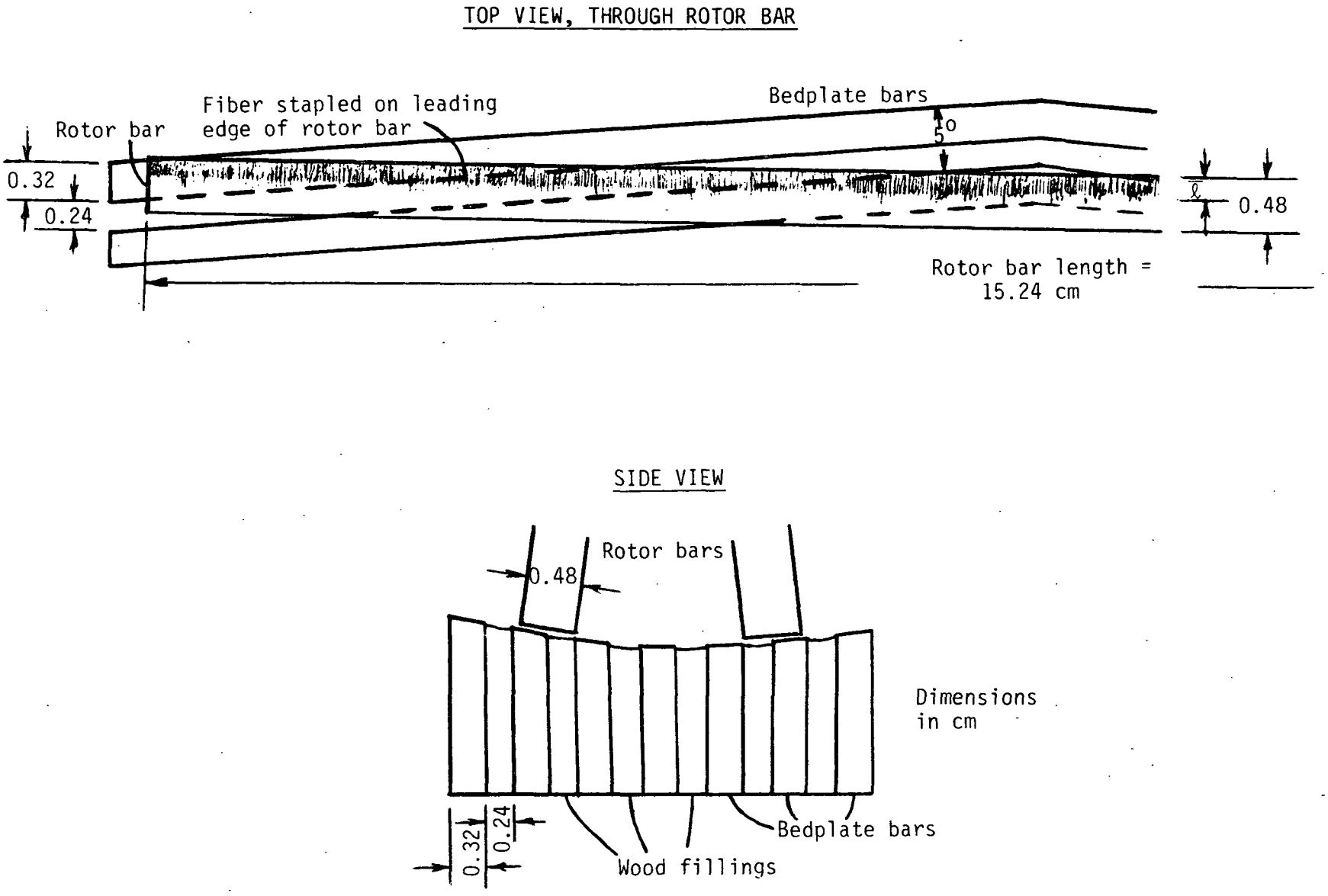

Figure 3. Valley beater bar geometry.

fiber which bears the load is $2[15.24-2(\frac{0.24}{\sin 5^\circ})]\bar{\ell} = 19.5\bar{\ell}$. This assumes that the width of stapled fibrages is indeed equal to $\bar{\ell}$(cm), and that it is less than the stator bar width of 0.32 cm.

Following the reasoning presented previously, the load or thrust T = $19.5\bar{\ell}\ \bar{P}_N$. If Λ equals the torque on the 19.38 cm diameter beater roll, then T = $\Lambda/9.69\ \mu$, and the expressions for fiber stress are:

$$\bar{P}_N = \frac{T}{19.5\bar{\ell}} = \frac{\Lambda}{189\mu\bar{\ell}} \tag{16}$$

$$\bar{\tau}_f = \frac{\mu_f T}{19.5\bar{\ell}} = \frac{(\mu_f/\mu)\Lambda}{189\bar{\ell}} \tag{17}$$

$$\bar{\sigma}_f = \frac{\mu_f T \ell_f}{19.5\bar{\ell}t_f} = \frac{(\mu_f/\mu)\Lambda\ell_f}{189\bar{\ell}t_f} \tag{18}$$

With the standard 5500 g load on the lever arm and the 17.9:9.0 ratio, the load T on the bedplate is 10939 g. For a pulp with average fiber length $\bar{\ell}$ = 0.2 cm, Eq. 16 would predict a $\bar{P}_N$ value of 41 psi; this is in contrast to values near 500 psi reported for larger refiners (10). For a fiber in such a slurry with

$$\ell_f = 3 \text{ mm},$$

$$t_f = 4\ \mu\text{m},$$

$$\mu_f = 0.15,$$

then the tensile stress $\bar{\sigma}_f$ would be 4500 psi. If we use long, relatively low strength sulfite pulp, a typical fiber strength level may be 5-6 times that. Hence, if this analysis is correct, P_N would have to hit a value of 5-6 times $\bar{P}_N$ in order to break the 3 mm long fiber in tension.

Clearly, if the beater is to be used to study fiber cutting, its severity of action should be increased. Preliminary experiments indicate that an effective way to accomplish this is to increase the load, up to 4.5 times the standard.

The task of measuring P_N on a scale which would correspond to fiber stresses was approached by replacing a 1/8-inch square bedplate bar segment with an instrumented post (Fig. 4). The top of the post experiences small deflections as the rotor bars pass during beating. Those deflections were detected by strain gages attached to the beam which forms an integral part of the post assembly (Fig. 5). Those strain gages were then connected to give signals proportional to normal and tangential deflections, as indicated in Fig. 5. Although the normal signal was the only one from which P_N was calculated, the tangential was of interest to check friction coefficient and was necessary for normal/tangential signal crosstalk corrections.

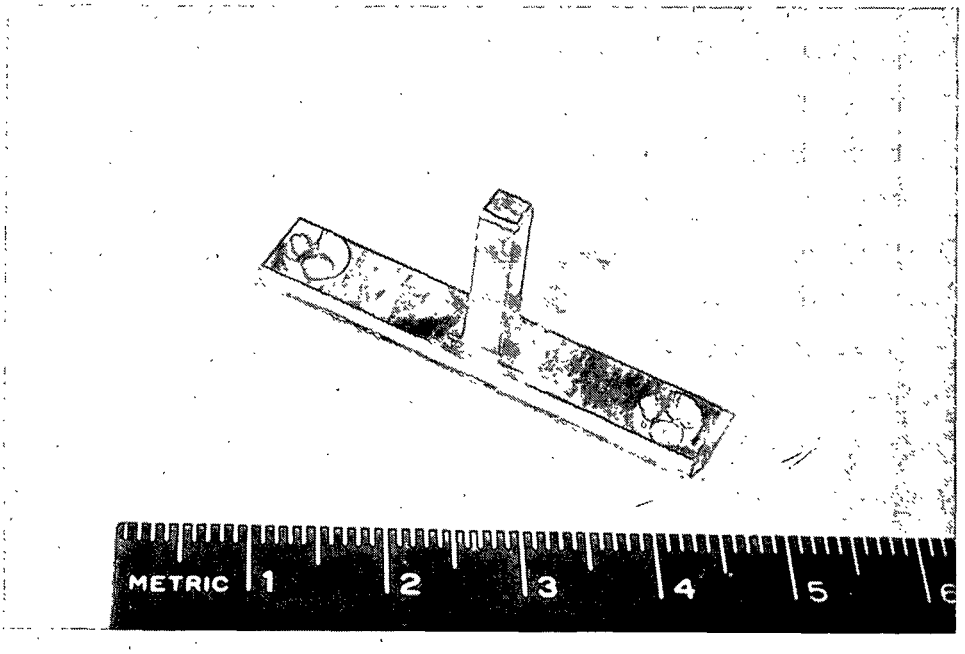

Figure 4. Bar segment and beam prior to strain gage attachment.

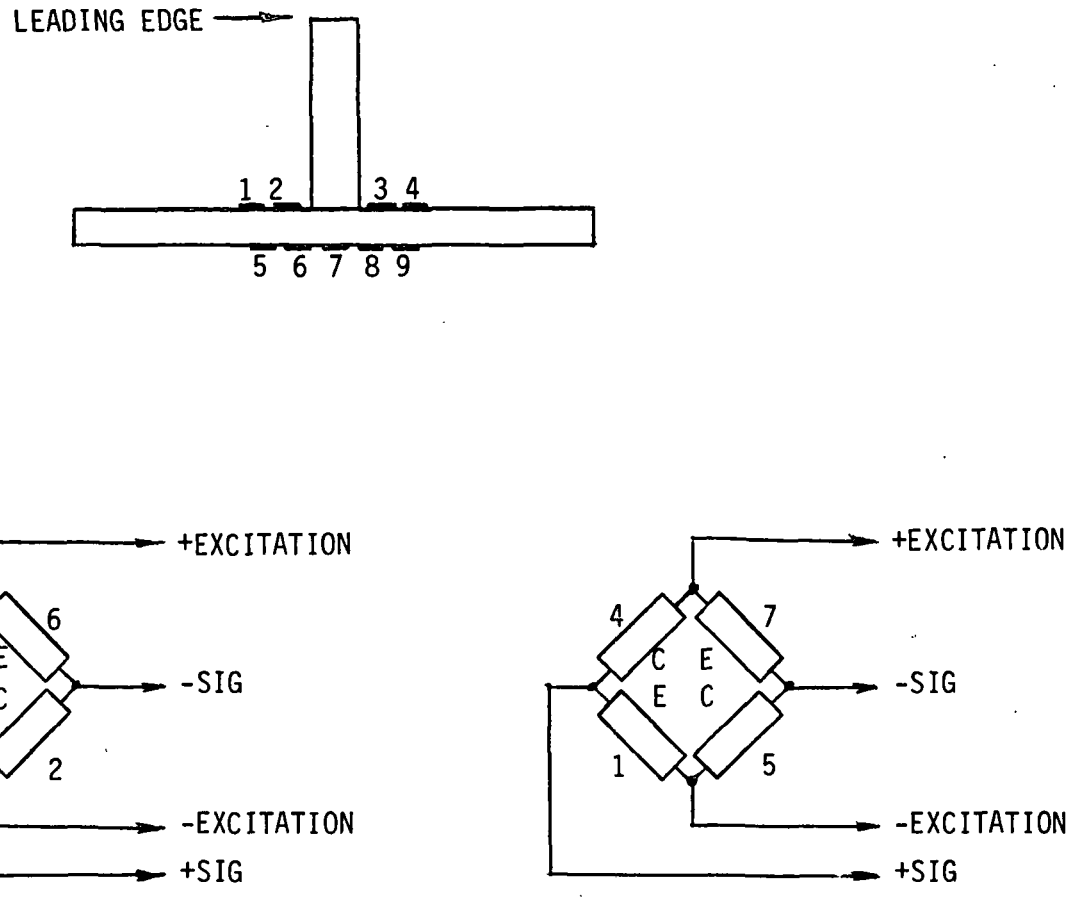

Figure 5. Placement of strain gages on post/beam assembly (top), and their connection into Wheatstone bridge circuits for normal (left) and tangential (right) deflections.

After the strain gages were attached to the beam and connected into the bridge circuits on the beam, the gages and connections were sealed with waterproof sealant, and the assembly was fitted into a specially made brass bedplate holder (Fig. 6). The central bar of a seven-bar bedplate assembly was cut in two and shortened prior to heat treating to provide an opening for the instrumented post. The bedplate bars were then heat treated, assembled with the oak fillings and riveted together, and placed in the brass holder over the post (Fig. 7). The area around the post was potted with a polymeric material, and the bar assembly was potted into the holder with a steel putty (Devcon). After installing the assembly in the beater, about 1 mm or less of bar surface was

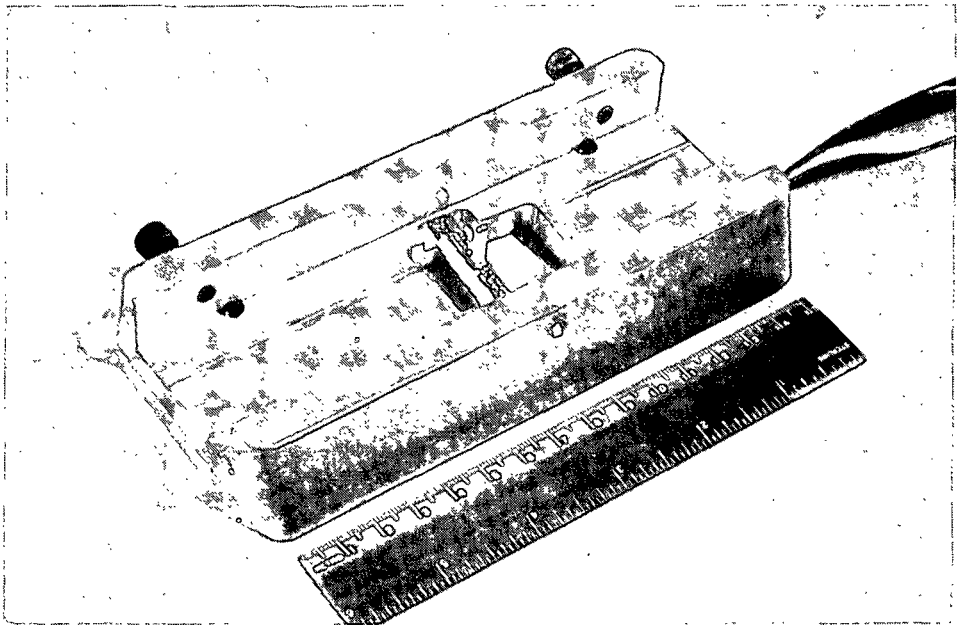

Figure 6. Strain gages attached to beam, installed in bedplate holder.

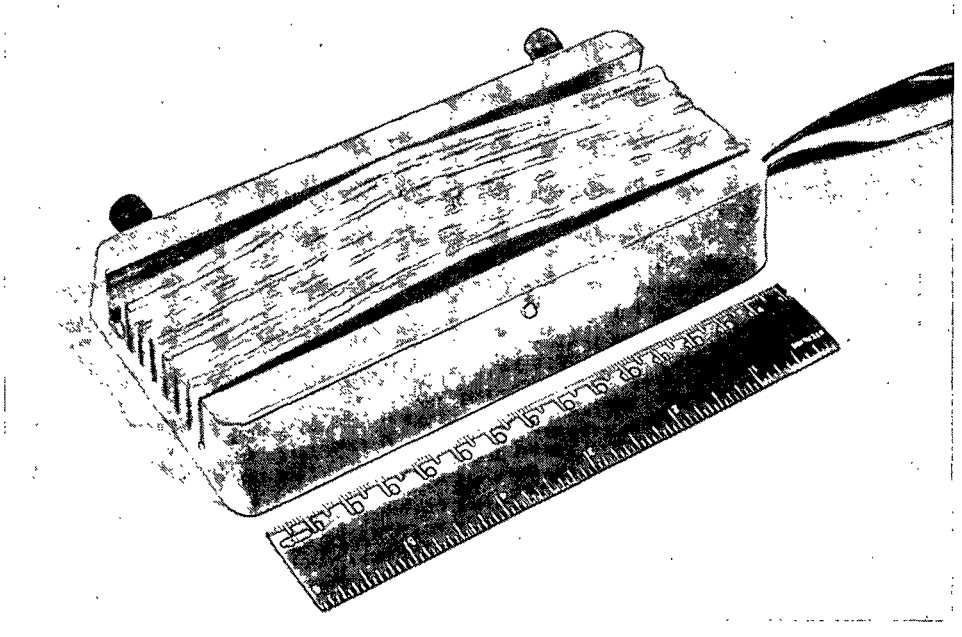

Figure 7. Beater bar assembly in place around instrumented post, prior to potting.

ground off with pulp-abrasive slurry, bringing the tops of the beater bars flush with the top of the post. At the point when a carbon paper impression revealed a uniform rotor bar contact across the entire bedplate, including the top of the post, then the assembly was removed and statically calibrated. By applying known forces to the post in the normal and tangential directions, calibration curves for bridge output voltages, including crosstalk, were determined. In the process of working out problems with strain gage and connection failures, potting techniques, signal noise, and other difficulties, several of these assemblies were put together. The later models featured a design whereby the instrumented post could be inserted into the bedplate holder from the bottom, without removing and repotting the bar assembly. Also, earlier designs incorporated potting in a space between the post and the wood spacers; later designs eliminated that space, and the resultant extraneous effects caused by potting in that location.

During operation, the normal and tangential signals are processed through amplifiers and fed to a data acquisition system. A triggering mechanism on the beater shaft initiates one data collection sweep per revolution. The normal and tangential voltage outputs as functions of time can be viewed on an oscilloscope screen and dumped to an Apple computer for manipulation. Software was written to accomplish the data transfer to the Apple and to convert the voltage values to force per the calibration (including crosstalk), then the normal force was converted to P_N by dividing by the calculated time-dependent bar segment crossing area. The computer program is also capable of determining the maximum level of P_N at each impact and calculating averages and standard deviations of P_N over several data sweeps.

The number of impacts which can be monitored in this way during beating is limited by data transfer time and disc storage capacity. In order to determine a more representative distribution of P_N, the normal voltage signal V_N can be monitored by a series of three electronic event counters. The event counters can be adjusted to increment when the normal voltage signal exceeds a preset value; this affords a distribution of V_N: x impacts/min exceed 1.0 volts, y impacts/min exceed 1.2 volts, etc. The distribution of P_N can then be closely inferred from this.

RESULTS AND DISCUSSION

EFFECTS OF LOAD AND ADDITIVES ON BEATING RESPONSE

In order to study fiber cutting and other severity-related phenomena, it is essential to use a long-fibered pulp which is sensitive to cutting. A western softwood bleached sulfite pulp was chosen. In addition, the beater must be operated in such a way as to effect a certain degree of cutting. Hence, a series of experiments was carried out with this pulp to establish base-line data and to determine the effects of load and certain additives on pulp property development.

Table 1 lists beating parameter data obtained at four levels of load, beating in tap water. The apparent coefficient of friction of the pulp rapidly decreases initially but eventually levels off as the pulp develops a slimy character. The values of initial coefficient of friction compare with the values of 0.06-0.14 reported by Steenberg (15) for dissolving pulp in a Valley

Table 1. Beating parameters as function of bedplate load[a].

Load, g on lever arm	Total Beating Time, min	Power, hp[b] No-load P_o	Gross P_t	Net P_n	Net Specific Energy E_n Sample	Cumulative	App. Coeff. of Friction, μ	Sp. Edge Load, Ws/m
5500	5	0.22	0.33	0.11	0.99	0.99	0.15	0.30
(standard)	10	0.21	0.30	0.09	0.82	1.81	0.12	0.23
	15	0.20	0.28	0.08	0.73	2.54	0.11	0.20
	20	0.19	0.26	0.07	0.80	3.34	0.11	0.20
	30	0.18	0.25	0.07	1.56	4.89	0.10	0.18
8250	3	0.21	0.38	0.17	0.88	0.88	0.15	0.44
(1.5 x std.)	8	0.20	0.33	0.13	1.20	2.08	0.12	0.34
	13	0.19	0.31	0.12	1.17	3.25	0.11	0.31
	18	0.18	0.30	0.12	1.22	4.47	0.11	0.31
	23	0.18	0.30	0.12	1.32	5.79	0.10	0.31
16500	3	0.22	0.52	0.30	1.61	1.61	0.14	0.80
(3.0 x std.)	6	0.21	0.45	0.24	1.37	2.98	0.11	0.63
	9	0.20	0.42	0.22	1.29	4.27	0.10	0.57
	12	0.19	0.41	0.22	1.36	5.63	0.10	0.57
	15	0.19	0.42	0.23	1.52	7.15	0.10	0.60
24750	2	0.22	0.70	0.48	1.69	1.69	0.15	1.28
(4.5 x std.)	4	0.22	0.56	0.34	1.25	2.94	0.11	0.89
	6	0.21	0.51	0.30	1.19	4.13	0.10	0.80
	9	0.21	0.50	0.29	1.83	5.96	0.09	0.77
	12	0.19	0.50	0.31	2.04	8.00	0.09	0.80

[a]Average of duplicate runs at each load.
[b]The rotor speed Ω was 500 $\pm$ 7 rpm.

beater, with higher levels observed at lower loads and higher consistencies. The changing frictional character of the pulp produced corresponding changes in both the no-load and the net power consumption, as well as the specific edge load. These values were high initially but dropped rapidly, then leveled off.

Figures 8-10 illustrate the effects of load on the energy efficiency of pulp property development. To achieve a given level of freeness, density, or tensile strength, less net energy is required under gentler refining conditions.

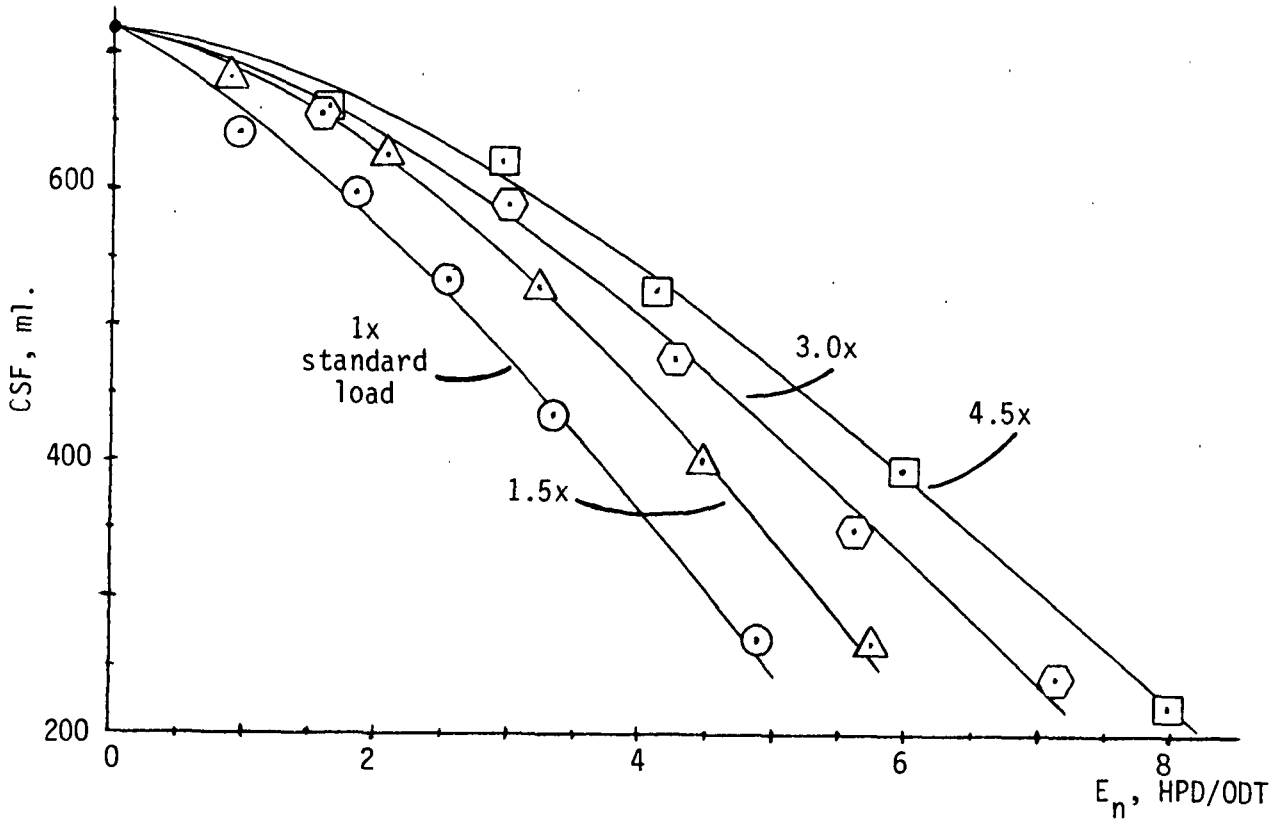

Figure 8. Freeness vs. net specific energy.

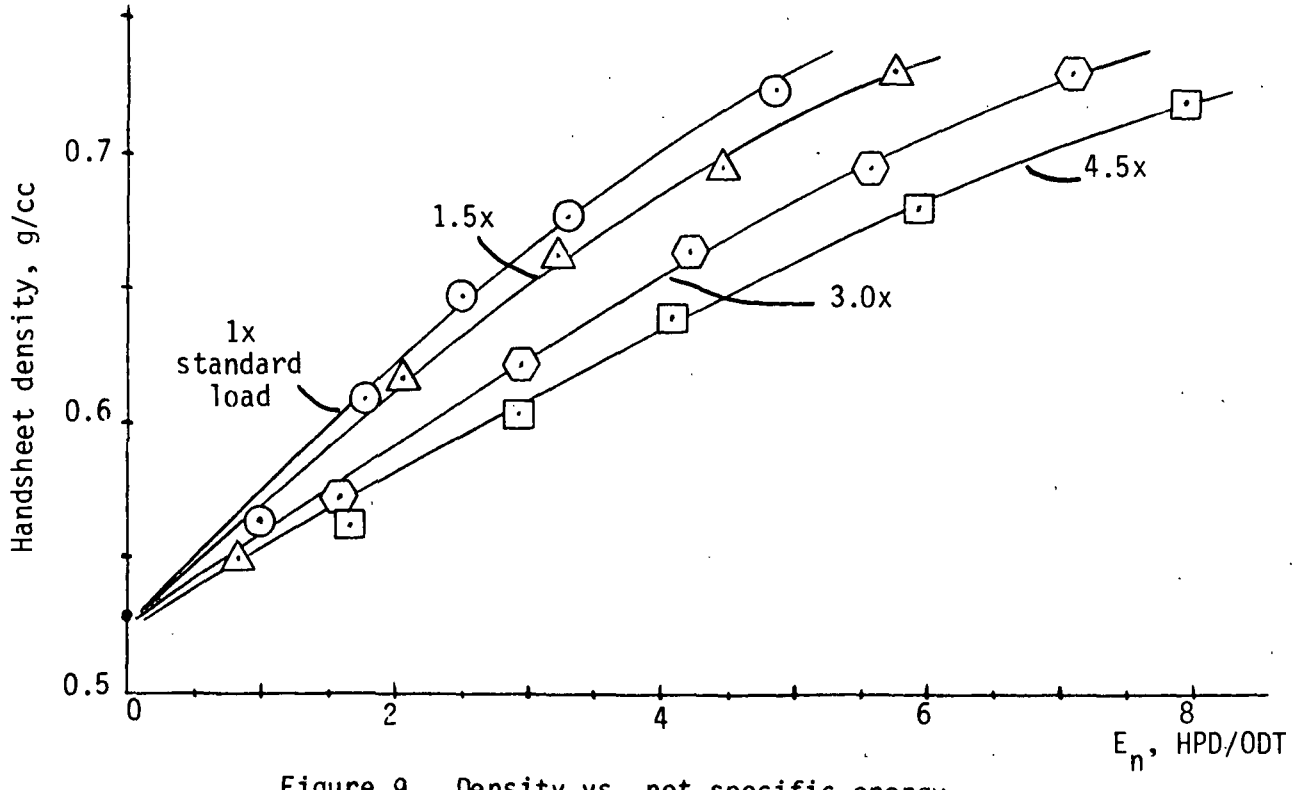

Figure 9. Density vs. net specific energy.

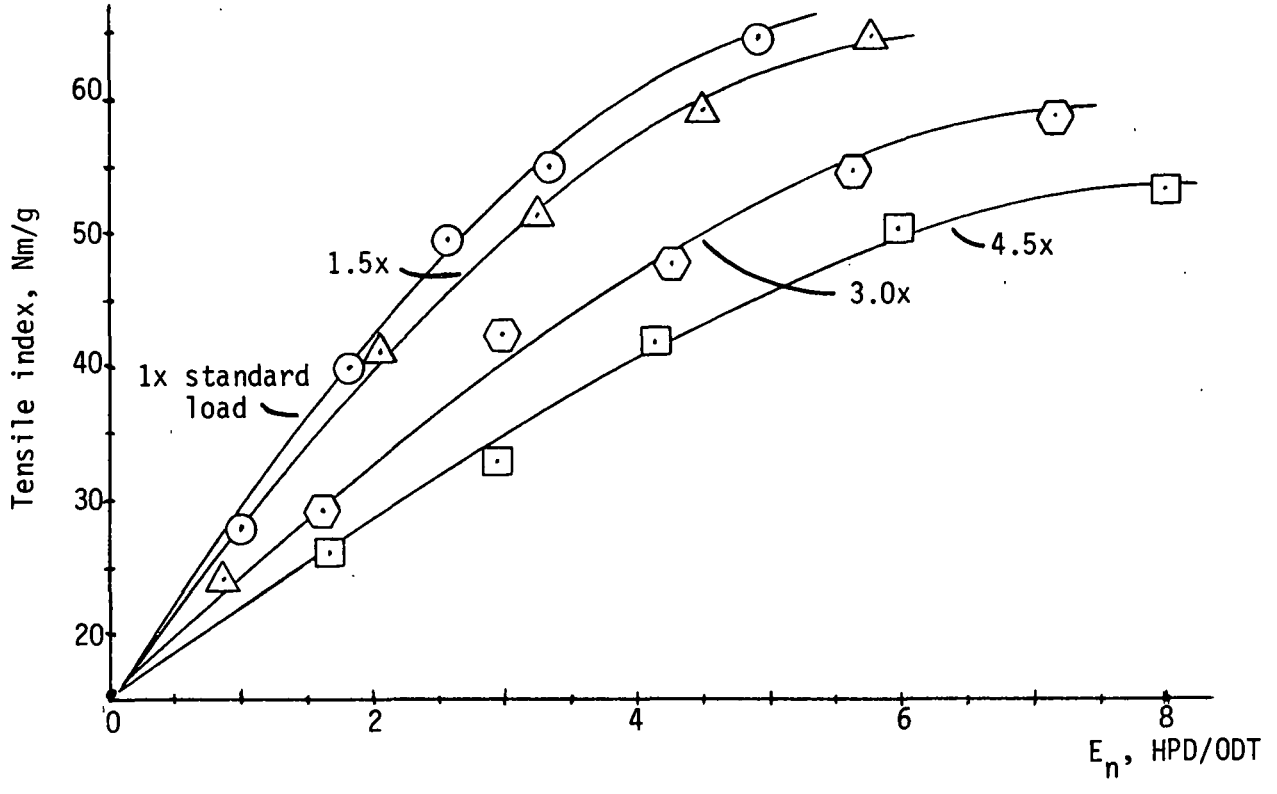

Figure 10. Tensile strength vs. net specific energy.

This is similar to the behavior of hardwood pulps, but is the opposite of that observed with softwood kraft (4, 6). Apparently the softwood sulfite pulp used in the present study possesses a sensitivity to refining severity which is totally different from softwood kraft pulps.

Figures 11-15 illustrate the pulp property relationships observed at the various loads. As functions of density, the levels of freeness, tear strength, and scattering coefficient are essentially unaffected by load, while the tensile strength at a given density is inferior at higher loads. The benefits of gentler refining on tear-tensile and tear-density are readily apparent. In addition, the initial rates of fiber cutting and fines generation are very sensitive to beating severity (Fig. 16).

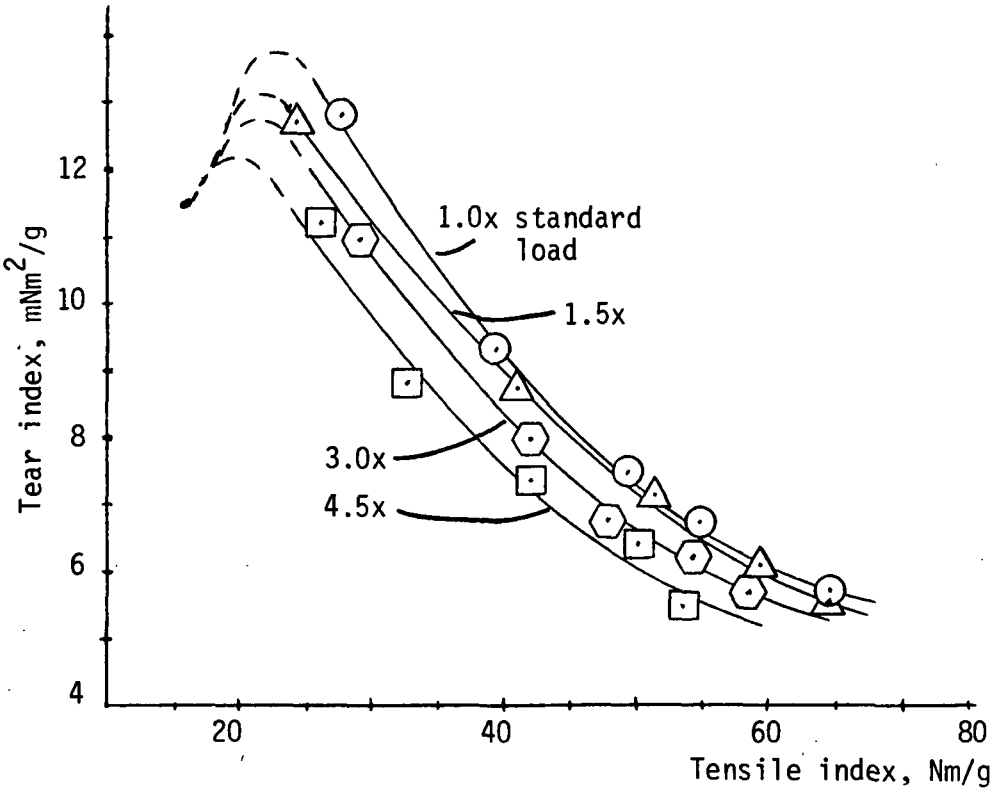

Figure 11. Tear vs. tensile strength.

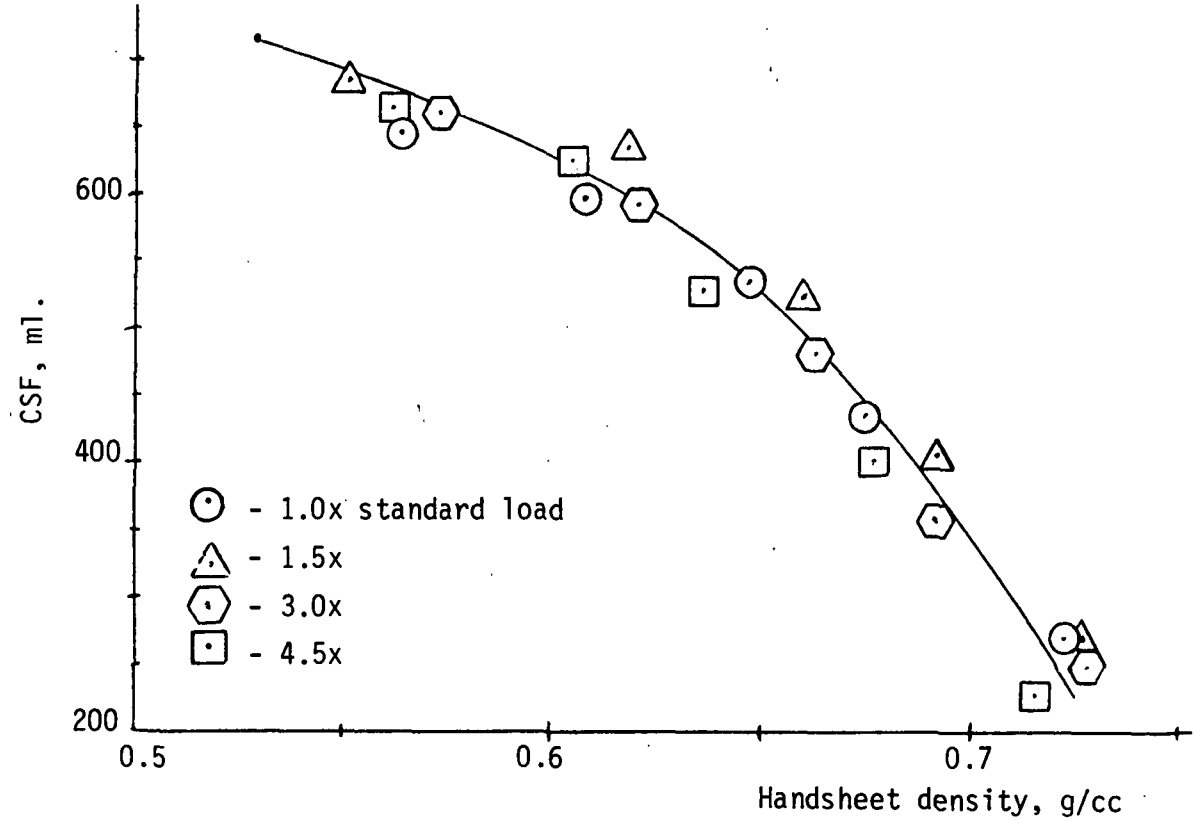

Figure 12. Freeness vs. density.

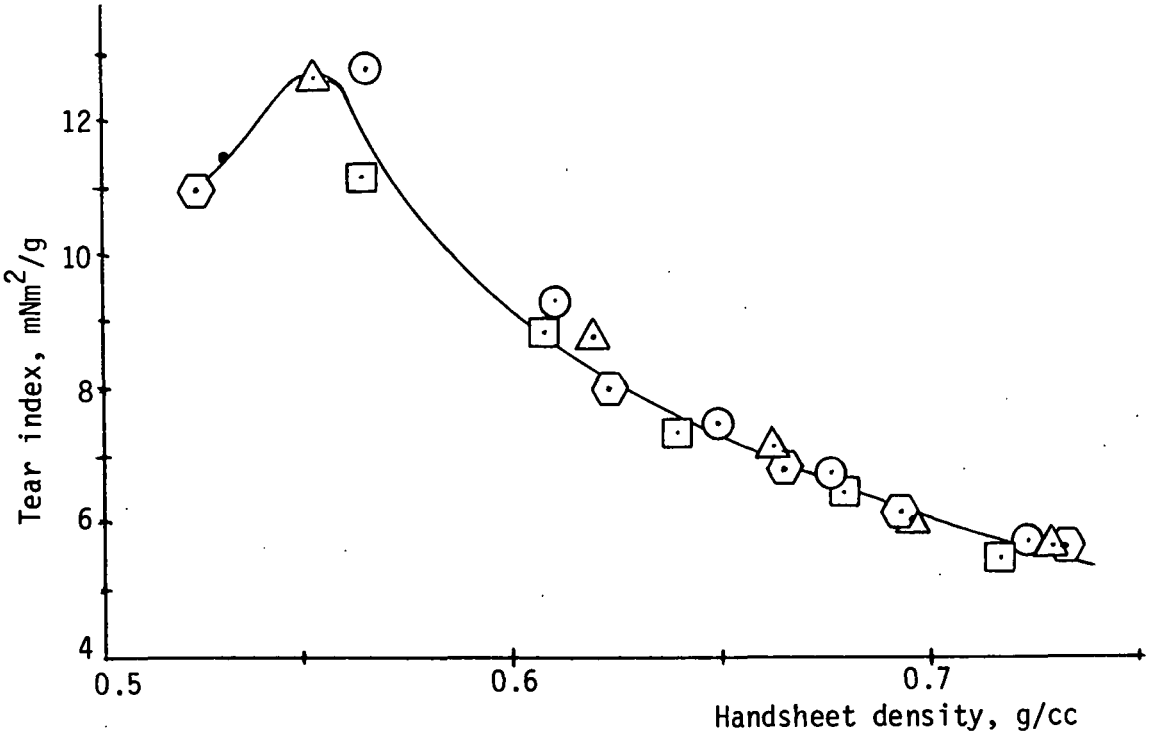

Figure 13. Tear strength vs. density.

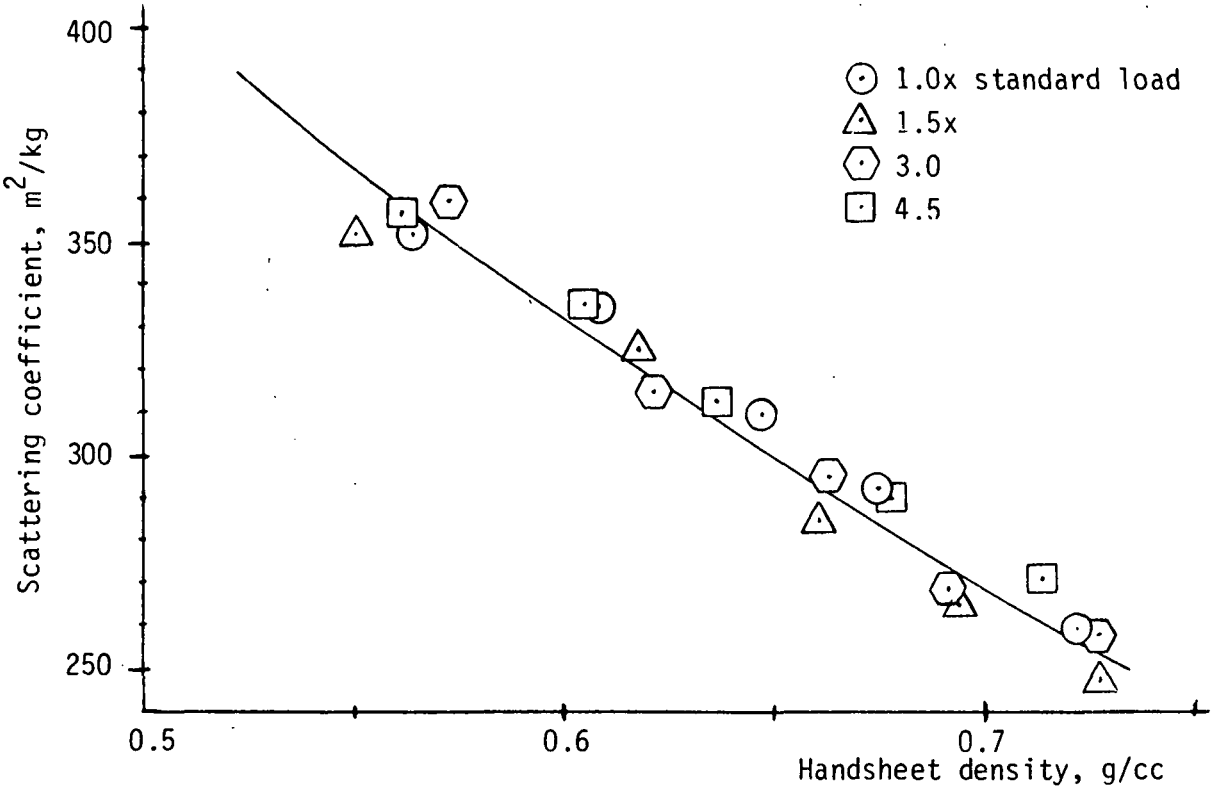

Figure 14. Scattering coefficient vs. density.

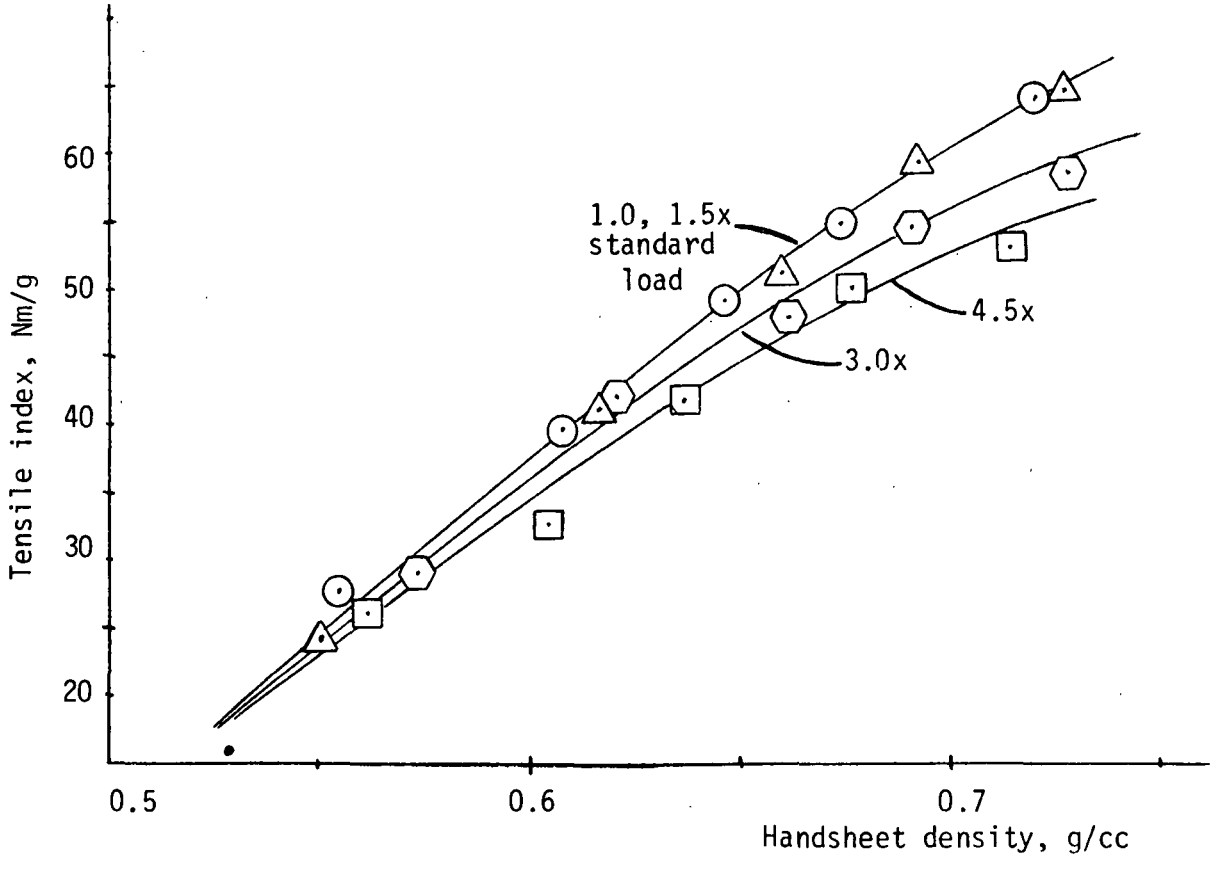

Figure 15. Tensile strength vs. density.

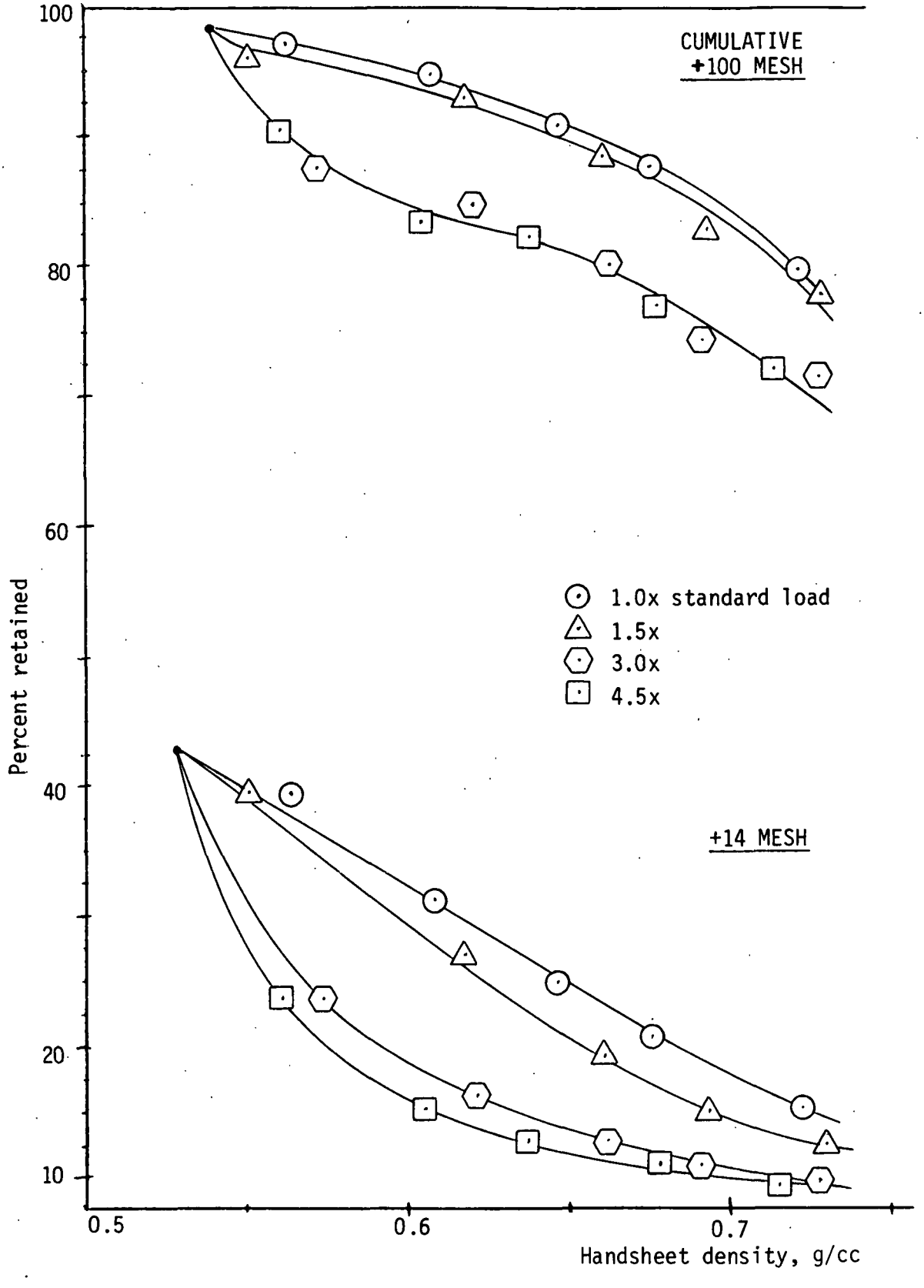

Figure 16. Fiber classification vs. density.

A later series of experiments was carried out with certain additives in deionized water, using a different bedplate. Listed in Table 2 are beating parameters calculated from torque readings recorded during those runs. Figures 17-21 compare the energy and pulp property relationships of deionized water runs with alum- and alkali-containing runs. Beating at pH 10 required somewhat less energy to reach a given level of freeness or density, while beating in the presence of 10 mg/ℓ alum required much less energy. Pulp property relationships, however, were identical with the three series. The magnitude of specific energy levels recorded in these runs was much higher than in the previous set.

Table 2. Beating parameters obtained with additives in deionized water[a].

Water Medium	Total Beating Time, min	Net HP	App. Coeff. of Friction, μ	Sp. Edge Load, Ws/m	Net Cum. Sp. Energy, HPD/ODT
Deionized[b]	0	0.13	0.15	0.32	0
	1.8	0.12	0.14	0.30	0.4
	6.5	0.10	0.13	0.26	1.3
	11.6	0.10	0.12	0.27	2.3
	21.5	0.10	0.12	0.27	4.3
	31.5	0.09	0.12	0.24	6.3
	41.7	0.09	0.12	0.25	8.6
10 mg/ℓ $Al_2(SO_4)_3 \cdot 18H_2O$	0	0.11	0.14	0.28	0
	2.7	0.09	0.12	0.24	0.4
	7.9	0.07	0.09	0.20	1.2
	11.9	0.07	0.09	0.20	1.8
	22.1	0.08	0.10	0.20	3.4
	42.6	0.09	0.11	0.23	7.5
	62.6	0.09	0.11	0.23	11.8
NaOH to initial pH = 10	0	0.14	0.17	0.35	0
	2.3	0.10	0.12	0.27	0.5
	6.8	0.07	0.09	0.20	1.2
	22.0	0.07	0.08	0.18	3.4
	42.4	0.11	0.14	0.30	7.6
	61.8	0.12	0.15	0.31	13.0

[a]Absolute levels may be in error due to torque sensor malfunction - see text.
[b]Average of duplicate runs.

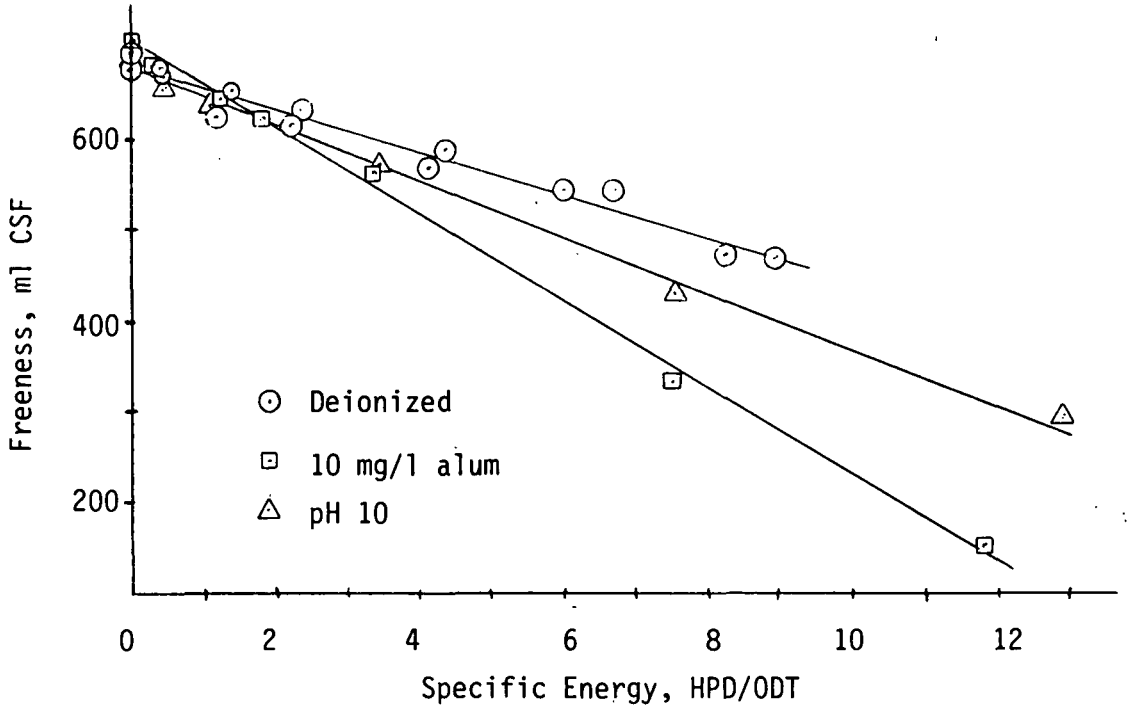

Figure 17. Freeness vs. net specific energy.

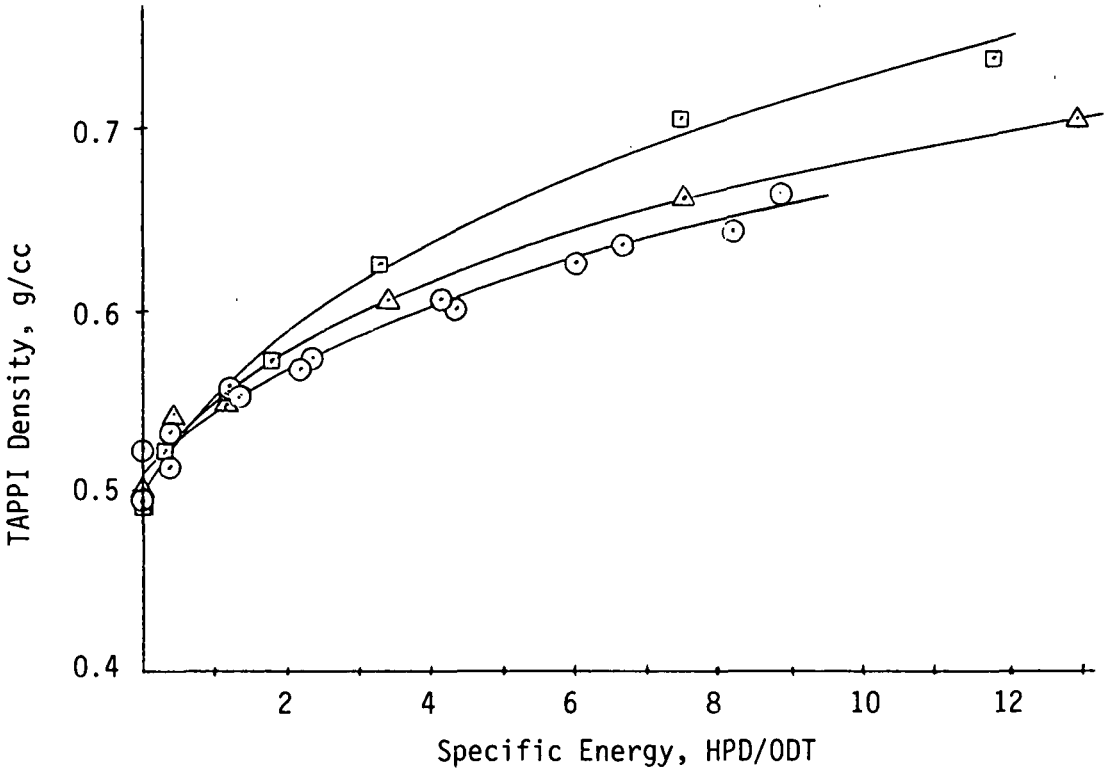

Figure 18. Density vs. net specific energy.

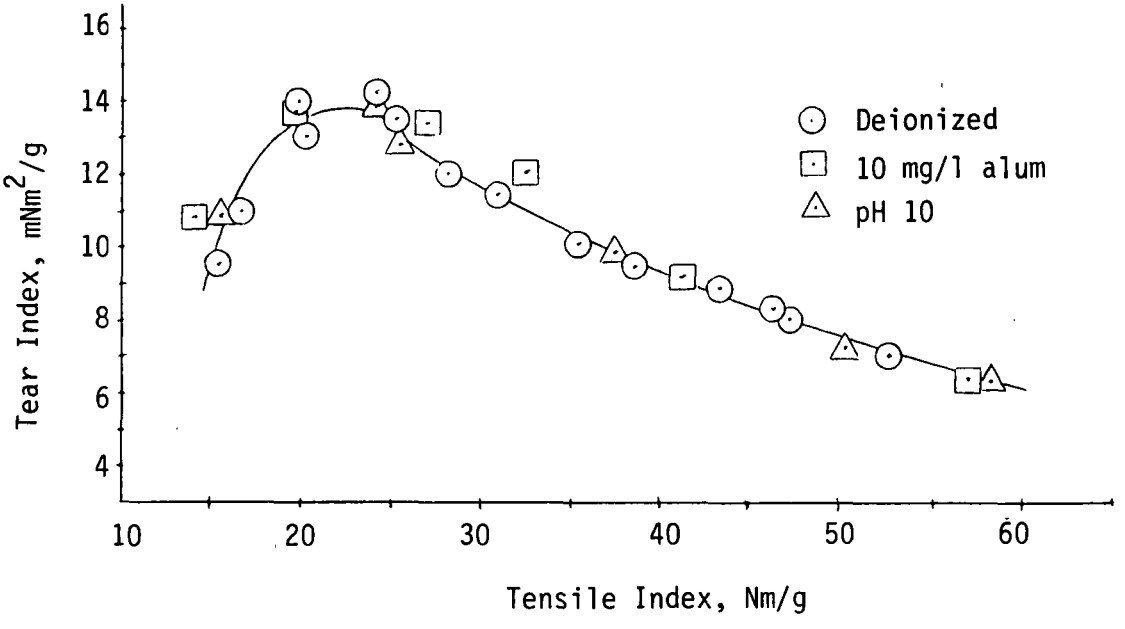

Figure 19. Tear vs. tensile strength.

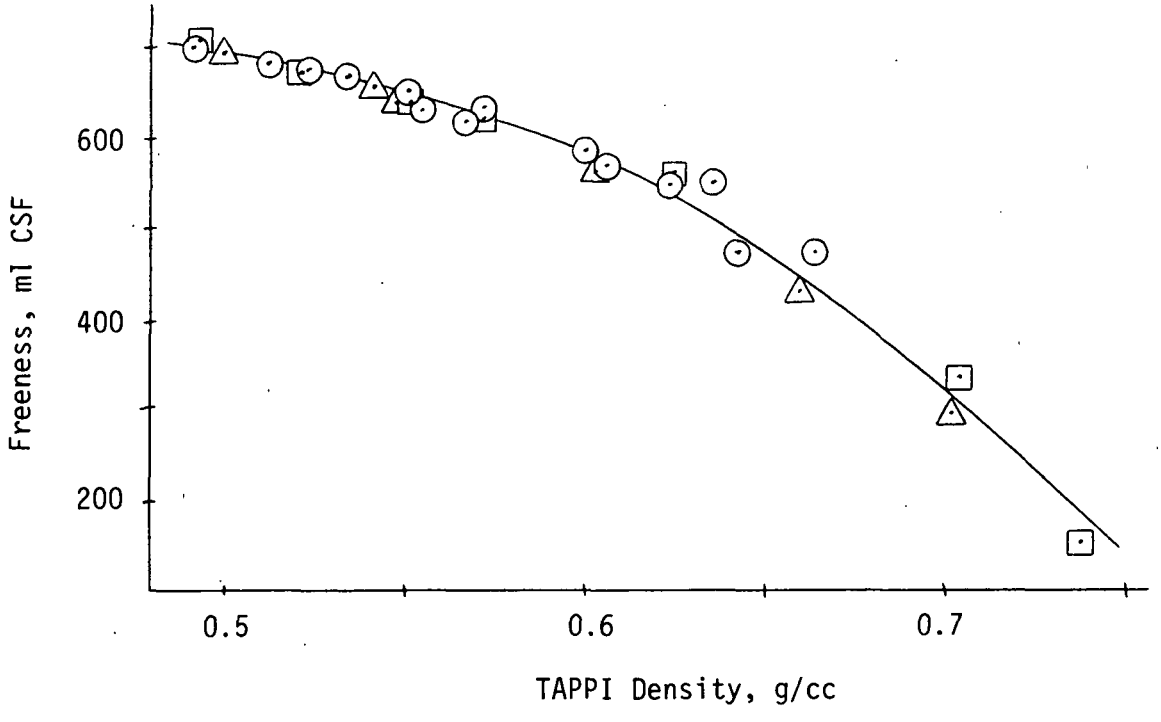

Figure 20. Freeness vs. density.

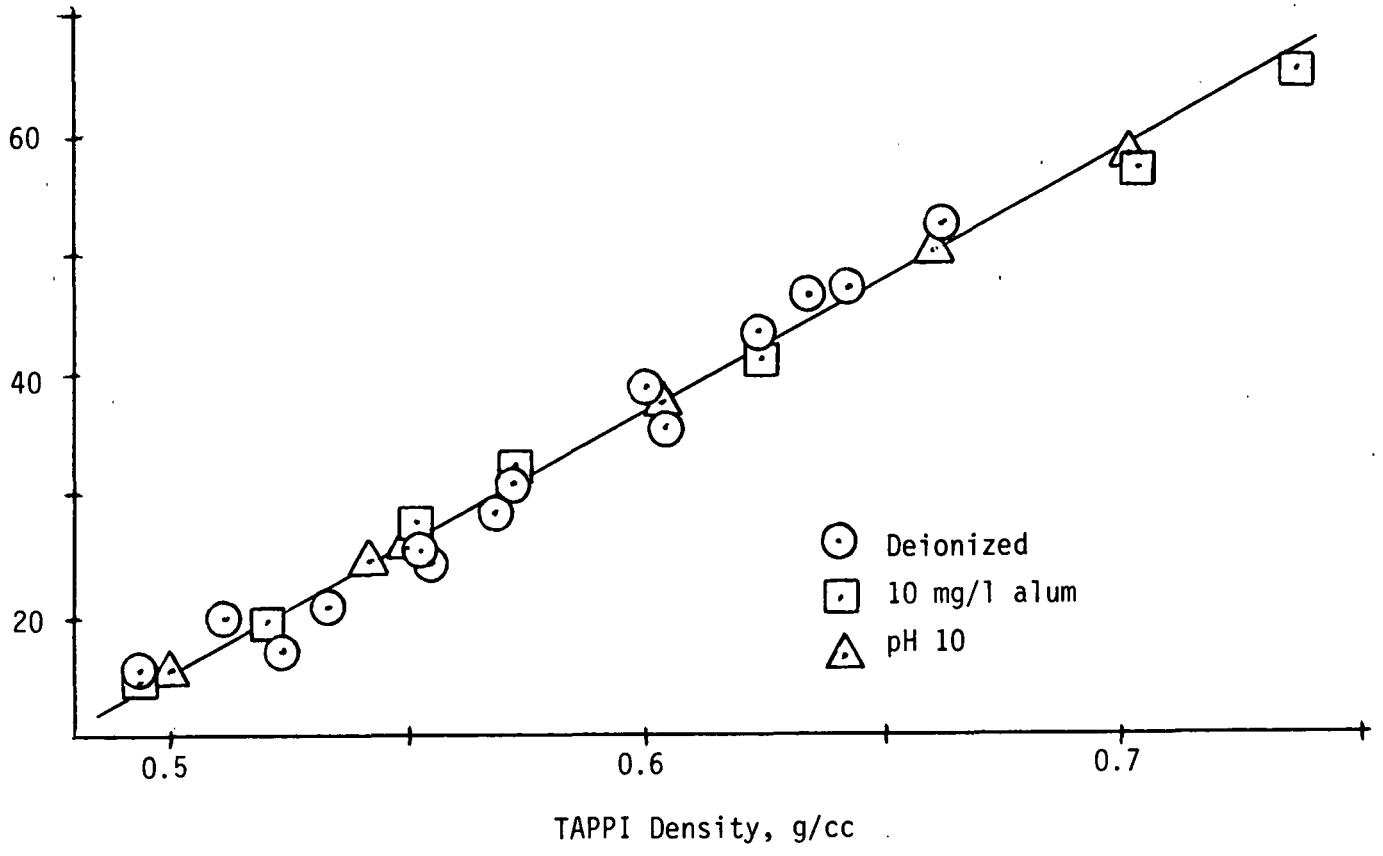

Figure 21. Tensile strength vs. density.

Although different bedplates were used in the two cases, the discrepancy is believed to be chiefly attributable to a malfunction in the torque sensor. Hence, the values in Table 2 are believed to be correct in their relationship to each other, but their absolute level may be in error. Similarly, the x-axes of Fig. 17 and 18 may be in error as well.

As expected, the coefficient of friction with initial pH 10 was lower than in the case with deionized water until after ca. 40 minutes beating time. The reason for the rise in friction thereafter is unclear, but it may have been related to a decreasing pH (not recorded) or other alkali-related fiber modification. The lower friction coefficient and rate of power consumption with alum

was a bit surprising. Other workers (16) reported substantial increases in friction coefficient and refining power consumption in the presence of alum at pH 4-5. Further substantiating work is needed to verify the opposite effect, as observed here at low alum concentrations (pH ca. 6.5).

NORMAL FORCE AND P_N CURVES

Figure 22 depicts a typical trace of the voltage output from the normal and tangential bridges. Three rotor bar crossings are recorded here. The highest peak in each impact, which starts as the leading edge of the rotor bar first reaches the post, represents the maximum force and pressure level of that bar crossing. This maximum typically occurs at ca. 0.8 mm from the leading edge of the post, as indicated in Fig. 23. A second force peak is often observed at a distance of 2.5-3.2 mm from the leading edge. However, because of the larger bar area at this point, the P_N level is much lower than in the 0.8 mm vicinity. Occasionally, sizable force readings are recorded as a rotor bar hits the next

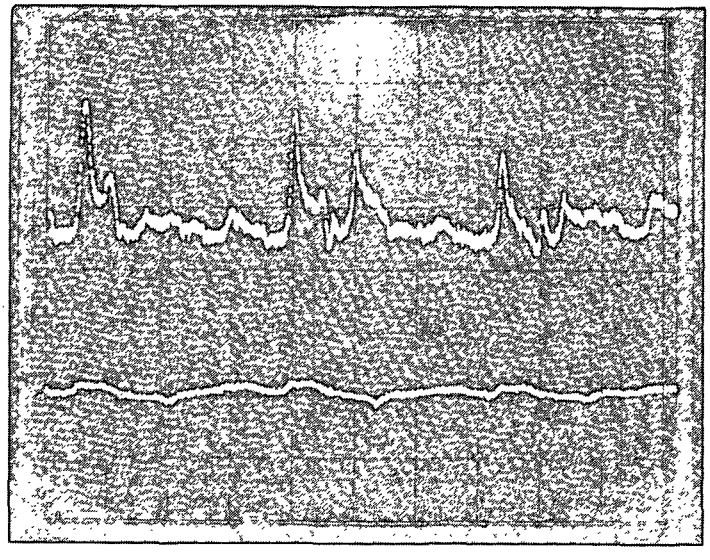

Figure 22. Oscilloscope trace of normal (top) and tangential (bottom) voltage outputs.

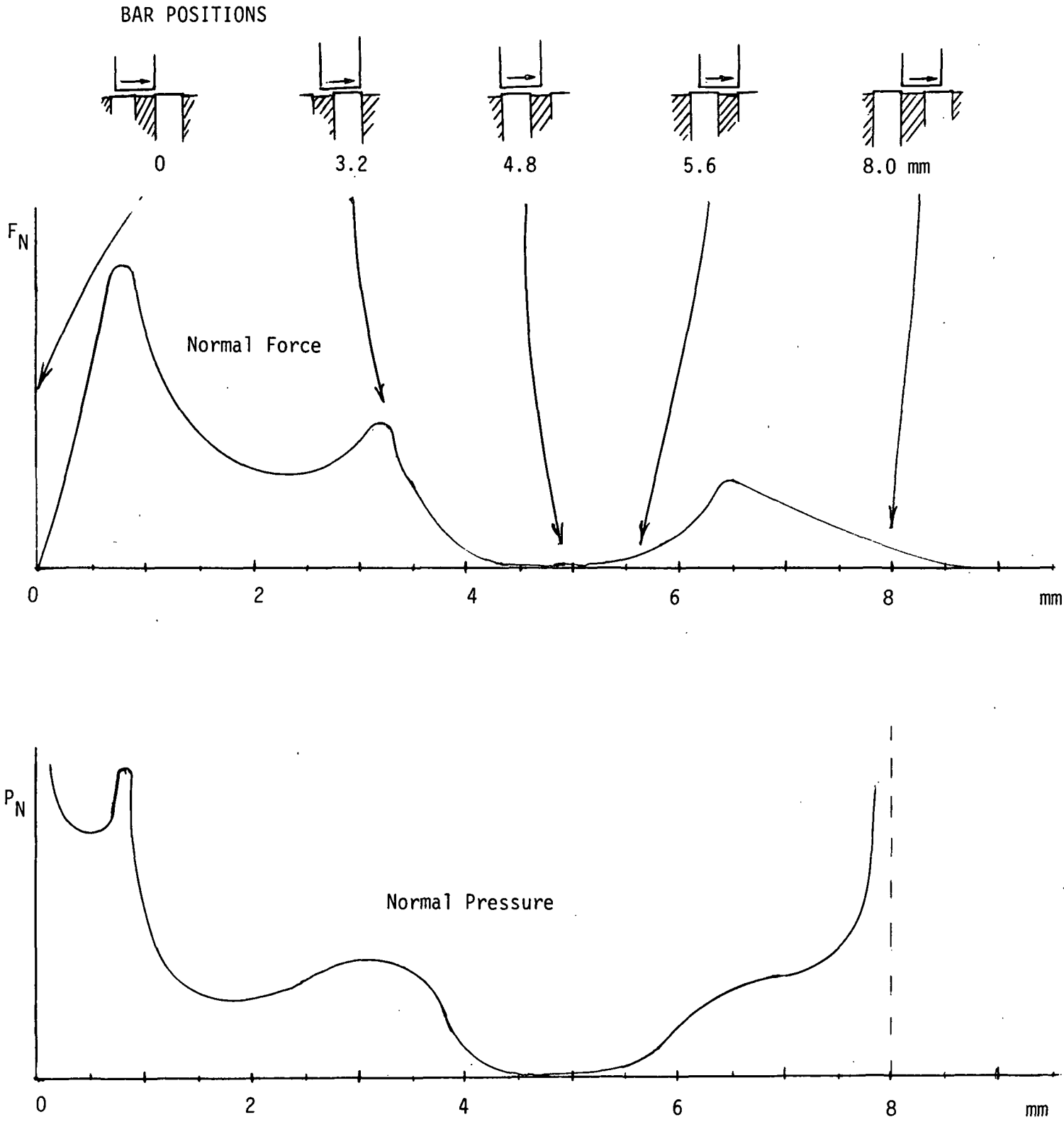

Figure 23. Typical relative levels of normal force F_N and normal pressure P_N, as functions of rotor bar position during a bar crossing. P_N equals F_N divided by the time-dependent bar crossing area. Bedplate bars are 3.2 mm wide, wood fillings 2.4 mm, rotor bars 4.8 mm.

bedplate bar following the instrumental post. This is exemplified by the second impact shown in Fig. 22, and illustrated by the peaks at 6.4 mm in Fig. 23. This is evidently due to normal force transmitted through the wood filling following the post, and is not a force experienced by fibers during the impact over the post. Since the maximum P_N level in each impact is consistently seen to be at the first peak, the computer program searches for the F_N maximum in the range of 0.50 to 1.25 mm from the leading edge, and computes P_N from that data point. In addition, the event counters used to count levels of V_N above a set point, operate through a trigger and an electronic gating mechanism so that they only monitor the first 300 μs (1.52 mm) of each bar crossing.

VARIABILITY OF NORMAL FORCE AND PRESSURE

Listed in Table 3 are values of P_N calculated by the Apple program operating on data obtained from the data acquisition system. At varicus times during a standard beating, 27 consecutive bar impacts were monitored (out of 32 in a complete rotor revolution). The variability from one impact to the next, and from minute to minute, is tremendous. It appears as though P_N may follow a Poisson distribution, with standard deviation equal to (or exceeding) the mean. Although it is difficult to declare it statistically significant, there does appear to be a consistent broad peak of P_N values in the middle portion of beating. Somewhat lower levels are typically observed in early beating, and lower levels yet after the freeness drops below about 300 ml CSF.

These observations are also confirmed by the counter data, as seen in Table 4. To obtain this data, the group of three counters was set to count the number of impacts which exceeded levels of 0.2, 0.8, and 1.6 V, for a one-minute period, then reset to levels of 0.4, 1.2, and 2.0 V for a second one-minute

Table 3. Values of P_N for 27 consecutive impacts, monitored at various times of beating softwood sulfite pulp at standard load and consistency in deionized water[a].

Beating Time, min	5	15	20	45	60	75
	0	1944	0	465	117	0
	29	266	779	0	210	37
	75	109	0	919	131	0
	117	0	85	6	424	141
	234	182	0	35	787	0
	350	185	0	124	141	498
	0	258	109	943	0	311
	102	715	59	85	0	0
	90	1012	137	0	242	124
	153	1287	960	779	0	92
	59	39	0	141	691	0
	177	2867	38	449	196	244
	0	604	0	241	525	0
	0	0	742	2629	148	29
	0	0	490	194	224	0
	75	0	1217	1679	154	0
	0	273	39	2860	442	0
	1600	664	195	778	0	0
	0	621	0	85	309	323
	237	6284	742	135	447	165
	0	47	2051	3768	234	0
	0	54	0	366	93	390
	0	0	844	599	213	92
	1949	1036	0	1072	100	0
	0	454	724	298	116	107
	777	670	0	604	29	233
	1018	0	2771	109	0	154
Mean	261	725	444	719	221	109
Std. Dev.	500	1297	686	956	210	140
Pulp Freeness, ml CSF	700	626	525	405	340	220

[a]Only 3.0 OD g freeness samples were removed during beating.

Table 4. Distribution of normal voltage output, as number of impacts per minute in various voltage ranges, as function of time of beating at standard load and consistency[a].

Beating Time, min	Voltage Range, V							Wtd. Av. Voltage, V[b]	Calc'd. Av. P_N, psi[c]
	0-0.2	0.2-0.4	0.4-0.8	0.8-1.2	1.2-1.6	1.6-2.0	>2.0		
0-10	8955	4741	1928	288	78	2	8	0.24	111
0-15	8693	4875	2095	243	87	2	5	0.25	116
5-20	8332	4811	2451	215	185	0	11	0.27	125
10-25	7501	5410	2607	259	212	6	5	0.28	130
15-30	7585	4997	2804	388	204	17	5	0.29	135
20-35	8257	4773	2361	496	90	23	0	0.27	125
25-40	9950	3593	1930	408	107	12	0	0.24	111
30-45	8896	5022	1504	449	127	2	0	0.25	116
35-50	5472	8204	1622	443	250	9	0	0.30	139
40-55	1290	11583	2409	501	199	18	0	0.37	172
45-60	1522	10900	2957	450	154	17	0	0.37	172
50-65	3401	9159	2983	419	26	12	0	0.33	153
55-75	7659	5848	2050	441	0	3	0	0.26	121
60-75	8512	6089	1120	279	0	0	0	0.23	107
70-75	11109	4270	597	24	0	0	0	0.17	79
Av.	7122	6285	2114	354	115	8	2	0.27	125

[a]Calculated as moving averages of three data points spaced 5 min apart.
[b]Calculated using the mid-point of each range, and 2.2 V for the last column.
[c]Assuming peak occurs at 0.8 mm from beginning of impact.

period. This procedure was repeated every five minutes during an entire beater run, during which only 3-gram freeness samples were removed (every 15 minutes). The lowest voltage range (0-0.2 V) was calculated as the difference between the 16,000 total impacts per minute and the 0.2 V counter reading, with the others determined by successive differences. Due to random variability between conditions in the first and second one-minute counting periods, moving averages of three consecutive data sets (each 5 minutes apart) were calculated. This procedure affords a well-defined distribution of force levels, as well as an estimation of the average P_N (assuming the location of the P_N maximum is at 0.8 mm from start of impact). The data in Tables 3 and 4 were taken during the same beater run. In early beating, and especially after extensive beating, one observes a trend toward

fewer very heavy impacts and lower average intensity. However, the levels of P_N calculated from counter data are significantly lower than those from the data acquisition system (Table 3). Of the two sources, the data calculated from the counters may be more representative. The counters monitor 32,000 impacts over a 5-minute period, while the other monitors only 27. In addition, the occasional readings in Table 3, which are in the thousands, are questionable, probably caused by an erroneously low assumption of area in calculating psi; the counter calculations all assume the P_N maximum occurs at the same bar crossing area.

SUMMARY AND CONCLUSIONS

A mathematical model has been formulated to describe fiber stresses during refining. It takes into consideration refiner bar angle and size and fiber length, thickness, and friction characteristics, as well as classical specific edge load parameters.

The response of softwood sulfite pulp to severe beating conditions was similar to that of hardwood pulps: low-intensity refining affords significant property improvement, plus savings in net specific energy.

Compared with Valley beating in deionized water, beating of sulfite pulp in 10 mg/ℓ alum solution resulted in a modest decrease in apparent coefficient of friction, but a sizable reduction in specific energy requirements. Beating at pH 10 gave a variable friction coefficient, with a small reduction in specific energy requirement. Pulp properties were unaffected by these two additives. The interpretation of this in terms of the model equations is yet to be established.

Means have been devised for successfully measuring the local normal pressure P_N in a Valley beater, a key parameter in the model equation. Measurements made to date indicate best-estimate values to be in the 100-200 psi range for TAPPI standard beating of the softwood sulfite pulp, with occasional values of several hundred or over 1000 psi. The variation of P_N from impact to impact, and from minute to minute, is tremendous; P_N appears to follow a Poisson-like distribution, with standard deviation of the same magnitude as the mean. It is not uncommon for an "impact" of 0 psi to be followed by one of several hundred psi. This provides support for Ebeling's theory regarding refining of flocs (1).

With this pulp, the maximum level of P_N during an impact occurs when the leading edge of the rotor bar is ca. 0.8 mm from the stator bar leading edge. In contrast to Goncharov's results with conical refiners (10), this early maximum is not sustained very long during the bar crossing. Rather, it forms a rather sharp peak, later followed by a smaller peak or peaks before the two bars part.

FUTURE WORK

The near-term plans with the Valley beater involve continuing the collection of P_N, μ, SEL, and specific energy data under various beating conditions with the softwood sulfite pulp, and correlation with pulp property data, and fiber length information by Kajaani analysis. Comparisons are to be made between:

- standard load and consistency
- 3x standard load
- 0.8 and 3.0% consistency

- pH 10
- alum addition (10 and 200 mg/ℓ)
- addition of karaya gum or CMC to study μ effects

A recent preliminary run with hardwood pulp showed a different P_N curve shape, with perhaps a quicker rise to the first peak (less than 0.8 mm), and a more prolonged duration at the elevated level. Hence, the first trials to obtain hardwood pulp data are planned soon, to confirm and explain these observations.

Longer-term plans for the Valley beater include running mixtures of dyed rayon fibers and softwood pulp, to test the postulated dependence of fiber cutting on ℓ_f, t_f, μ_f, and $\overline{\ell}$.

Beyond this, the P_N-monitoring scheme is to be applied to a soon-to-be installed 16-inch Beloit-Jones refiner.

REFERENCES

1. Ebeling, K. A critical review of current theories for the refining of chemical pulps. Progress Report Three to the members of The Institute of Paper Chemistry, Project 3384, Jan. 9, 1981.
2. Wultsch, F.; Flucher, W., Papier 12(13/14):334-42(1958).
3. Brecht, W.; Siewert, W., Papier 20(6):301-11(1966).
4. Levlin, J.-E. Some differences in the beating behavior of softwood and hardwood pulps. Preprint, International Symposium on Fundam. Concepts of Refining, Appleton, WI, Sept., 1980, p. 51-60; Pulp Paper Can. 81(12):51-9 (1980).
5. Levlin, J.-E. Characterization of the beating result. Ibid, p. 131-8.
6. Canon, J. G.; DeFoe, R. J. Benefits of low intensity refining. Proceedings, TAPPI Papermakers' Conf., Atlanta, GA, April, 1984, p. 41-5.
7. Arjas, A. Constant vs. variable rotational speed during the refining process and the Adapt-Set System. Preprints, International Symposium on Fundam. Concepts of Refining, p. 264-73, Appleton, WI, Sept., 1980.

8. Nilsson, H. A totally new concept in stock refining - the Vargo beater. Paper Trade J. 54-56(Oct. 26, 1970).

9. Leider, P. J.; Nissan, A. H. Understanding the disk refiner - the mechanical treatment of the fibers. Tappi 60(10):85-9(1977).

10. Goncharov, U. N. Force factors in a disk refiner and their effect on the beating process. Bumazh. Prom. no. 5:12-14(May, 1971).

11. Banks, W. A. Paper Technol. 8(4):363-9(1967).

12. Fox, T. S.; Brodkey, R. S.; Nissan, A. H. Tappi 62(3):55-8(1979).

13. Hartman, R. Mechanical treatment of pulp fibers for property development. Doctoral Dissertation. Appleton, WI, The Institute of Paper Chemistry, 1983. 127 p.

14. Corte, H.; Agg, S. On the shortening of pulp fibers during beating. Presented at International Symposium on Fundam. Concepts of Refining, Appleton, WI, Sept., 1980.

15. Steenberg, F. In Symposium on Beating. Proc. Tech. Sect. Brit. Paper and Board Makers' Assoc. 32(2):388-95(1951).

16. Barnet, A.; Leask, R. A.; Shaw, A. C. Alum pretreatment of high-yield sulfite. In Fiber-Water Interactions in Papermaking-Transactions of the Symposium held at Oxford, Tech. Div., BPBIF, Vol. I, p. 179, Sept., 1977.

THE INSTITUTE OF PAPER CHEMISTRY

Appleton, Wisconsin

Status Report

to the

ENGINEERING PROJECT ADVISORY COMMITTEE

Project 3480/3584

PROCESS FUNDAMENTALS OF WET PRESSING

September 11, 1985

PROJECT SUMMARY FORM

DATE: September 11, 1985

PROJECT NO.: 3480/3584 - Process Fundamentals of Wet Pressing

PROJECT LEADER: C. H. Sprague

IPC GOAL: Fundamentally increase the potential capacity of processes.

OBJECTIVE:

1. To increase press effectiveness through improvements to the water receiving system.

2. To determine the technical and economic feasibility of displacement pressing in achieving high dryness and/or property control.

3. To provide a fundamental model to describe the amount of water removal and the degree of web consolidation in a wet pressing process.

CURRENT FISCAL BUDGET: $140,000

SUMMARY OF RESULTS SINCE LAST REPORT: (April, 1985 - September, 1985)

1. This work has concentrated primarily on porous plates as potential replacements for felts in wet pressing. This work, initiated in response to the superior performance obtained with porous plates in the UMO study, has now been discontinued. When tested under common conditions, porous plates proved inferior to felts under all circumstances and for a fairly broad range of porous plate types.

2. Earlier work has already established the technical feasibility of displacement pressing. A third generation pressing head, designed to provide the data on which to base an engineering and economic evaluation, is now undergoing testing. Included are provisions for measuring air flow to determine air supply system requirements. Preliminary data suggest the air horsepower requirement may be reasonable.

3. Despite the contributions of the UMO work, the industry still does not have a wet pressing model to predict water removal and densification from fundamental sheet and felt conditions, and pressing conditions. The UMO model requires a nip efficiency factor which can only be obtained by running the furnish on a pilot or real press, which begs the point of having a model. The poorly understood part of the process occurs in the expansion and exiting zones of the nip, both ignored in the UMO work. With the development of thickness measuring equipment for whole sheets or any part, and the availability of full-nip simulators, we are now in a position to tackle the expansion part of the nip. This work is underway and has already produced some exciting results with regard to what controls nip efficiency and, therefore, water removal in a press.

WET PRESSING

Attached is an interim report on wet pressing submitted to the DOE in mid-summer. The report to DOE covers work on displacement pressing, pressing with porous plates as water receivers and some recently initiated work to describe the expansion section of a press nip. This supplemental report briefly describes the recent progress on the first and last of the above subjects. For background and continuity, the DOE report should be read first.

DISPLACEMENT PRESSING

TEST HEAD DESIGN

The DOE report presents information on laboratory tests with first and second generation displacement pressing heads. A third generation system has been designed and is now undergoing testing. The new head, shown schematically in Fig. 1, has a number of important features missing in earlier design, including:

1. An onboard air storage tank, short-coupled directly through a high-speed solenoid valve to the test chamber, to supply displacement air. This system avoids the long delay and slow rise of displacement air pressure common to the previous system. Oscilloscope traces of typical applied mechanical and air pressure pulses, shown in Fig. 2, illustrate this point. Compare this figure with Fig. 17 in the attached report. The air pressure rise time is about 5 ms.

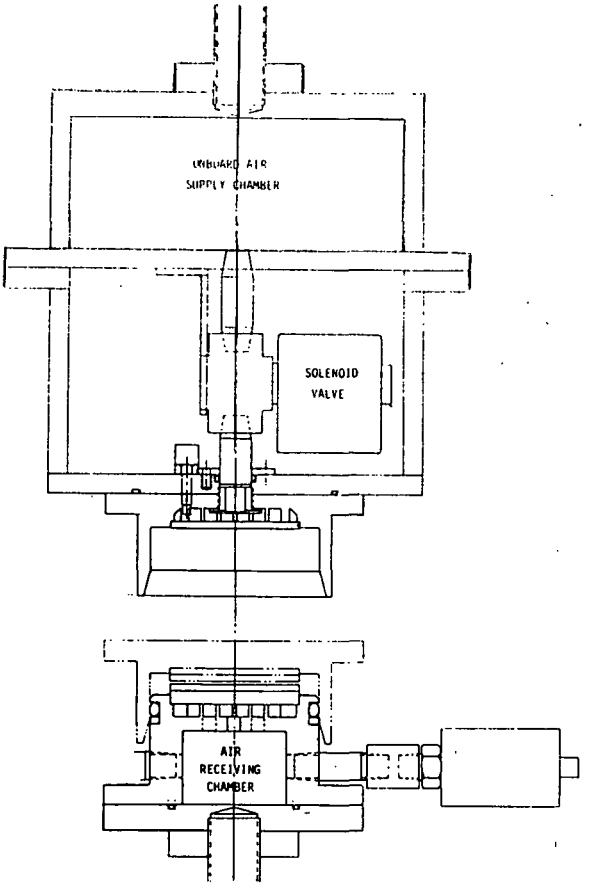

Figure 1. Schematic of displacement pressing head.

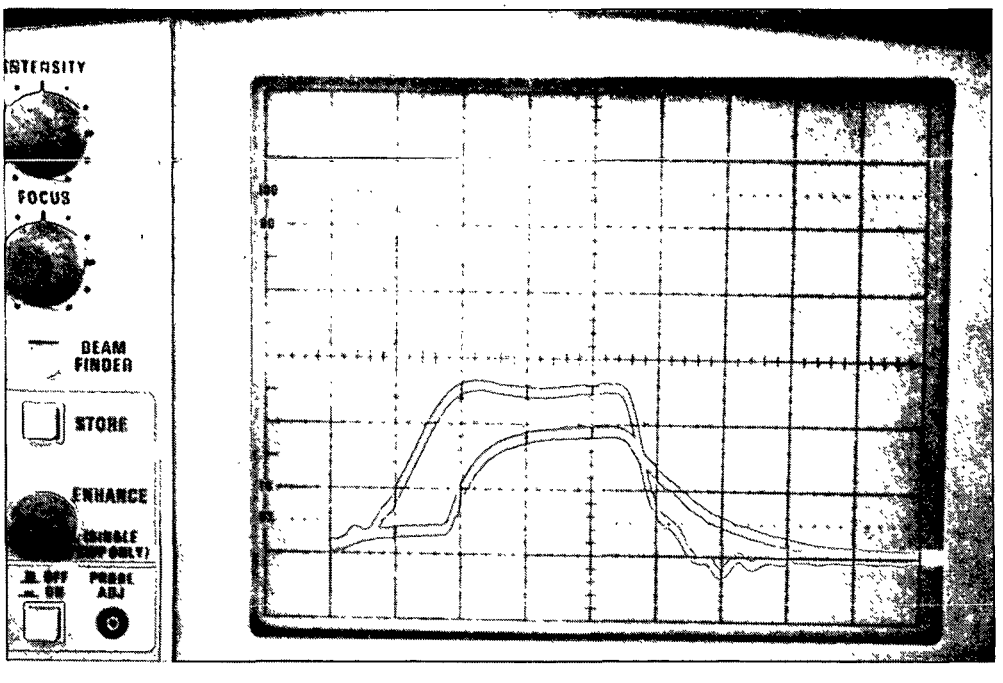

Figure 2. Load and air pressure traces.

2. A closed chamber below the sheet, equipped with a pressure transducer to measure the pressure rise caused by air flow through the sheet. This measurement and an appropriate assumption about the thermodynamics of the filling process can be used to calculate the superficial air velocity through the sheet and the displacement power consumption. Figure 3 shows typical load and lower chamber pressure pulses. Back pressure on the sheet is kept low by using a large receiver volume.

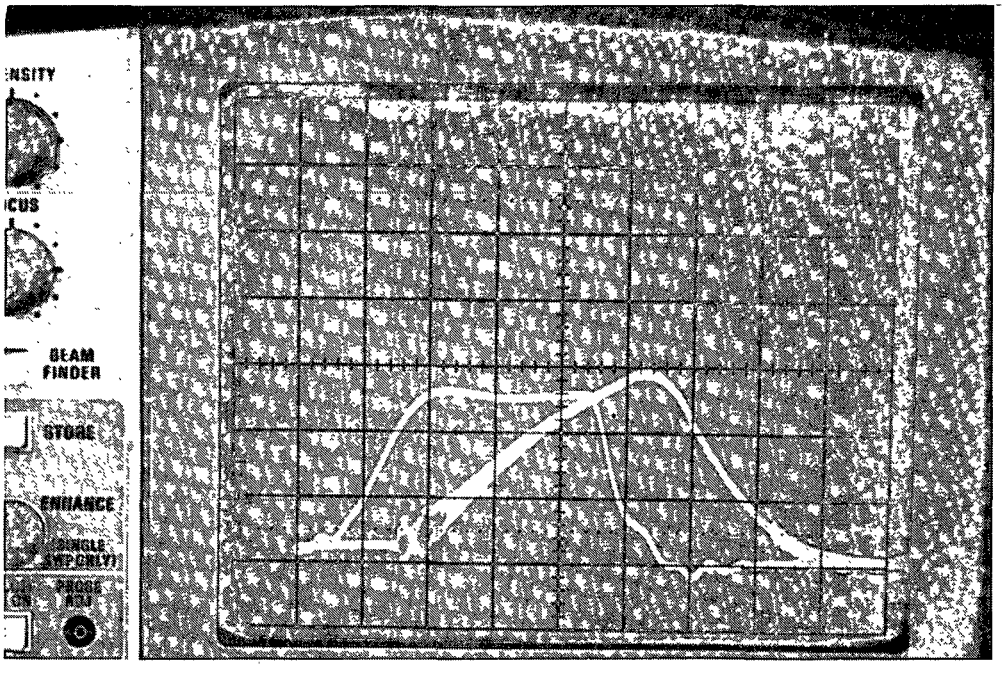

Figure 3. Load and receiving chamber pressure pulses.

3. Improved sealing of the test chamber to preclude leakage or bypass paths.
4. An improved air distributor for faster air pressure rises.

The resulting head and several of its details are illustrated in Figs. 4-7. Tests conducted to date show that the head functions as intended.

NEW RESULTS

An initial and limited set of tests, designed to explore the effects of applied mechanical pressure, displacement pressure (air flow rate) and the load spreader/water receiver configuration has been conducted. All tests were carried out with a pressure NRT of about 50 ms and a displacement NRT of about 40 ms. A once-dried northern softwood bleached kraft furnish with a freeness of about 680 mL was used in 50 gr/m^2 handsheets. All sheets were pressed to ingoing solids levels near 50%. These tests were carried out for mechanical pressures (P_p) of 500 and 800 psi and displacement pressures (P_d) of 40 and 80 psi.

These data are now being analyzed and results will be available for the meeting.

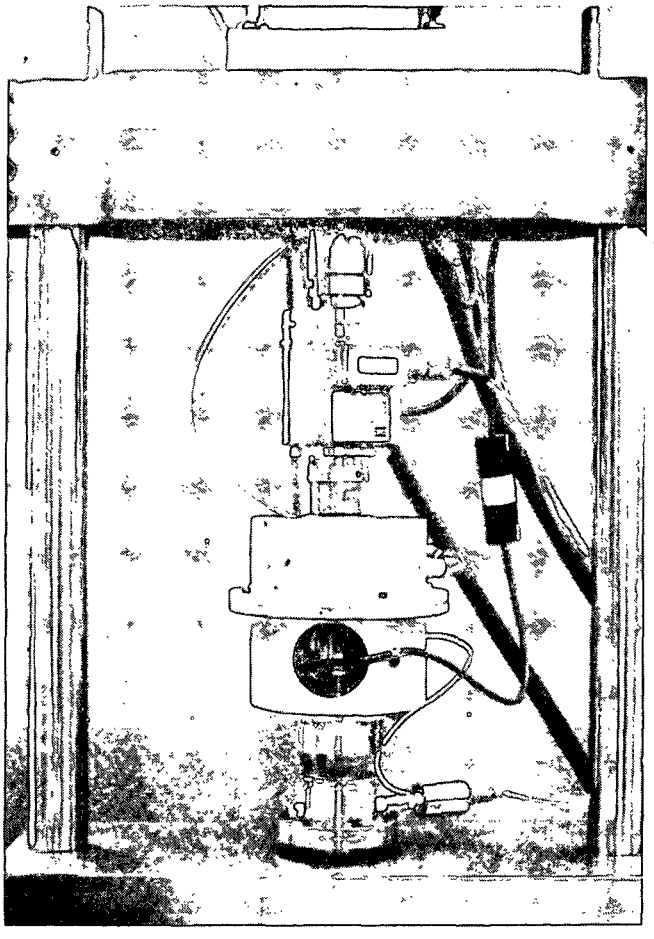

Figure 4. DP head installed in electrohydraulic press.

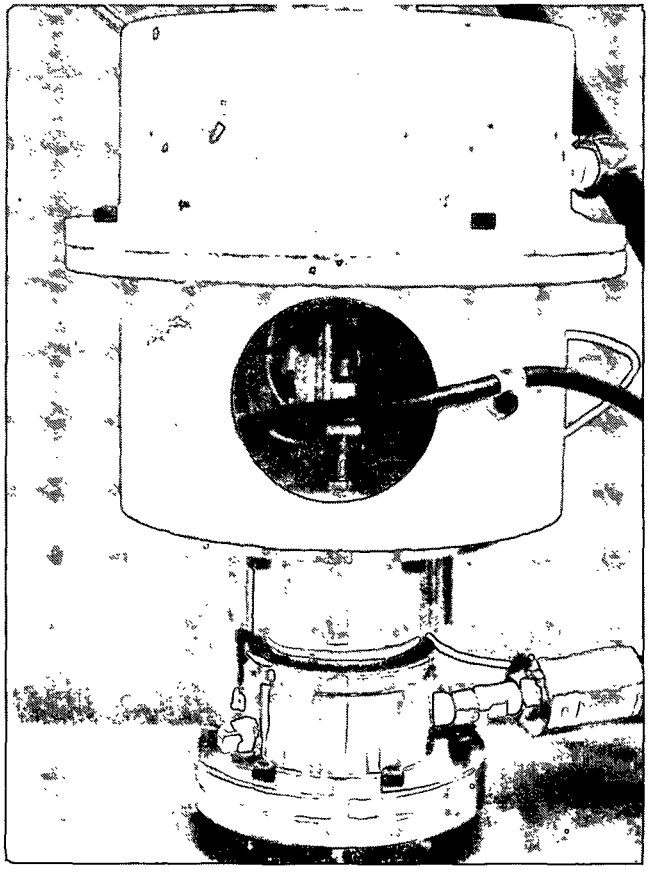

Figure 5. Close up view of head in a slightly open position.

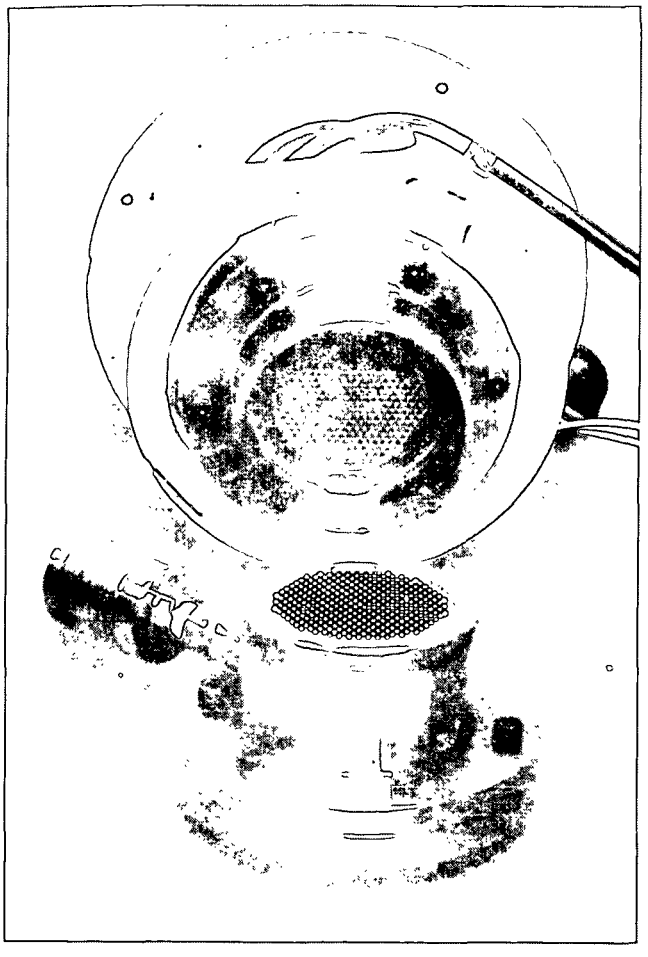

Figure 6. Upper and lower halves of head.

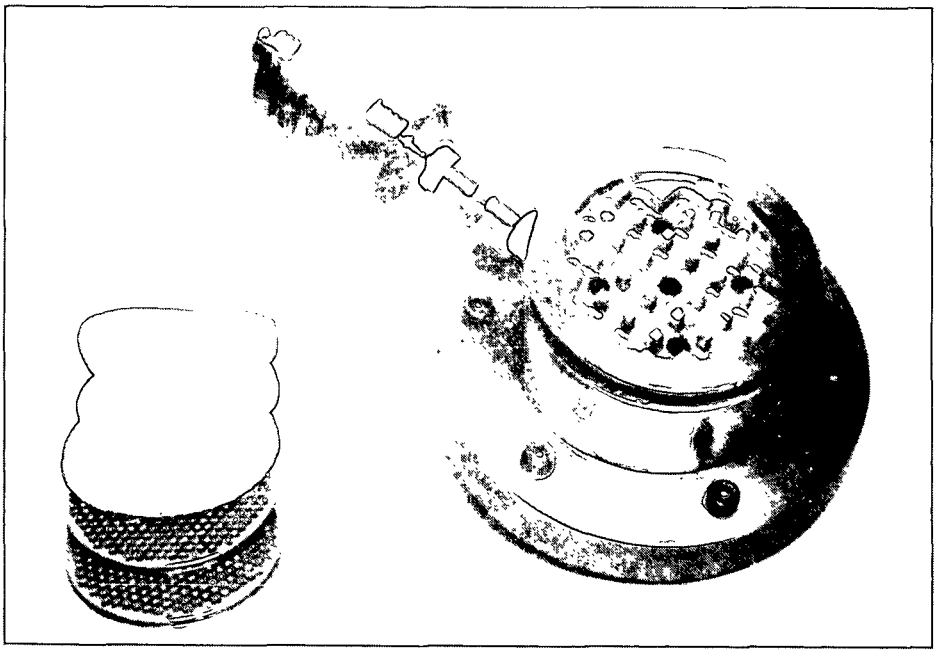

Figure 7. Lower chamber with various layers of load spreaders and water receivers.

WET PRESSING MODEL

In a recently completed study[1], the University of Maine at Orono developed a model to predict the water removal in a wet press. This model was successful in describing the behavior of a laboratory compression tester, but seriously over predicted water removal in a real press, although the trends were correct. A nip efficiency factor was defined to correct the model data to agree with real press data. Nip efficiencies can be estimated by running a given furnish on a real or pilot press and in the lab compression tester and comparing the results. Nip efficiency is a fairly strong function of furnish and pressing conditions. Given a nip efficiency, the model can be used to explore small perturbations in furnish, design and operating parameters. Large perturbations require a new efficiency to be determined. The limitations of this approach are self-evident.

To understand why a correction factor is required, it is helpful to examine the compression testing details and the UMO approach to modeling. The tester is described fully in the attached report and in Ceckler and Thompson, Ref. 1 of the attached report. Some of the salient details are repeated below:

1. The press uses a vented porous plate as the water receiver. A stainless steel plate with an average pore size of 40 was selected to correspond to the pore sizes in typical pressing felts.
2. Proximity detectors were used to measure the separation between the pressing platen and the incompressible porous plate. This separation corresponds to instantaneous sheet thickness which was used to determine the compression behavior of the sheet. By assuming that the sheet was

always saturated, instantaneous water removal was also obtained from sheet thickness. Total water removal in a given pressing simulation was taken to correspond to the minimum sheet thickness attained.

3. Saturation of the sheet and porous plate was assured by initially flooding the nip. A desired initial moisture ratio was established by presetting the sheet to the corresponding thickness for a saturated sheet.

Ceckler and Thompson originally suggested the smoothness and pressure uniformity supplied by the porous plates as the cause of the higher water removal in the lab compression tester. The data in the attached report tend to refute this, however, showing that felts yield more water removal than porous plates in every case tested.

It is more likely that the compression tester showed better water removal because the sheets were compressed from a presaturated state and because the expansion part of the process, with its attendant reabsorption of water, was ignored. Proper accounting of the deleterious effect of porous plates and of these two testing artifacts should permit estimation of the nip efficiency factor used by the UMO to correct the laboratory data to agree with pilot press data. More importantly, a mathematical description of the factors omitted in the UMO model will make it unnecessary to use a nip efficiency factor, thus providing a much more complete description of the pressing process. These areas are now being investigated by using a full-cycle press nip simulator with multilayer and instantaneous sheet thickness measurements, and modeling of the expansion process.

Full details on this modeling activity will be presented at the meeting, but Fig. 8 is included to illustrate the point and a part of the approach. In this figure, instantaneously recorded values of applied pressure and density (sheet thickness) are plotted versus time. The beginning and ending saturation points are indicated on the figure, the latter based on the water remaining in the sheet at the exit of the press.

For this relatively wet sheet saturation occurs quickly, but some time is required to compress the sheet to remove the air. At the minimum thickness point one would estimate a water removal value of about 180 gr/m^2, whereas the actual water removal was about 104 gr/m^2. Nip efficiency, based on water removal, would be assigned a value of about 57% for these data. More importantly, almost half the water initially removed returned to the sheet in the expansion portion of the nip. Almost all of this occurred late in the nip.

The equipment used to generate the data in Fig. 8 can be used either in a falling-weight press simulator or the electrohydraulic press to study a wide range of pressing conditions. Multiple targets in the sheet allow the measurement of mid region densities as well. Finally, these systems simulate a complete nip rather than just the compression part of the event.

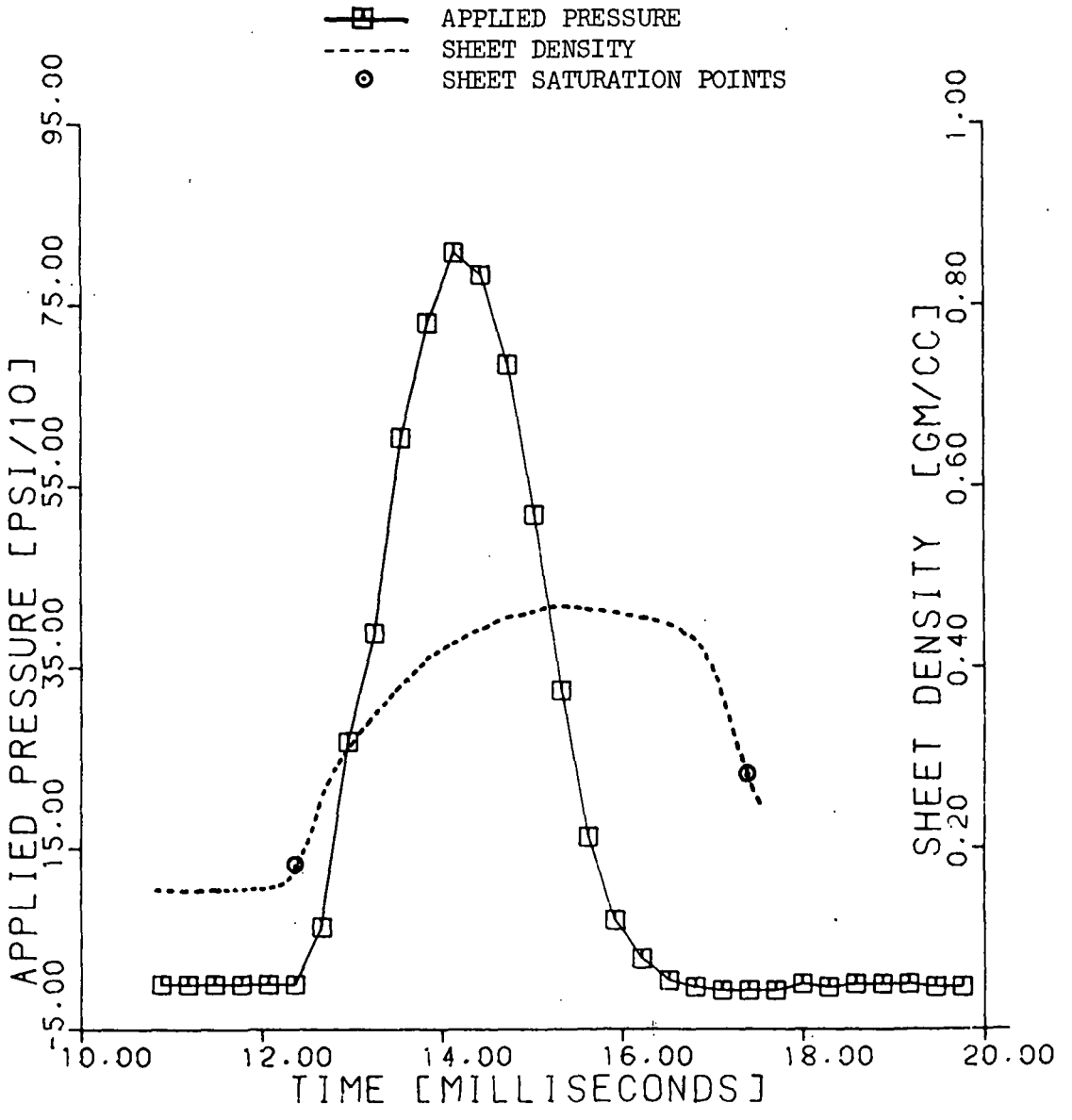

Figure 8. Instantaneous pressure and density curves for a typical wet pressing cycle.

NEW CONCEPTS IN WET PRESSING

PROGRESS REPORT ONE

BY
DR. CLYDE H. SPRAGUE

PROJECT NO. 3584
DOE CONTRACT NO. DE-AC02-84CE40685

June 28, 1985

TABLE OF CONTENTS

SUMMARY

This is an interim report in a year-long project to investigate two subjects; the technical feasibility of displacement pressing and the factors causing the differences in water removal between a laboratory compression tester and a pilot press, both used in the recently completed wet pressing study conducted by the Department of Chemical Engineering at the University of Maine at Orono (UMO). Because of the broad scope of the subject areas and the time and budget constraints on this project, only limited investigations of these subjects have been planned.

DISPLACEMENT PRESSING

Displacement pressing, a new concept for wet pressing, replaces or supplements the normal hydraulic pressure gradient in a pressed sheet with an externally imposed pressure gradient, generated by compressed air or steam. This concept has been explored through two generations of laboratory pressing heads in two pressing regimes; moisture levels in the 50% range, typical of third press or early dryer levels, and in the 25-45% range, typical of first or second presses. At low moisture levels, hydraulic pressures are difficult to generate, thus limiting the maximum dryness achievable in a conventional press. In this regime, displacement pressing has been shown to be effective in increasing dryness levels to at least 65%. For lightweight, relatively free sheets, this has been achieved with normal compression pressures, displacement air pressures of 50-100 psi and times in the 10-40 ms range. Heavier or lower freeness sheets are more difficult to dewater.

For wetter sheets where hydraulic pressure gradients can be developed readily, displacement pressing is used for bulk retention (control). Low compression pressure, combined with an external air pressure gradient, are used

to remove water from the sheet without significantly increasing density. In this way, a dry, bulky sheet can be produced, something which cannot be achieved in a conventional press. As an example, a 65 g/m^2 sheet of bleached northern softwood kraft at a freeness of 690 ml was displacement pressed at compression levels of 100, 400, and 1600 psi and for an ingoing solids range from 25-50%. For an ingoing solids level of 35%, the outgoing solids levels were all near 48%, but the density levels corresponding to the three compression pressures were about 0.43, 0.47, and 0.51, respectively. These data, and others, have shown that displacement pressing can be used to decouple the normal density-dryness relationship obtained in conventional pressing so dry, bulky sheets can be produced.

A simple model of the displacement pressing process, based on a two-zone description, shows that liquid permeability and thickness of the sheet (basis weight), and air pressure differential are the key variables. Thickness and permeability are both dependent on compression pressure in ways which oppositely affect water removal. Hence, there may be a need to schedule pressure during the displacement pressing event for optimum performance. This can be readily accomplished with the electrohydraulic pressing system in the IPC Pressing and Drying Laboratory.

When used for achieving high dryness levels, displacement pressing will offer improved paper machine productivity, better runnability through improved wet web properties in the open draw, and substantially reduced drying energy. Increasing the solids level into the dryer from 50 to 65% will reduce drying energy by 1/3 to 1/2, a large improvement. Using a displacement press in the first or second press position may afford a significant opportunity to achieve both high dryness and high bulk, a real advantage for a number of grades.

A third generation of displacement pressing heads for the laboratory press simulators is now under construction. This new system is designed to avoid air leakage paths, to provide a more uniform compression of the sheet and a more uniform air pressure gradient, and to provide a more controllable air pressure with a much faster rise time. It is also equipped with transducers for measuring air flow through the sheet for modeling and engineering calculations. Displacement pressing has already been shown to be effective. This generation of equipment should allow determination of the technical feasibility of the concept.

POROUS PLATES AND NIP EFFICIENCY

In their recently completed wet pressing study, the UMO showed that a laboratory compression tester was much more effective in removing water than a pilot press of conventional design. A number of experiments conducted in this follow-up study have shown that the difference is not attributable to the use of a porous plate as a water receiver in the compression tester. In fact, for every condition investigated and for several porous plate designs, felts have given better performance.

There is now mounting evidence that the compression tester showed better water removal because the sheets were compressed from a presaturated state and because the expansion part of the process, with its attendant reabsorption of water, was ignored. Proper accounting of the deleterious effect of porous plates and of these two testing artifacts should permit estimation of the nip efficiency factor used by the UMO to correct the laboratory data to agree with pilot press data. More importantly, a mathematical discription of the factors omitted in the UMO model will make it unnecessary to use a nip efficiency

factor, thus providing a much more complete description of the pressing process. These areas are now being investigated by using a full-cycle press nip simulator with multilayer and instantaneous sheet thickness measurements, and modeling of the expansion process. While it is expected that considerable progress in this area will be made, a full description is probably beyond the remaining time and budget for this project. It should be noted that this aspect of the investigation was prompted by the findings regarding porous plates and was not a part of the original proposal.

INTRODUCTION

WATER REMOVAL ON THE PAPER MACHINE

Figure 1 shows a schematic illustration of the water distribution in a typical papermaking process. Processing starts at the headbox with perhaps 200 parts of water for each part of fiber. Most of this water is removed before the presses through such forces as gravity, vacuum, centrifugal, and wire tension. In the presses, additional water is removed so the exiting web has about equal parts of water and fiber. The last bit of water is removed in the dryer, usually by direct evaporation. Although the relative amount of water removed in pressing and drying is small, it is profoundly important in terms of operating costs and energy consumption, machine runnability, and paper properties.

In wet pressing, the moist sheet, along with one or two felts, is passed through a press nip to mechanically compress the combination. Figure 2 shows an example of a two roll press with a single felt working against a vented roll. Within the sheet, part of the water is carried in the network pores ("free" water) and the remainder is carried in the fiber pores ("bound" water). For a relatively wet sheet (moisture ratio >2.0) much of the water is free and readily accessible for removal by this compression process. For dryer sheets, much of the water is bound making it more difficult to remove. As a consequence, two or three presses are needed to increase the solids content from 20% or so to the 40-50% range. In drying all of the water is evaporated requiring about 1.5 pounds of steam for each pound of water removed.

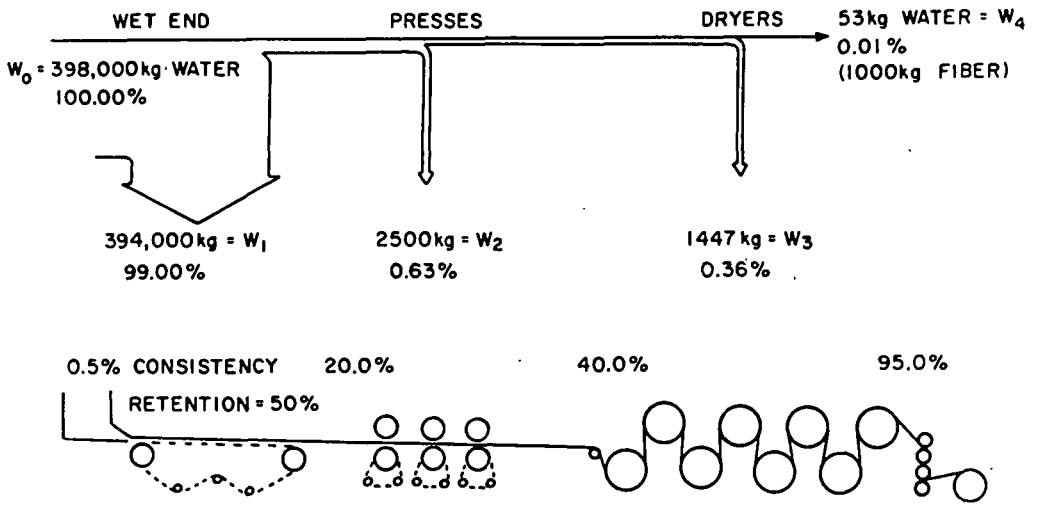

Figure 1. Water distribution on paper machine.

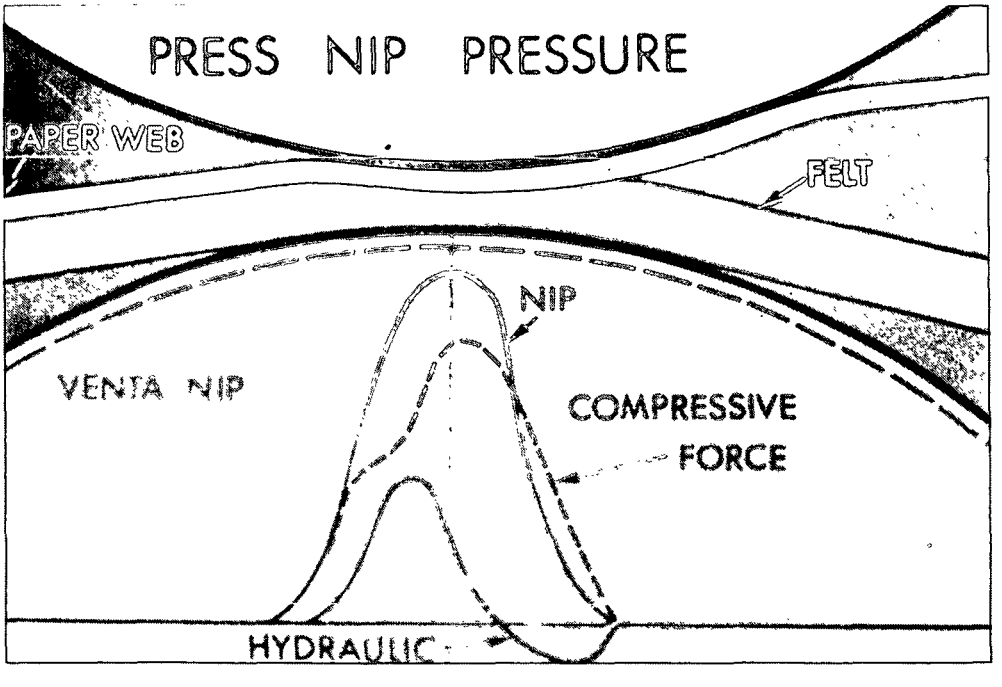

Figure 2. Roll press and pressure diagrams.

WET PRESSING

As the wet sheet passes into the nip, the pressing forces compress the fiber structure, thus reducing the pore volume available to hold water. At some level of compression, the pore volume and water volume become equal, creating a condition known as saturation. Additional compression beyond the saturation level causes a hydraulic pressure gradient to form, forcing water to flow from the sheet. Under these conditions, the total pressure applied by the roll is borne partly by the fiber network and partly by the hydraulic pressure or, in equation form,

$$P_t = P_h + P_s \quad (1)$$

where P_t = total applied pressure

P_h = hydraulic pressure

P_s = structural pressure (fiber network pressure)

As the sheet continues through the nip, the hydraulic pressure rises to a maximum, usually around mid-nip, and then declines through zero as the sheet expands on the exit side of the nip. Beyond this point, the hydraulic pressure gradient reverses and some water may flow from the felt back to the expanding paper web. Representative nip pressure profiles are shown in Fig. 2.

Flow Controlled Pressing

For sheets having high moisture, high basis weight, or low freeness, the primary impediment to water removal is the flow resistance of the fiber network. This regime is called "flow controlled". For flow controlled pressing, the amount of water removed depends on the hydraulic pressure available to force water from the sheet and the time available for flow. Under these conditions, the hydraulic pressure depends directly on the total applied pressure. Thus, in this regime, water removal depends almost totally on the area under the pressure-time curve, called the "impulse" of the press.

$$I = \int_{o}^{NRT} P_t dt \qquad (2)$$

NRT = nip residence time

Time and pressure may be freely interchanged to achieve equivalent water removal in the flow controlled region. This flow controlled behavior, typical of most first presses in a multi-press system, is illustrated by the left portion of the impulse diagram in Fig. 3. Water removal is independent of basis weight in this region.

Compression Controlled Pressing

As the free water leaves the sheet, removal of the bound water starts to dominate the pressing process. Considerable compression is necessary to free sufficient water from the fibers to saturate the sheet, even though the pore volume of the highly compressed sheet is small. Only a modest amount of water remains to be removed. This regime, called compression controlled pressing, is typical of third presses and is characterized by relatively dry sheets, low basis weights and high freeness furnishes. Press impulse remains an important driving force in the compression controlled regime, but here maximum pressure has an important independent effect, as shown in the righthand part of Fig. 3. Water removal is directly proportional to basis weight in the compression controlled zone. The transition between these zones is not sharply defined and certainly depends upon such situational factors as furnish, basis weight, freeness, and certain press design factors. Nevertheless, the concepts are well founded and very useful in understanding or describing pressing behavior.

NEW PRESSING CONCEPTS

Displacement Pressing for High Dryness

As a foregoing discussion suggests, one of the primary measures of press effectiveness is the dryness of the sheet going to the dryers. All of the

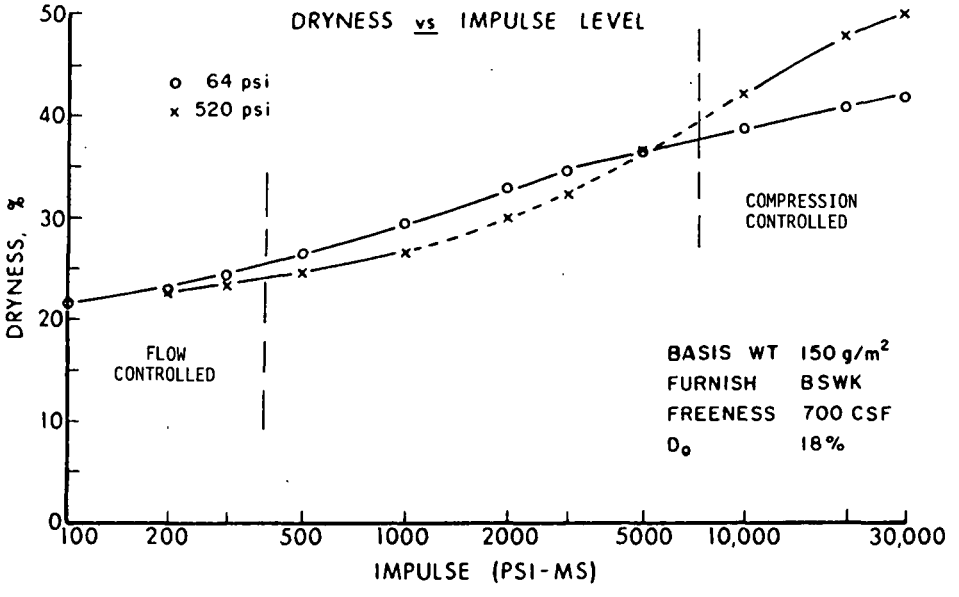

Figure 3. Pressing impulse diagram.

water not removed by the press must be evaporated in the dryer. About 36% of the gross energy consumption in an integrated kraft mill occurs in the paper mill with most of this going to paper drying. As a consequence, each percentage point increase in solids content out of the presses reduces dryer energy consumption by about 4.5%. Hence, there is a big energy cost incentive for improving press exit dryness.

On many machines, the first (or only) open draw occurs between the last press and the first dryer can. Many web breaks occur in this zone because of the poor mechanical properties of the wet web. These breaks cause a significant loss of productivity. Improved pressing usually increases the dryness of the web and, correspondingly, the mechanical properties of the web in the open draw, thus reducing the frequency of breaks. Hence, runnability, as well as dryer energy cost, is well related to press exit dryness.

In first presses, and in some second presses, double felting, extended or high impact nips, and increased loading are all examples of actions that are effective in increasing water removal. Third presses are normally compression controlled so that high pressures as well as long nips (time) are needed to effect significant additional water removal. Both have been improved by recent press developments, but the additional incremental improvements expected in these technologies seem unlikely to produce substantial increases in dryness. It is this combination of factors which lead to the concept of displacement as another pressing dimension to be used in improving the performance of presses, especially third presses.

For relatively dry sheets ($MR \leq 1.0$) it is still possible to press water from the fibers, but difficult to create a hydraulic pressure gradient to drive the water out of the sheet. In displacement pressing, the sheet is mechanically compressed as usual, but the water removal force is supplied as an externally imposed pressure gradient using compressed air, for example. With this approach, significant additional water can be removed, pushing sheet dryness levels 10-15 percentage points above those normaly achieved. One of the principal objectives of this project is to investigate the feasibility of the displacement pressing concept in achieving high press exit dryness levels and the benefits derived therefrom.

Displacement Pressing for Property Development

As a moist sheet passes through a pressing nip, it is first compressed to some minimum thickness, beyond which it expands, but not to its original thickness. If the sheet is dried promptly after pressing, much of the densification that occurs during pressing is permanently captured in the sheet. Because sheet density is at the root of many strength properties and some optical properties, densification in the presses has an important influence on paper

properties. Generally, if strength is the end-use property of most concern, more densification is desired in the wet presses.

For most presses of current design, density is very nearly a linear function of press exit dryness. Hence, any action taken to increase dryness will correspondingly increase density. Displacement pressing may also lead to much higher dryness levels but, because the water removal mechanism is different from that in more conventional pressing, the degree of incremental increase in density may be less. Some increase in density is expected, however.

For some paper grades, bulk is the property of interest and densification in the wet presses is undesirable. Absorbent grades, boxboard, and some printing papers, are all examples where part or all of the sheet should be bulky to effect the desired end-use properties. Bulk and high dryness are inconsistent in current pressing operations, but can be achieved by starting the displacement pressing process at solids levels of 25-35%. In this regime, low mechanical pressures are used to avoid densifying the sheet. The water is displaced with an external pressure source such as compressed air. A second major objective of this project is to determine the feasibility of displacement pressing as a means of decoupling the usual density-dryness relationship and producing a sheet that is both bulky and dry, something that cannot be achieved with current presses.

Pressing with Porous Plates

Under the sponsorship of the U. S. Department of Energy (DOE), the Department of Chemical Engineering at the University of Maine at Orono recently completed a major study of the wet pressing process. One major objective of that work was to develop a model to predict the performance of real presses, given proper information about the furnish, the press design and the pressing conditions. To develop this model, it was necessary for the UMO to obtain

compressibility, permeability and capillary pressure data on the furnish in question for conditions appropriate to the intended model use.

Moist web compression behavior is very time and moisture level dependent. Hence, the compressibility data had to be collected within the same time scale as occurs in a real press. To gather these data and also to simulate a pressing process, a laboratory compression tester was constructed, as shown in Fig. 4. An ample description of this tester is given in Ceckler and Thompson (1). Several aspects of design and test procedure should be noted, however.

1. The press uses a vented porous plate as the water receiver. A stainless steel plate with an average pore size of 40μ was selected to correspond to the pore sizes in typical pressing felts.

2. Proximity detectors were used to measure the separation between the pressing platen and the incompressible porous plate. This separation corresponds to instantaneous sheet thickness which was used to determine the compression behavior of the sheet. By assuming that the sheet was always saturated, instantaneous water removal was also obtained from sheet thickness. Total water removal in a given pressing simulation was taken to correspond to the minimum sheet thickness attained.

3. Saturation of the sheet and porous plate was assured by initially flooding the nip. A desired initial moisture ratio was established by presetting the sheet to the corresponding thickness for a saturated sheet.

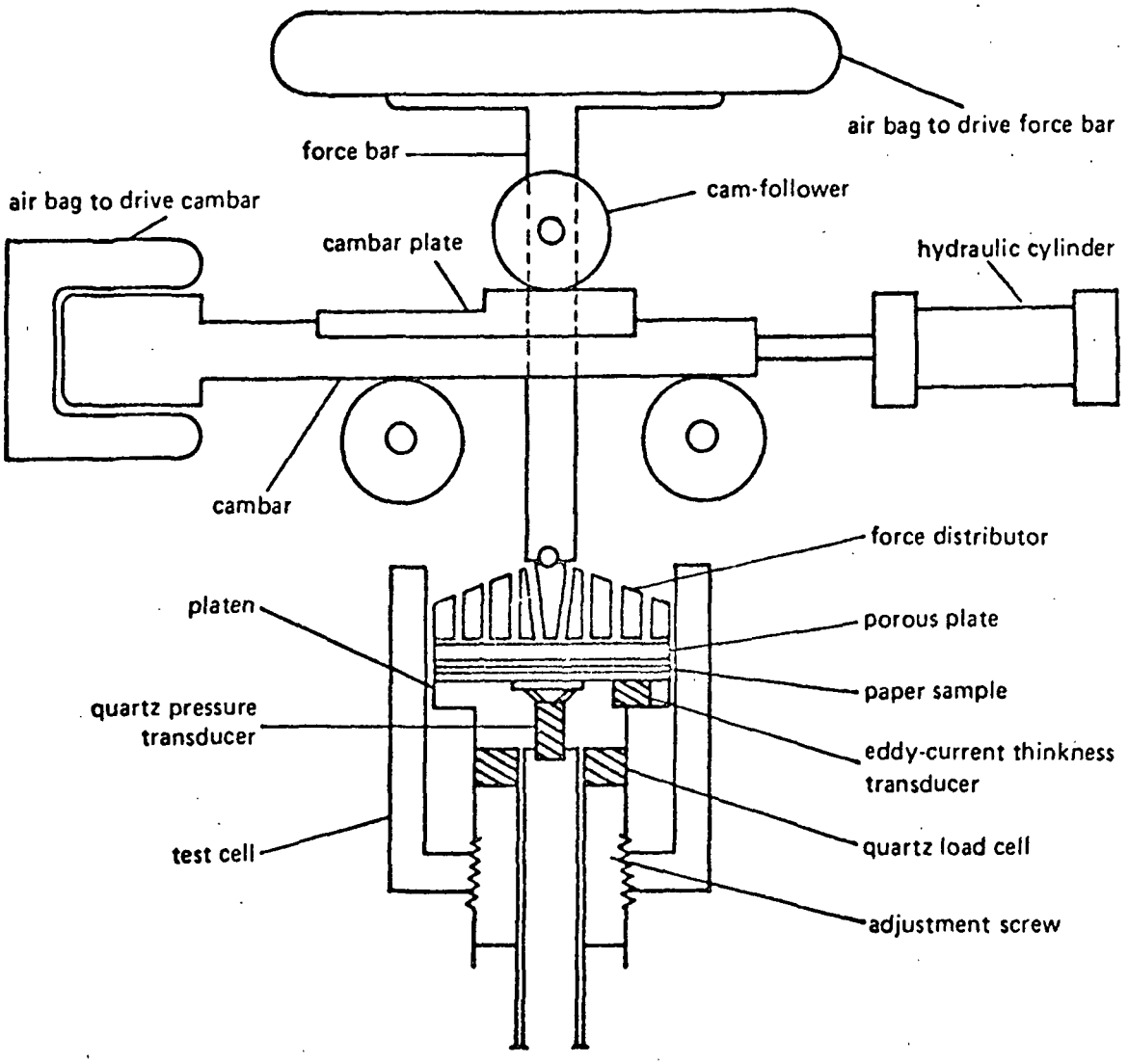

Figure 4. Schematic drawing of UMO compression tester.

Compressibility data, measured as described above, and permeability and capillary pressure data, measured initially in separate experiments, were used to develop a model to describe water removal in a press nip. This model was quite successful in describing water removal in the laboratory compression tester as illustrated by the data in Fig. 5. Absolute agreement between the water removal in the laboratory compression tester and a pilot press - Fig. 5 - was quite poor, however, although the trends were very similar. In general, the compression tester showed much higher water removal levels than the pilot press. Examination of the data showed that one set could be shifted by a common factor to coincide with the other set. This factor has been called a "nip efficiency" factor, but is more appropriately a correction factor to adjust the model data to agree with the real (pilot) press data. A given correction factor applies over only a very narrow range of furnish and pressing conditions, so a new one must be determined for each new set of conditions. The correction factor may vary over at least a 4 or 5 to 1 range; hence, the accuracy of the estimate of pressing behavior obtained with the model is critically dependent on the accuracy with which the correction factor is known.

Because the water removal determined in the lab press is always much higher than in the pilot press, the correction factor is always less than 1.0, sometimes substantially less, as in Fig., 5, for example. In the Phase I report (11), it was speculated that the porous plates used in the compression tester are more effective at water removal than are felts because they provide a more uniform application of pressing pressure. Whatever the cause, there were not sufficient details in the initial report to assign a real cause to the difference. Furthermore, the differences were so large as to support the concept of an advantage for porous plates. Interpretation of these results was con-

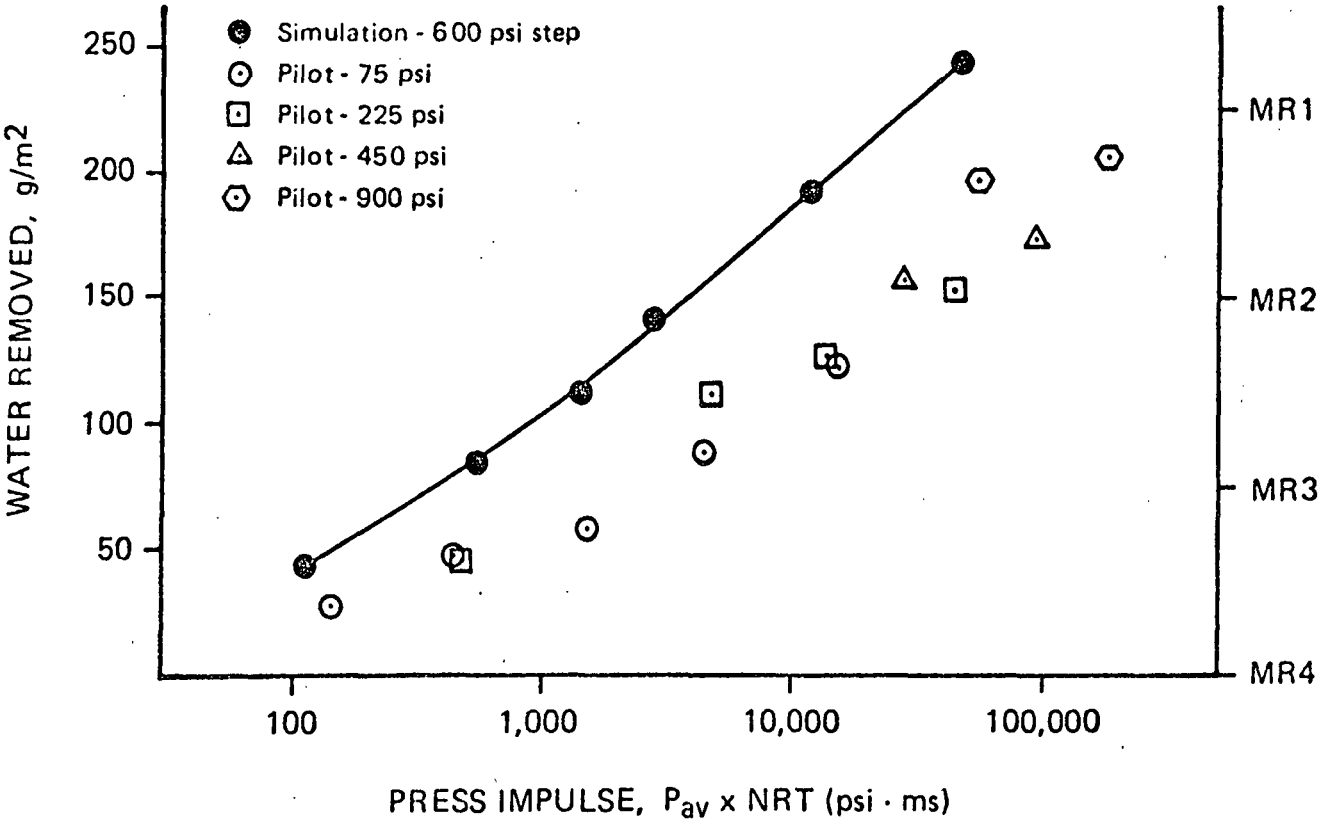

Figure 5. Comparison between pilot and laboratory simulations for 300 CSF bleached softwood kraft, 75 g/m^2.

founded by the differences in the test equipment used for comparison; a lab compression tester operating in a perpetually saturated state with thickness determined water removal on the one hand, and a pilot press operating normally with gravimetrically determined water removal on the other. A third objective of this project is to clarify this issue by comparing the performance of porous plates and felts under identical and realistic pressing conditions. This work is also expected to contribute to understanding of the correction factor necessary with the UMO model.

DISPLACEMENT PRESSING

The data in Fig. 3 show that increases in press impulse yield only small increases in sheet dryness when the sheet is in the compression controlled zone. The exact level of dryness at which the transition to compression control occurs depends somewhat on basis weight, freeness, and so on. But the point is clear; increasing impulse levels beyond those achievable with extended nip presses will have little impact on water removal/dryness for dryness levels above the 45-50% range. Pressing pressure has a small positive impact in this zone, but structural design considerations will preclude significant advances via this route. Based on all of these factors, it appears that major gains in sheet dryness out of the press will require a different pressing mechanism.

At high dryness levels, practical pressing pressures squeeze some water out of the fibers into the interfiber pores, but not enough to saturate the sheet. For this unsaturated condition, there is no hydraulic pressure gradient to drive the water from the sheet. In impulse drying, a similar state of sheet compression and saturation is achieved (12). There, however, appreciable liquid water removal is induced by the bulk flow of the vapor generated at the hot surface. In pressing at high dryness levels, the same mechanism can be invoked by driving air or steam through the sheet from an external source. As the gas stream flows through the compressed sheet, a portion of the available water is removed by displacement or entrainment. This mechanism, illustrated in Fig. 6., can be used to raise sheet dryness levels well above those achievable with conventional or extended nip presses without using any thermal energy. This concept is called "displacement pressing".

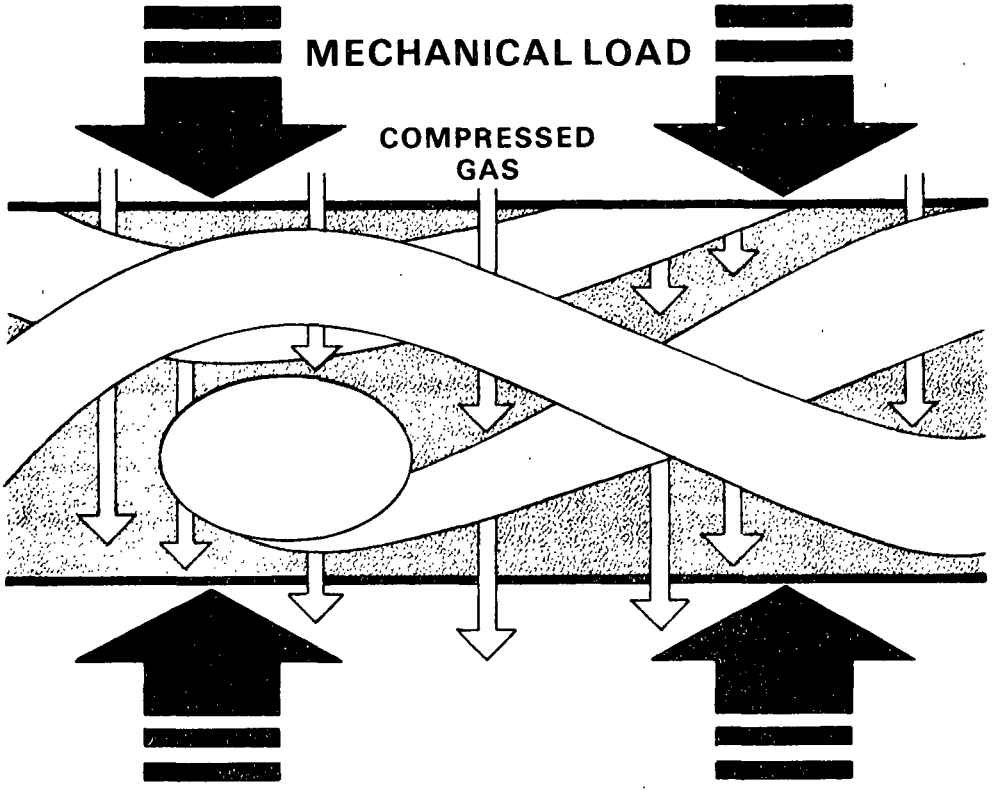

Figure 6. Illustration of displacement pressing concept.

FIRST GENERATION EXPLORATORY EXPERIMENTS

A simple displacement press chamber (Fig. 7) was constructed for obtaining preliminary data on the dryness levels attainable by displacement pressing. In this simple chamber, the wet sheet is sandwiched between two drilled plates which act as load spreaders while allowing air and water to pass. Various combinations of screens, felts, and porous plates are placed between the sheet and the load spreaders. For the initial experiments, the chamber assembly was placed in a static press to provide compression of the sheet. Compressed air was then passed through the sheet for a predetermined period of time to displace the water. A picture of the static press is shown in Fig. 8.

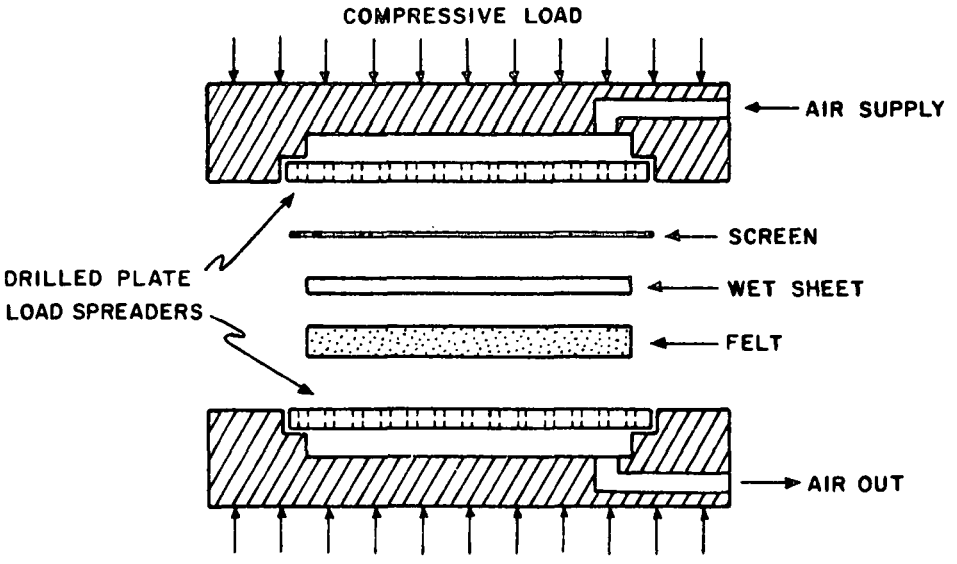

Figure 7. Displacement press chamber.

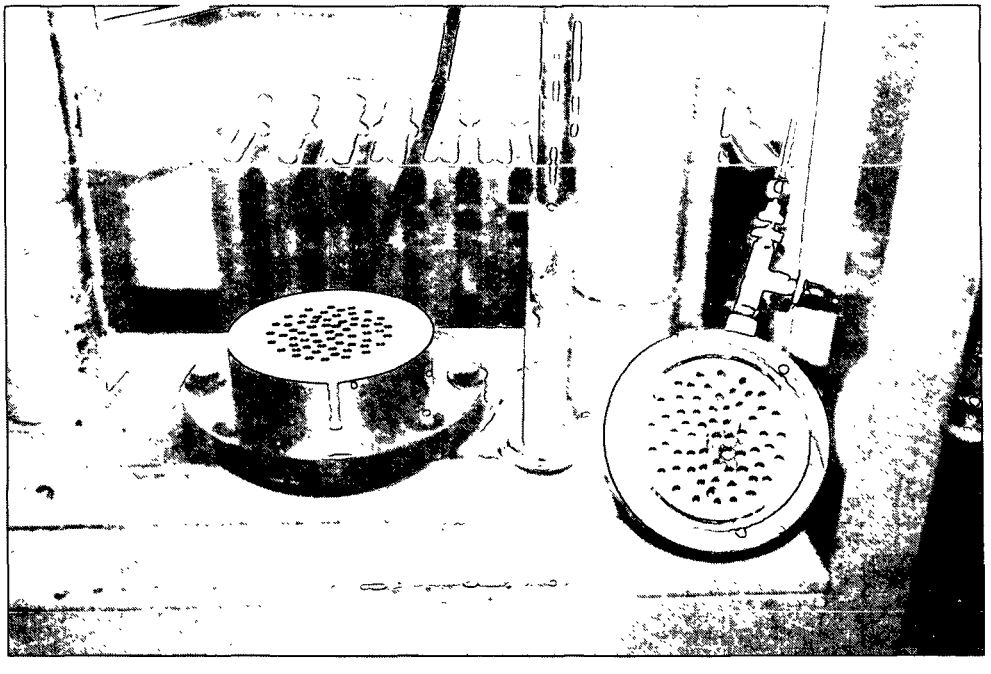

Figure 8A. Press chamber.

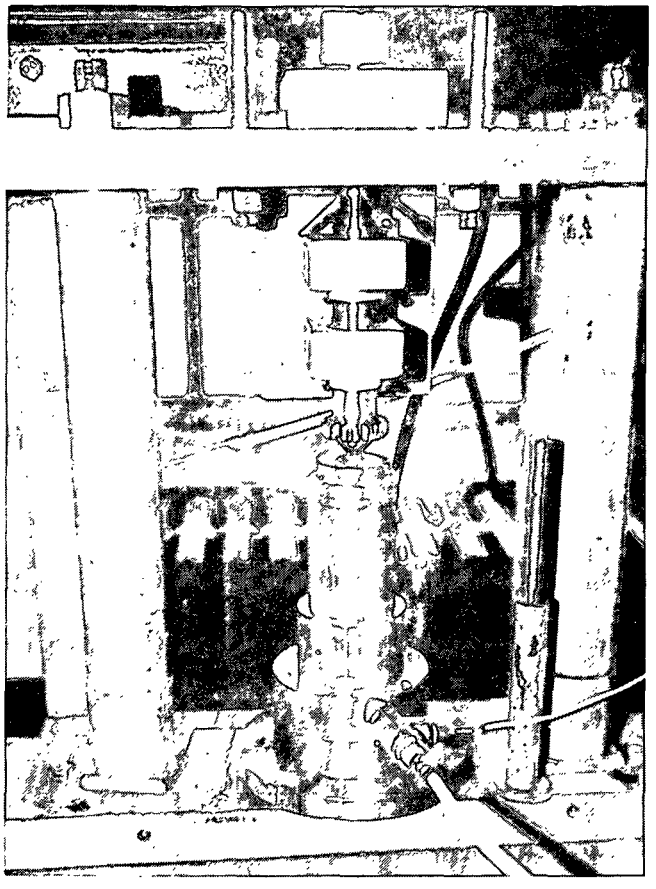

Figure 8B. Static press.

For each test, the wet sheet was pressed by conventional means to the desired initial solids content, usually near 50%, and weighed. It was then placed in the test chamber shown in Fig. 7, with the appropriate water receiver, usually a dry felt, and supplemental load spreader, such as a screen. This assembly was then placed in the static hydraulic press and loaded to a predetermined and constant pressure. At a controlled time after compression of the sheet, the air supply valve was opened and left open for a predetermined time. All timing operations were controlled as closely as possible by manual means. After pressing, the sheet was removed from the press and weighed to determine water removal. Care was taken to keep the post-pressing contact time between the sheet and felt constant and minimum, but still there was significant opportunity for rewet so the data presented later underestimate the true water removal.

The purpose of these initial tests was to determine if attractive sheet dryness levels could be reached with displacement pressing and to identify the parameters important to further study. A high freeness bleached softwood kraft furnish was selected and tested at two basis weights, 63 g/m^2 and 125 g/m^2. Representative test results are shown in Fig. 9 as sheet dryness versus the displacement pressure P_d, for the two basis weights.

From the data in Fig. 9, one can make the following observations:

1. Sheet dryness levels of 60-65% are readily achievable, despite the limitations of the apparatus used for these tests.

2. Displacement pressure and displacement time are important variables, but they appear to be somewhat interchangeable, so the product of the two may be the key quantity.

3. The external compression pressure, P_t, is a less important variable, especially for the lower basis weight. High compression pressures tend to make more water avaiable for removal but, at the same time, reduce sheet permeability. These counteracting effects seem to balance in the lower basis weight sheet and to favor water removal in the heavier sheet.

4. Higher basis weight sheets are more difficult to dewater by displacement pressing. For Darcy's law flow, assumed to apply here, both the permeability and the pressure gradient decrease with increasing basis weight, giving an inverse square law effect.

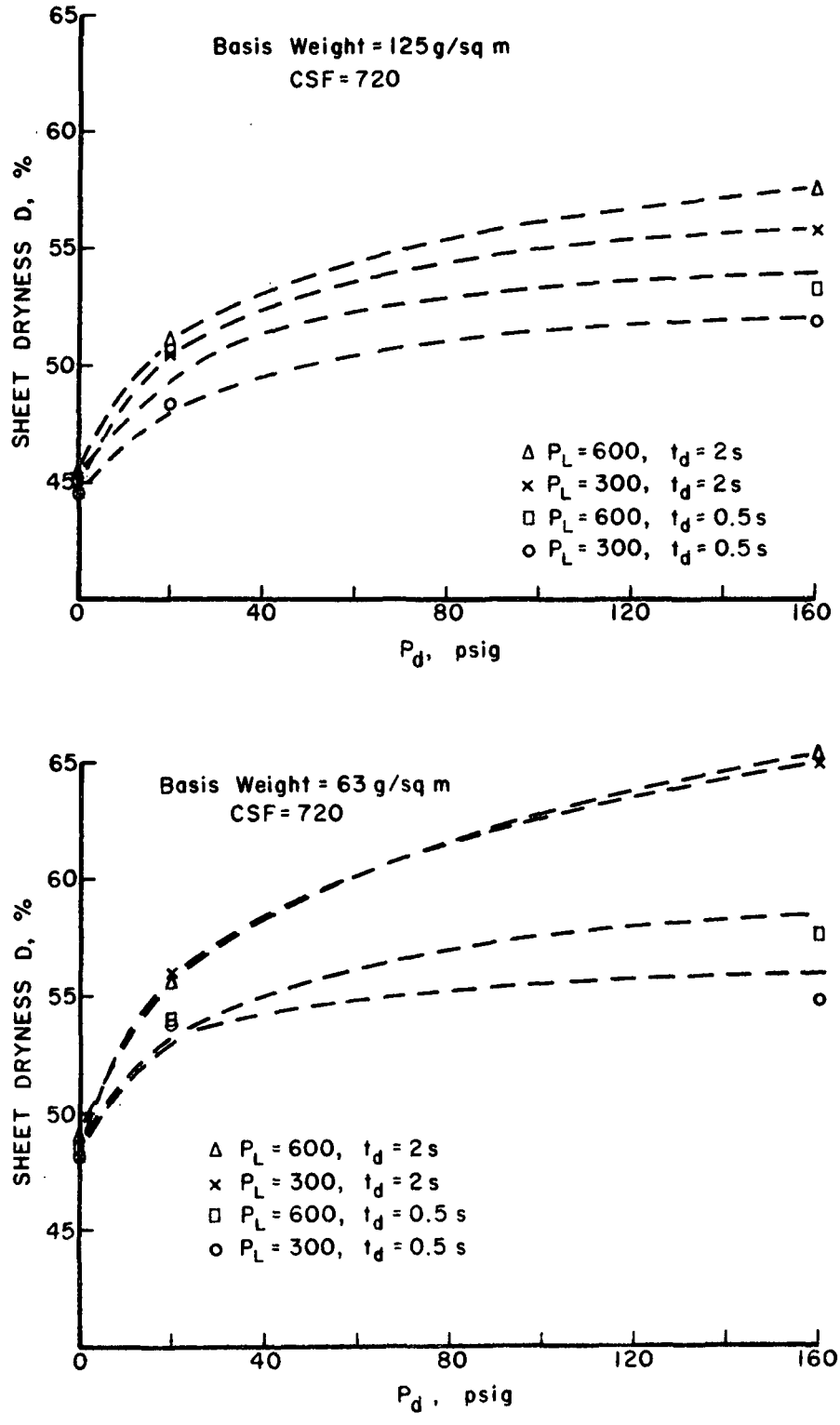

Figure 9. Sheet dryness resulting from displacement pressing at various displacement pressures.

5. Although it is not evident from these data, other results show that almost all of the water was removed by displacement and only very little by pressing alone. This is consistent with the small effectiveness of impulse in dewatering high solids sheets.

Several additional tests were conducted, primarily to explore the effect of press head configuration on displacement pressing performance. These data are shown in Table 1. From these data, one may make the following observations:

1. Replacing the felt with a screen substantially reduced water removal (tests 1 & 2). The data do not provide a valid comparison between use of a felt and porous plates above and below the sheets, but it appears that felts are better. These plates may introduce appreciable pressure drop, thus reducing the gradient across the sheet.

2. Increasing displacement pressure is shown to have a large positive effect by tests 2 and 3.

3. Displacement pressing should remove more water from a wet sheet than from a dryer one. This is supported - but certainly not proven - by the data from tests 4 and 5.

4. Applied pressure has only a minor effect as shown by tests 5 and 6.

5. Displacement time is an important variable, as shown by tests 7 through 10.

Table 1. Displacement pressing data for various press configurations.

	P_t	P_d	T	D_i	D_o	L_1	L_2	L_3	L_4	L_5	BW	ΔMR
1.	530	160	2	48.7	56.6	DP	SCR	SHT	SCR	DP	125	0.287
2.	530	160	2	48.7	61.1	DP	SCR	SHT	FLT	DP	125	0.417
3.	530	20	2	48.7	56.1	DP	SCR	SHT	FLT	DP	125	0.271
4.	530	40	10	50.3	64.1	DP	SCR	SHT	FLT	DP	125	0.428
5.	530	40	10	48.7	62.8	DP	SCR	SHT	FLT	DP	125	0.461
6.	300	40	10	48.7	62.5	DP	SCR	SHT	FLT	DP	125	0.453
7.	530	50	1	46.0	52.3	SSS	SHT	SSS	---	---	125	0.262
8.	530	50	5	46.0	55.4	SSS	SHT	SSS	---	---	125	0.369
9.	530	50	10	46.0	59.8	SSS	SHT	SSS	---	---	125	0.502
10.	530	50	20	46.0	66.6	SSS	SHT	SSS	---	---	125	0.672
11.	530	0	5	46.0	48.0	SSS	SHT	SSS	---	---	125	0.091
12.	530	50	5	43.4	57.7	SSS	SHT	SSS	---	---	60	0.571
13.	530	50	10	43.2	67.7	SSS	SHT	SSS	---	---	60	0.838

P_t = total applied pressure - psi

P_d = displacement air pressure - psig

T = displacement time - sec.

D_i = ingoing dryness - %

D_i = outgoing dryness - %

L_1-L_5 = layers of pressing system - top-to-bottom

BW = basis weight - g/m^2

ΔMR = change in moisture ratio through press

DP = drilled plate

SCR = screen

SHT = sheet

SSS = sintered stainless steel plate - 40μ pore size

FLT = felt

6. The pure pressing effect - i.e., without displacement - is small as shown by tests 8 and 11.

7. Finally, basis weight has a large negative effect as indicated by tests 8 and 12 and by tests 9 and 13.

These observations are consistent with, but expand upon, those made earlier.

While freeness has not been considered as a variable in these tests, decreasing freeness would be expected to have a significant negative impact on displacement pressing performance.

These results show favorable sheet dryness levels for displacement pressing, even though the times involved were excessive for commercial machines. With the simple, manually controlled equipment, it was not possible to effectively test at shorter time intervals. There were several other deficiencies in this first generation system, as well. These included poor distribution of the compression load, extensive rewet because of the long post-pressing contact time, compression of the web well before and after the displacement pulse, severe radial leakage of air, thus reducing and disguising the true displacement pressure, and manual control. Given these qualifications, the results were regarded as sufficiently encouraging to warrant further work.

SIMPLIFIED ANALYSIS OF DISPLACEMENT PRESSING

In order to gain understanding of the primary effects of web and operating parameters, a highly simplified analysis of displacement pressing has been performed. Because of the success of zonal models in describing high intensity drying, a two-zone model has been adopted (see Fig. 10). In this model, the water available for displacement by an air pressure gradient is considered to be displaced from the web as a unit (wet zone), leaving behind (in

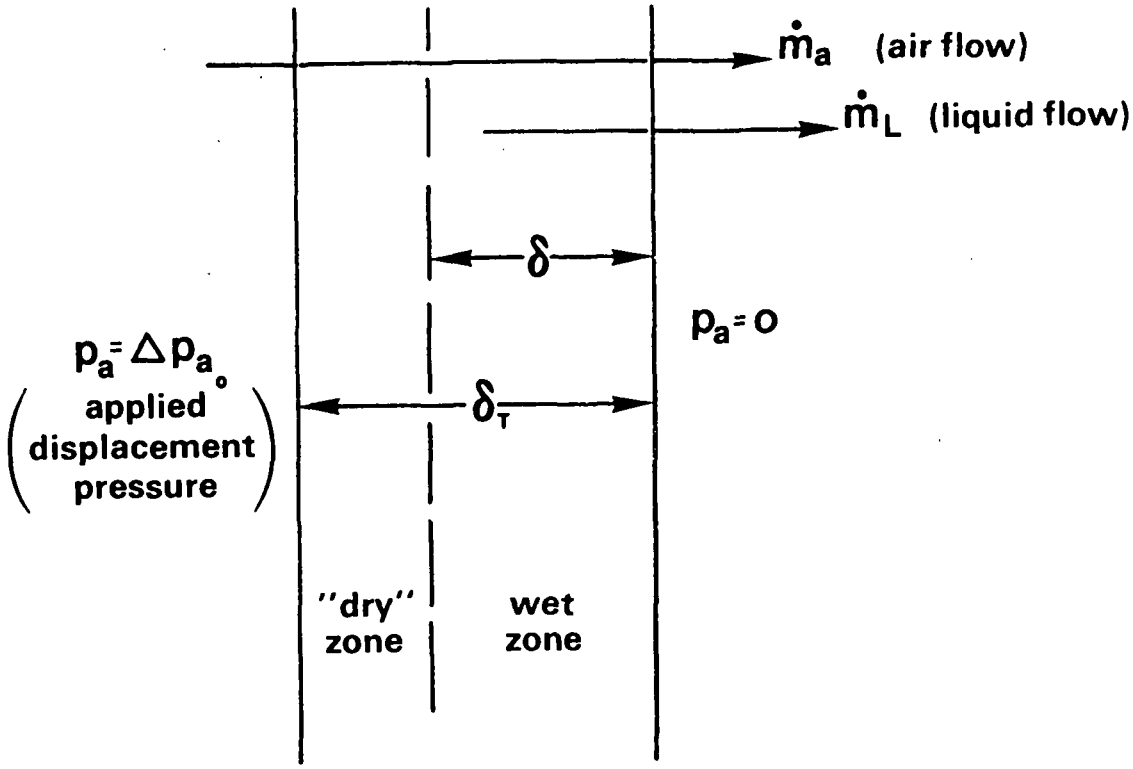

Figure 10. Two-zone model of displacement pressing.

the "dry" zone) that water which is unavailable for displacement. The analysis was performed for the general case in which air flows through the entire web removing water by viscous entrainment. However, the special case of a saturated wet zone, with water removal by a "push-through" mechanism, is readily handled in the model by setting the air permeability of the wet zone to zero.

A brief outline of the analysis is as follows. As a result of mechanical compression, the web has a thickness (δ_T), an effective density of water available for displacement ($\bar{\rho}_L$), air permeabilities for the wet and "dry" zones

(k_{a_w}, k_{a_d}), and a liquid permeability in the wet zone (k_L). The above quantities, as well as the applied air pressure difference (Δp_{a_o}), are considered constant. For simplicity, the compressibility of the air is neglected [i.e., the air density (ρ_a) is treated as constant].

It is assumed that Darcy's law adequately describes both the air and water flows. Although the wet zone thickness will decrease with time, a quasi-steady-state analysis is employed. Thus, the air flow rates ($\dot{m}_a$) through the "dry" and wet zones must be equal at every instant, yielding:

$$\dot{m}_a = \frac{\rho_a \, k_{a_d}}{\mu_a} \frac{\Delta p_{a_d}}{(\delta_T - \delta)} = \frac{\rho_a \, k_{a_w}}{\mu_a} \frac{\Delta p_{a_w}}{\delta} \tag{3}$$

where μ_a = air viscosity

Δp_{a_d} = air pressure drop across "dry" zone

Δp_{a_w} = air pressure drop across wet zone

Of course, the total pressure drop is fixed:

$$\Delta p_{a_d} + \Delta p_{a_w} = \Delta p_{a_o} \tag{4}$$

If capillary pressure effects are neglected, it is Δp_{a_w} that drives the liquid flow. Thus, the liquid flow rate ($\dot{m}_L$) is given by:

$$\dot{m}_L = \frac{\rho_L \, k_L}{\mu_L} \frac{\Delta p_{a_w}}{\delta} \tag{5}$$

where ρ_L = density of water

μ_L = viscosity of water

Finally, the rate of change of the wet zone thickness (δ) can be obtained from a mass balance on the wet zone:

$$\overline{\rho}_L \frac{d\delta}{dt} = - \dot{m}_L \tag{6}$$

with $\delta(o) = \delta_T$.

All of these equations are based on unit area.

The above equations have been solved, yielding the following expression for the wet zone thickness as a fraction of the total thickness:

$$\frac{\delta}{\delta_T} = \frac{-\bar{k} + \sqrt{1 - (1-\bar{k}^2)\bar{t}}}{1 - \bar{k}}, \quad o \leq \bar{t} \leq 1 \tag{6}$$

where $\bar{k} = k_{a_w}/k_{a_d}$

$\bar{t} = t/t_D$

$$t_D = \text{"pressing time"} = \frac{(1+\bar{k})\mu_L m_L'' \delta_T}{2 \rho_L k_L \Delta p_{a_o}} = \frac{(1+\bar{k})\mu_L \rho_L \delta_T^2}{2 \rho_L k_L \Delta p_{a_o}} = \frac{(1+\bar{k})\mu_L \delta_T^2}{2 k_L \Delta p_{a_o}} \tag{7}$$

$m_L'' = \bar{\rho}_L \delta_T$ = mass of water available for displacement per unit area

Of course, for $\bar{t} > 1$, no further water removal occurs, since $\delta = o$. The relative water removal (cumulative) is easily derived from the above result as:

$$\bar{M}_{out} = 1 - \delta/\delta_T. \tag{8}$$

Figure 11 shows the predicted behavior for the physically meaningful range, $o \leq \bar{k} \leq 1$.

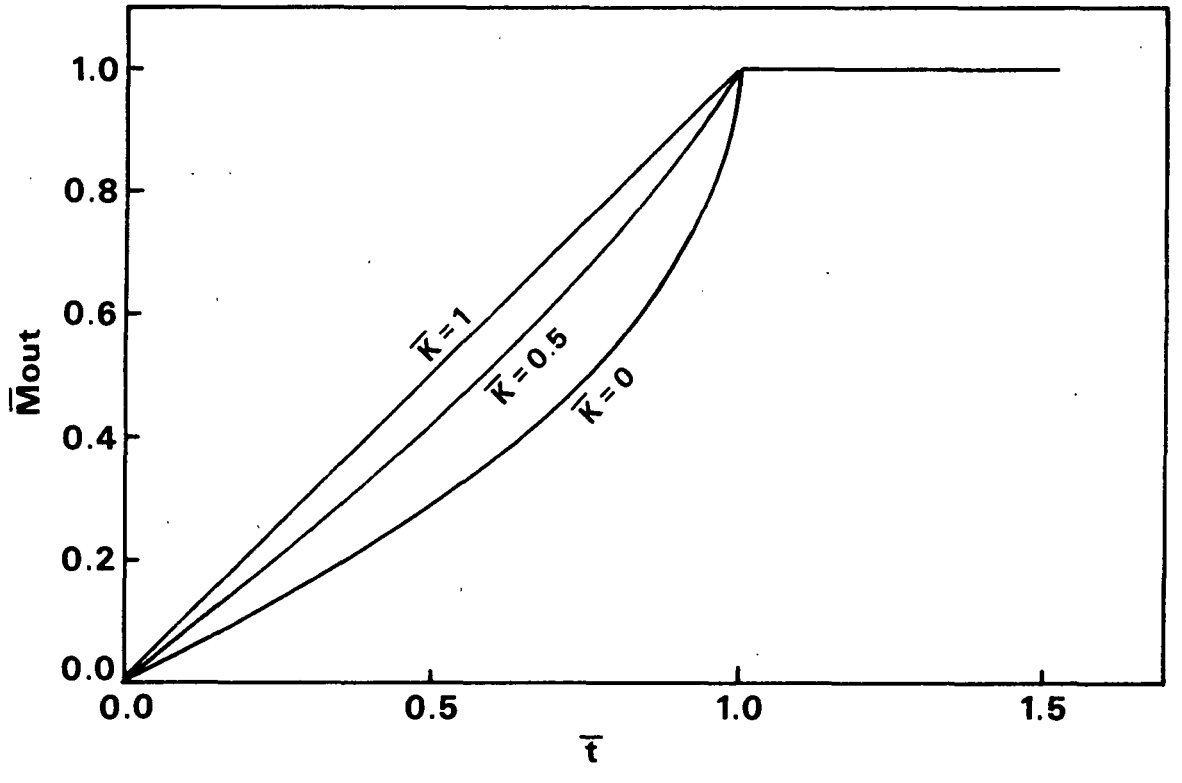

Figure 11. Dimensionless cumulative water removal ($\bar{M}_{out}$) as a function of dimensionless displacement time ($\bar{t}$).

Perhaps the most important result of the analysis is the expression for "drying time" (t_D) listed above. It, in conjunction with the expression for $\bar{m}''_L$, indicates that drying time is proportional to the square of the web thickness (basis weight) and inversely proportional to applied air pressure and web liquid permeability (a strong function of compression level, moisture ratio, and freeness for a given pulp).

According to the model, there is no incentive to perform displacement pressing for times longer than t_D. The real challenges, then, are to minimize t_D, while maximizing $\bar{m}''_L$ (the water available for displacement). This will require understanding and use of optimal operating strategies.

EXPLORATORY EXPERIMENTS WITH A SECOND GENERATION PRESS

The initial exploration of displacement pressing reported in an earlier section involved tests performed in a static press device. That is, the sheets were precompressed for several seconds, after which displacement (air) pressure was applied. Although the dryness levels attained (up to about 65%) were very encouraging, the compression and displacement times ($\geq$ 0.5 sec.) used were long compared to residence times typical of commercial pressing equipment.

To learn whether these high dryness levels could be attained or exceeded within a time period more typical of currently practical pressing operations, a second generation of displacement pressing equipment was developed. A new test head, shown in Fig. 12, included a sheet/felt edge seal, improved load distributors, a pressure transducer for measuring the actual displacement pressure on the sheet, and an improved air supply/distribution system.

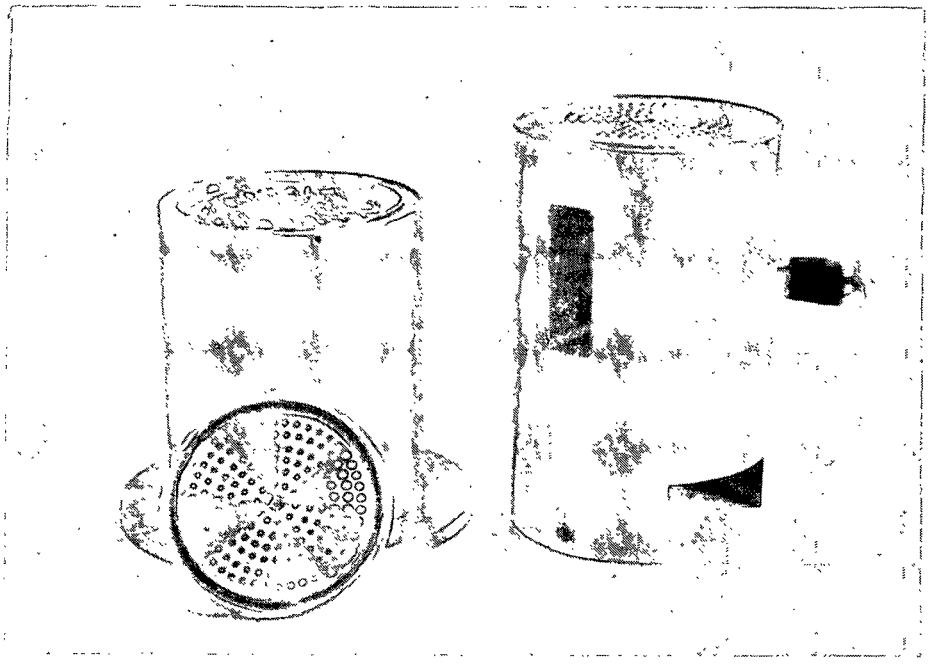

Figure 12. Displacement pressing head.

To permit short duration, dynamic testing, this test head was installed in a falling-weight press nip simulator, shown schematically in Fig. 13 and described more fully in ref. (13). In this device, peak pressure, nip residence time, and impulse are set by selecting appropriate values for the falling weight, the height from which the weight is dropped and the amount of elastic material in the system. While short, hard nips proved easy to simulate, great difficulty was encountered in going to nip residence times beyond a few milliseconds, an area of particular interest for displacement pressing. For this reason, testing of the displacement pressing concept was shifted to an electrohydraulic press.

The electrohydraulic press uses a hydraulic cylinder, servovalve and position and force transducers to form a closed loop, load and position control

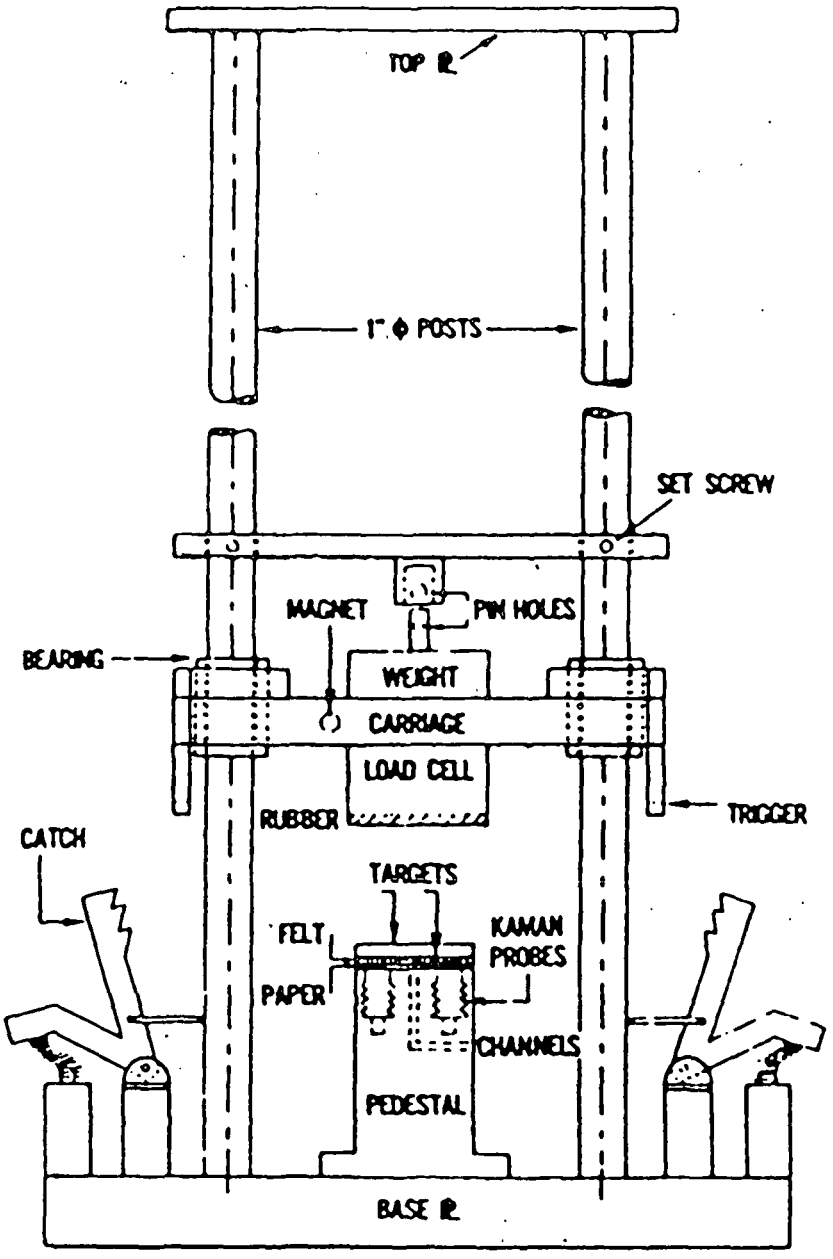

Figure 13. Falling weight press nip simulator.

system. A special electronic control package was developed to allow simulation of a single pressing event. Pressure-time pulses of a wide variety of shapes and sizes may be commanded electrically to simulate various types of nips. This device is extremely well suited to simulating any press configuration with a nip residence time of 10 ms or more. Figure 14 shows the press servo with the displacement pressing head installed.

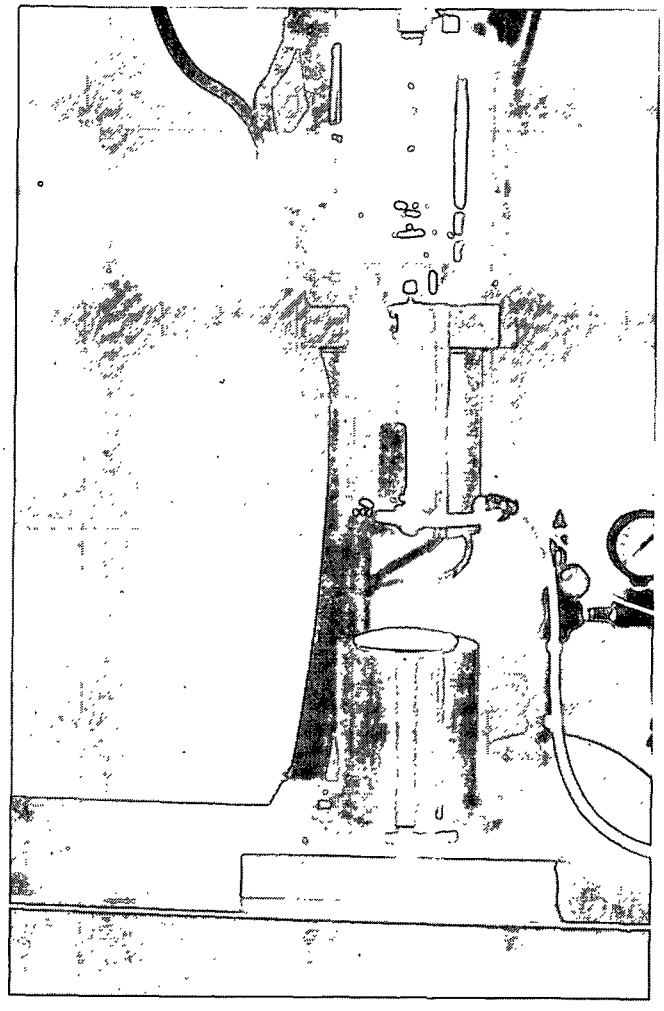

Figure 14. Electrohydraulic displacement pressing system.

Results

Initially, scoping experiments were performed to examine the effects of certain operating variables on displacement pressing performance. For these experiments, 63 g/m^2 handsheets formed from 720 CSF bleached softwood kraft (once-dried) pulp were utilized.

In one series, the peak mechanical pressure and nip residence time (displacement time) were varied. The tests were performed using sheets at 43-45% initial dryness. The pressing configuration used comprised a bronze wire/handsheet/felt sandwich pressed between the drilled plates of the two test heads with the wire at the air supply side. A soft rubber gasket surrounded the sandwich to minimize air leakage. A haversine-shaped mechanical pressure pulse was applied and the air supply was triggered just prior to initiation of the mechanical pulse. Example mechanical pressure and air pressure responses for this operating mode are given in Fig. 15.

The results of this test series are presented in Fig. 16. It is seen that nearly 50% of the water initially in the sheet (corresponding to final dryness levels of 60% or more) was removed under the maximum time and pressure conditions. For the range of conditions represented in Fig. 16, the peak air pressures ranged from 40 to 80 psi, increasing with mechanical pressure and with displacement time. Air pressure levels were very erratic, however, because of poor sealing. Some of the factors contributing to the beneficial effect of higher mechanical pressures may be: larger quantities of water squeezed from the fibers and available for displacement, increased air pressure differential across the web due to its increased saturation (air flow resistance), and decreased web thickness. The potentially impeding effect of increased liquid

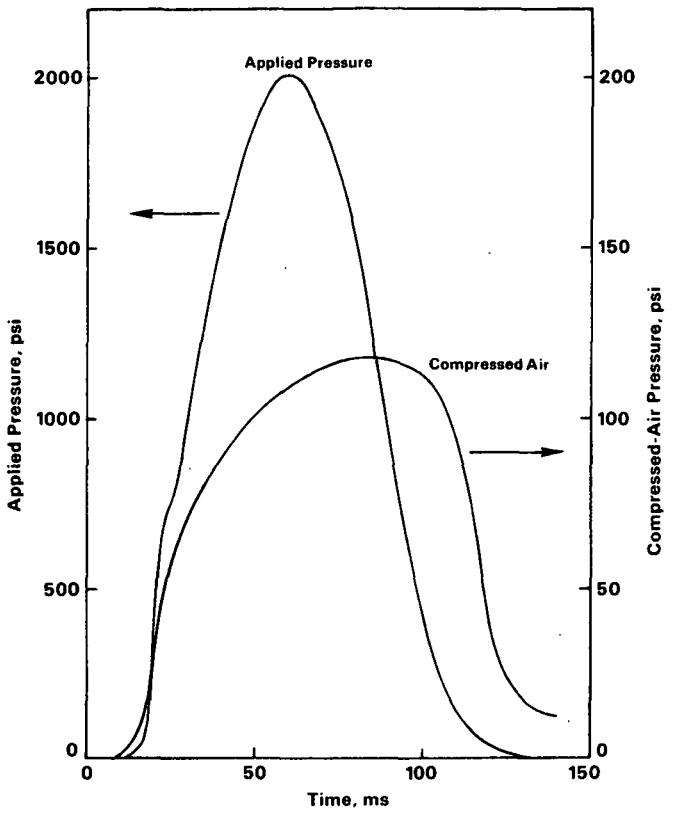

Figure 15. Example applied mechanical pressure and air pressure responses for the harversine mechanical pulse mode.

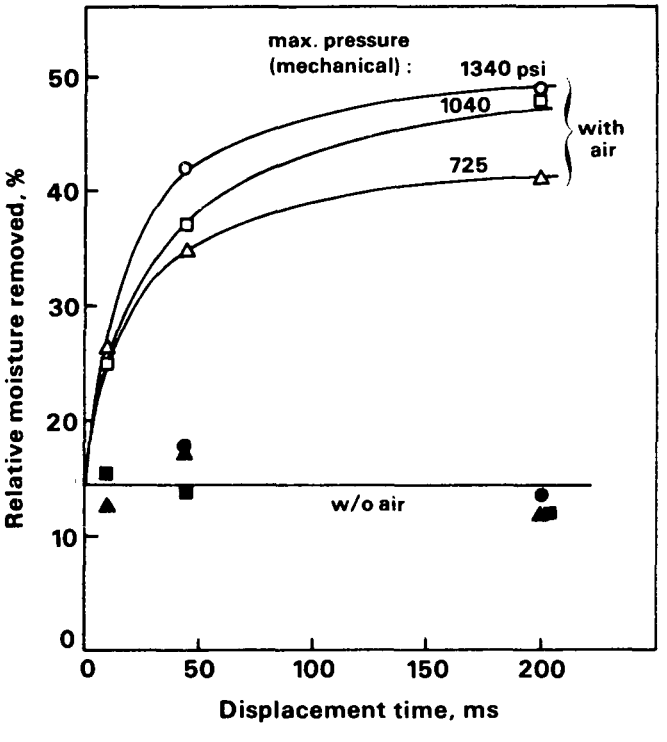

Figure 16. Results of displacement pressing of 63 g/m^2 handsheets of once-dried bleached softwood kraft pulp at 720 CSF. Initial dryness = 43-45%.

flow resistance at higher compression levels is apparently insufficient to overcome these beneficial effects. These displacement pressing results are particularly encouraging because they indicate that significant dewatering occurs in time approaching those for available pressing equipment (e.g., up to 50 ms).

Because the bronze wire/drilled plate combination yielded marked (dimpled) sheets after pressing, other load spreader/air distributor materials were tried. These included plastic wires and porous metal plates. The use of porous plates tended to result in somewhat reduced water removal. The plastic wire was stiffer than the bronze wire and reduced dimpling without significantly changing water removal. Therefore, it was adopted for use in subsequent experiments.

Although not studied thoroughly, several tests using "square," rather than haversine, mechanical pulse shapes were performed. In some cases, the displacement air application was delayed by 50 ms, as shown in Fig. 17, to determine the effect of precompression. No appreciable differences in water removal were observed with these pressing modes, as compared to the use of haversine pulses with mechanical precompression, for similar displacement times. These results support the notion that displacement time is a critical variable rather than compression time, consistent with the results obtained in the static press.

Increases in peak mechanical pressure (to 2000 psi), air supply pressure (to 200 psi) and sheet initial dryness (to ~49-51%) were also explored. The combined effect of these changes was an increase of several percentage points in final sheet dryness (up to the 64-65% range) within the same time range as shown in Fig. 16. These higher air supply pressure and initial dryness levels were then retained in subsequent tests.

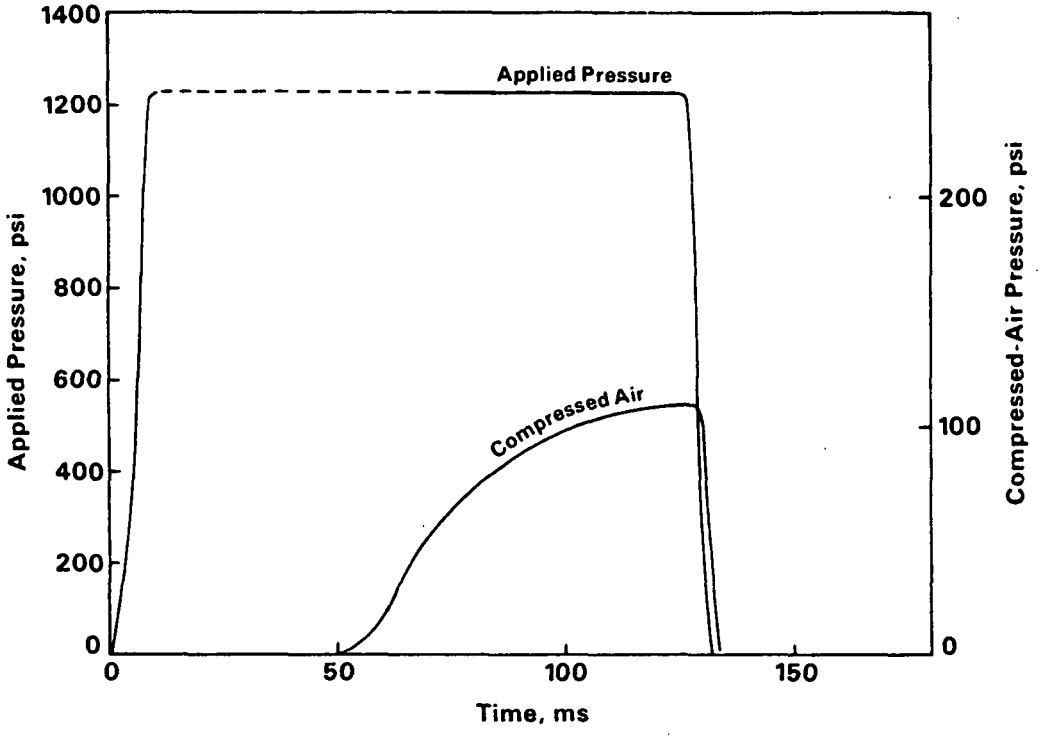

Figure 17. Mechanical and air pressure responses for "square" pulse with air supply "triggered" after 50 ms of sheet compression.

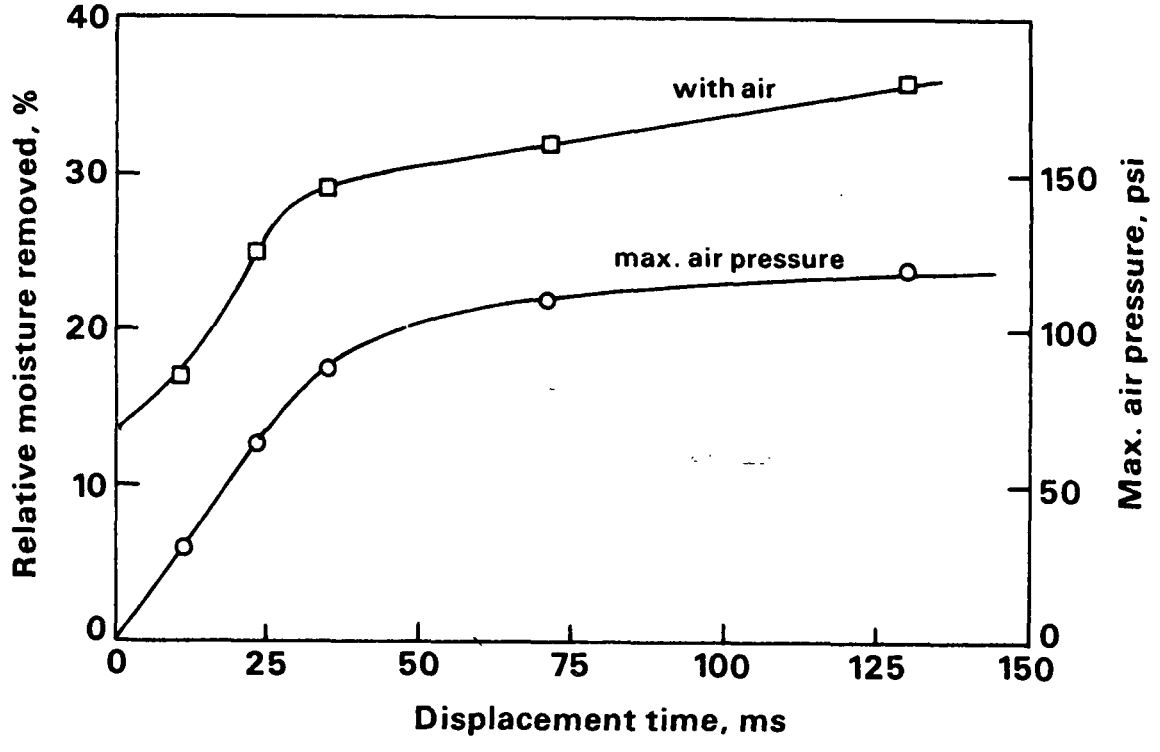

Figure 18. Results of displacement pressing of 63 g/m^2 handsheets of never-dried bleached northern softwood kraft pulp at 690 DSF. Initial dryness -50%.

The next phase of experimentation involved comparing the displacement pressing behavior of never-dried pulp (bleached northern softwood kraft), at two freeness levels (690 and 300 CSF), with that of the previously discussed once-dried pulp. One of the operating conditions used a "square" mechanical pulse, with 50 ms precompression time and 130 ms displacement time, at a level of 1200 psi. For 63 g/m^2 handsheets at about 49% initial dryness, the water removal amounts for the 720 CSF once-dried, the 690 CSF never-dried, and the 300 CSF never-dried pulp handsheets were 47%, 33%, and 20%, respectively. Rather similar results were found using other pulse shapes and somewhat shorter displacement times. For all three sheet types, pressing without displacement air yielded about 15% water removal.

The effects of displacement time and pulp freeness have been investigated in one of the most definitive portions of the displacement pressing study so far. Handsheet samples of 63 g/m^2 basis weight, formed from never-dried, bleached northern softwood kraft pulp at freeness levels of 300 and 690 CSF and having an initial dryness of about 50%, were employed. Mechanical pressure pulses of "square" shape, at a level of about 1200 psi, were used. The compressed air supply was "triggered" after 50 ms of sheet compression. Typical mechanical and air pressure responses are shown in Fig. 17. The water removal curves resulting from these tests are shown in Fig. 18 and 19. In the case of the 690 CSF pulp, the displacement times needed to achieve significant dryness increases were on the order of 25 ms and, thus, comparable to the response time of the air supply system (i.e., about 40 ms). As a consequence, the maximum air pressure applied to the sheet increased with displacement time (see Fig. 18). Instantaneously applying a given air pressure would probably increase water removal for short displacement times and flatten the curve for longer times.

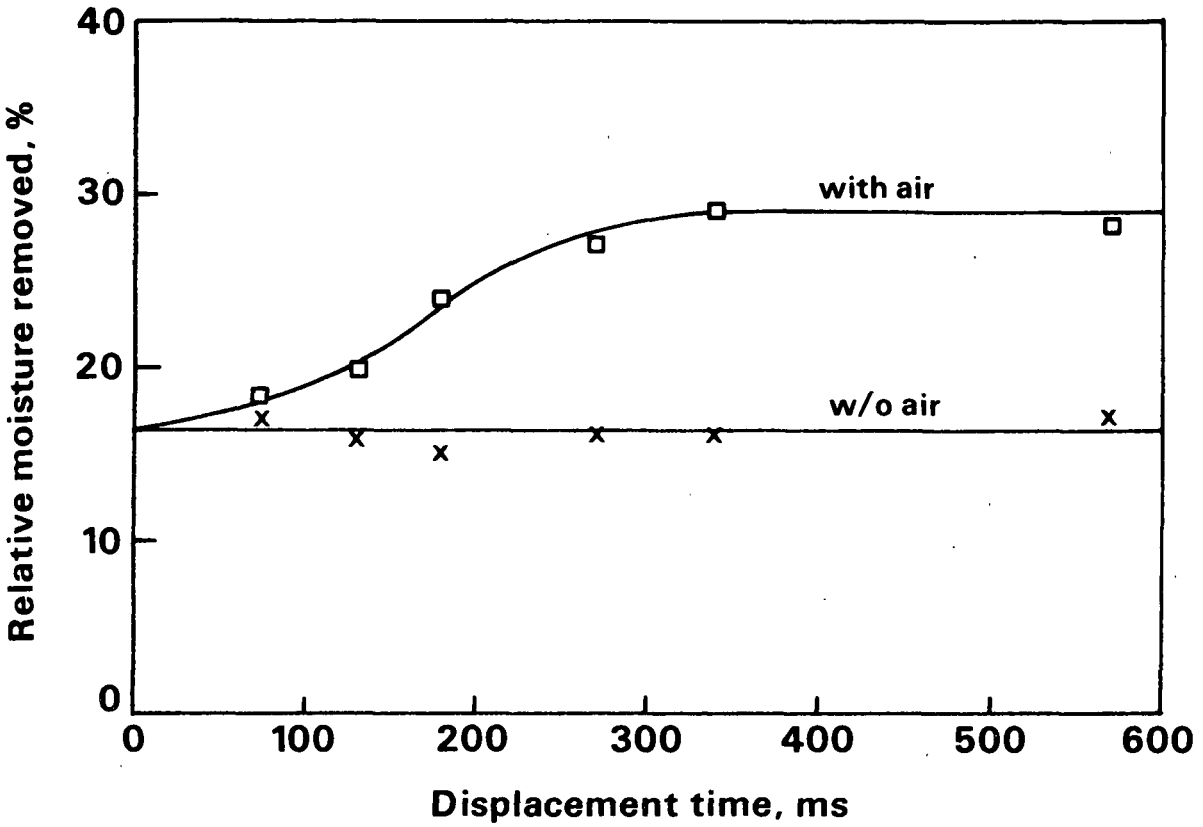

Figure 19. Results of displacement pressing of 63 g/m^2 handsheets of never-dried bleached northern softwood kraft pulp and 300 CSF. Initial dryness - 50%.

In the case of the 300 CSF pulp, the time required for significant water removal was well beyond the response time of the air system, so the peak air pressures were about the same for all tests. Interestingly, the peak air pressure was greatest for the low freeness pulp (180 psi vs. 120 psi), probably due to differences in sheet flow resistance.

The data presented in Fig. 18 and 19 indicate that significant increments of water removal via displacement pressing are achievable at high ingoing dryness levels. The amount of water available for displacement appears to be somewhat greater for the high freeness case. Importantly, the majority of the water removal occurred in a time period (<35 ms) comparable to the residence time in an extended nip press in the 690 CSF case. For the 300 CSF pulp, the dewatering time was nearly an order of magnitude longer (~300 ms).

The shapes of the displacement pressing curves in Fig. 18 and 19 are in good agreement with that predicted by the simplified model presented earlier in the report. Furthermore, the experimental dewatering times are in reasonable quantitative agreement with those calculated (using estimated parameter values where necessary) from the "pressing time" equation resulting from the simplified analysis.

A few very preliminary experiments were conducted to test the effects of preheating the web and of blinding the back side of the felt to prevent air flow-through. The results are too limited to permit definite conclusions, but suggest that preheating will increase water removal and that blinding the nip has little effect. If the latter observation holds up under more complete testing, it may be significant in reducing air flow and, therefore, power consumption for supplying the displacement air.

DISPLACEMENT PRESSING FOR BULK CONTROL

As stated previously, pressing usually increases final sheet density in direct proportion to the increase in dryness. For some grades, higher densities are undesirable. Examples include absorbent grades, boxboard and some printing paper. For all grades, high dryness out of the press is desirable for good runnability, productivity and low drying energy costs. To achieve both low density and high dryness, it is necessary to decouple the density-dryness relationship common to conventional wet pressing.

Density is developed by compressing the sheet to remove water from the fiber. This density is at least partially retained in the final product if the water remaining in the sheet after pressing is removed before the sheet can reswell. Because conventional pressing relies on strong compression of the sheet for water removal, dryness and density are closely linked. In displace-

ment pressing, however, the sheet can be compressed slightly to make water available for removal. The water is then displaced (removed) by air flowing into the sheet from an external pressure source. In this fashion, sheet dryness can be increased without significantly densifying the sheet. The degree of bulk retention depends on the moisture level at which displacement pressing is started.

Exploratory Experiment with High Bulk Displacement Pressing

Displacement pressing (DP) for high bulk uses the same equipment and procedures previously described for pressing to high dryness levels. Here, however, the DP process is started at a low solids content and much lower compression levels are used. For this type of operation, a displacement press would replace a conventional first or second press rather than a third or fourth press, as in the high dryness case.

To evaluate this concept, a number of tests have been carried out using 63 g/m^2 sheets made from a bleached northern softwood kraft furnish with a Canadian standard freeness of 690 ml. These sheets were displacement pressed with air and compression schedules like those shown in Fig. 17, i.e., 60 ms of precompression followed by 60 ms of displacement for a total time of 120 ms. Compression levels of 100, 400 and 1500 psi and ingoing dryness levels of about 25, 35, and 50% were used. Displacement pressed sheets were dried on a hot plate to determine final density. Outgoing dryness levels and density levels are shown in Figs. 20 and 21, respectively. Figure 20 also shows outgoing dryness levels without displacement, i.e., the conventional presssing component alone.

From the data in Fig. 20, one can make the following observations:

1. Displacement pressing is very effective in removing water, especially for low ingoing dryness levels.

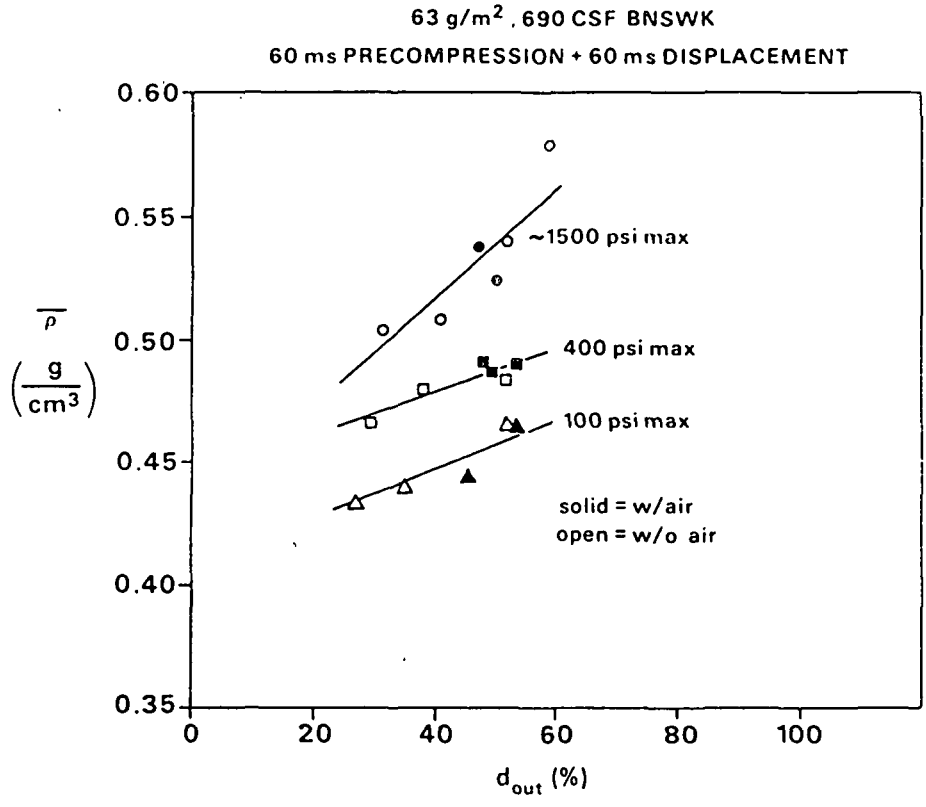

Figure 20. Dryness gains in displacement pressing.

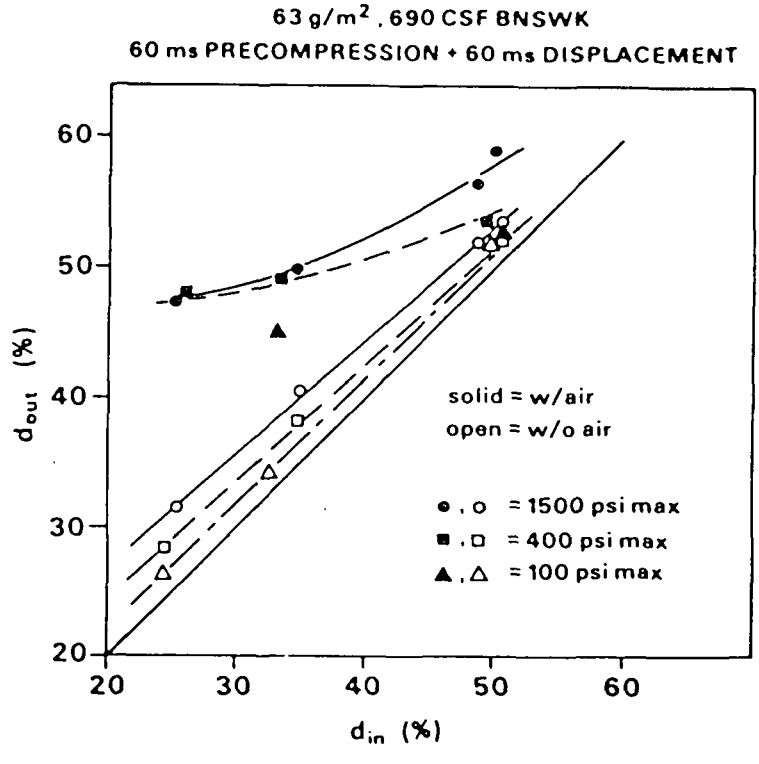

Figure 21. Density development in displacement pressing.

2. Very little of the water is removed by pressing only. Hence, most must be removed by displacement.

3. Outgoing dryness changes are about 1/3 of ingoing dryness changes. This is equivalent to the rule-of-thumb applied to conventional presses.

4. Water removal is quite insensitive to compression level, especially for low ingoing dryness levels. It is quite remarkable that the solids level can be increased from 25 to 48% in a press operating at a load of 100 psi.

From the data in Fig. 21, it is clear that displacement pressing at low ingoing solids levels can be used to decouple the normal density-dryness relationships. At an outgoing dryness level of 50%, for example, the density ranges from about 0.45 g/cm^3 for pressing at 100 psi, to about 0.54 g/cm^3 for pressing at 1500 psi. For conventional pressing to 50% solids, the density would be fixed, almost totally independent of the specific pressing configuration.

REVIEW OF POLISH WORK ON BLOWTHROUGH DEWATERING OF PAPER WEBS

Drainage or pressing of paper by passing (blowing) air through the wet web is not a new concept. Several devices for this purpose are described in a patent by Holden (1), filed for in March, 1963, and granted November 8, 1966. His work and that of Brundrett and Baines (2) were extended by Kawka and co-workers in Lodz, Poland. Several articles (3-10) have been published since.

Most of the work in Poland has been aimed at the use of the blow-through principle to raise the solids content of the sheet from values in the 10-30% range up to 40-45%. Two representative devices due to Holden (1), used

by Kawka, are shown in Fig. 22. An additional device, developed in Poland and called an air press, is shown in Fig. 23. Several other similar devices have been proposed or used (3-10). All have the following characteristics:

a. low mechanical compression forces on the wet fiber network

b. long exposure times (0.1-several seconds)

c. a porous fabric or structure backing the wet web

d. modest pressure differentials through the wet web (1-30 psi)

e. low load levels (50-100 pli) on the pressing components, where they were used

f. low operating speeds (up to 300 m/min)

g. unheated blowthrough air, in most cases.

Blowthrough dewatering has been applied primarily to lightweight grades where bulk, absorbency, and porosity are important, such as tissue, toweling, and bag papers. There is mention of application to heavyweight board pulp dewatering (9), but no data are given.

Some typical results for a 70 g/m^2 bag paper are presented in Figs. 24-26. These data were obtained by subjecting sheets with initial solids contents of 18.8, 25.3, and 31.4% to one, two, or three passes through an air press (Fig. 23). Corresponding exposure times were 0.2, 0.4, and 0.6 seconds. Press loads were about 50-100 pli.

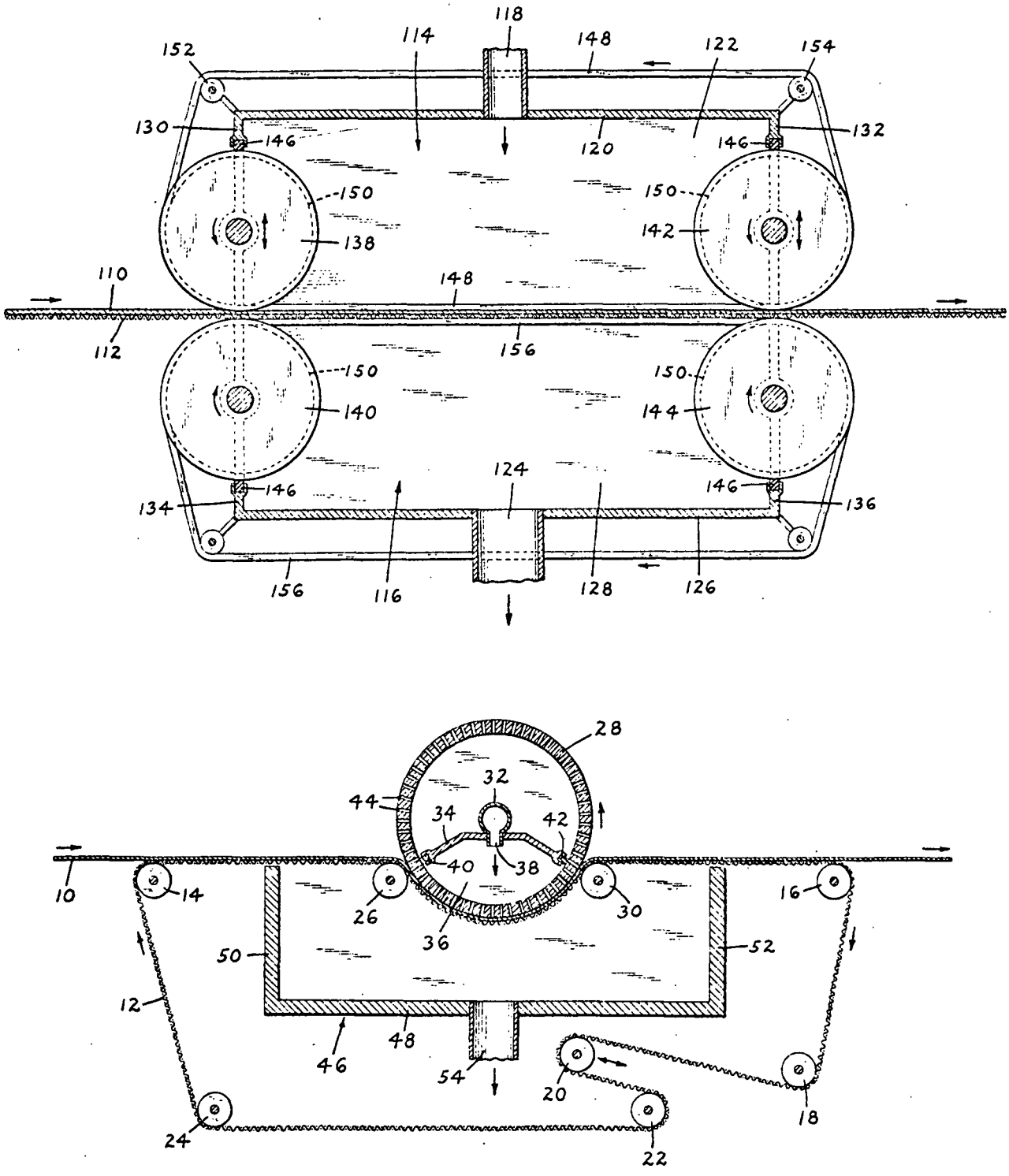

Figure 22. Two blowthrough configurations due to Holden (1).

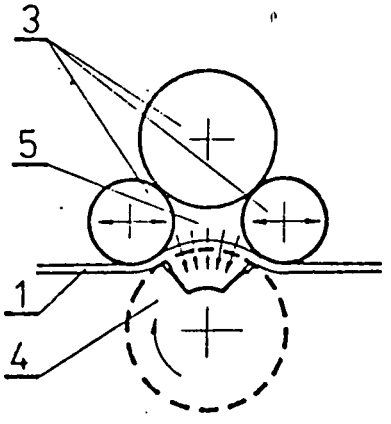

Figure 23. Polish "air press".

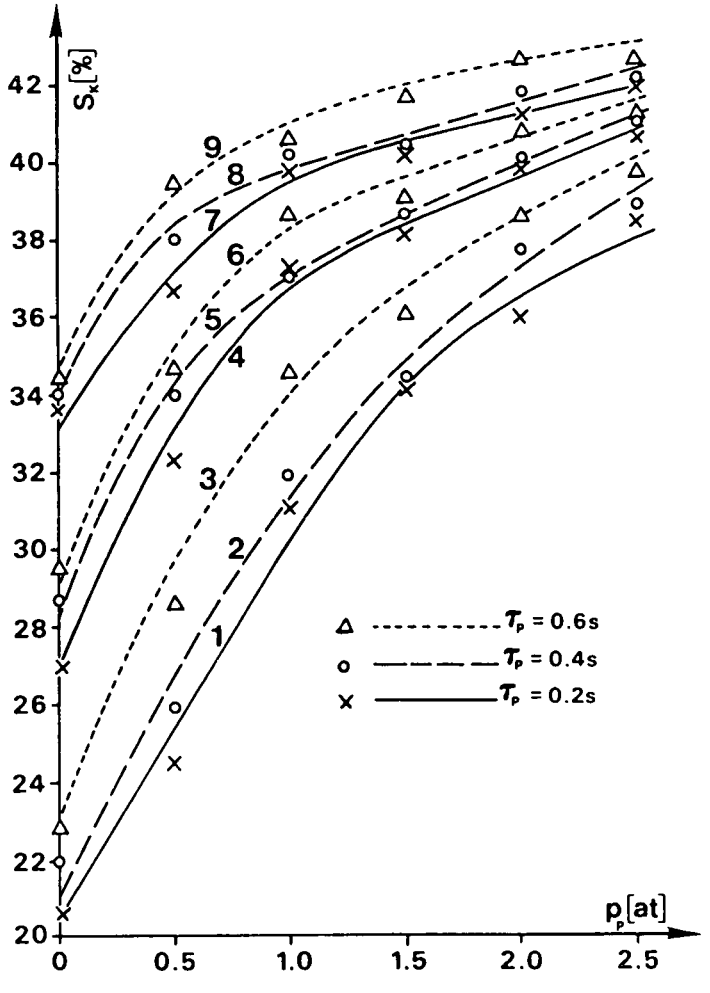

Figure 24. Final dryness (s_k) as a function of blowthrough air pressure differences (p_p) and blowthrough time ($_p$), initial dryness as a parameter. Initial dryness: 18.8% for 1-3, 25.3% for 4-6, 31.4% for 7-9.

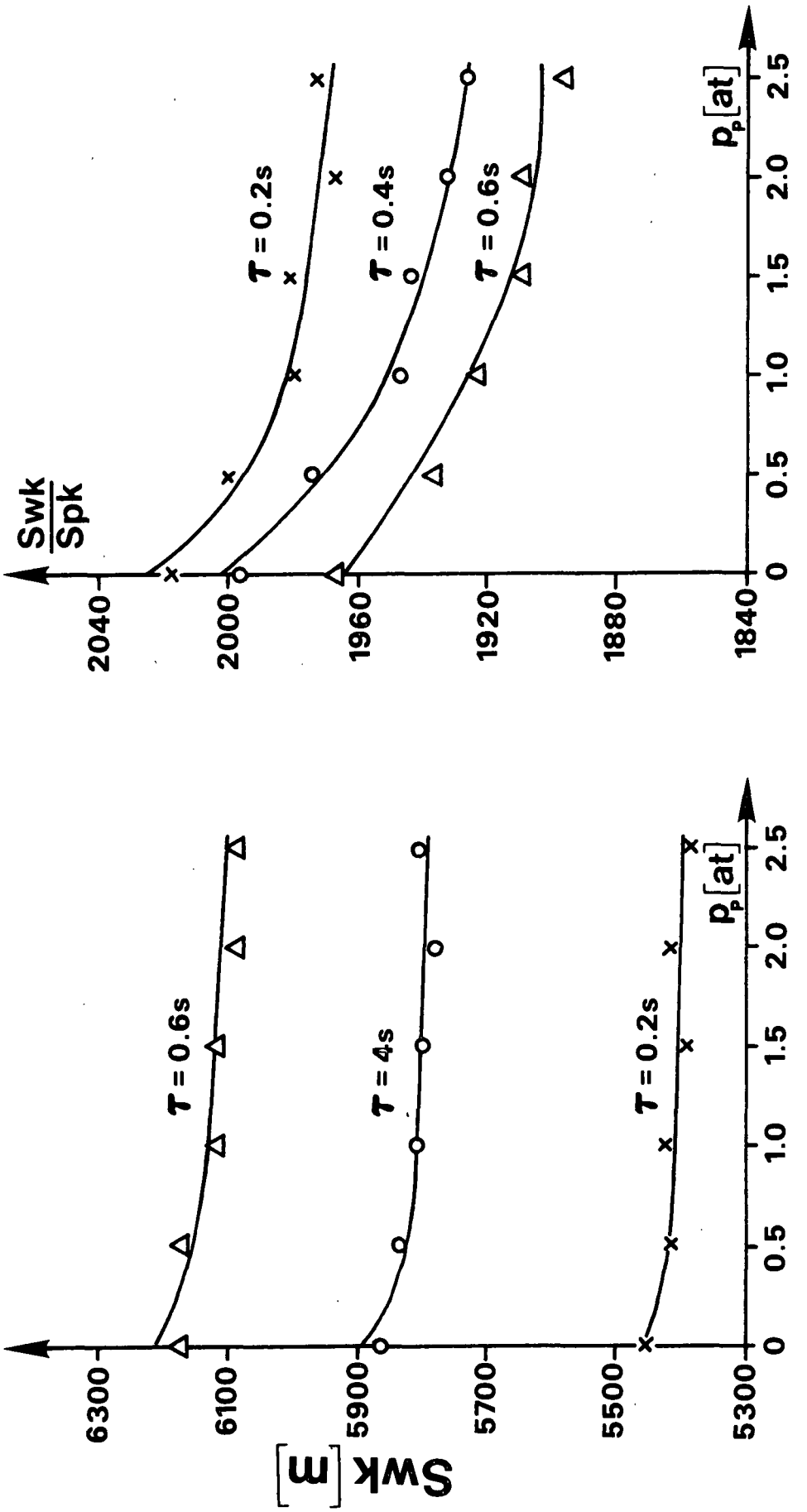

Figure 25. Breaking length and squareness as functions of blowthrough pressure differential.

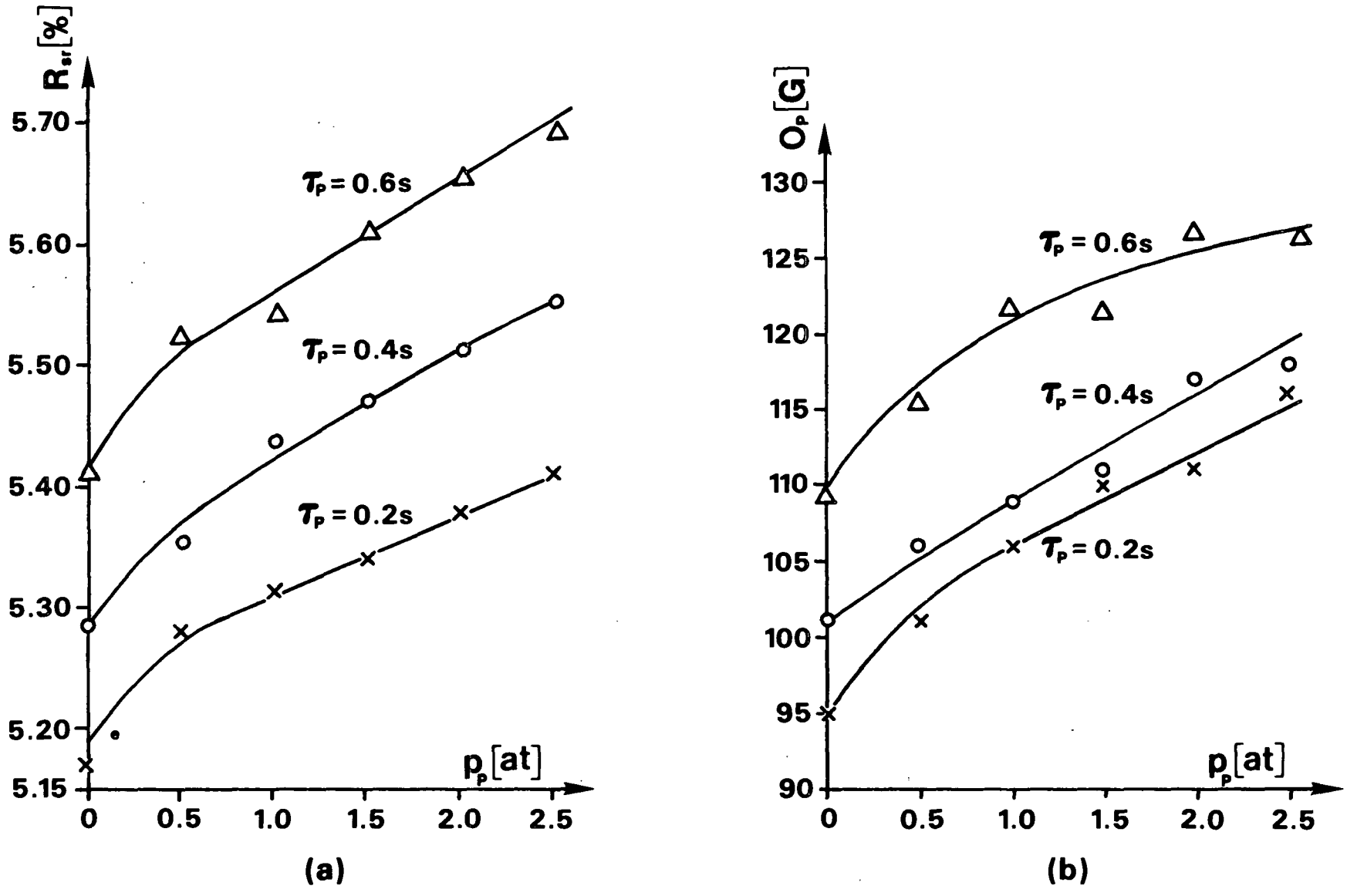

Figure 26. Elongation at failure and tear strength as functions of blowthrough pressure differential.

Figure 24 shows final solids values as a function of the blowthrough air pressure differential. The following observations apply to these data:

a. This type of blowthrough water removal is most effective on wet sheets (10-20% solids).

b. Increased dryness from additional passes - more blowthrough time - seems mostly due to mechanical pressing and not to blowthrough.

c. For the web tested and the prevailing dewatering conditions, the maximum solids level is limited to about 42%.

d. More air pressure gives higher dryness levels, but the effect diminishes at a transition pressure (1.0-1.7 atm) which decreases with increasing initial dryness.

Figure 26 shows elongation at failure and tear strength as functions of blowthrough pressure. Both show significant improvement with mechanical pressing (p_p = o) and even more dramatic improvement with increased blowthrough.

Other properties, not shown in these figures, were also altered. Blowthrough dewatering tends to give much higher bulk (100% more), higher porosity, and higher absorbency than conventionally consolidated papers.

Air pressing is thus effective in dewatering wet webs ($\leq$40% solids) and in promoting bulk, absorbency, stretch, tear, and squareness. Tensile strengths tend to be degraded slightly. The efficiency (cost) of such pressing is hard to assess, but in one example cited (3) the direct air power delivered to the web was about 4 million Btu/ton which is substantial. The authors state that the primary advantage is in property control and not in energy cost reductions.

In some of the papers, experiments involving high temperature air and long exposures are cited. These constitute through drying experiments and are not germane to the IPC projects.

The work outlined above has been cited because it is relevant and complementary to the IPC work, and it supports the expectation that displacement pressing of low solids sheets will result in high bulk levels. Most of the IPC work, however, is aimed at quite different objectives and operating regimes. For example, the displacement pressing process under study in this project has been shown to have the potential to:

a. extend pressing solids levels from 50 up to 65% thus augmenting conventional drainage and pressing elements and displacing dryers,
b. work over a range of mechanical pressures up to high levels to permit improvement and control of properties, including strength or bulk, thus making it attractive for use on several grades,
c. reduce drying energy levels substantially and reduce dryer size or increase productivity, and
d. work over the short time intervals characteristic of modern, high-speed machines.

All of these expectations fall well outside the range of the previously completed work and the capability of the various presses that have been developed. None has the potential for extension to the displacement pressing regime.

PRESSING WITH POROUS PLATES

BACKGROUND

Figure 3 [replotted from Ceckler and Thompson (11)] shows press exit dryness levels (total water removed) as a function of press impulse for a typical furnish and basis weight sheet. For sheets with less than 45-50% dryness, these and other data clearly show that press impulse is the dominant controlling variable. In this regime, pressure and time are largely interchangeable with the absolute level of pressure playing a small role. For higher dryness levels, impulse loses its dominance and pressure and other variables become important. These zones are often referred to as "flow controlled" (impulse controlled) and "compression controlled" (pressure controlled), respectively. Current extended nip technology provides impulse levels that nearly span the flow controlled range and can lead to dryness levels around 50%.

In their DOE sponsored wet pressing study, Ceckler and Thompson performed a number of experiments in the flow controlled regime to compare laboratory and pilot press performance. The laboratory unit used porous metal plates to receive the water whereas the pilot press used a felt. Under some test conditions, the laboratory press removed almost twice as much water as the pilot press for a given impulse level. Ceckler and Thompson attributed the greater effectiveness of the laboratory press to the uniformity of pressure provided by the porous plate as opposed to great variability in the local pressure delivered by the felt. As will be shown later, there is little evidence to support this hypothesis.

Ceckler and Thompson coined the term "nip efficiency" to describe the correction necessary to make the laboratory compression data agree with the pilot press data. Nip efficiencies tend to vary widely depending on furnish,

moisture level and pressing conditions, but are always well below 100%. Hence, the nip efficiency data show porous plates (the UMO laboratory compression tester) to be far superior to pilot press and, hence, real presses. Direct comparison of the UMO laboratory data with pilot press data is not appropriate however, for two very important reasons. First, laboratory tests were started with the sheet saturated and precompressed to the thickness corresponding to the desired initial moisture ratio. For sheets starting from a saturated state, hydraulic pressure builds instantly and follows the applied compression pressure. Water removal also begins instantly. For most real pressing situations, the ingoing sheet is not saturated and, thus, carries some air with it. The initial portion of the compression pulse is used to drive the air from the sheet and reach a saturated state, at which point water removal begins. This difference in initial sheet state allows the compression tester to remove more water than the real press. A part of the nip efficiency correction term can be attributed to this difference.

Secondly, in the UMO laboratory tests, water removal was calculated from the minimum thickness achieved by the sheet in the pressing cycle, by assuming the sheet to be saturated at this point. This calculation does not take into account the water that flows from the felt back into the sheet as the sheet expands in the exiting part of the cycle. This amount of water can be quite large and is believed to account for much of the remainder of the correction factor relating the UMO press to real presses.

All of the work in this part of the project is motivated by the UMO results and has three objectives:

1. To compare porous plates and felts under common pressing cycles to see if porous plates really effect more water removal.
2. To determine which porous plate characteristics are important to water removal.
3. To test the above hypothesis regarding the factors that control the UMO nip efficiency term.

POROUS PLATE - FELT COMPARISONS

Because the emphasis of this pressing study is initially on determining whether porous plates promote greater water removal than felts, a variety of porous plates was obtained for use in the experiments. The plates used in the work reported here are identified in Table 1.

Table 1. Porous plate characteristics.

Designation	Material	Approx. pore size, μ	Surface
SB10	Sintered bronze	10	Unground
SB30	Sintered bronze	30	Unground
SB40	Sintered bronze	40	Unground
SS40[a]	Sintered stainless steel	40	Ground
SS100	Sintered stainless steel	100	Ground

[a] This is similar to the plate used in the UMO study.

A pressing pedestal (Fig. 27) was fabricated for use in the water removal experiments. It is a vented nip configuration (drilled plate) and has provision for use with any of the porous plates. When a felt is employed, it is

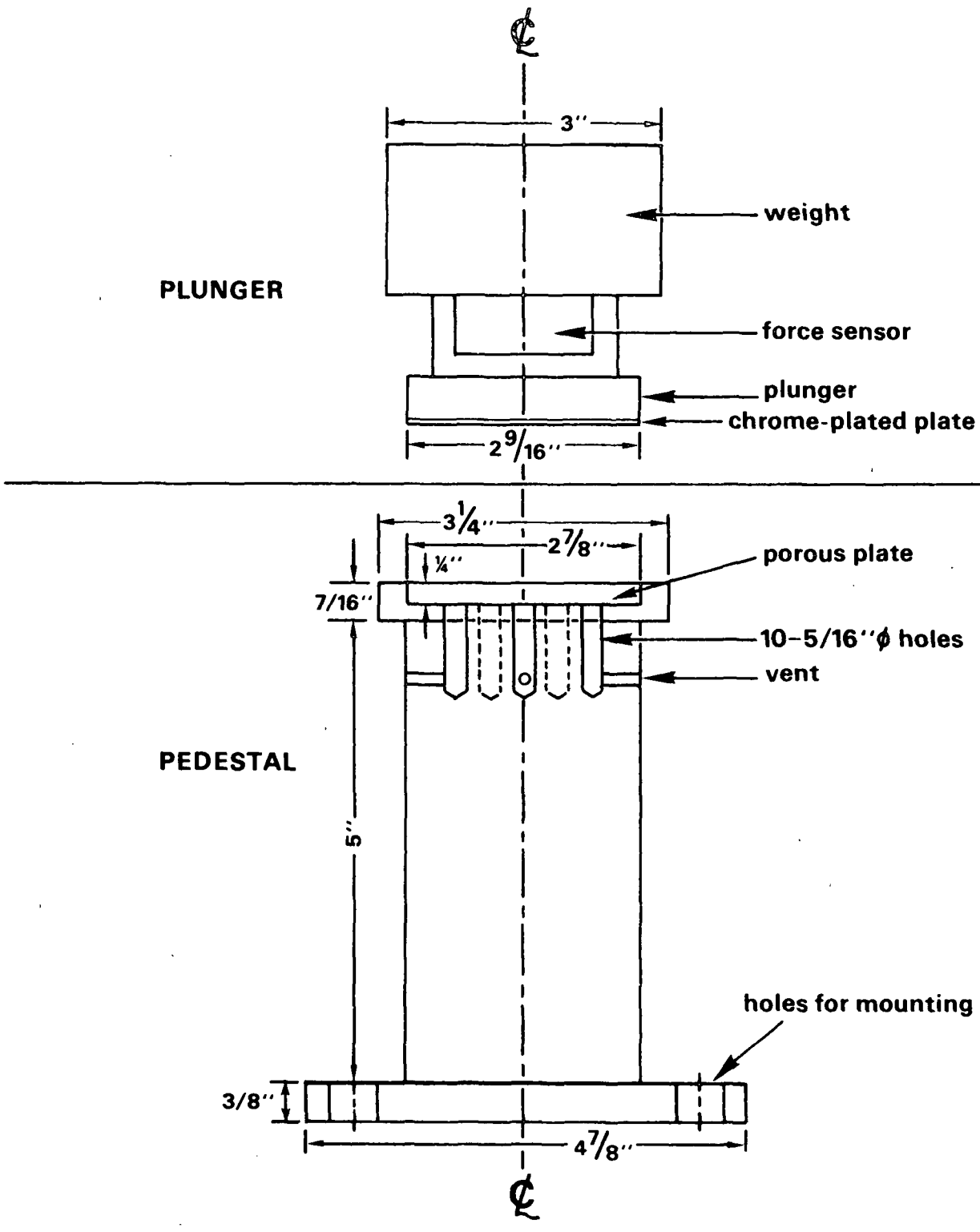

Figure 27. Pressing configuration for high-efficiency pressing study.

placed on top of a very coarse (250μ pore size) porous plate installed in the pedestal as a load spreader.

Many of the results reported here were obtained by using a falling-weight press simulator with this test head installed. Chang and Beck (13), have shown that the falling-weight (Wahren-Zotterman) press simulator provides a very good simulation of a real press nip, including both the compression and expansion parts of the cycle. This system is particularly well suited for modest pressing pressures (~500 psi peak) and nip residence times up to 10 ms or so.

For high pressures and longer nip residence times, an electrohydraulic press has been used with the same pressing heads or variants thereof. In both presses, water removal was measured directly from initial and final weights. Pressed sheets adhere to the chrome plated surface assuring instantaneous separation of sheet and water receiver to avoid post-nip rewetting.

Results

Initial, exploratory experiments were performed using 60 g/m^2 handsheets formed from (once-dried) bleached softwood kraft pulp at about 700 CSF. The initial moisture ratio of the samples was 3.0 for all the tests.

For the purpose of comparison of porous plate performance with felt performance, it was considered appropriate to operate each water receiver at that initial moisture ratio for which water removal from the sheet is maximized. Based on tests at an operating condition of 600 psi peak mechanical pressure and 6.0 ms nip residence time, it was found that all the porous plates performed best when initially dry, while the felt performance was 6-7% better at 0.3 moisture ratio (the optimum value) than when dry. These "best" moisture conditions were then used in subsequent experiments, except as noted.

The water removal data from the tests just described and from tests at a higher impulse level are presented in Fig. 28 for the felt and the three best porous plates. For these test conditions, the felt promotes greater water removal than that achieved with any of the porous plates for both pressing conditions. The ranking of the three porous plates seems to be in agreement with expectations. That is, the rather smooth, small-pored plate is best; the very smooth, but larger-pored, plate is next; and the least-smooth plate is worst. Two other, still coarser, plates yielded even poorer performance.

A few other felts were tested, at the same two operating conditions, to ascertain the importance of felt type. These included: a felt similar to the one used previously but unconditioned, a coarser felt, and a layered felt with one coarse layer. While the original felt remained at the top of the performance ranking, two of the other three had nearly as good performance, giving about 10 g/m^2 less water removal. The layered felt performed approximately the same as the best porous plate (SB10). The felt performance ranking was in accordance with expectations, since the coarser felts performed more poorly than the finer ones. The main conclusion from this test series is that, as a group, felts give better water removal than porous plates, at least for the (small) range of operating conditions studied.

To take the investigation a step closer to the conditions covered by the UMO study, sheets were prepared from (never-dried) bleached northern softwood kraft (BNSWK) pulp at 300 CSF. This is similar to the pulp used in many of the tests performed in the original UMO study. For tests at the same basis weight, initial moisture and impulse conditions used in the work discussed above, the results were as given in Fig. 29. While the quantities of water removal are about half those in Fig. 28, reflecting the greater difficulty of

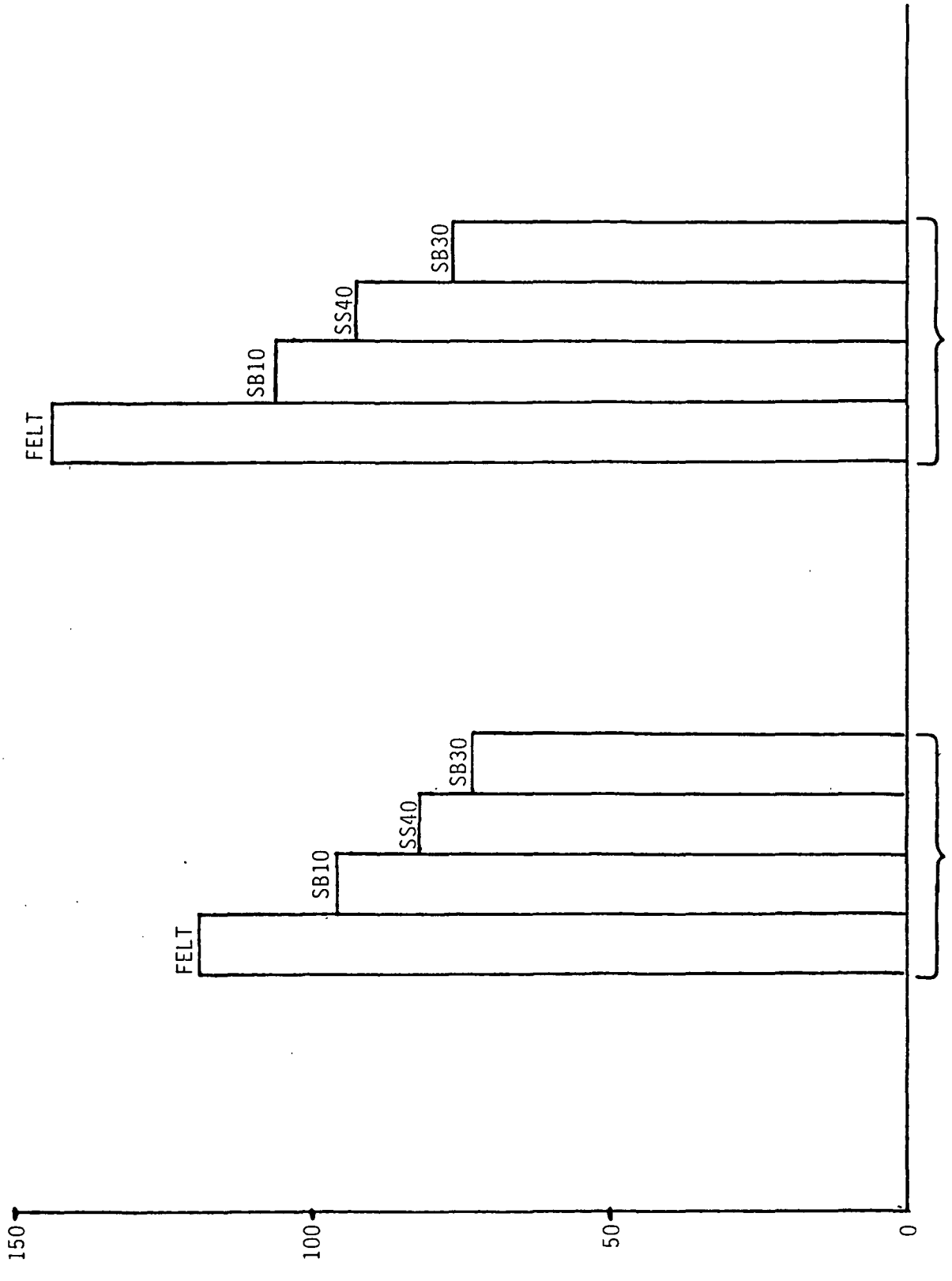

Figure 28. Effect of water receiver on water removal for 60 g/m^2 sheets of 700 CSF (once-dried) BSWK at 3.0 initial moisture ratio.

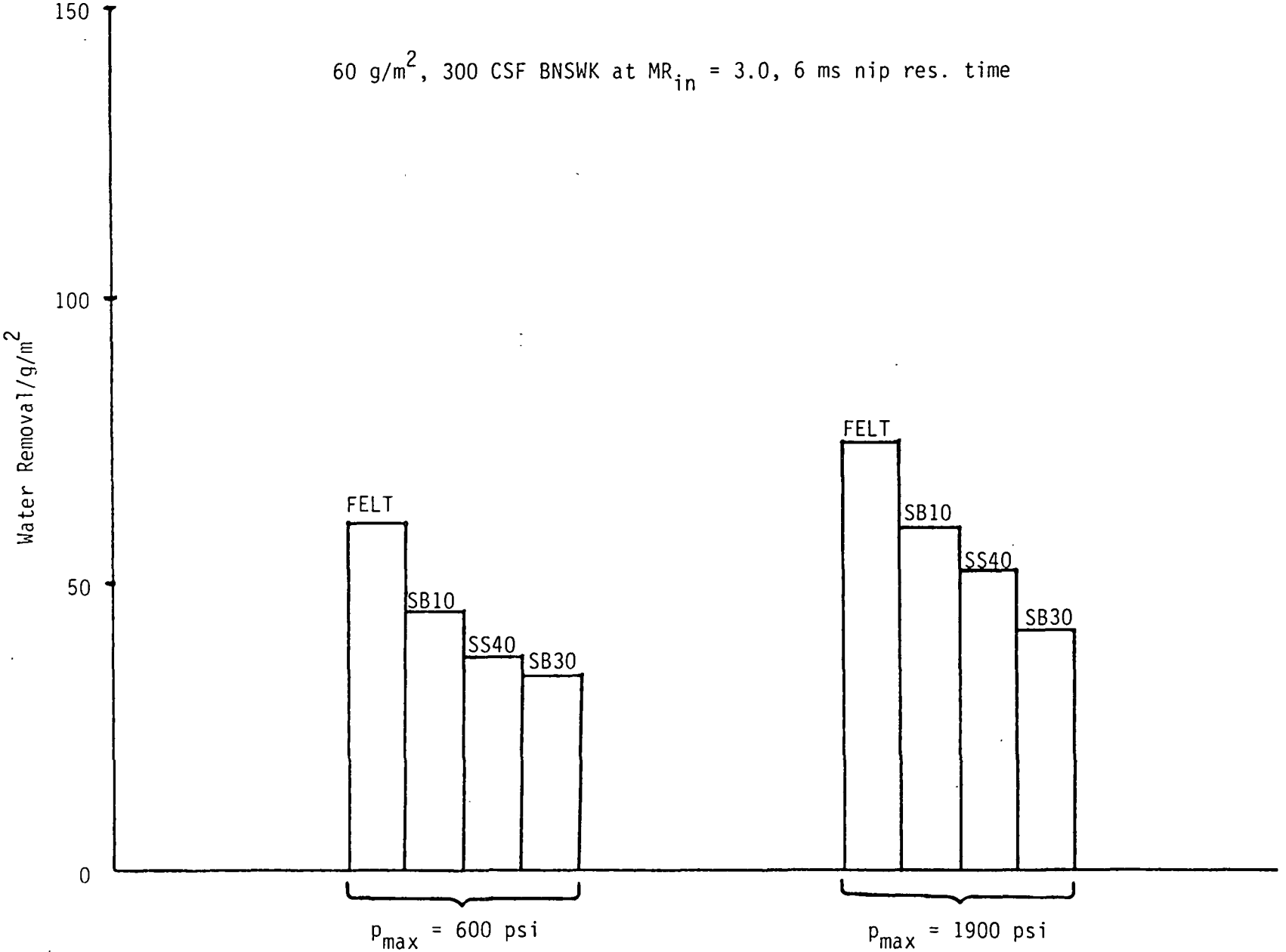

Figure 29. Effect of water receiver on water removal for 60 g/m^2 sheets of 300 CSF BNSWK at 3.0 initial moisture ratio.

removing water from low freeness pulps, the ordering is the same; the felt again has superior performance. In some similar tests at a higher basis weight (75 g/m^2), the SS40 plate showed slightly better performance than the SB10 plate, but still the felt was best.

With the availability of the electrohydraulic press system, it became possible to duplicate an operating condition (225 psi average pressure, 20 ms nip residence time) for which UMO water removal data were available over a range of basis weights, for both the felt and the SS40 plate as water receivers. Thus, a rather direct attempt at corroboration of the UMO data was possible. The results of recent IPC tests and the UMO data are compared in Fig. 30. With the exception of the data at basis weights of 75 and 100 g/m^2, which seem to be out of line, the IPC data follow the UMO (Beloit) pilot press data (based on felt as the water receiver) fairly closely. For the conditions represented in Fig. 30, the IPC measurements indicate that felt performance continues to exceed porous plate performance at low basis weight, while the two water receivers behave rather similarly at high basis weight.

To even more closely simulate conditions used in many of the UMO laboratory tests, some tests similar to those just described, but with a "square" compression pressure pulse rather than a haversine pulse, were performed with the SS40 plate as water receiver. The water removal levels resulting from these tests showed a similar trend with basis weight, but slightly lower magnitudes, as compared to those shown in Fig. 30.

Finally, a series of tests over a range of impulse values was conducted with each of several water receiver configurations, each unvented. Sheets with

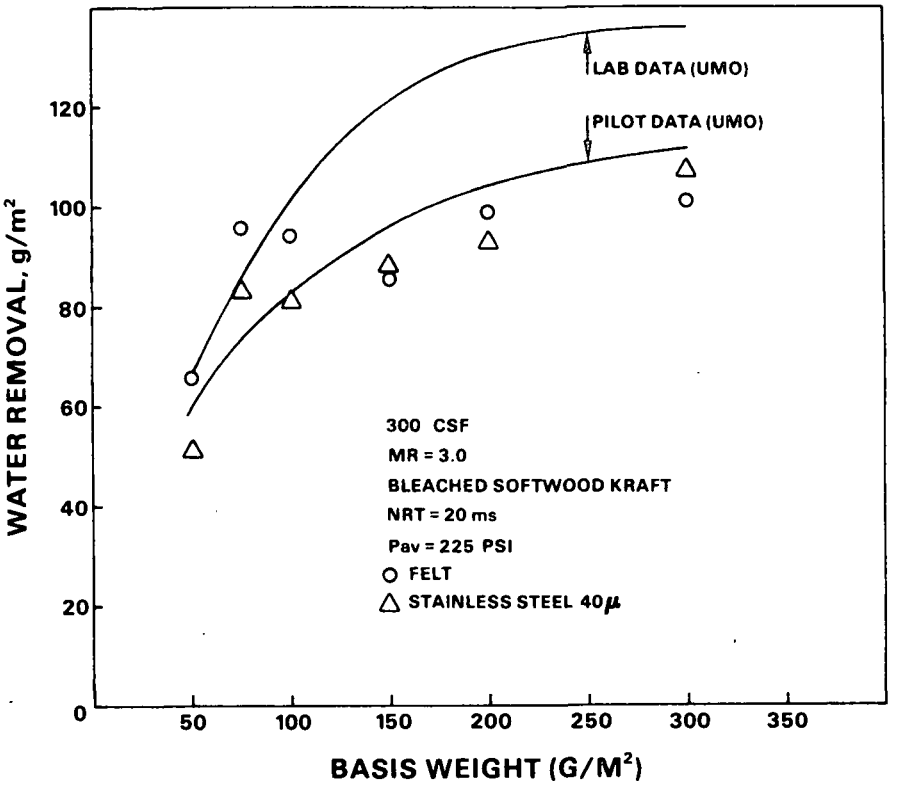

Figure 30. Comparison of data from the MTS system with results of the UMO study.

a basis weight of 245 g/m^2, made from a bleached sulphate softwood pulp, were used. A falling-weight press simulator, operating at nip residence times of 5-8 ms and pressures to about 1300 psi, was used for the tests. Results are shown in Fig. 31 for four sintered bronze plates with pore sizes of 10, 30, 40, and 90μ, for a felt alone, for a porous stainless steel plate with a pore size of about 40μ, and for the stainless steel plate backed by the felt. Ingoing moisture ratios were about 3.5.

These data show clearly that pressing with a felt removes more water than with any of the porous plate configurations. As previsouly noted and as expected, the smooth, smaller pore size plates do the best job, but none can compete with the felt.

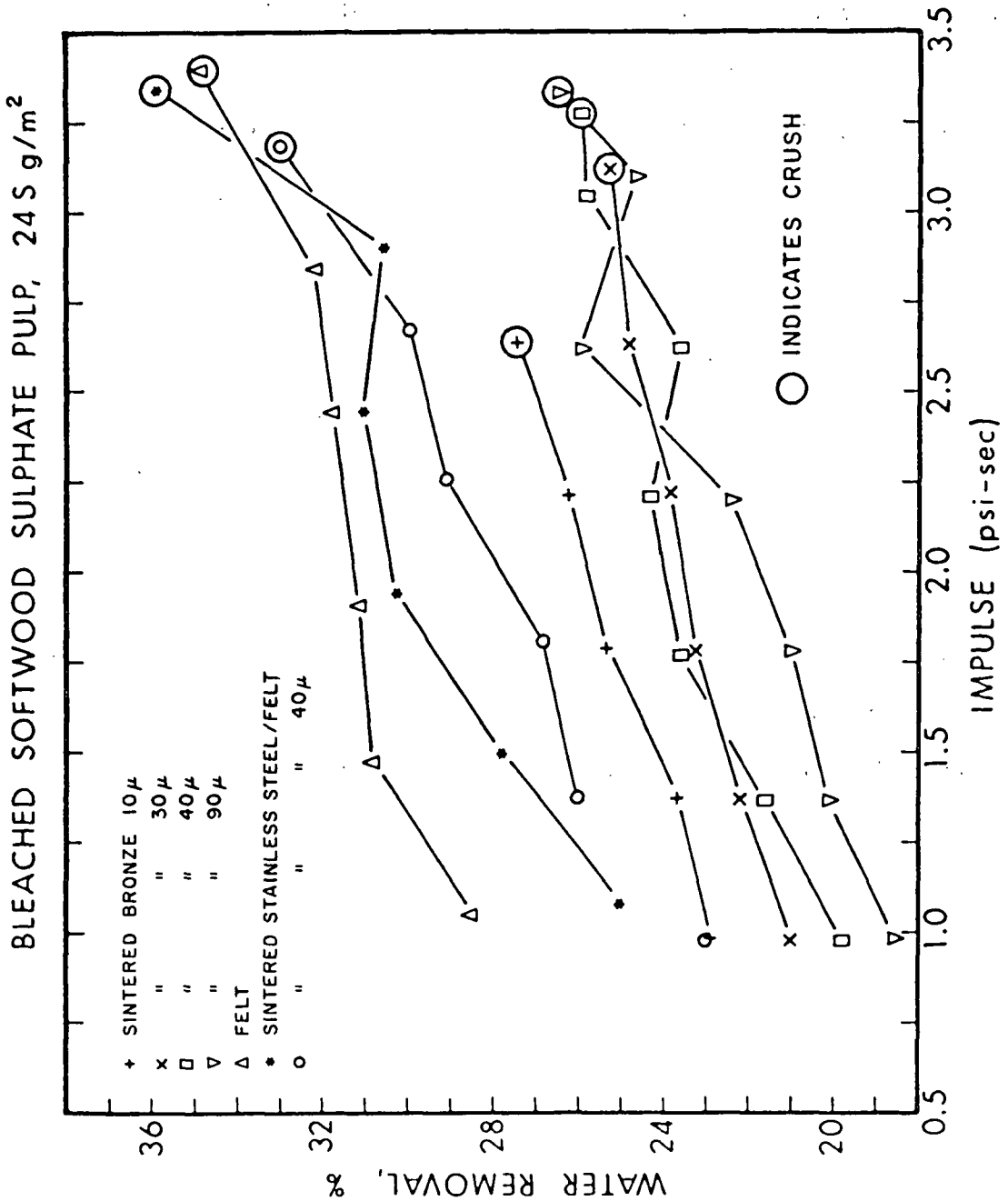

Figure 31. Water removal as a function of impulse for various water receivers.

Although more data are required to prove the point, the results presented above strongly suggest that porous plates are inferior to felts as pressing water receivers. Furthermore, porous plates tend to plug, to contaminate and to seriously peen under pressing impact. Thus, their practical use as replacements for felts in wet pressing seems highly unlikely. The data also show that porous plates are not responsible for the exceptionally high water removal levels attributed to the UMO press.

NIP EFFICIENCY

Failure of the UMO compression tester to produce results comparable to a real press has given rise to the use of a nip efficiency correction factor. Results presented in the previous section show that the differences between porous plates and felt tend to reduce water removal, rather than increase it. Hence, a basis for the correction factor must be sought elsewhere. While seeking to identify the factors that determine this correction was not part of the original scope of this project, it now appears as an important objective and will be pursued within the time and budget constraints of the project.

REFERENCES

1. Holden, G. R., U. S. pat. 3,284,285(Nov. 8, 1966).
2. Brundrett, E.; Baines, O., Tappi 49(3):97-101(1966).
3. Kawka, W.; Rogut, R., Przeglad Papierniczy 26(2):52-6(1970).
4. Kawka, W.; Ingielewicz, H., Przeglad Papierniczy 28(11):381-7(Nov., 1972).
5. Kawka, W., Przeglad Papierniczy 30(1):10-18(Jan., 1974).
6. Kawka, W.; Ingielewicz, H., Przeglad Papierniczy 34(2):53-8(Feb., 1978).
7. Kawka, W.; Ingielewicz, H.; Marek, I., Przeglad Papierniczy 34(3):82-7 (March, 1978).
8. Kawka, W.; Stepien, K., Przeglad Papierniczy 35(11):402-4(Nov., 1979).
9. Kawka, W.; Szwarcsztajn, E., EUCEPA-79 International Conf., London, May 21-24, 1979, Paper No. 31.
10. Kawka, W.; Przeglad Papierniczy 39(11/12):403-7(Nov.-Dec., 1983).
11. Ceckler, W. H., and Thompson, E. V., The University of Maine at Orono Wet Pressing Project, Final Report, DOE, August, 1982.
12. Arenander, S., and Wahren, D., Tappi 66(9):123-126(1983).
13. Chang, N., Nett, M., Beck, D., "A Comparison of a Wahren-Zotterman Press Simulator and a Pilot Press Nip", 70th Annual Meeting, Technical Section, Canadian Pulp & Paper Association Preprints.

THE INSTITUTE OF PAPER CHEMISTRY

Appleton, Wisconsin

Status Report

to the

ENGINEERING PROJECT ADVISORY COMMITTEE

Project 3479

HIGHER CONSISTENCY PROCESSING

September 11, 1985

PROJECT SUMMARY FORM

DATE: September 11, 1985

PROJECT NO.: 3479 - Higher Consistency Processing

PROJECT LEADER: T. E. Farrington

IPC GOAL:

Reduction of the complexity of screening, cleaning, and forming systems.

OBJECTIVE:

To identify or develop methods and principles for applying forces of controlled magnitude to various particles in 2-6% consistency slurries, so as to enable practical separation and forming processes to be carried out at these levels.

CURRENT FISCAL BUDGET: $130,000

SUMMARY OF RESULTS SINCE LAST REPORT: (April, 1985 - September, 1985)

Experiments with a single roll separator have continued with a new stock delivery system. A lightly refined softwood kraft furnish has been used to test the ability of the system to remove shives and fiber bundles. Test data for consistencies up to 2% have now been obtained; based on the results from these tests, a decision regarding testing at higher consistencies will be made.

While the objectives of this project remain constant, the approach is being carefully reviewed and some changes in direction or further activities are likely.

INTRODUCTION

The tendency of fibers to lock together in slurries and form coherent networks inhibits independent movement of fibers, shives, and contaminant particles in the unit operations of interest. The flocculating tendency of fibers has always been overcome by adding sufficient water to minimize fiber-fiber interactions. Unfortunately, this approach leads to tremendous capital and operating costs for the transport and removal of large amounts of water. It has long been a dream to be able to carry out these unit operations at higher consistencies, thereby drastically reducing equipment and system sizes, pumping costs, and the need for large water-removal equipment. There clearly seems to be a need for developing and implementing new principles of handling higher consistency (HC) stock.

Concepts which promise efficient HC fiber separation abound in the patent literature. For example, usable feed consistencies claimed for screens vary from the 2-5% range (1), up to 12% for an apparatus claimed to be useful for both screening and cleaning applications (2). These examples, like many others, are based on the use of rapidly moving bumps, ribs, bars, dimples, etc., to induce a fluidizing turbulence to the stock in the vicinity of the screening slots or holes. Drawbacks often encountered include a considerable dewatering of rejects (so that the accepted stock may not be such high consistency after all), and high energy requirements. Wahren (3) has noted that the power dissipation per unit volume required for fluidization of fiber networks increases with consistency to the 5.3 power: from 0.06 hp/gal at 1% consistency, to 20 hp/gal at 3%, to 11,000 hp/gal at 10%. Obviously then, to practically achieve really good turbulent fluidization at HC levels would require restricting power application to very small volumes.

A different method proposed for separating the components of slurries for HC screening, cleaning, and fractionating involves the use of a spray atomizer (4-6). This method combines the effects of surface tension and inertia, as particles in suspension on an atomizing wheel suddenly change direction at the wheel edge (6, 7). The optimum consistency range is stated as 3-6%. The failure of this concept to attain wide commercialization is apparently related to energy requirements, scale-up factors, and separation efficiencies.

In the area of HC forming, possibly the most significant work of recent years is that of Grundstrom et al. (8, 9). Their development of a HC (3-6%) former has been shown to be industrially feasible. However, in contrast to conventionally-formed sheets, these HC-formed sheets have a felted structure, due to considerable z-direction fiber orientation. This improves pressing and drying rates, and imparts improved compressive strength and Scott bond values. The reduction in MD and CD strength, however, is a serious drawback for most grades. Hence, the challenge of HC forming of sheets, with properties like those of conventionally-formed paper, remains. Control of fiber orientation is a major aspect of this challenge.

Our substantial knowledge of the behavior of HC fiber slurries and network structures, as applied to the unit operations of interest here, was summarized by Wahren (3). In the last ten years, and especially the last five years, little progress has been reported in developing new principles, or applying established principles, to acquiring practical technology for HC processing. Given the widely acknowledged need for such technology, perhaps we are facing a dearth of good ideas.

In light of these and other considerations, the present work is aimed at developing knowledge and principles which may be useful in practical HC technology development, particularly in the processes of forming and contaminant removal (screening and cleaning). Successful development of HC principles in these areas would seem to have especially high potential payback.

APPROACH

A number of alternative approaches, or directions of study, were considered and judged according to odds for favorable result, potential benefit, ease of study, and uniqueness and aptness as a potential IPC contribution. Among several possible means for minimizing the influence of interfiber interactions, one potentially effective and energy-efficient concept is most intriguing. It involves physically separating fibers prior to the application of forces which would effect fiber orientation and/or contaminant separation. Potential practical means of getting some distance between particles in a well-dispersed slurry include (1) spraying, and (2) spreading the slurry into a film thin enough that particles would contact each other in relatively few places. Fiber orienting and separating forces could then be applied to such a film, with much less effect of network forces.

Accordingly, an apparatus embodying the thin film principle was designed to study fiber orientation and particle separation in such films (Fig. 1). A well-dispersed slurry film is made to move down a stationary apron and then contact a rapidly moving roll surface. As illustrated in Fig. 2, the acceleration and shear at that point are expected to cause substantial fiber orientation in the film, thereby minimizing the number of interfiber contact points. Due to centrifugal force, particles of certain characteristics would be

SINGLE ROLL WITH AIR DOCTOR

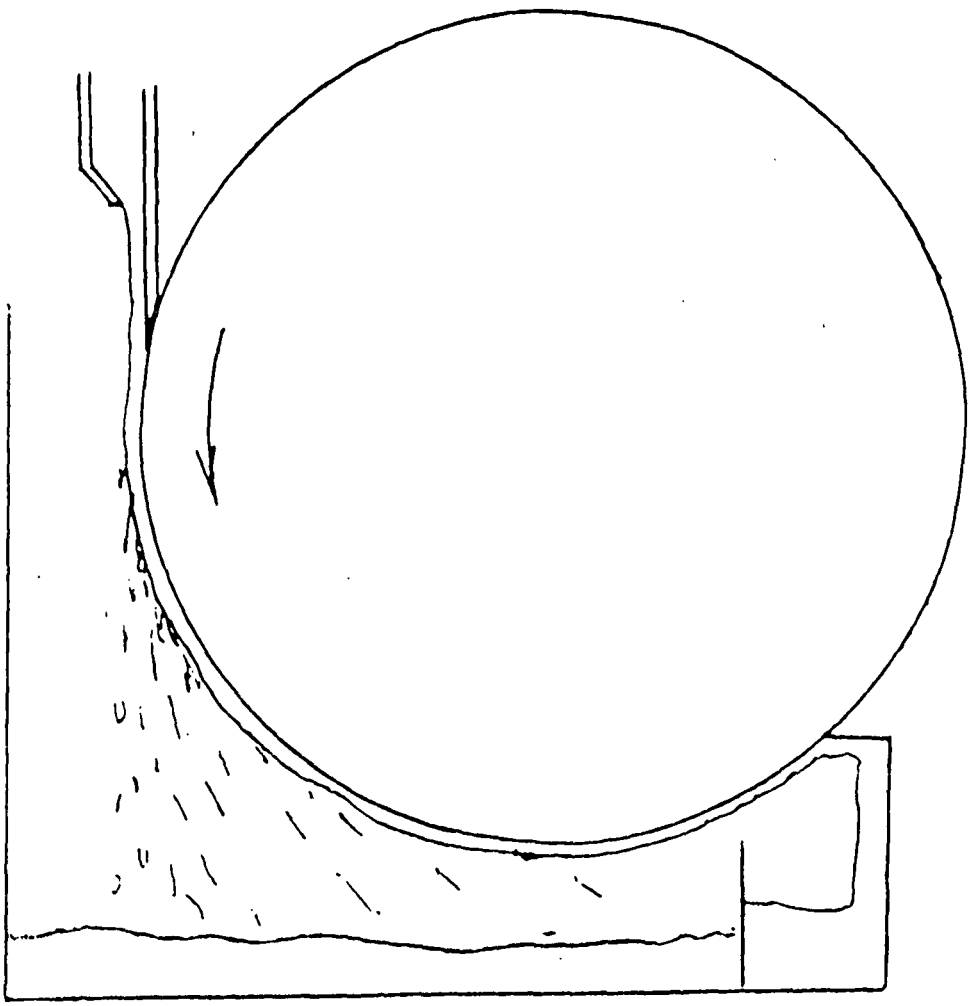

Figure 1. Concept for applying film of slurry to a blade and then to a moving roll.

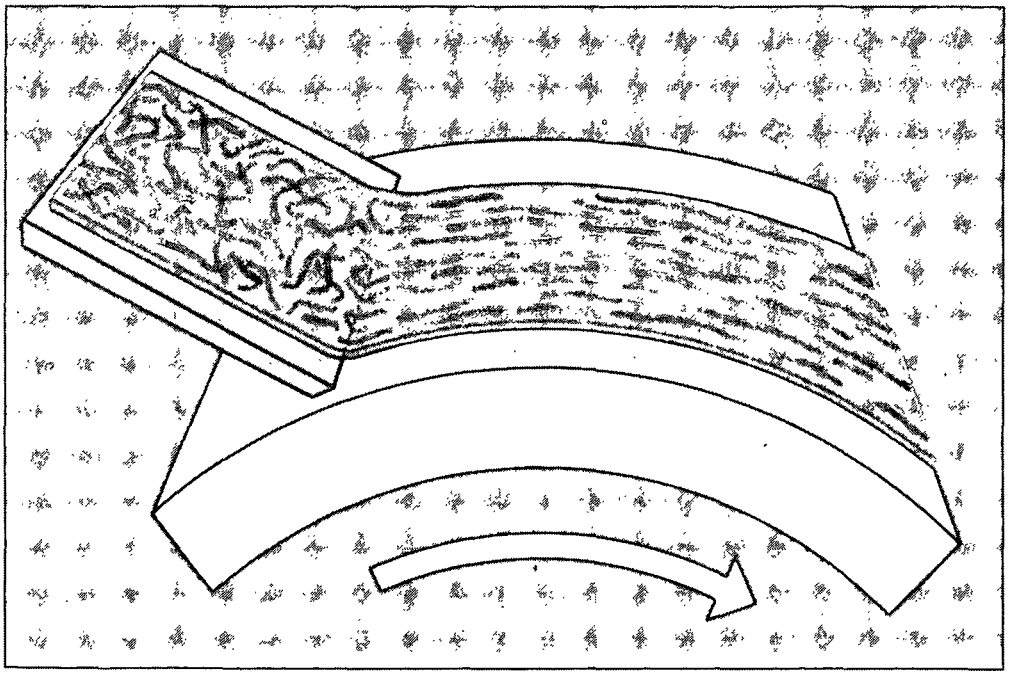

Figure 2. Means for employing shear and acceleration to fiber slurry films, illustrating anticipated fiber orientation effect.

thrown free of the film on the roll (Fig. 3), while particles with other characteristics would remain in the film, so they could be removed from the roll and collected.

In order to establish design and operating conditions whereby separations of interest might occur, the assumption was made that only two major forces are exerted on the particle in the film: centrifugal and surface tension. Hence, a balance of force/unit mass on a particle of length ℓ, width w, and thickness t, yields the expression in Fig. 4, where v is particle velocity, R the roll radius, γ the surface tension, θ the contact angle, and ρ the particle density. If μ is the particle coarseness, then the right-hand term becomes $\cos \theta/\mu$. Using a roll of 24.6 cm diameter, the substitution of other appropriate numerical quantities yields the values in Table 1 for wood particles. This predicts that a shive with a size near the 6-cut screen slot width would be ejected when it attained a speed of about 2500 cm/s. Given the coarseness of a typical "acceptable" softwood fiber, however, one would predict an order-of-magnitude higher rejection velocity (25,000 cm/s for a fiber of 15 micron thickness), or a centrifugal force per unit mass of 100 times that of the 6-cut shive. Hence, it should be possible to realize very efficient separation of

Table 1. Predicted size of ejected wood particles as a function of speed.

Particle Velocity		Centrifugal force per unit mass,	$\sqrt{wt}$	
cm/s	ft/min	N/g	cm	in.
500	984	0.20	0.075	0.029
1500	2954	1.83	0.025	0.010
2500	4923	5.08	0.015	0.006
3500	6892	9.96	0.011	0.004
25000	49225	50.0	0.0015	0.0006

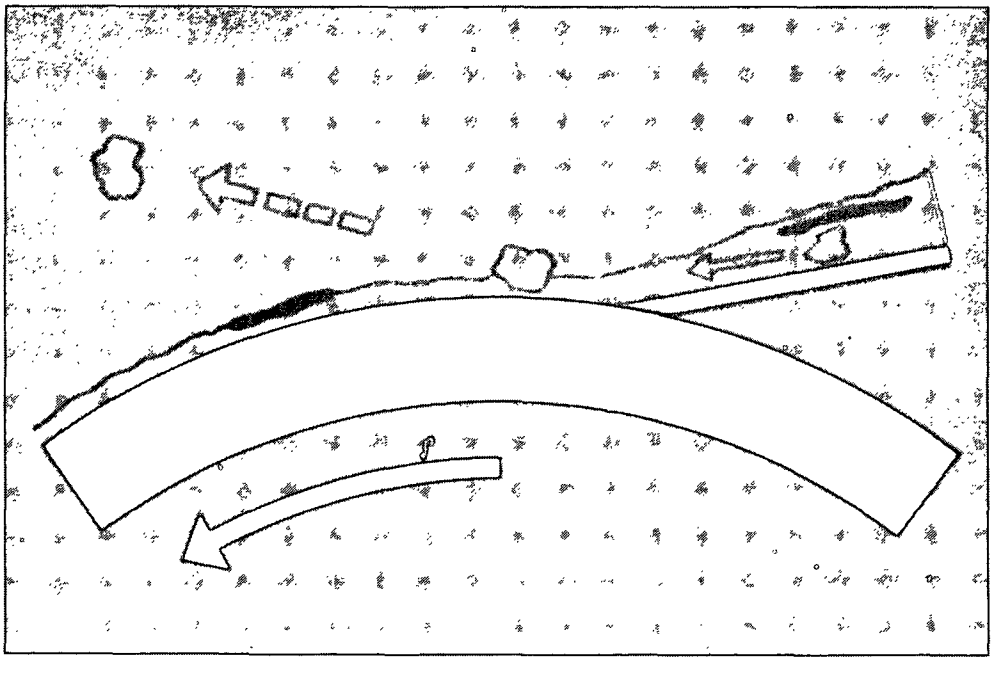

Figure 3. Illustration of particle separation from slurry film on moving roll surface.

$$\frac{v^2}{2\gamma R} = \frac{\cos\theta}{\rho w t}$$

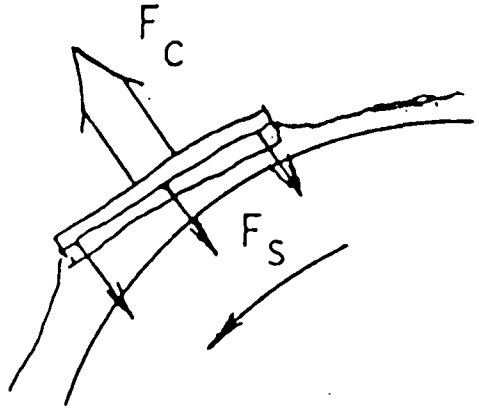

Figure 4. Theoretical basis of separation.

such shives or large, dense dirt particles from pulp fibers. However, this approach would not necessarily be useful for good separation of different types of pulp fiber from each other. At reasonably low levels of centrifugal force and velocity, all normal single pulp fibers should be retained in the film surface.

The dependence on contact angle also indicates an effective novel method for removing "stickies" from pulp. The values in Table 1 were obtained by assuming a contact angle of 30° for wood pulp fibers (10). The contact angles for water-wetted surfaces of paraffin, polethylene, and other typical polymeric components of stickies are usually well over 70° and often over 90° (11, 12). Hence, the surface tension force retaining such particles is much less than that of the more wettable pulp fibers, so that even less dense sticky particles should be easily ejected.

It should be pointed out that the basis for particle separation envisioned here is quite different from that established to be operating in the atomizing spray fractionator mentioned above (4-7, 10). Both approaches employ surface tension as the force restraining particle escape from the surface of a film. The atomizer, however, employs a combination of centrifugal and inertial forces to eject particles from the film as it turns the sharp corner at the disc shoulder (Fig. 5). With that geometry, no separation occurs unless the liquid film makes an abrupt turn and runs over a wettable lip of the proper length and angle. Centrifugal force imparts momentum to the particles before reaching the lip, and it assists in detachment after the corner is turned. However, inertial force resulting from the change in direction appears to be primarily responsible for separation: if the corner is rounded rather than sharp, allowing a gradual change in direction of film flow, then no separation occurs (7). The atomizer

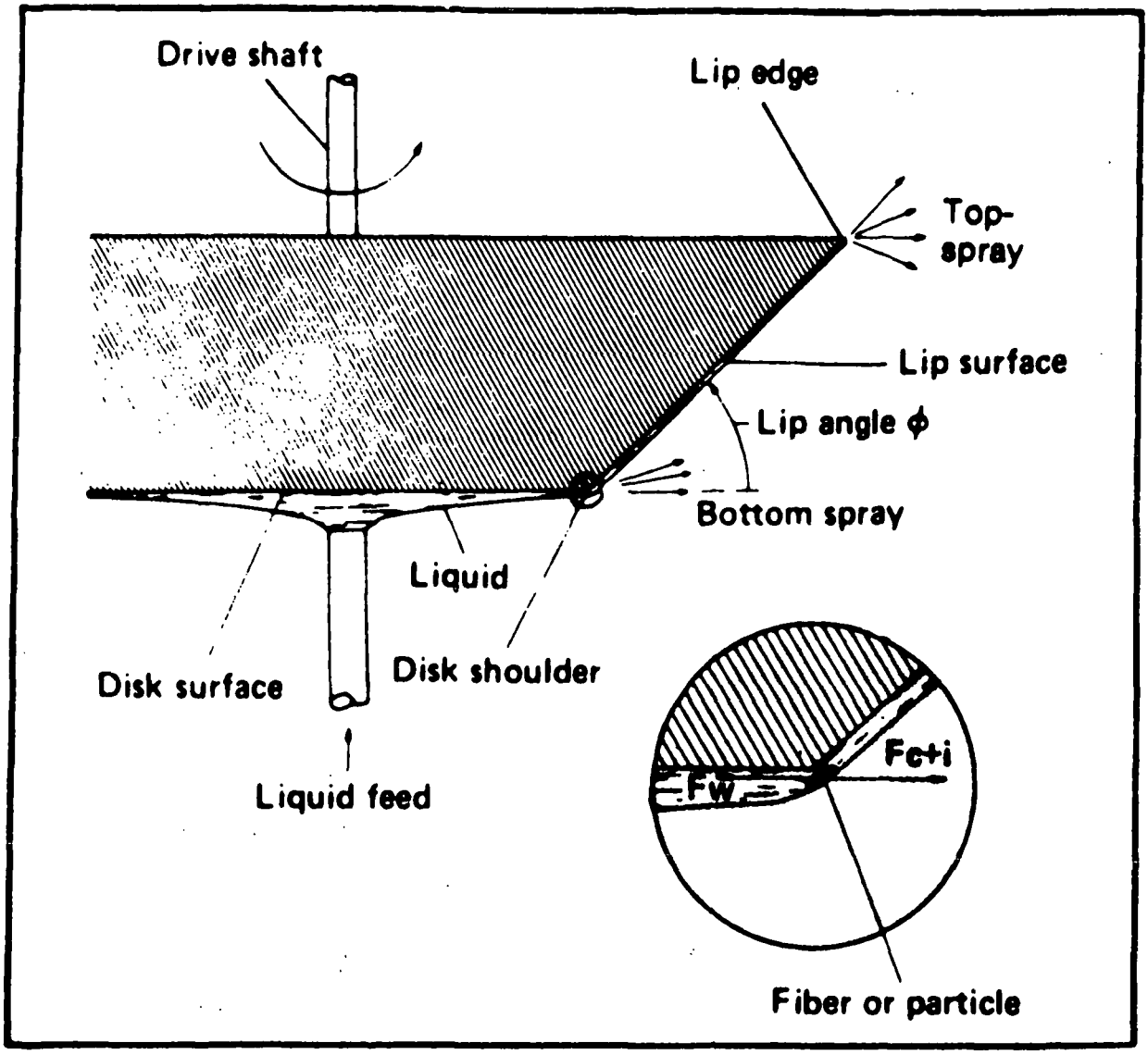

Figure 5. Particle separation from a spinning disc. From Klungness et al. (10).

typically requires much higher levels of centrifugal force to impart that momentum than envisioned here. The geometry of the present concept would apply lower levels of centrifugal force, but for periods of time sufficient to overcome surface tension forces on rejectable particles.

Of course, the objective of this work is not merely to develop a piece of equipment, but rather an understanding of HC fundamentals in such a system, as relevant to both separation and forming. In order to do this, the following steps were planned:

1. Build a laboratory model, and establish if separation occurs as predicted by the theory, and establish conditions and limitations for practical separations to be carried out.
2. Conduct a phenomenological study, using photographic and other techniques, to establish the effects of shear and acceleration of particles in a slurry film on fiber orientation and flocculation/deflocculation, with an eye to application of the principle to the wet end of a HC former.
3. Identify and investigate bottlenecks to operating at higher consistencies, including the nature of the feed dispersion.

The following section describes activity in the first area, and the beginnings of effort in the second.

RESULTS AND DISCUSSION

APPARATUS AND ITS OPERATION

A chrome-plated 24.6 cm diameter roll, as illustrated in Fig. 1, is cantilevered and connected via pulleys to a 10 HP variable speed drive. The system is theoretically capable of attaining roll surface speeds of about 5000 cm/s (nearly 4000 rpm). For most of the work to date, the pulp slurry was

applied to the stationary apron through a spray nozzle, arranged so that a uniform film was distributed to about a 4-inch width before contacting the moving roll. Flow rates were typically in the range of 1-2 gallons/min. It is essential that the apron contact the roll in such a way as to disrupt the boundary layer of air which follows the roll. Any air which passes between the apron and the roll destabilizes and disrupts the film on the roll.

Depicted in Fig. 6 is the apparatus running water only. The white apron can be seen near the top center of the photograph, receiving flow from the nozzle (obscured by the upper beam), and distributing the water film to the moving roll. Virtually all the flow adheres to the roll, and is doctored off into the last chamber, from which it is collected. The doctor blade is connected to an oscillating mechanism (right center of photo), to prevent fiber hang-up on the blade edge which would prevent complete removal of the film. The collection chambers have recently been modified so that the separation of "accepts" and "rejects" (the reject rate) can be infinitely variable, at nearly any physical location between the apron and the doctor blade.

Figures 7, 8, and 9 illustrate the operation of the apparatus when running a 50:50 mixture of TMP and kraft pulps. Several features described above can be better seen here. The coarsest shives and fiber bundles are collected in the left-most chambers, while clean fibers are doctored off into the last chamber. The very coarsest material, which is shown in chambers 2 and 3 in the photos, comes off the roll in a relatively dewatered state. It consists of both kraft shives, and shives and chop from the TMP.

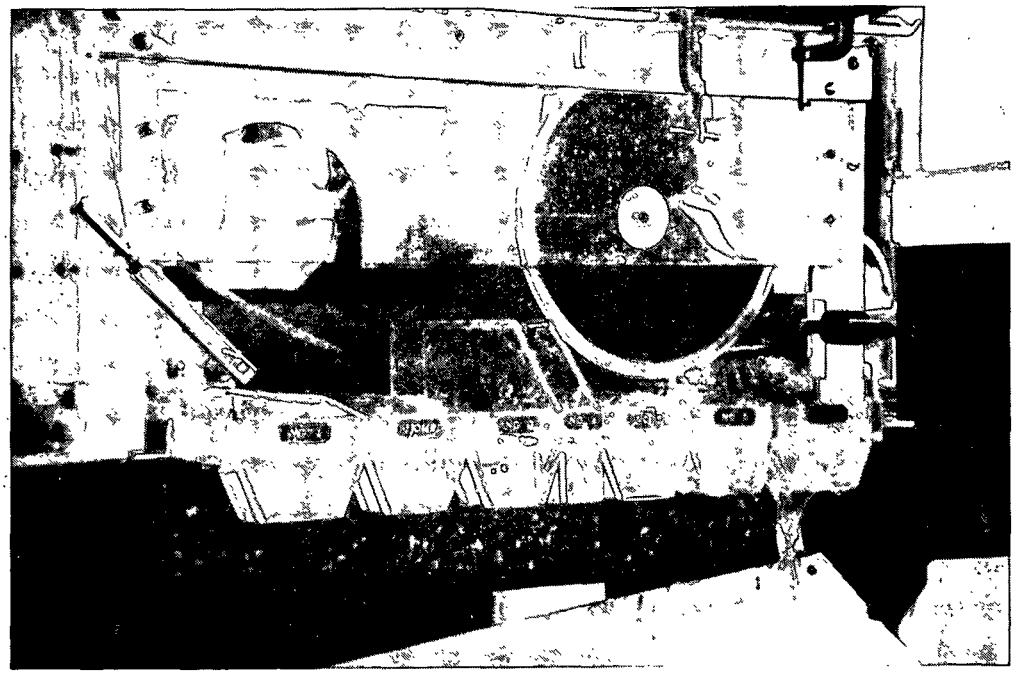

Figure 6. Roll separator operating on water only.

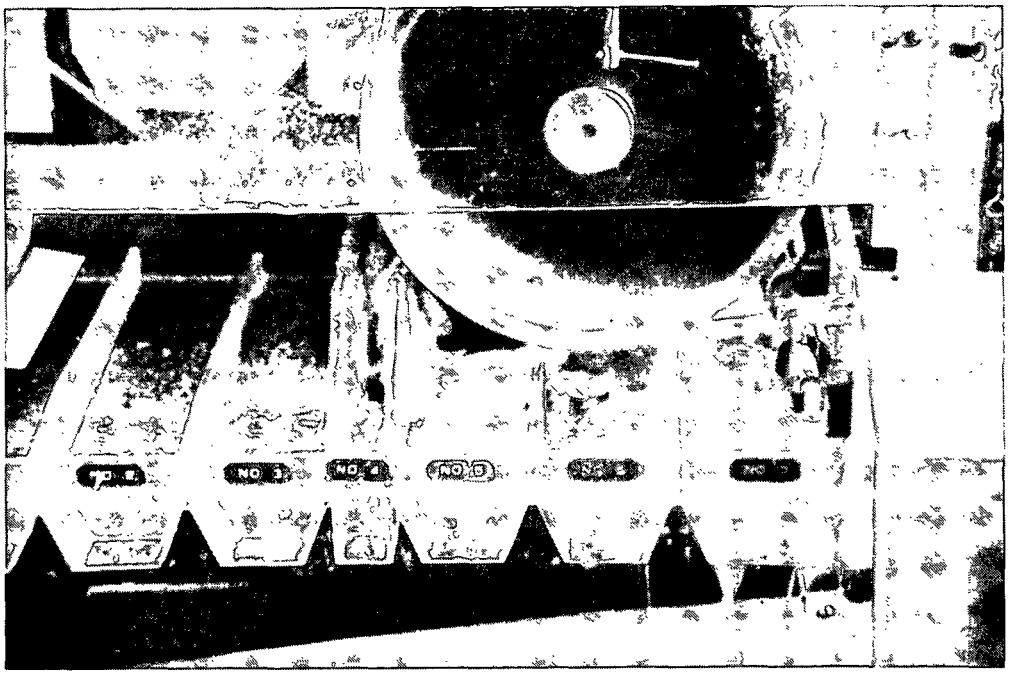

Figure 7. Roll separator operating on 50:50 TMP/kraft pulp.

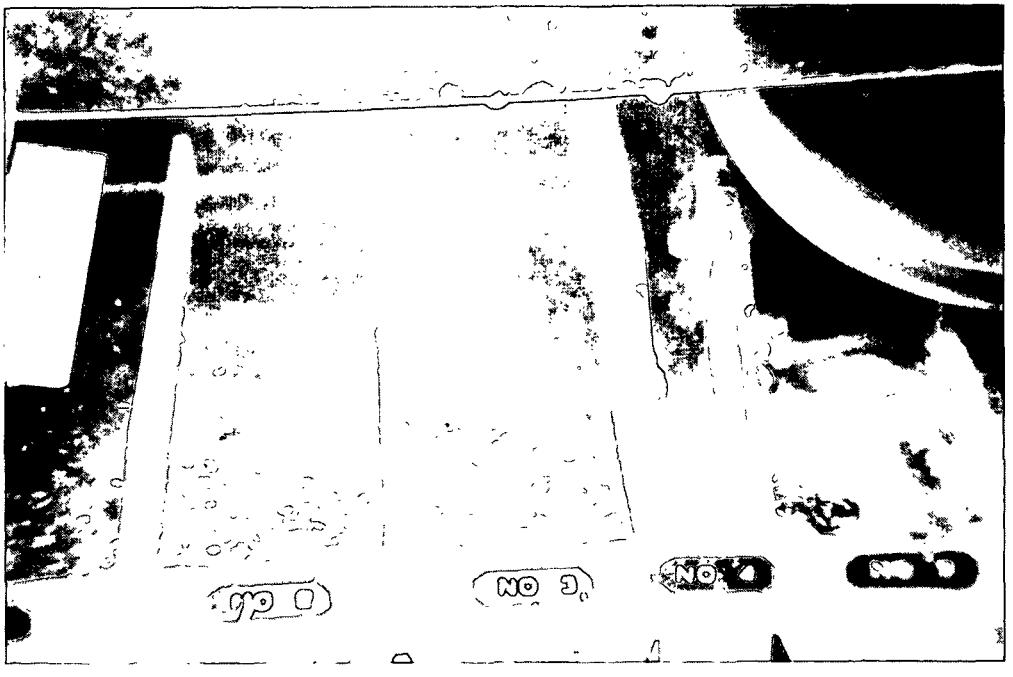

Figure 8. Rejected material from 50:50 TMP/kraft pulp.

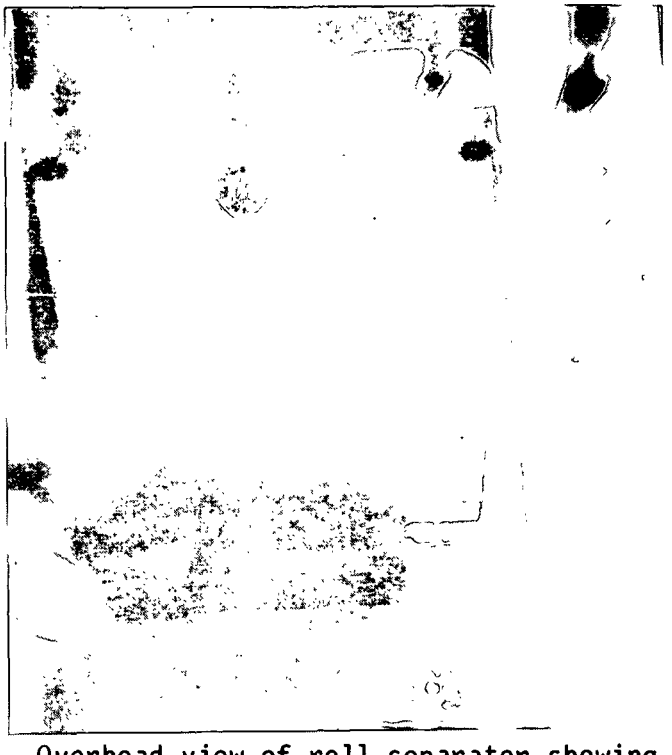

Figure 9. Overhead view of roll separator showing nozzle, apron, the pulp film, and reject chambers.

EFFICIENCY OF SHIVE REMOVAL

Figure 10 shows the efficiency of removal of shives from the TMP-kraft mixture, as a function of several parameters. Shive content is determined by screening on a 6-cut (0.006-inch slotted) flat screen. Removal efficiency is the percentage of shives in the feed which are removed on the apparatus. The speed effect is consistent with the theory outlined above: 6-cut shives are much more efficiently removed at speeds above 5000 fpm. There was a substantial difference between 3000 and 5000 fpm, while going beyond, to 7000 fpm, approached complete removal with little effect on reject rate (loss of good fiber). At the highest speed, efficient separation was seen even at low reject rates.

The consistency effect at a given reject rate is greater at low speeds than at higher speeds. For example, at 20% reject rate, doubling the consistency dropped the efficiency from 80 to 65% at 3000 fpm (Fig. 10). At 7000 fpm, however, that consistency change only dropped efficiency from 98 to about 96%. At a given set of operating conditions, using the same reject chamber locations, doubling the consistency tended to increase both the reject rate and the efficiency. Apparently the higher consistency did not inhibit the escape of rejectable material, but it increased the loss of good fiber along with shives. The good fiber may have been taken off with individual shives, or as flocculated entities separate from shives.

EFFICIENCY OF STICKIES REMOVAL

A quantity of kraft wrapping paper stock was slushed and defibered in a large beater, and processed on the roll separator at 1.2% consistency. The 6-cut rejects content of the feed in this base-line experiment, ca. 0.05%, was

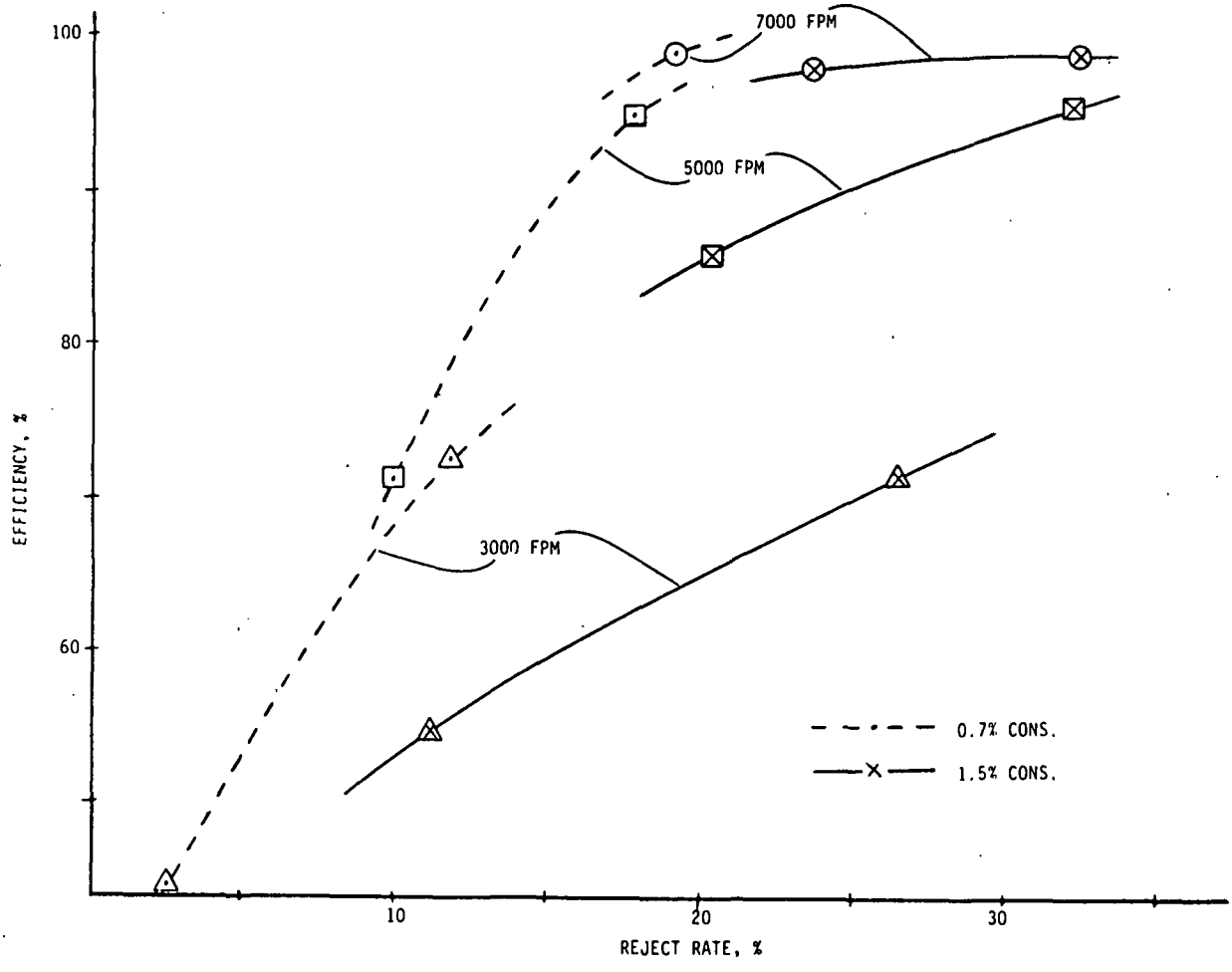

Figure 10. Efficiency of removal of 6-cut shives from 50:50 TMP/kraft mixture, as function of reject rate, roll speed, and consistency.

reduced to 0.01% in the accepts at 5000 fpm speed and 7% reject rate, and to less than 0.002% at 7000 fpm and 14% reject rate. A quantity of "stickies" was obtained in the form of adhesive applied to 15 x 24-inch sheets of paper. Pieces of this material were applied to pieces of the kraft wrapping paper, then processed in a Waring Blendor until completely dispersed. A quantity of the dispersed stickies was then added to the feed tank containing the kraft wrapping

paper stock. Separation results are given in Table 1. Although most of the stickies were retained on a 6-cut screen, a 6.5-hour toluene extraction was used as an additional analytical determination for stickies. The results indicate excellent separation of larger sticky particles (6-cut rejects), and good separation of even the smaller ones, as shown by the extraction method.

Table 1. Roll separation of stickies from kraft wrapping paper stock.

Feed: 1.29% cons.; 0.59% 6-cut rejects; 0.66% toluene extr.

Roll Speed, ft/min	Reject Rate, %	Percent Removal Efficiency	
		6-cut rejects	Stickies by extn.
3000	5.6	82.9	73.9
	11.6	97.1	78.3
5000	8.0	98.4	75.9
	20.4	99.7	92.6
7000	16.0	98.7	86.0
	25.6	98.5	92.0

PHOTOGRAPIC WORK

Attempts at high-speed, still photography were made, using 3000 ASA film in a Nikon camera equipped with a Polaroid attachment and a strobe of 2 μs duration. A low magnification shot at the slurry film on the early portion of the roll is shown in Fig. 11. The film on the apron is shown at the upper right; the blurry image at the upper left is a reflection on the Plexiglas at the edge of the roll. Two noteworthy aspects of the photograph are the ring-type instabilities, which are evident immediately after the film hits the roll, and the trajectory of escaping particles in the lower left.

Figure 12 shows a good dispersion of fibers at 1.5% consistency on the apron. The large black line is a focusing mark. These bleached kraft fibers,

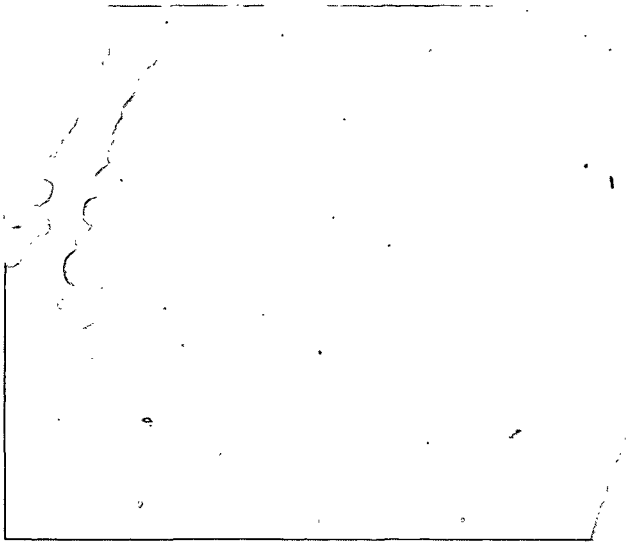

Figure 11. Slurry film on early portion of roll.

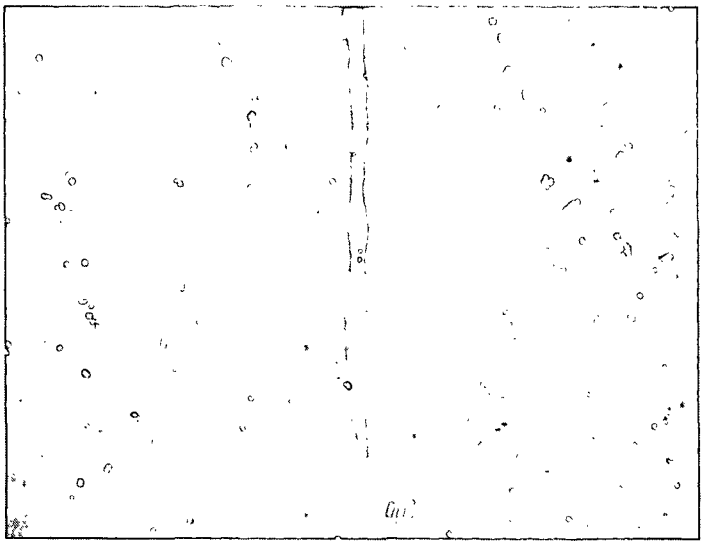

Figure 12. Dyed fibers on apron leading to roll (3X).

which have been dyed with Chlorazol Black E, are easily seen against the white plastic apron. Unfortunately, neither dyed nor undyed fibers have been successfully photographed on the moving roll to date. The poor contrast with the chromed surface, and the presence of ripples on the film surface, make the visualization of fibers very difficult. Future options to be considered include applying a white coating to the roll, or if necessary, utilizing a transparent roll or a window in the roll.

Figure 12 was taken at approximately 3X magnification. Because of the short focal length of the lenses used, the proximity of the camera to the roll made lens splattering a continual problem. New lenses will enable us to obtain the proper magnification at a 1-2 foot distance from the roll.

Attempts to take double exposure photographs of the fibers on the apron, as a means of determining fiber velocity, were unsuccessful. Two strobe units were fired through an electronic unit which allowed controllable duration between flashes. Apparently the portions of the film unexposed in the first flash are exposed sufficiently in the second flash, so that no fibers are visible in the photo. It appears that velocity measurements will have to be carried out with high-speed motion picture equipment rather than still photography. This will also allow more particles of interest to be captured on film - the probability of seeing a shive in a given single shot is low.

CONCLUSIONS

By applying centrifugal force to a slurry film, it is possible to obtain separation of particles of certain characteristics. That is, the roll separator apparatus is indeed a laboratory system wherein separation can be

carried out according to a new principle which holds promise for higher consistency application.

The results obtained to date are consistent with the hypothesized mechanism; at consistencies employed thus far, it appears that centrifugal and surface tension forces are the only significant separating forces. The conditions (speed, etc.) at which particles of a given size are ejected are consistent with a force balance which considers only those two forces.

In addition to providing a means for studying a new separation principle, the laboratory system also permits the investigation of HC phenomena and fundamentals in thin films, with possible application to forming processes.

FUTURE WORK

Near-term plans include completion of an experimental matrix for studying practical separation of shives from pulp slurries. Various flow and reject rates are being studied in the surface speed range of 5000 to 9000 ft/min. Consistencies will be evaluated as high as practicable over 2%, with some experimentation with simple flow dispersion techniques in the feed nozzle area.

Preliminary experimentation with the separation of colored nylon filament (cut fish line) from bleached kraft fiber indicated the possibility of operating at speeds where the filament just begins to separate. Hence, experimental work is under way to test the model equation for separation, using these easily characterized filaments. It is specifically designed to confirm or refute the predicted dependence on particle coarseness and velocity and the independence of fiber length.

Planned photographic work aims to:

- improve particle visualization with white coating of the roll or other techniques
- perfect the lens system to get reasonable focal length (distance from the spray), yet with adequate magnification
- investigate high-speed filming techniques for indications of fiber orientation and flocculation/deflocculation behavior on the roll and quantification of particle velocity in the slurry film

It is expected that the photographic visualization will be a useful tool to study the effectiveness of dispersion techniques at high consistencies. The application of photographic methods with this apparatus does indeed appear to hold promise for providing insight into fundamental effects of shear and acceleration on HC slurry films. It is hoped that the basic knowledge gained will have useful application to HC particle separation and/or sheet forming.

REFERENCES

1. Seifert, P. Directionally biased slotted screening system with rotational velocity generator. U. S. pat. 3,849,302; Can. pat. 974,936(Aug. 22, 1973).
2. Gullichsen, J. E. Method and apparatus for treating fibrous suspensions. Can. pat. 1,102,604(June 9, 1981).
3. Wahren, D. Fiber network structures in papermaking operations. Proc. Conf. Paper Science and Technol. - The Cutting Edge. The Institute of Paper Chemistry, Appleton, WI, May 8-10, 1979.
4. Moller, K.; Duffy, G. G.; Moller, J. T.; Foghmar, P. High-consistency of pulp fractionation with an atomizer. Tappi 63(9):89-91(1980).
5. Duffy, G. G.; Pedersen, M. L.; Petersen, J. H. Efficient fiber separation at high consistency by spray atomization. Presented at Appita Annual Meeting, Rotorua, N.Z., April 6-10, 1981.

6. Crosby, E. J.; Oroskar, A. R. Method and apparatus for spray fractionation of particles in liquid suspension. U. S. pat. 4,427,541(Jan. 24, 1984).

7. Oroskar, A. R. Spray Fractionation. Doctoral Dissertation. Madison, WI, University of Wisconsin, 1981.

8. Grundstrom, K.-J.; Norman, B.; Wahren, D. High-consistency forming of paper. Tappi 56(7):81-4(1973).

9. Grundstrom, K.-J.; Meinander, P. O.; Norman, B.; Reiner, L.; Waris, J. A high-consistency former. Tappi 59(3):58-61(1976).

10. Klungness, J. H.; Oroskar, A. R.; Crosby, E. J. Fiber separation with a vaneless spinning disc: Application. Tappi J. 67(6):78-81(1984).

11. Miller, B. Surface Characteristics of Fibers and Textiles. Part II. M. J. Schick, ed., Marcel-Dekker, Inc., New York, 1977, p. 436-7.

12. Valko, E. I. Chemical After-Treatments of Textiles. N. S. Wooding and S. M. Atles, eds., Wiley-Interscience, New York, 1971, p. 89.

THE INSTITUTE OF PAPER CHEMISTRY

Appleton, Wisconsin

Status Report

to the

ENGINEERING PROJECT ADVISORY COMMITTEE

Project 3470

FUNDAMENTALS OF DRYING

September 11, 1985

PROJECT SUMMARY FORM

DATE: September 11, 1985

PROJECT NO.: 3470 - Fundamentals of Drying

PROJECT LEADER: H. P. Lavery

IPC GOAL:

Reduction of the "necessary minimum" complexity (number and/or sophistication) of process steps.

OBJECTIVE:

To develop an understanding and a data base sufficient to support commercialization of advanced water removal systems, impulse drying in particular.

CURRENT FISCAL BUDGET: $150,000

SUMMARY OF RESULTS SINCE LAST REPORT: (April, 1985 - September, 1985)

Plans and procedures for conducting a broad technical performance evaluation of impulse drying have been developed. An initial series of screening experiments on 8 or 9 grades is nearly complete. Empirical relationships to describe water removal and densification as a function of impulse drying conditions have been worked out for these grades. Strength, surface and optical properties have also been measured. These data all show the extremely high water removal rates and the significant degree of densification afforded by impulse drying. Dramatic increases in smoothness and decreases in porosity, permeability and liquid penetration have all been shown. Finally, brightness and opacity are decreased slightly by impulse drying.

Two major reports have been completed and a DOE grant for $1.5 million has been received.

I. INTRODUCTION

The Papermaking Processes Group at The Institute of Paper Chemistry is continuing its investigation of high-intensity drying processes as alternatives or adjuncts to conventional or can drying. Most of the early work was devoted to exploratory and feasibility studies of three drying processes; drying at significantly higher pressure and temperature than normally used, drying under thermally induced vacuum conditions and impulse drying. The results of these early investigations are fully documented in Progress Report One for Project 3470, which is being published and will be distributed shortly. In Report One, it is concluded that impulse drying holds the greatest potential for a significant contribution to the pulp and paper industry. Accordingly, all project activities are now focused primarily on impulse drying with very modest continuing attention to thermal-vacuum drying. This report will document all of the recent progress with impulse drying.

IMPULSE DRYING

A precise and fully satisfactory definition of impulse drying is yet to be devised. Two concepts are important, however. First, in impulse drying, the moist paper or board web is subjected to pressures and temperatures much above those normally used, but for very short exposure times. Longer exposure times are virtually impossible to generate in practical equipment and could lead to damage of the web from overdrying. Second, the transport and densification mechanisms at work in impulse drying are very different from those in conventional drying. All of these issues are discussed fully in Report One.

The nature and intensity of the transport processes lead to several advantages for impulse drying, including:

1. Drying rates 2 to 3 orders of magnitude greater than in conventional drying. Much smaller dryers and lower capital costs should result.
2. A significant component of liquid dewatering which may reduce energy consumption to about half that of a conventional dryer.
3. Large and controllable levels of additional sheet densification. Density levels above 1.0 gr/cc have been easily achieved.
4. An I-beam type of density distribution which leads to dense, stiff outer layers and a bulkier middle layer. This may have an advantage in several grades.
5. Significant improvements in some surface properties including smoothness, pick resistance, air permeability, and water and ink penetration.
6. A potential for achieving required product properties from lower cost furnishes and processing.

Many of these performance characteristics will be explored more fully in subsequent sections of this report.

PROJECT PLAN

The basic objective of this project is to provide the data base necessary to encourage and support commercial implementation of the impulse drying process. Figure 1 is a project flowchart showing the basic steps necessary to achieve this goal and the interactions among them. Most of the exploratory and feasibility work has been completed and is documented in Progress Report One[1]. Considerable progress has also been made on step 2, investigation of the fundamental physical phenomena involved in the process,

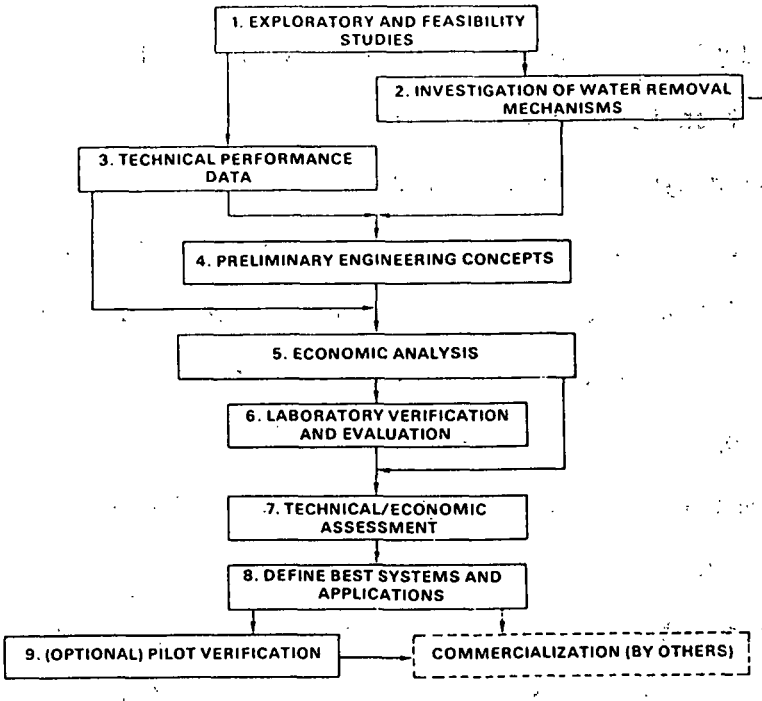

Figure 1. Project plan flowsheet.

mostly by students. In a recently completed Ph.D. thesis[2], Joe Pounder developed a model to describe some of the transport processes that occur in impulse drying. Chris Devlin is nearing completion of an experimental study to identify the water removal mechanisms in high-intensity drying. In his experiments, the sheets are exposed to the intense conditions long enough to produce complete drying. Steve Burton is investigating the dynamics of sheet density and property development. When completed in 1986, Steve's work is likely to produce good quantitative descriptions of both the transport and densification processes.

Most of the recent work in the Institute's dues funded research program has been devoted to the technical performance evaluation of step 3. Some preliminary work on step 4 has been completed; more will be undertaken as step 3 progresses.

II. TECHNICAL PERFORMANCE EVALUATION PLANS AND PROCEDURES

Impulse drying may be better suited, technically and economically, for some paper grades than for others. To more completely characterize the performance of this drying system and to determine the most attractive applications, bench-scale tests covering a representative range of paper grades, furnishes, and operating conditions are being conducted. A significantly expanded data base, compared to that developed during the completed exploratory work, covering drying rates, energy consumption, paper properties, etc., will be the primary result of this comprehensive test program. These technical data will be used to establish system configurations (i.e., hardware requirements, size estimates, heat source options, etc.) and operating conditions appropriate for the various paper and board grades being considered. Economic analyses, based on these data, will be used to establish the overall merits of impulse drying for various applications.

An improved understanding of the heat and mass transfer processes governing water removal from the paper web and of the web consolidation mechanisms under high-intensity operating conditions can be expected to follow from analysis of the test data. This will provide additional guidance for the successful development and design of advanced water removal systems.

In this section, the background planning for the technical performance evaluation program is reviewed. Areas covered include: grade/furnish selection, drying system design, test procedure specification, paper properties evaluation, test program definition, and data acquisition, processing, and storage. Almost all of the work is completed, and the actual experimental program is well under way. Results obtained thus far will be presented in subsequent sections.

GRADE/FURNISH SELECTION

Unfortunately, it is not practical to experiment with all combinations of fiber furnish, refining level, basis weight, etc., over a broad range of operating conditions. Therefore, a limited selection of these combinations, representative of certain important paper and board grades, has been selected for use in evaluating the performance of impulse drying. Based partly on production figures, the grades listed in Table 1 have been initially selected for this study. Overall, these grades represent over 70% of total U.S. paper and board production. Several grades have been included because they represent potentially interesting applications of impulse drying or because they may provide additional insight into process mechanisms.

Table 1. Grades for technical performance tests.

		Percent of Total U.S. Production[a]			Percent of Total U.S. Production[a]
1.	Newsprint	7.7	6.	Recycled paperboard	11.6
2.	Uncoated printing or writing paper	13.2	7.	Lightweight coating	- -
			8.	Recycled linerboard	- -
3.	Tissue	7.2			
			9.	Recycled corrugating medium	- -
4.	Linerboard	23.1			
5.	Corrugating medium, virgin	7.3	10.	High-yield experimental pulp	- -

[a]Combined paper and board production.

Stocks for grades 1-8, except 6, have been obtained by in-mill extraction as close to the headbox as possible to obtain materials representative of actual production. A recycled paperboard furnish has not yet been obtained. The high-yield experimental pulp is to be obtained from an IPC pulping project. The recycled corrugating medium will be 100% old corrugated containers.

In a subsequent section of this report, impulse dryer performance data will be given for each grade. Each furnish will be characterized, in detail, in that section.

DRYING SYSTEM

The technical performance evaluation program requires a drying system capable of operating over a wide range of mechanical pressure, surface temperature, and drying time combinations. Ideally, the system should permit the pressure-time profile to be varied, as well. Finally, the system should accommodate both atmospheric and vacuum ambient conditions. None of the previously used drying systems can meet these requirements so a new system has been designed and constructed.

The new drying system is based on the use of electrohydraulic servo components, obtained from Materials Testing Systems (MTS). A large hydraulic actuator (22,000 lb force) with integral LVDT stroke transducer, two parallel servovalves with accumulators, a load cell, hydraulic power supply with remote control unit and a servo control package were all purchased from MTS. A load frame, designed and constructed by the IPC, along with the servo actuator components and a test head are shown in Fig. 2.

The stroke and load transducer signals are used, in combination, to form a two-loop feedback control system, as shown schematically in Fig. 3. A logic system, also developed at the IPC and shown as the remainder of Fig. 3, is used to move the test head toward the sample, detect contact with the sample, command a suitable load pulse from a commercial function generator, and withdraw the head from the sample at the conclusion of the test. An electronic integrator calculates the area under the load-time curve to produce an electrical signal

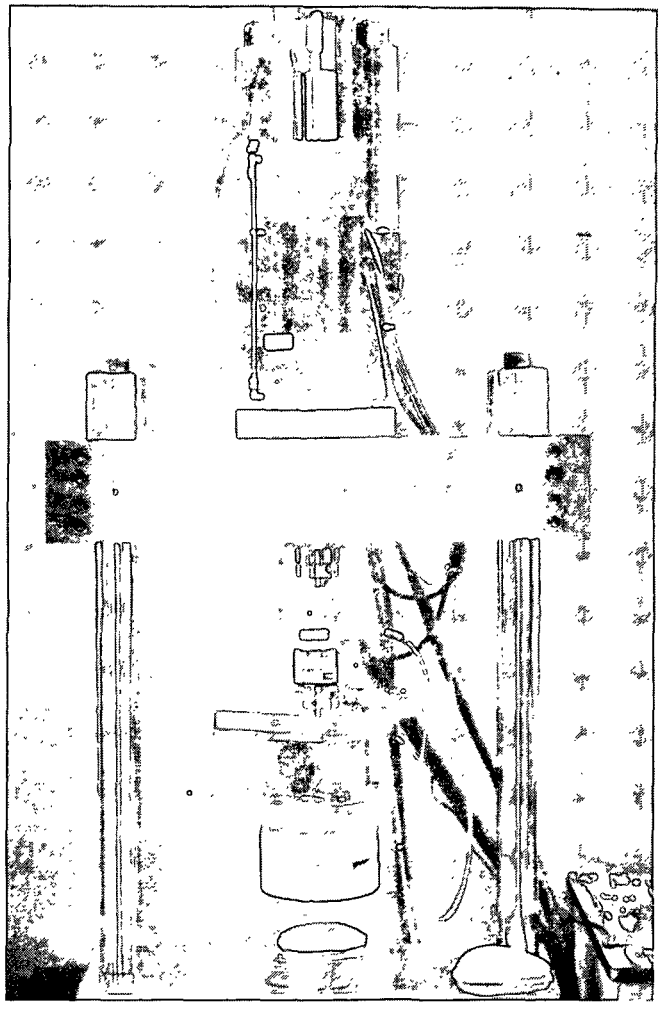

Figure 2. Servo actuator and load frame assembly.

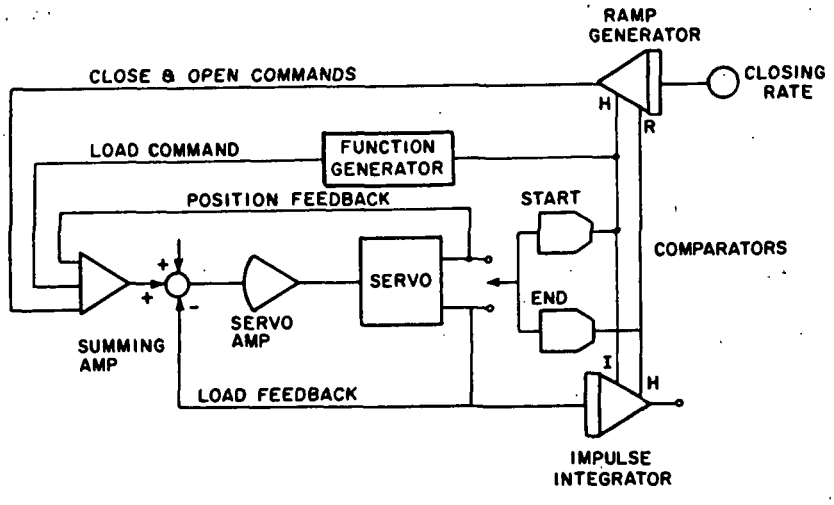

Figure 3. Schematic diagram of electrohydraulic press control system.

proportional to press impulse. Figure 4 shows a schematic representation of a complete test cycle; Fig. 5 shows a recording of an actual test cycle. While approaching and retracting from the sample, the stroke signal changes are large and the load signal changes are small, so the system behaves like a position control system. Conversely, during a test, the head is in contact with a fairly incompressible sample yielding large load changes and small stroke changes. Thus, the servo behaves like a load control system. This simple scheme works well and avoids the complexity of the high-speed mode switching sometimes used in such applications. The resulting system can produce load pulse from about 50 to 15,000 pounds with durations from about 10 ms up to unlimited values. Almost any pulse waveform can be used, but sine, haversine, rectangular and triangular are readily available from the function generator.

An impulse drying test head, with associated base plates and couplings, has been designed and constructed for use in the electrohydraulic pressing system. This head, shown in Fig. 6, accommodates 5-inch diameter handsheets, which are large enough for paper properties evaluation, but small enough to allow mechanical pressures in excess of 1000 psi to be applied during a drying experiment. Heat transfer to the sheet during a drying test is provided from a large steel block, preheated to the required temperature by a cartridge heater and temperature controller. The head is instrumented with a 0.25-inch diameter Medtherm surface thermocouple (iron-constantan) for use in heat transfer calculations, and a pressure tap and transducer to measure the vapor pressure developed at the hot surface. The opposing head, used to support the water receiver and handsheet, is supported by a spherical washer so it is self-aligning. A bellows chamber can be installed around the test head and evacuated for thermal/vacuum drying tests. A large pre-evacuated tank, connected through a

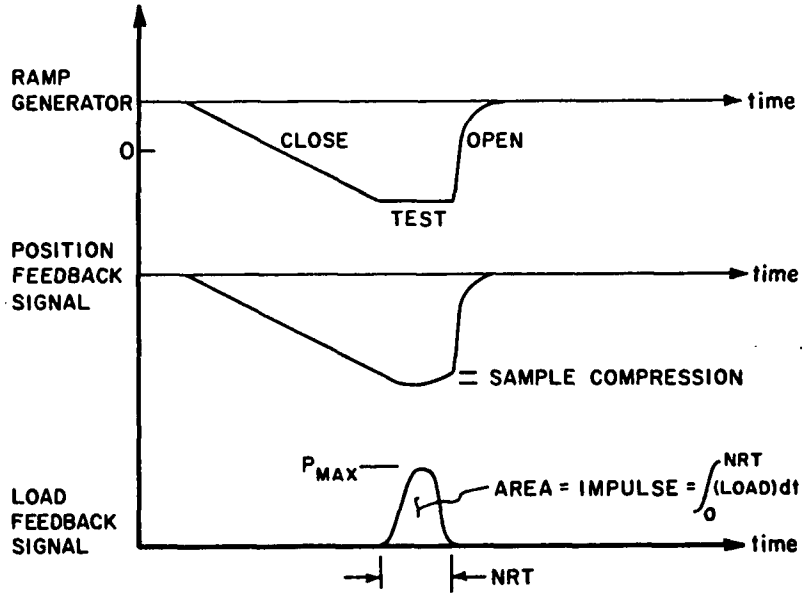

Figure 4. Schematic representation of a test cycle.

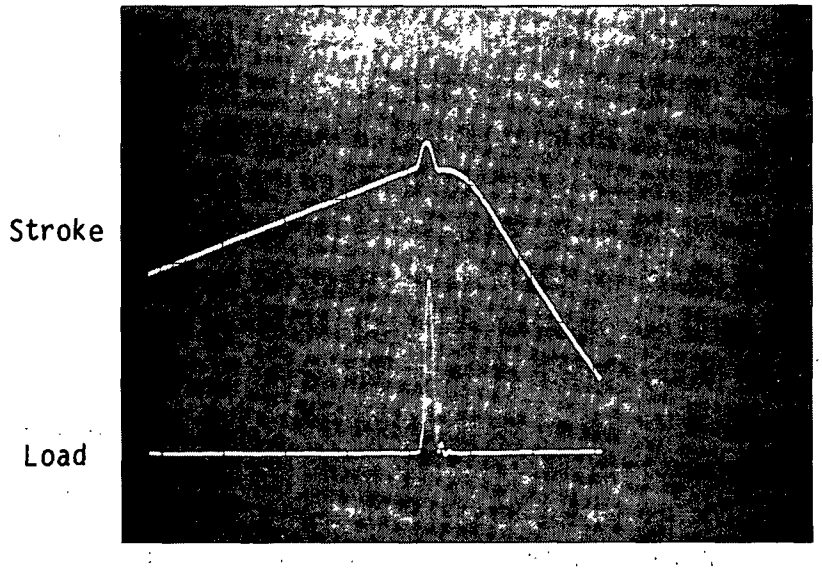

Figure 5. Electrohydraulic press test cycle.

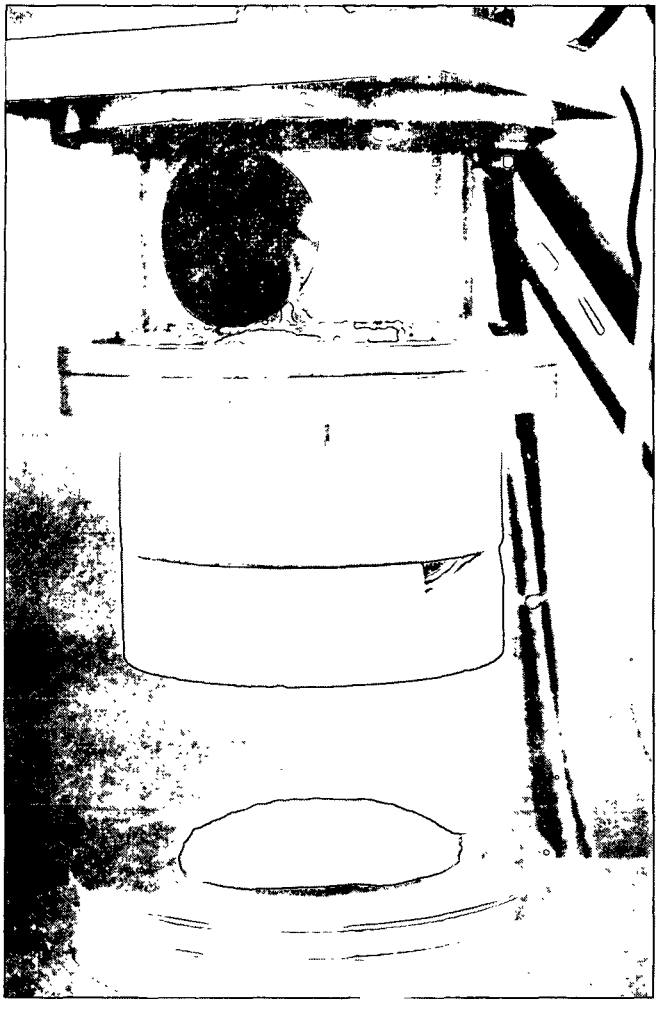

Figure 6. Impulse drying test head.

solenoid valve to the bellows section, is used to quickly develop the vacuum ambient at the start of a test. A low-pressure steam distribution system is being designed for preheating of the sheets before drying.

An APPLE computer-based data acquisition system is being used in the test program to acquire temperature, load and vapor pressure histories for selected tests. Temperature histories can be used in a separate heat transfer model for the heated block to calculate heat fluxes and cumulative energy transfer.

HANDSHEET PREPARATION AND HANDLING

A standard handsheet mold, modified by installation of a 5-inch diameter tube, is used to make 5-inch handsheets. The wire is sealed under the tube to control drainage. Standard procedures are used to produce handsheets in batches, each batch being large enough for 2-3 days of testing. All sheets are stored at high moisture contents in sealed bags under refrigeration until they are used, usually no more than 4-5 days.

Immediately prior to being impulse dried, each sheet is pressed to the desired moisture ratio. A roll press (Fig. 7), designed to yield pressure levels and nip residence times comparable to commercial presses, is used for this purpose. Each sheet is sandwiched between two blotters, placed between carrier strips, and passed through the roll press one or more times to achieve the desired moisture level. Pretest calibration runs are used to establish the pressing conditions required for a given test.

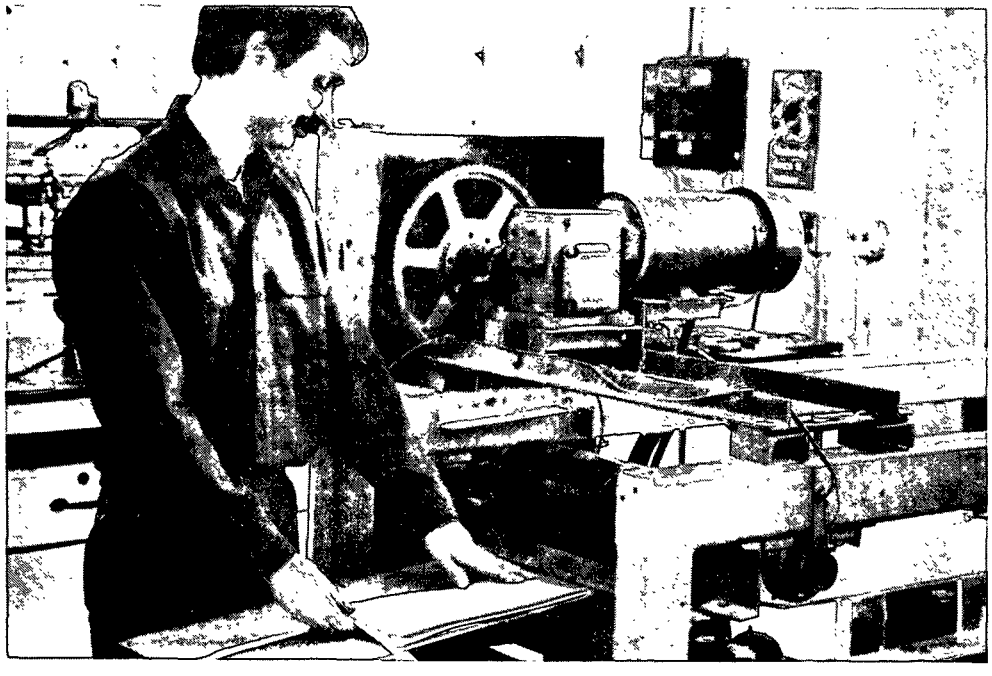

Figure 7. Roll press for pre-pressing sheets.

Many of the impulse drying tests result in only partial water removal. A temperature-controlled, low-intensity dryer (i.e., low temperature and pressure), Fig. 8, located adjacent to the impulse drying system, is used for post-test drying to a 5-6% moisture level for subsequent final conditioning and paper properties evaluation. For a few special tests, this system is used for both pre- and post drying. Here, too, calibration tests are required to establish the drying time required to achieve the desired final moisture content. These are carried out before starting an impulse drying test.

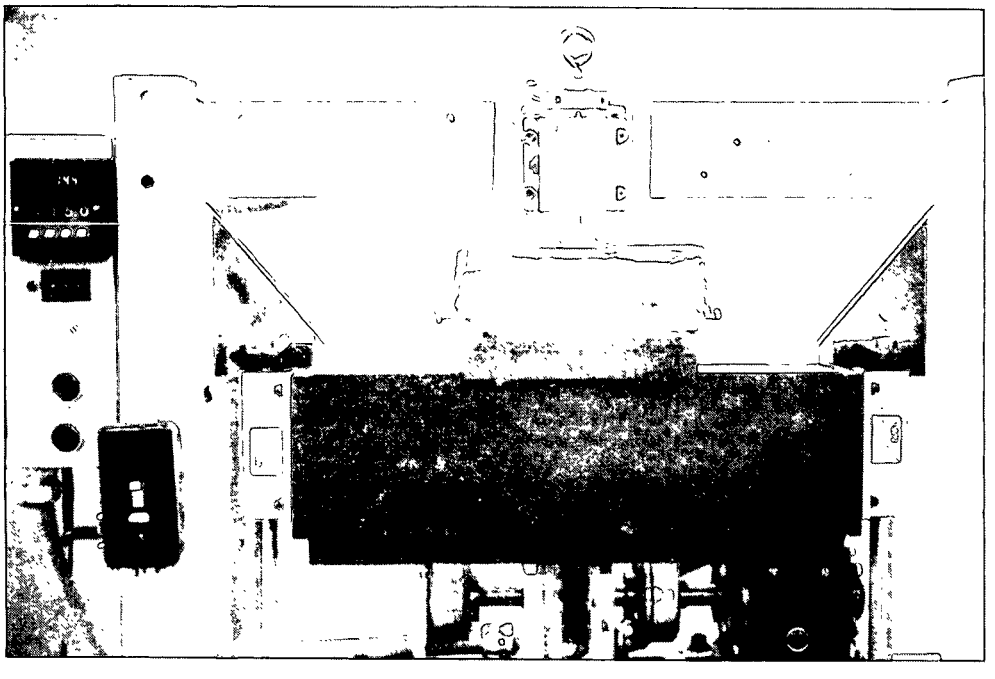

Figure 8. Low-intensity drying system.

A flowchart of all the steps in the evaluation of performance at a given impulse drying condition is shown in Fig. 9. After manufacture, handsheets are taken through the appropriate pre-processing steps (pressing or pressing and pre-drying). Most of the sheets are them impulse dried under given conditions to produce a corresponding dryness level, usually well below 95%. These sheets are then post-dried under conventional conditions to 94-95% solids. A few sheets bypass impulse drying and go directly to the conventional drying stage and act as control sheets for the experiment. All sheets are then forwarded to the Paper Testing Laboratory for property evaluation, as specified below.

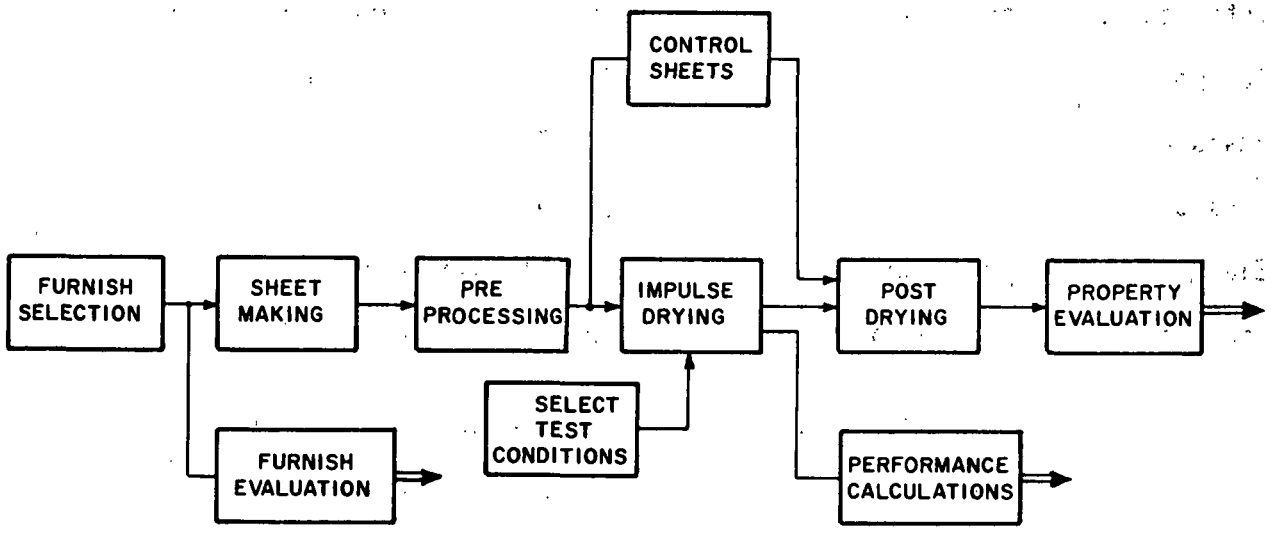

Figure 9. Elements of performance evaluation.

PAPER PROPERTY EVALUATION

For each paper and board grade included in the technical performance evaluation, a set of relevant physical properties has been established. These properties are measured on samples dried under various operating conditions and compared with those obtained from corresponding control sheets to establish the effect of impulse drying on property development.

The property sets can be divided into two groups: those common to all grades and those that are grade-specific. Most of the property evaluations are being made according to standard procedures, while others require special procedures, as noted below. The properties common to all grades are identified in Table 2. The properties specific to given grades are identified in Tables 3-8.

Table 2. Properties common to all grades.

Property	Comments on Procedure
Tensile stiffness	TAPPI, using five 1 by 3-inch samples
Tensile strength	TAPPI, using five 1 by 3-inch samples
Stretch	TAPPI, using five 1 by 3-samples
Total energy absorption	TAPPI, using five 1 by 3-inch samples
Caliper	IPC rubber platen method
Basis weight, o.d.	TAPPI standard
Density	Calculated
Elastic moduli (in-plane, out-of-plane)	IPC ultrasonic method
Shear moduli (in-plane, out-of-plane)	IPC ultrasonic method

Table 3. Additional properties for newsprint.

Property	Comments on Procedure
Tear	Elmendorf
Opacity	TAPPI standard
Smoothness	PRINTSURF, manufacturer's procedure
Porosity	Bendtsen
Brightness	TAPPI standard
Ink penetration	Hercules
Pick	IGT; fiber pick and blister endpoint
Water resistance	Water drop; four trials

Table 4. Additional properties for writing paper.

Property	Comments on Procedure
[All properties as listed in Table 3 for newsprint.]	
Folding endurance	MIT

Table 5. Additional properties for tissue.

Property	Comments on Procedure
Water absorption	Water drop
Water capacity	IPC; dip sample, let free water drain off; use tensile specimens
Stiffness	TAPPI/Clark; use tensile specimens
Wet strength	IPC; tensile with sheet wetted by spray bottle
Porosity	Bendtsen
Brightness	TAPPI standard
Light-scattering coefficient	Standard
Bulk	IPC; calculated from density of stacked sheets

Table 6. Additional properties to for linerboard (primary).

Property	Comments on Procedure
Burst	Mullen
Smoothness	Bendtsen
STFI compression	Standard, 20 replicate tests

Table 7. Additional properties for corrugating medium.

Property	Comments on Procedure
Concora	Shorter strip than standard (fewer flutes)
Water absorption	Water drop
STFI compression	Standard

Table 8. Additional properties for carton stock (recycled paperboard).

Property	Comments on Procedure
Stiffness	Taber; using 1-inch wide samples
Plybond	ZDT
STFI compression	Standard
Smoothness	Bendtsen
Ink absorption	Water drop
Pick	IGT; fiber pick and blister endpoint

Based on the numbers and sizes of samples required for the various property evaluations indicated in the preceding tables, the number of handsheets that must be dried at a given test condition has been estimated and tabulated in Table 9.

Table 9. Number of handsheets rquired for each test condition.

Grade	Number of Handsheets
Newsprint	12
Writing paper	12
Tissue	13
Linerboard (primary)	5
Corrugating medium	5
Carton stock (recycled paperboard)	10

In addition to providing test samples for paper properties evaluation, the drying experiments will provide extensive performance data on water removal and energy use. The quantities to be measured in the test program include: instantaneous applied mechanical pressure, instantaneous hot surface temperature, instantaneous vapor pressure at the hot surface, total water (weight) loss, and chemical tracer loss. Certain of these variables will be used in subsequent calculations, e.g., the temperature data will be used to calculate the heat flux and cumulative thermal energy input to the sheet, the mechanical pressure data can be used to calculate impulse, and the chemical tracer data will be used to estimate the amount of liquid dewatering.

TEST PROGRAM

Of the many variables of possible interest in the technical performance evaluation program, the following variables are considered to be of primary importance: (1) grade (furnish), (2) basis weight, (3) initial moisture ratio, (4) initial sheet temperature, (5) ambient pressure, (6) peak applied mechanical pressure, (7) initial hot surface temperature, and (8) residence time at drying

conditions. Other variables, likely to warrant early, limited investigation, are expected to emerge in this study. Possible candidates include mechanical pressure pulse shape, water receiver type and moisture content, preprocessing conditions, hot surface treatment, two-sided impulse drying, and so on. These have received or will receive attention, as required, to meet the full objectives of this project.

Some comments on the primary variables are appropriate. Several are discrete or have limited ranges, requiring only two or three levels of testing. These include: grade, basis weight, initial moisture ratio, initial web temperature (room temperature and approximately 212°F), and ambient pressure (atmospheric and vacuum). Basis weight values will be dictated primarily by grade, even for experimental furnishes where a target grade can be identified. Residence time is somewhat special; only those times less than or equal to the drying time are meaningful. Drying time depends on surface temperature, applied mechanical pressure, and other variables, and is thus not known a priori. To avoid this problem, drying time relationships are determined approximately in preliminary experiments as a partial basis for selecting test times for the main study. Figure 10 shows an approximate basis weight nip residence time chart for typical grades and two nip widths, 1.2" and 8". These data are also used for guidance in selecting initial impulse drying times. The control case corresponds to a nip residence time of zero (no impulse drying).

Temperature values of interest range from room temperature up to 1000°F. Pressure values up to 1000 psi are of interest although pressure and nip residence time (NRT) values should be coordinated to reflect the line pressure limitations of current press technology.

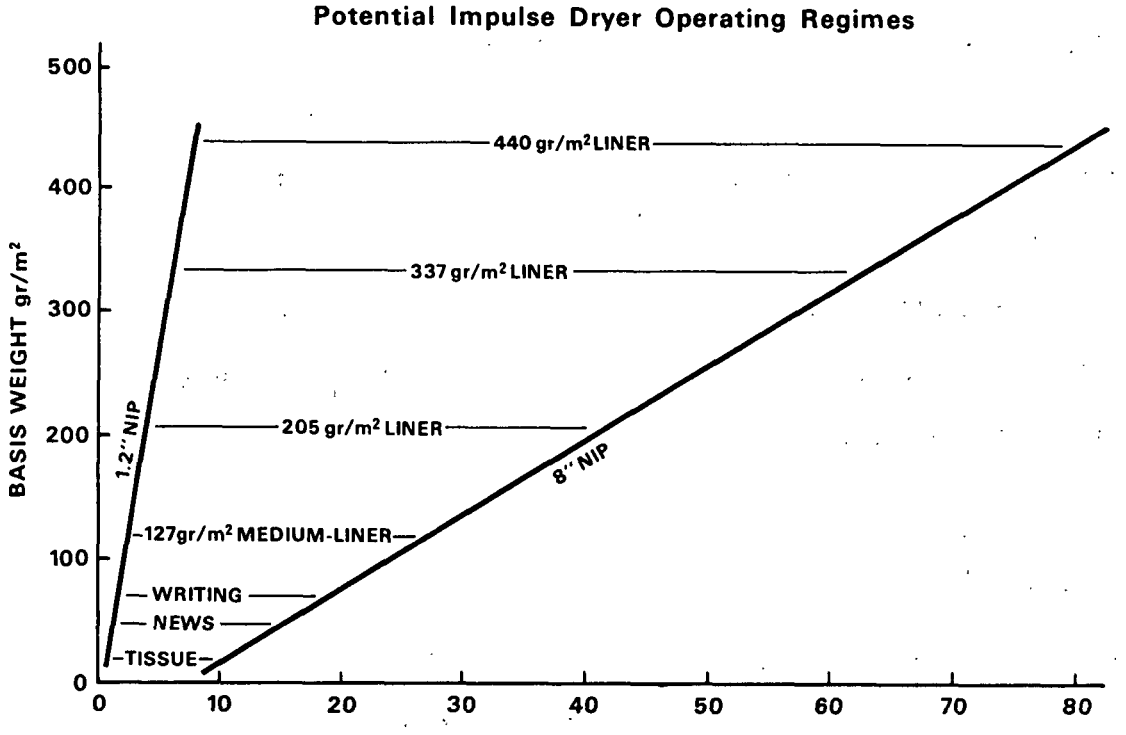

Figure 10. Nip residence time range (milliseconds).

Because the full test program suggested by the primary variables given above is quite large, an overview or screening series of tests is now being conducted. These tests are being used to explore limited ranges of the test variables and to identify interesting avenues of special investigation. Results from these tests will be used to fine-tune the final test program to avoid excess testing or testing in areas where impulse drying has little appeal.

DATA ACQUISITION, PROCESSING, AND STORAGE

Because of the wide scope of the technical performance evaluation program, it is especially important to have an efficient system for acquiring, manipulating, storing, retrieving, and presenting the data. The present plan is to use an APPLE microcomputer linked to the Burroughs mainframe computer,

via a BURPLE interface, to provide the necessary hardware capability. The APPLE is installed as an integral part of the drying test system. It serves primarily for acquisition of instantaneous mechanical pressure, vapor pressure and surface temperature. All other slow speed and discrete data are acquired manually, including such items as operating conditions, water removal and sheet properties. These data are all stored in a large data base system called INSYTE for easy retrieval, reporting and manipulation. The intent is to build a long-term data base via this mechanism.

Transient data, delivered to the mainframe by the APPLE, are analyzed for key results such as heat flux values and cumulative energy transfer. These data are then stored in INSYTE along with all of the other information. The net result is a single, comprehensive data base that can be readily searched on the basis of almost any test attribute including test conditions, initial sheet characteristics, property values, date, grade, test ID numbers, and so on. Only averages for a given test (5-15 sheets tested at one condition) are recorded. Individual sheet values are retained in hard copy form.

For data analysis, the appropriate data set from INSYTE is downloaded to an IBM XT for processing in a software package called STATGRAPHICS.

III. TECHNICAL PERFORMANCE EVALUATION TEST RESULTS

As noted earlier, the initial phase of this technical performance evaluation is devoted to limited screening tests on each grade. A more comprehensive test program, based on the results of these screening tests and devoted to the most promising applications, will follow. Tests conducted to date have been aimed primarily at determining water removal rates and paper property values. Although some transient data have been recorded, measurements of the fraction of water removed in liquid form and of heat fluxes and total heat transfer are being delayed for the next series of tests. These measurements are time consuming and expensive and, hence, will be carried out only on a limited subset of experiments known to be of high interest. Considerable information on liquid dewatering and energy consumption was obtained in the exploratory phase of this project and is documented in Report One (1).

To date, screening experiments on several furnishes and a few special experiments have been completed. Results from and discussions of these experiments are presented below, as they are available. Additional data will be available at the meeting.

FURNISH DEFINITIONS AND EVALUATIONS

For the eight furnishes available to date, fiber makeup data are given in Table 10, compressibility properties are given in Table 11, and surface and water retention properties are given in Table 12.

Table 10. Fiber makeup of furnishes.

	Fiber Makeup		
Linerboard 1 (virgin)	100% UBSWK		
Linerboard 2 (recycled)			
Corrugated Medium 1	91% SCSC	1.5% UBHWK	7.3% UBSWK
Corrugated Medium 2	100% OCC		
Tissue	47% BHWK	53% BSWK	
Writing	73% BHWK	27% BSWK	
Newsprint 2	22% BSWK	78% GW	
Lightweight Coating	47% BSWK	53% TMP	

Table 11. Compressibility properties of furnishes.

Linerboard	$C = 0.050P^{0.364}$
Tissue	$C = 0.064P^{0.434}$
Writing	$C = 0.074P^{0.332}$
Newsprint 2 (GW&K)	$C = 0.071P^{0.294}$
Lightweight Coating (TMP&K)	$C = 0.073P^{0.305}$
Corrugating Medium	$C = 0.068P^{0.319}$

C = GR/CC P = KPa

Table 12. Surface and water retention properties of furnishes.

	Surface Area cm^2/gr	Specific Volume cc/gr	CWR $\frac{gr\ H_2O}{gr\ fiber}$	CSF cc
Linerboard	4,000	2.43	- -	730
Tissue	12,100	2.31	1.73	635
Writing	16,200	2.80	2.70	495
Newsprint 2 (GW&K)	29,100	3.38	3.03	175
Lightweight Coating (TMP&K)	35,300	3.57	3.04	115
Corrugating Medium	19,800	3.45	3.08	310

IMPULSE DRYING PERFORMANCE BY GRADE

Linerboard - Virgin Fiber

Test Conditions

All tests on linerboard have been conducted using $127g/m^2$ sheet made entirely of base stock. No attempt has yet been made to evaluate duplex sheets. Four test subsets have been carried out: an overview study, typical of the tests conducted on each furnish; a set of tests at various levels of predrying; another set corresponding to constant press line loading; and one two-sided impulse drying test. For all tests, the sheets were prepressed to about 46% solids; some were also predried. Table 13 shows the ingoing sheet conditions and the impulse drying conditions.

Table 13. Test conditions for virgin linerboard base sheets.

Test subset	NRT ms	Peak Pressure psi	Initial Temp. °F	Ingoing Solids %
	Control	- -	- -	46.0
	27.2	715	700	46.5
	28.7	703	400	45.7
	29.8	407	400	46.2
Overview	30.3	417	700	46.2
	14.9	407	400	46.0
	15.2	404	700	45.9
	14.3	716	700	46.2
	14.3	715	400	46.4
	32.0	601	500	45.0
	34.0	602	700	45.0
	34.0	607	900	45.0
Constant	66.0	314	500	45.0
line load	66.0	309	700	45.0
tests	66.0	313	900	45.0
	127.0	153	500	45.0
	127.0	148	700	45.0
	127.0	152	900	45.0
Predried	23.1	748	700	57.6
to various	23.2	741	700	65.2
soilids	23.3	756	700	72.4
levels	23.3	750	700	82.7
Impulse dried two sides	27.7	756	700	46.4

Water Removal Rates

Water removal rates for all virgin linerboard base stock sheets are shown in Fig. 11 as a function of temperature divided by the square root of NRT. Several important observations can be made from this plot:

1. Water removal rate is strongly correlated to and linear with temperature divided by the square root of NRT. This relationship holds over a broad range of drying conditions.
2. Temperature is the dominant variable in determining water removal rate.

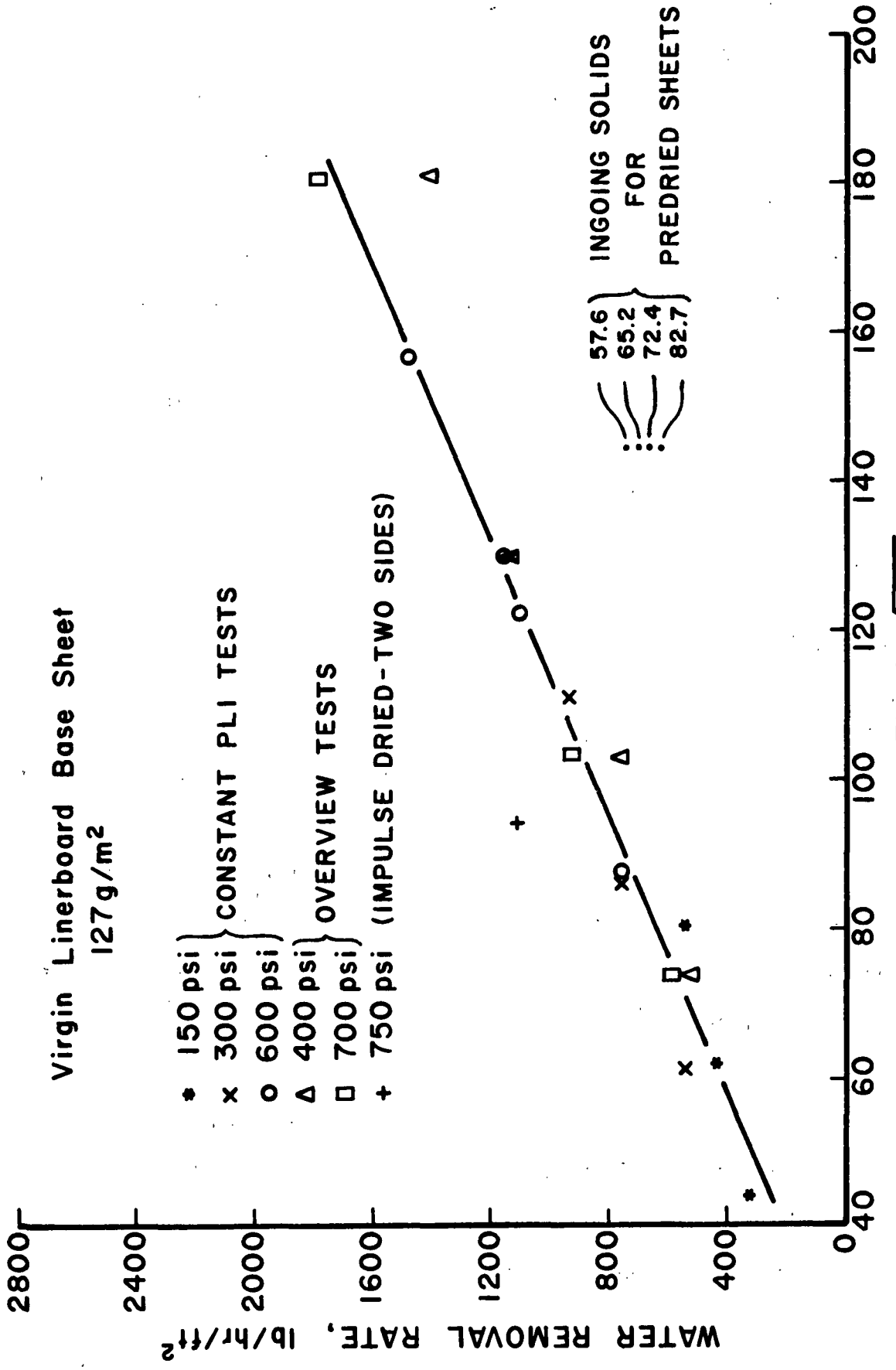

Figure 11. Water removal rates for virgin linerboard base stock.

3. Pressure has a positive but modest influence on water removal rate.
4. Short nips produce high water removal rates as $\sqrt{NRT}$ becomes small. Long nips produce greater total water removal in proportion to $\sqrt{NRT}$.
5. Drying on opposite sides with two nips of length X appears to provide more water removal than drying on one side with one nip of length 2X.
6. Sheets slightly predried and then impulse dried from the same side show a large reduction in water removal rate. Additional predrying causes only small additional degradation of drying rate.

Figure 12 shows water removal rate as a function of ingoing solids levels. This graph further illustrates the serious negative impact of predrying.

Property Development

Linerboard density, as determined from thickness measurements made on the IPC rubber platen caliper gauge, is plotted versus thermal impulse (temperature·NRT) in Fig. 13. Applied pressure is used as a plotting parameter. These same density data are presented in Fig. 14 as a function of outgoing solids level. The following observations are made from these data sets:

1. Linerboard density can be increased dramatically by impulse drying.
2. Density varies almost linearly with thermal impulse for pressures from about 300 psi on up.
3. Pressure has a significant and positive influence on density, especially above 300 psi or so.

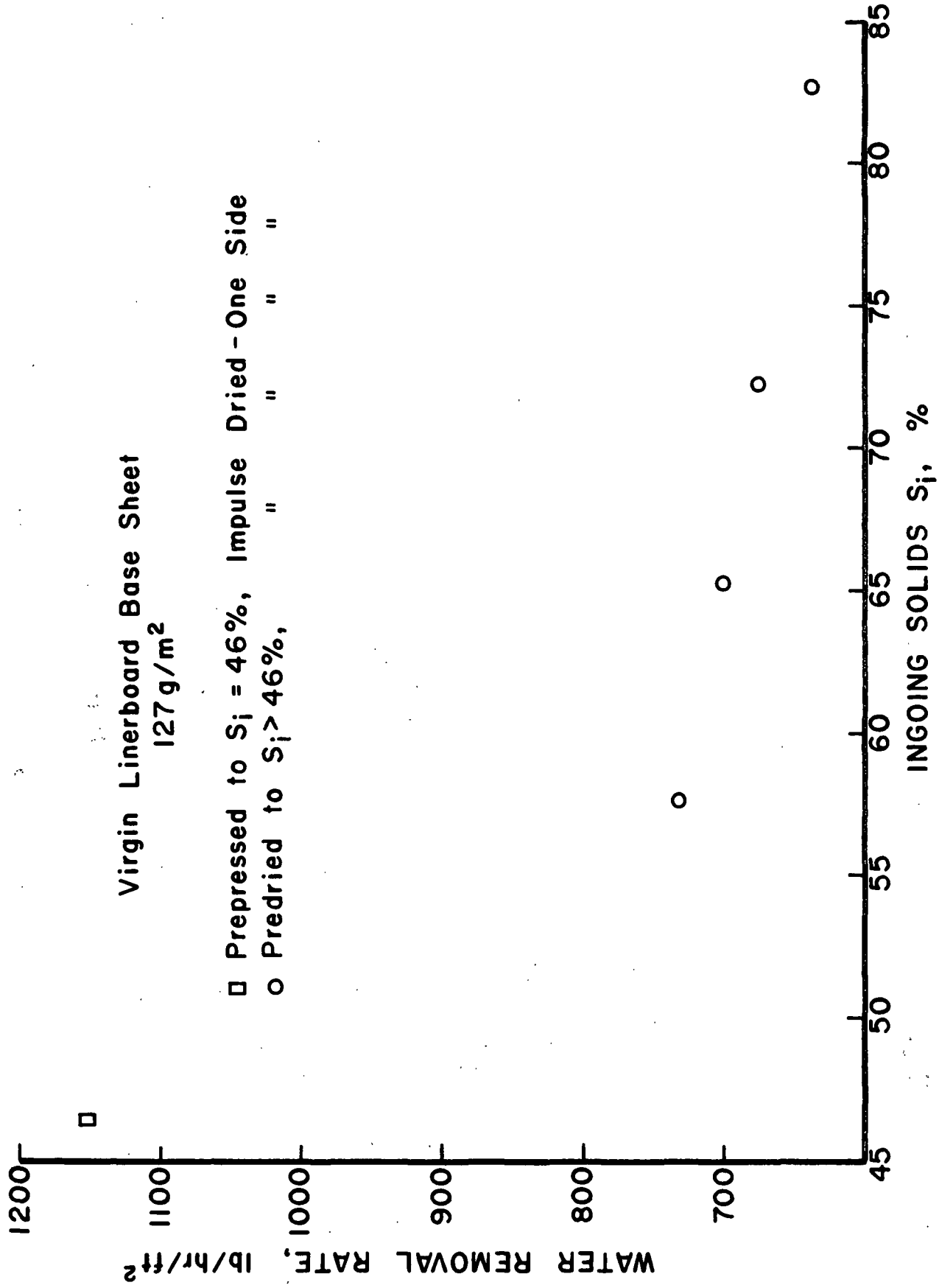

Figure 12. Effect of predrying on water removal rate for virgin linerboard base sheet.

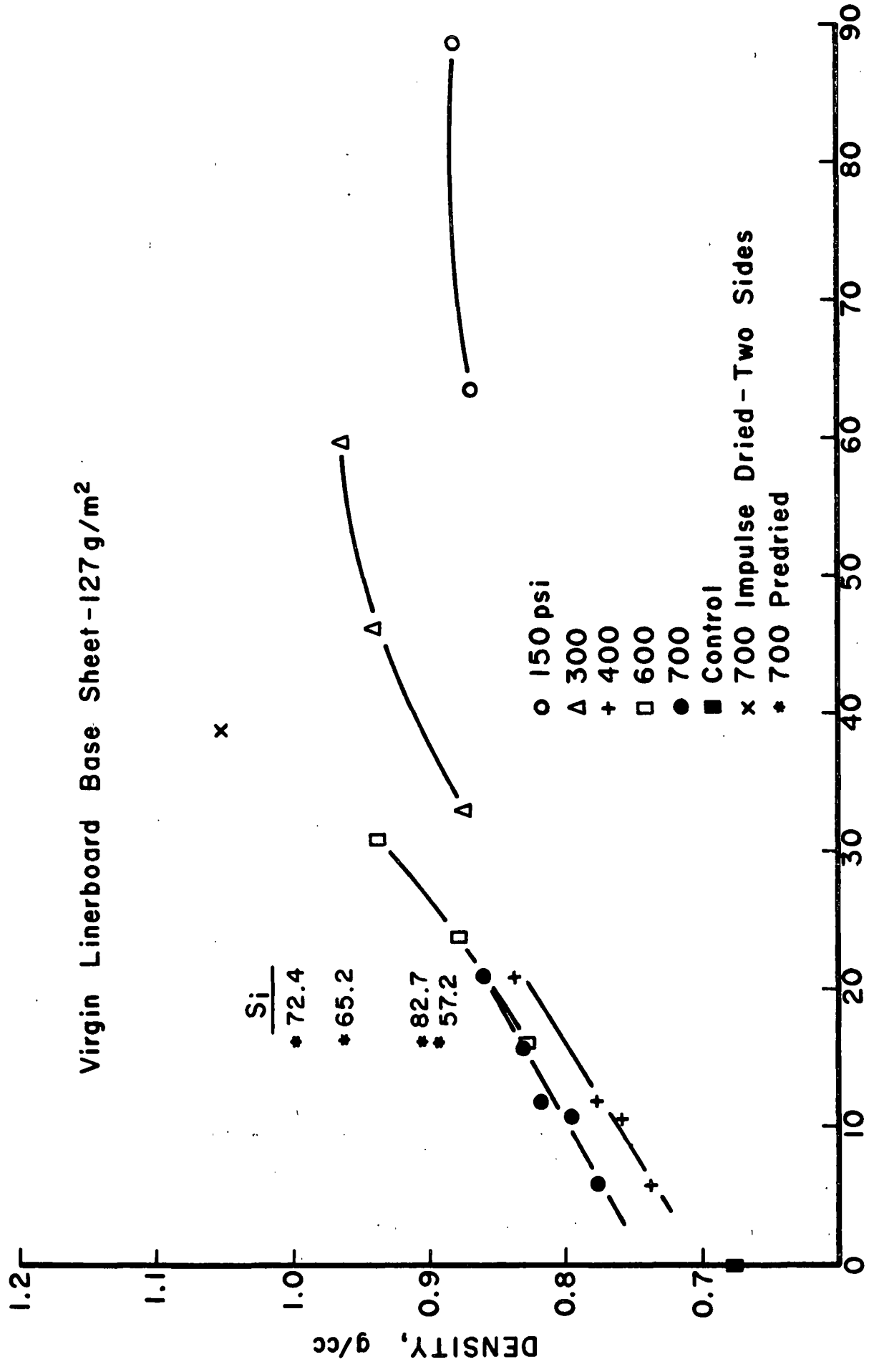

Figure 13. Density development for virgin linerboard base sheet.

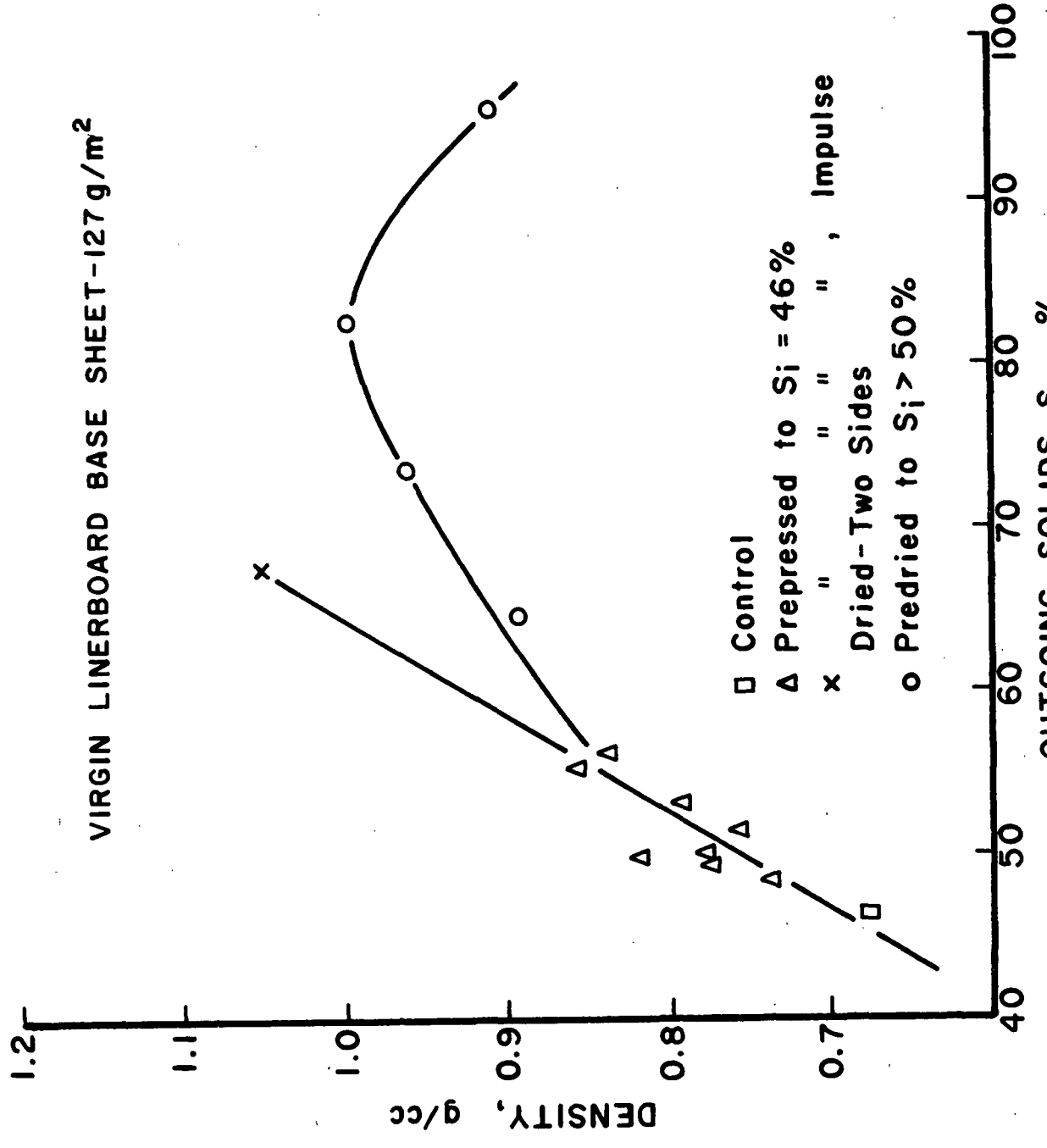

Figure 14. Density development with dryness for virgin linerboard base sheet.

4. The density curves for pressures of 150 and 300 psi tend to flatten out, or even drop off, for large values of thermal impulse. Similar trends may occur for the higher pressures, but this has never been investigated.
5. Drying on opposite sides with two nips of length X appears to produce a density equivalent to drying on one side with one nip of length 2X.
6. Density varies linearly with outgoing solids for sheets prepressed to a given moisture content. This seems to hold for two-sided drying, too.
7. Predrying tends to increase the density developed in the impulse dryer, but substantially degrade the density-outgoing solids relationships.

Figures 15-18 show plots of STFI compressive strength index, burst index, tensile index and the Z-direction sheet modulus, measured ultrasonically, all plotted versus density. All of these mechanical properties show the expected linear trend with density for all sheets prepressed only, even the sheet impulse dried on both sides. For the predried sheets, however, these properties tend to decline with increasing density. This is a most unusual type of behavior, requiring further investigation.

Habeger and Whitsitt[3] have developed a fundamental model relating compressive strength to certain in-plane and out-of-plane elastic properties. One form of this model relates compressive strength to a linear function of $E_Z^{1/4}\ E_X^{3/4}$ (where E_Z is the out-of-plane elastic modulus divided by density and E_X is the corresponding in-plane modulus). As shown in Fig. 19, the data from this study fit this model quite well, including those from the predrying experiments.

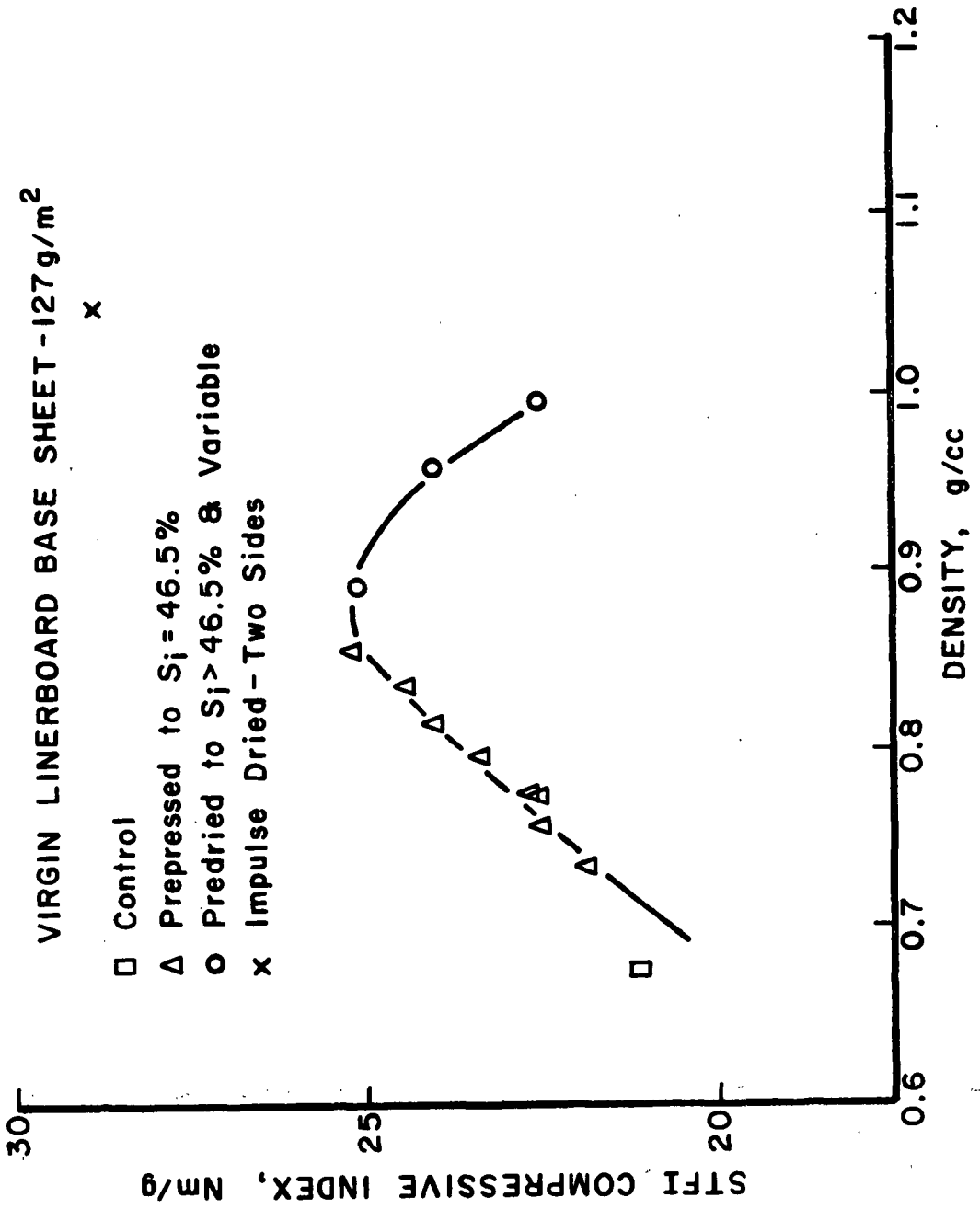

Figure 15. Compressive strength variation with density for virgin linerboard base stock

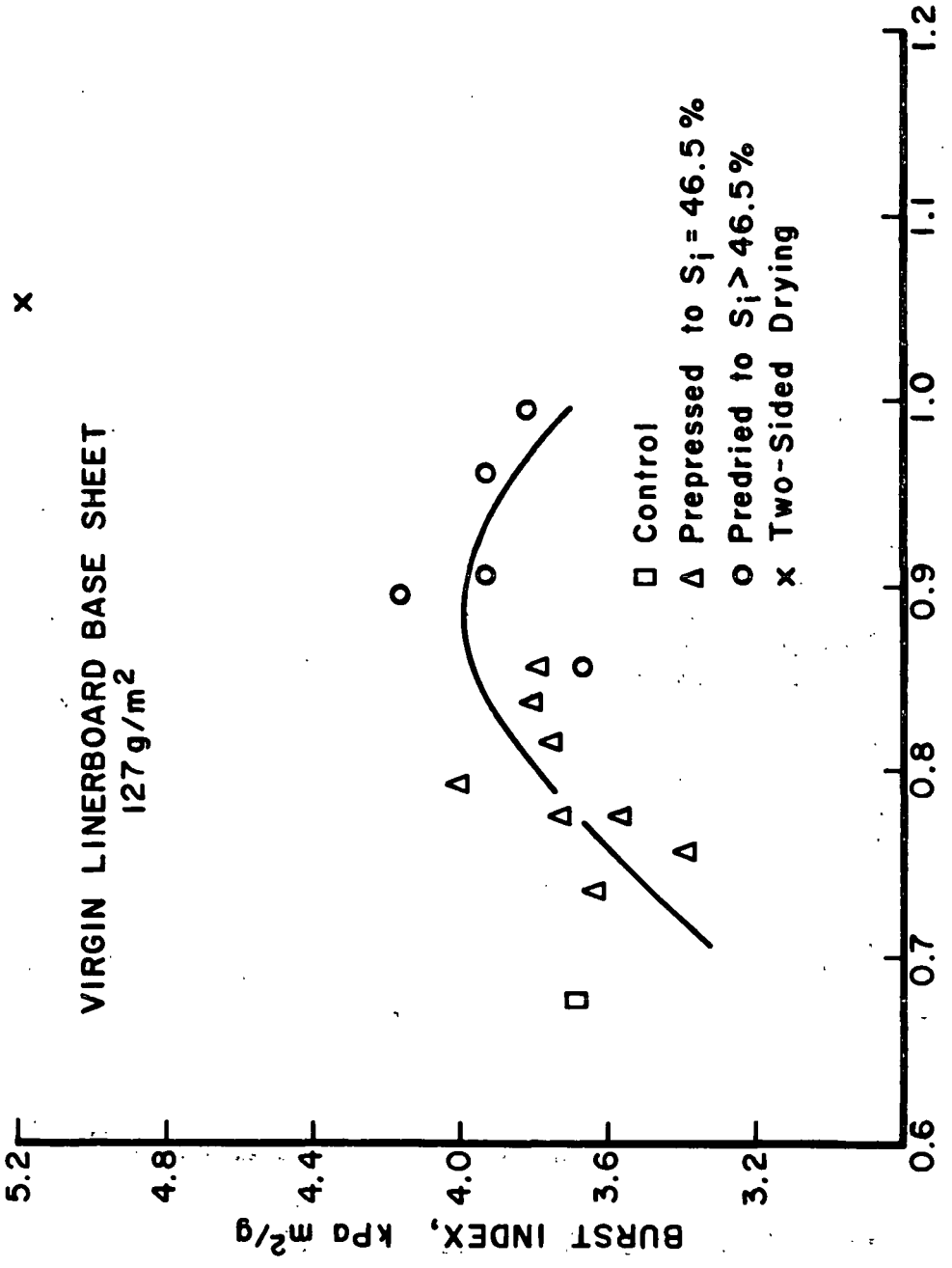

Figure 16. Burst development with density for virgin linerboard base sheets.

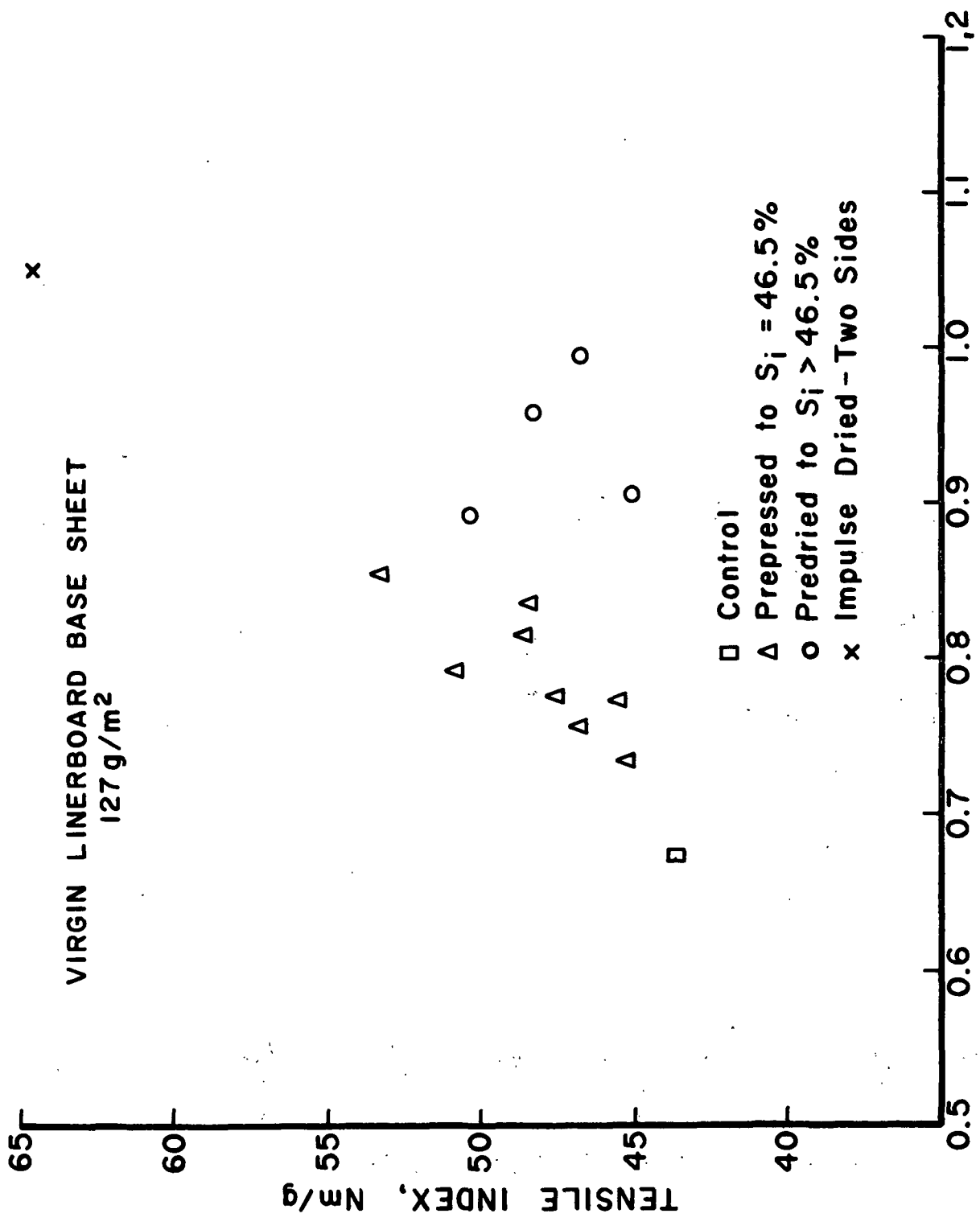

Figure 17. Tensile strength development with density for virgin linerboard base sheet.

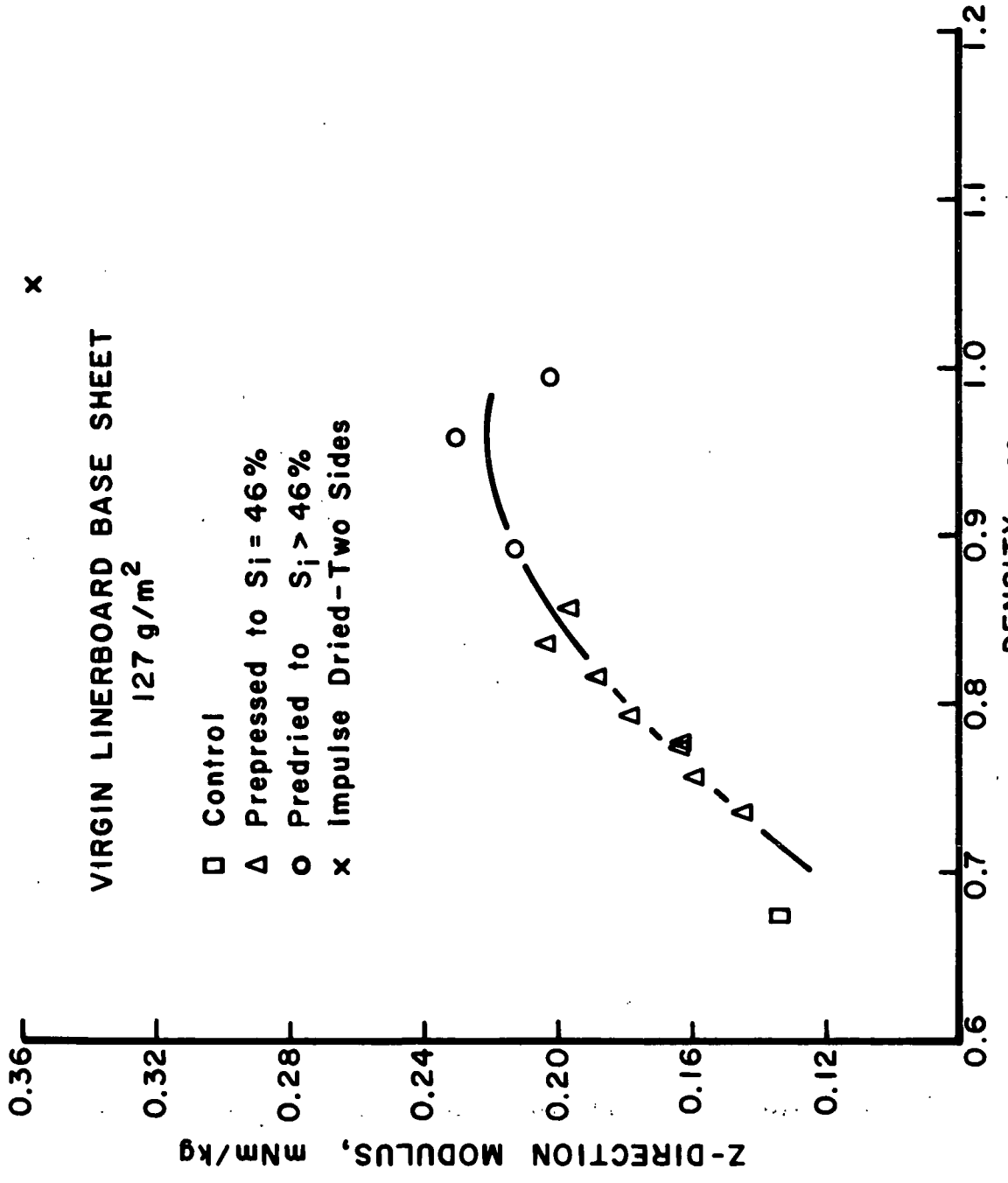

Figure 18. Z-direction modulus variation with density for virgin linerboard base sheet.

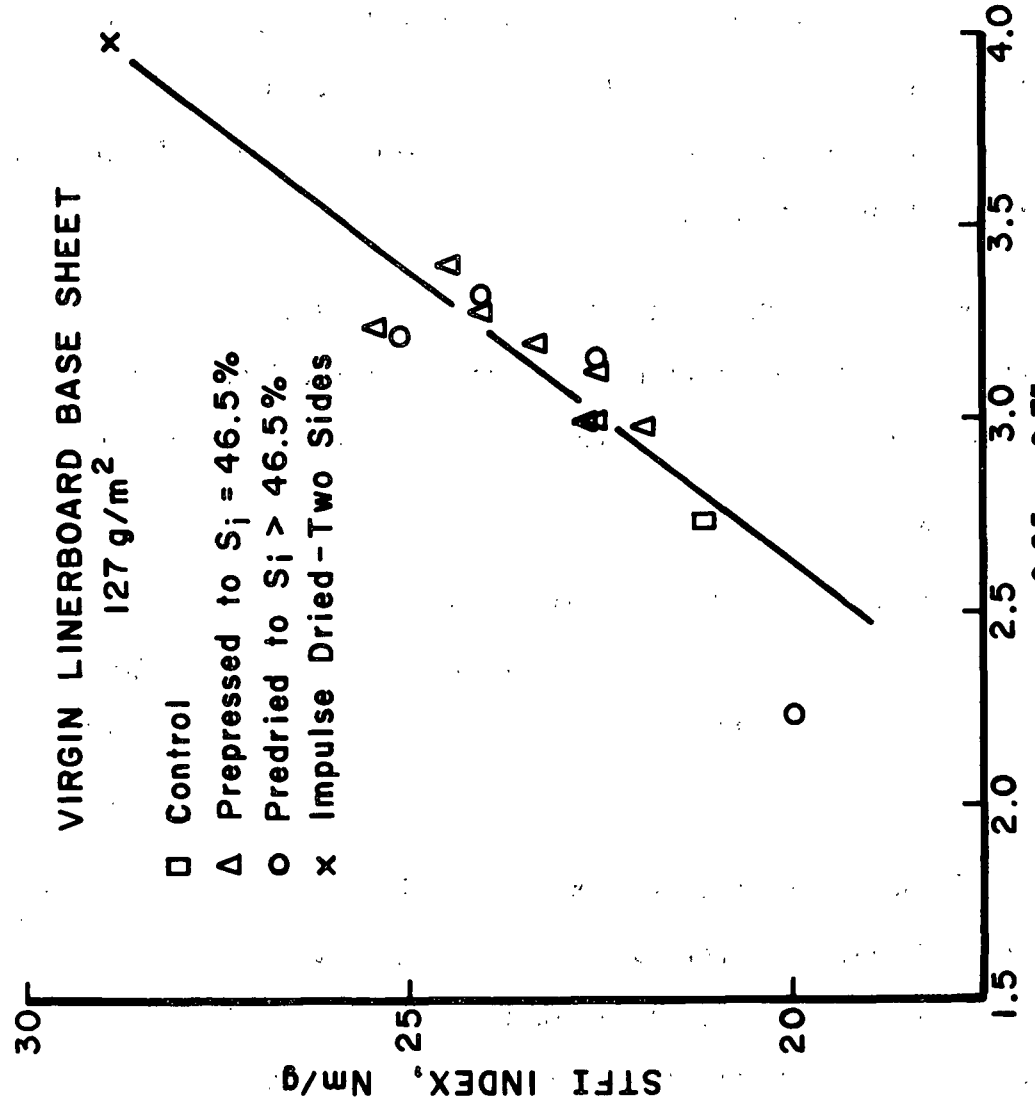

Figure 19. Habeger-Whitsitt compressive strength model for virgin linerboard base sheet.

Surface roughness is a property of only limited interest for linerboard base sheets, but it was evaluated in this study. Surface roughness (Parker Print surf) for each side is plotted versus outgoing solids in Fig. 20. Felt-side roughness is not significantly influenced by impulse drying. The smoothness of the heated side is greatly improved, somewhat in proportion to the degree of impulse drying. Modest predrying does not seem to alter this behavior; high levels of predrying tend to slightly limit smoothness development. Two-sided drying tends to equalize smoothness by roughening what was initially the heated side and smoothing what was initially the felt side.

Local unevenness in felt compressibility tends to generate a corresponding sheet topography not discernible in smoothness/roughness measurements. This will be discussed more fully in subsequent sections.

Linerboard - Recycled Fiber

A few tests on linerboard base sheets made from recycled fiber have been conducted. Results from these tests are presented and compared with corresponding data for virgin fiber sheets in the following sections.

Test Conditions

All sheets for this study were also 127 gr/m^2 and prepressed to about 45% solids. Once-dried fibers are relatively easy to dewater so higher levels of wet pressing may have been an advantage. The intent, however, was to compare with the virgin liner tests under comparable conditions.

Test conditions are presented in Table 14.

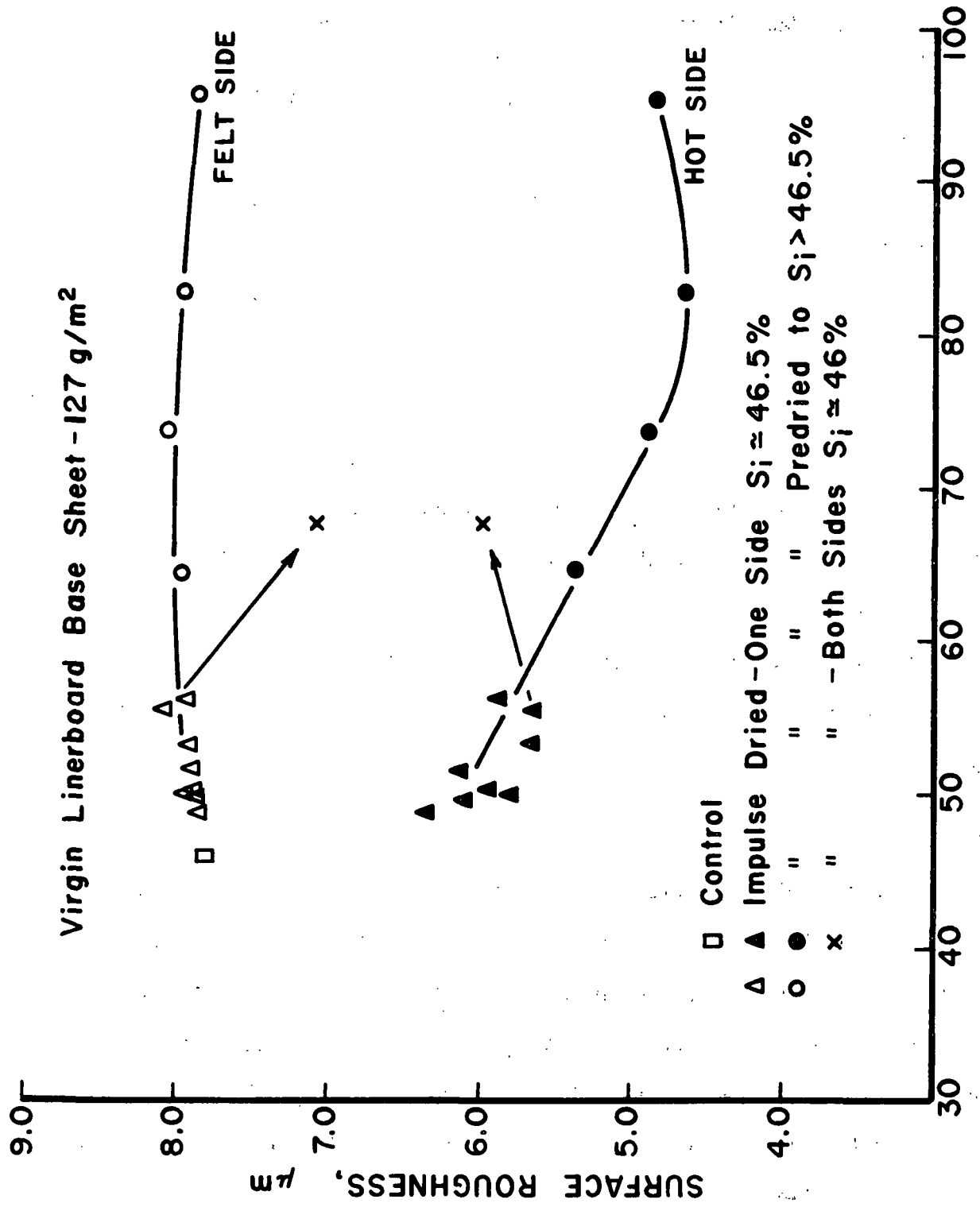

Figure 20. Roughness changes with dryness for virgin linerboard base sheet.

Table 14. Test conditions for recycled fiber linerboard base sheets.

NRT ms	Peak Pressure psi	Initial Temp. °F	Ingoing Solids %
29.5	717	400	45.7
28.9	389	400	45.2
29.1	418	700	45.7
14.0	408	700	45.6
14.5	655	550	45.4
14.7	661	700	45.5

Water Removal Rates

Water removal rates are plotted as a function of temperature divided by the square root of NRT in Fig. 21. These data increase with $T/\sqrt{NRT}$ at about the same rate as for virgin fiber, and also show a modest and probably positive impact of pressure. However, the actual water removal rates are larger than for virgin fiber by at least 400-500 $lb/hr/ft^2$, reflecting the ease of dewatering once-dried fibers.

Property Development

Density development with thermal impulse and with outgoing solids are presented in Figs. 22 and 23, respectively. The density levels for the recycled fiber are about 15% lower than those for the virgin fiber, reflecting the lower strength potential of the fiber (see data for control sheet) or the need for more pressing, or both. Density increases with outgoing solids are about the same for both sheets, but density increses more rapidly with thermal impulse for the recycled fiber.

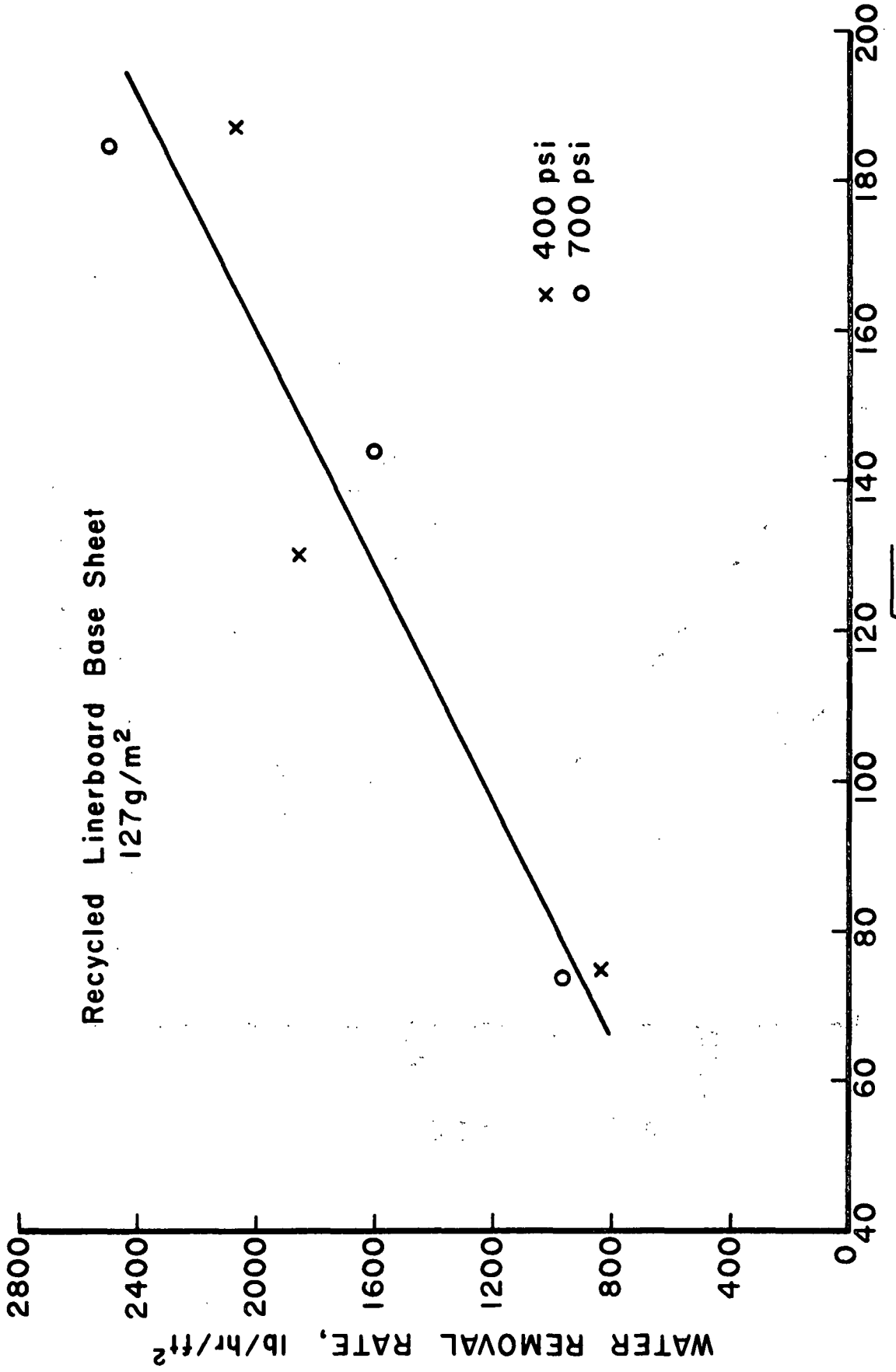

Figure 21. Water removal rates for recycled linerboard base stock.

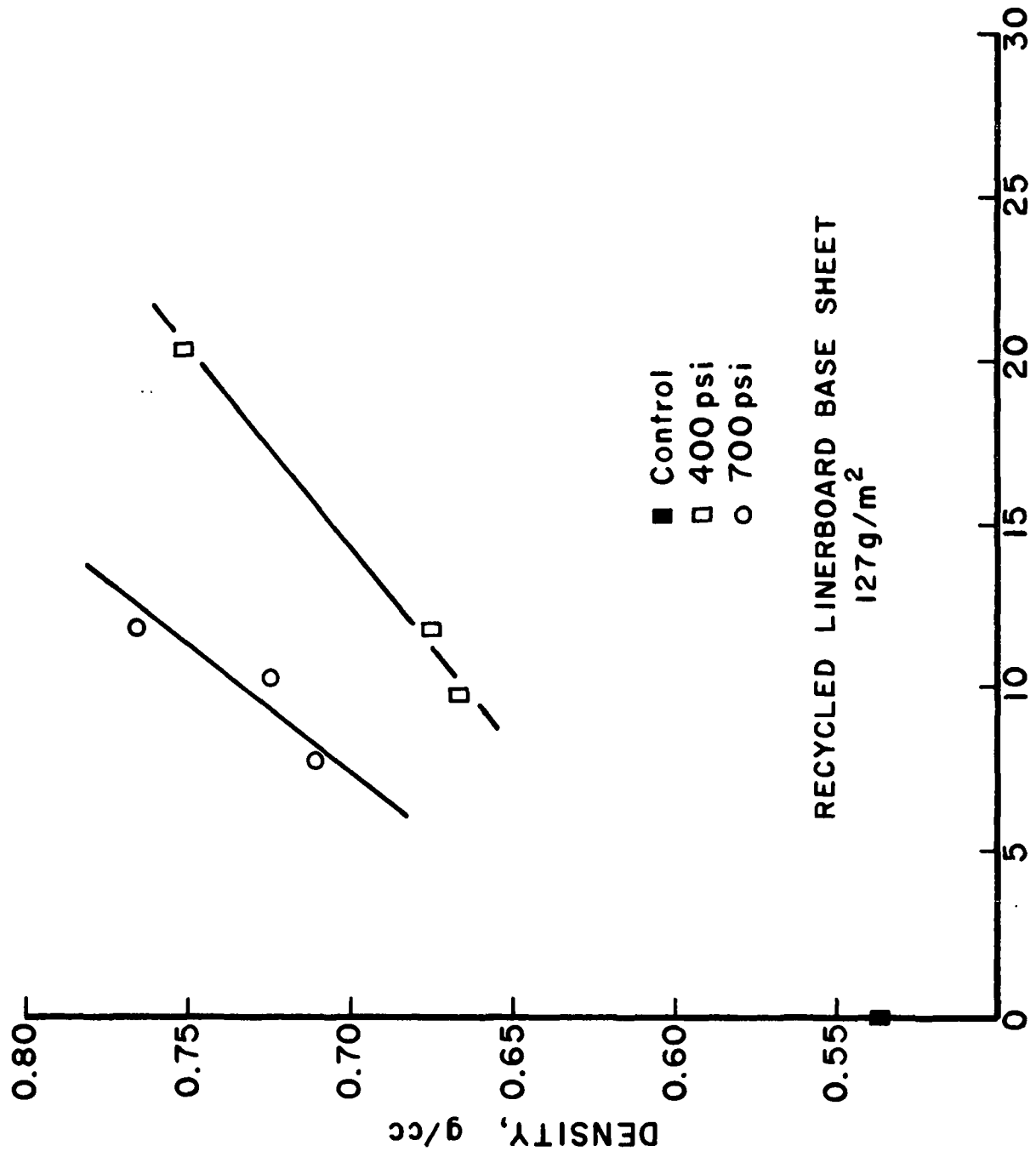

Figure 22. Density development for recycled linerboard base sheet.

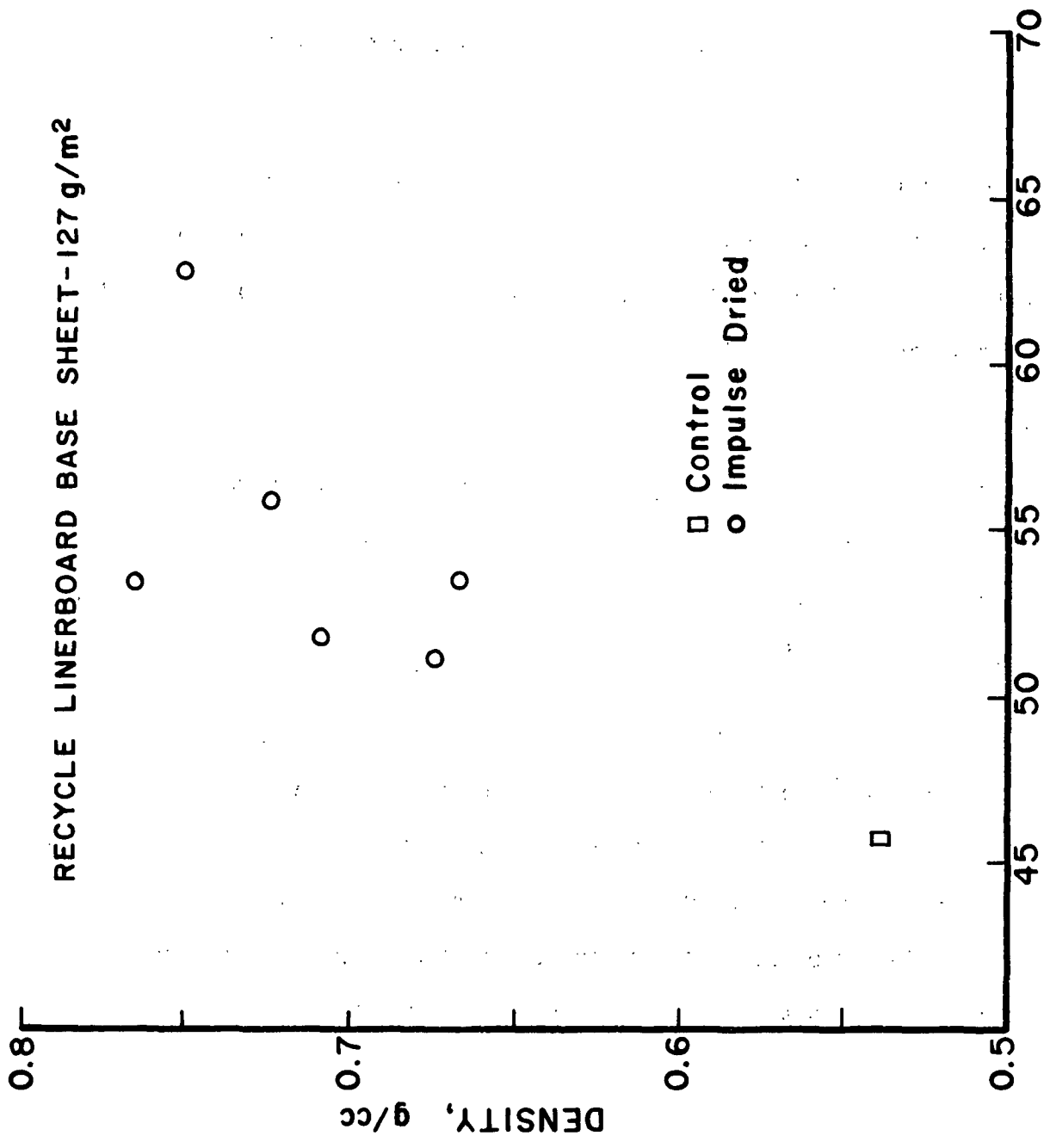

Figure 23. Density development with dryness for recycled linerboard base sheet.

STFI compressive strength variation with density for both the recycled and virgin linerboard furnishes are shown in Fig. 24. The trends are similar for both furnishes, but the absolute values are higher for the virgin fiber, as expected. The compressive strength data for the recycled fiber sheet fit the Whitsitt-Habeger[3] model, as shown in Fig. 25. Burst properties show similar trends.

In summary, impulse drying of a recycled linerboard furnish leads to higher water removal rates and equivalent density and strength development rates, but lower absolute densities and strengths, as compared to impulse drying of a virgin linerboard furnish.

Corrugated Medium

The corrugating medium used in this study was a sodium carbonate semi-chemical virgin fiber furnish. This proved hard to dewater, as the data will show, and only a few tests were conducted. More work is planned, both with this furnish and a recycled fiber furnish.

Water removal rates for the corrugating medium, Fig. 27, show the normal trends with $T/\sqrt{NRT}$, but seem to be somewhat more sensitive to pressure and lower in value than the linerboard data. These rates are still about 200 times higher than for a conventional dryer. Density and strength values, shown in Fig. 28-30, exhibit the usual trends, but there is considerable scatter in the data, largely as a result of the small range of values tested.

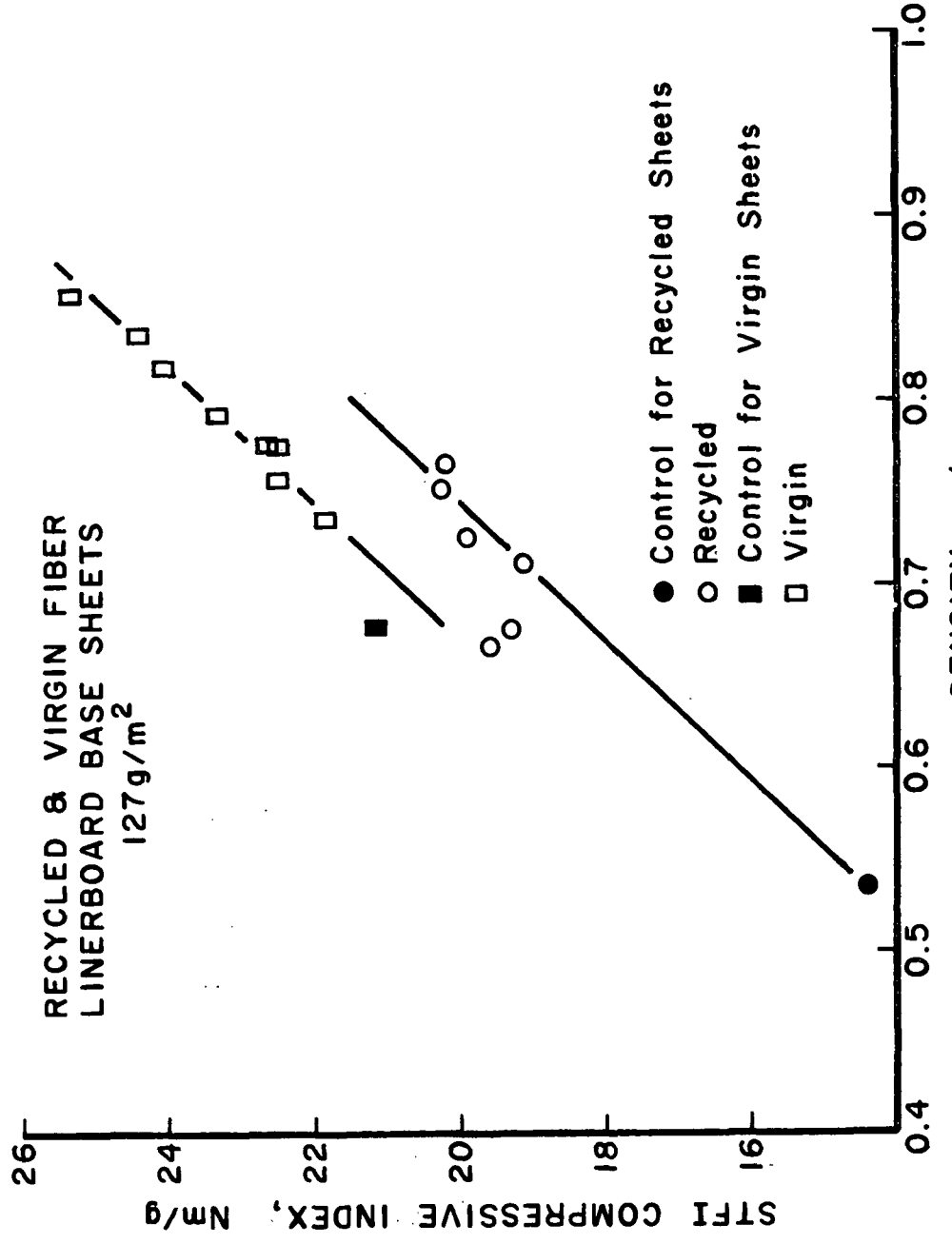

Figure 24. Compressive strength - density relationships for virgin and recycled linerboard.

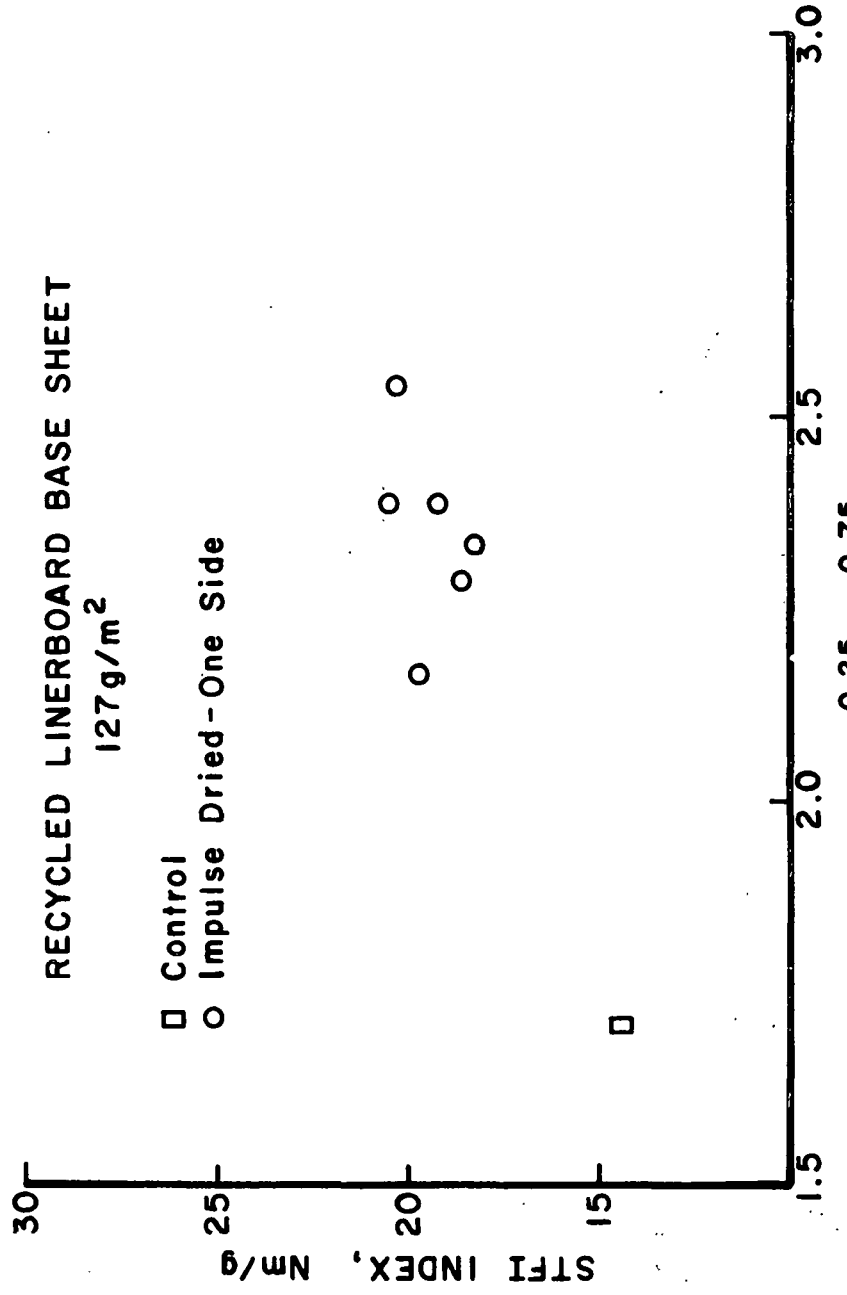

Figure 25. Habeger-Whitsitt compressive strength model for recycled linerboard base sheet.

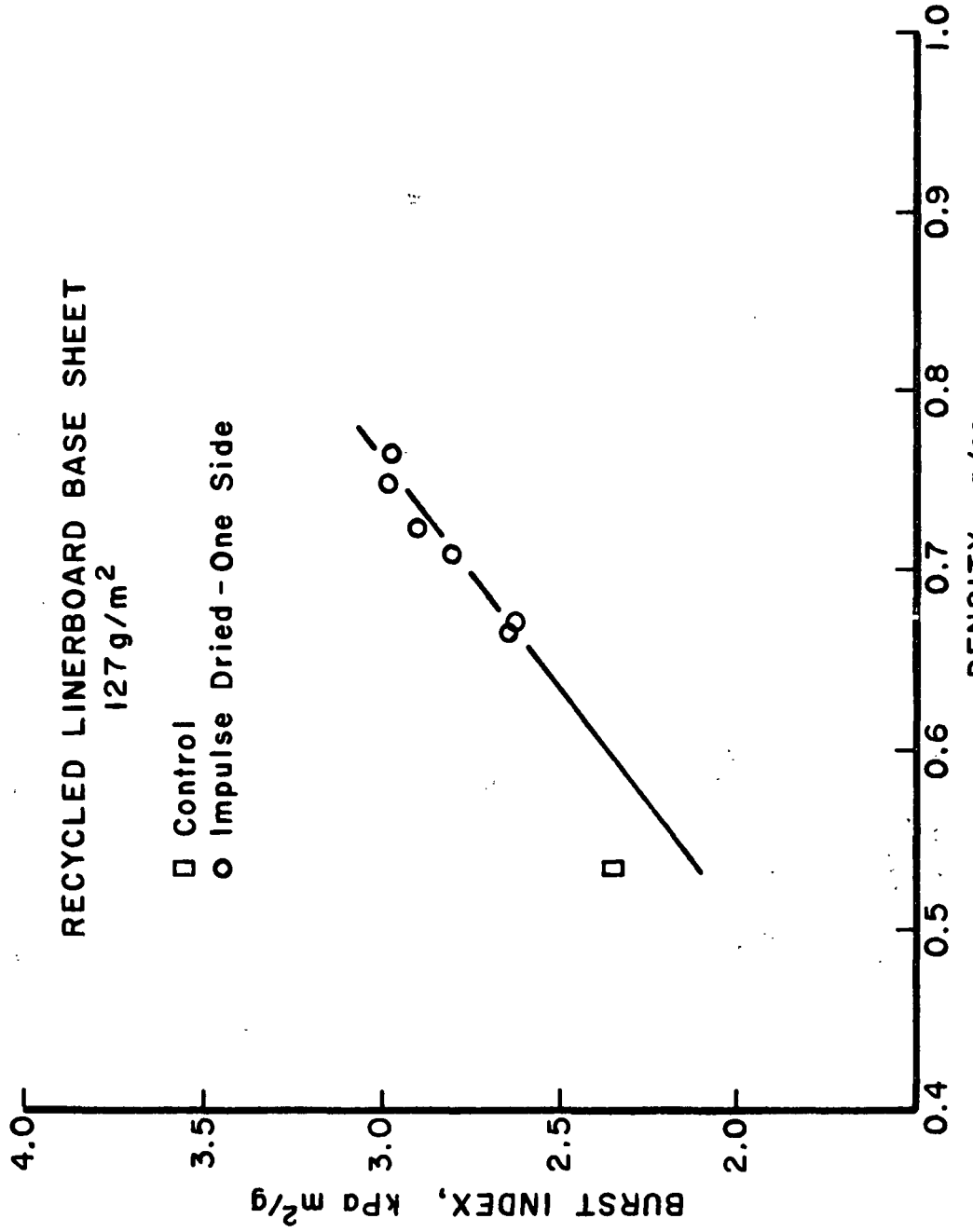

Figure 26. Burst development with density for recycled linerboard base sheet.

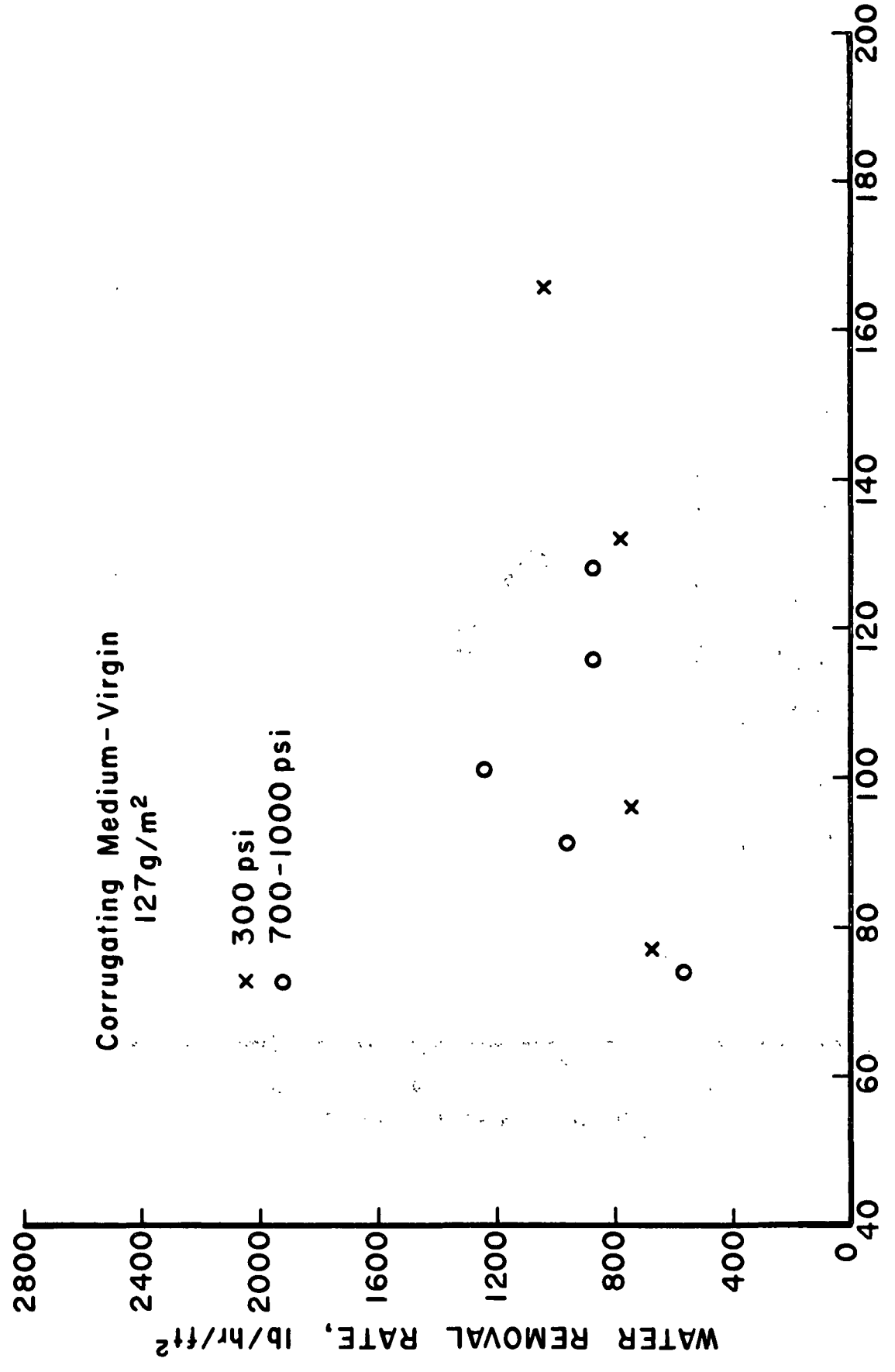

Figure 27. Water removal rates for virgin corrugating medium.

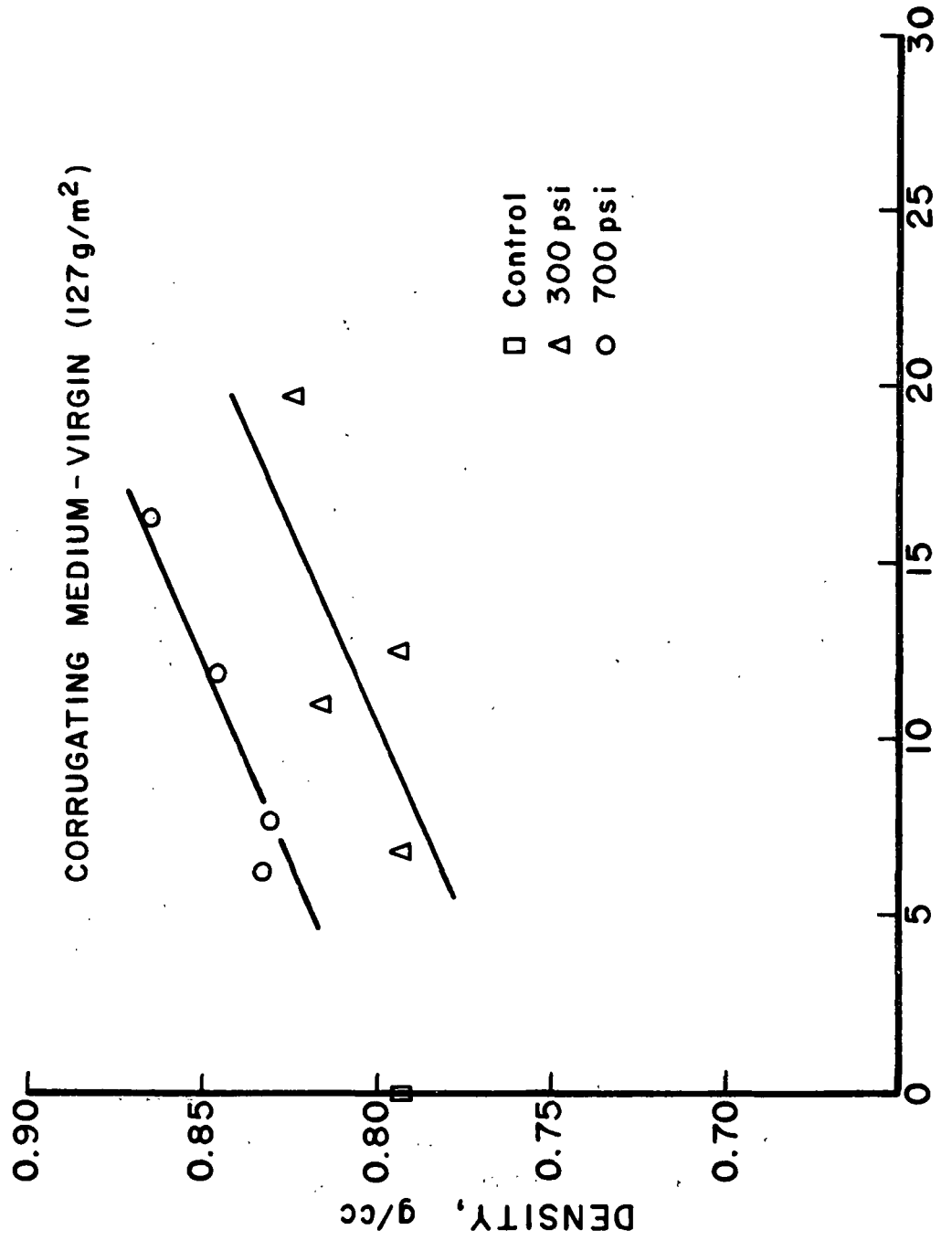

Figure 28. Density development for corrugating medium.

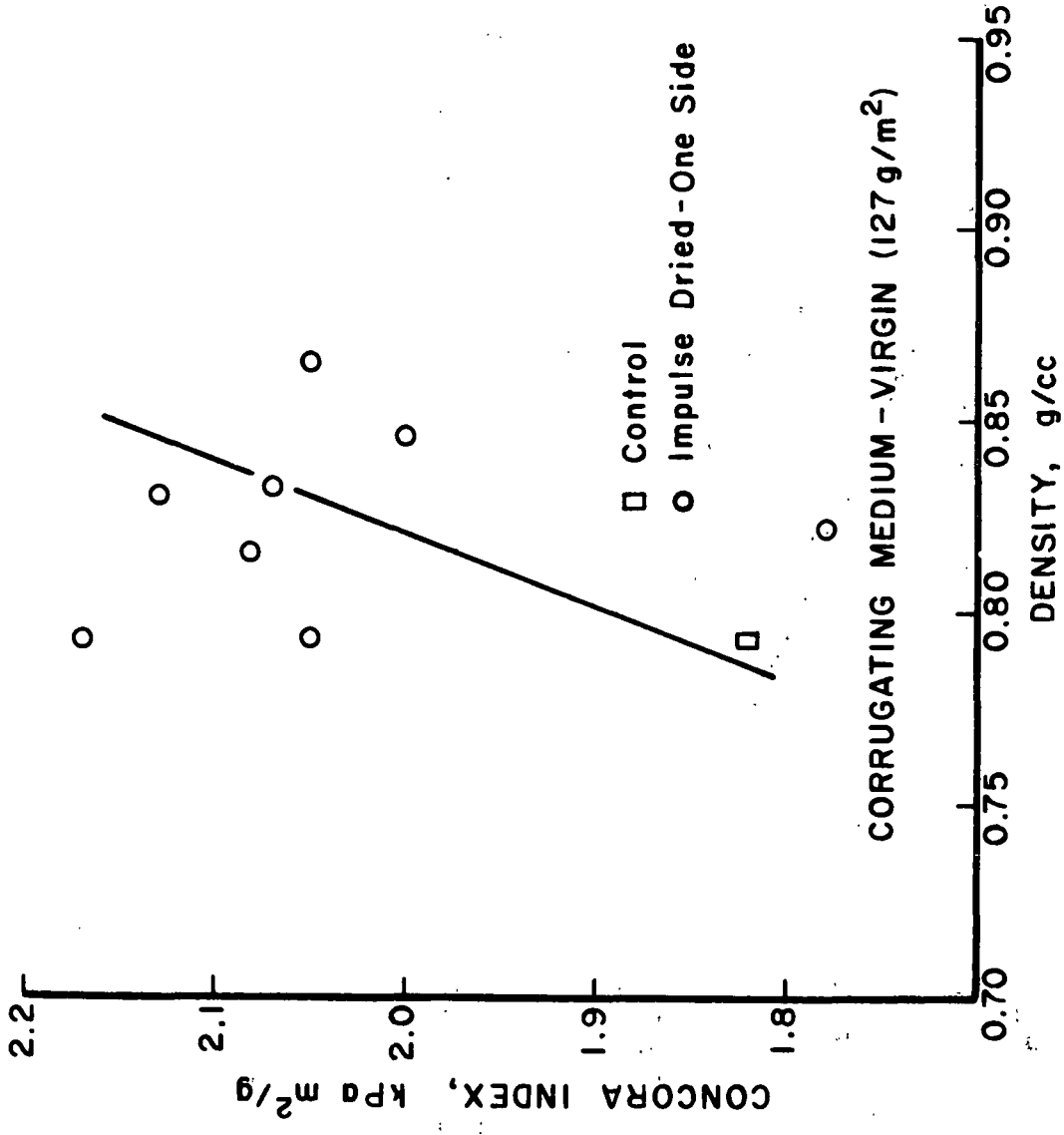

Figure 29. Concora variation with density for virgin corrugating medium.

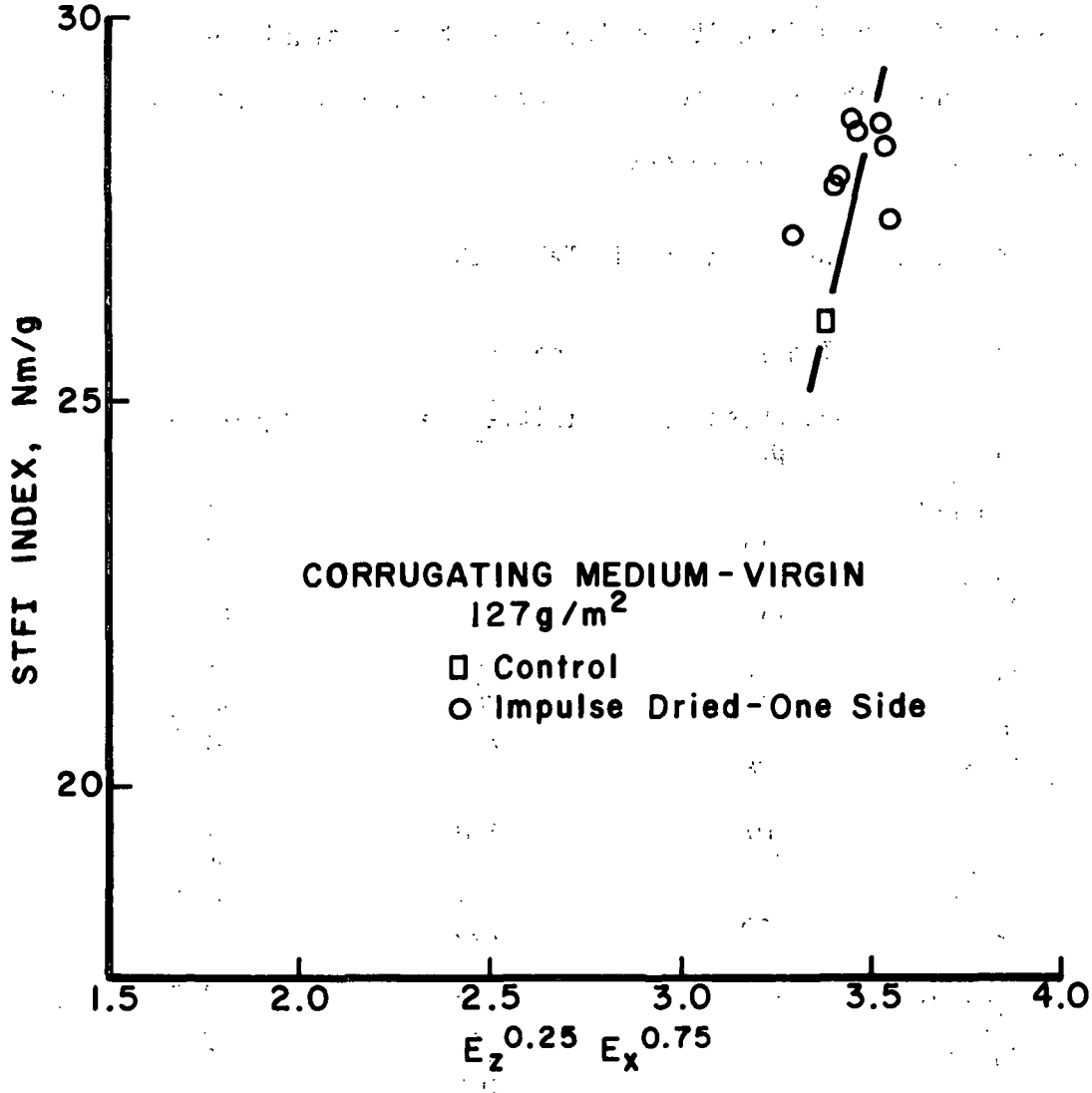

Figure 30. Habeger-Whitsitt compressive strength model for corrugating medium.

Lightweight Coating Grade

Test Conditions

This furnish was originally delivered to the IPC as a newsprint furnish; however, the actual fiber makeup is more typical of a lightweight coating (LWC) grade. Before the true identity of the furnish was established, sheets were made up for a basis weight of about 55 gr/m^2, typical of newsprint weights. All tests were conducted at this weight.

Test conditions are given in Table 15.

Table 15. Test conditions for LWC

NRT ms	Peak Pressure psi	Initial Temp. °F	Ingoing Solids %
Control	- -	- -	51.1
19.3	516	400	51.8
35.5	712	400	51.7
30.7	715	700	51.7
36.0	319	400	51.5
35.6	310	700	51.2
15.4	584	700	51.3
21.5	306	400	50.9
21.4	307	700	51.0
30.0	712	700	35.9
Control	- -	- -	36.6
30.0	720	700	38.0
Control	- -	- -	38.2
30.0	718	700	43.0
Control	- -	- -	43.1
30.0	723	700	56.5
Control	- -	- -	56.6
300	715	700	51.7
Control	- -	- -	51.1

Water Removal Rates

This grade also shows water removal rates that are essentially linear with $T/\sqrt{NRT}$ and mildly influenced by pressure, Fig. 31. Also included in Fig. 31 are data that show water removal rates that rapidly decrease with ingoing solids content. These data are presented more explicitly as water removal rate and outgoing solids as functions of ingoing solids in Fig. 32. Outgoing solids variations are leveled to about one-third of ingoing variations, a figure typical of may pressing operations, and indicative of the profile leveling capability of impulse drying.

Property Development

Density development with thermal impulse and with outgoing solids are presented in Figs. 33 and 34, respectively. Tensile-density and tensile-tear relationships are shown in Figs. 35 and 36, respectively. None of these relationships show any new feature or unexpected behavior.

TAPPI brightness and opacity data are presented as a function of density in Fig. 37 and as a function of outgoing solids in Fig. 38. Brightness tends to decline very slightly for the highest levels of drying intensity whereas opacity tends to decline slowly over the whole range, dropping by about five percentage points for outgoing solids levels of about 85%.

Roughness values for both sides, plotted against outgoing solids in Fig. 39, show a strong smoothing trend on the hot side of the sheet and a slight roughening trend on the felt side. Such sheets would normally be impulse dried on both sides which, as noted before, tends to equalize smoothness.

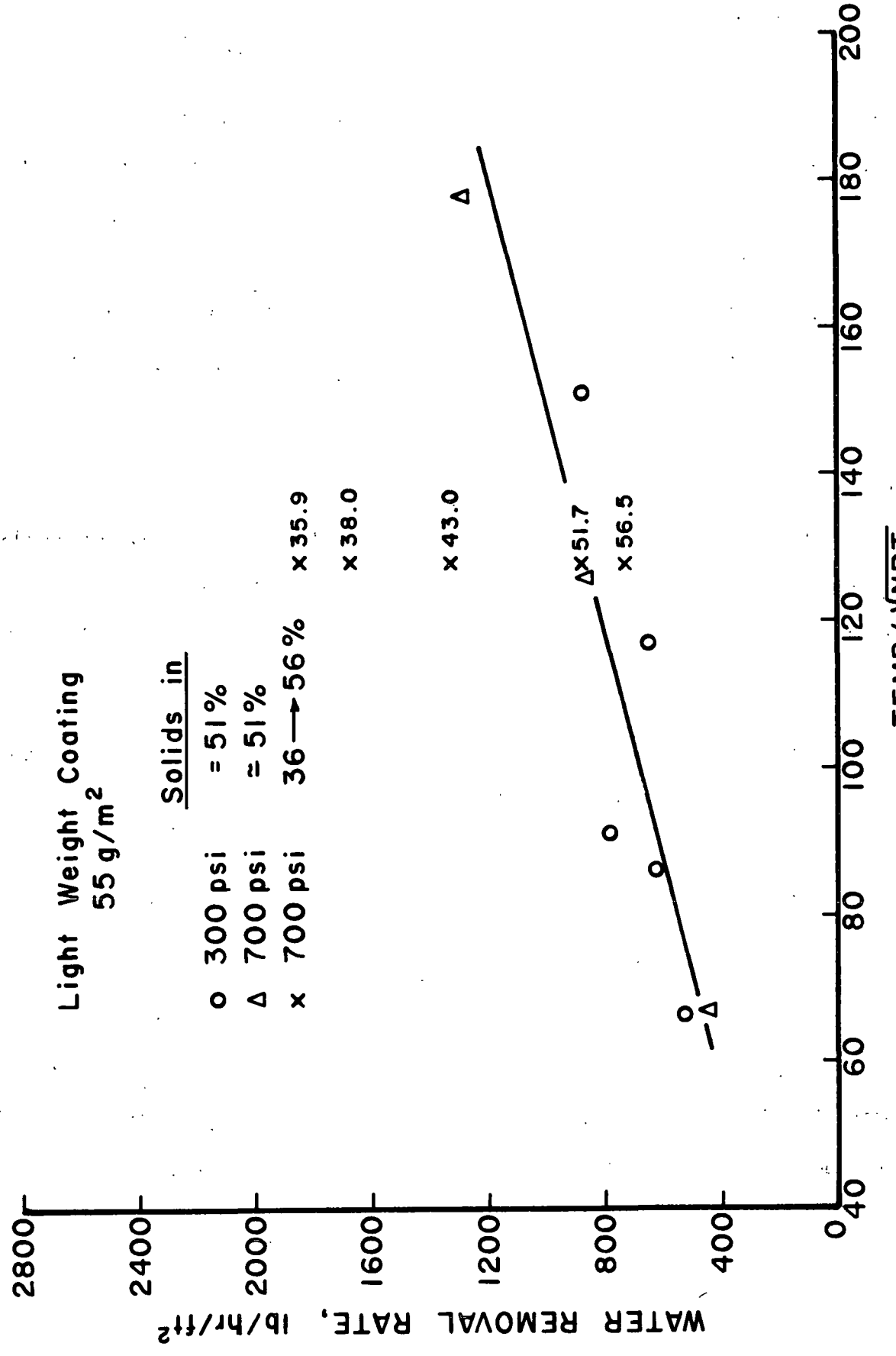

Figure 31. Water removal rates for lightweight coating paper.

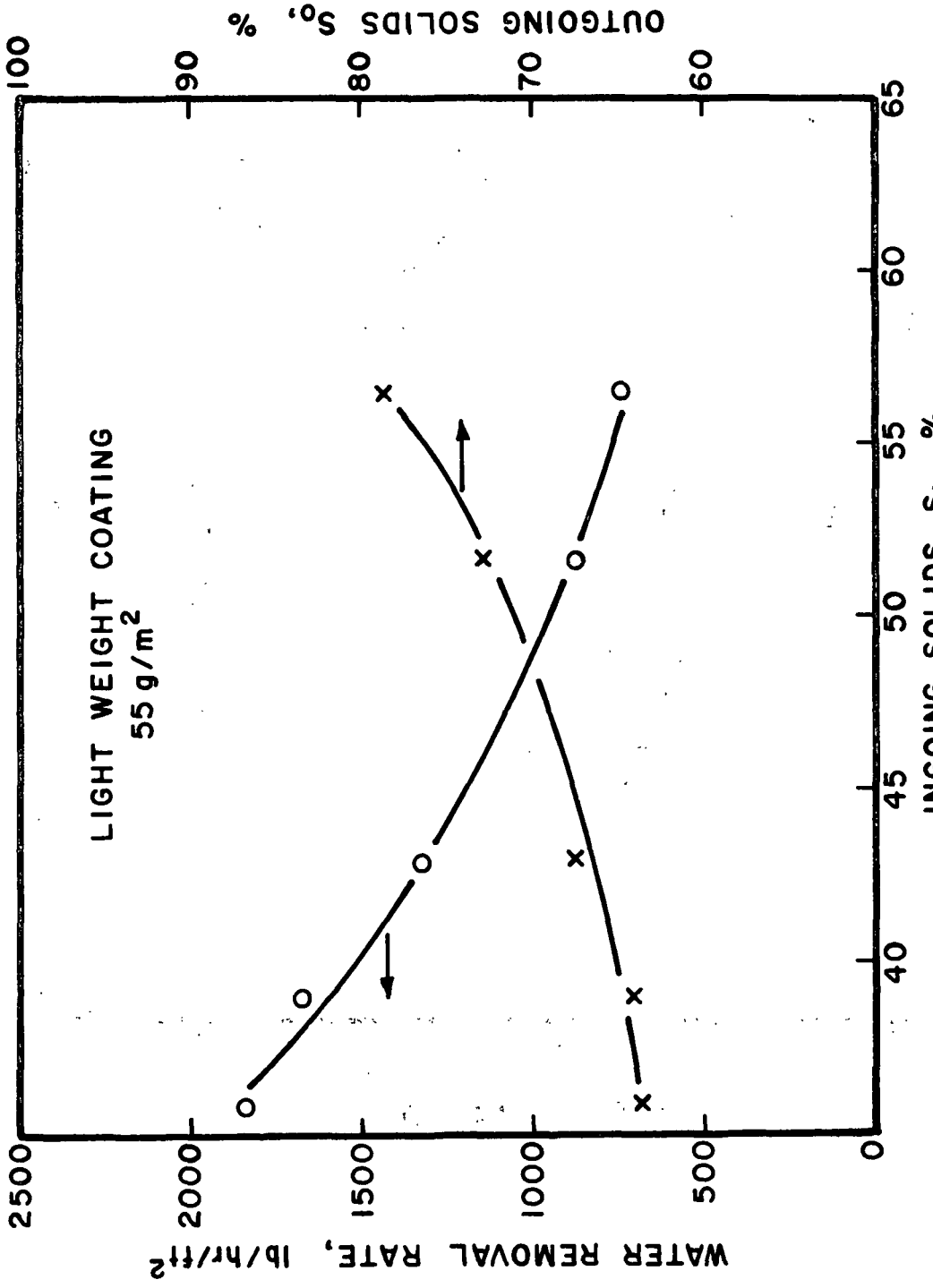

Figure 32. Water removal rate and outgoing solids variations with prepressing level for lightweight coating paper.

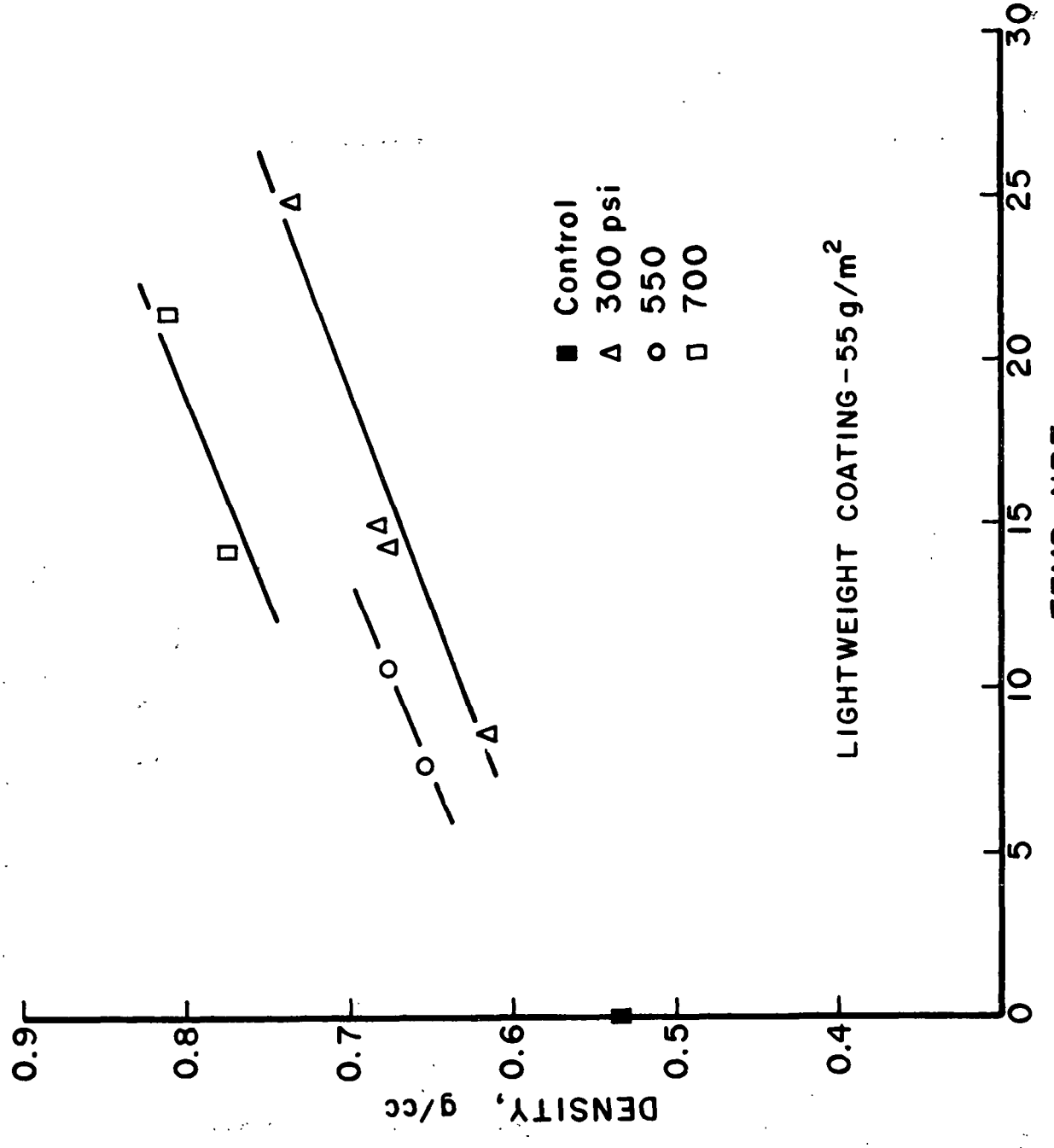

Figure 33. Density development for lightweight writing paper.

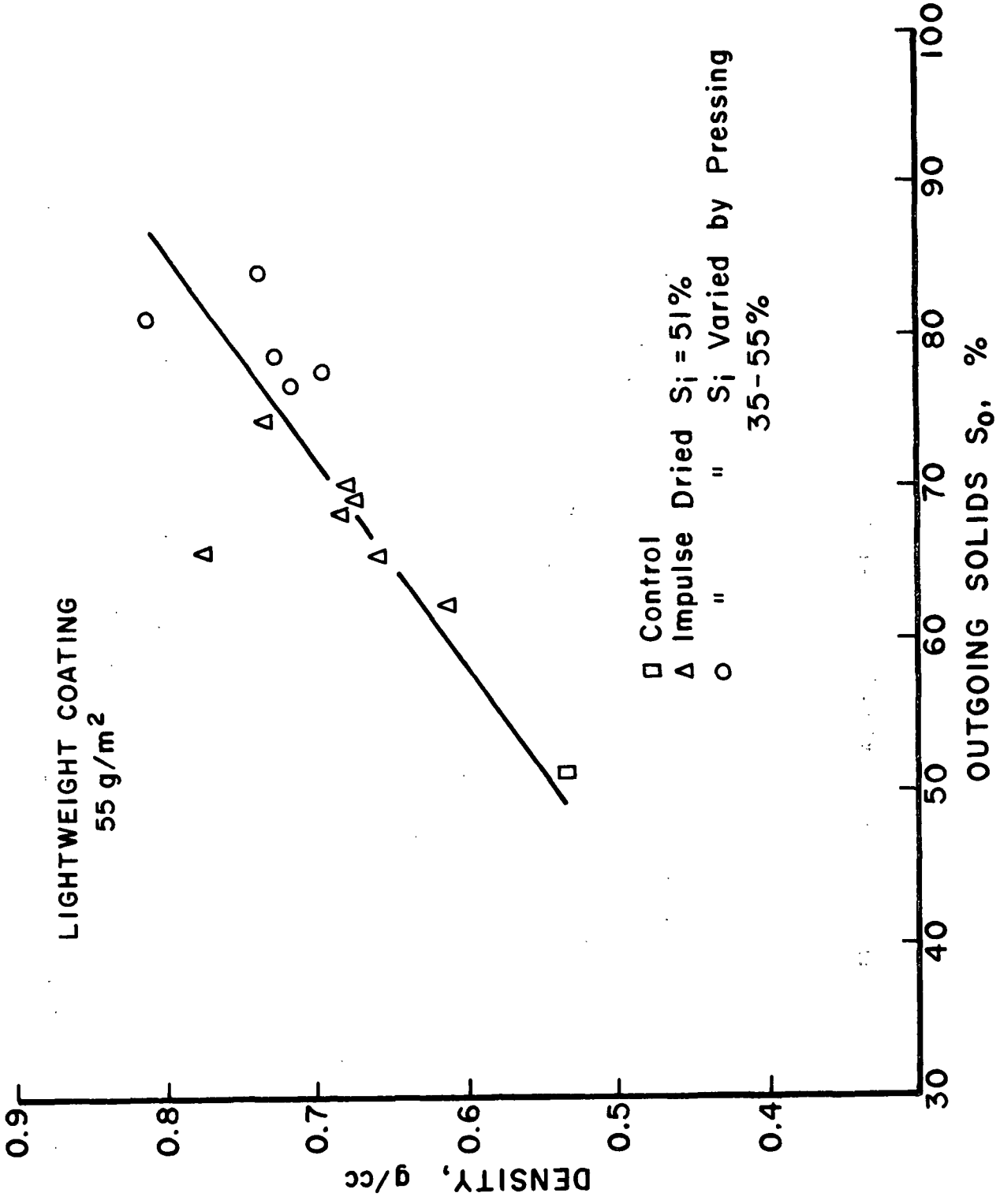

Figure 34. Density development with dryness for lightweight coating grade.

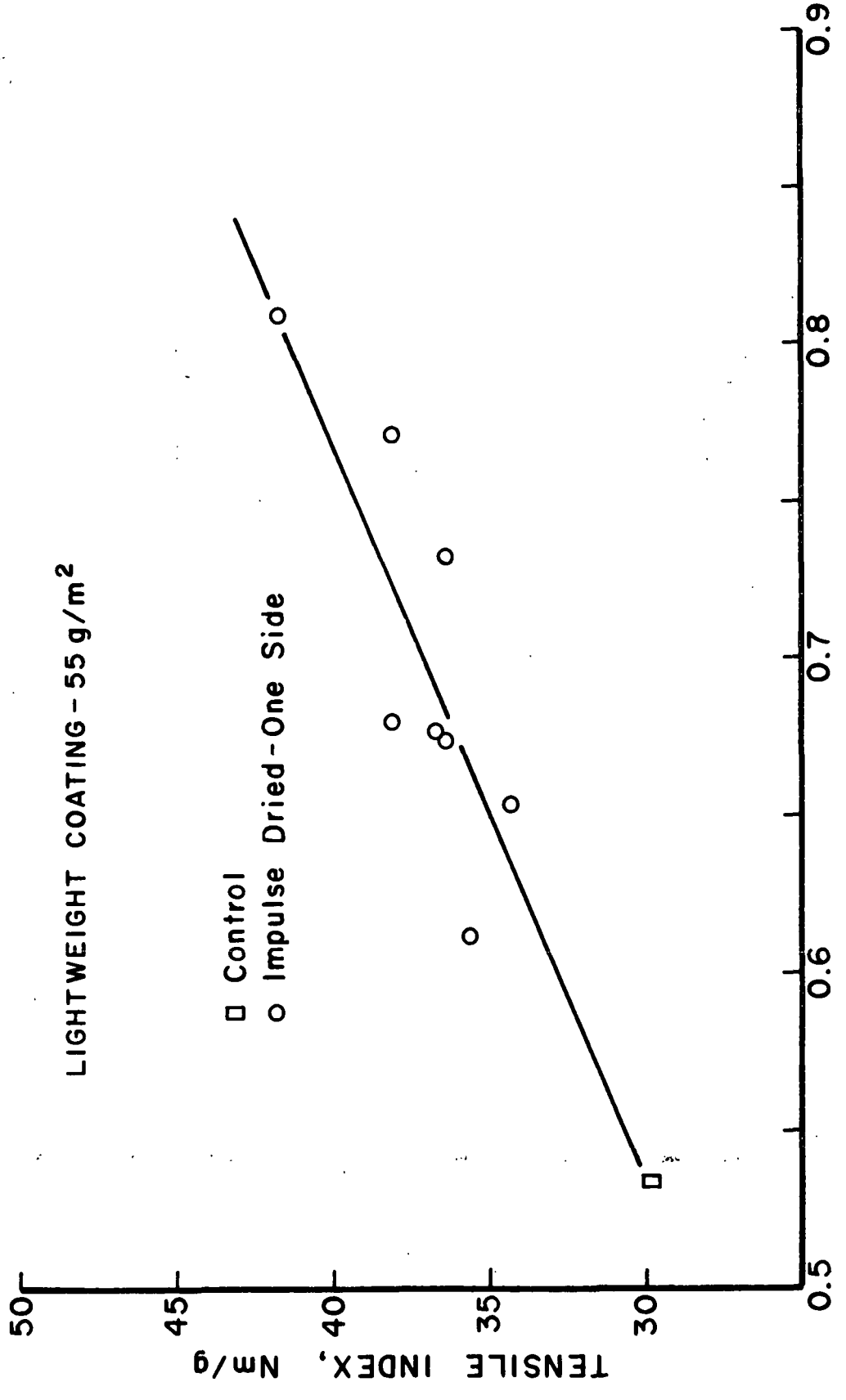

Figure 35. Tensile strength development with density for lightweight coating paper.

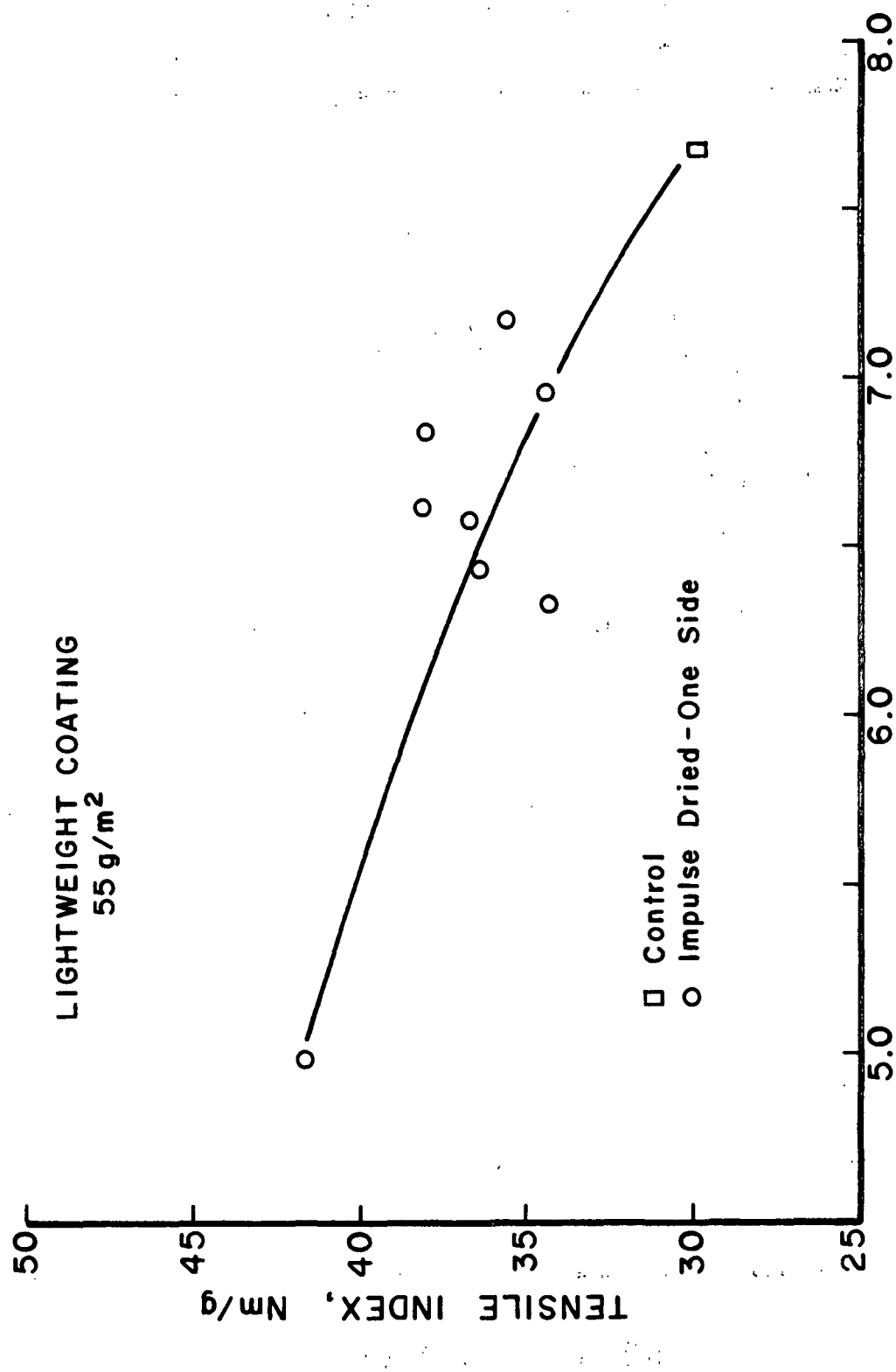

Figure 36. Tensile-tear relationship for lightweight coating paper.

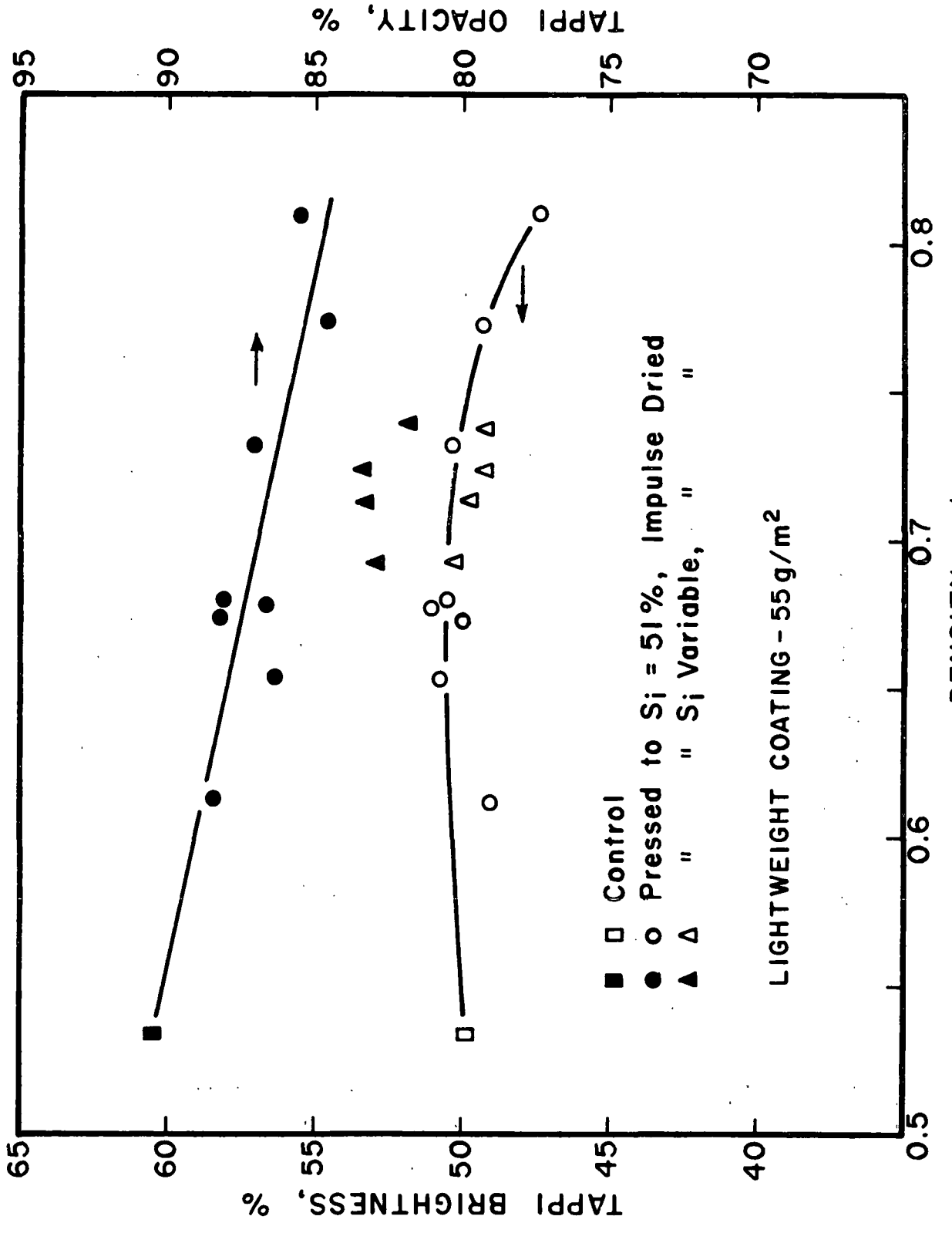

Figure 37. Brightness and opacity changes with density for lightweight coating paper.

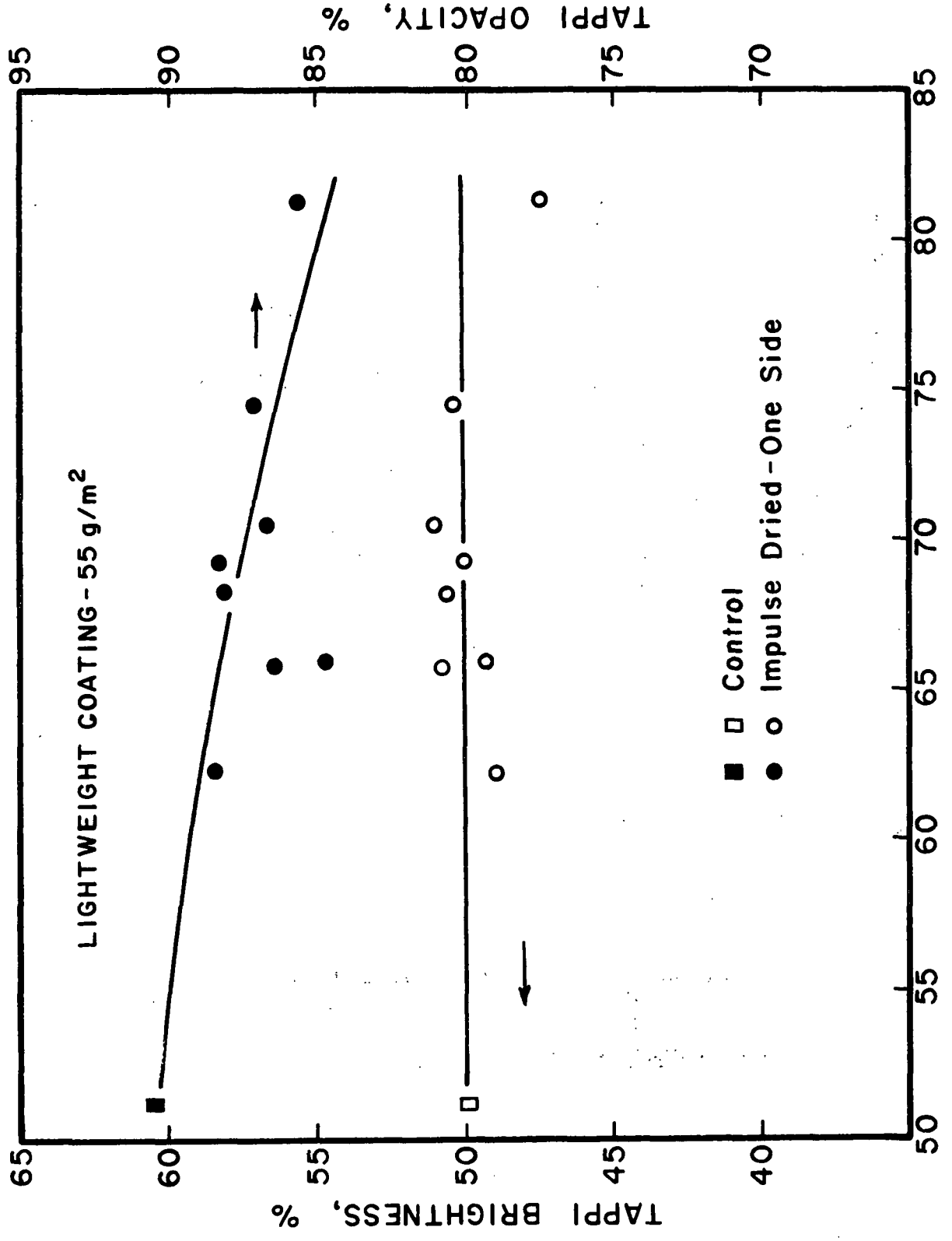

Figure 38. Brightness and opacity changes with dryness for lightweight coating paper.

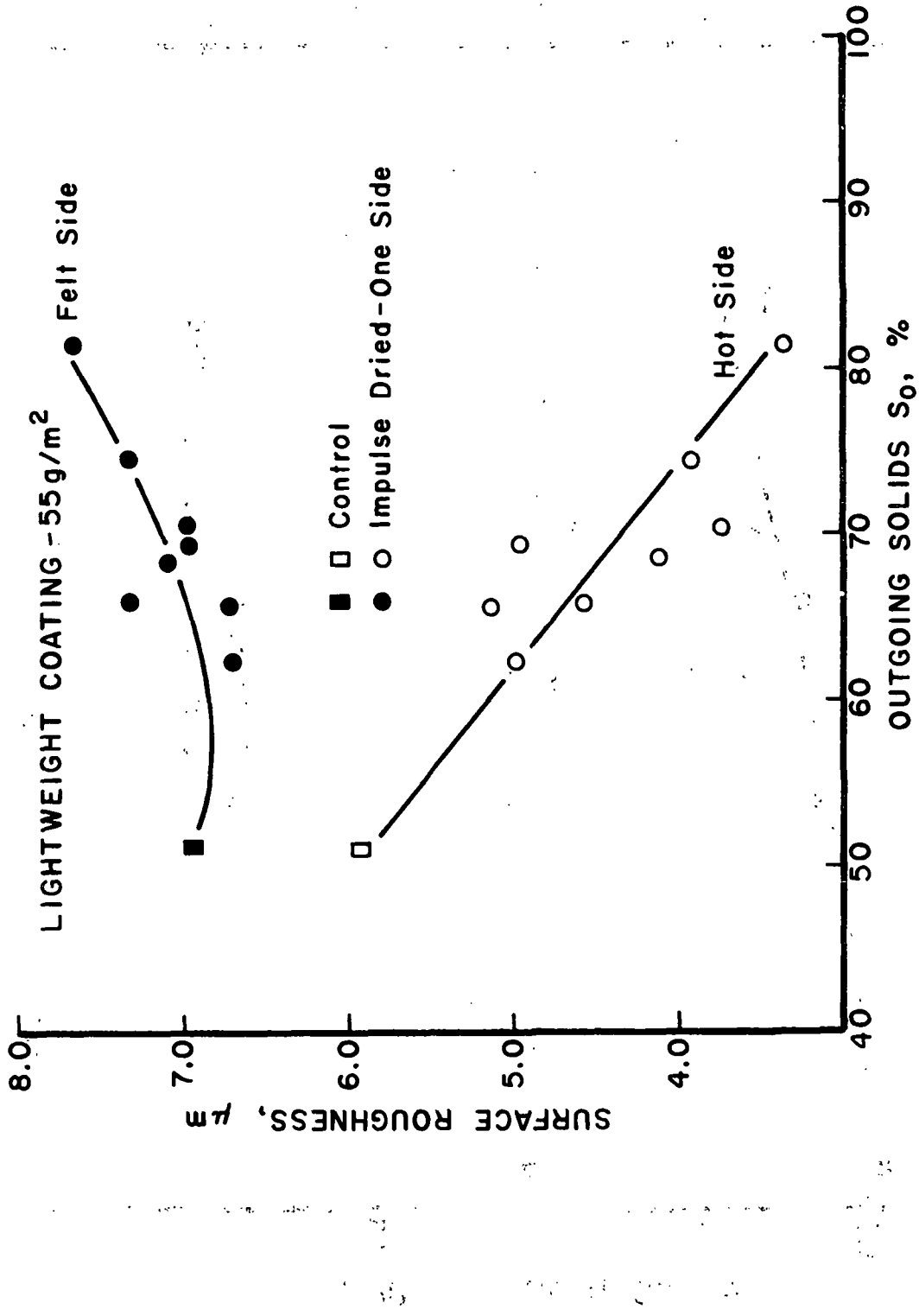

Figure 39. Roughness changes with dryness for lightweight coating paper.

Air permeability declines rapidly with increased levels of drying, as shown in Fig. 40, presumably because the sheet pores become quite closed at the sheet surface on the hot side. Perhaps for similar reasons, ink penetration, shown in Fig. 41, is also reduced, although the data are quite scattered. Ink penetration seems to be reduced by even the lightest intensity of impulse drying, and then remains constant or increases with increased drying. More data are needed to clarify this picture.

Newsprint

Test Conditions

This furnish was produced by blending about 20% BSWK and 80% GW. The target basis weight value was 49 gr/m^2, but actual values were closer to 52 gr/m^2. Test conditions are given in Table 16. In each of the subsequent plots, the datum for the two-sided drying test carries a separate symbol for ease of identification.

Table 16. Test conditions for newsprint.

NRT ms	Peak Pressure psi	Initial Temp. °F	Ingoing Solids %
Control	- -	- -	52.9
25.4	733	400	52.5
25.2	734	700	52.8
20.1	327	400	53.2
19.9	321	700	52.4
16.1	304	400	53.5
16.0	306	700	53.3
14.3	701	400	52.5
14.5	532	700	52.6
*14.6	558	700	53.6

* Two-sided Drying - NRT = Nip Time - Each Side

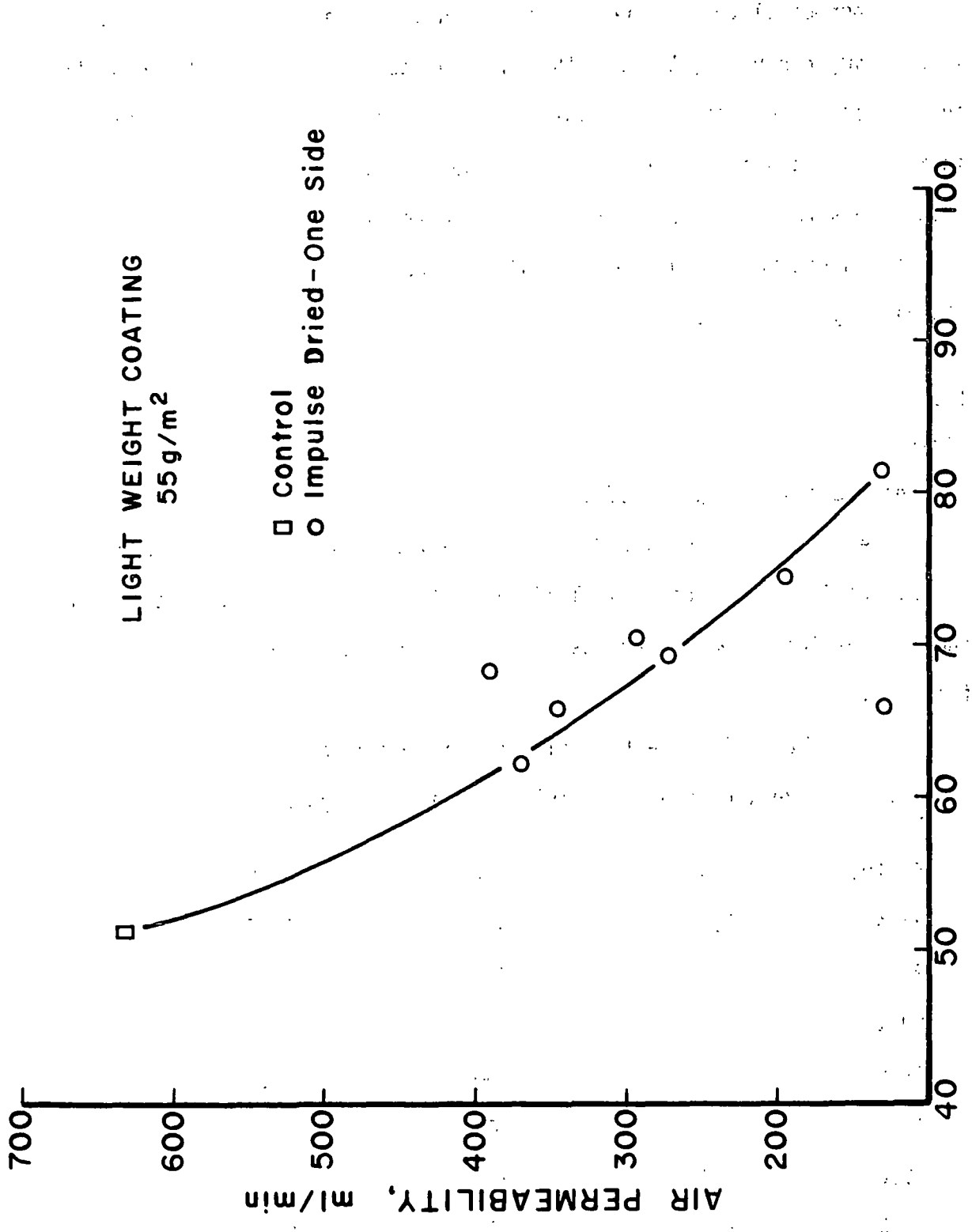

Figure 40. Air permeability variations with outgoing solids for lightweight coating paper.

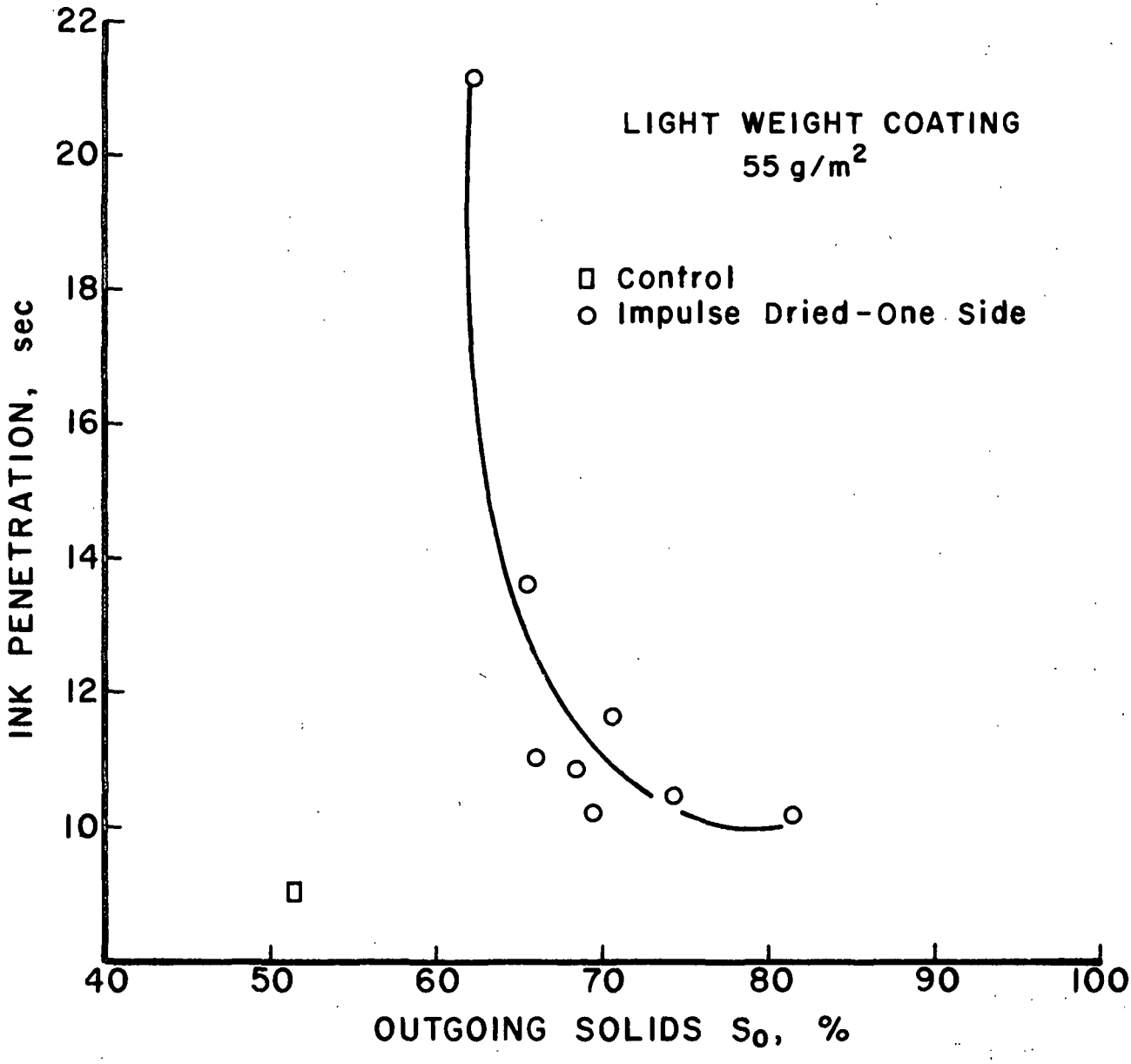

Figure 41. Ink penetration variation with outgoing solids for lightweight coating paper.

Water Removal Rates

Water removal rates, shown in Fig. 42, are linearly and closely related to $T/\sqrt{NRT}$, but show almost no sensitivity to pressure. The absolute values are well below those for a higher freeness furnish such as linerboard, despite the low basis weight.

Property Development

Density in relation to thermal impulse and to outgoing solids is shown in Figs. 43 and 44, respectively. As with all grades, density varies linearly with thermal impulse, increases significantly with pressure, and is linearly related to outgoing solids. The value for two-sided drying fits the same pattern.

The tensile-density and tensile-tear relationships, shown in Figs. 45 and 46, exhibit expected characteristics, except for the datum from the two-sided drying experiment. This sheet showed both increased tensile and tear, relative to the control, an unexpected and important trend, if it is real. Tear values were not measured on the linerboard sheets dried on two sides, so no additional data are available. This point deserves additional attention.

Surface roughness for the two sides of the sheets, plotted against outgoing solids in Fig. 47, show behavior typical of all impulse dried sheets.

Brightness and opacity both trend downward with increasing levels of drying degree or outgoing solids, as shown in Fig. 48. In both cases, the loses are about 6-7 percentage points over the solids range from 50-90%. Relative to the LWC grade with about 50% BSWK, this opacity loss is about the same, but the brightness loss is much greater.

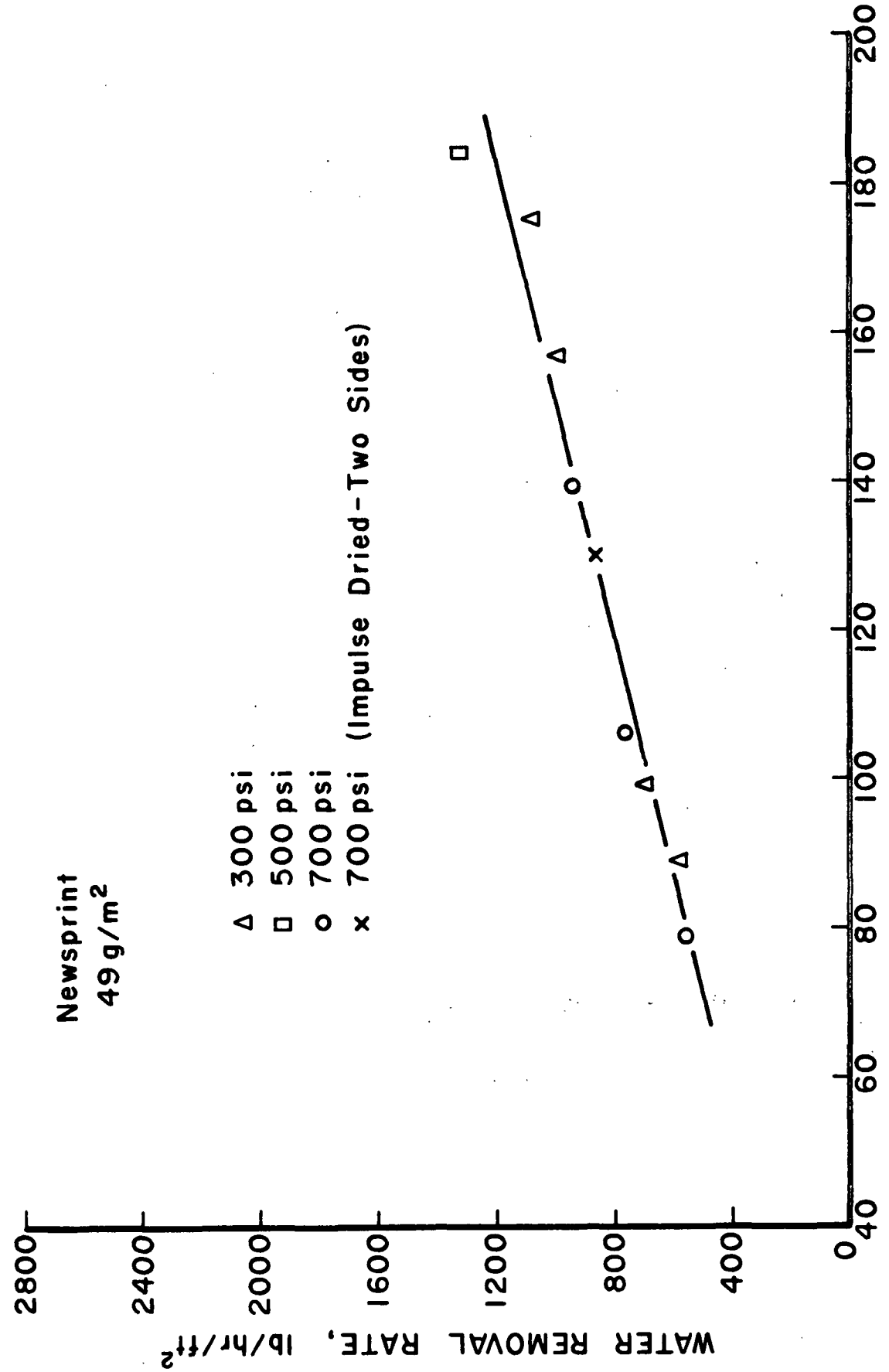

Figure 42. Water removal rates for newsprint.

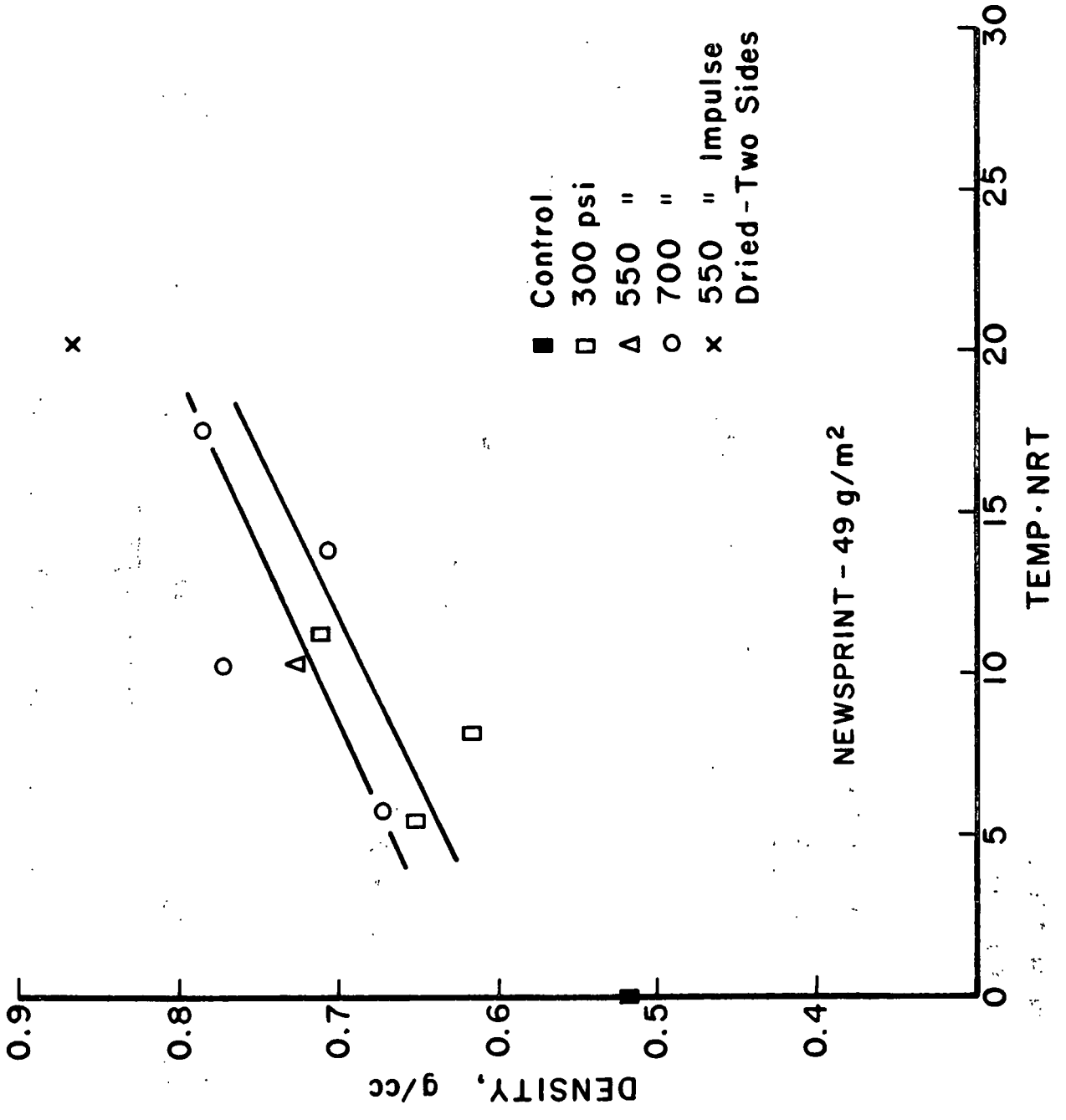

Figure 43. Density development for newsprint.

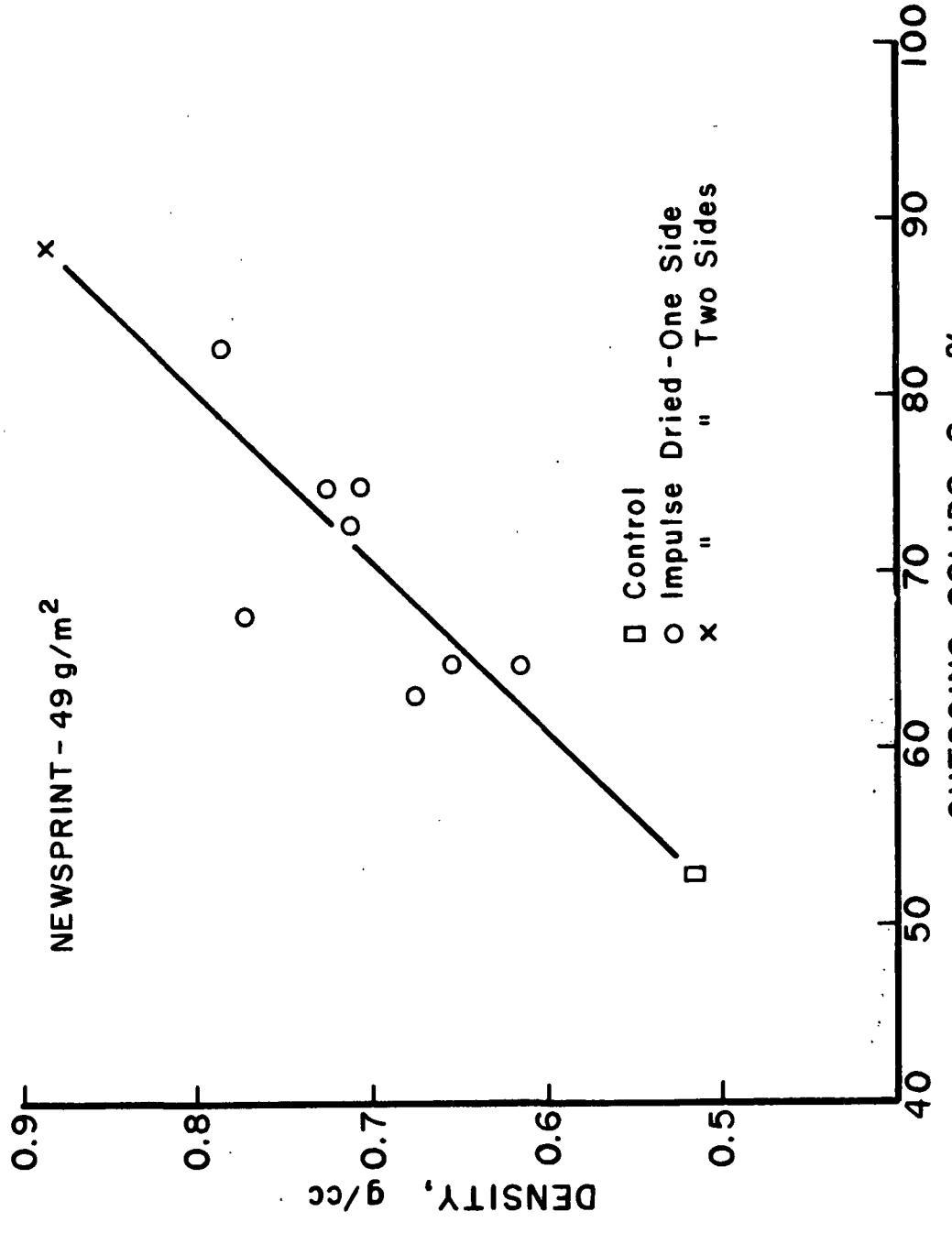

Figure 44. Density development with dryness for newsprint.

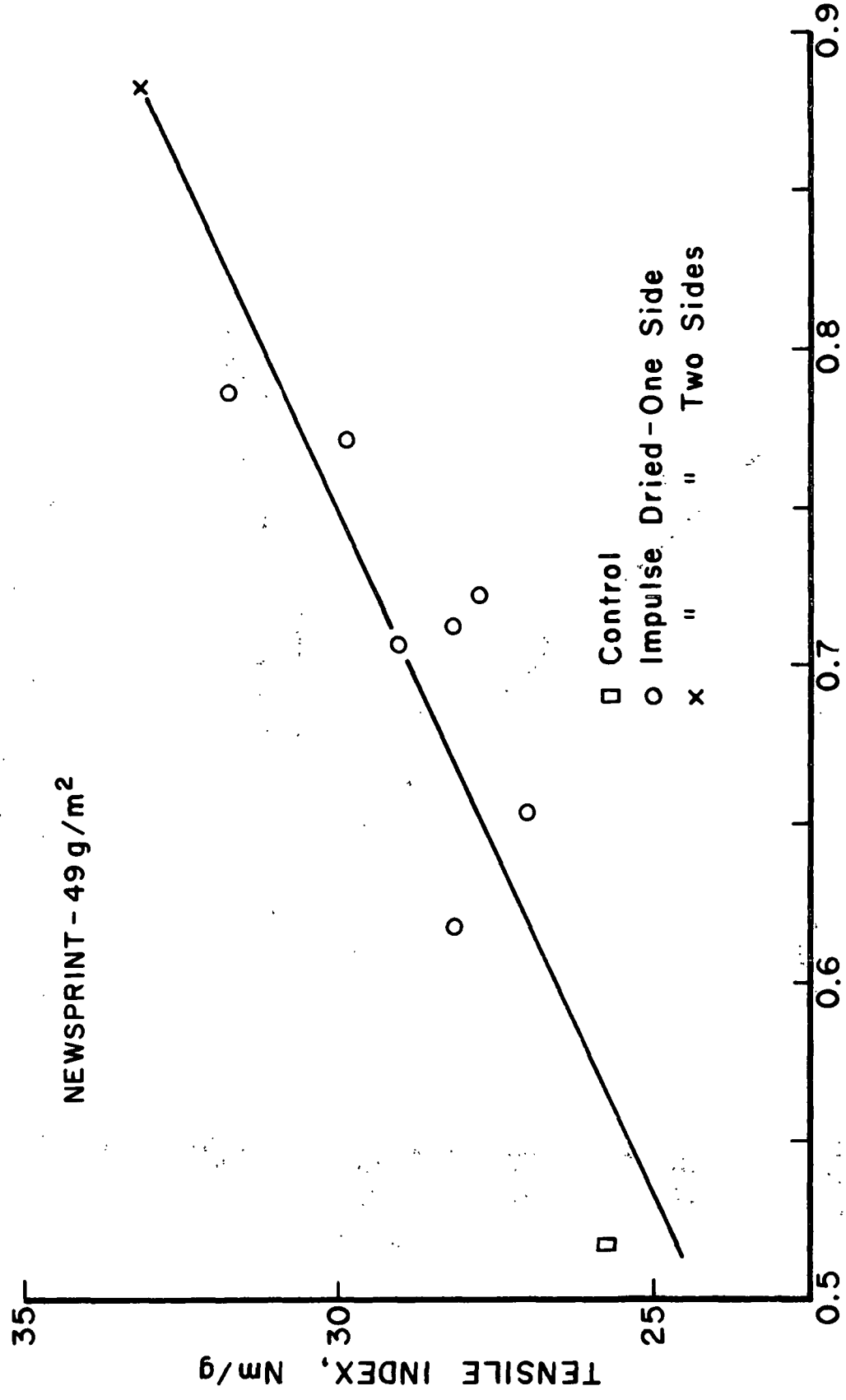

Figure 45. Tensile strength development with density for newsprint.

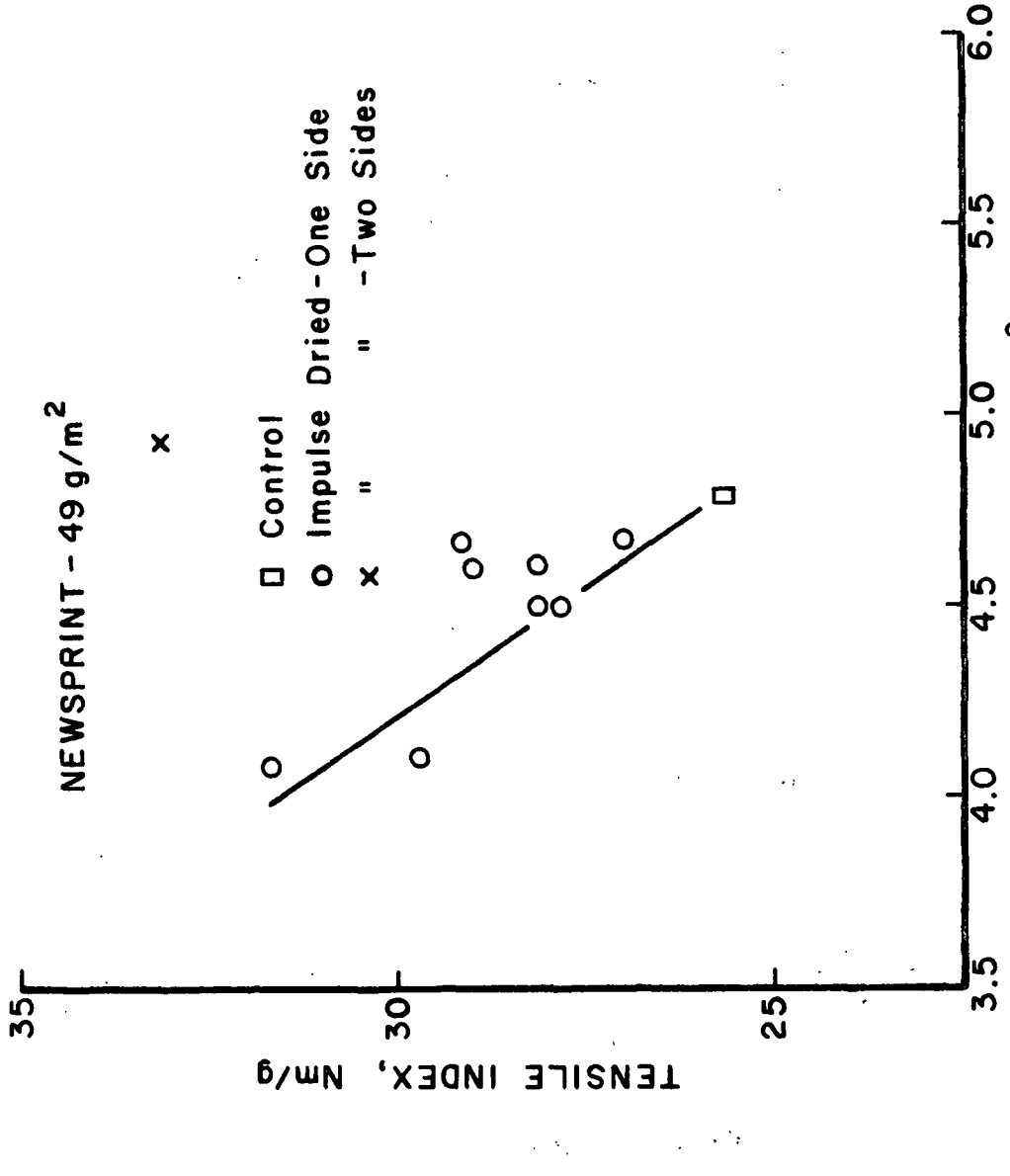

Figure 46. Tensile-tear relationship for newsprint.

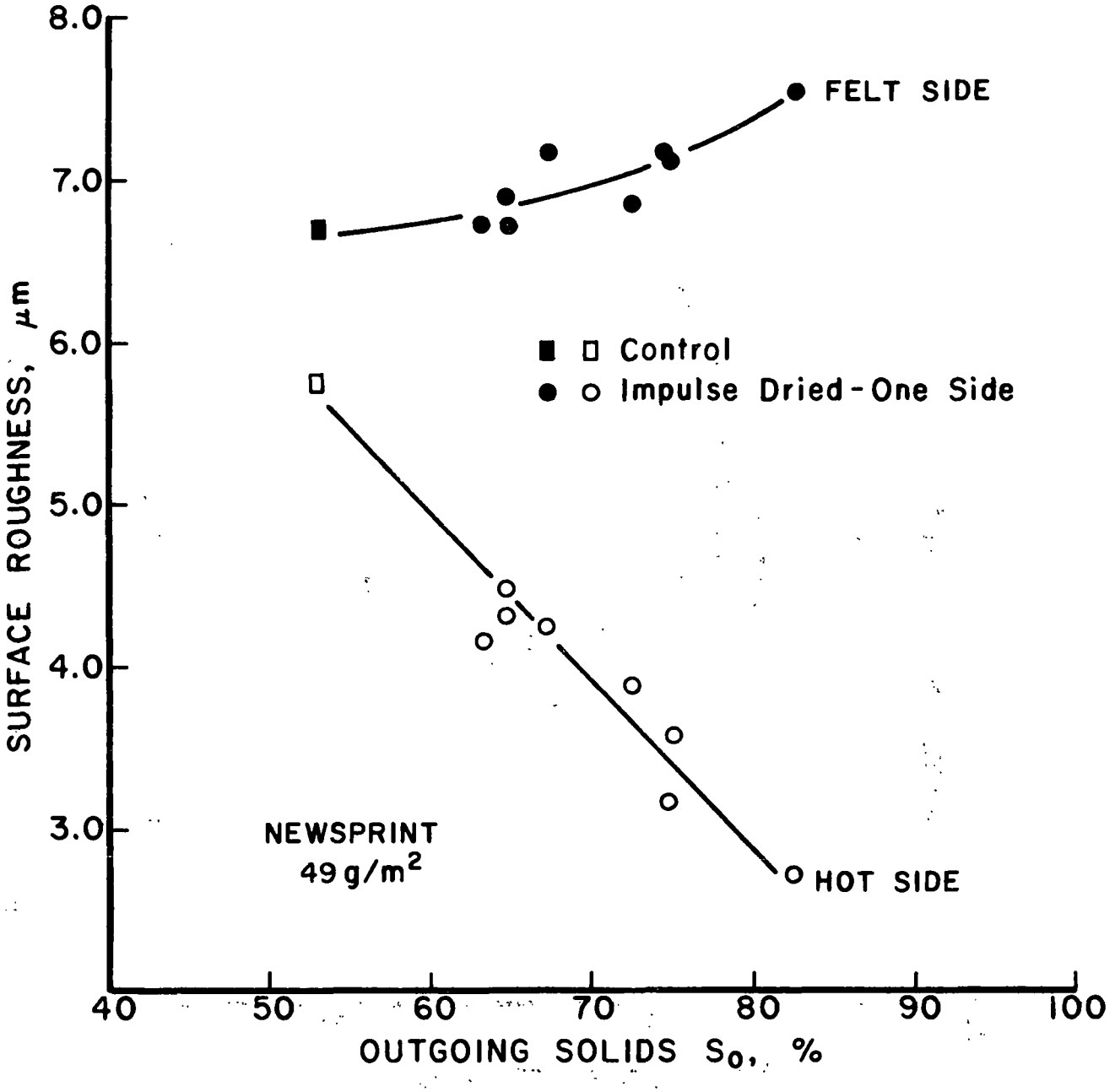

Figure 47. Roughness changes with dryness for newsprint.

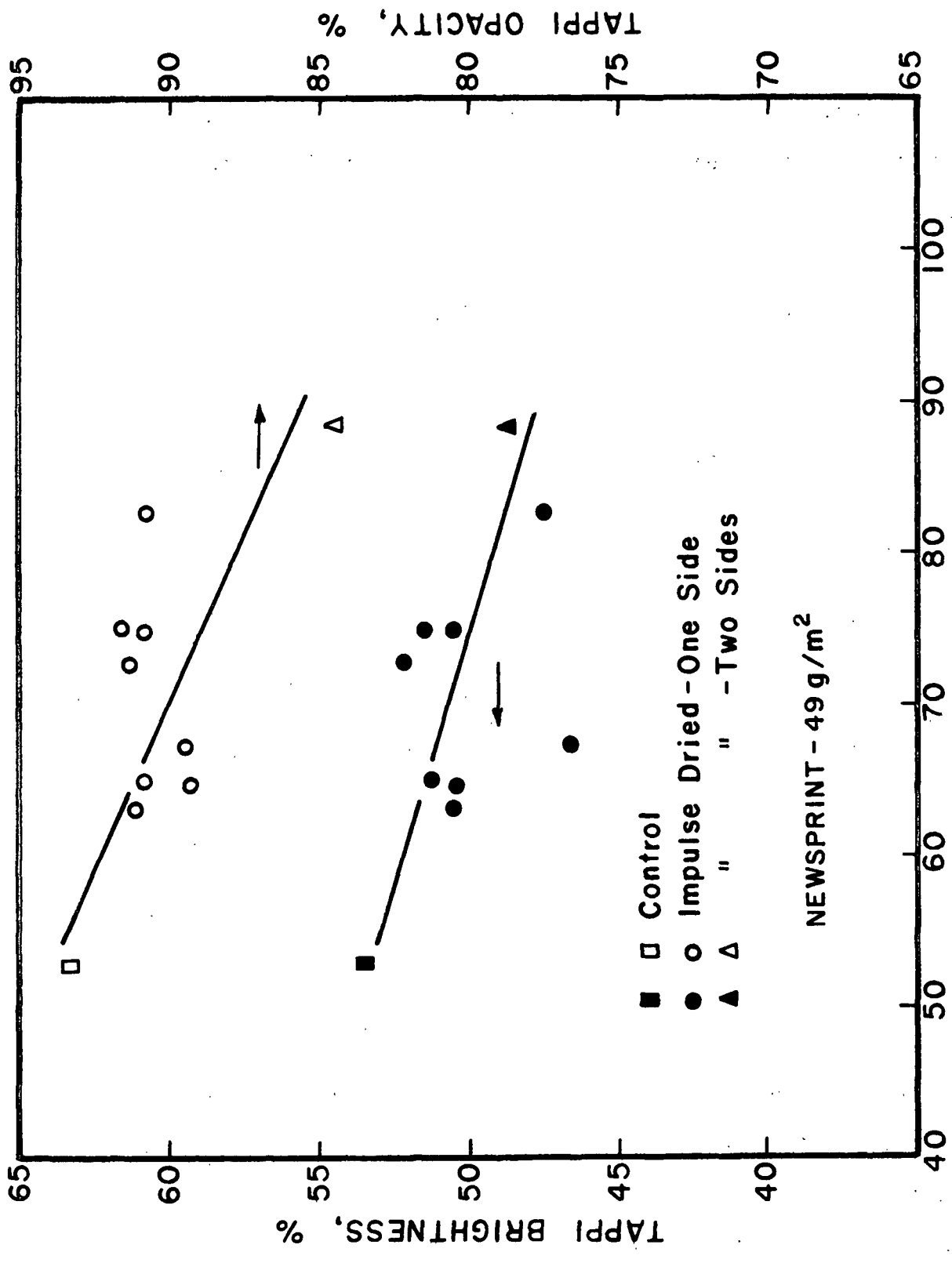

Figure 48. Brightness and opacity changes with dryness for newsprint.

WRITING OR FINE PAPER

Test Conditions

This grade was composed of about 73% BHWK and 27% BSWK, made up in sheets with a basis weight of about 80 g/m^2. Test conditions are given in Table 17.

Table 17. Test conditions for writing paper.

NRT ms	Peak Pressure psi	Initial Temp. °F	Ingoing Solids %
Control	--	--	48.4
26.5	732	400	48.1
26.1	728	700	48.1
25.2	324	400	48.1
25.6	316	700	47.9
15.9	324	400	48.0
16.4	309	700	48.0
14.3	646	400	48.4

Water Removal Rates

This grade dewatered fairly readily and shows typical trends and relationships, as indicated by the data in Fig. 49.

Property Development

Impulse drying does densify this grade, as shown in Fig. 50, but the control sheet density is already high, limiting the rate and amount of additional densification with increasing thermal impulse. The usual positive effect of pressure is clearly indirect with this grade.

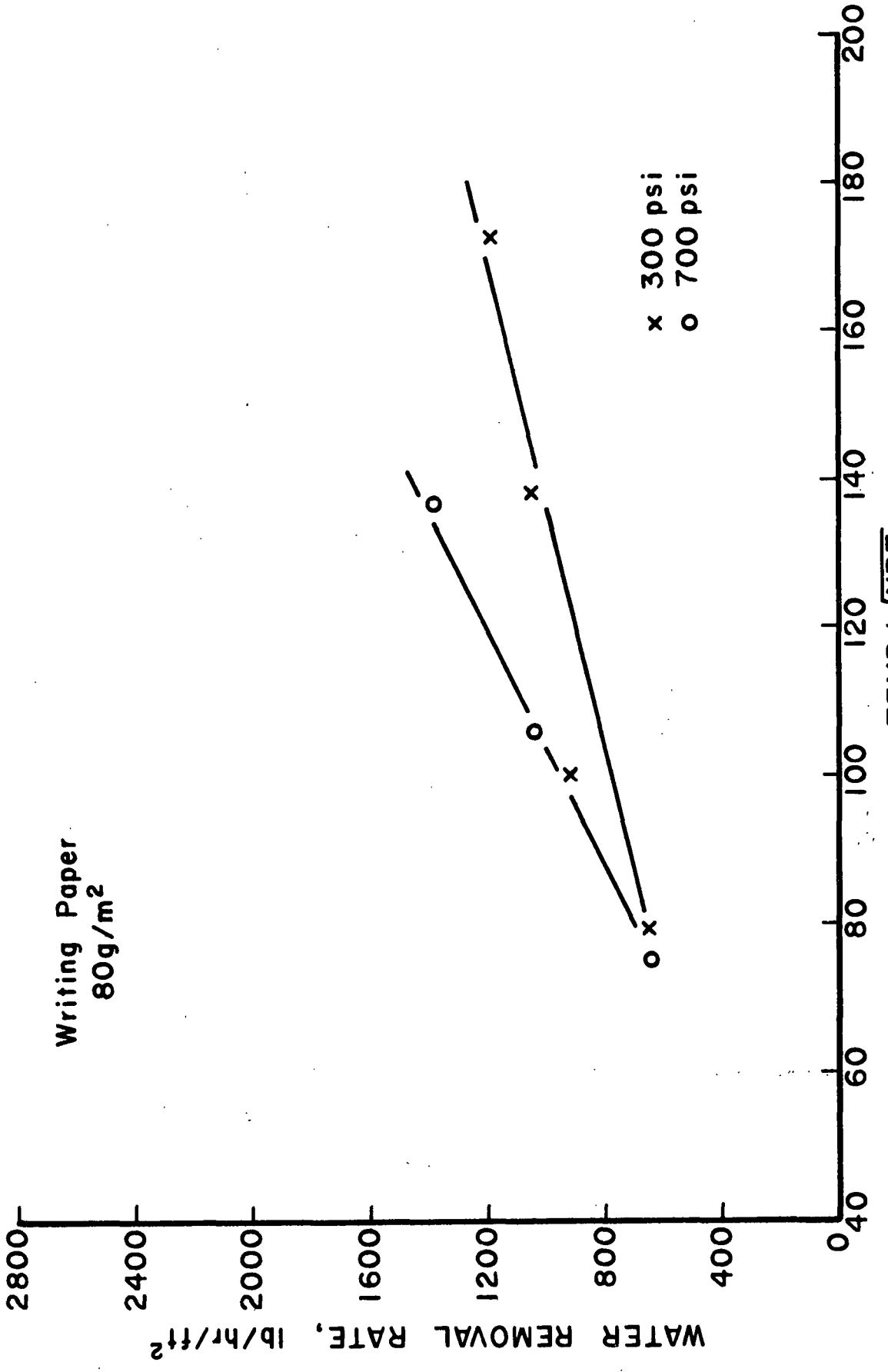

Figure 49. Water removal rates for writing paper.

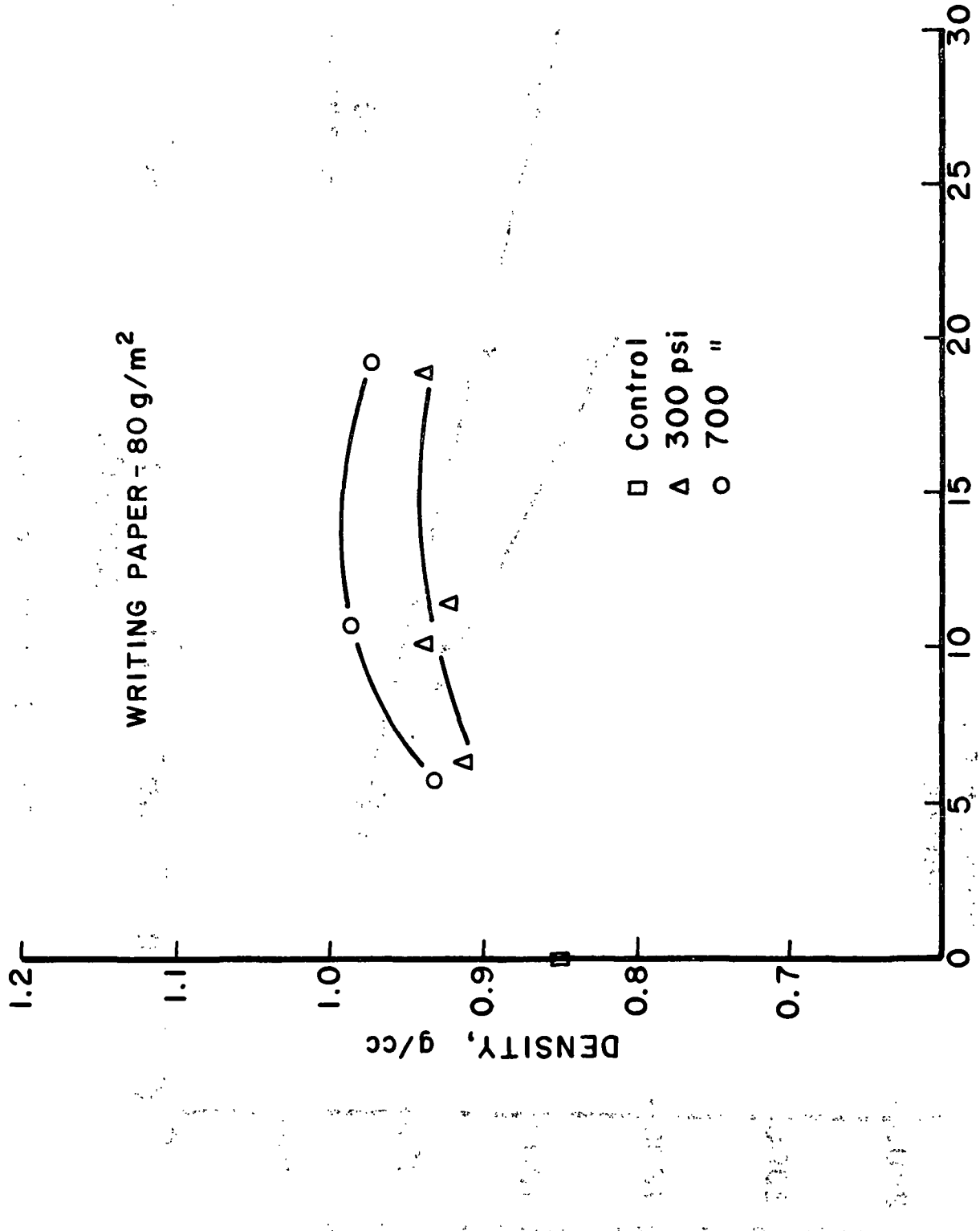

Figure 50. Density development for writing paper.

The tensile-tear relationship in Fig. 51 is typical. Folding endurance, measured only on this grade, is shown as a function of density in Fig. 52. Impulse drying seems to improve this property so it will be measured on some other grades in future work. The roughness relationships in Fig. 53 show that a small amount of impulse drying greatly reduces the roughness of the hot side of the sheet; more impulse drying does not give further improvement. Felt-side roughness tends to increase with degree of impulse drying, as usual. Finally, opacity and brightness values decline by only about 2-3 percentage points over the solids range from 48-72%.

TISSUE

Because impulse drying tends to increase bonding and density rather than bulk, tissue is expected to be a poor application grade. Nevertheless, for completeness, tissue has been included in the screening grades and a number of tests conducted to establish a proper test range. As of this writing, property data are still pending so only water removal results can be presented. All tests were conducted on sheets with a basis weight of about 15 g/m^2. Test conditions, necessarily mild because of the light weight, are shown in Table 18. All initial moisture values were obtained by blotting rather than pressing.

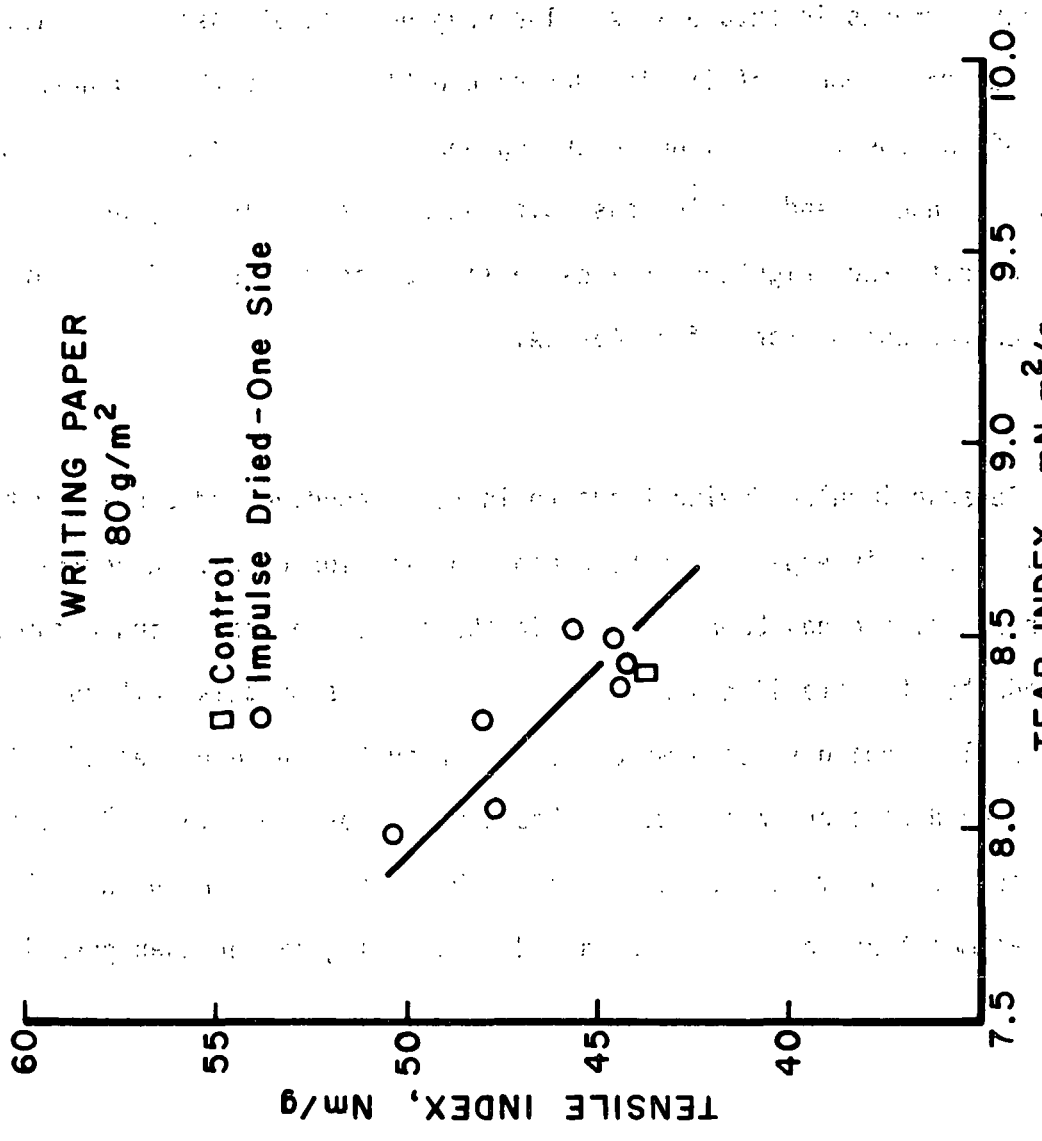

Figure 51. Tensile-tear relationship for writing paper.

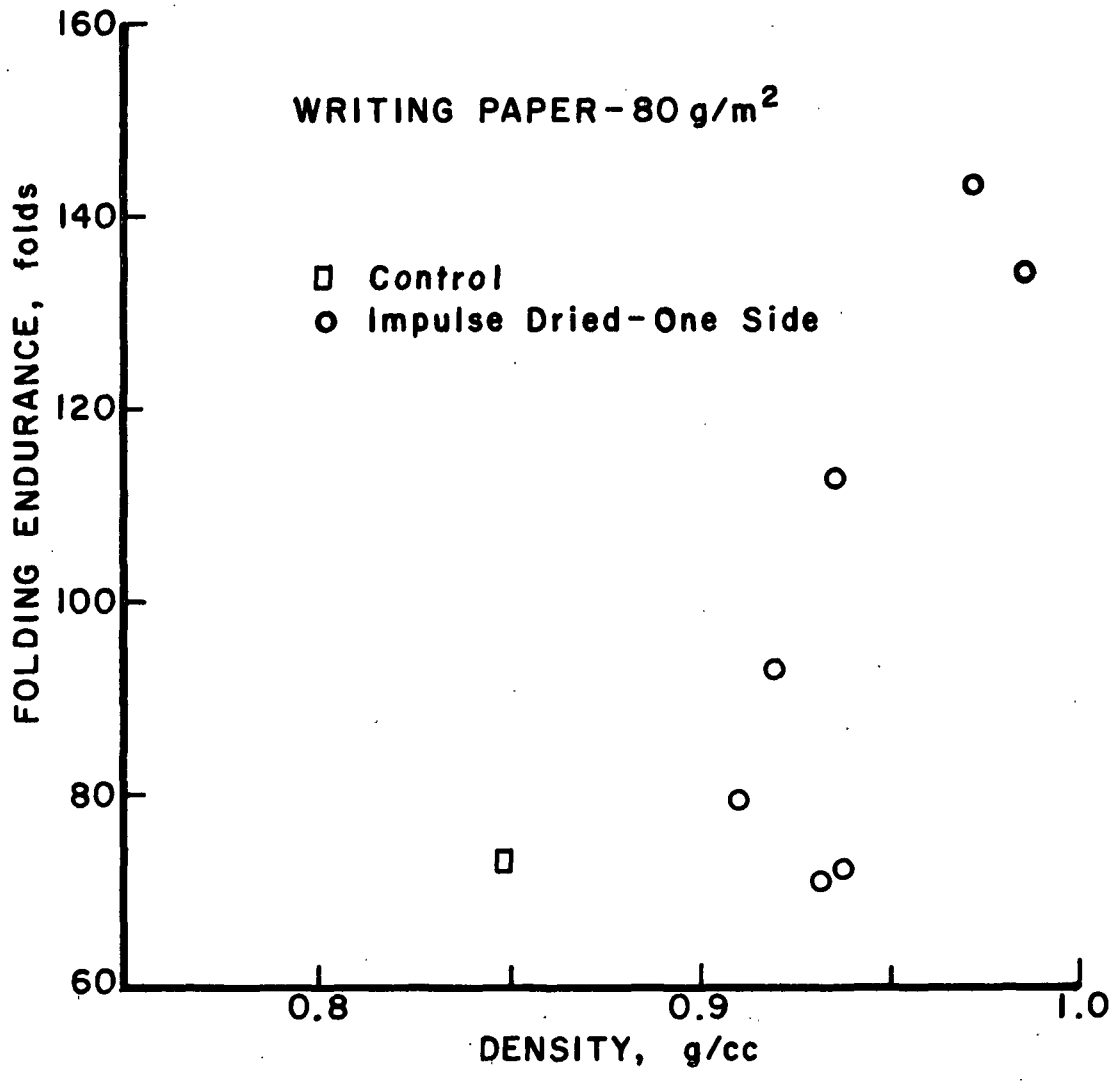

Figure 52. Fold endurance variations with density for writing paper.

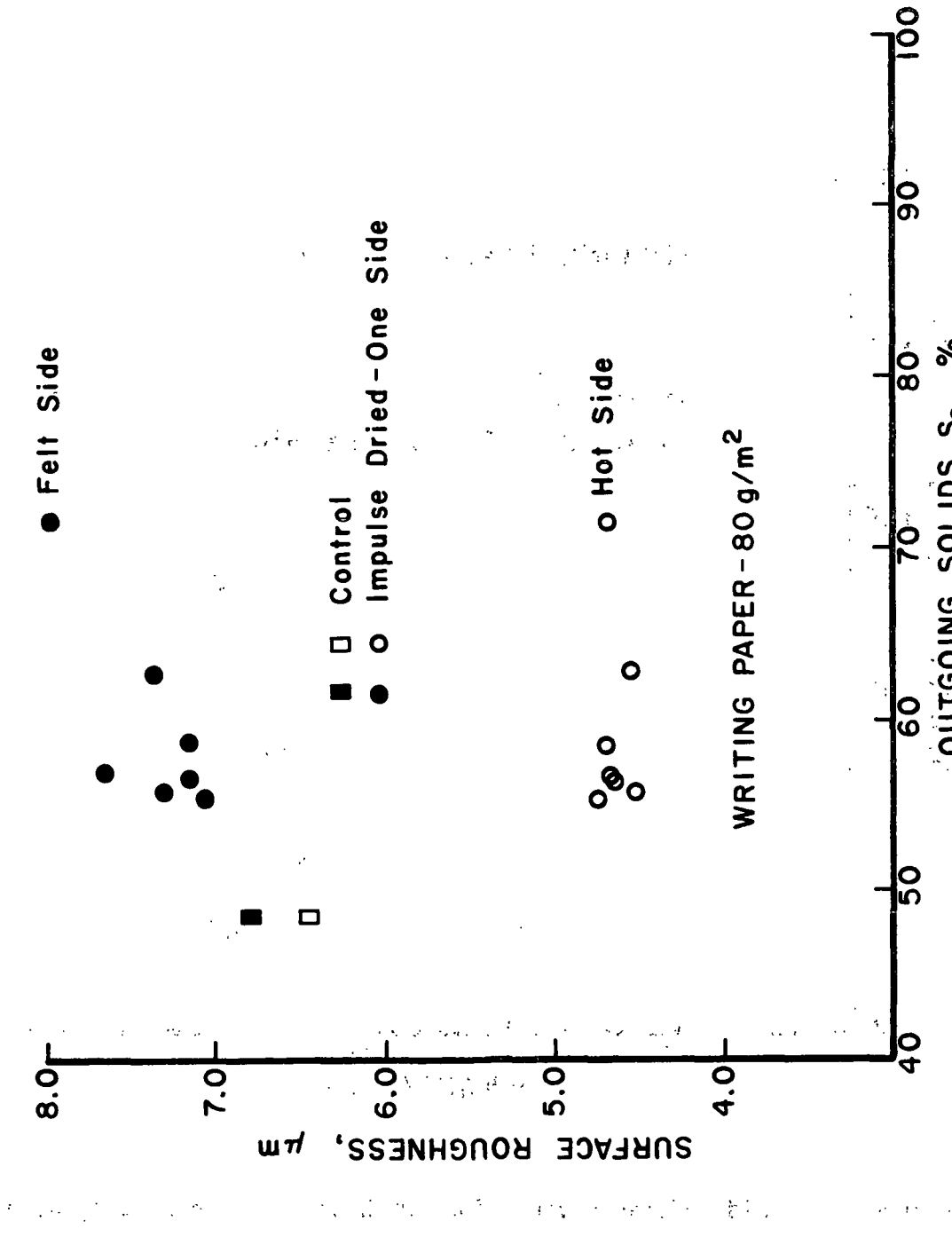

Figure 53. Roughness changes with dryness for writing paper.

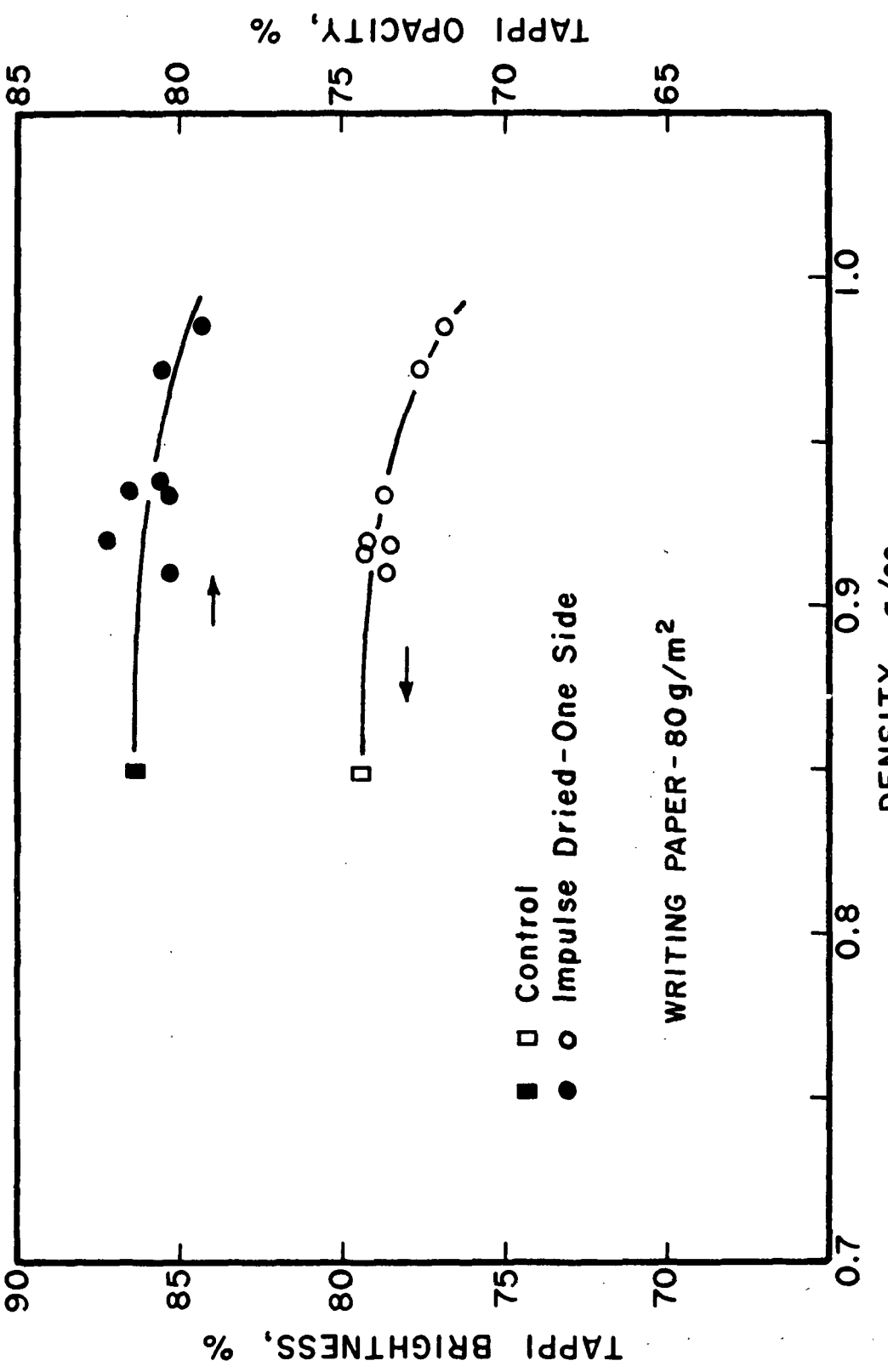

Figure 54. Brightness and opacity changes with density for writing paper.

Table 18. Test conditions for tissue.

NRT ms	Peak Pressure psi	Initial Temp. °F	Ingoing Solids %
Control	--	--	
22	63	310	47.5
19	50	410	49.5
23	60	502	49.0
19	95	320	47.8
18	100	405	48.5
19	93	508	49.3
19	87	560	49.3
20	80	590	48.8
14	90	300	48.8
13.5	110	400	48.8
14	103	500	48.5
16	180	305	49.5
16	170	420	48.5
16	180	410	48.3
15	205	450	48.8
16	200	500	48.8
15	300	305	48.3
15	300	400	49.3
15	300	420	48.5
15	300	450	48.8
15	300	500	48.3
12	420	300	48.3
12	400	400	48.8
12	400	450	49.5
12	400	500	48.3

Water Removal Data

In Fig. 55, water removal rates are plotted as a function of $T/\sqrt{NRT}$. Although WRR depends strongly on this variable, the relationships depart from the straight lines and the small pressure dependence exhibited for other grades.

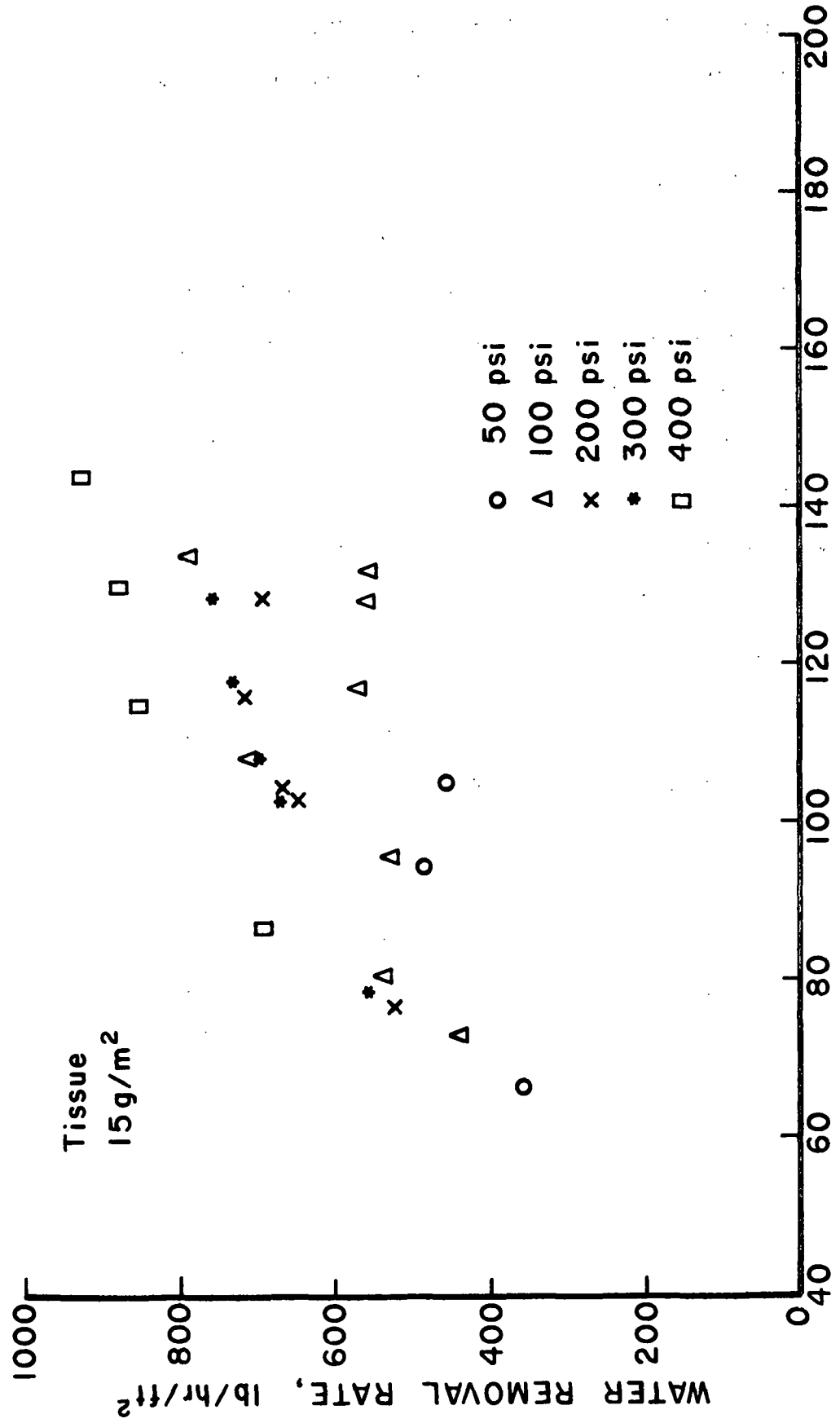

Figure 55. Water removal rates for tissue.

This is probably a function more of basis weight and test conditions than of grade. For 15 g/m^2 sheets, low pressures and temperatures are necessary to prevent overdrying of the web. Over the range from 50-150 psi, water removal is sensitive to pressure, and pressures in this range were used in these tests. Most of these sheets were more completely dried than for any other grade, again because of the low basis weight. Outgoing solids levels range from about 72 to 94%, but most were in the 85-90% range, whereas the sheets for most other grades came out of the impulse drier at 80% solids or less. At high solids levels, much more of the water being removed is bound to the fibers, making removal more difficult. Hence, more of the water is likely to be removed by an evaporation process, reducing removal rates and changing the interrelationships. Finally, these data were taken over a short range of nip residence time values. Future testing with tissue will probably be carried out on a falling-weight press simulator to allow much shorter NRT values.

Some of these data have been replotted in Fig. 56 using pressure as the independent variable and temperature as a parameter, all with nearly constant NRT. This presentation emphasizes the large effect of temperature, the small but discernible effect of pressure, and also, that pressures can be too high for best water removal under some operating conditions. Most of the other grades were not tested in ranges where this negative effect of pressure is evident.

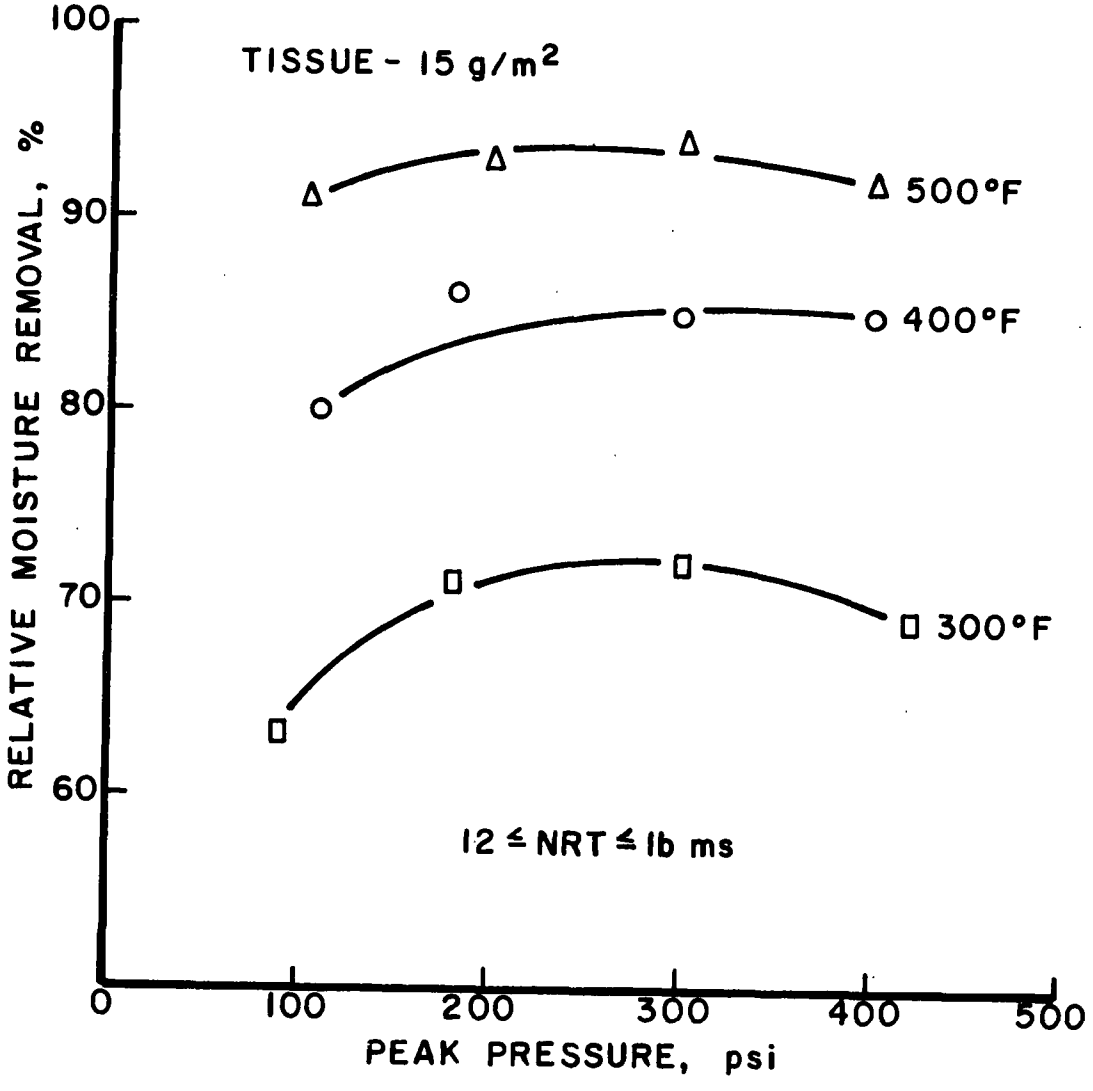

Figure 56. Variation of relative moisture removal with pressure for tissue.

IV. SUMMARY OF RESULTS FROM TECHNICAL PERFORMANCE EVALUATION

Procedures for the technical performance evaluation were presented in Section II. Results obtained to date from the screening portion of this evaluation were presented in Section III. The purpose of this section is to integrate the data from the various grades and discuss the performance of the impulse dryer with respect to (1) water removal, (2) strength development, and (3) surface property development. Data on liquid dewatering and specific energy consumption will be gathered in the next series of tests. Some aspects of future testing will be discussed at the end of this section.

WATER REMOVAL RATES

For all of the grades tested, impulse drying leads to water removal rates that are 60 to 500 times higher than for a conventional dryer. Recycled linerboard dewaters most readily; a complete ranking for a specified $T/\sqrt{NRT}$ is given in Table 19.

Table 19. Example water removal rates ranked by grade.

Grade	WRR, lb/hr/ft^2	Basis Weight, g/m^2
Recycled liner	1750	127
Virgin liner	1300	127
Corrugating medium	1200	127
Writing	1450	80
Lightweight coating	920	55
Newsprint	920	49
Tissue	860	15

$T/\sqrt{NRT}$ = 140; P selected for maximum WRR.

With these grade-specific tests, basis weight and furnish changes occur together making it difficult to discern the separate effect of either. WRR seems to trend directly with basis weight, however, and some evidence of the effect of furnish is provided by the liner and medium data. High freeness or once-dried furnishes dewater more readily. These issues will be explored more fully in subsequent tests.

As illustrated by most of the grades (Fig. 11, 21, 27, 31, 42, 49, and 55), WRR can be described by a relationship of the form

$$WRR = A + BP + CT/\sqrt{NRT}$$

Although they are not yet available, these correlations will be worked out, by grade, for presentation at the meeting. From the data, it is evident that WRR increases linearly with temperature, over a wide range, and for all grades. For values above about 150 psi, pressure seems to be a relatively unimportant variable; below 150 psi, pressure becomes quite important. Based on these results, rapid water removal requires high temperatures, short nips, and a pressure of 150 psi, or more. The amount of water removed is given by the average water removal rate multiplied by NRT. In equation form this is

$$\text{Total water removal (TWR)} = [A + BP + CT/\sqrt{NRT}] \times NRT$$
$$= A\ NRT + BP \cdot NRT + CT \cdot \sqrt{NRT}$$

The first term is a small contributor. The second term is proportional to press impulse and also a small contributor. The third term, which depends on temperature and the square root of NRT, dominates the total water removal function. Because of the square root term, doubling NRT increases total water removal by something over 40%. Hence, to remove a lot of water, high temperature, pressure above 150 psi, and the longest possible nip are required.

DENSITY AND STRENGTH DEVELOPMENT

For all grades tested for which property data are available, impulse drying contributes greatly to densification, producing density values well above those available from more typical processing. Most of the data (Fig. 13, 22, 28, 33, 43, and 50) correlate well in the following form

$$\rho = D + EP + F(T \times NRT)$$

where D, E, and F are regression coefficients. These coefficients will all be worked out for the meeting presentation, but are not now available. Generally, however, density increases rapidly with thermal impulse (T x NRT), but also depends strongly on pressure. This linear regression model holds well except for the writing paper, Fig. 50, and for very large values of T x NRT, Fig. 13.

For most impulse drying conditions, density also correlates linearly and closely to outgoing solids level, almost independently of the impulse conditions used to achieve the given S_o value. Fig. 14, 23, 34, and 44 show this relationship. Hence, more impulse drying means more density, especially for S_o values below 85%.

In a Ph.D. thesis project, it has been shown that impulse drying produces significant density gradients. Typically, densities for parts of the sheet near the hot surface are well above those for conventional processing. Near the open surface, density may be somewhat higher. In the center of the sheet, however, lower densities may develop. Overall, this gives rise to an unsymmetric I-beam type of material distribution. This effect is important and will be exploited in grades where bending stiffness or z-direction compressibility is needed.

In traditional papermaking practice, most strength properties - except tear - depend linearly and strongly on density. These relationships carry over to impulse drying as illustrated by Fig. 15, 16, 17, 24, 26, 29, 35, and 45. An exception to this rule, evident in Fig. 15-17, occurs when sheets are partially predried conventionally and then impulse dried. This will be discussed below.

With the large increases in density available from impulse drying, correspondingly large increases in strength can be obtained, even for those properties where declining caliper is an issue. For linerboard base stock, STFI values increased by 36% as the sheet was impulse dried from 46.4% to 67.7% solids, despite a corresponding 34% drop in caliper.

As tensile strength improves with impulse drying, tear tends to decline, Fig. 36 and 46, a normal relationship. The lone exception is a LWC sheet, impulse dried on both sides, that showed increases in both tear and tensile, relative to the control as shown in Fig. 46. This observation clearly calls for further investigation.

Compressive strength data for three furnishes, Fig. 19, 25, and 30, are characterized in terms of elastic properties by the Habeger-Whitsitt model[3]. All of these data are described reasonably well by the model, despite the diversity of furnishes and processing conditions. Even more importantly, this model describes the data for the predried linerboard samples, where the typical density relationship breaks down - compare Fig. 15 and 19. This also deserves further investigation.

Folding endurance was only measured on the writing paper grade for which the data are shown in Fig. 52. Clearly, this property improves with impulse drying. A few tests will be conducted later on linerboard to see if this change holds there as well.

SURFACE AND OPTICAL PROPERTIES

Opacity and brightness are only slightly degraded by impulse drying, as shown versus density in Fig. 37 and 54 and versus S_o in Fig. 38 and 48. For a bleached furnish, Fig. 54, the brightness and opacity drops are limited to about 2.5 percentage points. The higher lignin furnishes, Fig. 37, 38, and 48, show about twice as much degradation, i.e., about 5 percentage points.

Surface roughness (smoothness) characteristics for four furnishes are shown in Fig. 20, 39, 47, and 53. All show similar trends. The hot-side surface becomes progressively smoother with impulse drying, usually by 25 to 50% with Newsprint (NP2) showing the greatest improvement. In contrast, the felt side becomes roughened or stays about the same.

Usually the felt mass distribution pattern tends to "print" through to the hot surface, yielding a readily discernible surface topography of a scale not included in the roughness measurement. Caliper measurements using a stiff metal plate reflect the height of the tops of these topographic features whereas the IPC rubber platen caliper gage tends to reflect the average height. One formula for quantifying the topography is

$$TI = \frac{S-R}{R} \times 100$$

where TI = topographic index

S = caliper measured with a steel platen

R = caliper measured with a rubber platen

As example data, NP2 impulse dried at 700°F and 700 psi yielded

$$TI = \frac{100.9 - 63.7}{63.7} \times 100 = 58.4$$

For the corresponding control sheet

$$TI = \frac{141.9 - 96.9}{96.9} \times 100 = 46.4$$

The "print through" tendency is evident from these data. Sheet topography may be an important factor in dictating felt design, so some measure is needed. The above is but one possible approach. Some additional testing with various water receivers will be completed shortly to further evaluate this issue.

All properties that reflect liquid uptake through the surface are reduced by impulse drying, often to a great degree. This property is presented as ink penetration time (Hercules) for the LWC grade in Fig. 41. Although not presented in this report, NP2 shows similar trends.

Air permeability, a measure of surface openness, is greatly reduced by impulse drying as shown by the data in Fig. 40. Other grades for which this property is important show similar trends.

SPECIAL TESTS

Two-Sided Impulse Drying

One sample each of two different furnishes has been impulse dried on two sides. After drying on one side, the sample was weighed and then dried on the opposite side so there were a few seconds of elapsed time between events. The resulting data points are shown in the plots for LB1 (Fig. 11-12) and for NP2 (Fig. 42-48).

In each case, drying on the second side is as effective as drying on the first in removing water from and densifying the sheet. In fact, for a specified total drying time, it is better to divide it between nips drying on opposite sides than to use the full interval on one side. Hence, the early worries

about the closed surface on the first side degrading drying performance on the second side are unfounded. For the LB1 in particular, two-sided drying produced a density of 1.05 g/cc at an outgoing solids level of only 68%. Two-sided drying tends to equalize surface smoothness as shown in Fig. 20.

Predrying

A few LB1 samples were pressed to about 46% solids, predried at low temperature and pressure to various higher solids levels, and then impulse dried. The results from these tests are included in Fig. 11, 12, and 14-20. Predrying has the following serious and negative effects on impulse dryer performance:

1. WRR is reduced by more than 44%, even for slight predrying (Fig. 11).
2. Density development with outgoing solids level is sharply impaired by predrying (Fig. 14).
3. Strength-density relationships are also impaired by predrying giving a double negative impact on strength (Fig. 15-17).
4. Despite the changes in the density and density-strength relationships, the data for the predried sheets still fit the Habeger-Whitsitt model (Fig. 19). This observation suggests the elastic constants provide a more useful and universal sheet description than do the traditional strength tests.

In contrast, as noted above, predrying by impulse drying on one side does not have a negative effect.

It has already been shown[1] that preheating the ingoing sheet to about 210°F with live steam greatly improves the performance of impulse drying. The above data suggest that preheating by predrying will have an opposite effect. These observations also deserve further study.

Prepressing Levels

A few of the LWC sheets were pressed to ingoing solids levels from about 35-55% and then impulse dried. Property measurements on these sheets were limited to density, brightness, and opacity. The resulting data, shown in Fig. 31, 32, 34, and 37, yield the following tentative conclusions:

1. WRR varies directly with ingoing moisture level - the wetter the sheet, the greater the water removal rate (Fig. 31). The significant pressing component of impulse drying may partially account for this.
2. Both outgoing solids and density variations, Fig. 32 and 34, are much less than the ingoing moisture variations giving a leveling effect on both solids and moisture.
3. Brightness and opacity, Fig. 37, are not greatly influenced by ingoing solids level, achieved by prepressing, although the opacity data do not match those from a previous experiment with this furnish.

FUTURE WORK

The data and empirical equations presented in this report are precisely what is needed to carry out the engineering and economic analysis in Steps 4 and 5 of the plan. Although the experiments that produced these data were screening in nature, they have revealed much of the behavior of impulse drying and will serve as a planning base for the next series of experiments, to begin shortly. From these data, it is clear that impulse drying can effect extremely rapid water removal and that it has a profound effect on properties. It is also clear that there is opportunity to trade off and manipulate these effects to achieve a given desired end point.

While this work is experimental in nature, it is being complemented by Steve Burton's Ph.D. work on the fundamental mechanisms of impulse drying, including densification. Some of this work will be highlighted at the meeting. For the future, the technical performance evaluation and the important side bar experiments spawned by it will continue. Work has already been initiated on a pilot press for use in moving web impulse drying experiments. Finally, work on the engineering concepts appropriate to impulse drying, initiated by Matt Nightingale in his M.S. work, and on the economics of impulse drying will be reopened. All of this work is now proceeding under a $1.5 million grant from the DOE, $350,000/yr for each of the first two years and then $400,000/yr for two more.

REFERENCES

1. Progress Report One, Project 3470, Ahrens, F.W., The Institute of Paper Chemistry, October, 1985.

2. Pounder, J.R. A Mathematical Model of High Intensity Paper Drying. Doctoral Dissertation. Appleton, WI, The Institute of Paper Chemistry, Jan. 1986.

3. Habeger, C.C., Whitsitt, W.J. A mathematical model of compressive strength in paperboard. Fiber Science & Technology 19(1983) 215-329.

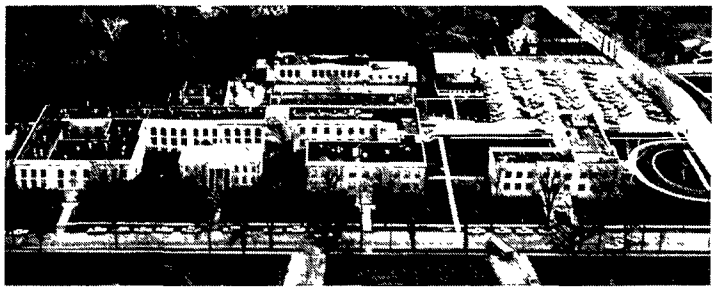

THE INSTITUTE OF PAPER CHEMISTRY, APPLETON, WISCONSIN

SLIDE MATERIAL

for the

Engineering Project Advisory Committee

October 23-24, 1985
The Institute of Paper Chemistry
Continuing Education Center
Appleton, Wisconsin

TABLE OF CONTENTS

Project 3556

FUNDAMENTALS OF KRAFT LIQUOR CORROSIVITY

David Crowe

PROJECT 3556

FUNDAMENTALS OF KRAFT LIQUOR CORROSIVITY

David C. Crowe

FUNDAMENTALS OF KRAFT LIQUOR CORROSIVITY

OBJECTIVE

REDUCE COSTS OF CORROSION OF CARBON STEEL BY KRAFT LIQUORS

APPROACH

- MONITOR CORROSIVITY
- DETECT HIGH CORROSIVITY
- TRACE ORIGINS OF HIGH CORROSION RATE
- CORRECT

PROGRESS

- ° CONTINUED MONITORING OF CORROSIVITY IN THE FIELD
  - LPR
  - ER
  - WEIGHT LOSS
  - LIQUOR SAMPLING
  - VELOCITY EFFECT
- ° CONSTRUCTION AND PROGRAMMING OF MICROPROCESSOR FOR REMOTE DATA ACQUISITION

PROGRESS (Contd.)

- ° COMPLETION OF STUDY OF THIOSULFATE ADDITIONS ON CORROSION RATE
- ° COMMENCEMENT OF STUDY OF SULFITE ADDITIONS ON CORROSION RATE
- ° CONSTRUCTION OF APPARATUS TO STUDY VELOCITY EFFECTS BY MEANS OF ROTATING CYLINDER ELECTRODE

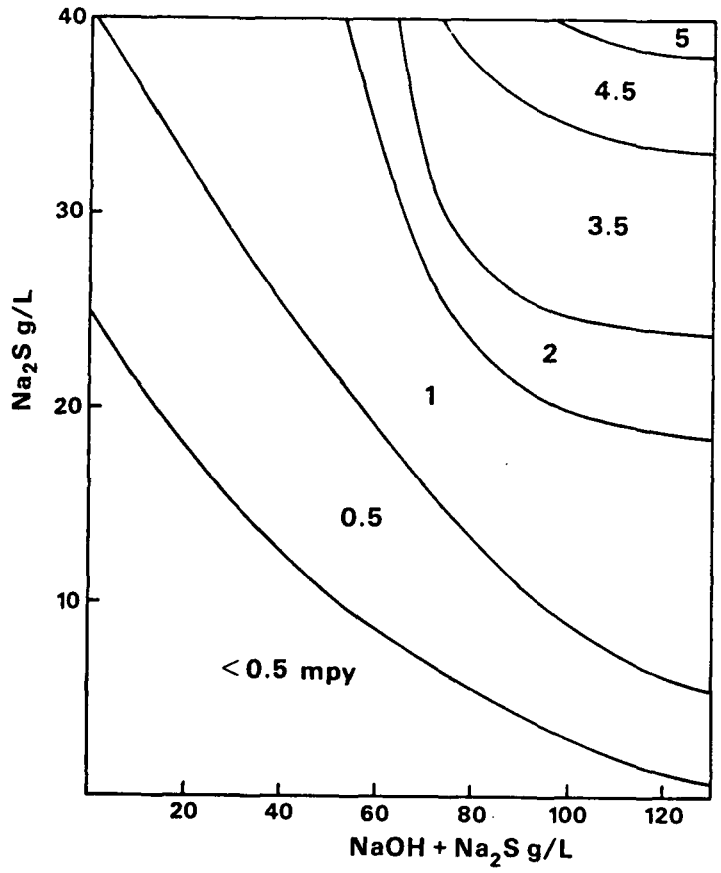

Iso-corrosion plot for NaOH + Na_2S solutions.

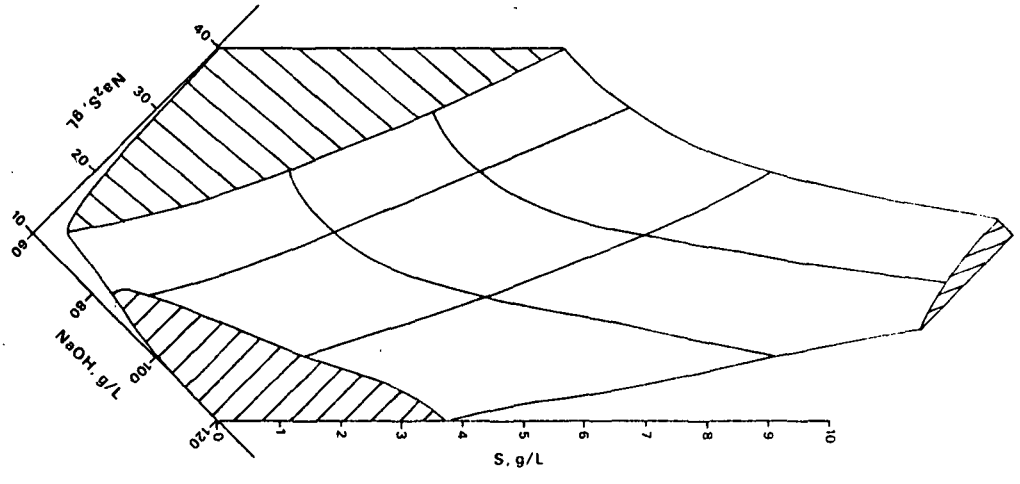

Isocorrosion surface 5 mpy in NaOH + Na_2S + S solution after 2 weeks exposure.

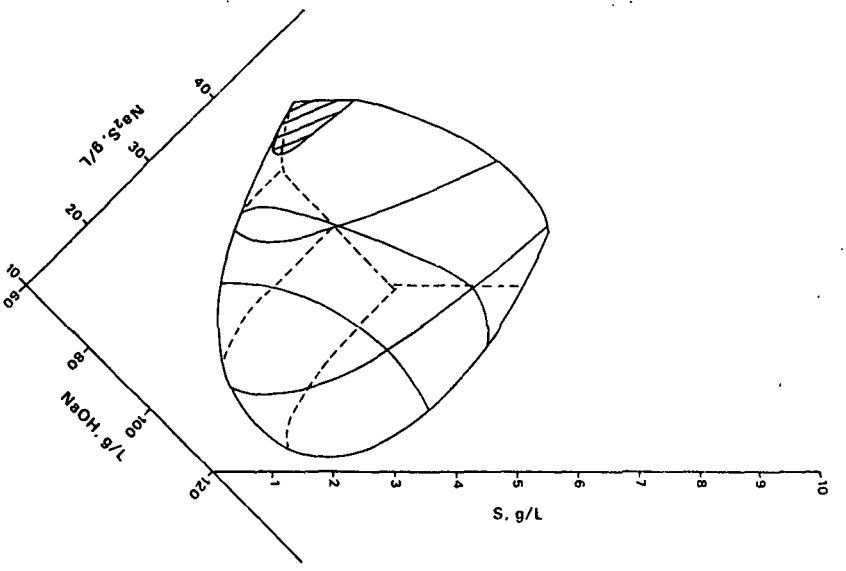

Isocorrosion surface 5 mpy in NaOH + Na_2S + S solution after 8 weeks exposure.

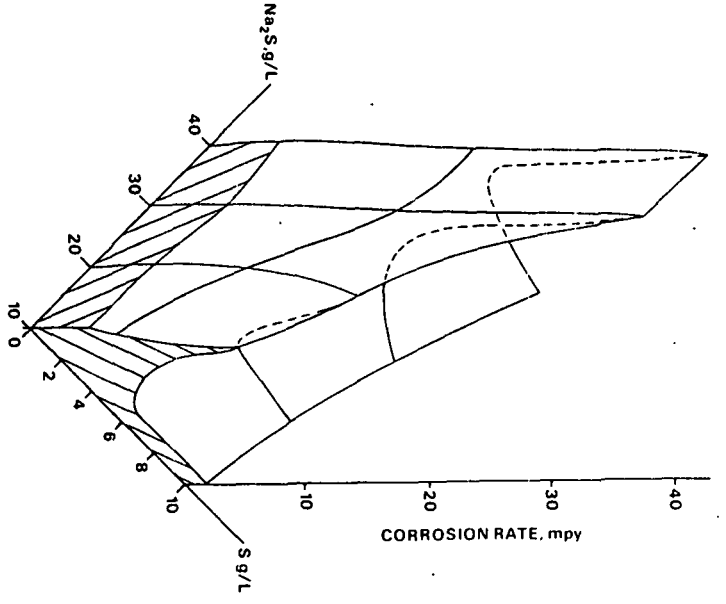

Corrosion rates in Na_2S + S + 120 g/L NaOH solution after 2 week exposure.

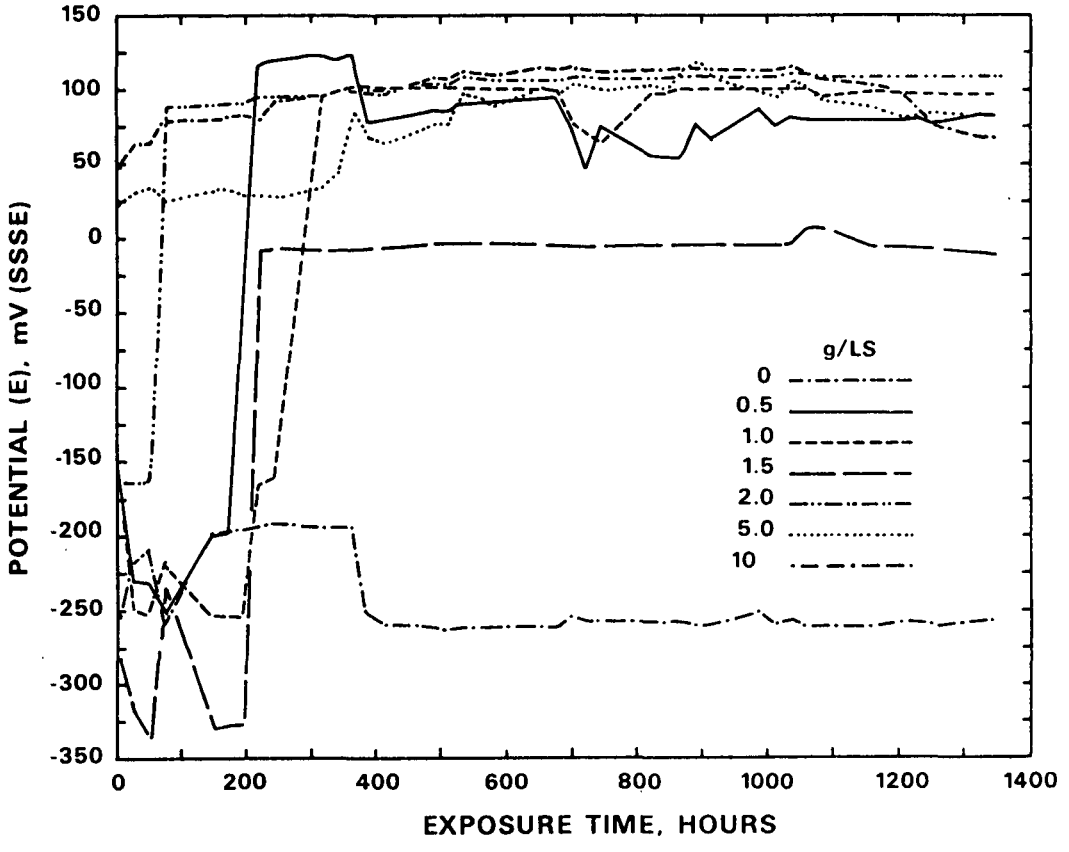

Corrosion potential as a function of exposure time in 100 g/L NaOH + 30 g/L Na_2S + 0-10 g/L S.

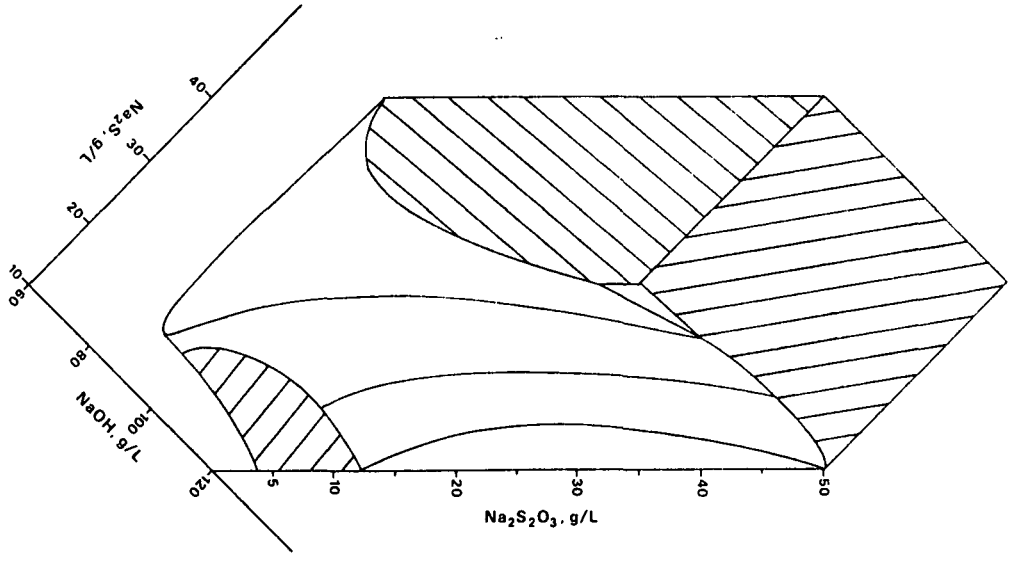

Isocorrosion plot of 15 mpy surface in NaOH + Na_2S + $Na_2S_2O_3$ solutions after 2 weeks exposure.

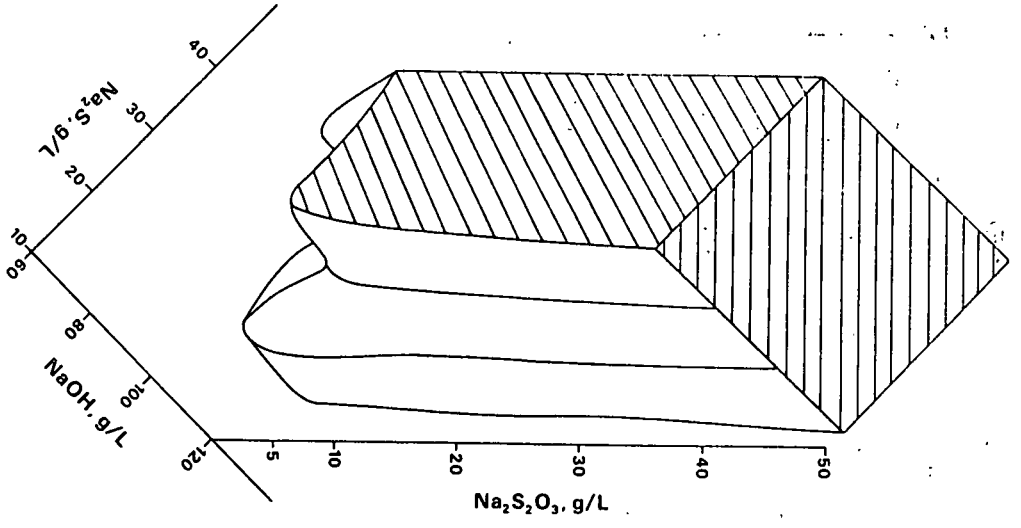

Isocorrosion plot of 15 mpy surface in NaOH + Na_2S + $Na_2S_2O_3$ solutions after 8 weeks exposure.

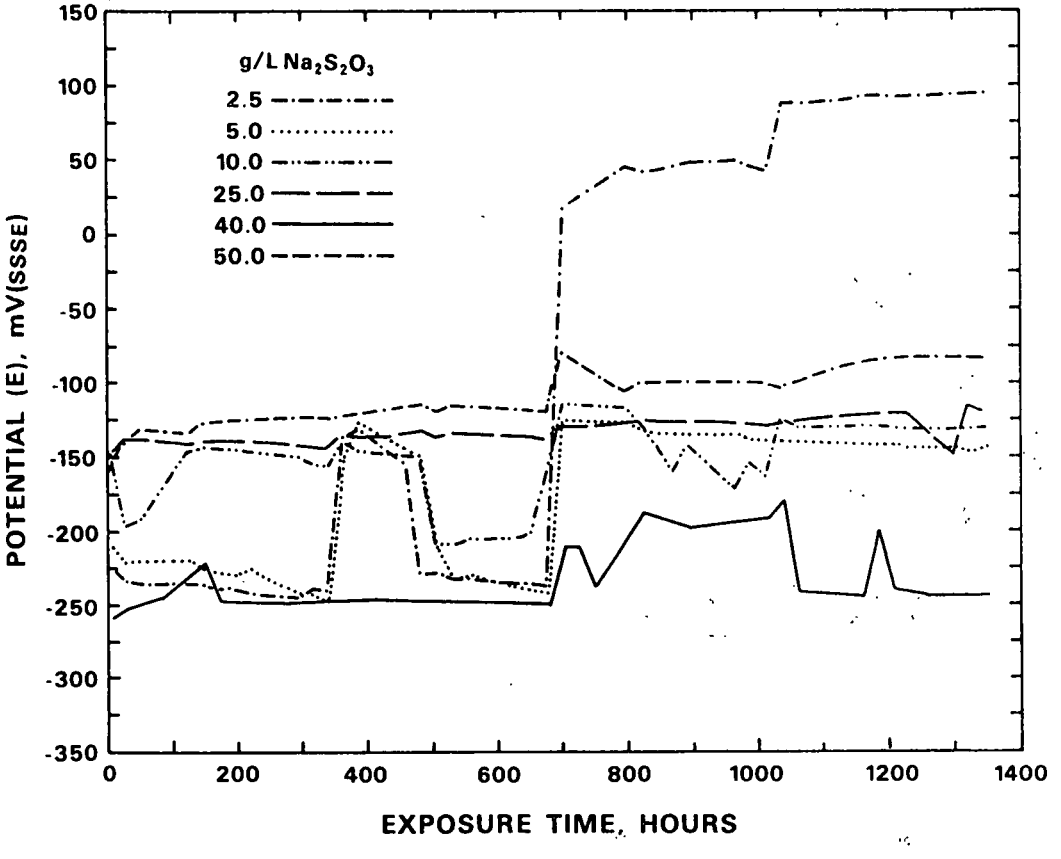

Corrosion potential during exposure in 80 g/L NaOH + 40 g/L Na_2S + 0-50 g/L $Na_2S_2O_3$.

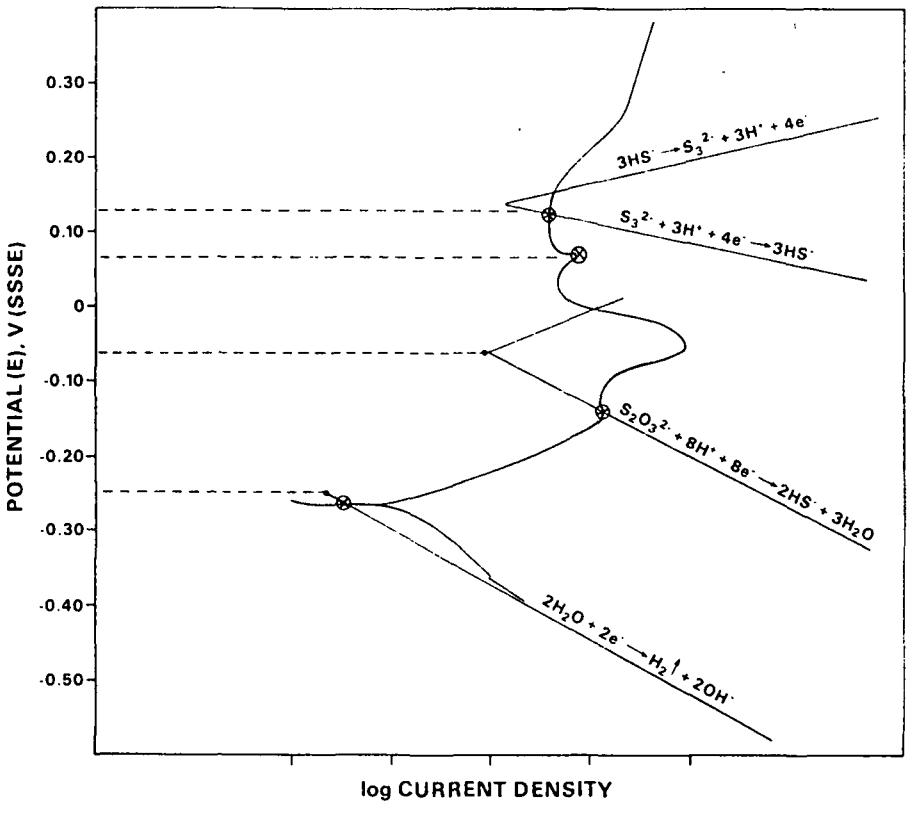

Schematic diagram illustrating the reactions which may control the corrosion potential.

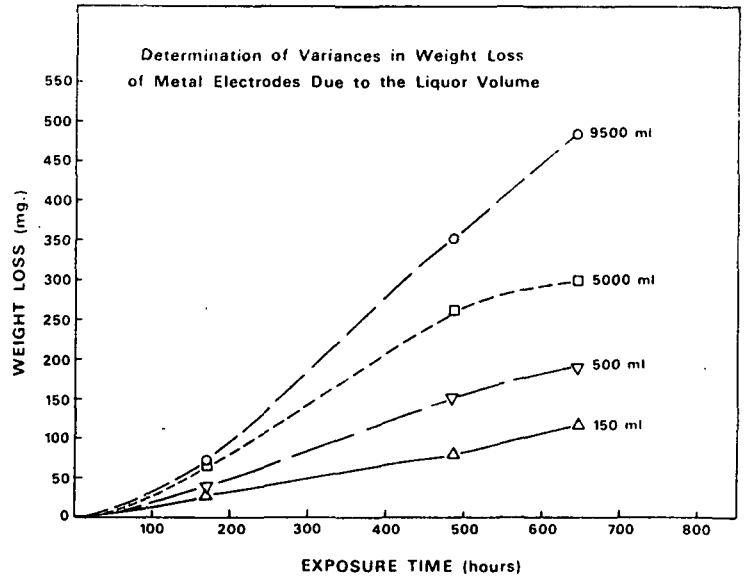

Determination of variances in weight loss of metal electrodes due to the liquor volume.

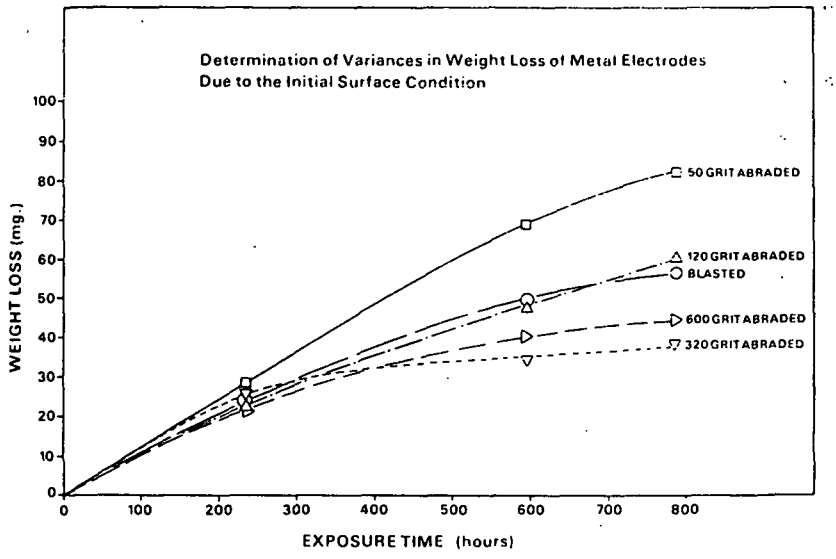

Determination of variances in weight loss of metal electrodes due to the initial surface condition.

IN-MILL LPR RESULTS

- MEASURED VALUES AGREED VERY WELL WITH WEIGHT LOSS, WHEN APPROPRIATE CORRECTIONS ARE APPLIED, CONSISTENT WITH TAFEL SLOPES MEASURED FROM IN SITU POLARIZATION CURVES.
- GIVES AN INSTANTANEOUS MEASUREMENT OF CORROSION RATE.

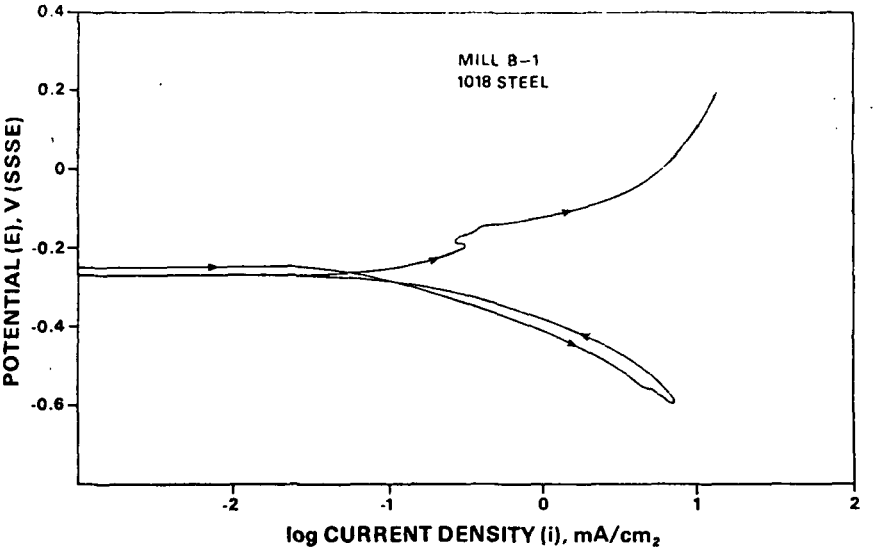

Representative polarization curve
for 1018 steel in mill white liquor

ELECTRICAL RESISTANCE RESULTS

- EXCELLENT AGREEMENT WITH WEIGHT LOSS TESTS.
- A PERIOD OF EXPOSURE OF AS MUCH AS ONE MONTH IS NECESSARY TO OBTAIN AN ACCURATE MEASUREMENT.
- NEEDS NO CORRECTION OR INTERPRETATION.

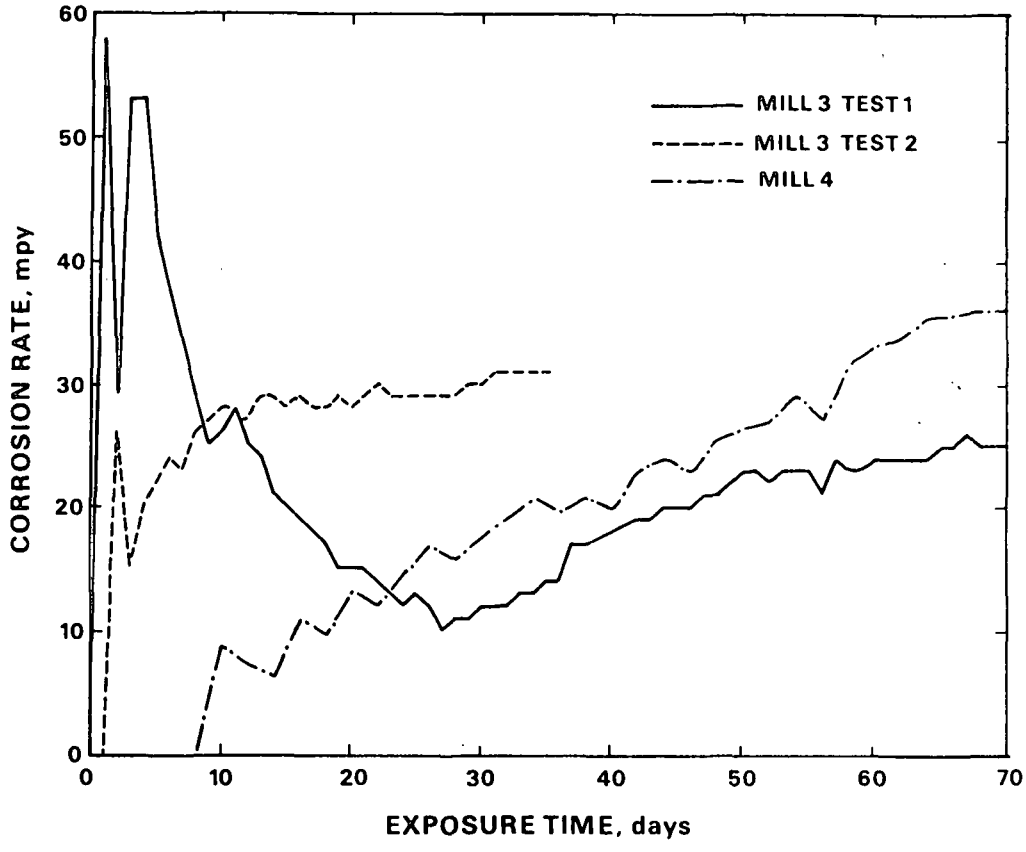

Corrosion rate measured by electrical resistance technique in mill white liquor

MATERIALS

- MATERIALS, IN ORDER OF DECREASING CORROSION RESISTANCE:

  A285 SPECIAL
  A283
  A285C
  1018

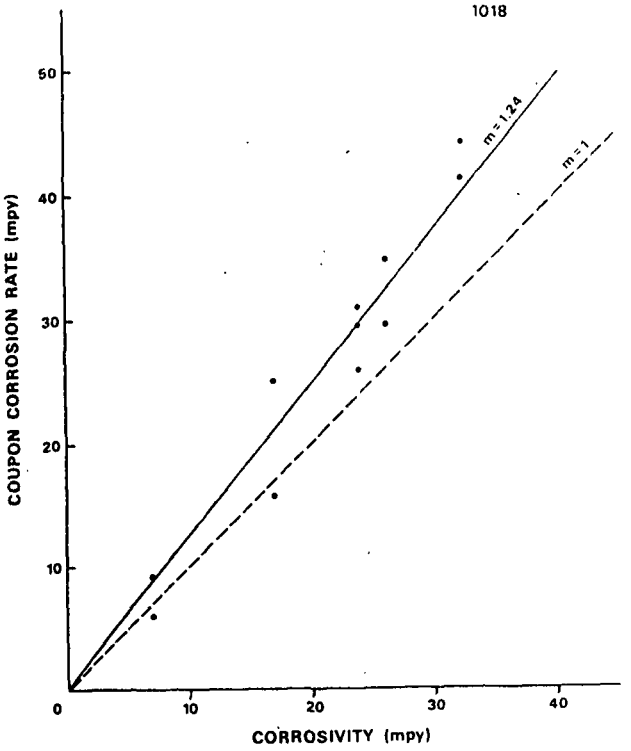

Corrosion rate of 1018 steel in mill white liquors of various corrosivity

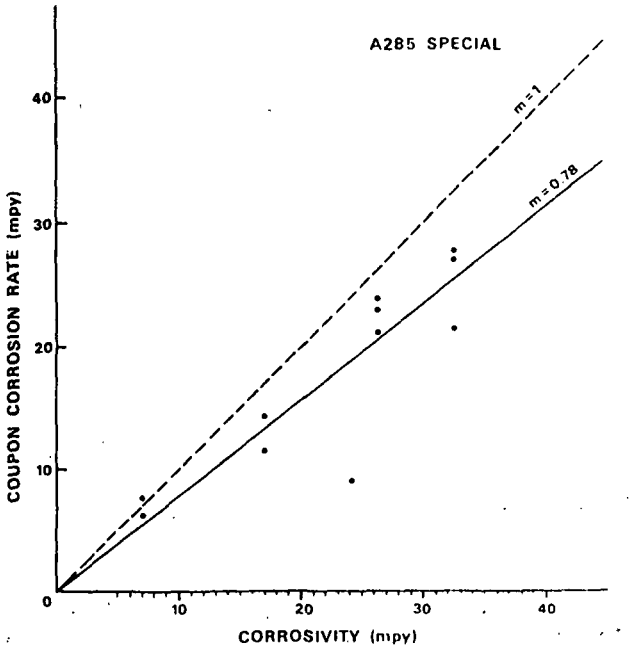

Corrosion rate of A285 - special steel in mill white liquors of various corrosivity

LIQUOR CORROSIVITY

- THE MOST SIGNIFICANT FACTOR
- THIOSULFATE, SULFIDE, HYDROXIDE } AFFECTED CORROSION RATES IN-MILL

PLANS FOR NEXT PERIOD

- FIELD TEST THE MICROPROCESSOR-BASED DATA ACQUISITION SYSTEM
- COLLECT MORE MILL DATA
- MEASURE EFFECTS OF SULFITE ON CORROSION RATES
- TESTING OF VELOCITY EFFECTS WITH A ROTATING CYLINDER ELECTRODE
- COMPLETE MODIFICATIONS TO FLOW LOOP AND RESUME TESTING
- TESTING OF A NEW DESIGN OF Ag/Ag_2S REFERENCE ELECTRODE

SIGNIFICANCE TO THE INDUSTRY

- CORROSION MONITORING METHODS MAY BE APPLIED RELIABLY IN WHITE LIQUOR SYSTEMS
- CORROSION RATE IS INFLUENCED MORE STRONGLY BY LIQUOR CORROSIVITY THAN BY STEEL COMPOSITION
- CORROSION IS STIMULATED BY THIOSULFATE AND POLYSULFIDE RESULTING FROM LIQUOR OXIDATION

Project 3309

FUNDAMENTALS OF CORROSION CONTROL IN PAPER MILLS

Ronald Yeske

FUNDAMENTALS OF CORROSION CONTROL IN PAPER MILLS

Project 3309

OBJECTIVE

° IMPROVE LIFETIME OF SUCTION ROLLS

SHORT TERM OBJECTIVES

° IDENTIFY A PREDICTIVE LABORATORY TEST

° NORMALIZE DIFFERENT FATIGUE METHODS

A PREDICTIVE LABORATORY TEST

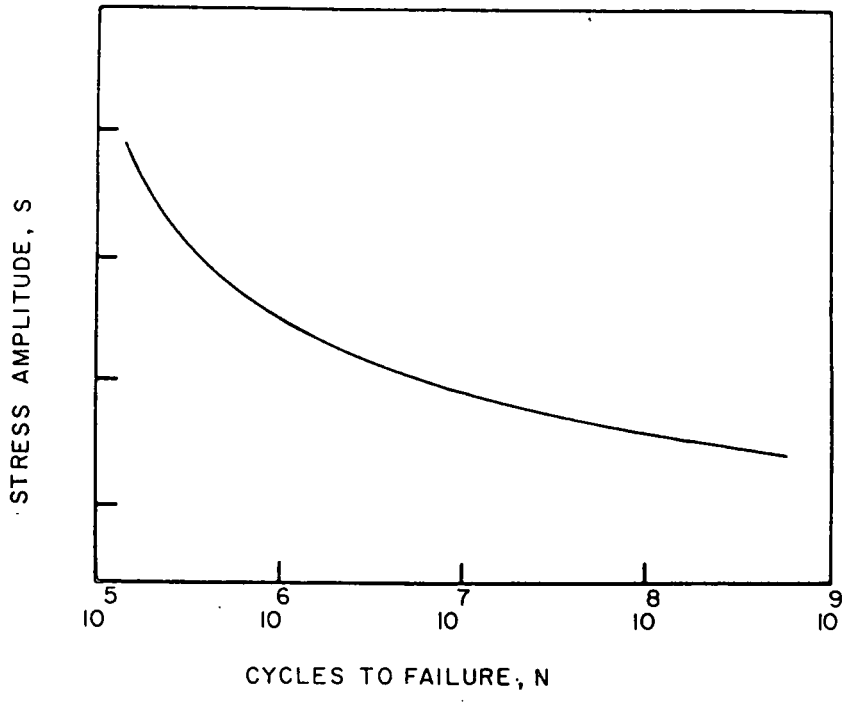

Schematic S-N curve depicting resistance to fatigue crack initiation.

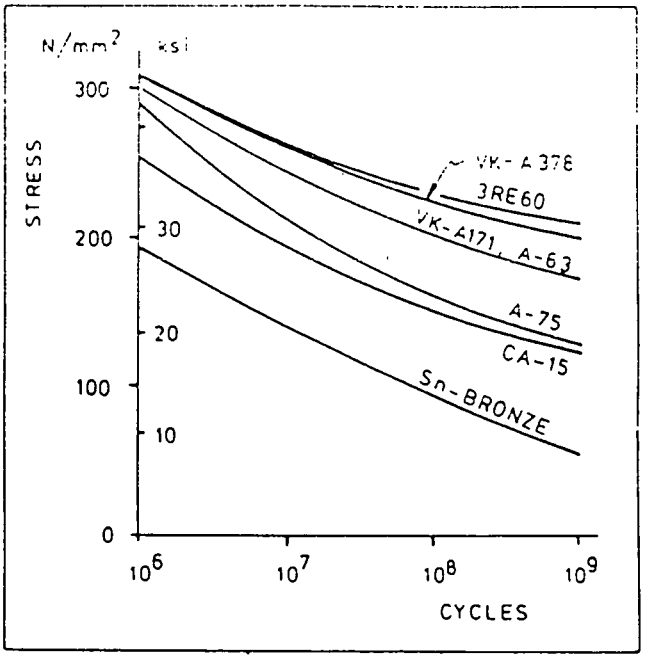

S-N curves for seven suction roll alloys in white water (pH 3.5, chloride 20-400 ppm, sulfate 250-1000 ppm) from rotating beam tests at 1500-1750 rpm

Although Alloy 75 is superior to Alloy 63 in service, the results of this S-N curve generated in the laboratory would indicate otherwise.

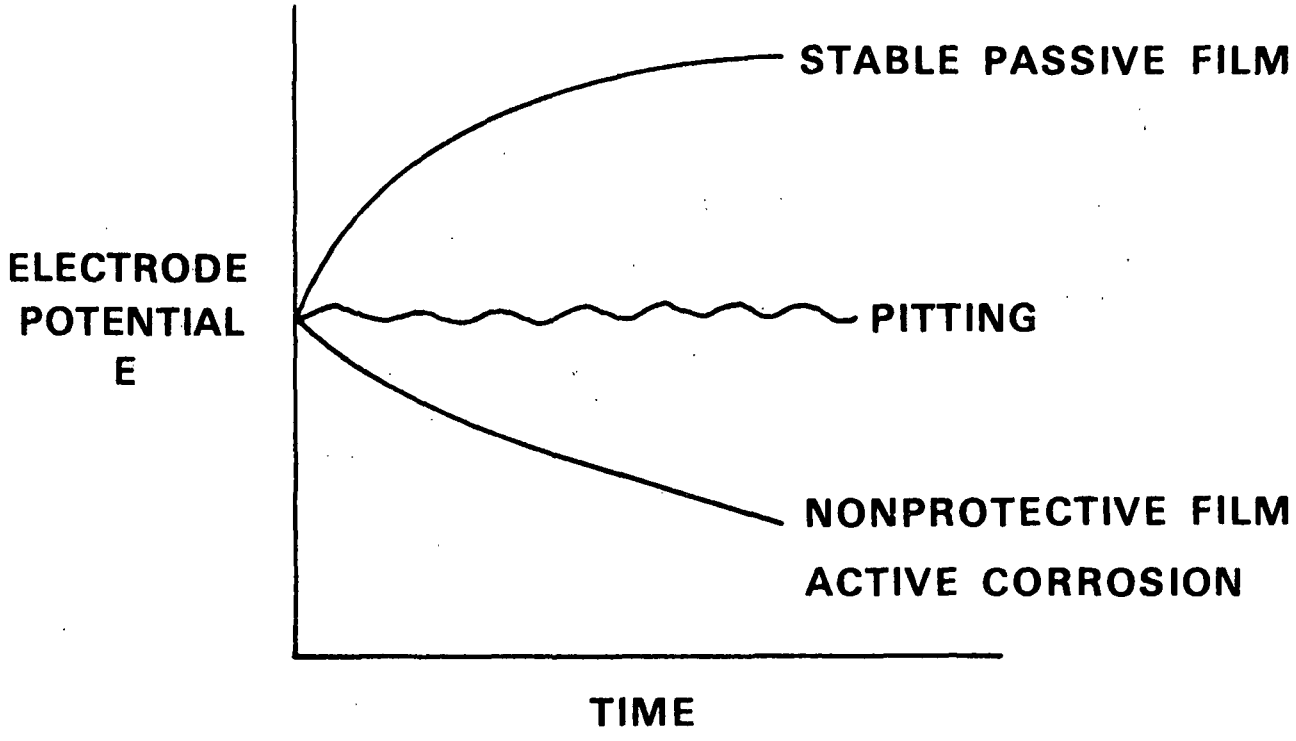

Variation in electrochemical potentials developed at the wetted surfaces of suction roll specimens exposed to a simulated white water.

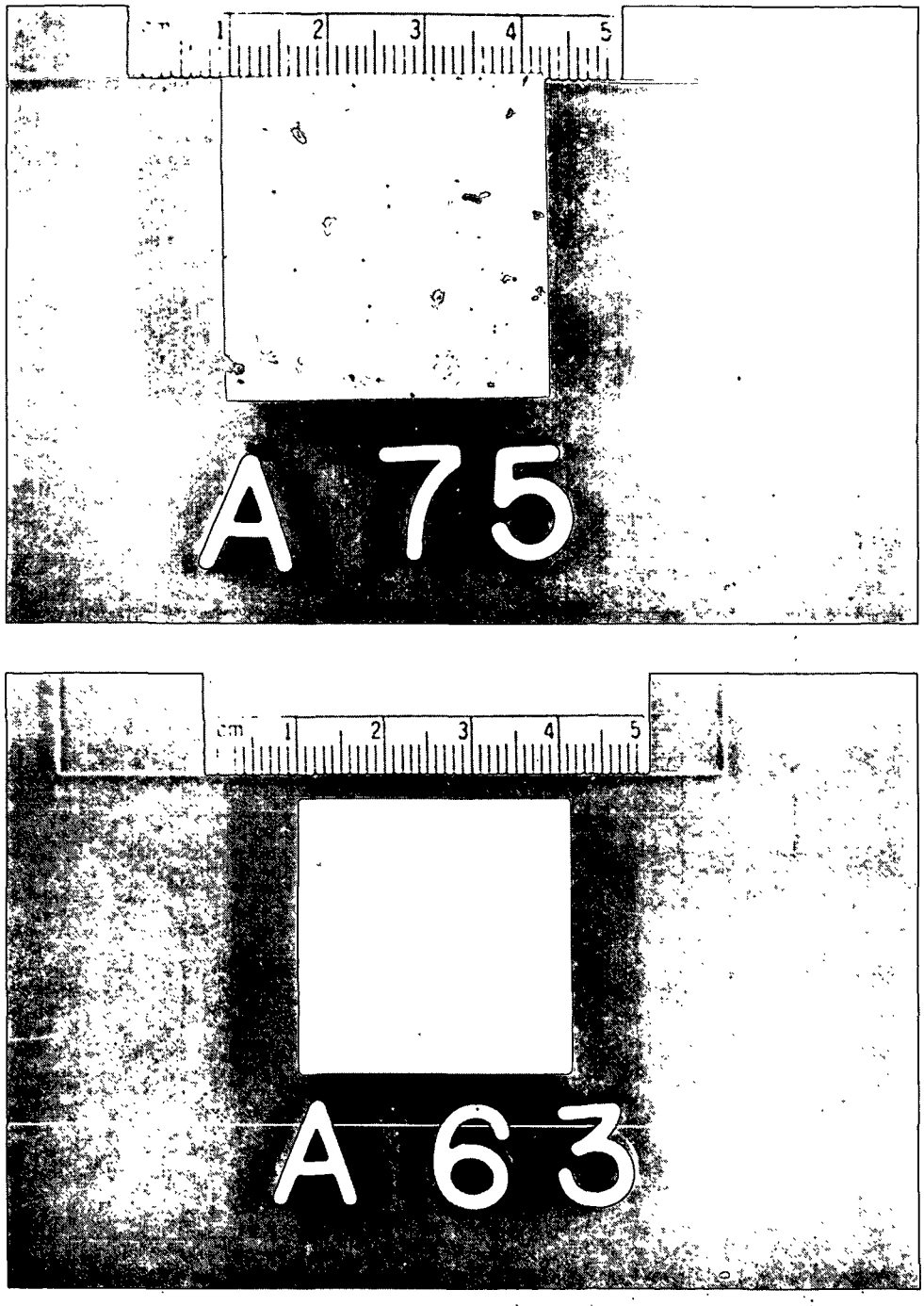

Examples of pitting corrosion resistance of Alloys 75 and 63 in simulated paper machine white waters. Alloy 75 has a superior service record.

NORMALIZE FATIGUE METHODS

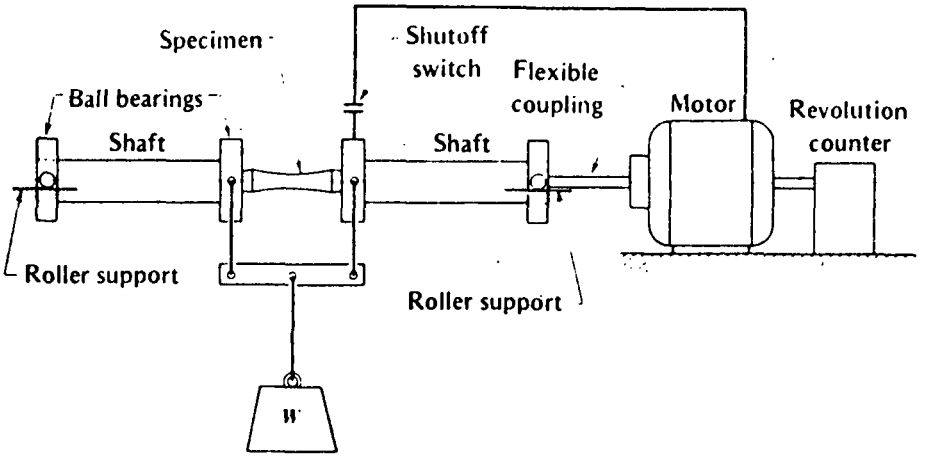

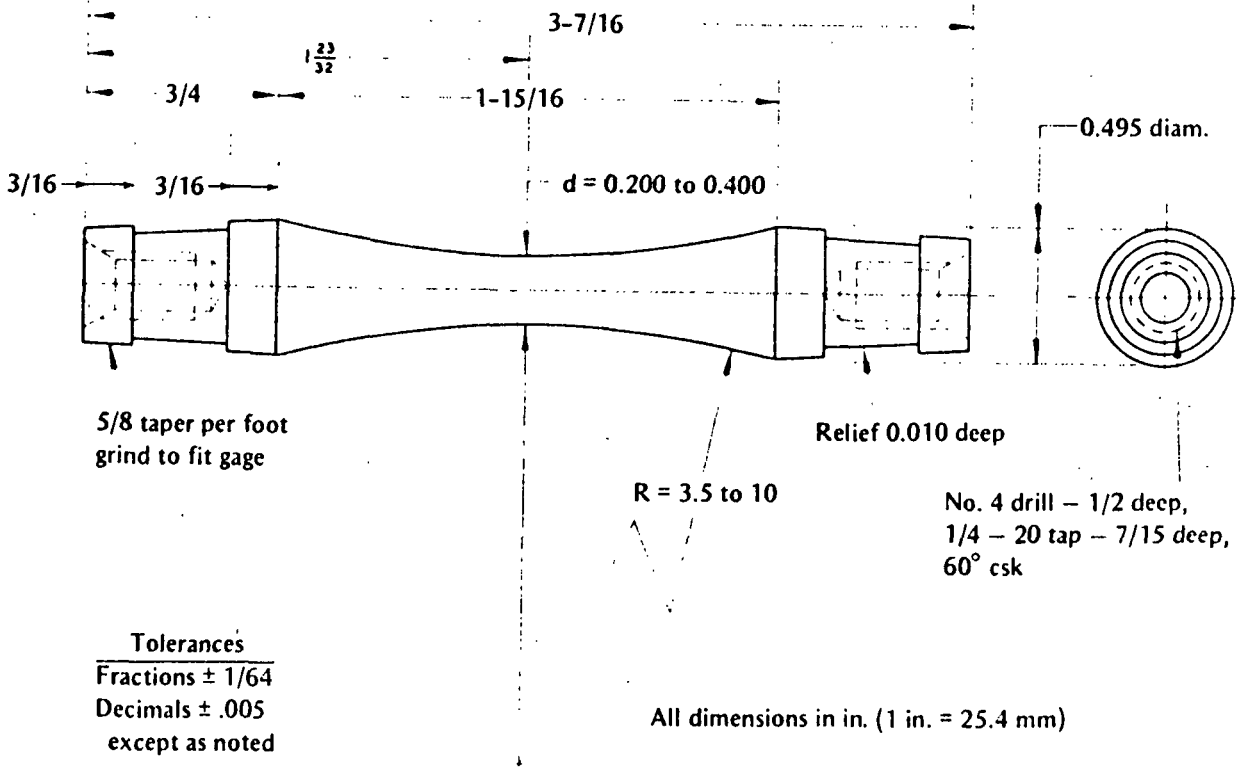

Schematic illustration of rotating beam testing machine (upper) and geometry/dimensions of the specimen (R. R. Moore type).

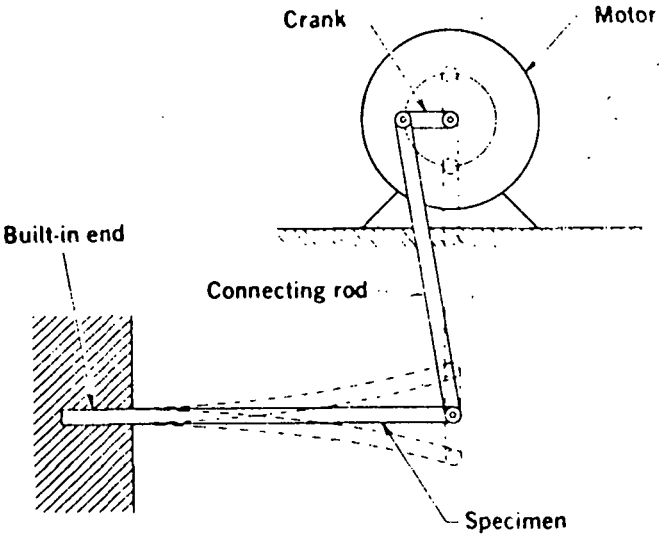

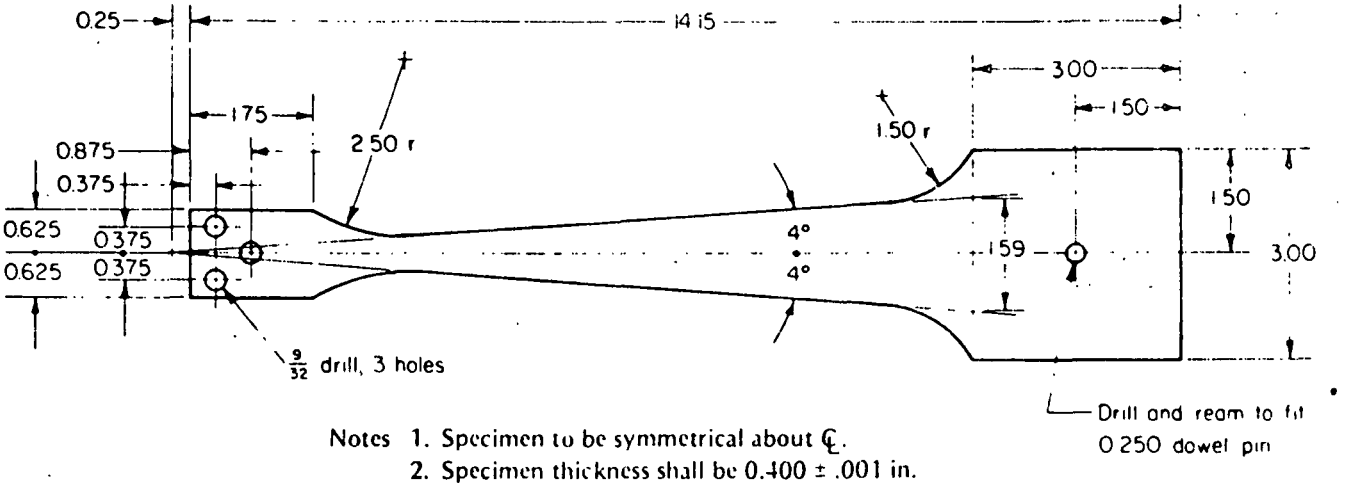

Notes 1. Specimen to be symmetrical about ℄.
2. Specimen thickness shall be 0.400 ± .001 in.
3. All dimensions in inches.

Schematic illustration of reversed plate bending test machine (upper) and specimen geometry/dimensions, below.

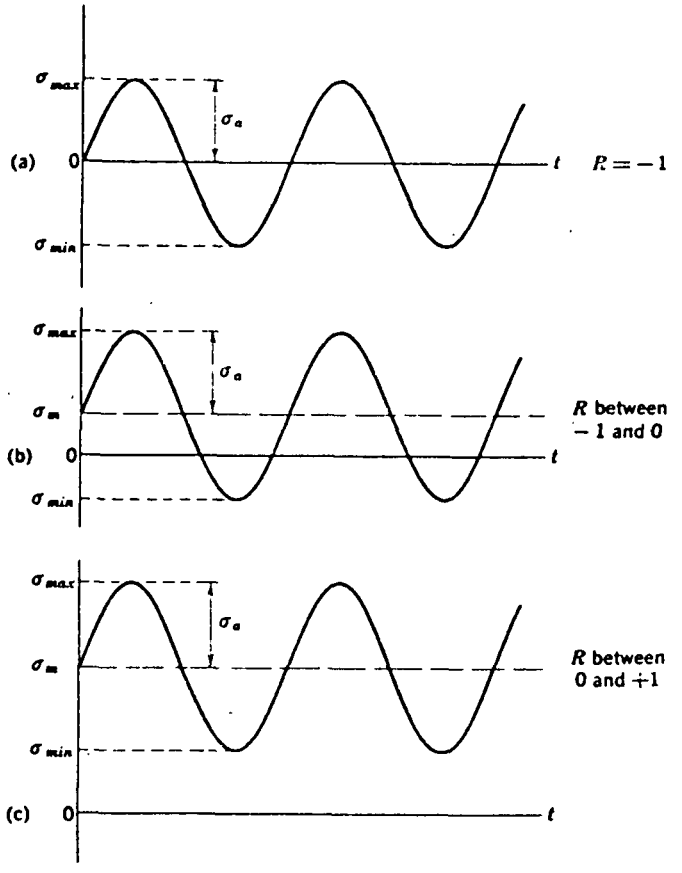

Schematic illustration of three alternating load forms as a function of time (t) in fatigue

IMPORTANT VARIABLES

- STRESS AMPLITUDE
- MEAN STRESS
- SPECIMEN GEOMETRY
- FREQUENCY
- NOTCH/SMOOTH
- SURFACE FINISH
- TEMPERATURE
- Cl^-, $S_2O_3^=$ CONCENTRATION
- pH

CORROSION TESTING PROGRAM

COMPARISON OF WEIGHT LOSSES
DUE TO PITTING OF SUCTION ROLL ALLOYS

ALLOY	CORROSION RATE, mpy	ALLOY	CORROSION RATE, mpy
A75	3.4	CF3M	1.0
CA15	12.1	1811	0.1
KA171	0.04	1804	0.5
2505	0.7	304L	3.0
KA171	0.08	VKA 378	0.06
A63	0.0	1300	14.3

NORMALIZATION OF FATIGUE METHODS

- ACQUISITION OF ALTERNATING BENDING APPARATUS
- ACQUISITION OF THREE ROTATING BENDING MACHINES
- TEST CHAMBER DESIGN, SHAKEDOWN

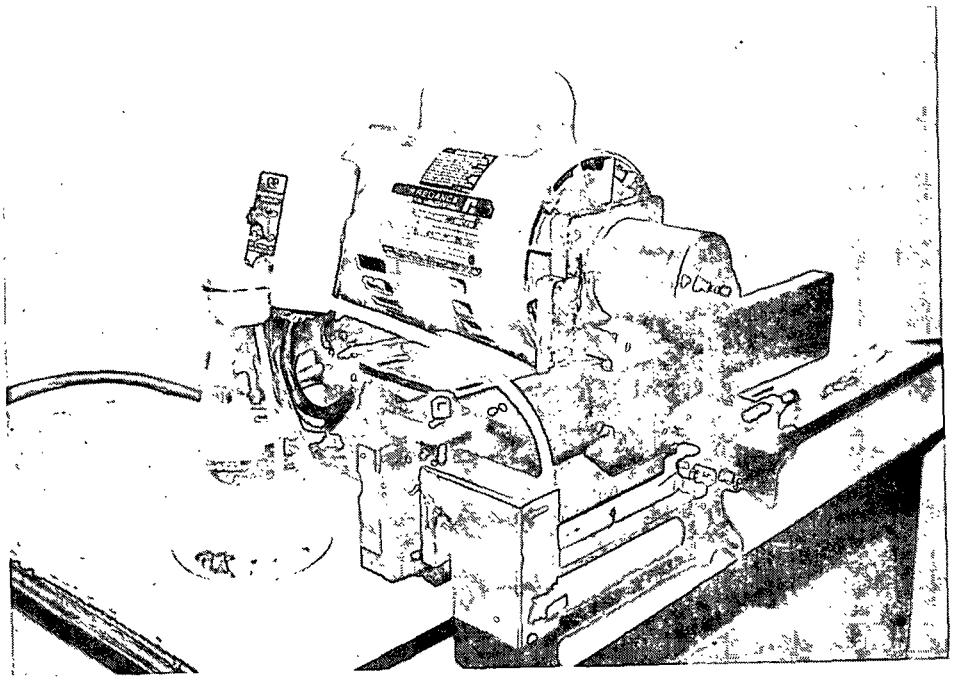

Tatnall Krause alternating bending fatigue machine fitted with a wick arrangement for delivery of corrosive solutions to a stress concentrating hole in the test plate.

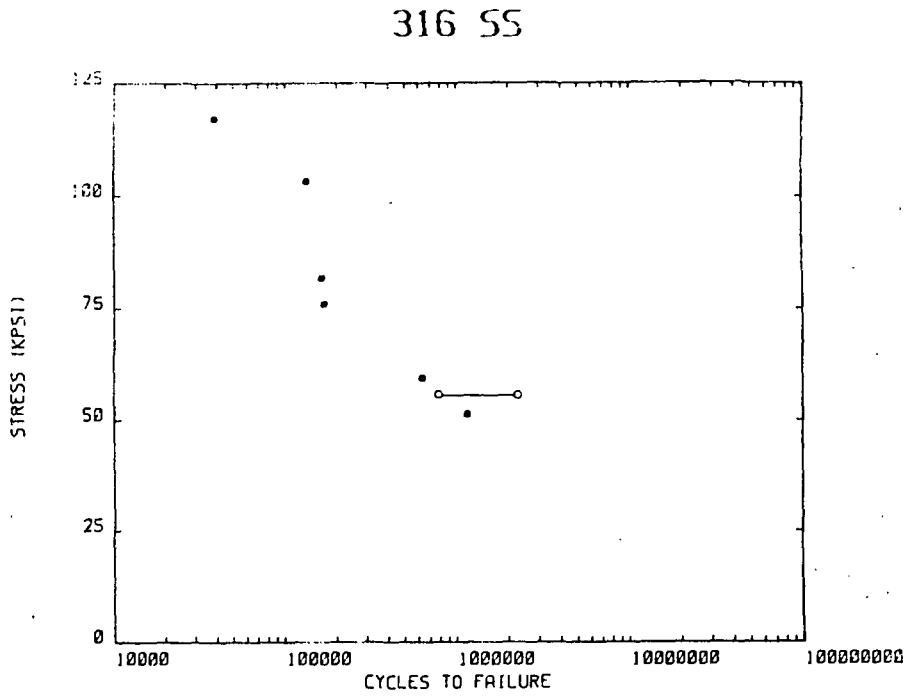

S-N curve for 316L stainless steel exposed to Environment #1 (1000 ppm chloride, pH 4.7), as generated with the Tatnall Krause alternating bending machine.

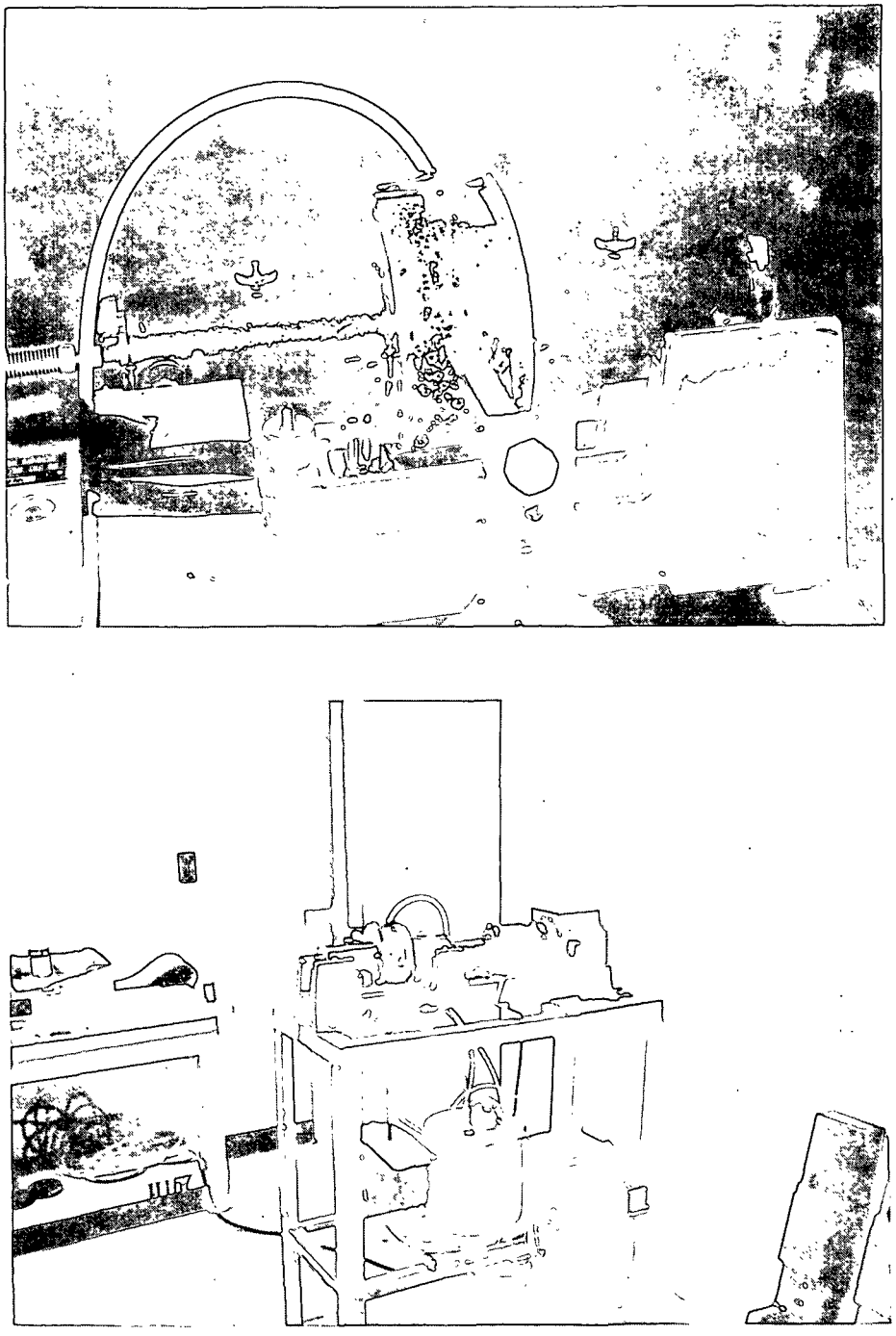

R. R. Moore rotating bending fatigue machine fitted with a recent version of a corrosion test chamber.

PREDICTIVE TEST DEVELOPMENT

INITIATION VS. PROPAGATION

STRESS INTENSITY CONCEPT

$$\text{DRIVING FORCE FOR GROWTH} = \begin{cases} \text{NOMINAL STRESS} \\ \text{CRACK LENGTH} \\ \text{GEOMETRY} \end{cases}$$

$$\Delta K = (\text{STRESS RANGE})\ (\text{CRACK LENGTH})^{\frac{1}{2}}\ (\text{GEOMETRY})$$

$$= S_R (a)^{\frac{1}{2}}\ fn\ (a/w)$$

STRESS INTENSITY NORMALIZES

- LONG CRACK, LOW STRESS
- SHORT CRACK, HIGH STRESS
- LOADING GEOMETRY

MEAN STRESS EFFECTS

"R" RATIO = K_{max}/K_{min}

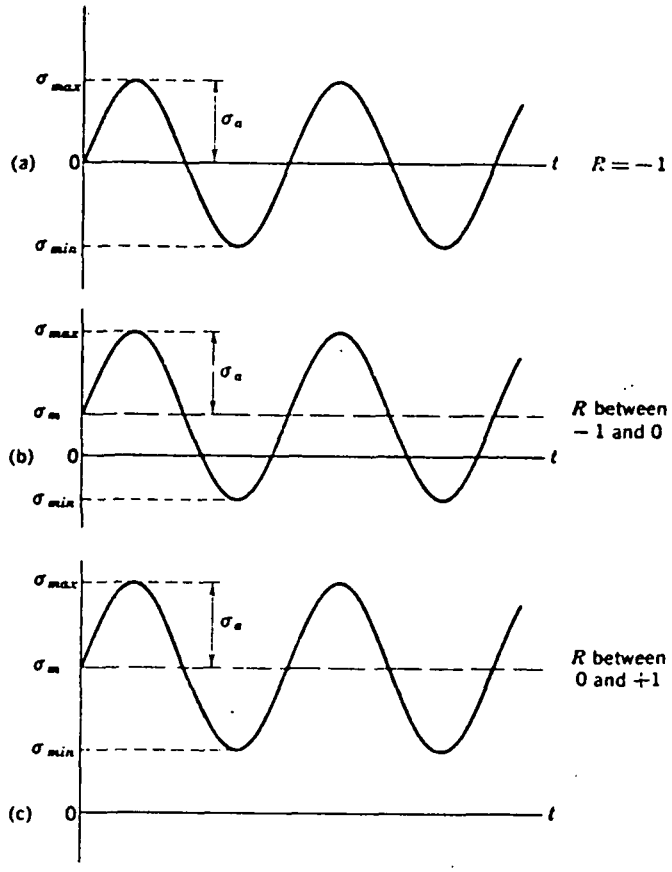

Schematic illustration of three alternating load forms as a function of time (t) in fatigue

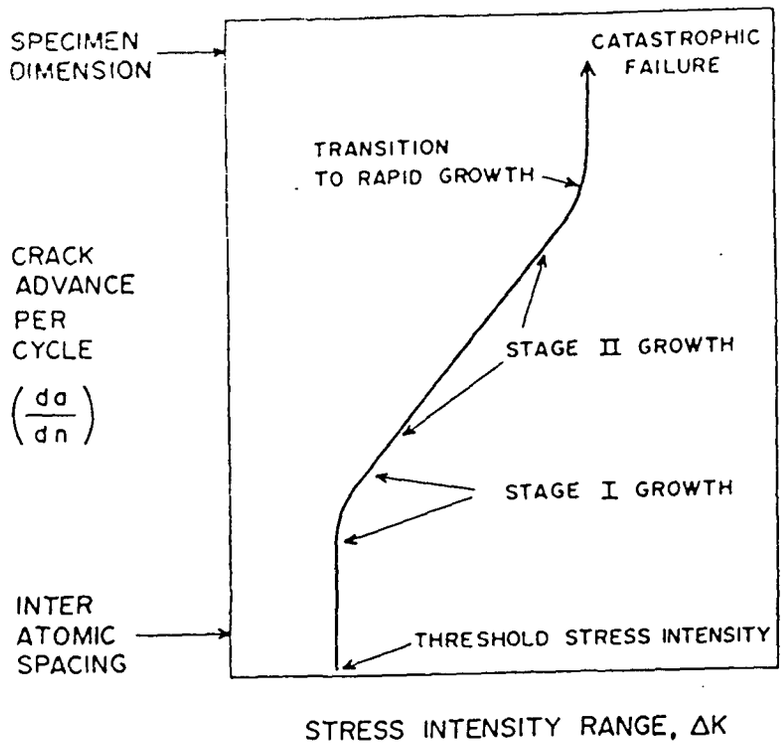

Schematic diagram showing the dependence of crack growth rates on the cyclic stress intensity.

ΔK_{th} DETERMINATION

- CRACK SHARPNESS
- LOAD SHEDDING
- COMPRESSIVE RESIDUAL STRESSES

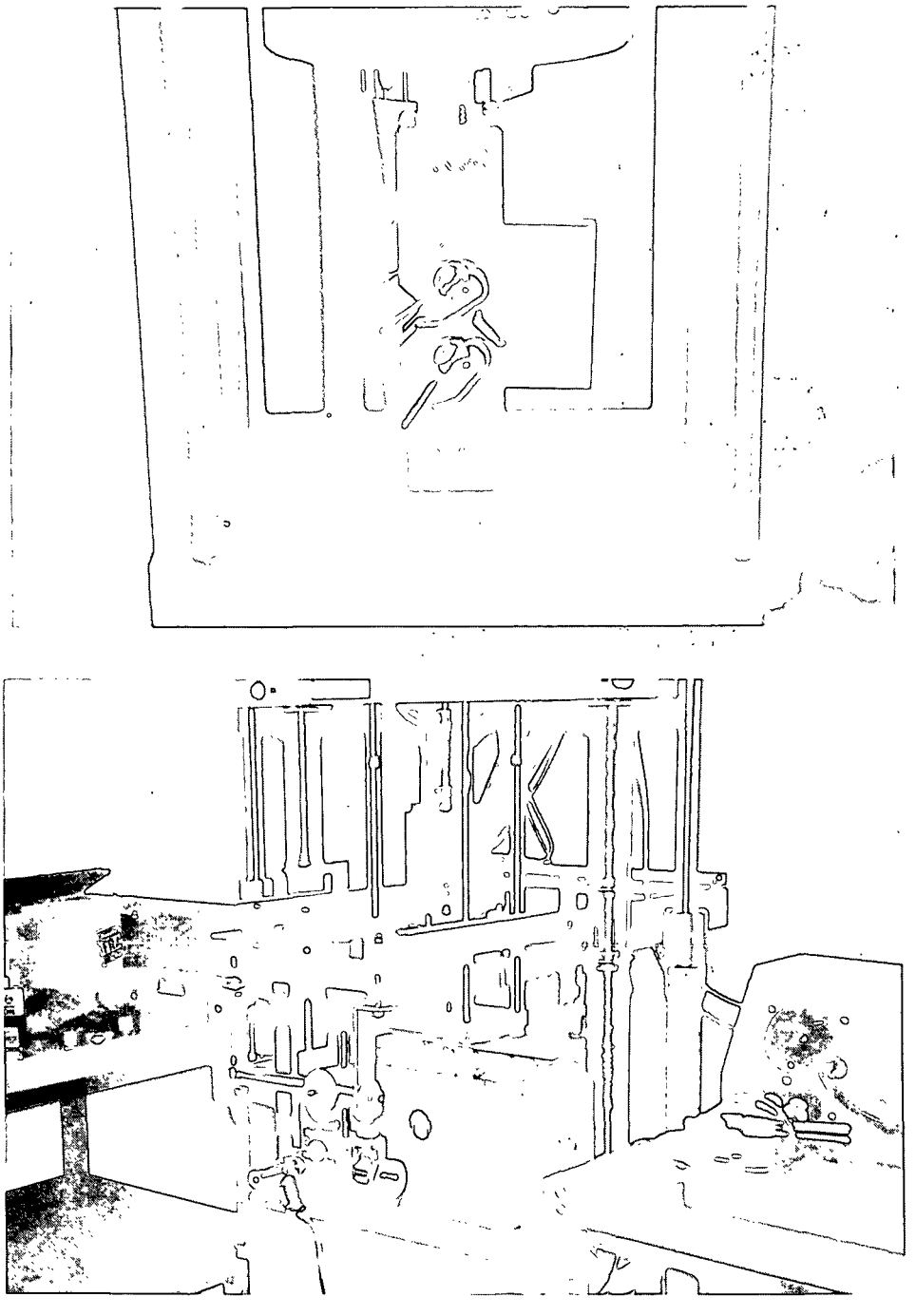

The MTS electrohydraulic testing machine equipped with modified test frame and environmental chamber for fatigue testing in simulated paper machine white waters.

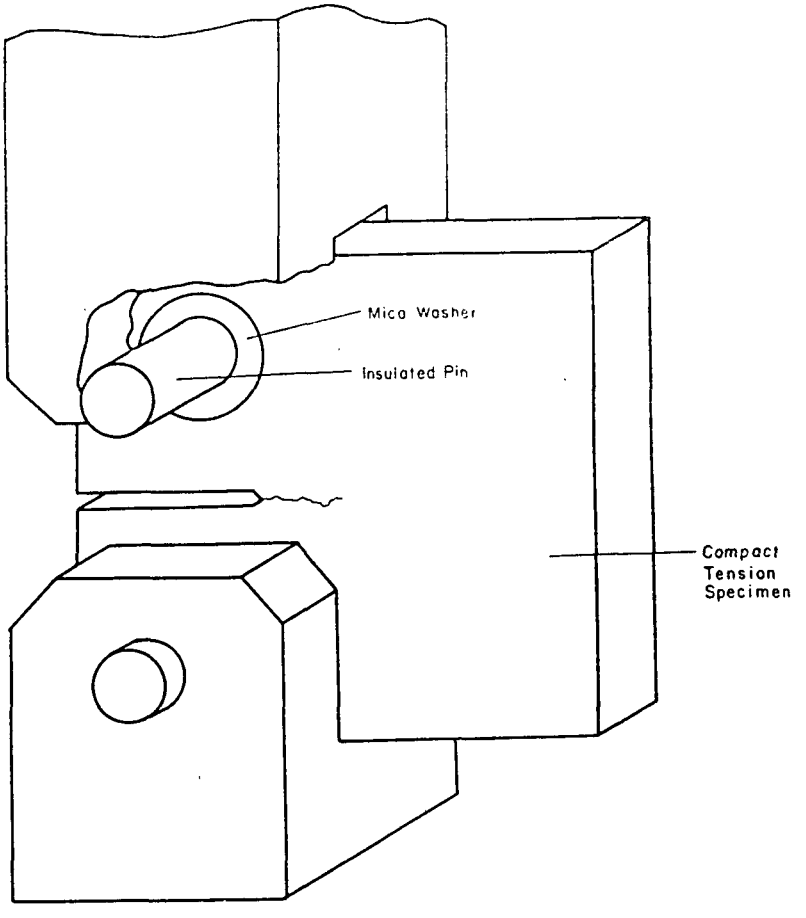

Cut-away view of the gripping arrangements used in near-threshold fatigue testing.

TEST ENVIRONMENTS

ENVIRONMENT	CHLORIDE, ppm	SULFATE, ppm	THIOSULFATE, ppm	pH
A	1000	0	0	4.7
B	100	1000	0	3.6
C	1000	1000	0	3.5
D	200	500	50	4.1

REPRODUCIBILITY

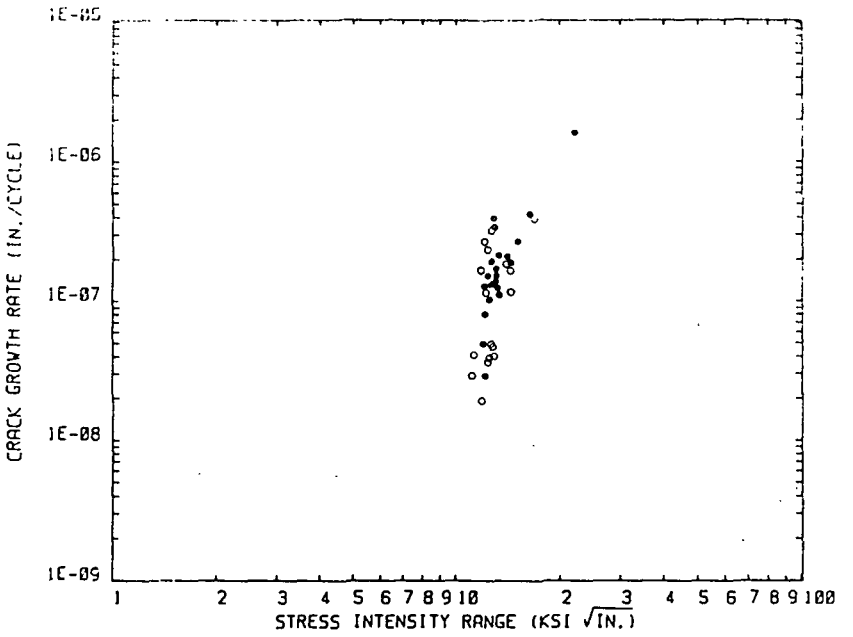

A comparison of fatigue crack growth rates measured in two separate tests on Alloy 63 in Environment A.

ENVIRONMENTAL EFFECT

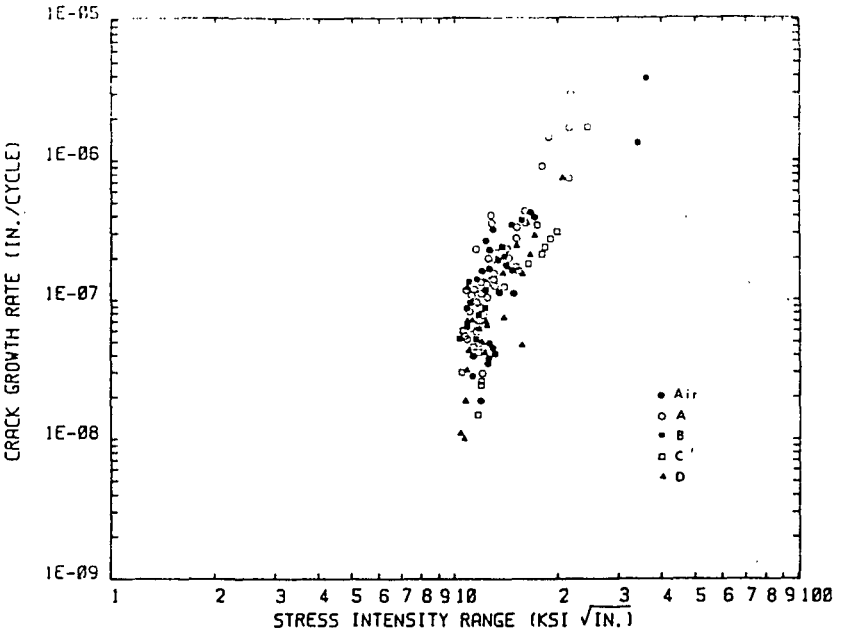

Comparison of the effects of test environment on fatigue crack growth in Alloy 63. R = 0.1, T = 50°C.

ALLOY 63 VS. ALLOY 75

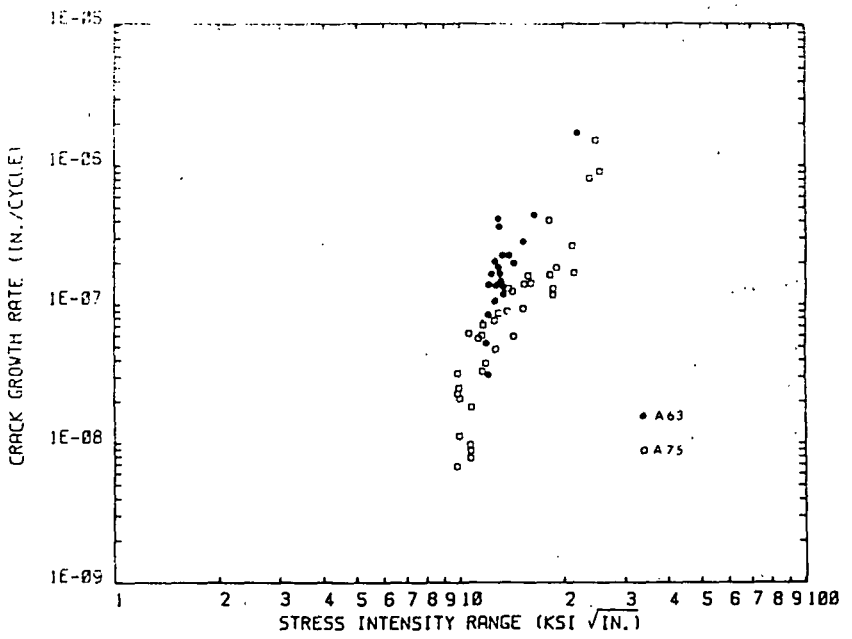

A comparison of the fatigue crack growth characteristics exhibited by Alloys 75 and 63 in a simulated white water containing 1000 ppm chloride.

MEAN STRESS EFFECTS (RESIDUAL STRESS)

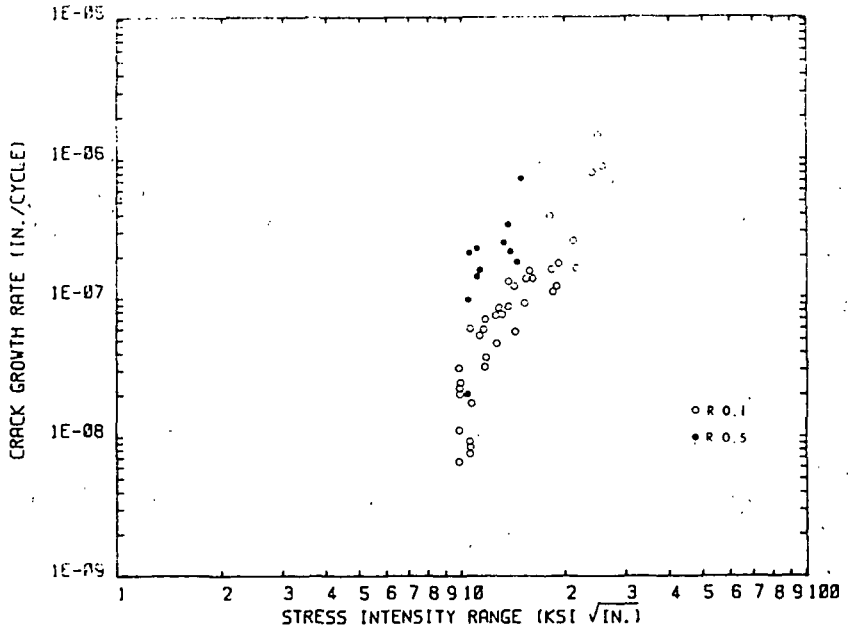

Crack growth rate data for Alloy 75 in a simulated paper machine white water showing the effects of mean stress on growth rate.

FRACTOGRAPHY

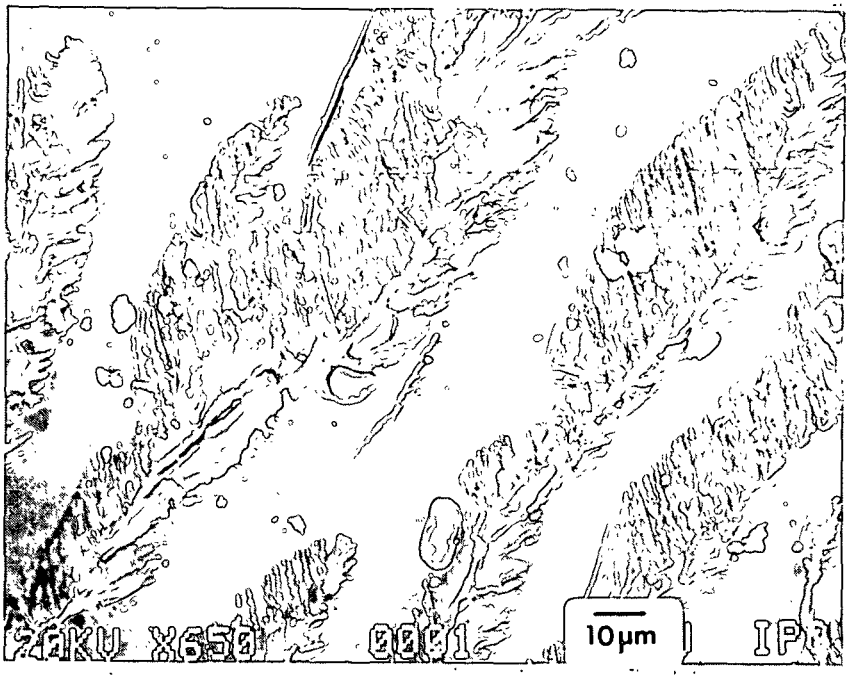

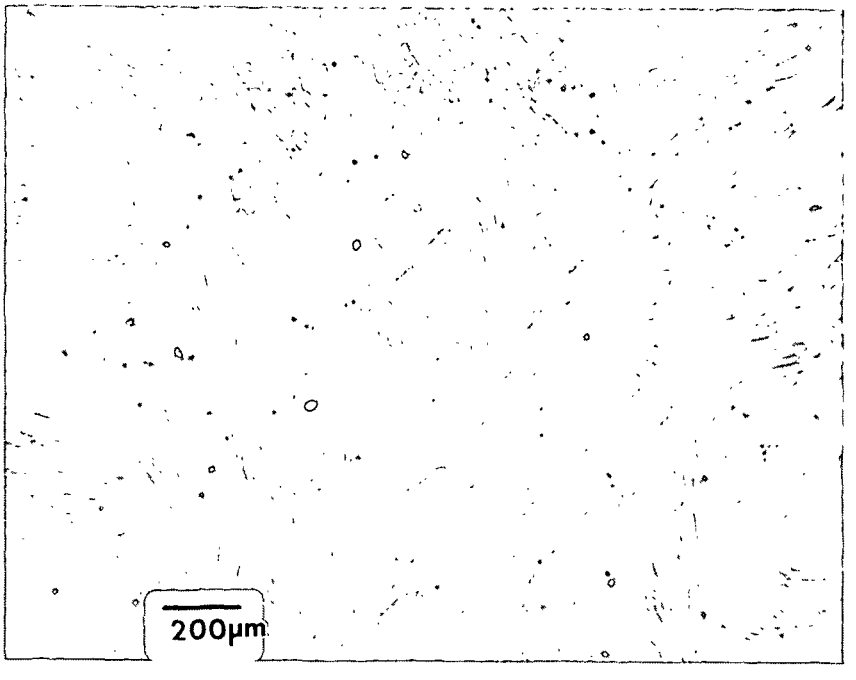

A typical scanning electron fractograph showing features on the fracture surface of an Alloy 63 specimen used in the fatigue crack growth studies.

CONCLUSIONS — NEAR THRESHOLD CRACKING

- MEAN STRESS EFFECT IN STAGE I ONLY
- NO STRONG ENVIRONMENT EFFECT
- NO APPARENT CORRELATION WITH SERVICE

SLOW STRAIN RATE TESTING

MATERIALS ACQUISITION

ALLOY 75

VKA 378

AVESTA 3RE60

VKA 171

ALLOY 63

FUTURE WORK

- NEAR THRESHOLD, STRONGER ENVIRONMENT
- NEAR THRESHOLD, LOWER FREQUENCY
- S-N TESTING
- SLOW STRAIN RATE TESTS
- PITTING, CREVICE CORROSION TESTING
- METALLOGRAPHY

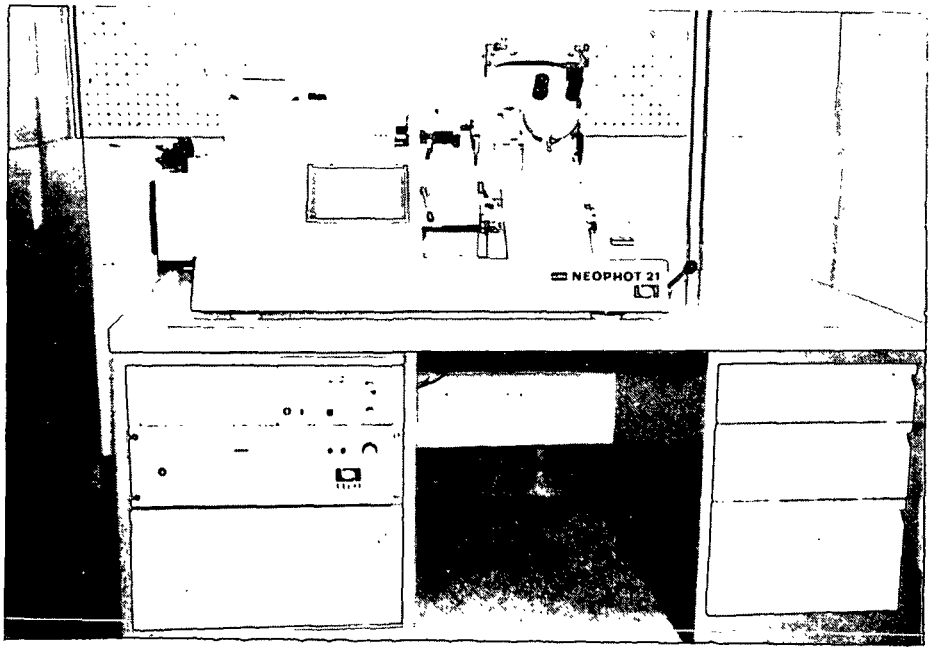

METALURGICAL MICROSCOPE RECENTLY INSTALLED IN THE CORROSION RESEARCH BUILDING.

SIGNIFICANCE TO THE INDUSTRY

- EMBRYONIC STAGE, BUT...
- BRIGHT PROSPECTS FOR REDUCING SUCTION ROLL COSTS

Project 3384

REFINING OF CHEMICAL PULPS FOR IMPROVED PROPERTIES

Clyde Sprague

PROJECT 3384 - REFINING OF CHEMICAL PULPS FOR IMPROVED PROPERTIES

OBJECTIVES

- ON-LINE MEASURE OF REFINING INTENSITY
- MODEL BETWEEN INTENSITY AND PROPERTIES
- ON-LINE CONTROL OF PROPERTY DEVELOPMENT

CONTROL OF REFINING SEVERITY

SPECIFIC EDGE LOAD $SEL = \frac{P}{\Omega Z^2 L}$

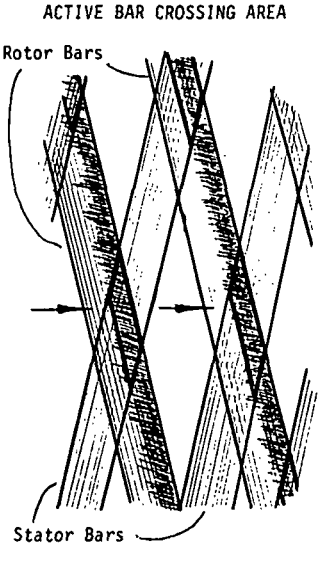

$$\text{Normal stress } \bar{P}_N = \frac{T}{Z^2 L \bar{\ell}} = \frac{P}{\pi\mu\Omega Z^2 L \bar{\ell}(D - \frac{1}{2}L\cos\theta)}$$

$$\text{Shear stress } \bar{\tau}_f = \mu_f \bar{P}_N = \frac{\mu_f T}{Z^2 L \bar{\ell}} = \frac{(\mu_f/\mu)P}{\pi\Omega Z^2 L \bar{\ell}(D - \frac{1}{2}L\cos\theta)}$$

$$\text{Tensile stress } \bar{\sigma}_f = \frac{\mu_f \bar{P}_N \ell_f}{t_f} = \frac{\mu_f T \ell_f}{Z^2 L \bar{\ell} t_f} = \frac{(\mu_f/\mu)P\ell_f}{\pi\Omega Z^2 L \bar{\ell}(D - \frac{1}{2}L\cos\theta)t_f}$$

EXPERIMENTAL APPROACHES

- IN-REFINER MEASUREMENT OF P_N
- VERIFICATION OF $\bar{\tau}_f$ AND $\bar{\sigma}_f$ EXPRESSIONS

MODEL EQUATIONS FOR VALLEY BEATER

$$\bar{P}_N = \frac{\Lambda}{189\mu\bar{\ell}}$$

$$\bar{\tau}_f = \frac{(\mu_f/\mu)\Lambda}{189\bar{\ell}}$$

$$\bar{\sigma}_f = \frac{(\mu_f/\mu)\Lambda\ell_f}{189\bar{\ell}t_f}$$

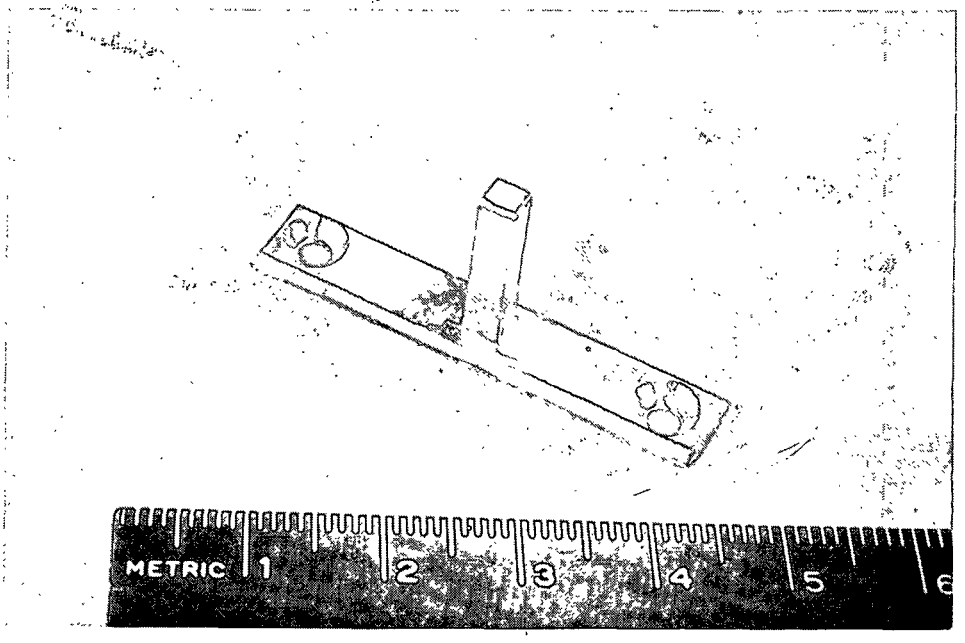

Bar segment and beam prior to strain gage attachment.

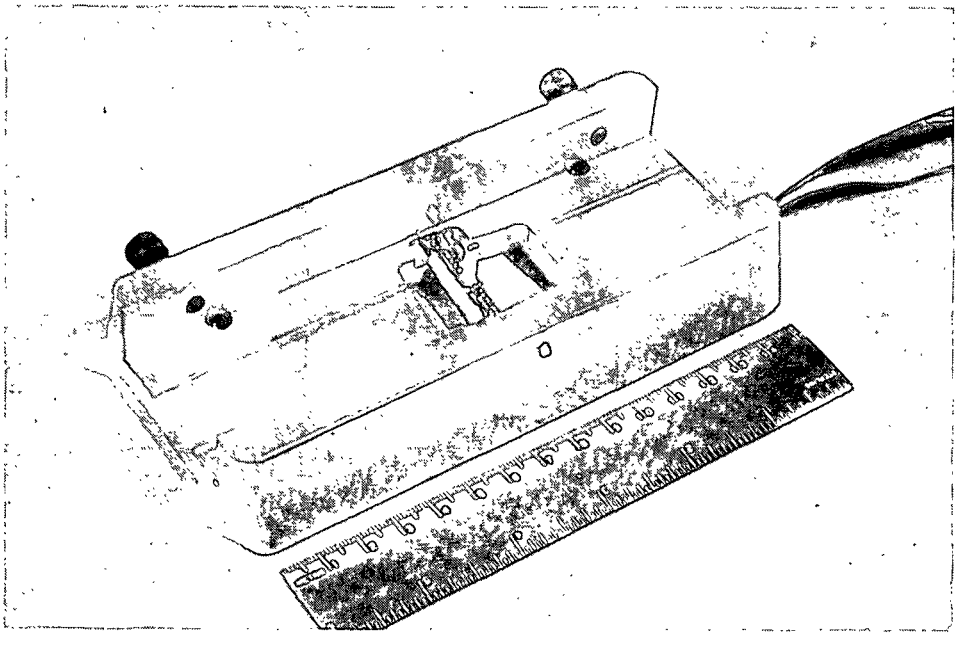

Strain gages attached to beam, bar segment installed in bedplate holder.

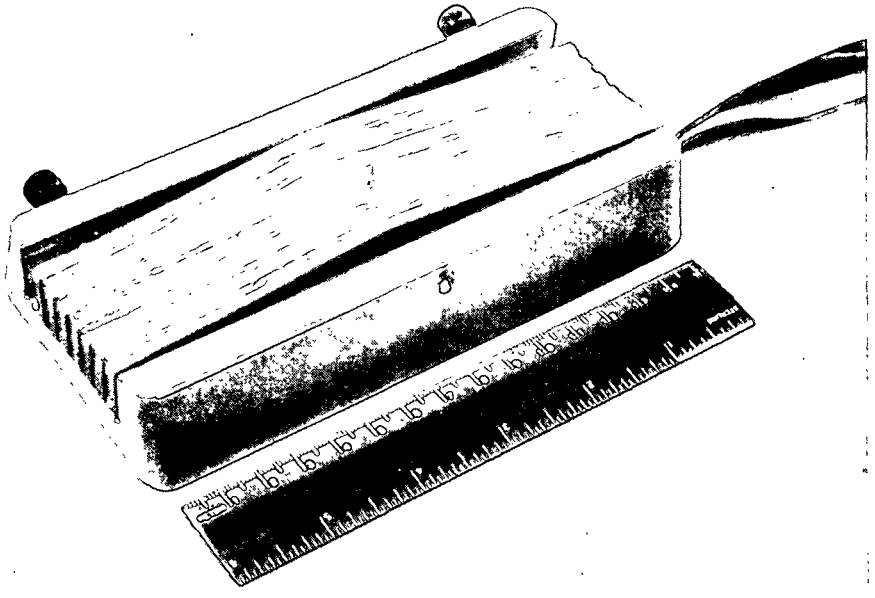

Beater bar assembly in place around instrumented bar segment, prior to potting.

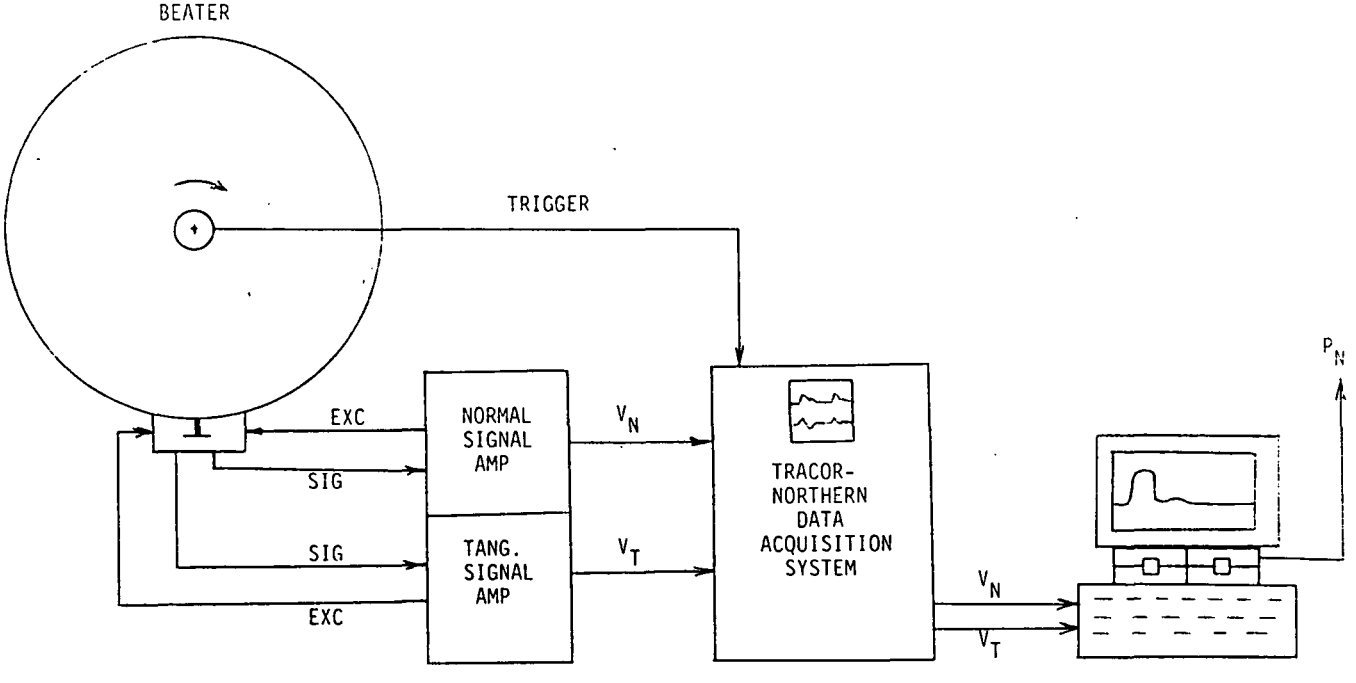

NORMAL PRESSURE MEASURING SYSTEM

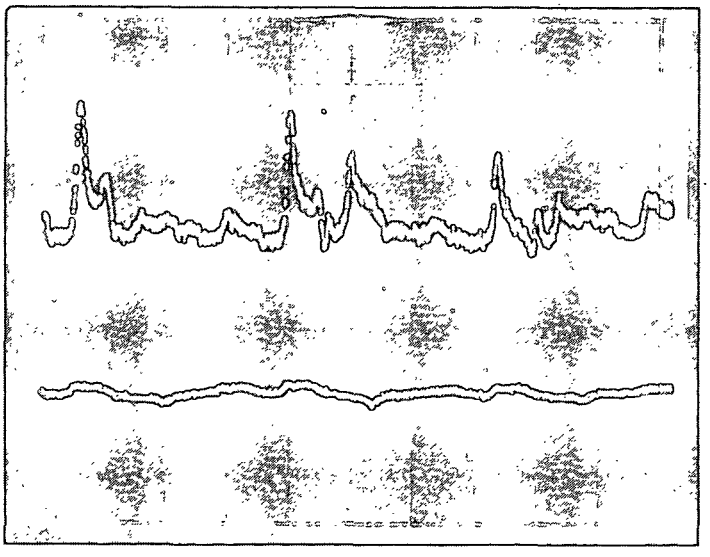

Oscilloscope trace of normal (top) and tangential (bottom) voltage outputs.

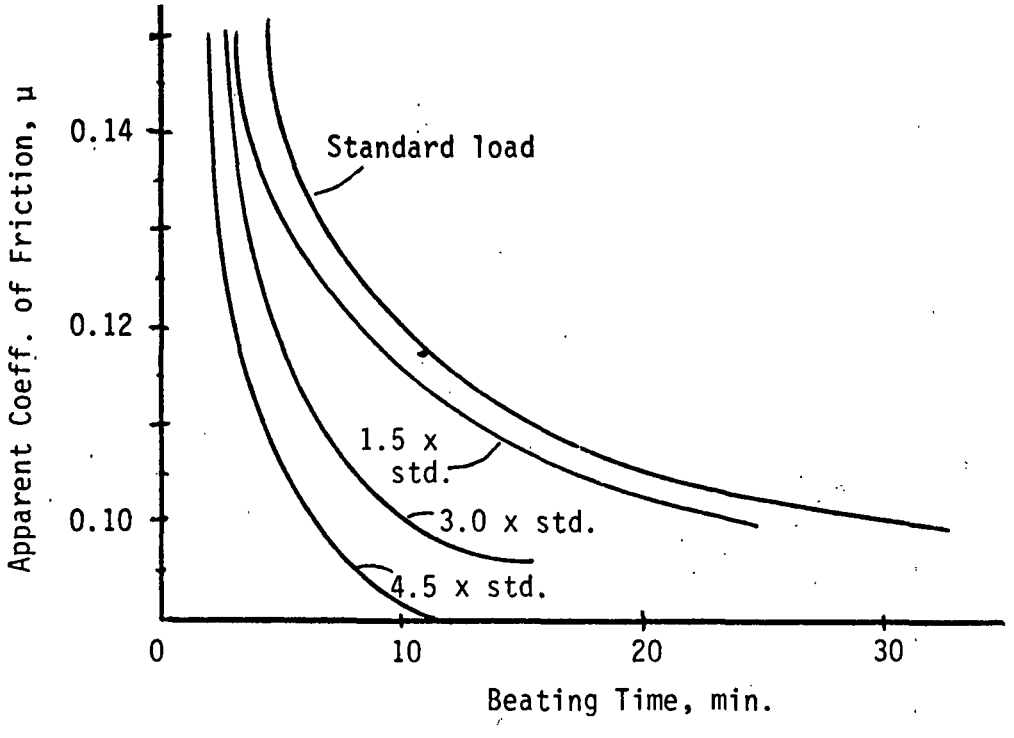

Apparent coefficient of friction as a function of beating time for several load levels.

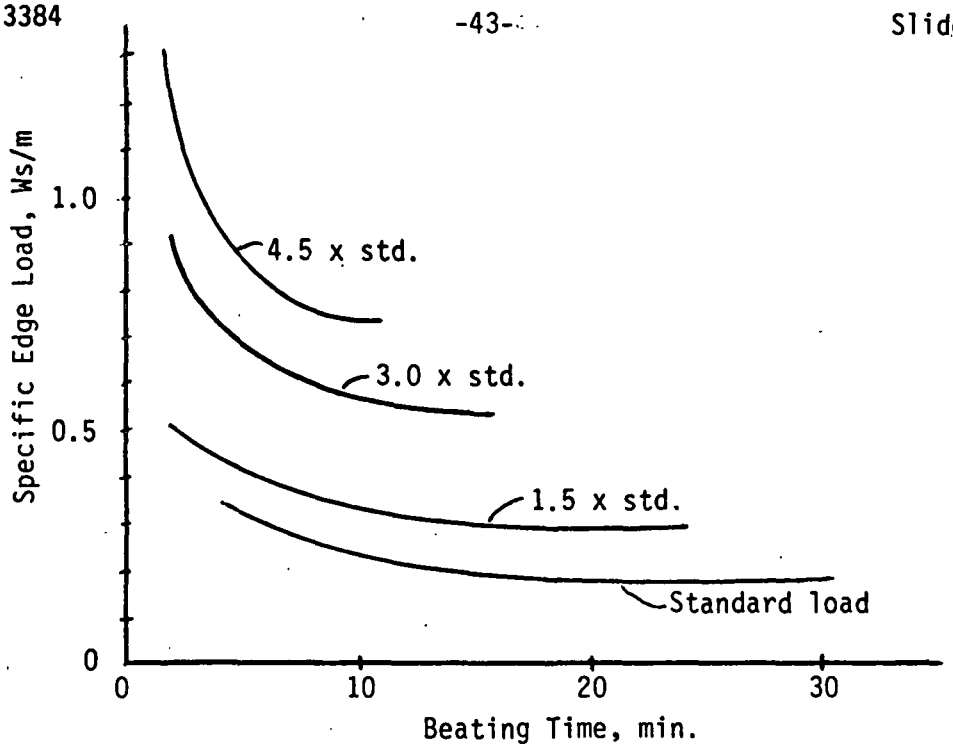

Specific edge load as a function of beating time for several levels of load.

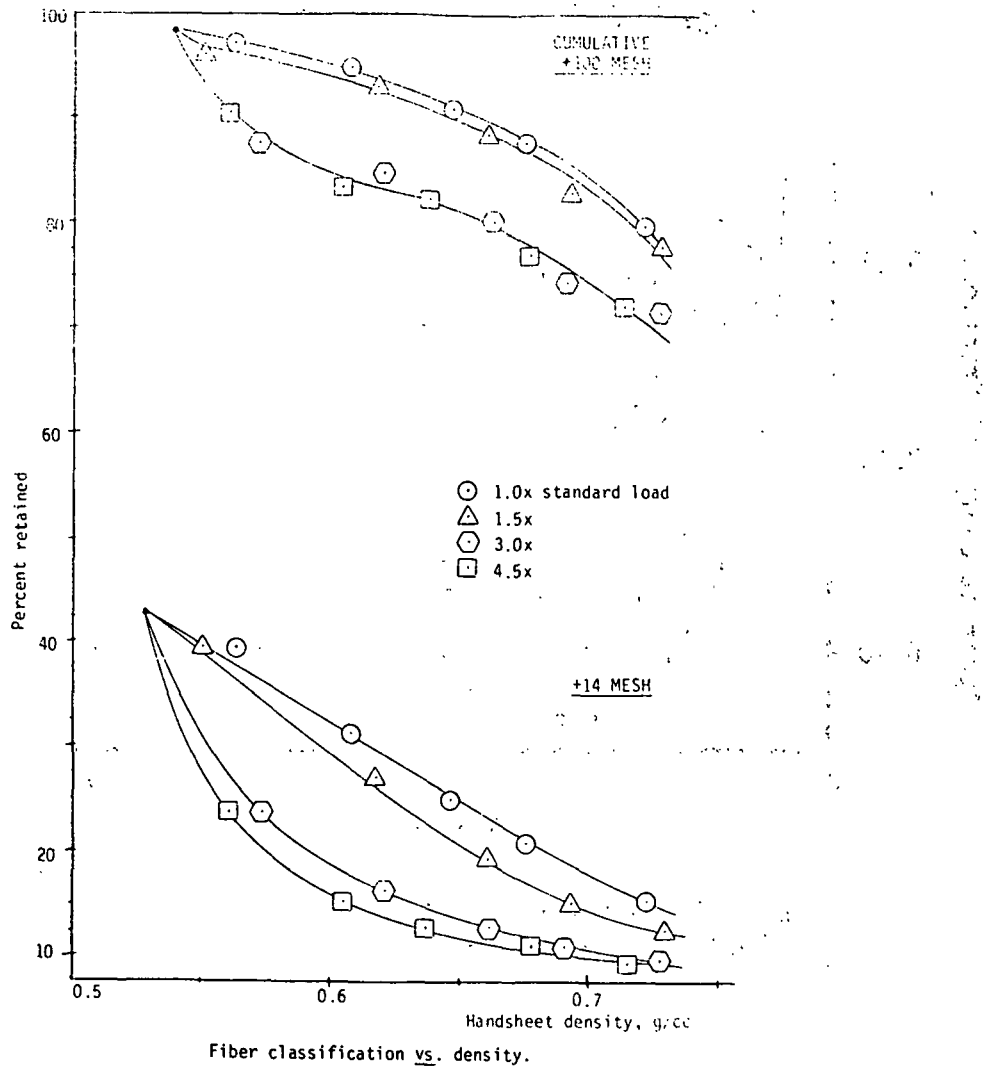

Fiber classification vs. density.

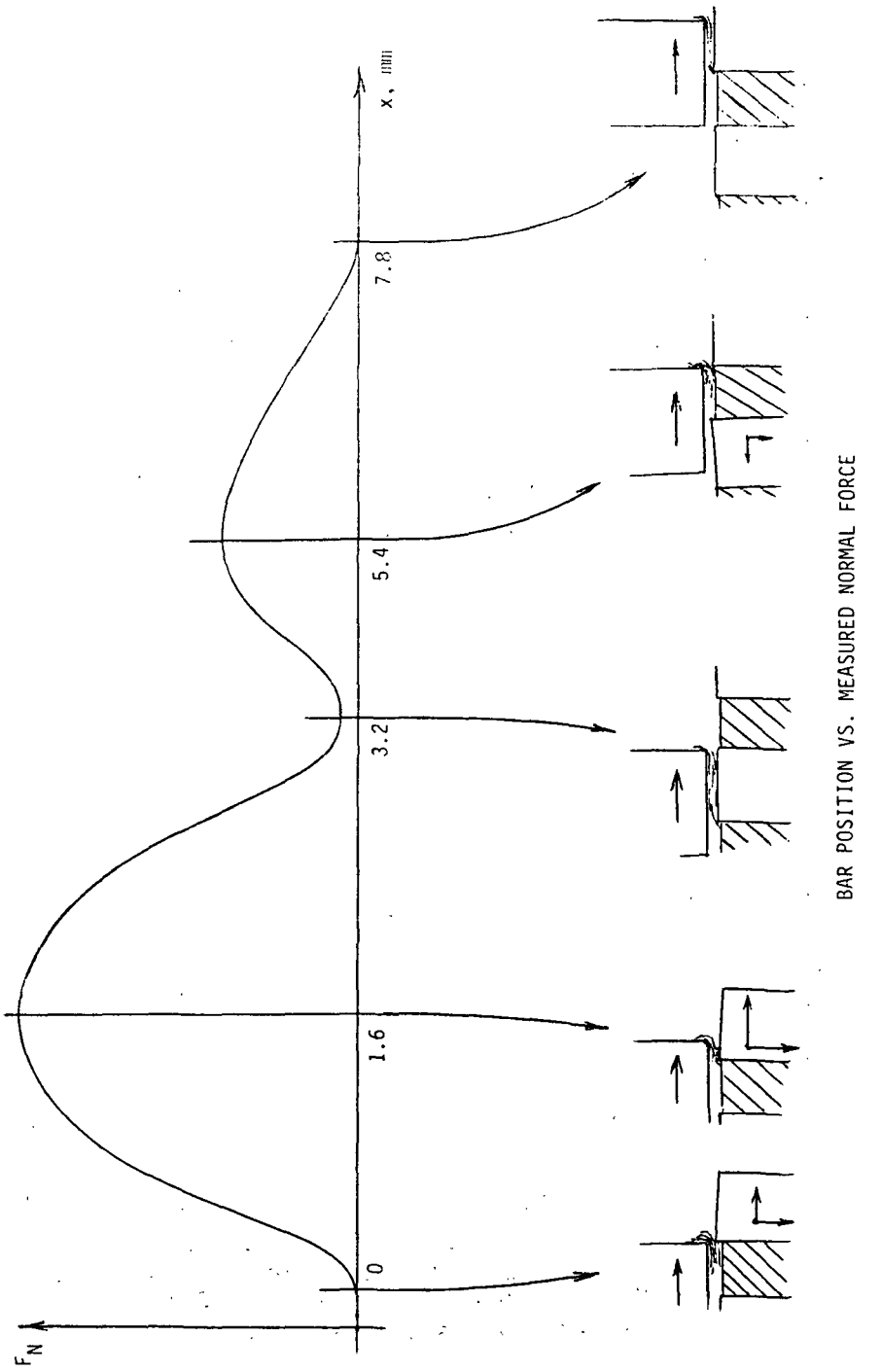

BAR POSITION VS. MEASURED NORMAL FORCE

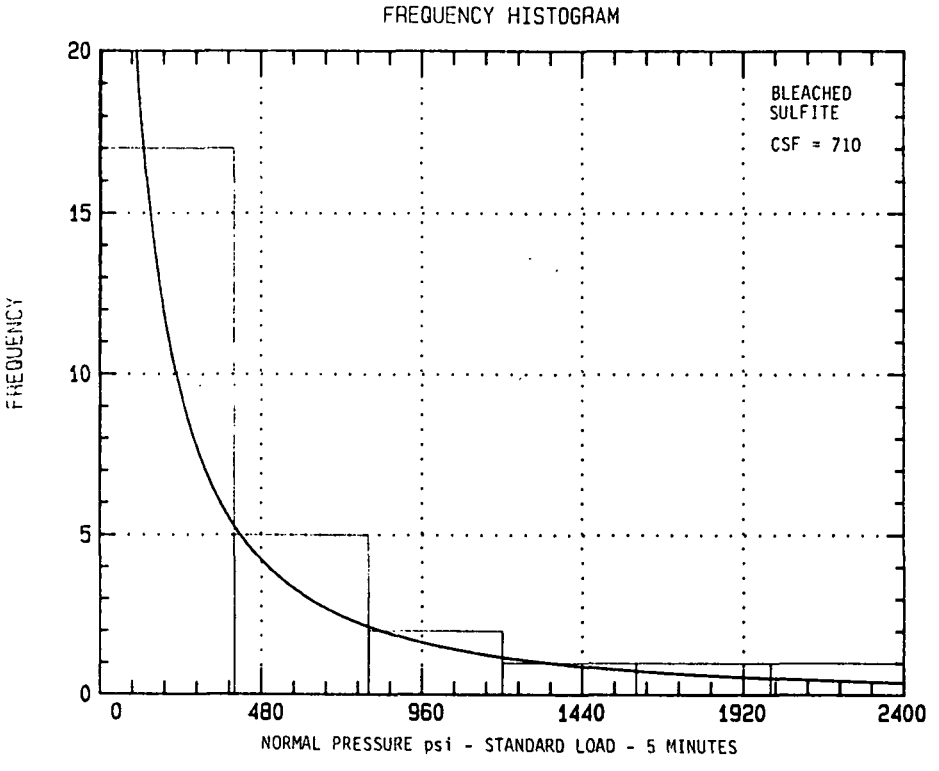

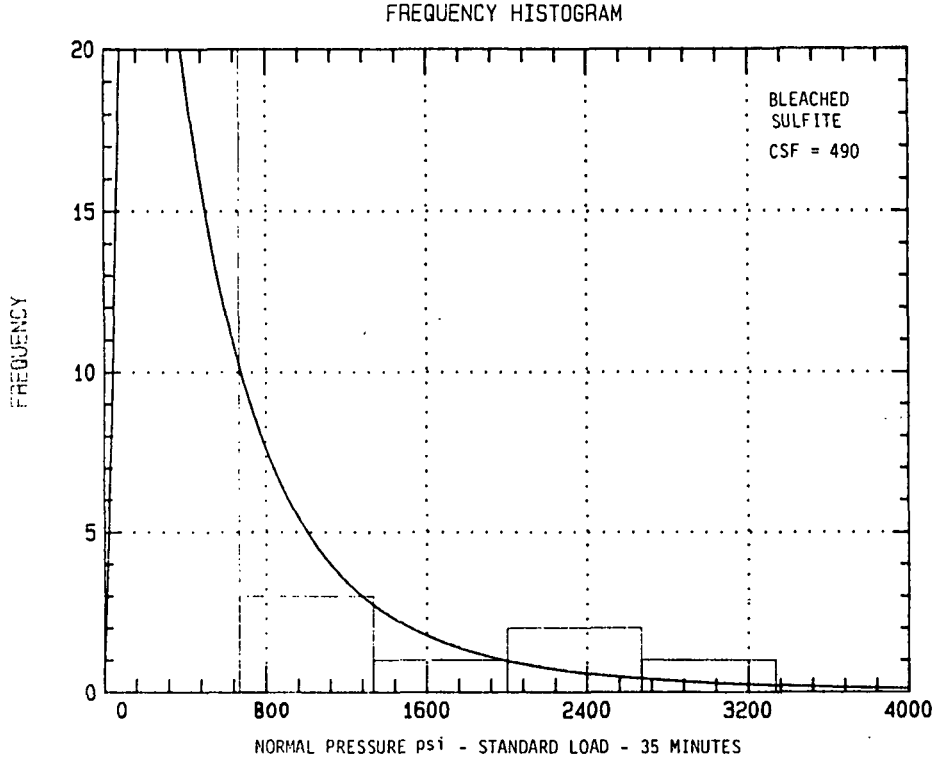

Valley Beater normal pressure histogram and log-normal fitted frequency distribution for a bleached sulfite softwood pulp.

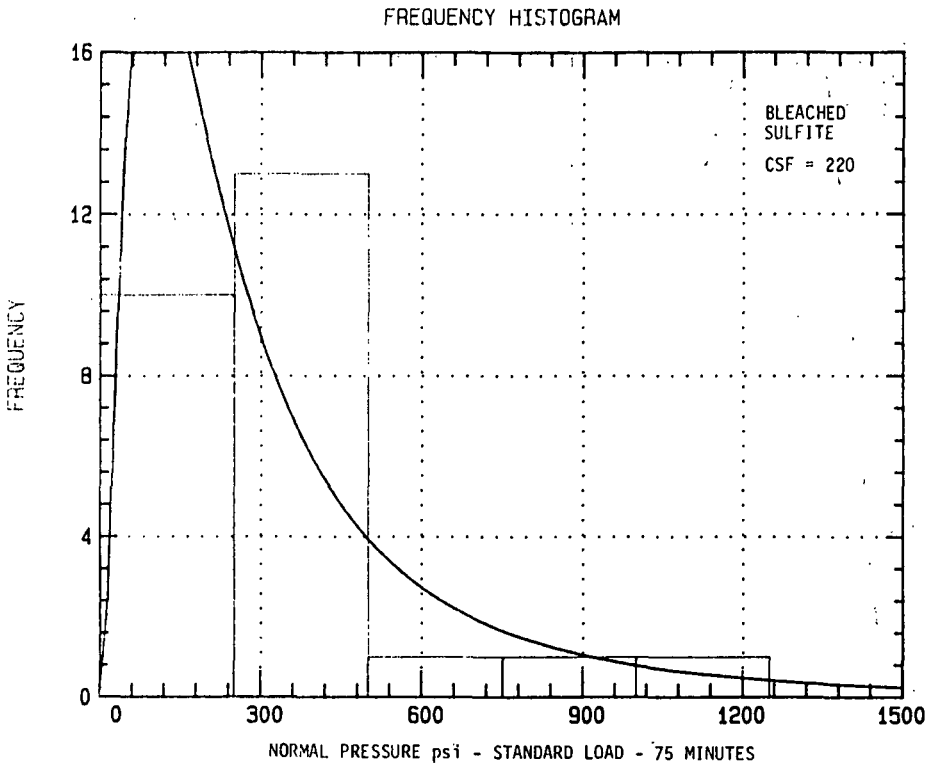

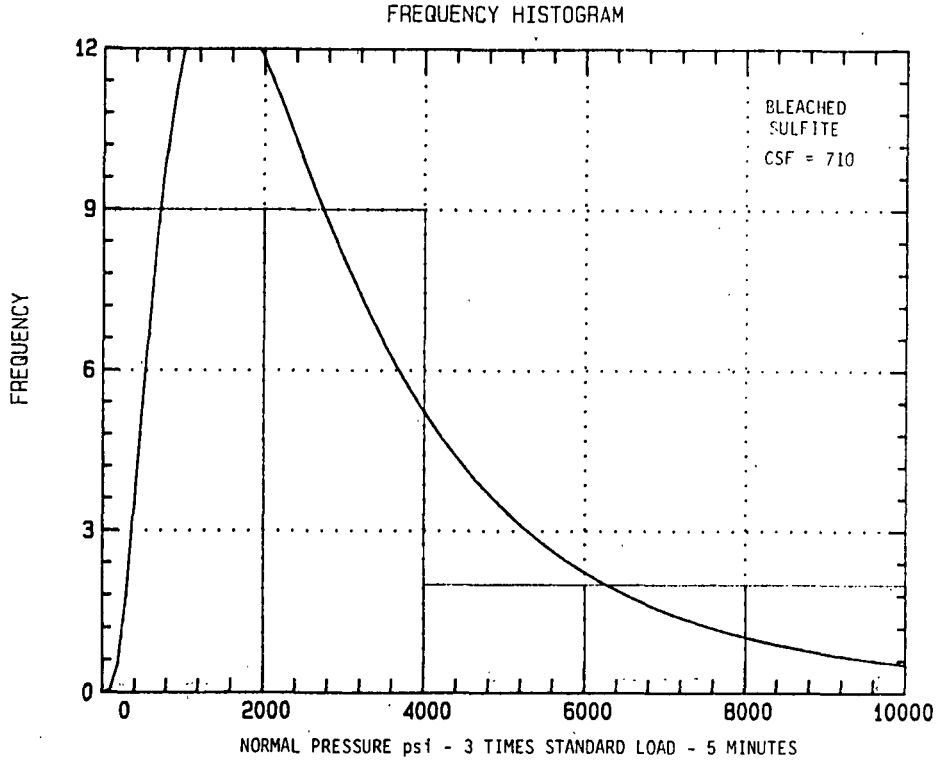

Valley Beater normal pressure histogram and log-normal fitted frequency distribution for a bleached sulfite softwood pulp.

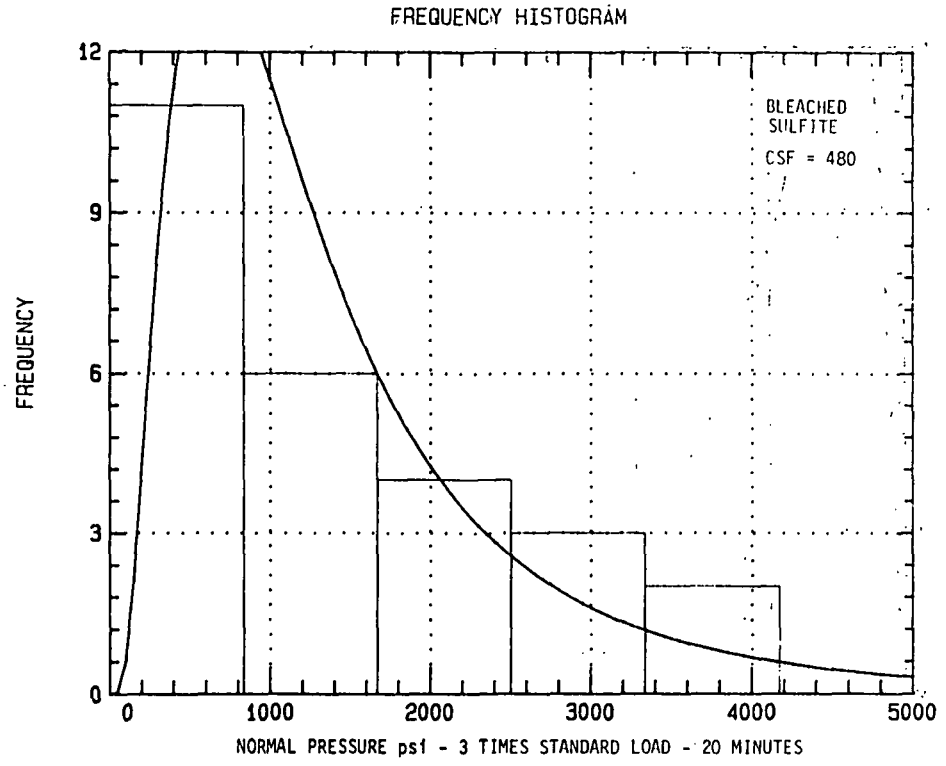

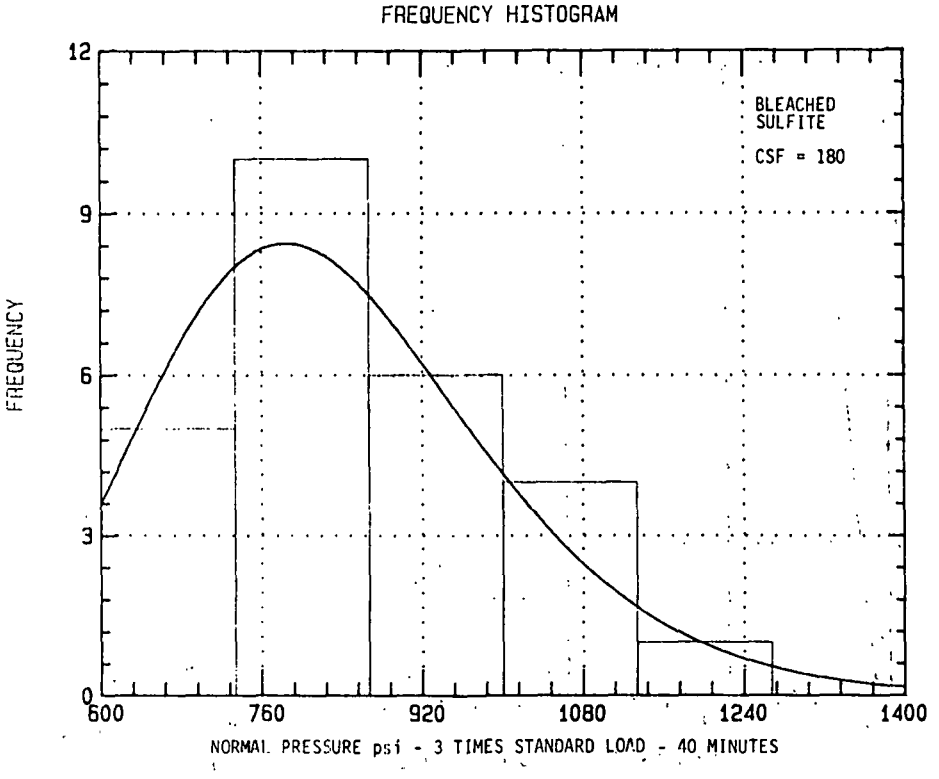

Valley Beater normal pressure histogram and log-normal fitted frequency distribution for a bleached sulfite softwood pulp.

VALLEY BEATER DATA - BLEACHED SULFITE PULP

LOAD	BEATING TIME	CSF	AVE. FIBER LENGTH	SEL WS/M
1X	5	710	2.19	0.263
	20	595	2.04	0.229
	40	450	1.90	0.229
3X	5	710	2.16	0.604
	10	630	1.82	0.553
	20	480	1.68	0.536

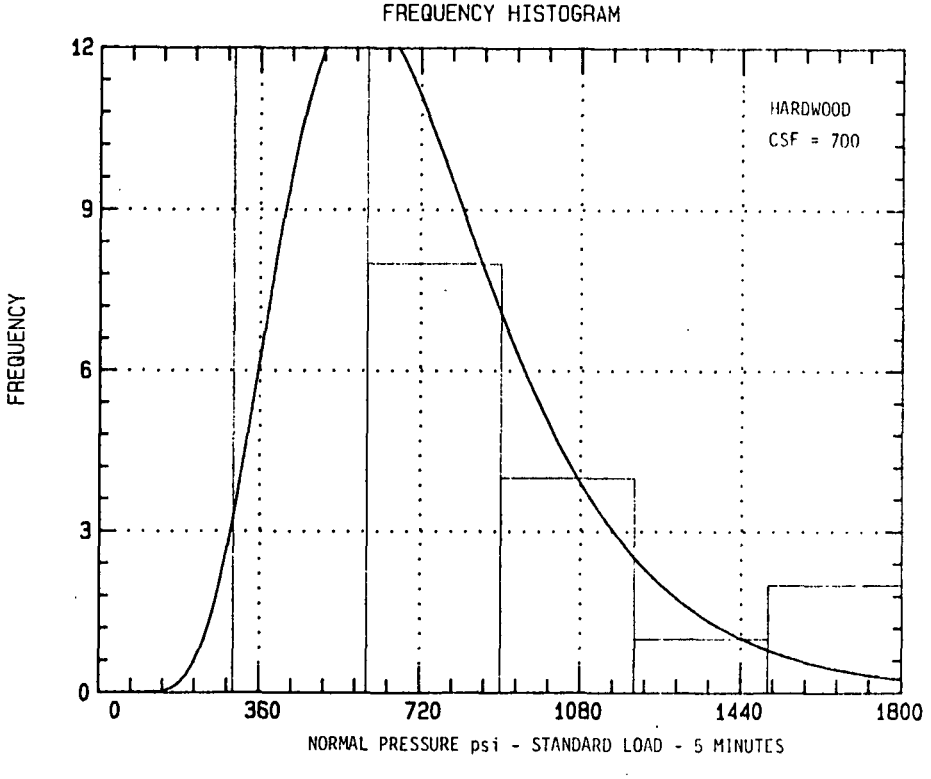

Valley Beater normal pressure histogram and log-normal fitted frequency distribution for hardwood pulp.

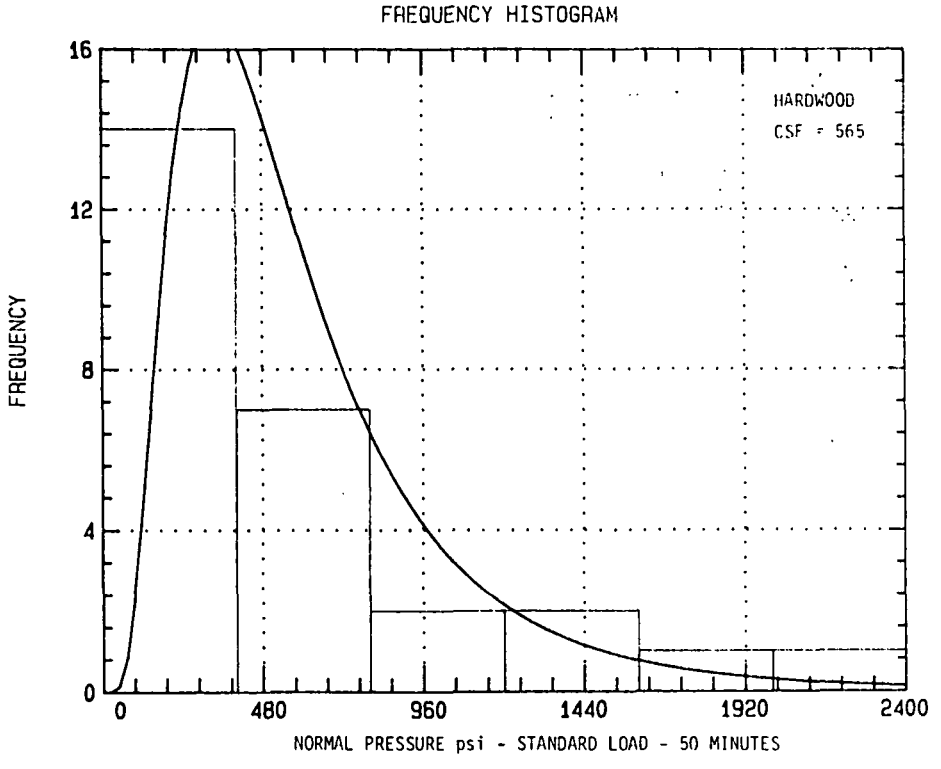

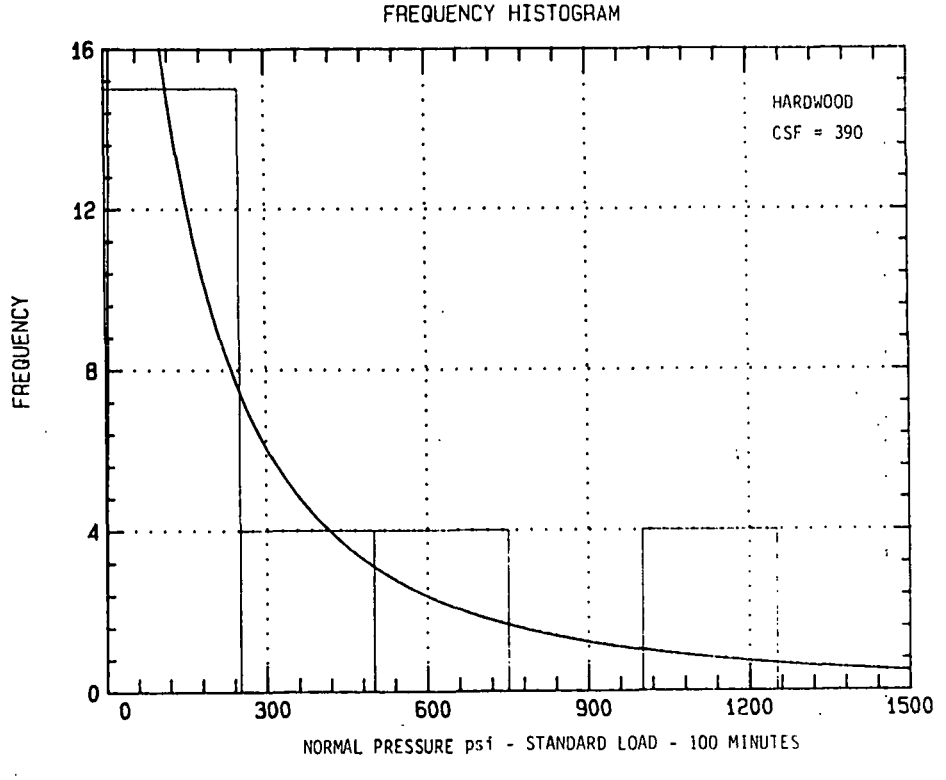

Valley Beater normal pressure histogram and log-normal fitted frequency distribution for hardwood pulp.

Project 3480/3584

PROCESS FUNDAMENTALS OF WET PRESSING

Clyde Sprague

PROJECT 3480/3584

WET PRESSING FUNDAMENTALS

OBJECTIVES: DETERMINE FEASIBILITY AND PERFORMANCE OF DISPLACEMENT PRESSING

DEVELOP A PREDICTIVE MODEL FOR WET PRESSING

DISPLACEMENT PRESSING

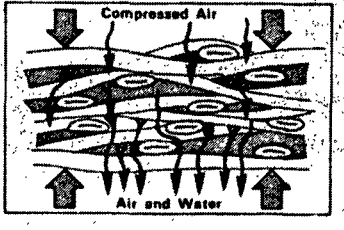

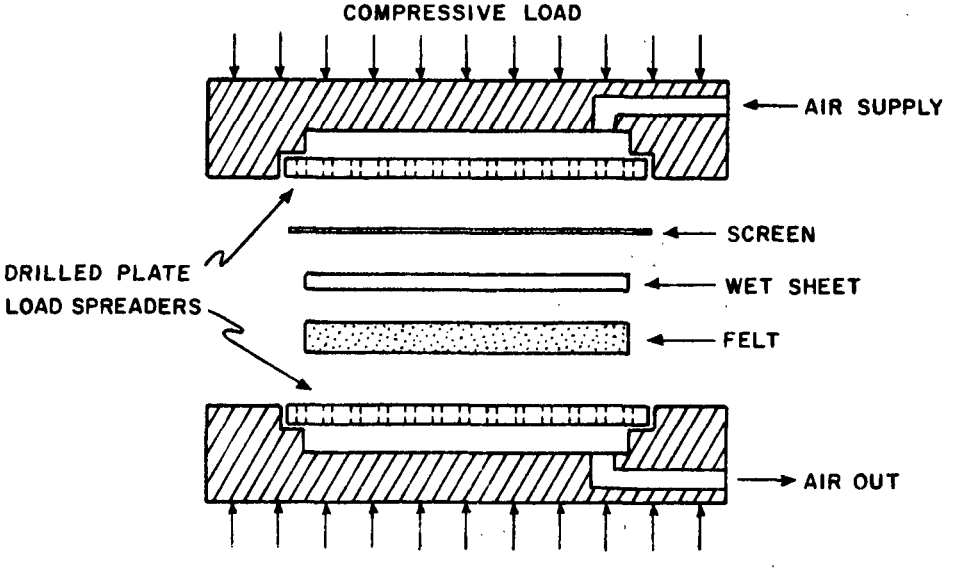

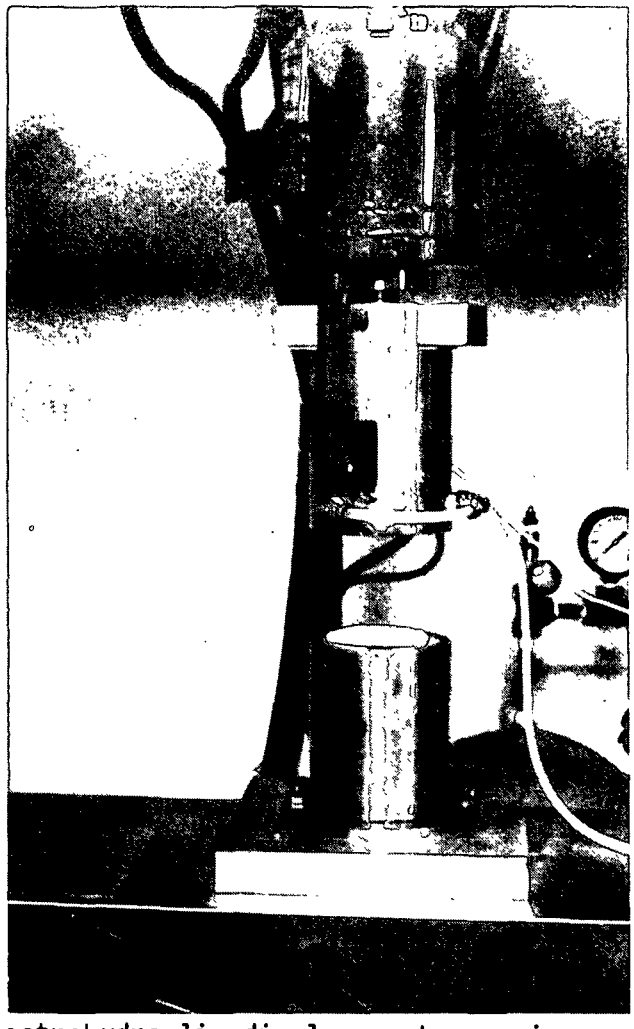

Electrohydraulic displacement pressing system.

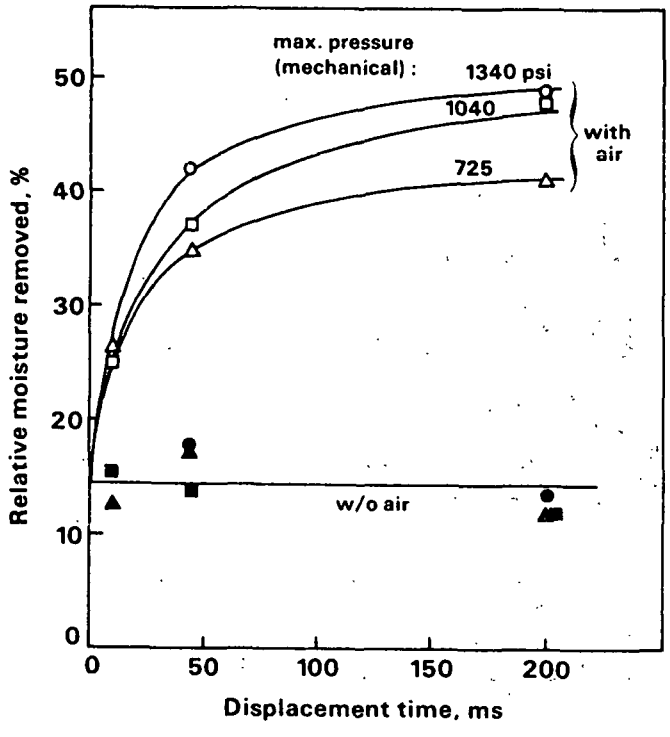

Results of displacement pressing of 63 g/m^2 handsheets of once-dried bleached softwood kraft pulp at 720 CSF. Initial dryness = 43-45%.

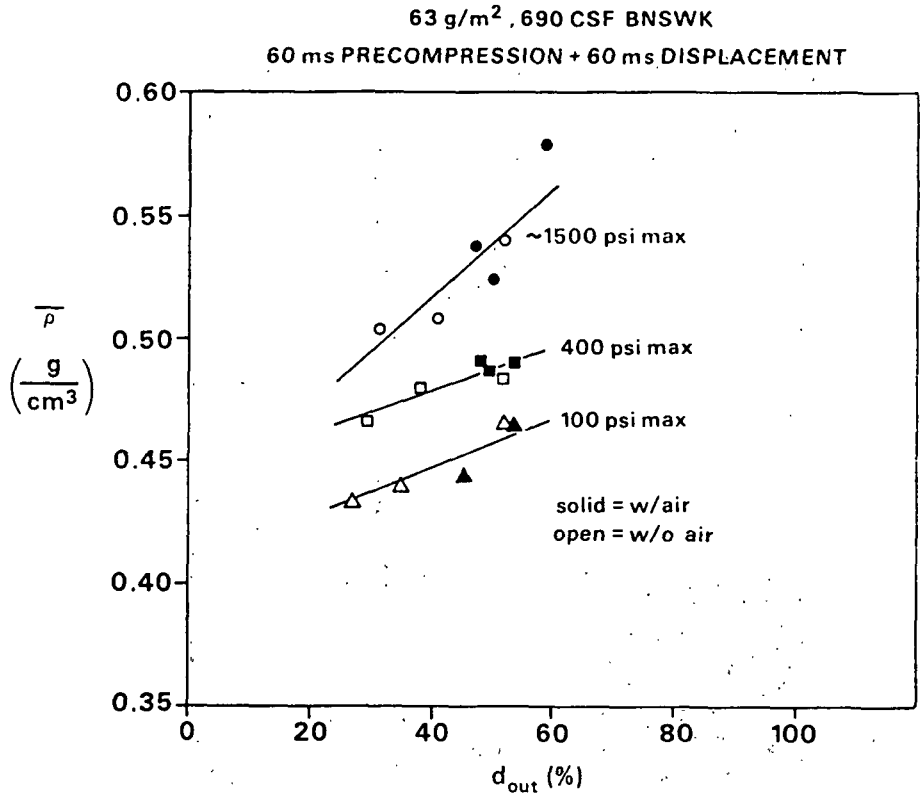

Density - dryness relationships for various pressing conditions.

THIRD GENERATION EQUIPMENT REQUIREMENTS

- FASTER RISE ON AIR PRESSURE
- EFFECTIVE PRESS CHAMBER SEALING
- INTERCHANGEABLE LOAD SPREADERS
- AIR FLOW MEASUREMENTS
- SYNCHRONIZED AIR DELIVERY

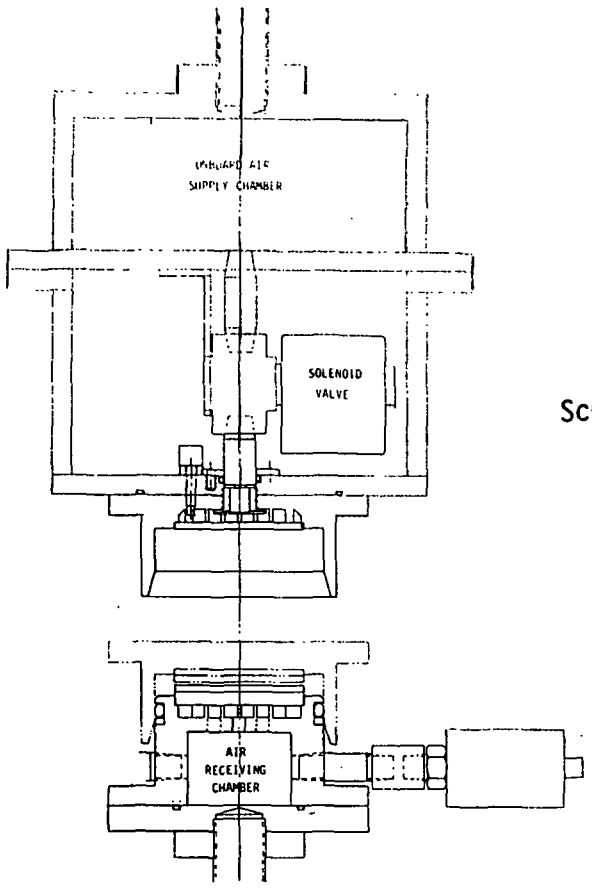

Schematic of displacement pressing head.

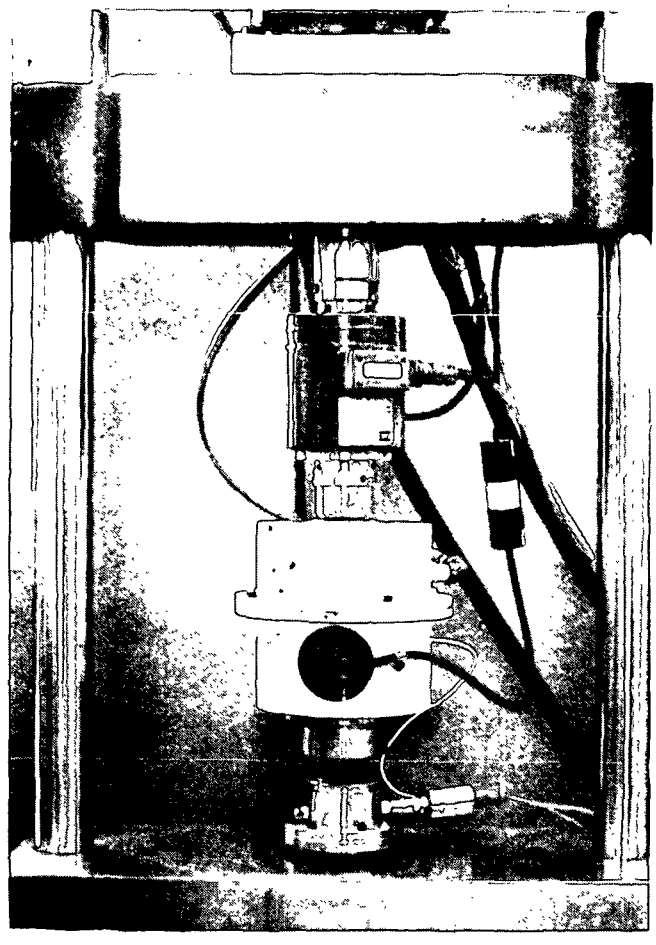

DP head installed in electrohydraulic press.

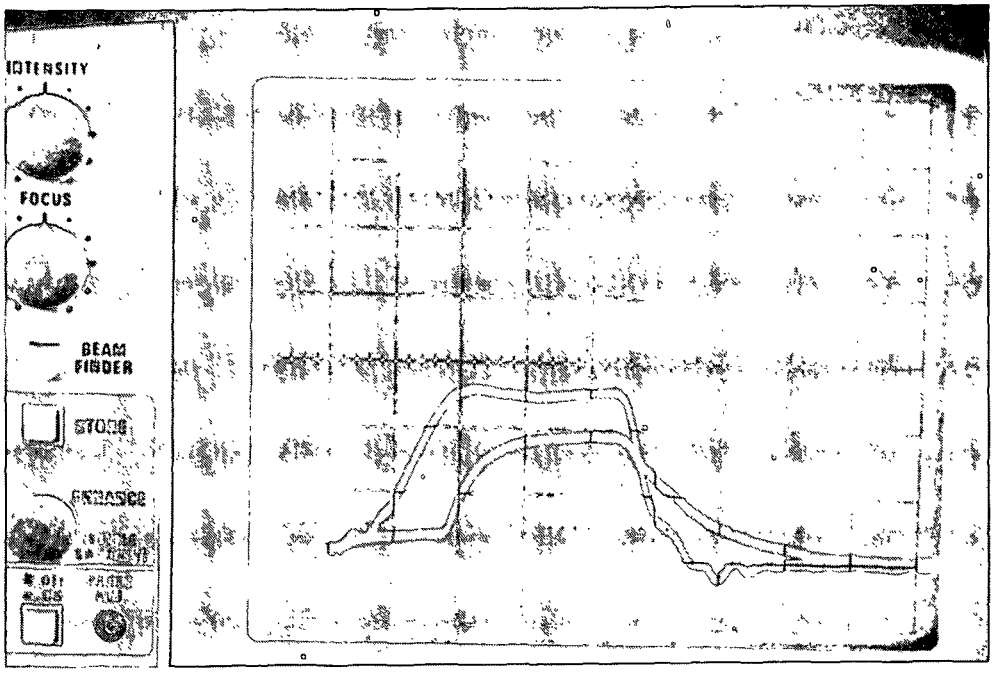

Load and air pressure traces.

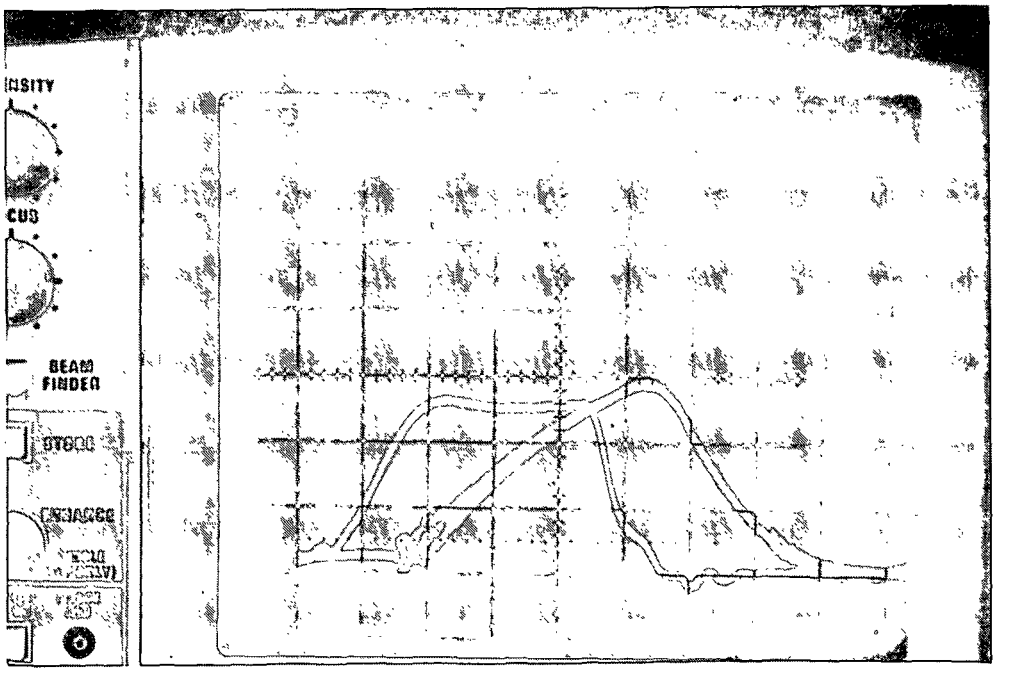

Load and receiving chamber pressure pulses.

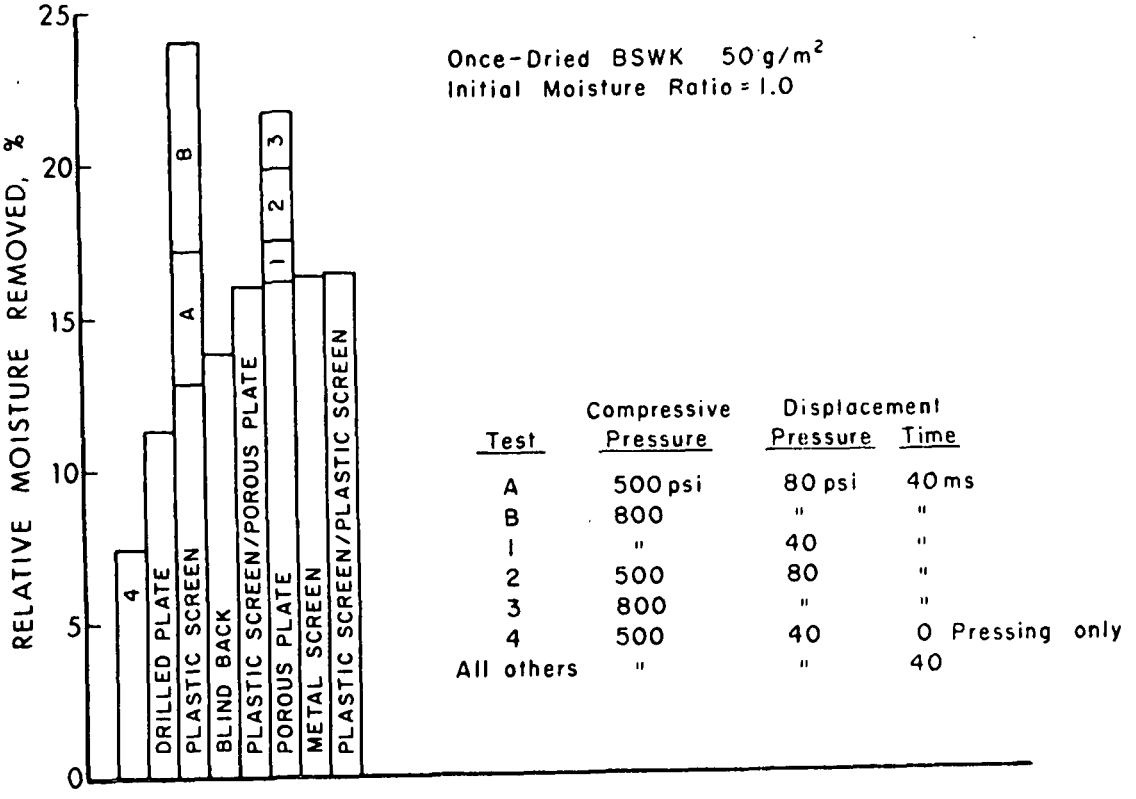

Relative moisture removal values for various displacement pressing conditions.

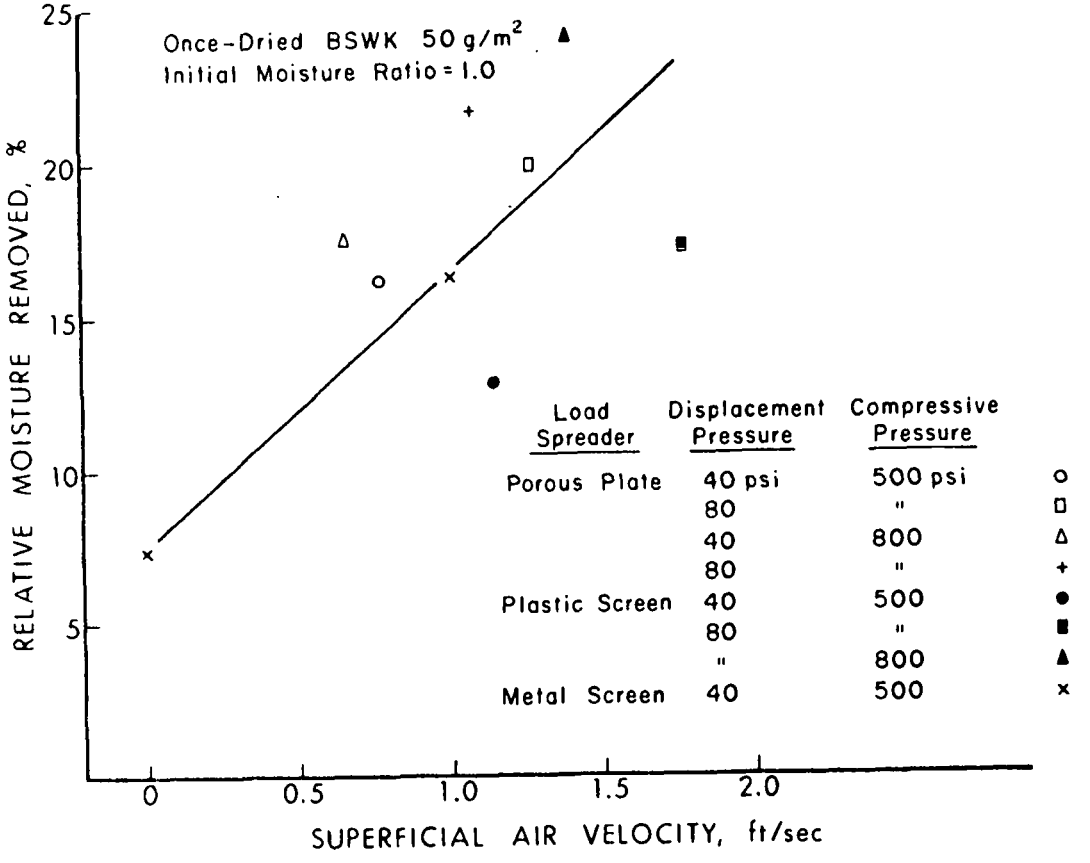

The effect of superficial air velocity on water removal.

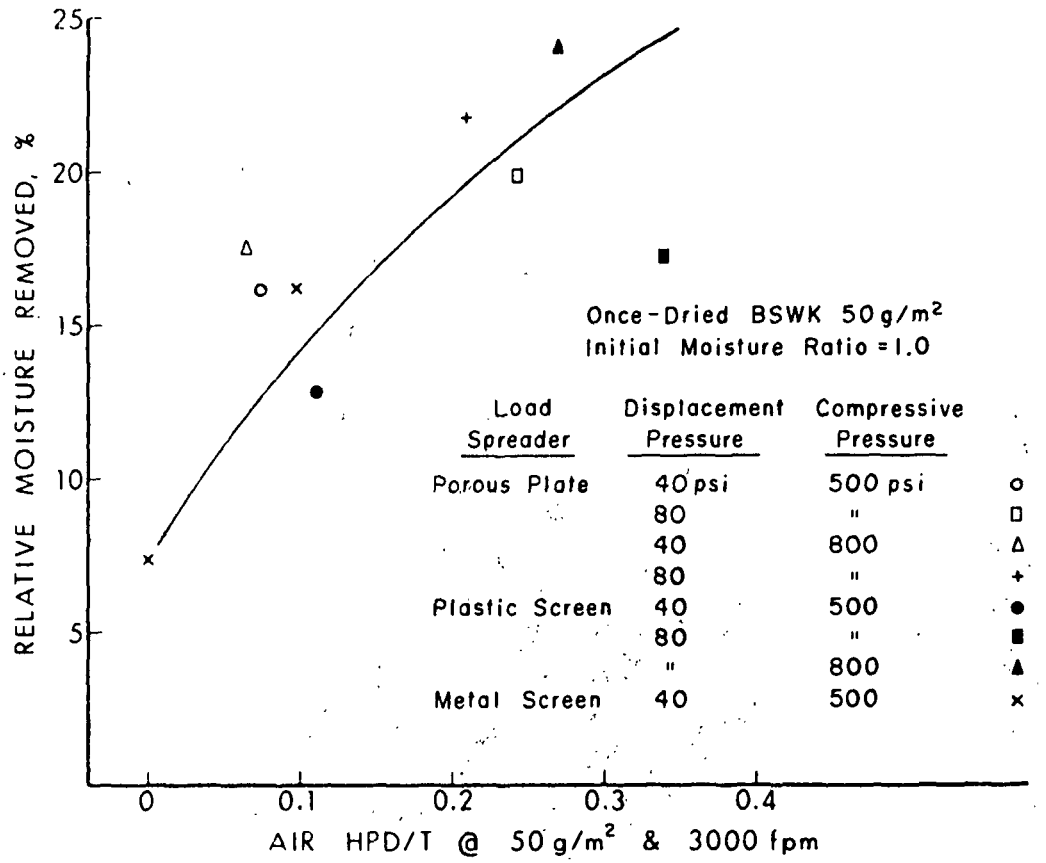

Air horsepower requirements for displacement pressing.

DISPLACEMENT PRESSING

PERFORMANCE

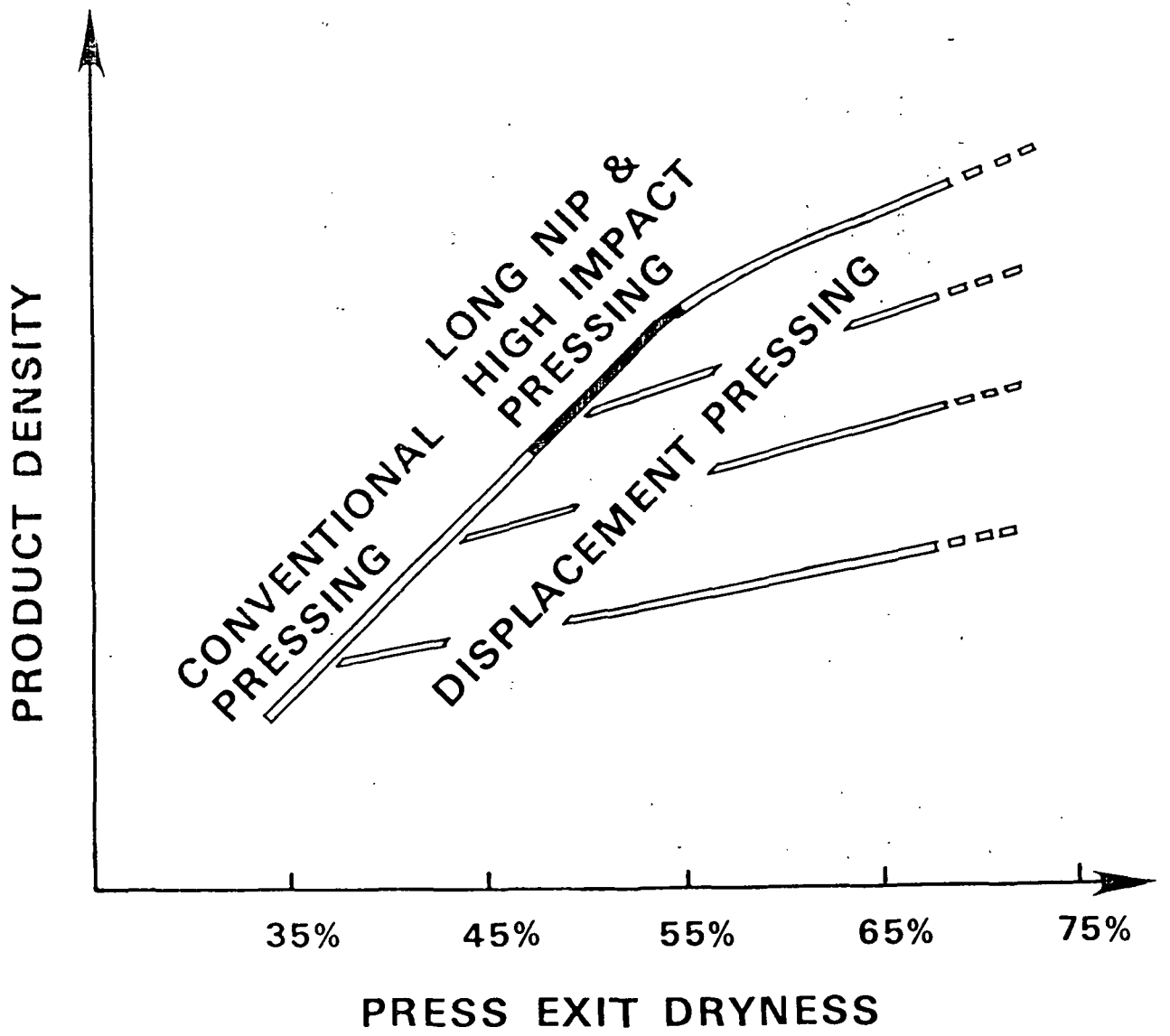

PROJECT 3480/3584

WET PRESSING FUNDAMENTALS

OBJECTIVES: DETERMINE FEASIBILITY AND PERFORMANCE OF DISPLACEMENT PRESSING

DEVELOP A PREDICTIVE MODEL FOR WET PRESSING

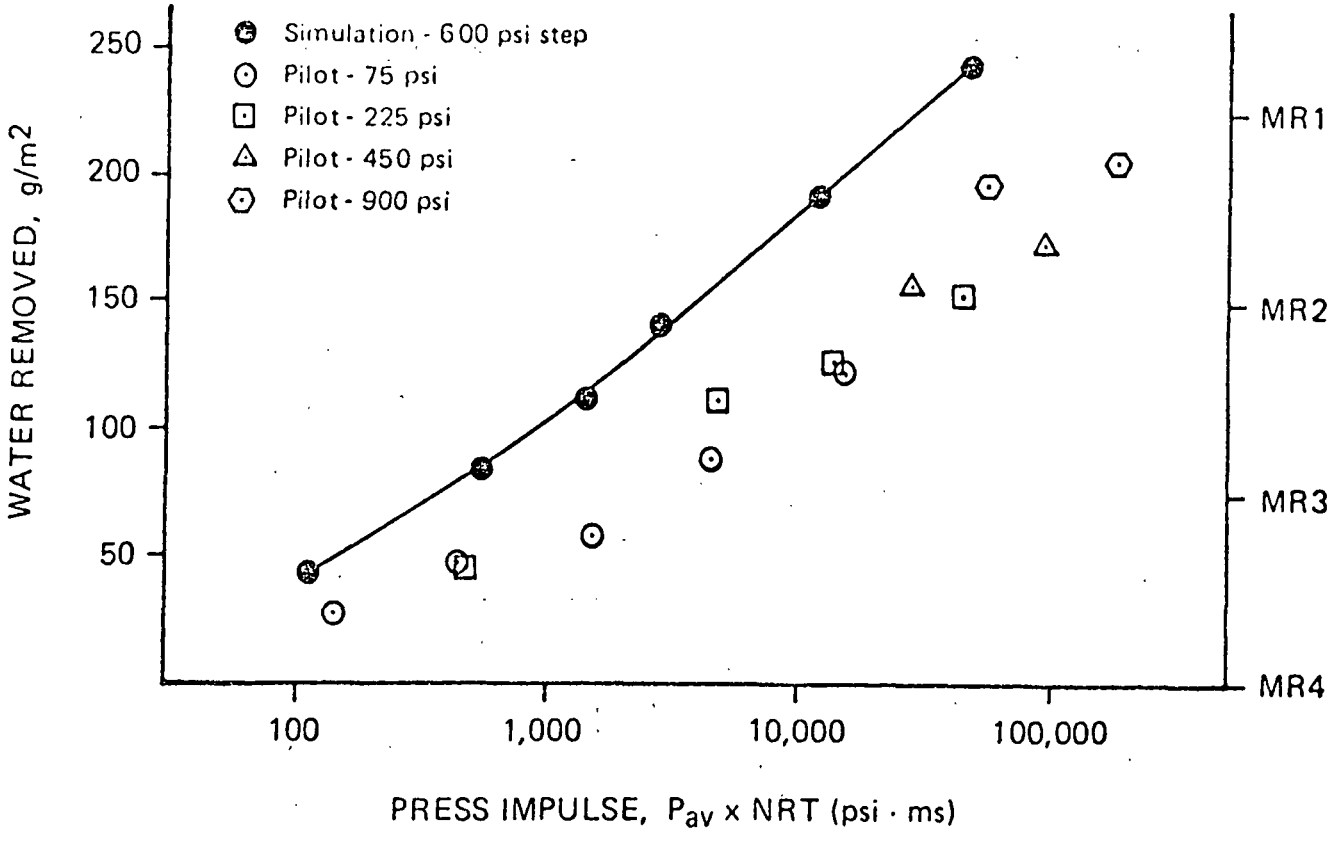

Comparison between pilot and laboratory simulations for 300 CSF bleached softwood kraft, 75 g/m^2.

PILOT PRESS

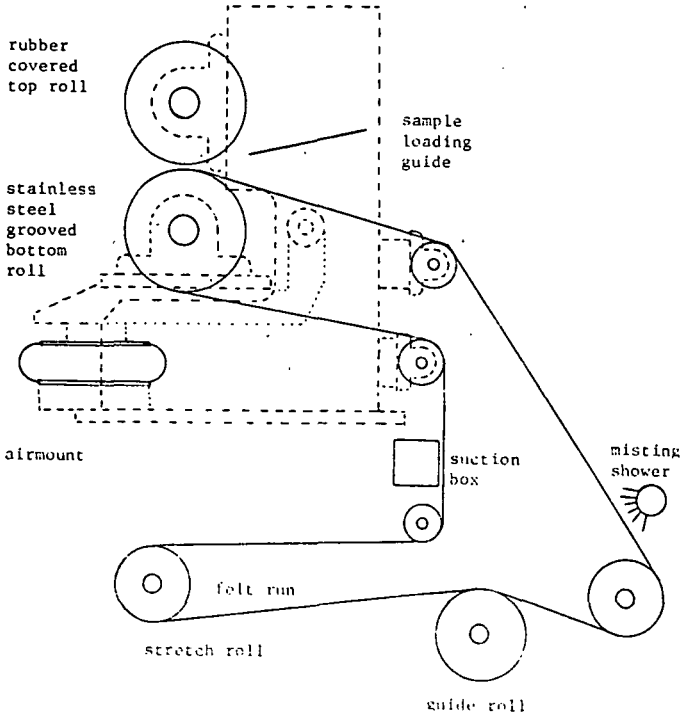

Broken or dotted lines indicate parts of frame or bearings.

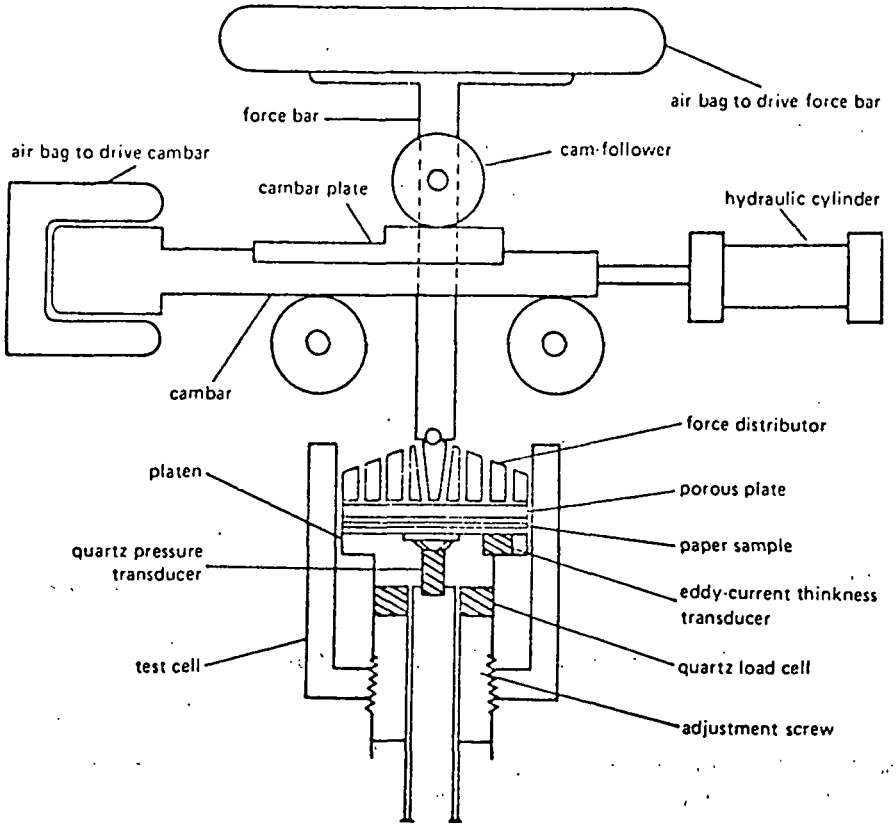

Schematic drawing of UMO compression tester.

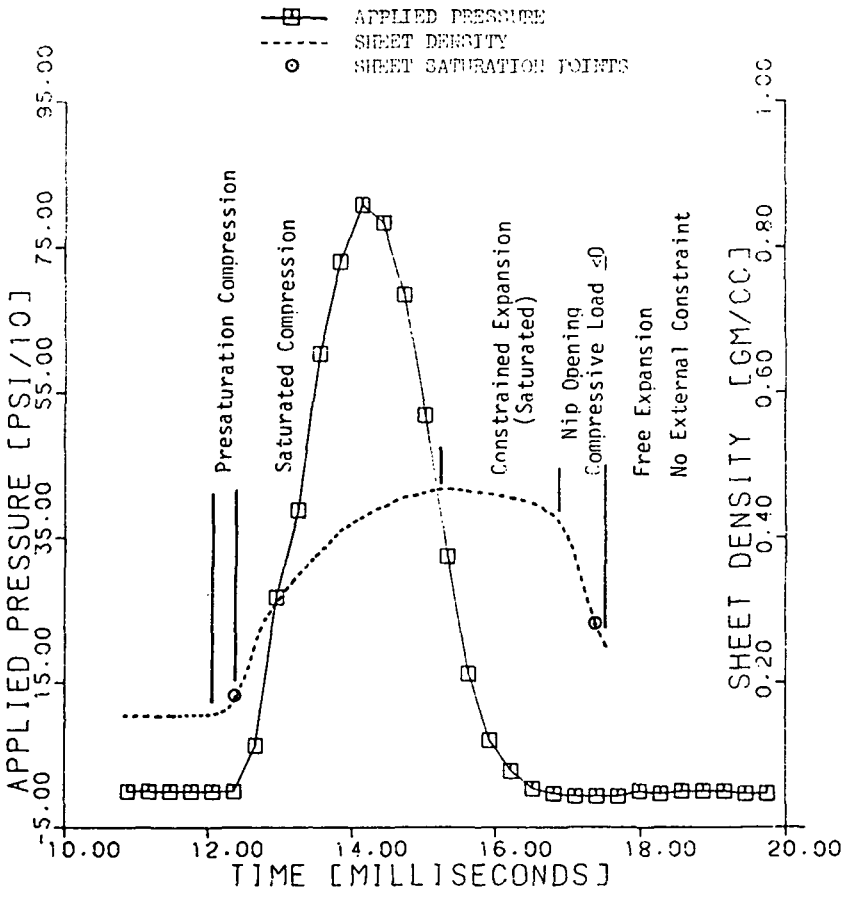

R1L 55.6 GM/SQ-M MR = 4.8
70 F 420 CSF

Instantaneous pressure and density curves for a typical wet pressing cycle.

NIP EFFICIENCY MUST ACCOUNT FOR:

- PRESATURATION COMPRESSION
- CONSTRAINED EXPANSION
- NIP OPENING
- POST-NIP CONTACT
- DIFFERENCES IN WATER RECEIVERS

MODELING OBJECTIVE

DEVELOPMENT OF A MODEL TO PREDICT THE PERFORMANCE OF A WET PRESS, GIVEN BASIC FURNISH PROPERTIES

TASKS

- COMPARATIVE TESTING OF POROUS PLATES/FELTS
- COMPRESSION/EXPANSION MODEL FOR COMPLETE CYCLE
- ADD TRANSPORT PROCESSES TO MODEL
- TREAT NIP OPENING & POST CONTACT

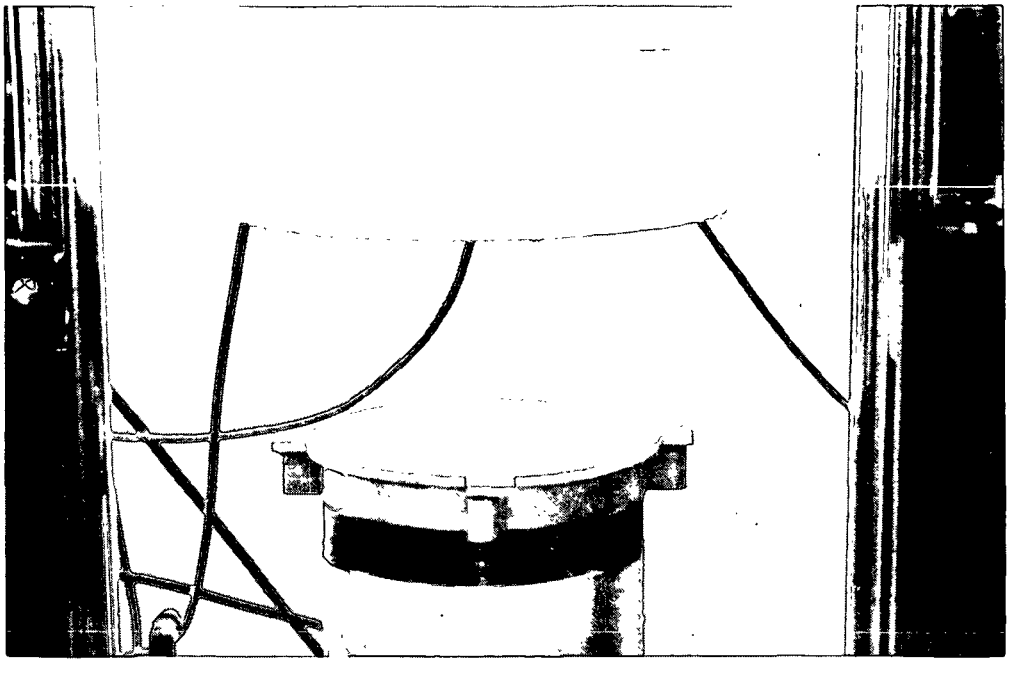

Impulse drying simulator nip. Upper platen is heated, lower platen is water receiver.

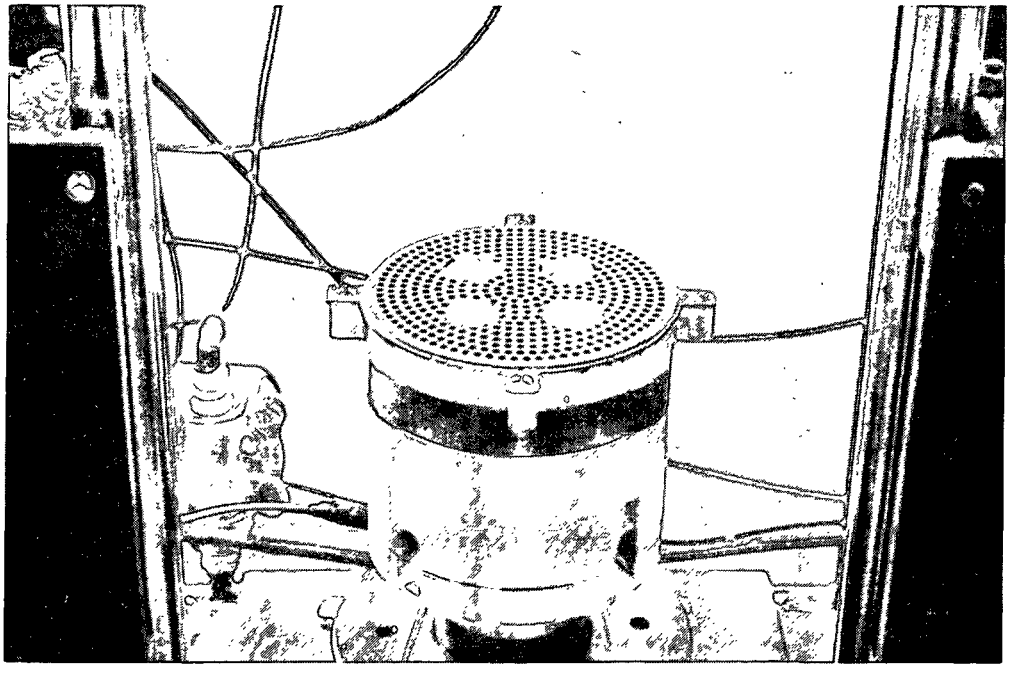

Lower pedestal of impulse drying simulator with ceramic removed revealing displacement transducers and drilled plate.

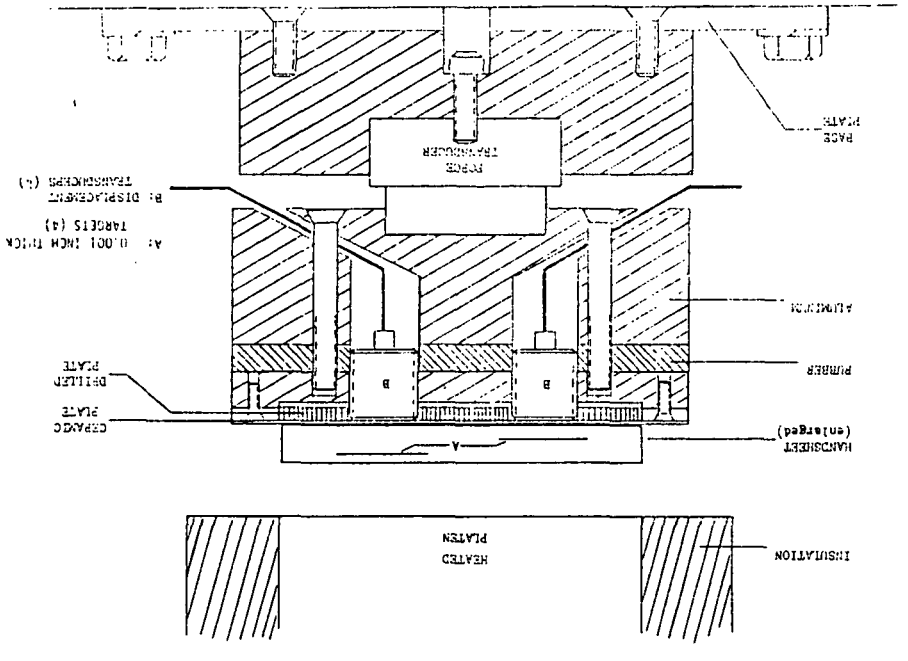

Impulse drying simulator pedestal.

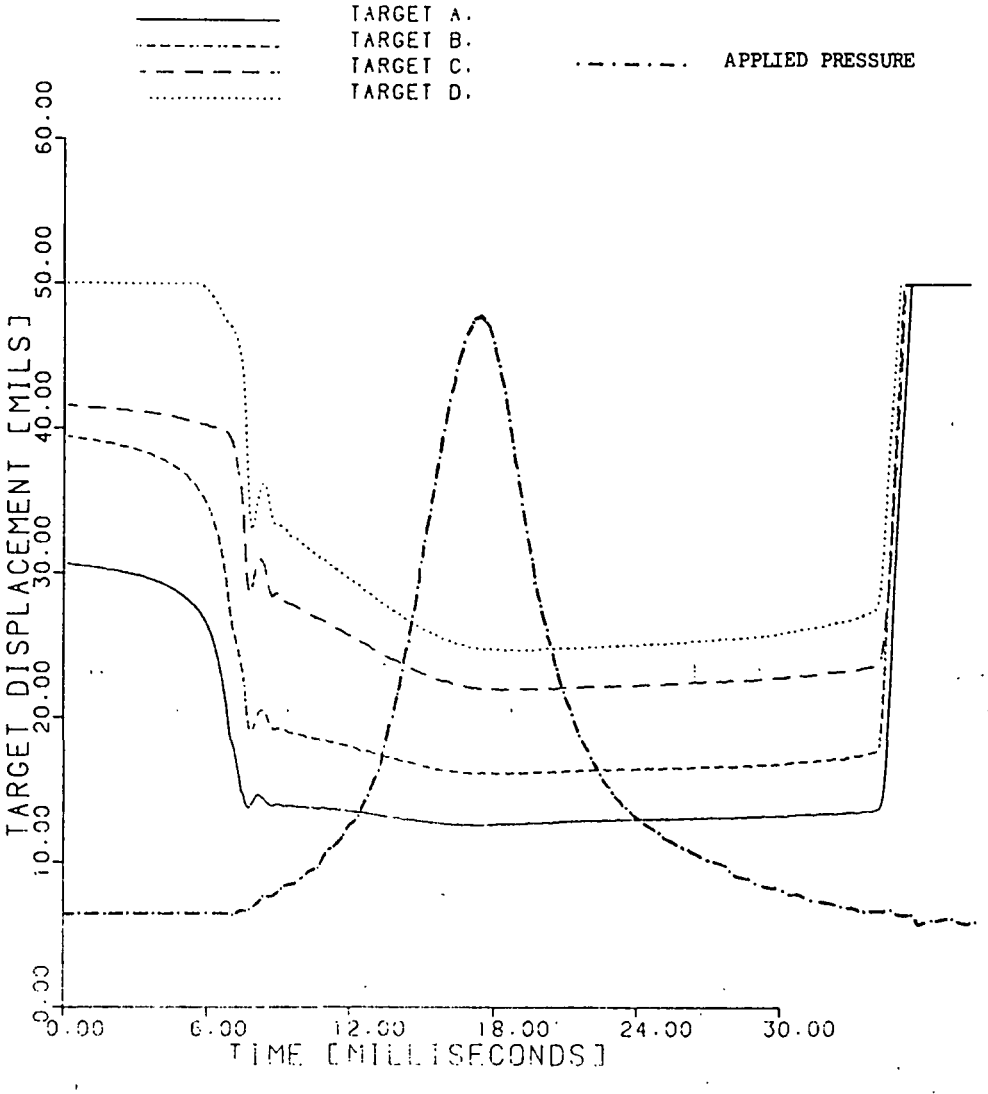

DISPLACEMENT HISTORIES OF FOUR TARGETS PLACED AT DISTINCT POSITIONS WITHIN THE FIBER MAT, WET PRESSED AT ROOM TEMPERATURE, PEAK PRESSURE OF 614 PSI AND A NIP RESIDENCE TIME OF 25 MILLISECONDS. THE HANDSHEET IS A 168 g/m^2 BASIS WEIGHT, 2.3 INITIAL MOISTURE RATIO, 735 CSF.

Target material used in thickness measurement - 0.001 inch thick copper mesh.

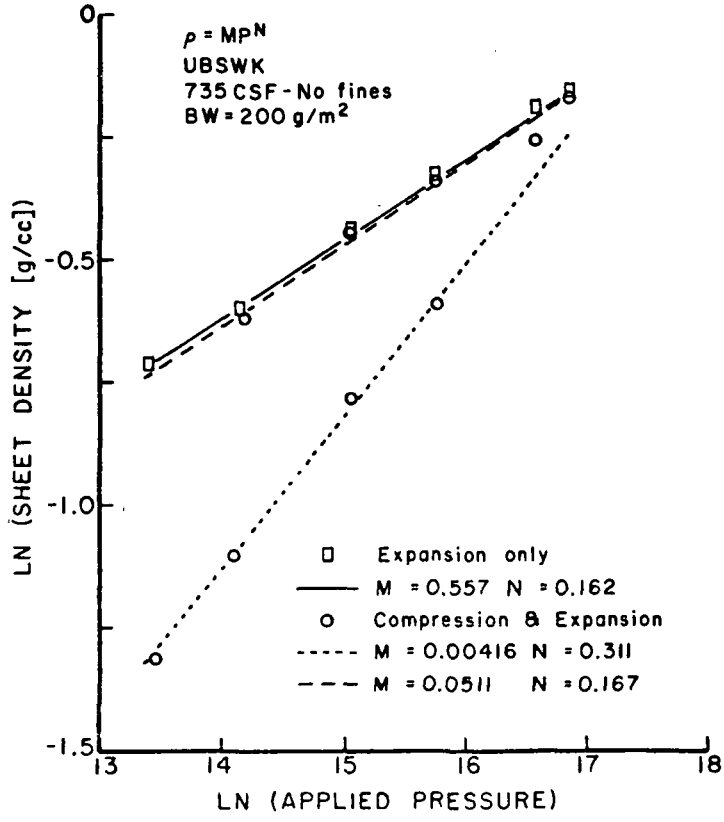

Compression-expansion curves for a "slow" process.

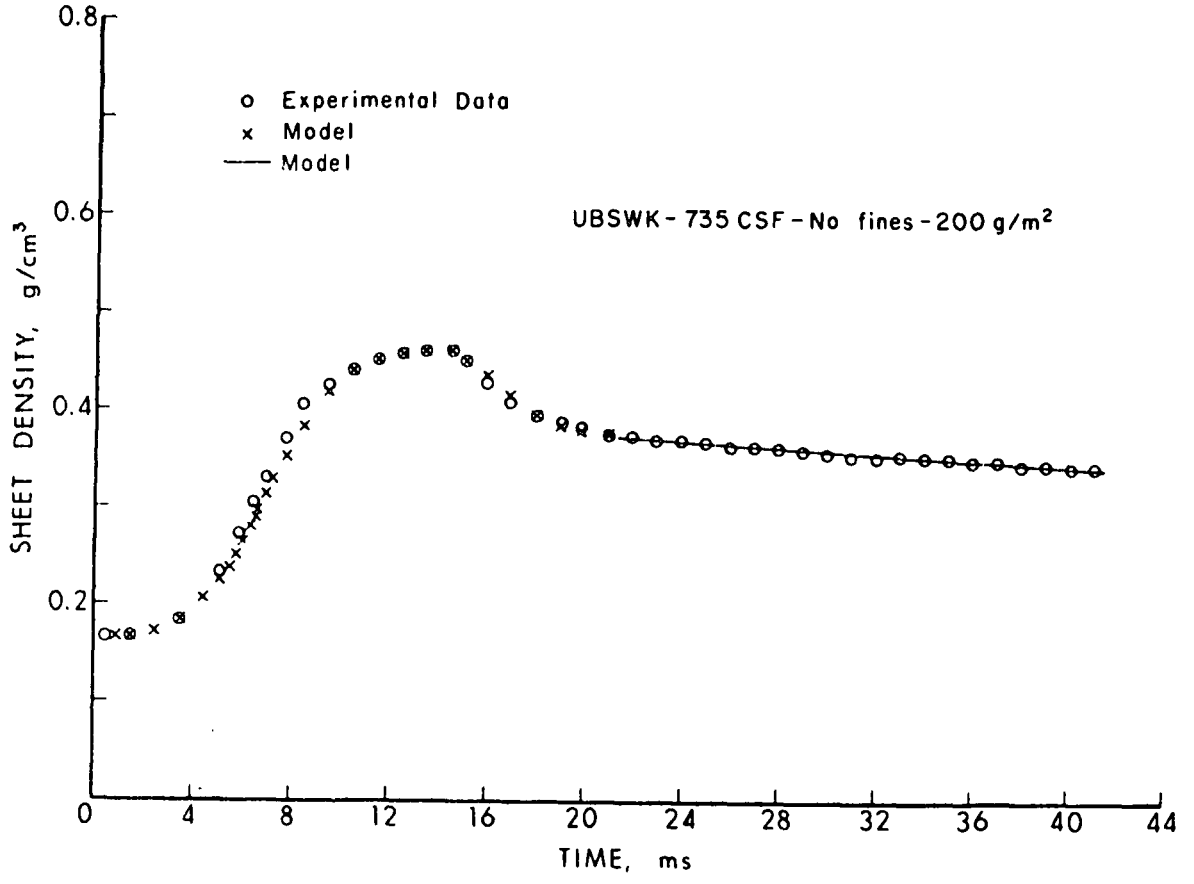

Typical compression-expansion curve including post-nip expansion.

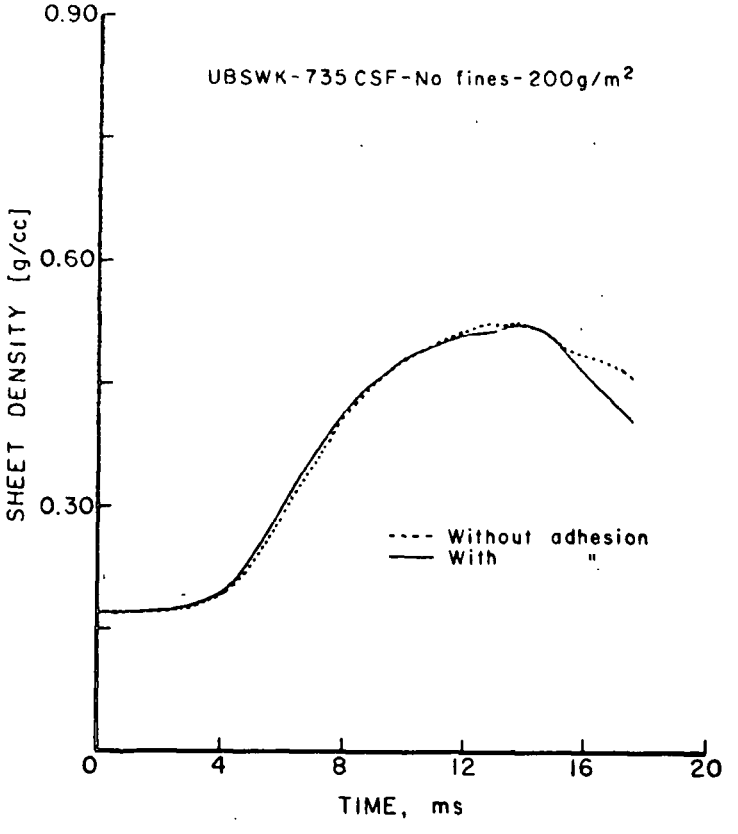

Wet pressing density curve with and without adhesion.

FUTURE WORK

- COMPRESSION-EXPANSION MODEL FOR UNSATURATED WEBS
- HYDRAULIC PRESSURE MEASUREMENTS FOR SATURATED WEBS
- DESCRIBE NIP OPENING PROCESS
- COMBINE WITH TRANSPORT EQUATIONS TO COMPLETE MODEL
- VERIFY ON NEW LABORATORY ROLL PRESS

Project 3479

HIGHER CONSISTENCY PROCESSING

Clyde Sprague & Ted Farrington

PROJECT 3479: HIGHER CONSISTENCY PROCESSING

OBJECTIVE

DEVELOP THE BACKGROUND AND METHODS FOR PRACTICAL SEPARATION AND FORMING AT ELEVATED CONSISTENCIES.

APPROACH

- SELECT A WORKABLE METHOD FOR ONE PROCESS
- IDENTIFY FUNDAMENTAL LIMITATIONS TO METHOD
- DEVELOP UNDERSTANDING OF FUNDAMENTALS NECESSARY TO REMOVE LIMITATION

SINGLE ROLL WITH AIR DOCTOR

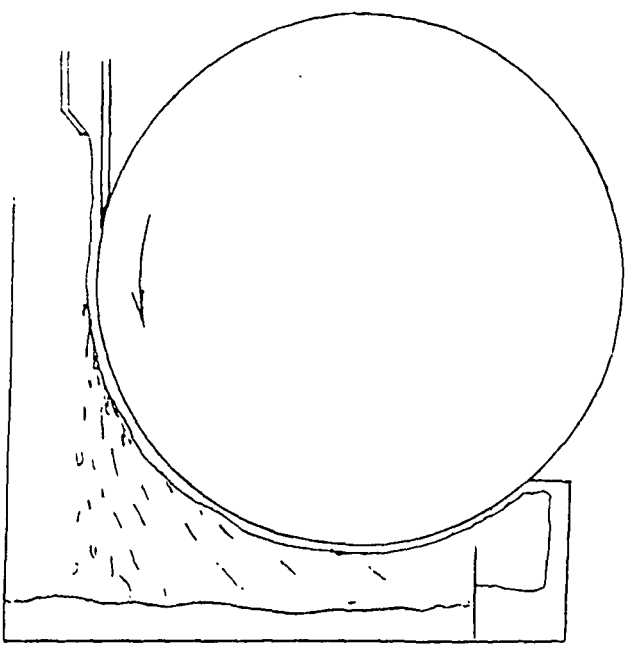

Concept for applying film of slurry to a blade and then to a moving roll.

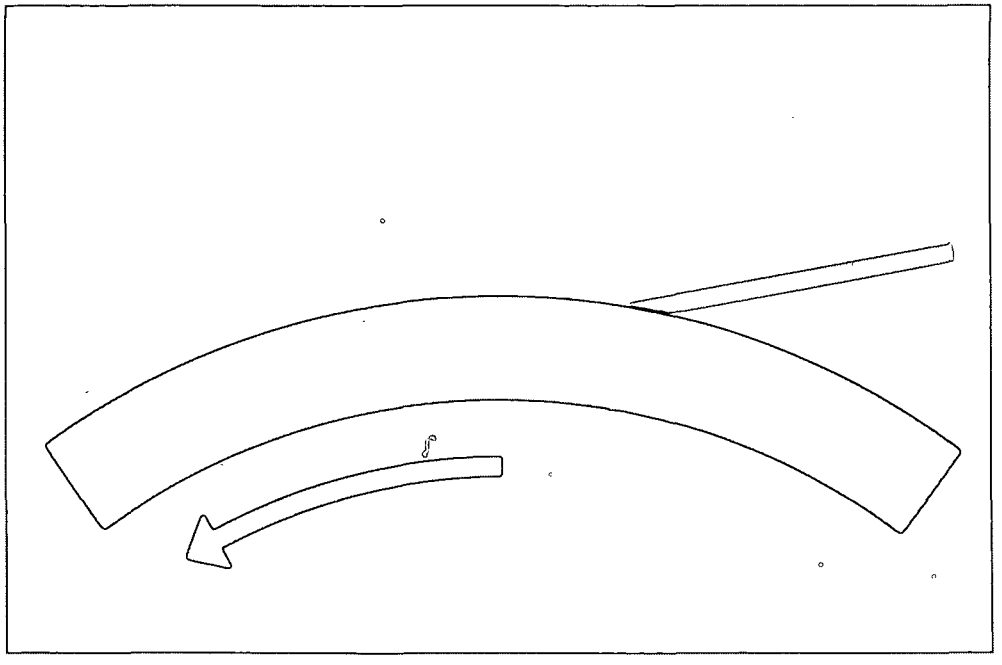

Illustration of particle separation from slurry film on moving roll surface.

$$\frac{v^2}{2\gamma R} = \frac{\cos\theta}{\rho w t}$$

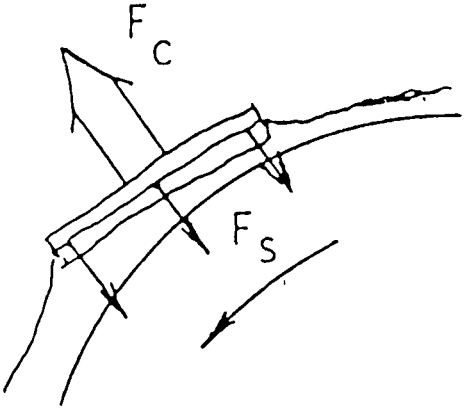

Theoretical basis of separation.

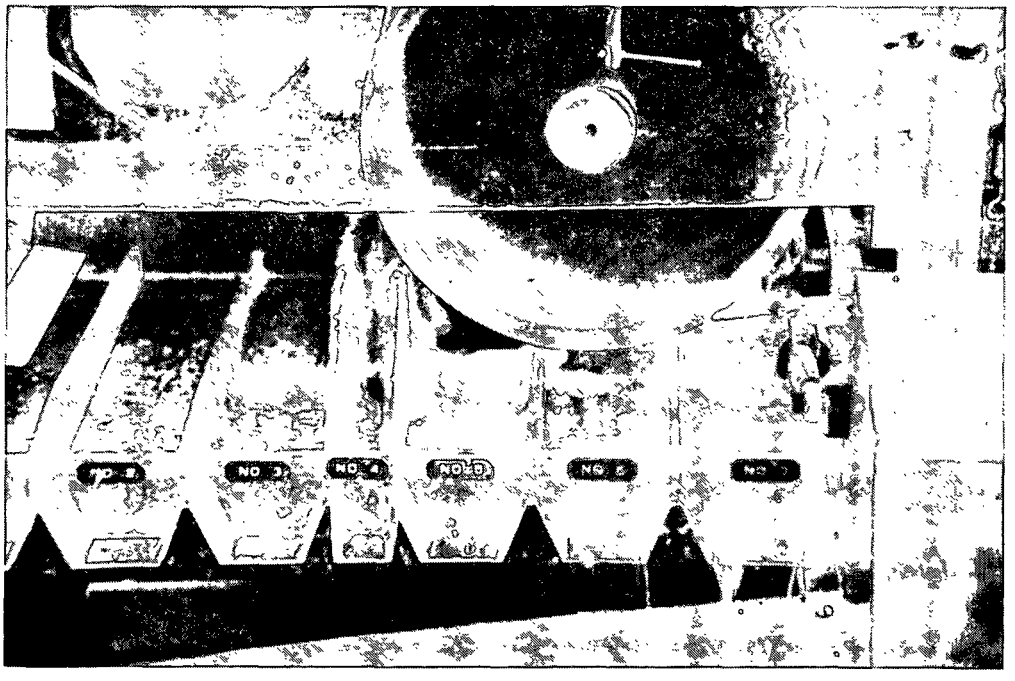

Roll separator operating on 50:50 TMP/kraft pulp.

ROLL SEPARATION OF STICKIES FROM RAFT WRAPPING PAPER STOCK

Feed: 1.29% cons.; 0.59% 6-cut rejects; 0.66% toluene extr.

Roll Speed, ft/min	Reject Rate, %	Percent Removal Efficiency	
		6-cut rejects	Stickies by extn.
3000	5.6	82.9	73.9
	11.6	97.1	78.3
5000	8.0	98.4	75.9
	20.4	99.7	92.6
7000	16.0	98.7	86.0
	25.6	98.5	92.0

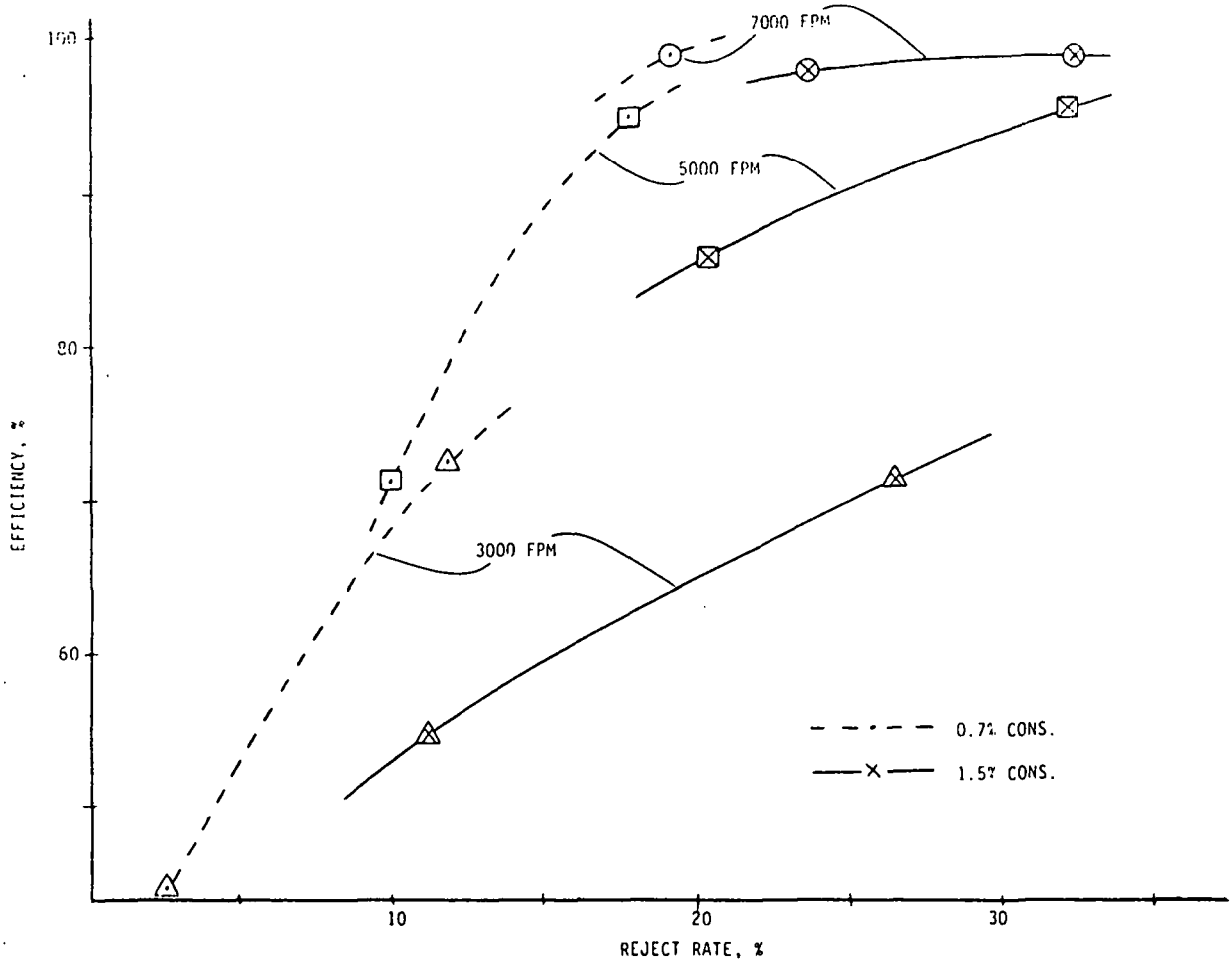

Efficiency of removal of 6-cut shives from 50:50 TMP/kraft mixture, as function of reject rate, roll speed, and consistency.

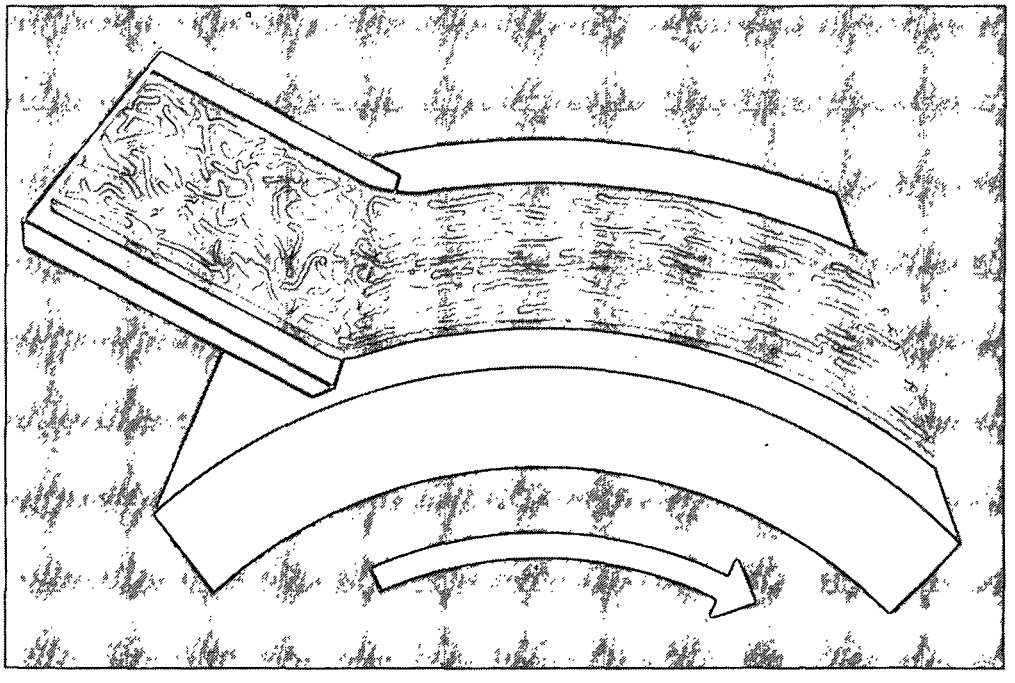

Means for employing shear and acceleration to fiber slurry films, illustrating anticipated fiber orientation effect.

HIGH CONSISTENCY PAPERMAKING

PROJECT 3479

INITIAL PROJECT CONCEPTS

OUTLINE

I. PROBLEM DEFINITION

II. ACTIVITIES THUS FAR

III. INITIAL PROGRAM CONCEPTUALIZATION

IV. POTENTIAL ACTIVITIES

V. TARGETS FOR FIRST YEAR

PROBLEM DEFINITION

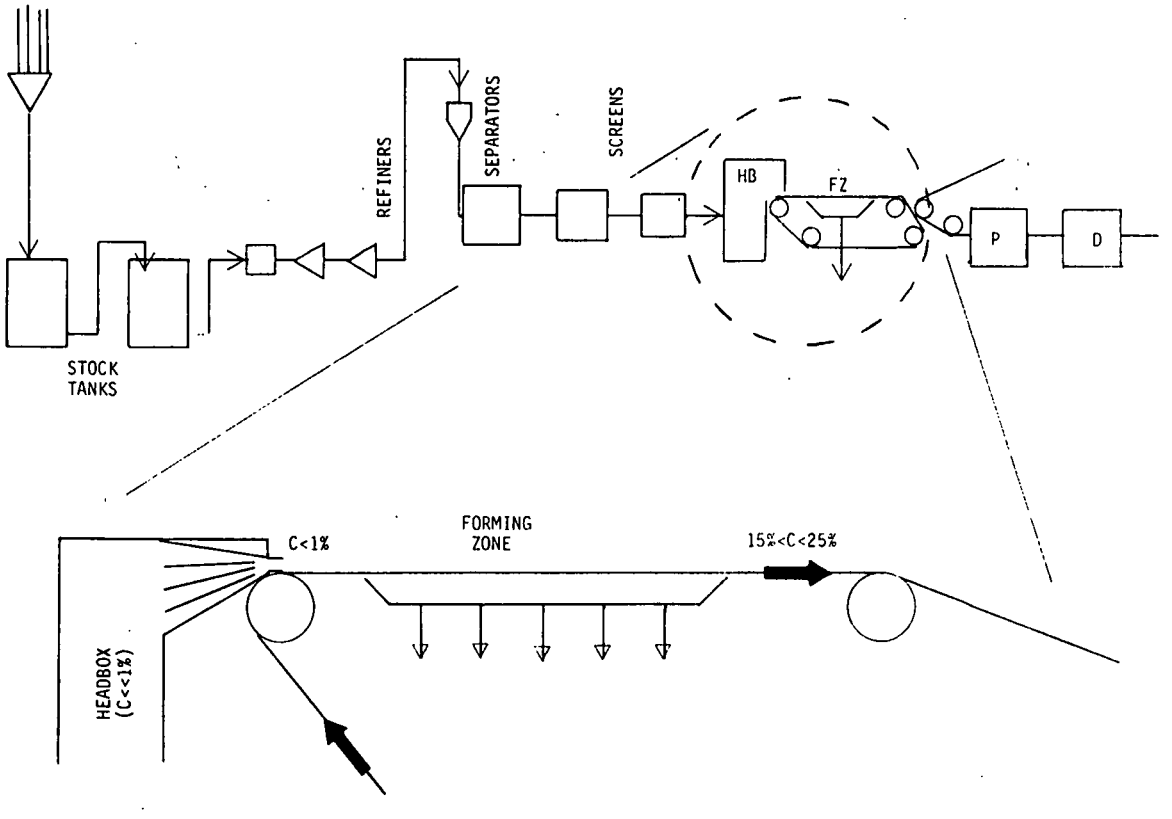

POTENTIAL BENEFITS FROM HIGH CONSISTENCY PAPER MAKING (HCPM)

- REDUCED CAPITAL COSTS
- IMPROVED PAPER QUALITY (REDUCED RAW MATERIAL COSTS)
- IMPROVED FINES RETENTION
- LOWER ENERGY COSTS

ACTIVITIES THUS FAR

I. WHAT'S BEEN DONE?
WHAT'S GOING ON?

A. LITERATURE SURVEYS

1. DOCUMENTED PROBLEMS WITH HCPM
2. COLLOIDAL PROPERTIES
3. RHEOLOGY OF FIBROUS SUSPENSIONS
4. FLOWFIELD - FIBER FLOC INTERACTION
5. FORMATION
6. FLOW THROUGH POROUS MEDIA
7. PATENTS
8. FLOW VISUALIZATION

II. PROJECT DEFINITION AND PLANNING

- RANDOM SURVEY OF PROBLEMS AND POSSIBLE PROJECT ACTIVITIES
- LIST OF REASONABLE PROJECT ACTIVITIES
- SET SOME PRIORITIES
- DEFINE A PLAN OF ATTACK

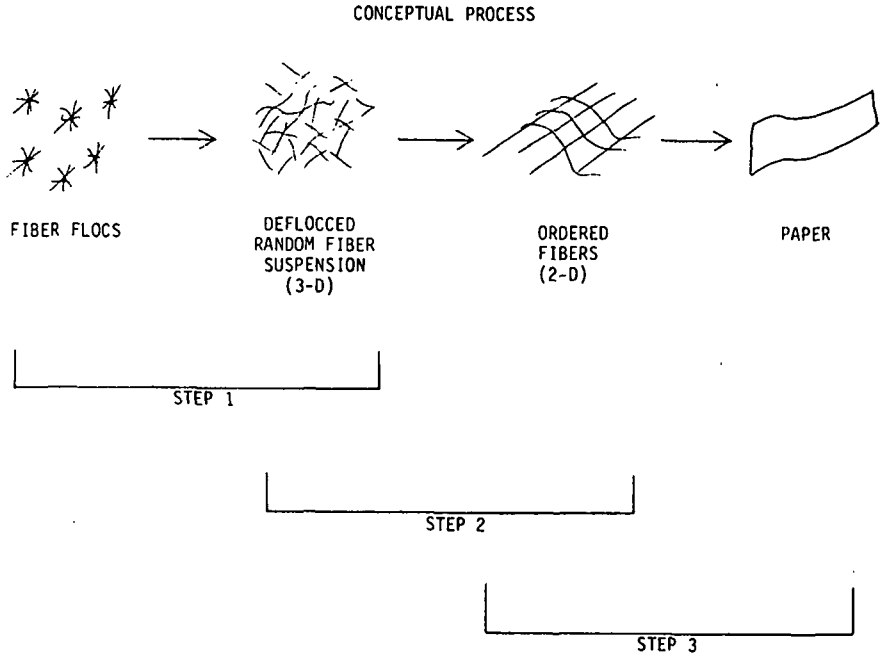

POTENTIAL ACTIVITIES FOR INVESTIGATION OF STEP 1

1. COLLOIDAL BEHAVIOR
   - ° MAGNITUDE OF ATTRACTIVE FORCES (VDW))
   - ° ELECTROKINETIC EXPERIMENTS
   - ° FLOCCULATION EXPERIMENTS
   - ° FLOCCULATION MODELS (SETTLING, SHEAR)

POTENTIAL ACTIVITIES FOR INVESTIGATION OF STEP 1 (CONTINUED)

2. FIBER FLOC-FLUID DYNAMICS INTERACTION
   - ° BEHAVIOR OF SINGLE AND MULTIPLE FLOCS IN
     - SHEAR & ELONGATIONAL FLOWS
     - LAMINAR & TURBULENT REGIMES
   - ° FLOC STABILITY

POTENTIAL ACTIVITIES FOR INVESTIGATION OF STEP 1 (CONTINUED)

3. FUNDAMENTAL FIBER NETWORK PROPERTIES

° NETWORK INFLUENCE ON RHEOLOGY

° INHERENT NETWORK STRENGTH

POTENTIAL ACTIVITIES FOR INVESTIGATION OF STEPS II AND III

I. CONTROL OF FIBER ORIENTATION

° EXPERIMENTAL STUDY OF EFFECT OF VARIOUS FLOW FIELDS ON ORIENTATION
- SHEAR, ELONGATION, CONVERGING FLOWS

° COMPARISON OF RESULTS WITH THEORETICAL PREDICTIONS

II. RELATIONSHIPS BETWEEN FIBER ORIENTATION AT START AND FINISH OF FORMATION PROCESS

° FLOW THROUGH POROUS MEDIA

III. PILOT PAPER MACHINE EXPERIMENTS

AND FINALLY:

FLOW VISUALIZATION

OBJECTIVE: TO ASSESS FIBER ORIENTATION DISTRIBUTION IN FIBER SUSPENSIONS FROM <1% to 5% CONCENTRATION

INVESTIGATION POTENTIAL USE OF:

OPTICAL TECHNIQUES

X-RAY WITH TRACER

HOLOGRAPHY

HIGH SPEED MOVIES

ELECTRICAL PROPERTIES

LIST OF ACTIVITIES

COLLOIDAL BEHAVIOR

FIBER FLOC-FLUID INTERACTION

FUNDAMENTAL FIBER NETWORK PROPERTIES

CONTROL OF FIBER ORIENTATION

PILOT PAPER MACHINE STUDIES

FLOW VISUALIZATION

CONCEPTUAL PROCESS

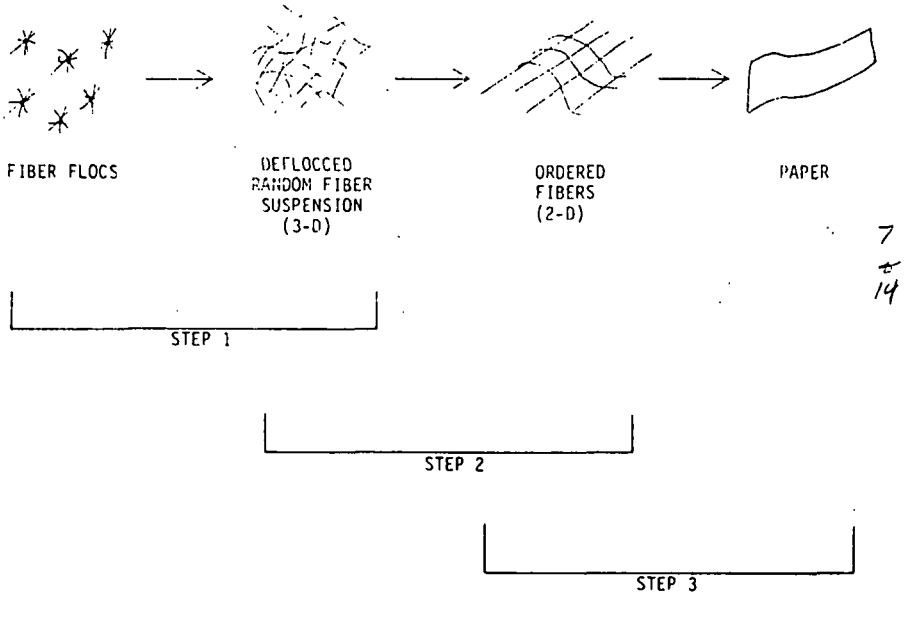

7 of 14

TOP PRIORITIES

1. FLOW VISUALIZATION TECHNIQUE FOR HIGHER CONCENTRATIONS
2. EFFECT OF VARIOUS FLOW FIELDS (SHEAR, ELONGATIONAL, CONVERGING) ON FIBER ORIENTATION AT HIGHER CONCENTRATIONS
3. PILOT MACHINE STUDIES TO QUANTIFY PROBLEM

PROBLEM DEFINITION

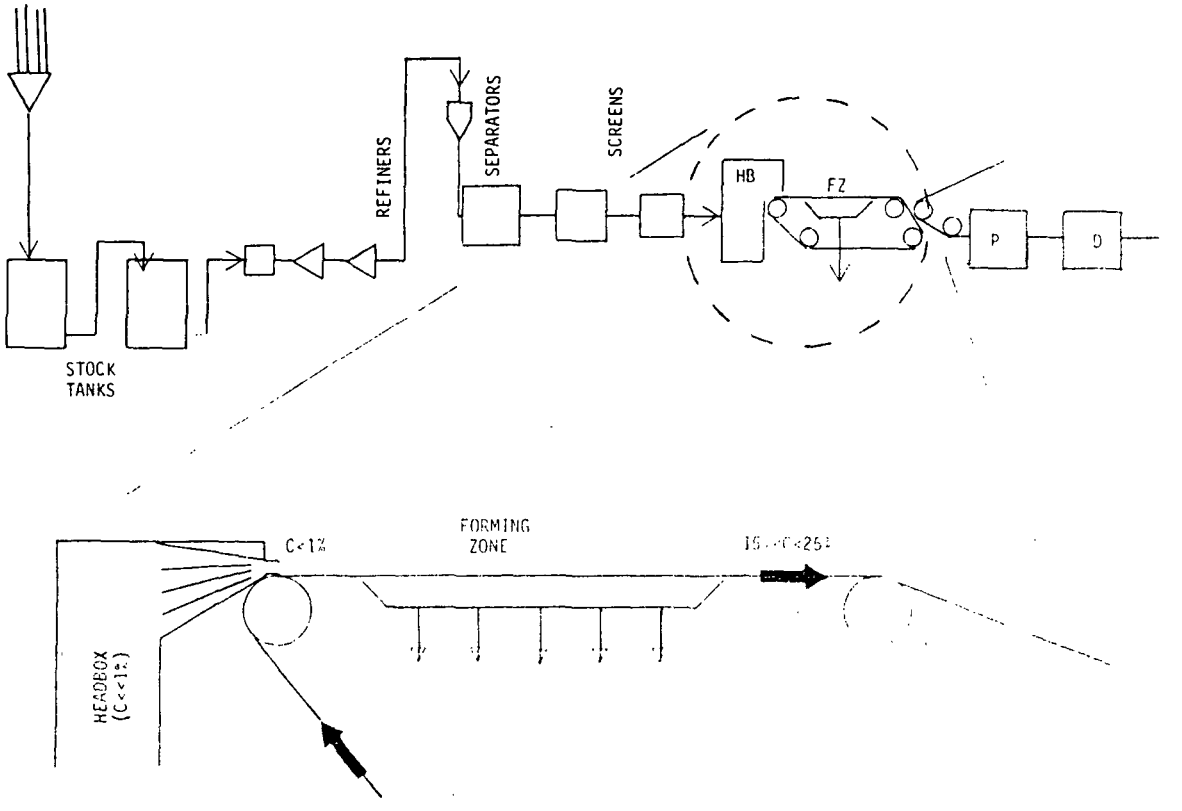

Project 3470

FUNDAMENTALS OF DRYING

Clyde Sprague & Hugh Lavery

PROJECT 3470

FUNDAMENTALS OF DRYING

OBJECTIVE: DEVELOP THE INFORMATION NECESSARY FOR COMMERCIALIZATION OF IMPULSE AND THERMAL/VACUUM DRYING PROCESSES

IMPULSE DRYING

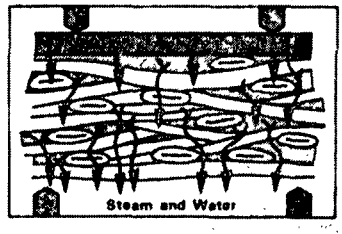

WATER REMOVAL MECHANISMS

° THERMALLY AUGMENTED PRESSING

° HIGH RATE EVAPORATION

° LIQUID PHASE DEWATERING

IMPULSE DRYING GIVES:

° EXTREMELY HIGH DRYING RATES
- VERY SMALL DRYERS
- HIGH PRODUCTION RATES

° LIQUID PHASE WATER REMOVAL
- LESS DRYING ENERGY

° SHEET DENSIFICATION
- PROPERTY DEVELOPMENT
- PRESS DRYING EFFECTS

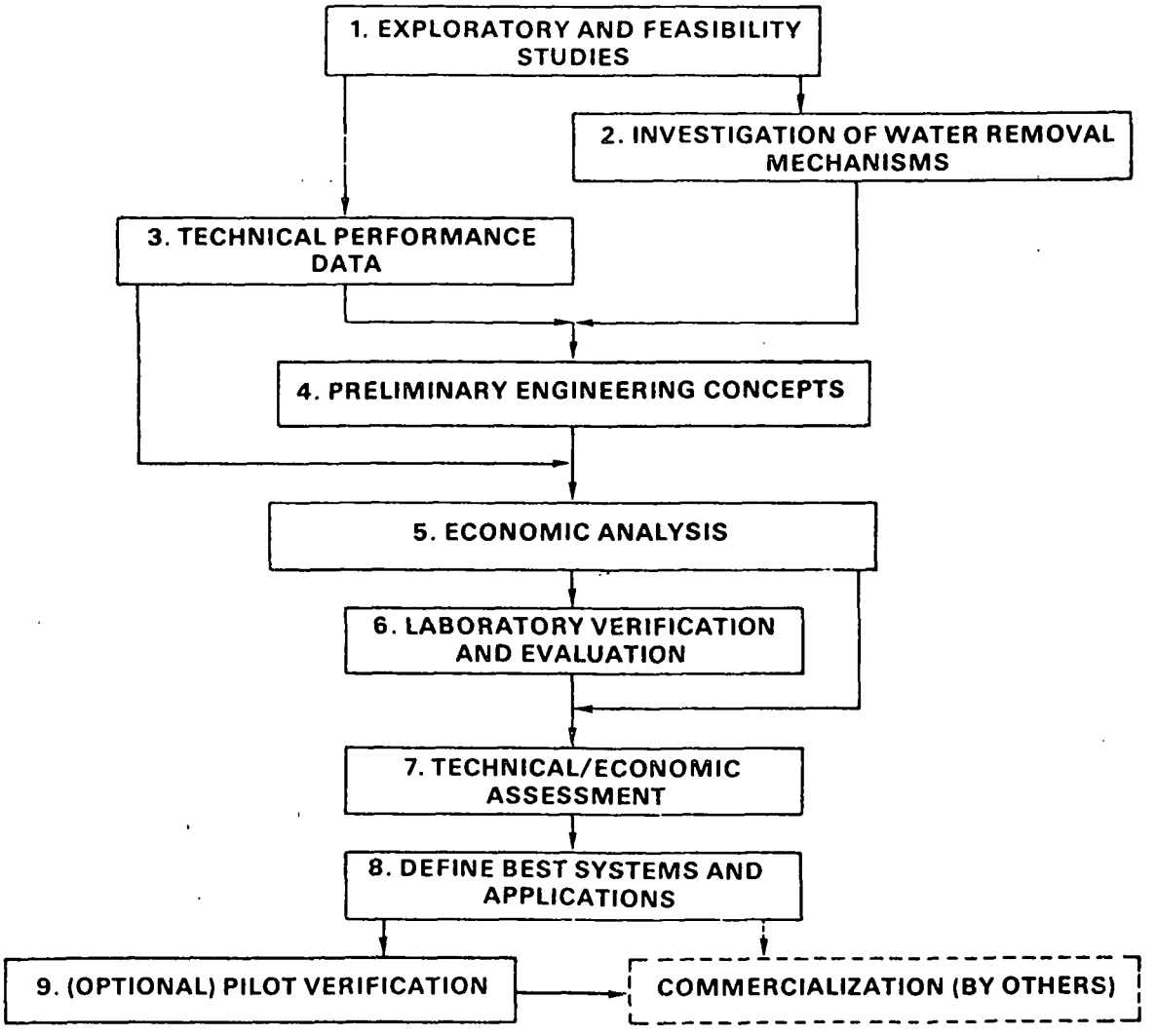

PROJECT PLAN FLOWSHEET.

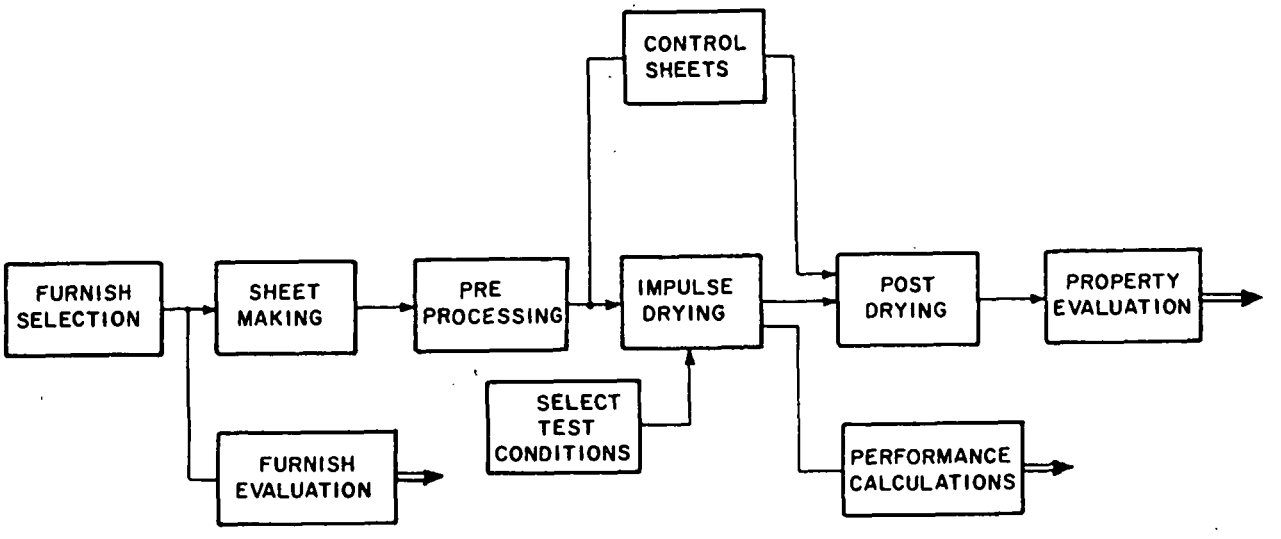

ELEMENTS OF PERFORMANCE EVALUATION.

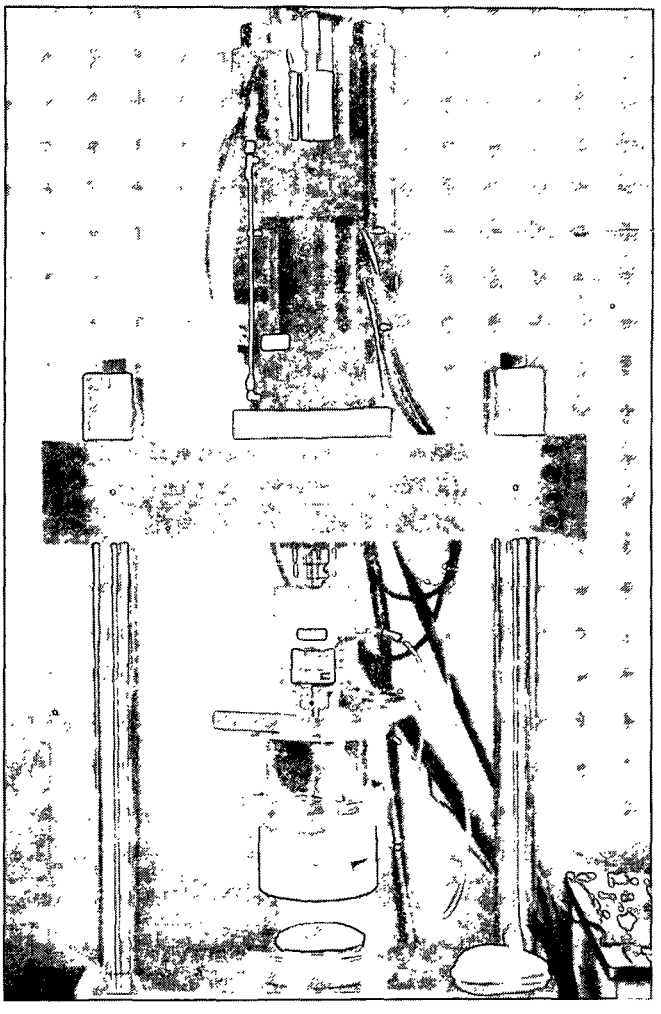

SERVO ACTUATOR AND LOAD FRAME ASSEMBLY.

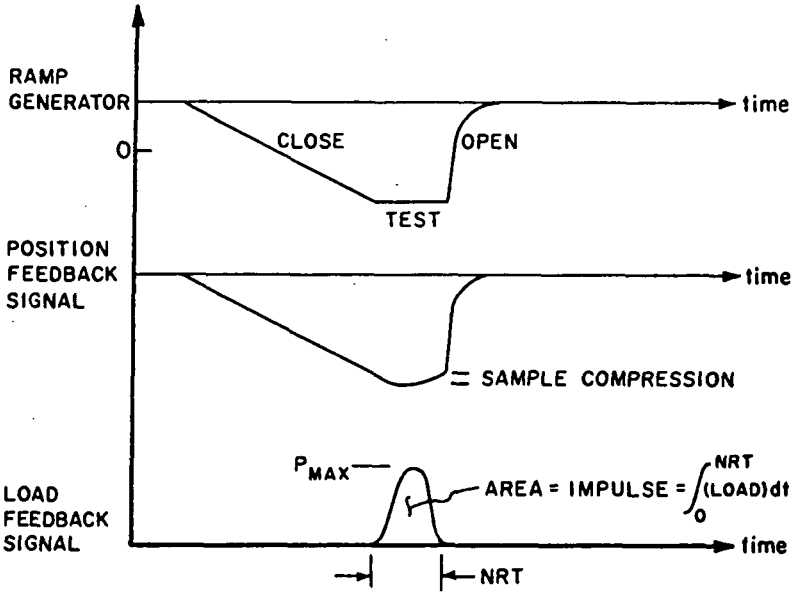

SCHEMATIC REPRESENTATION OF A TEST CYCLE.

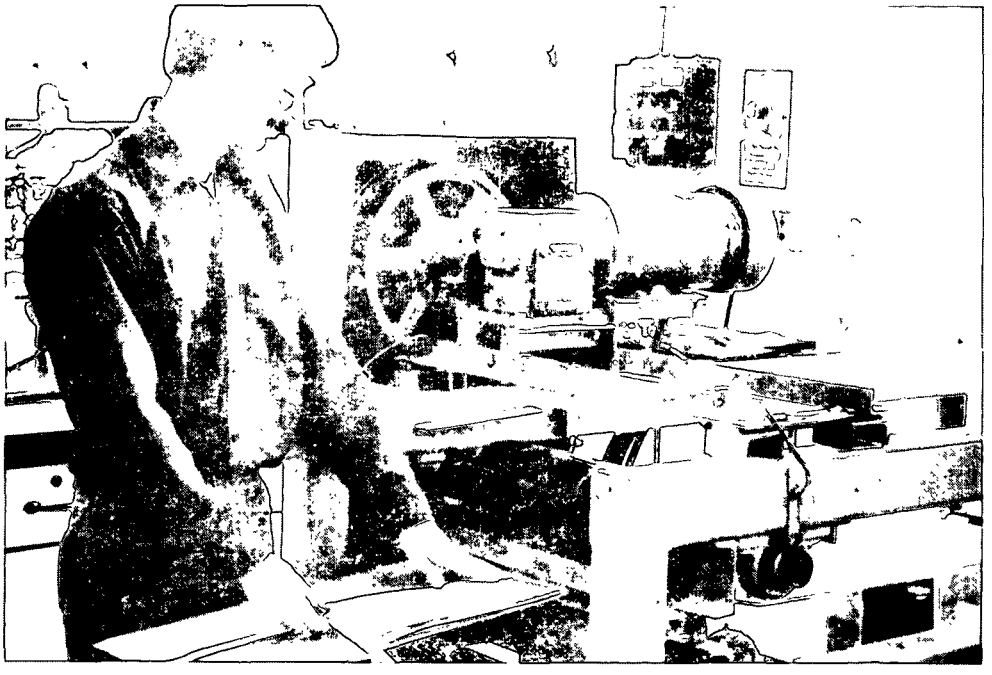

ROLL PRESS FOR PREPRESSING SHEETS.

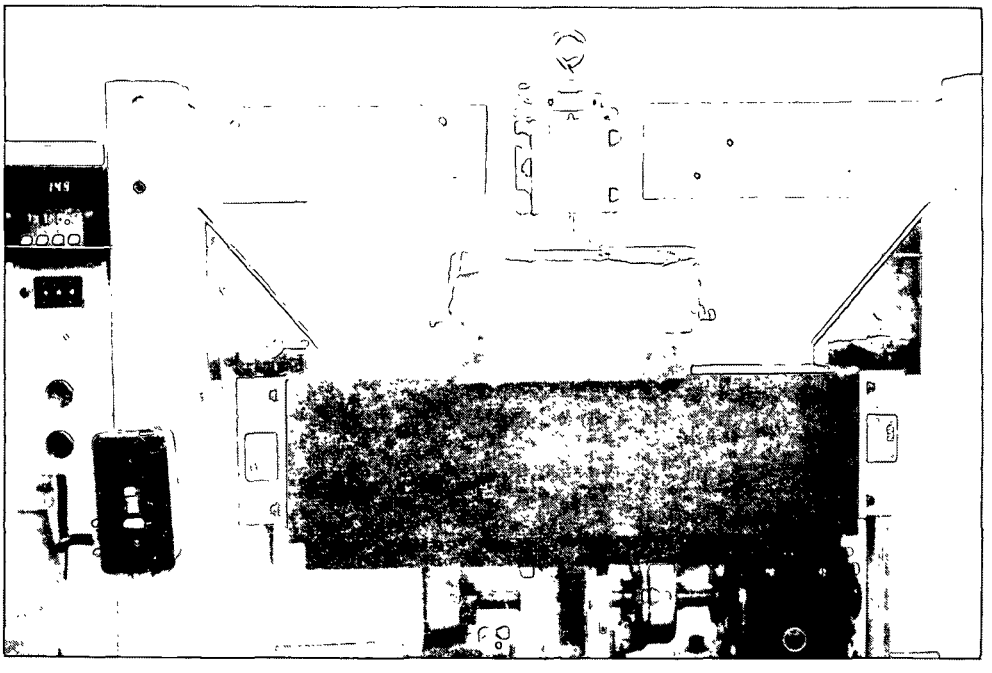

LOW-INTENSITY DRYING SYSTEM.

TEST PROGRAM VARIABLES

- GRADE (FURNISH)
- BASIS WEIGHT
- INITIAL MOISTURE RATIO
- INITIAL SHEET TEMPERATURE
- AMBIENT PRESSURE (ATMOSPHERIC OR VACUUM)
- PEAK APPLIED PRESSURE
- INITIAL HOT SURFACE TEMPERATURE
- RESIDENCE TIME*

GRADES FOR TECHNICAL PERFORMANCE TESTS

		Percent of Total U.S. Production[a]			Percent of Total U.S. Production[a]
1.	Newsprint	7.7	6.	Recycled paperboard	11.6
2.	Uncoated printing or writing paper	13.2	7.	Lightweight coating	- -
3.	Tissue	7.2	8.	Recycled linerboard	- -
4.	Linerboard	23.1	9.	Recycled corrugating medium	- -
5.	Corrugating medium, virgin	7.3	10.	High-yield experimental pulp	- -

[a]Combined paper and board production.

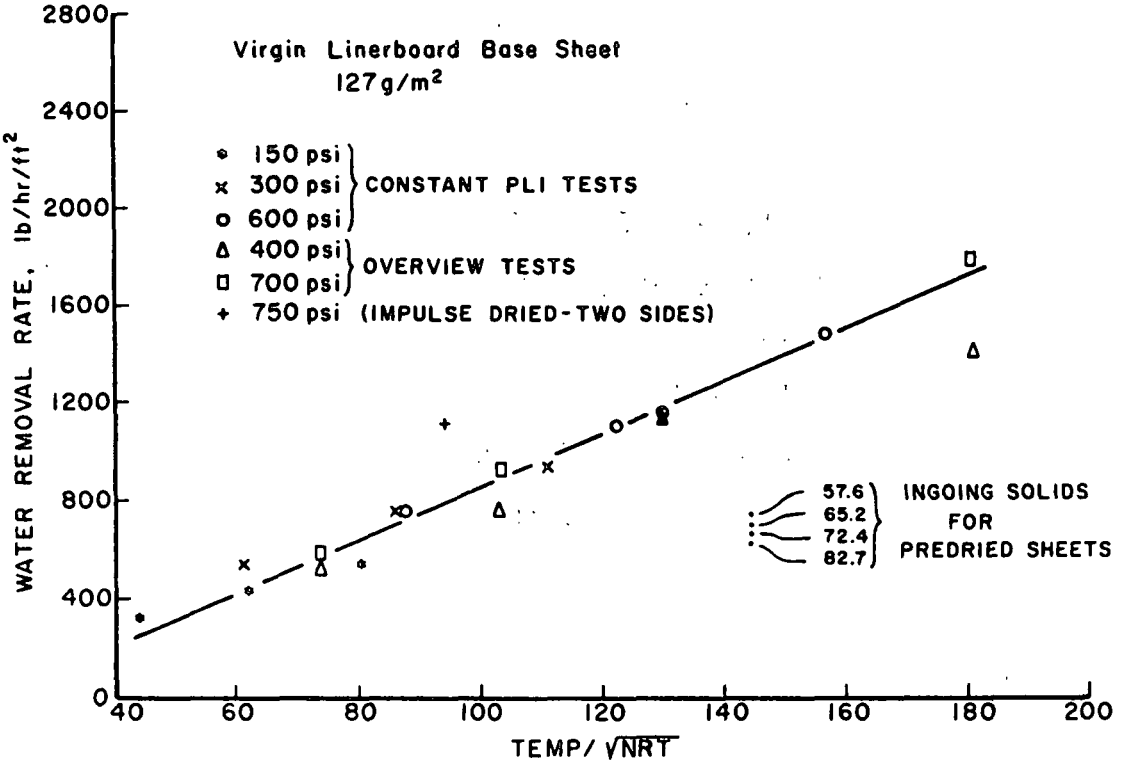

WATER REMOVAL RATES FOR VIRGIN LINERBOARD BASE STOCK.

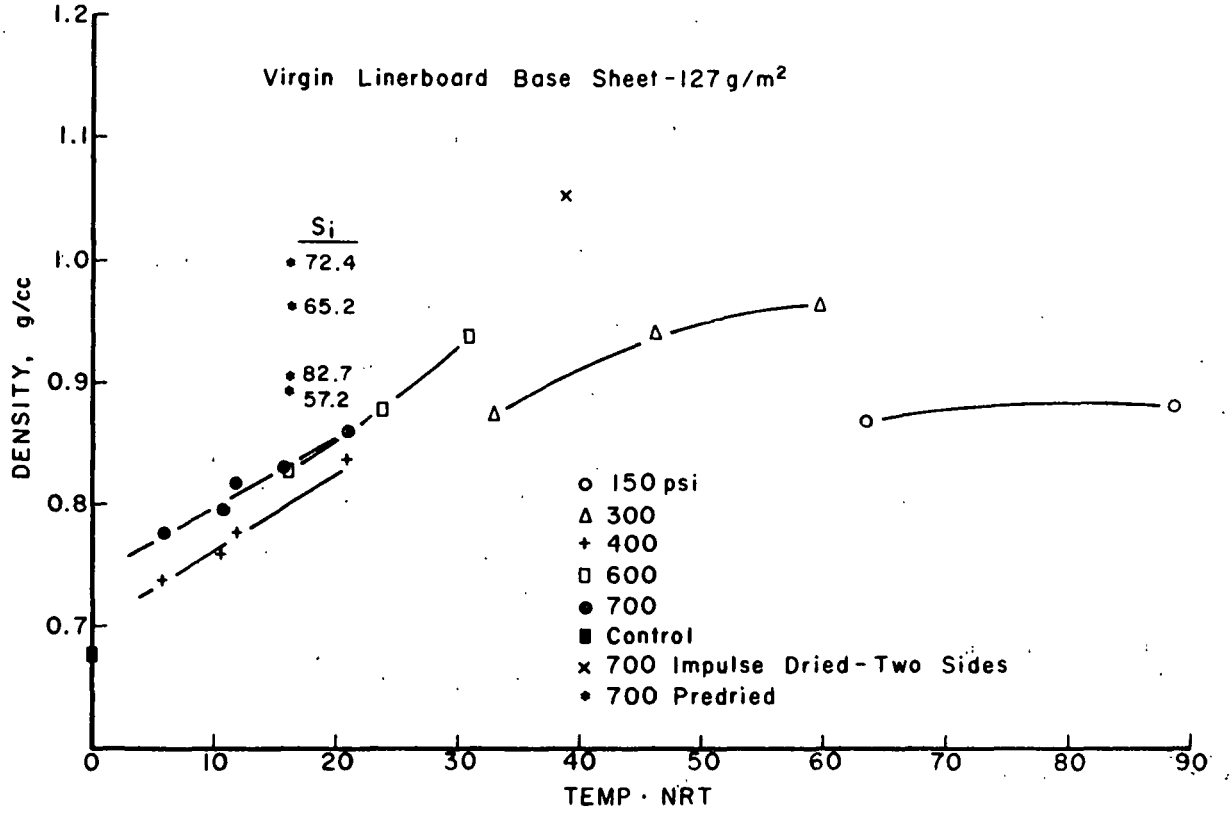

DENSITY DEVELOPMENT FOR VIRGIN LINERBOARD BASE SHEET.

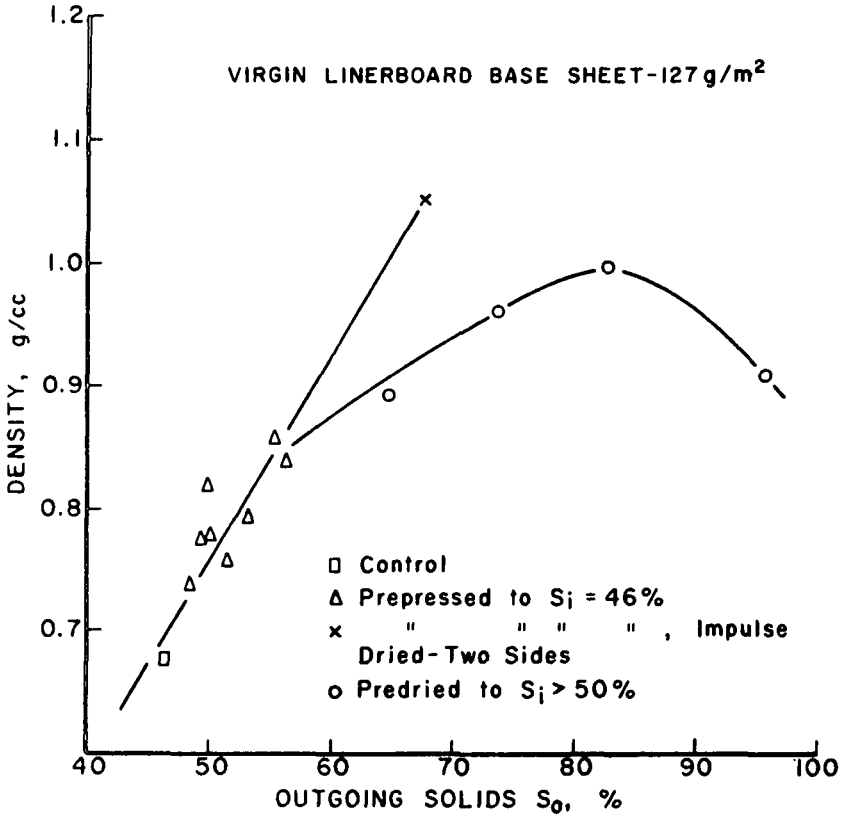

DENSITY DEVELOPMENT WITH DRYNESS FOR VIRGIN LINERBOARD BASE SHEET.

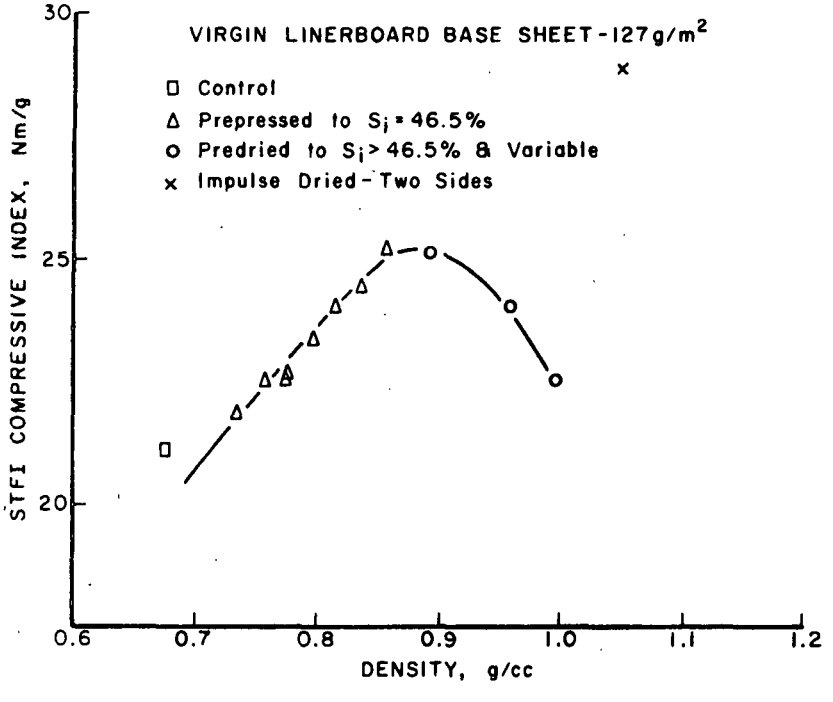

COMPRESSIVE STRENGTH VARIATION WITH DENSITY FOR VIRGIN LINERBOARD BASE STOCK.

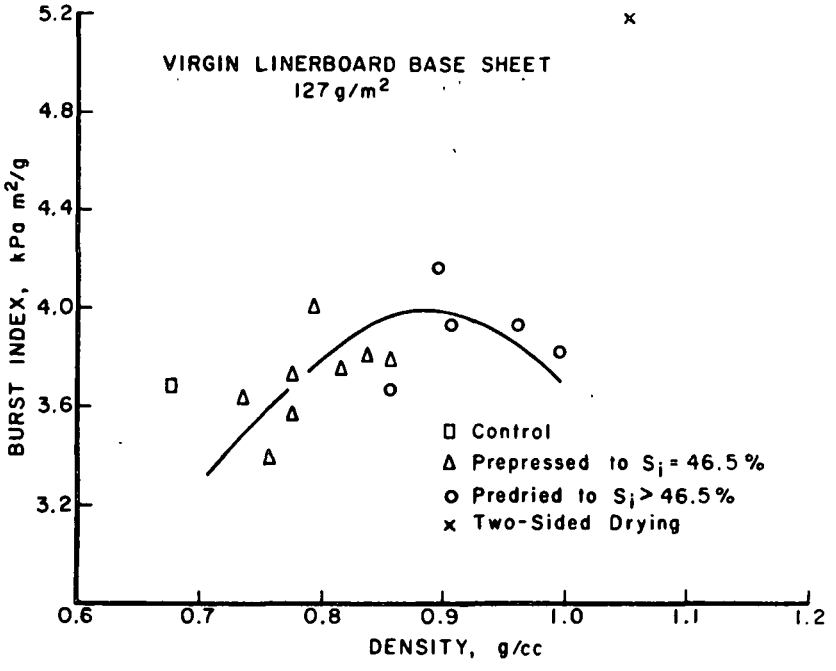

BURST DEVELOPMENT WITH DENSITY FOR VIRGIN LINERBOARD BASE SHEET.

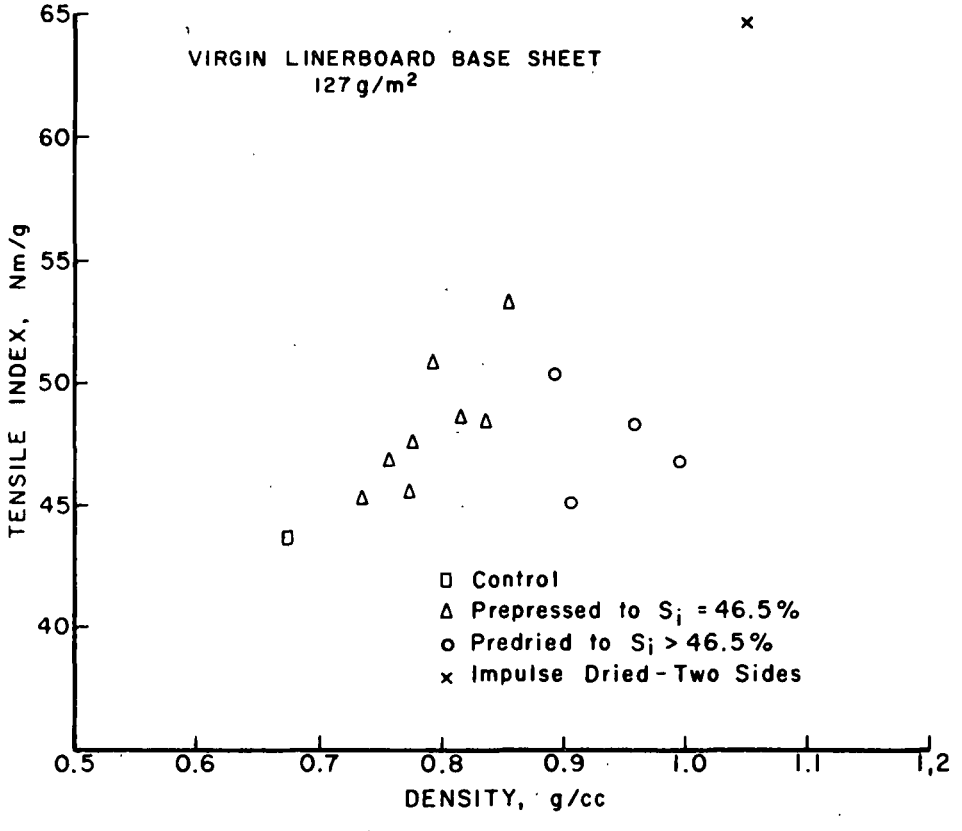

TENSILE STRENGTH DEVELOPMENT WITH DENSITY FOR VIRGIN LINERBOARD BASE SHEET.

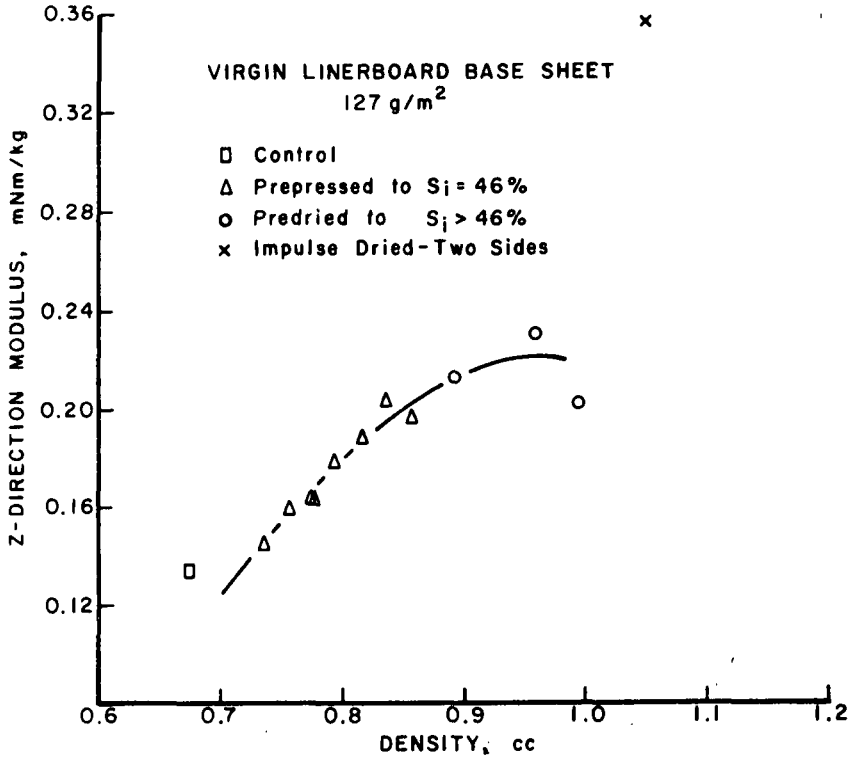

Z-DIRECTION MODULUS VARIATION WITH DENSITY FOR VIRGIN LINERBOARD BASE SHEET.

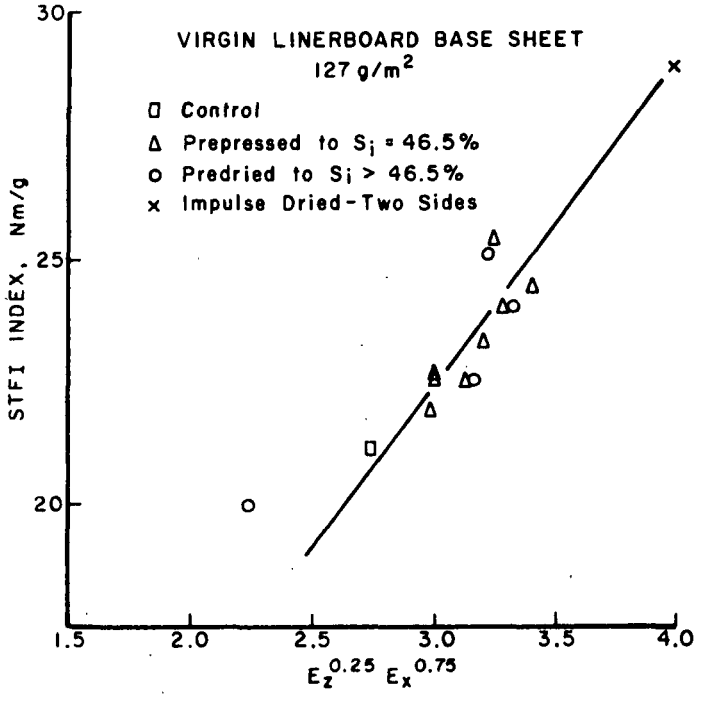

HABEGER-WHITSITT COMPRESSIVE STRENGTH MODEL FOR VIRGIN LINERBOARD BASE SHEET.

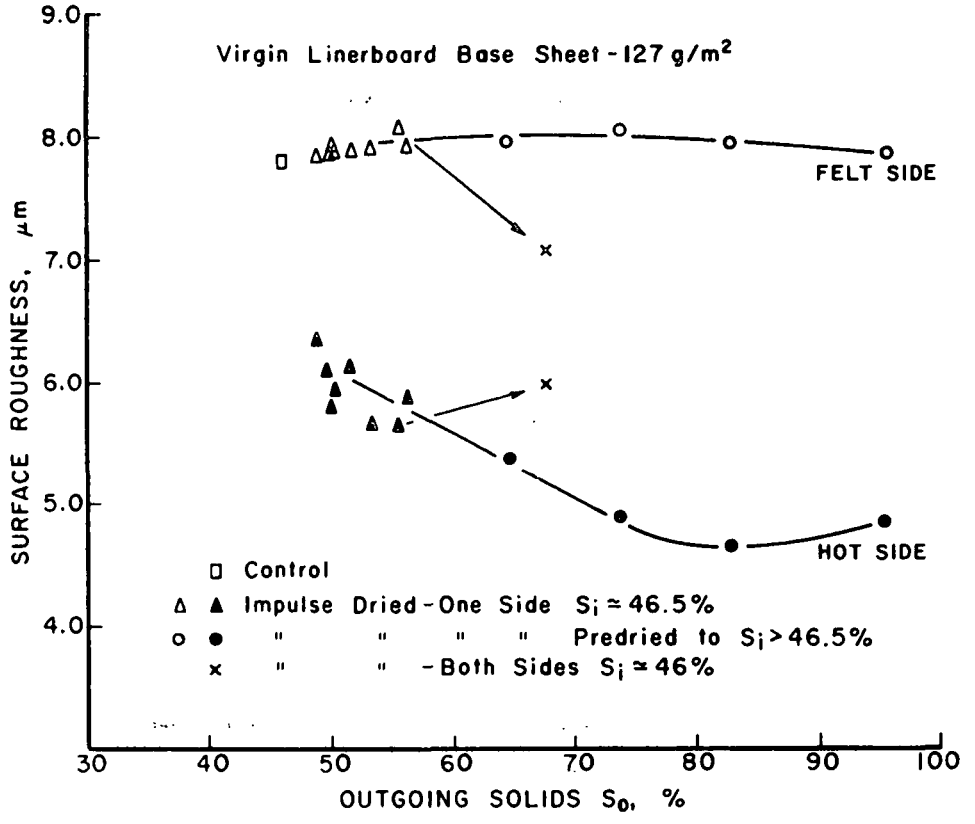

ROUGHNESS CHANGES WITH DRYNESS FOR VIRGIN LINERBOARD BASE SHEET.

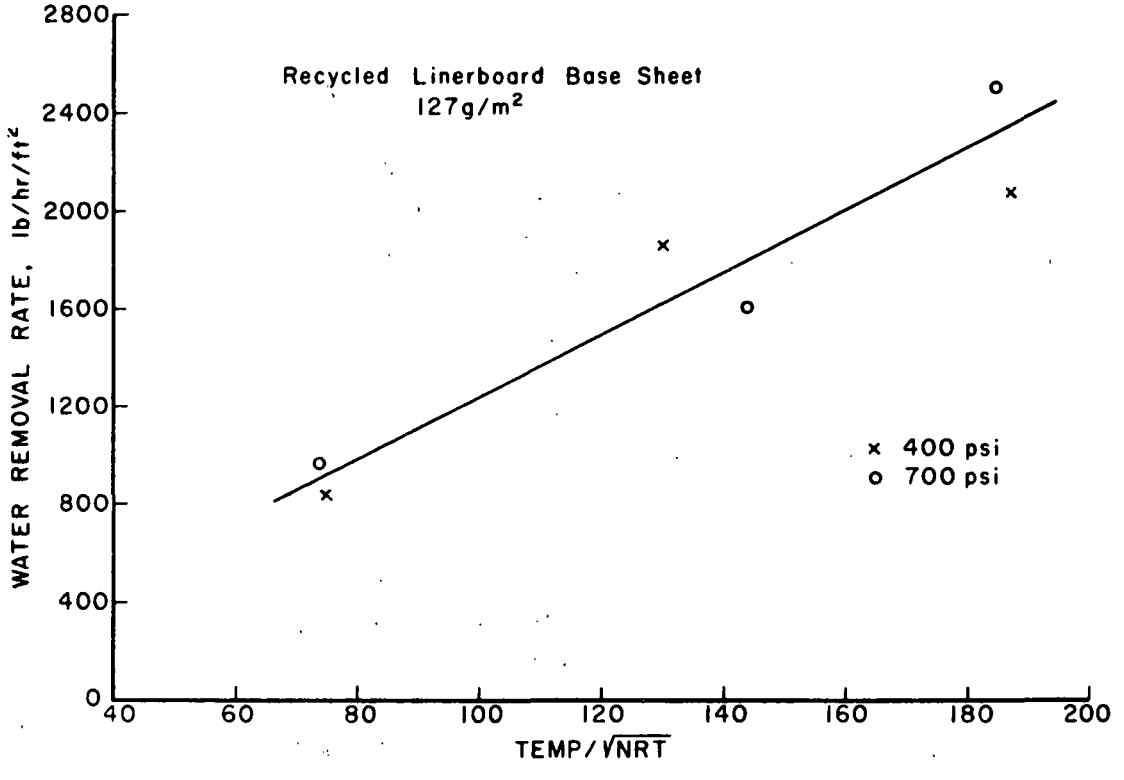

WATER REMOVAL RATES FOR RECYCLED LINERBOARD BASE STOCK.

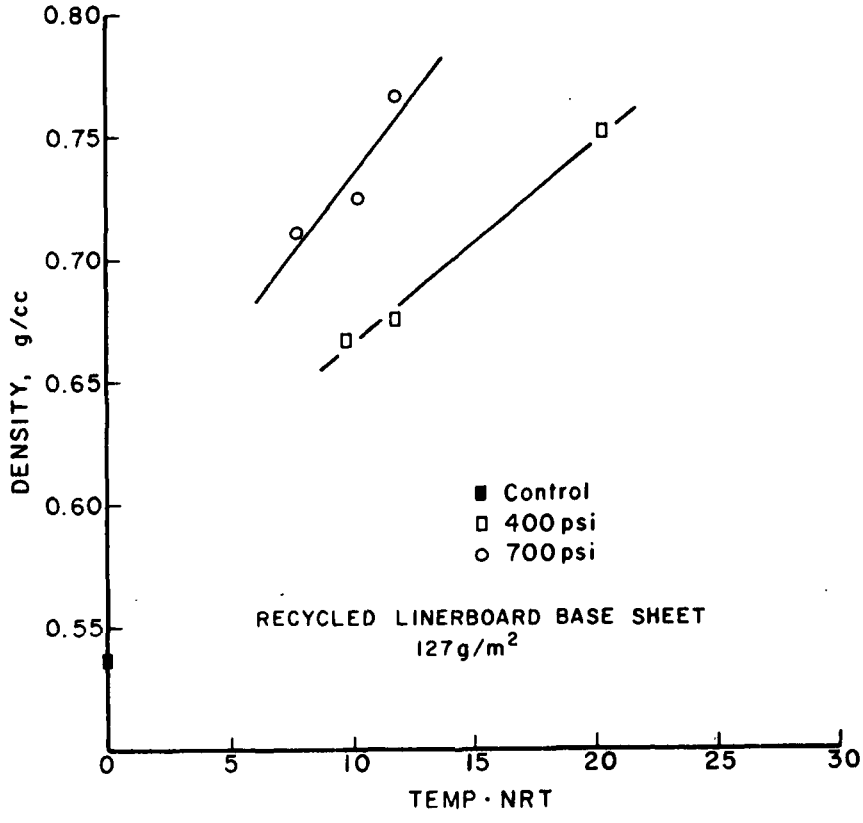

DENSITY DEVELOPMENT FOR RECYCLED LINERBOARD BASE STOCK.

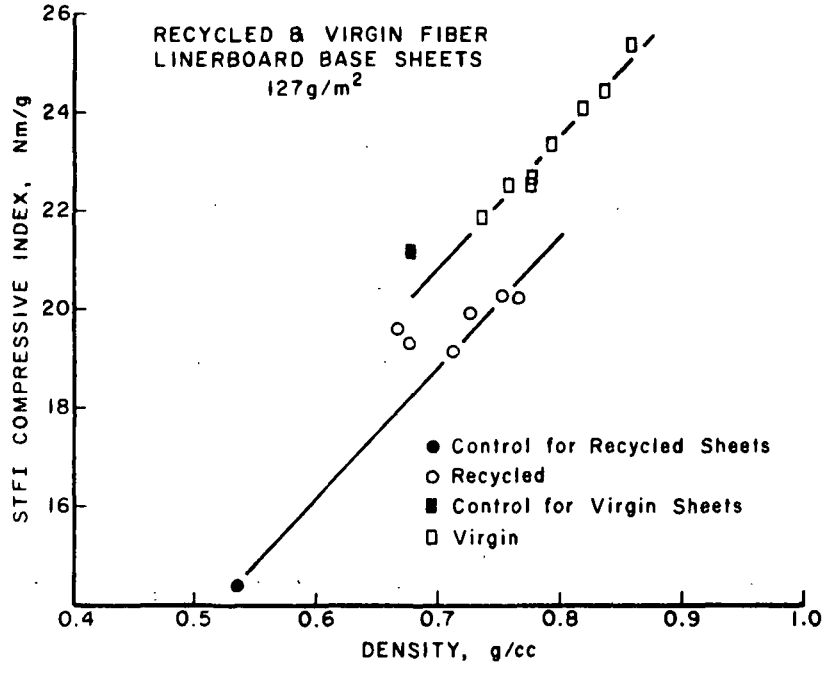

COMPRESSIVE STRENGTH - DENSITY RELATIONSHIPS FOR VIRGIN AND RECYCLED LINERBOARD.

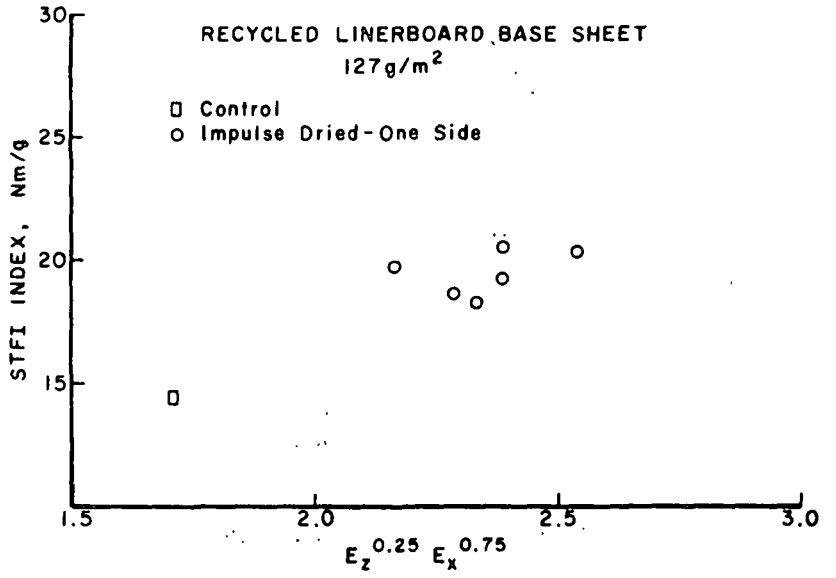

HABEGER-WHITSITT COMPRESSIVE STRENGTH MODEL FOR RECYCLED LINERBOARD BASE SHEET.

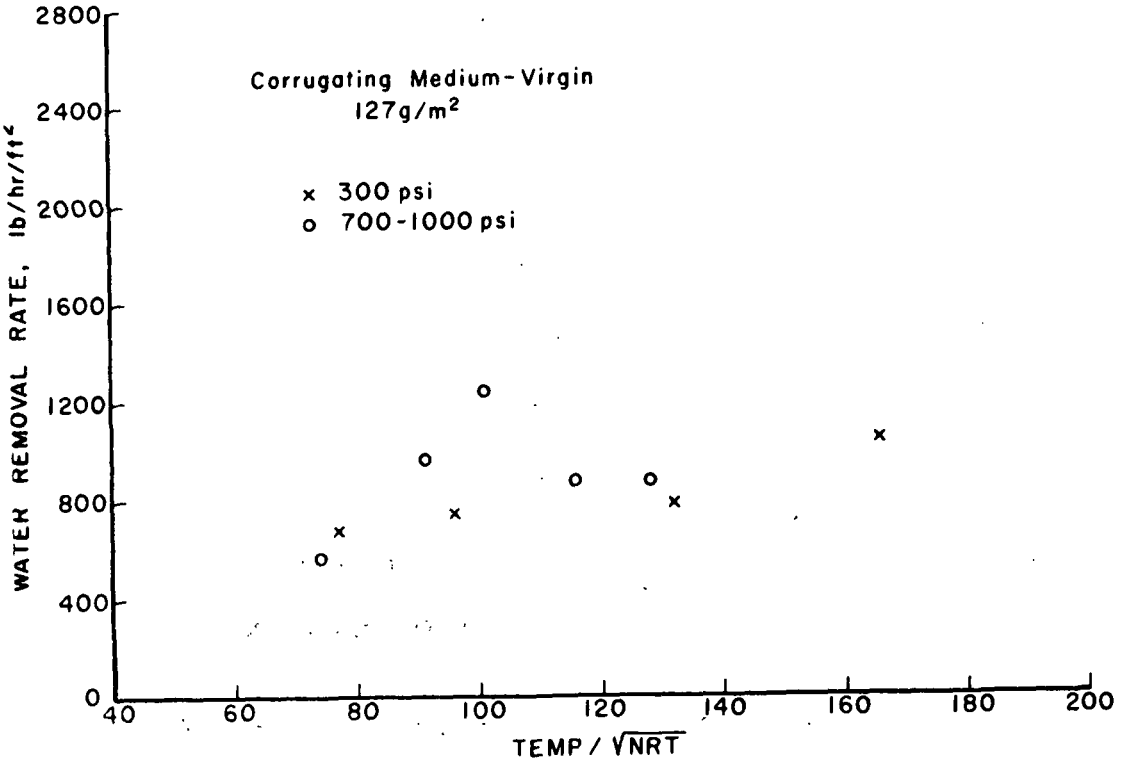

WATER REMOVAL RATES FOR VIRGIN CORRUGATING MEDIUM.

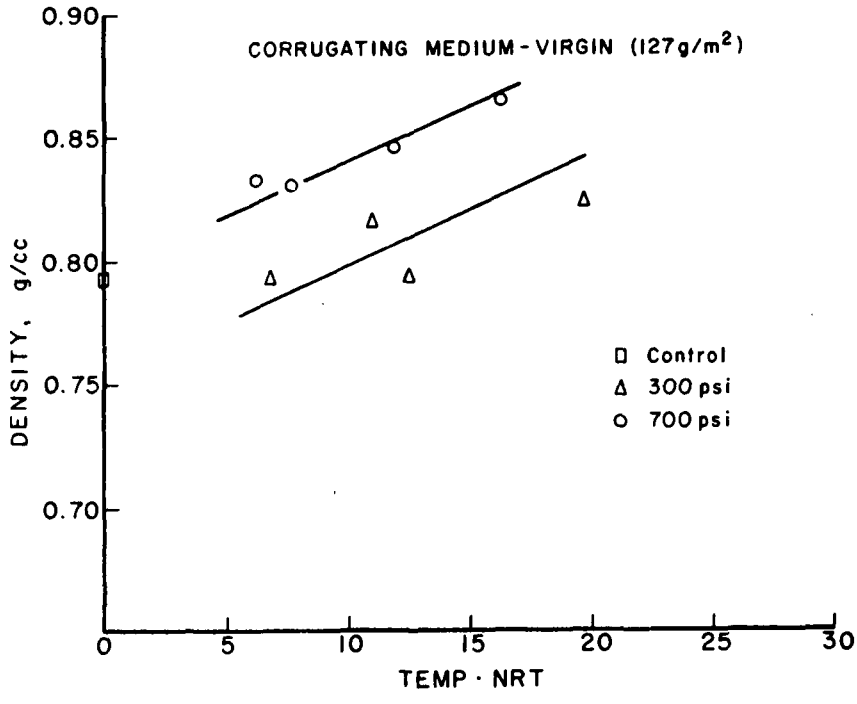

DENSITY DEVELOPMENT FOR CORRUGATING MEDIUM.

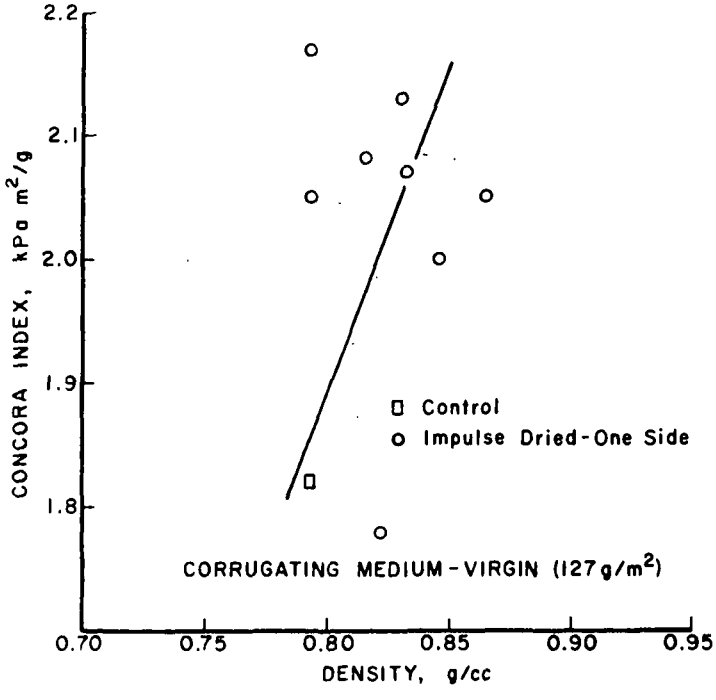

CONCORA VARIATION WITH DENSITY
FOR VIRGIN CORRUGATING MEDIUM.

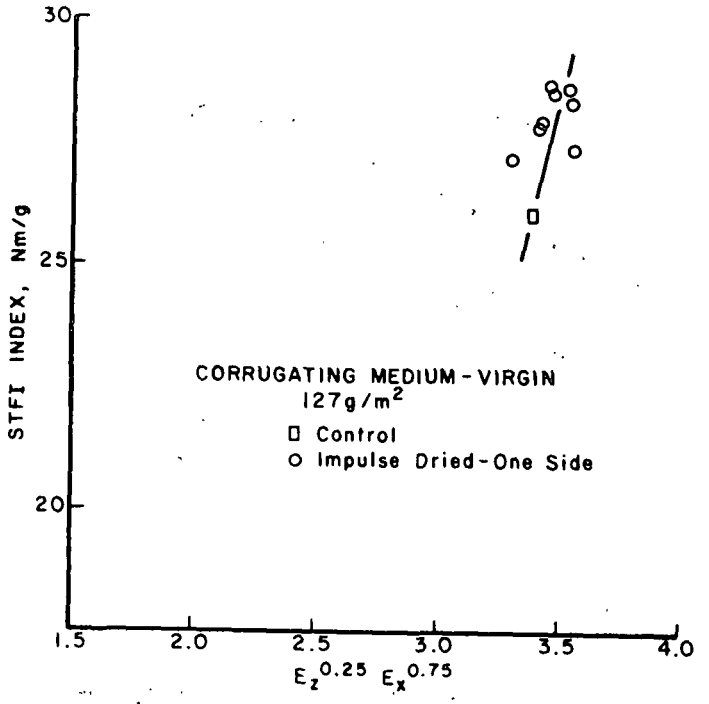

HABEGER-WHITSITT COMPRESSIVE STRENGTH MODEL FOR CORRUGATING MEDIUM.

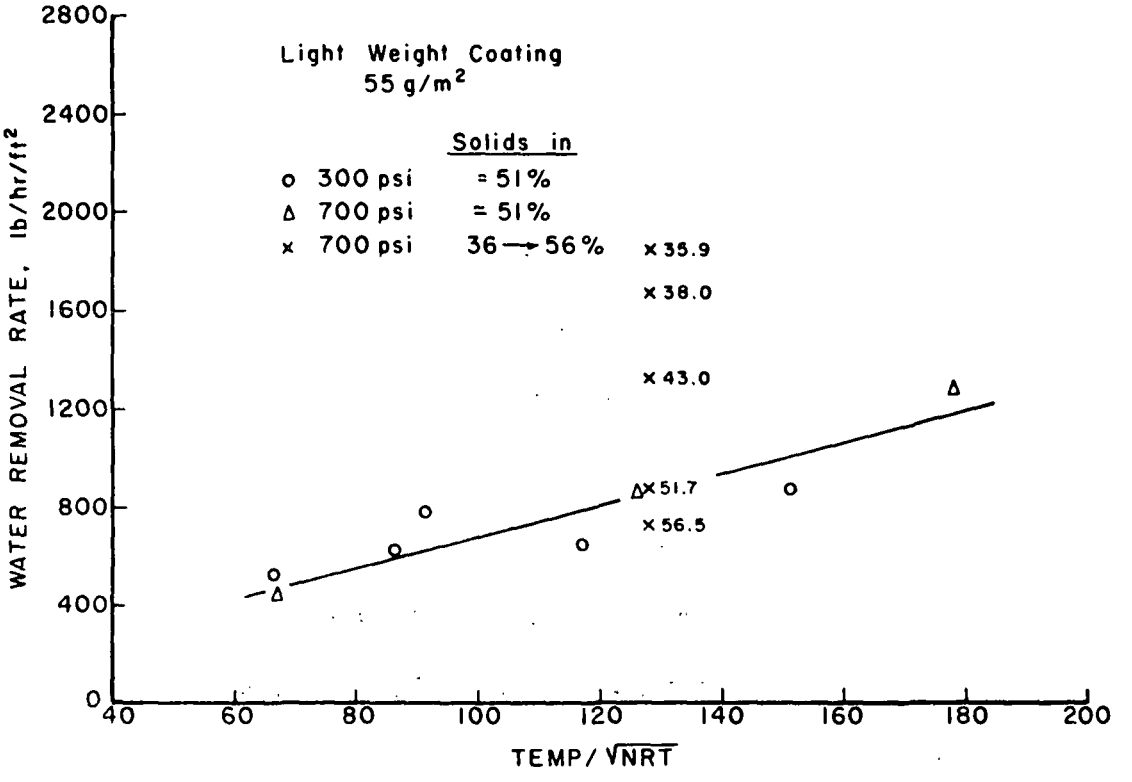

WATER REMOVAL RATES FOR LIGHTWEIGHT COATING PAPER.

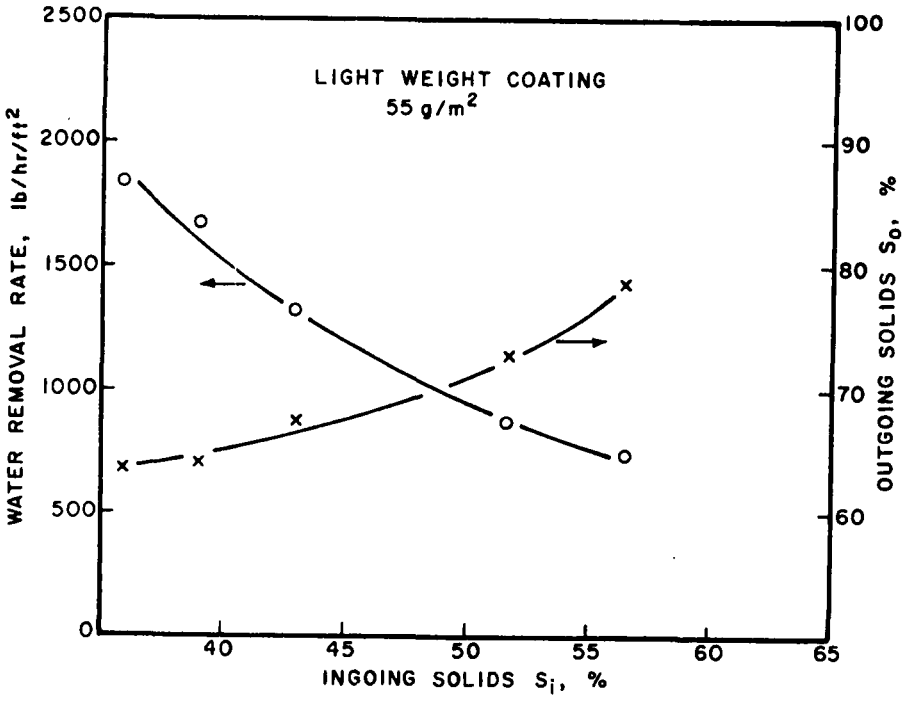

WATER REMOVAL RATE AND OUTGOING SOLIDS VARIATIONS WITH PREPRESSING LEVEL FOR LIGHTWEIGHT COATING PAPER.

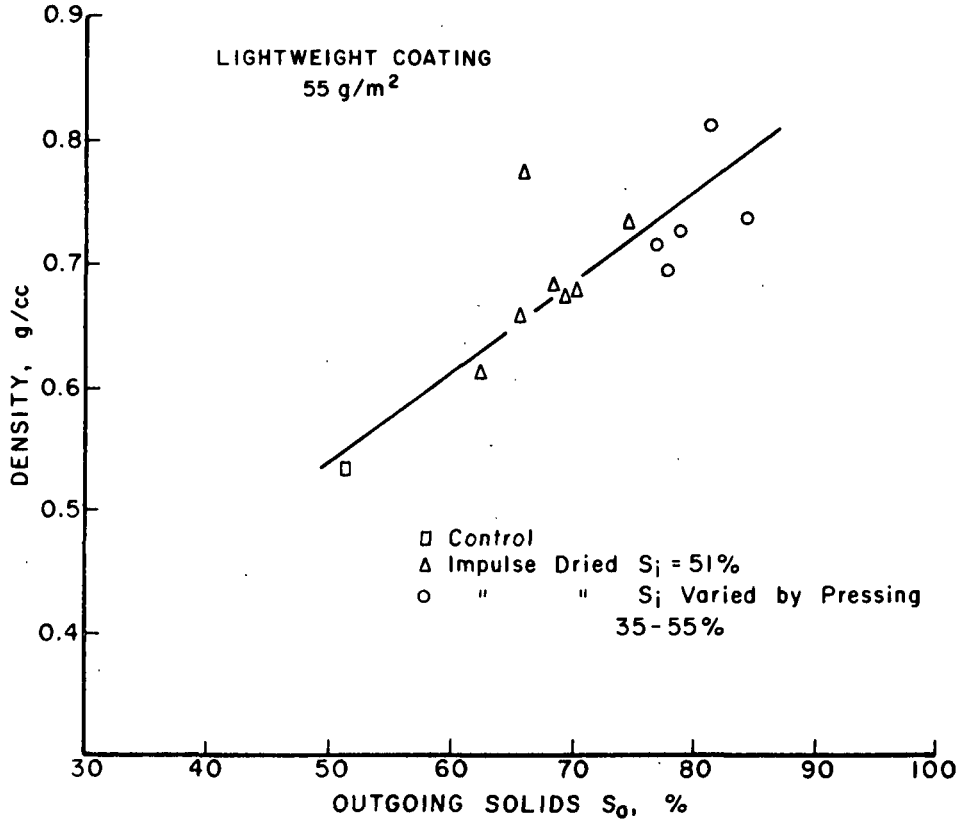

DENSITY DEVELOPMENT WITH DRYNESS FOR LIGHTWEIGHT COATING GRADE.

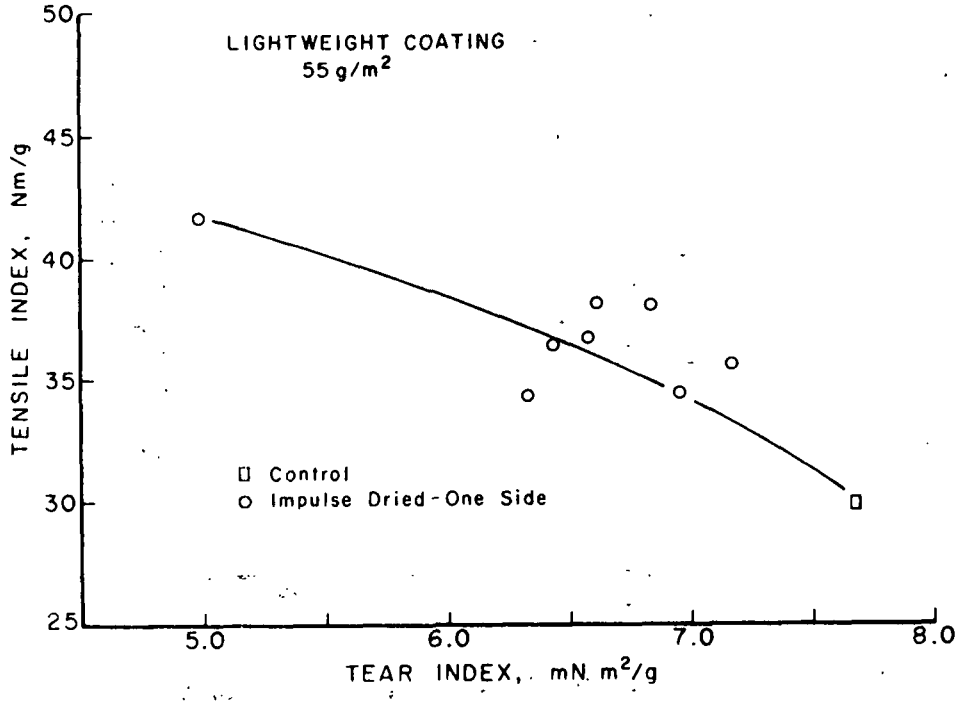

TENSILE-TEAR RELATIONSHIP FOR LIGHTWEIGHT COATING GRADE.

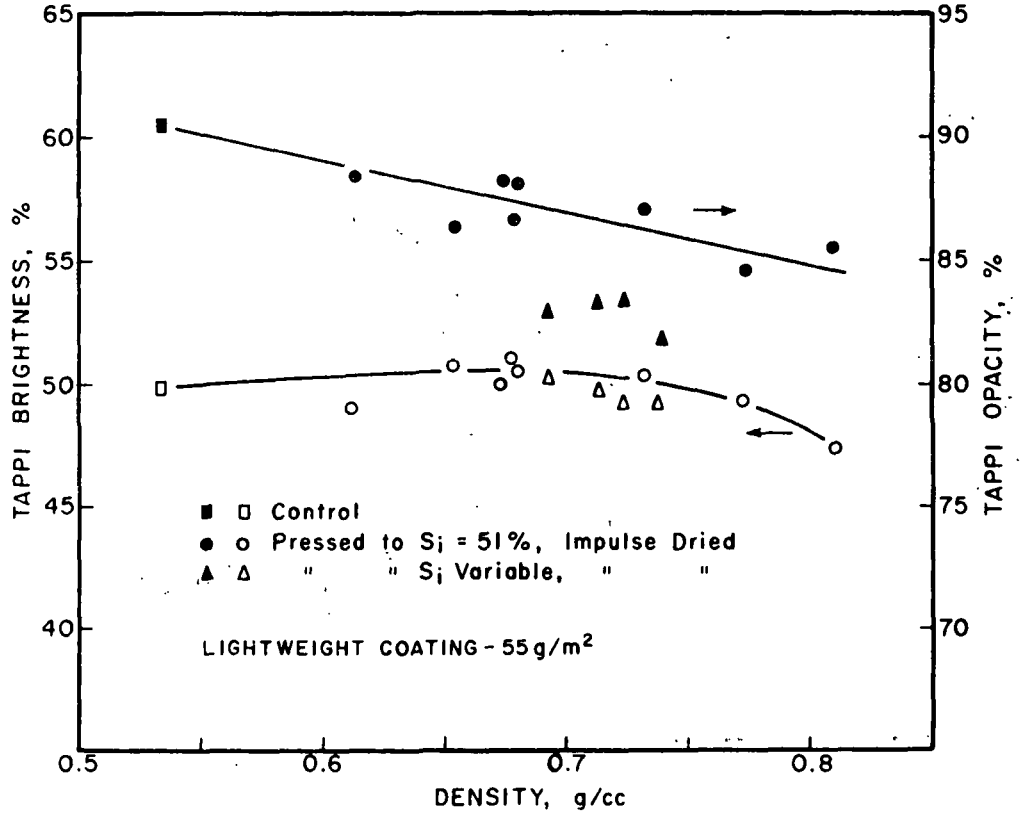

BRIGHTNESS AND OPACITY CHANGES WITH DENSITY FOR LIGHTWEIGHT COATING PAPER.

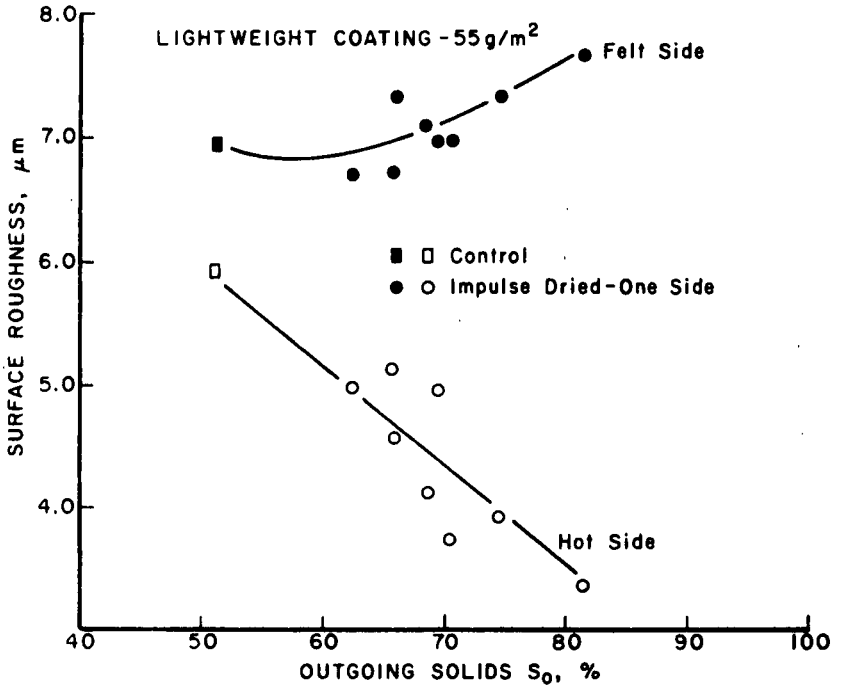

ROUGHNESS CHANGES WITH DRYNESS FOR LIGHTWEIGHT COATING PAPER.

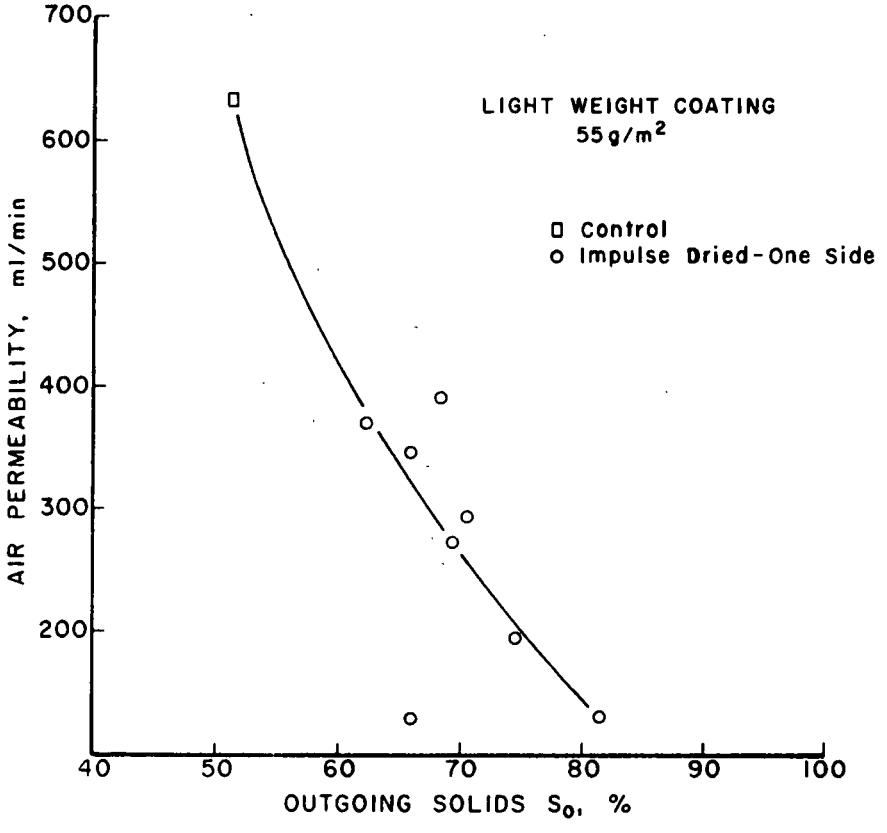

AIR PERMEABILITY VARIATIONS WITH OUTGOING SOLIDS FOR LIGHTWEIGHT COATING PAPER.

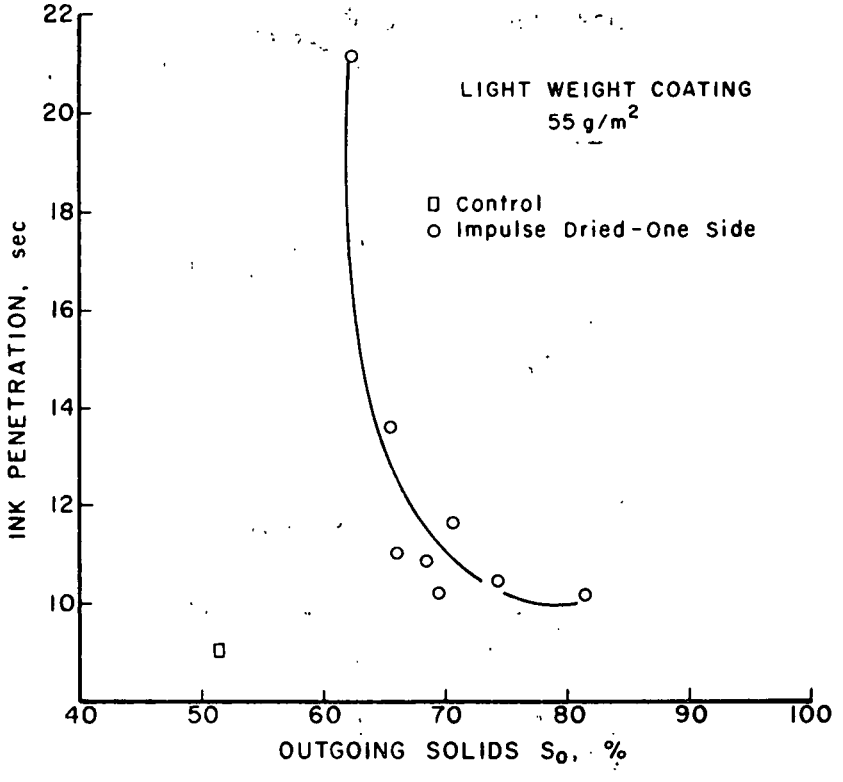

INK PENETRATION VARIATION WITH OUTGOING SOLIDS FOR LIGHTWEIGHT COATING PAPER.

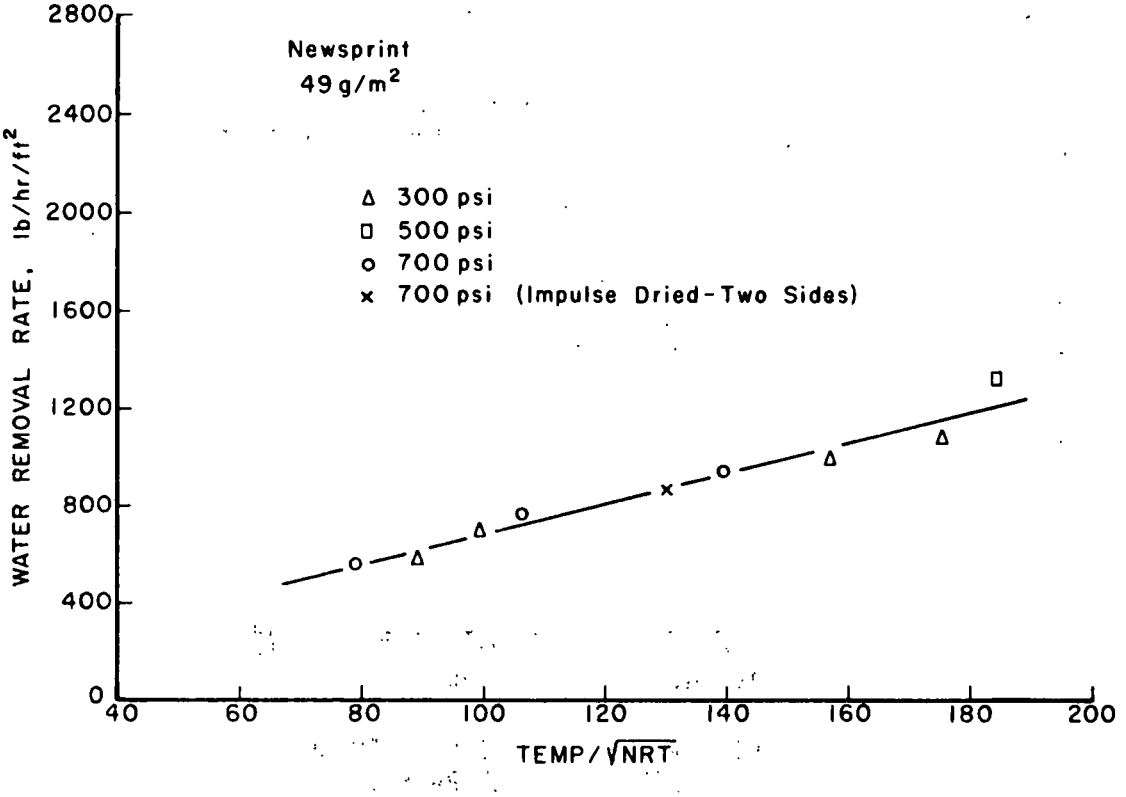

WATER REMOVAL RATES FOR NEWSPRINT.

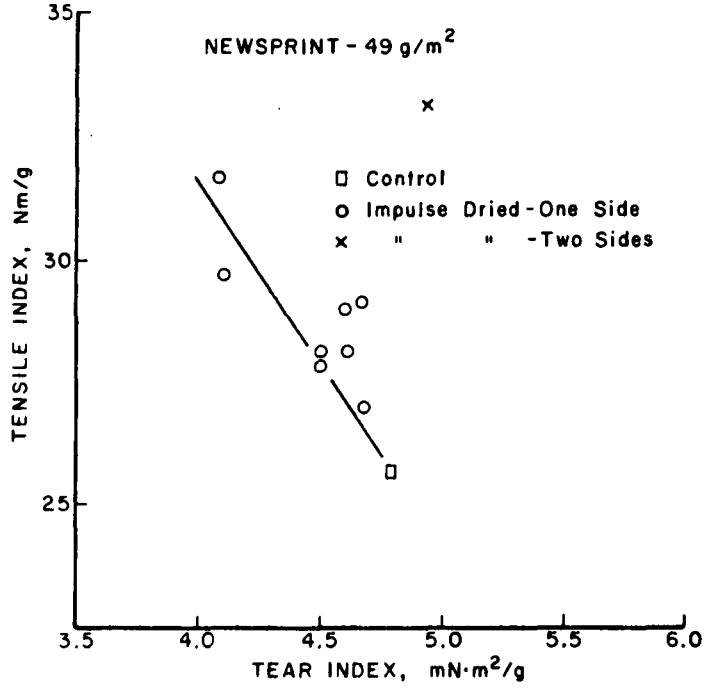

TENSILE-TEAR RELATIONSHIP FOR NEWSPRINT.

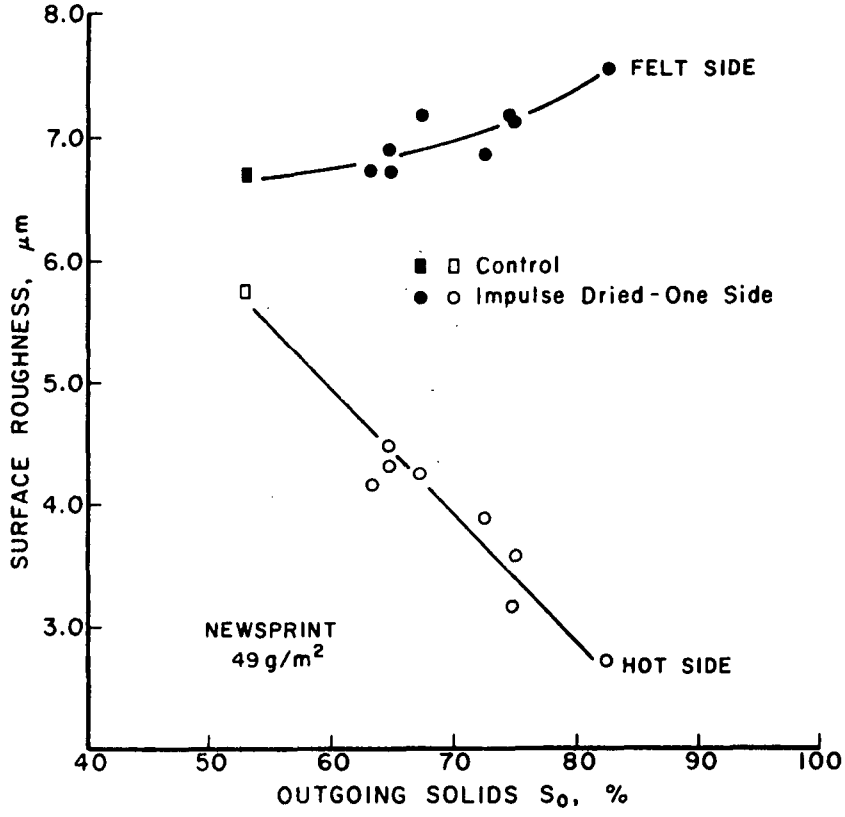

ROUGHNESS CHANGES WITH DRYNESS FOR NEWSPRINT.

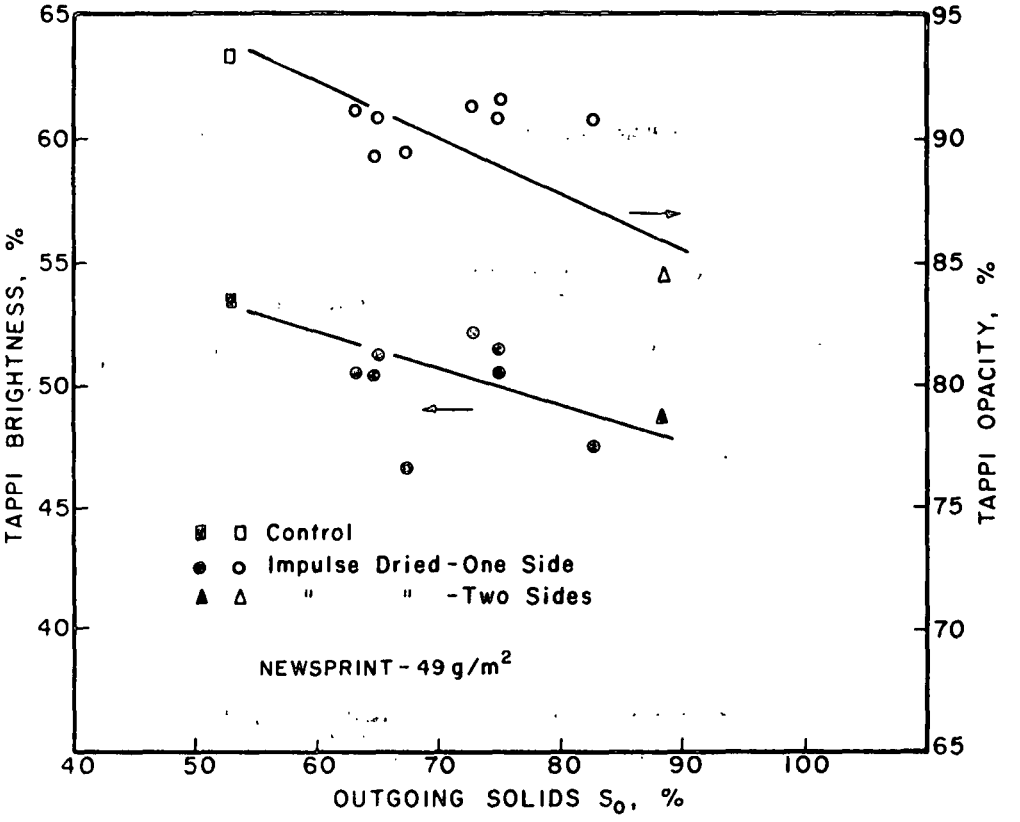

BRIGHTNESS AND OPACITY CHANGES WITH DRYNESS FOR NEWSPRINT.

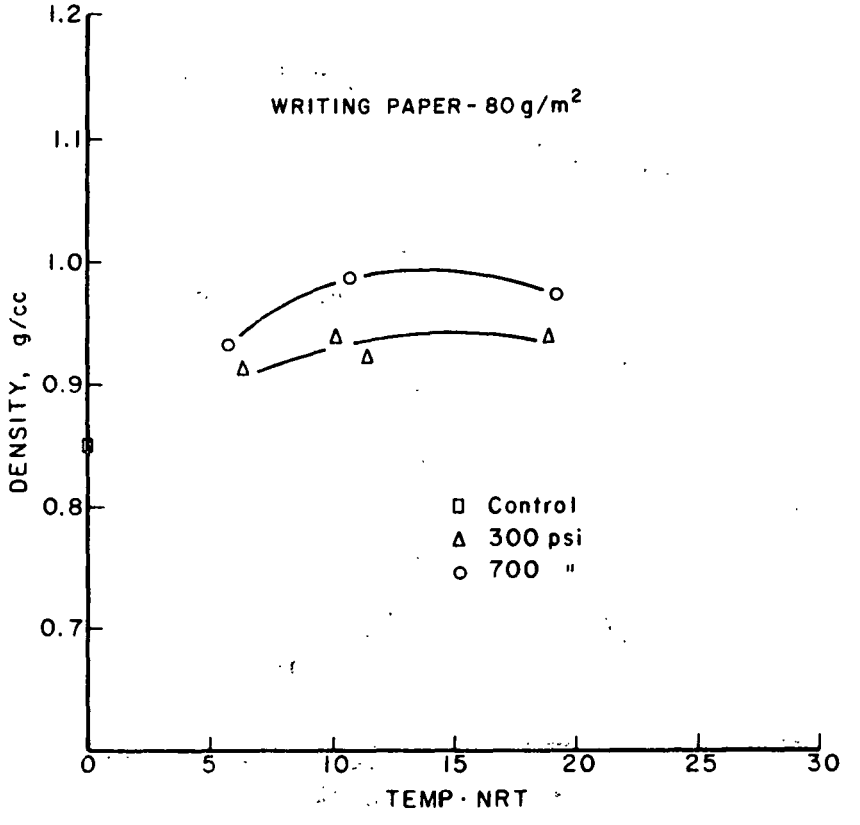

DENSITY DEVELOPMENT FOR WRITING PAPER.

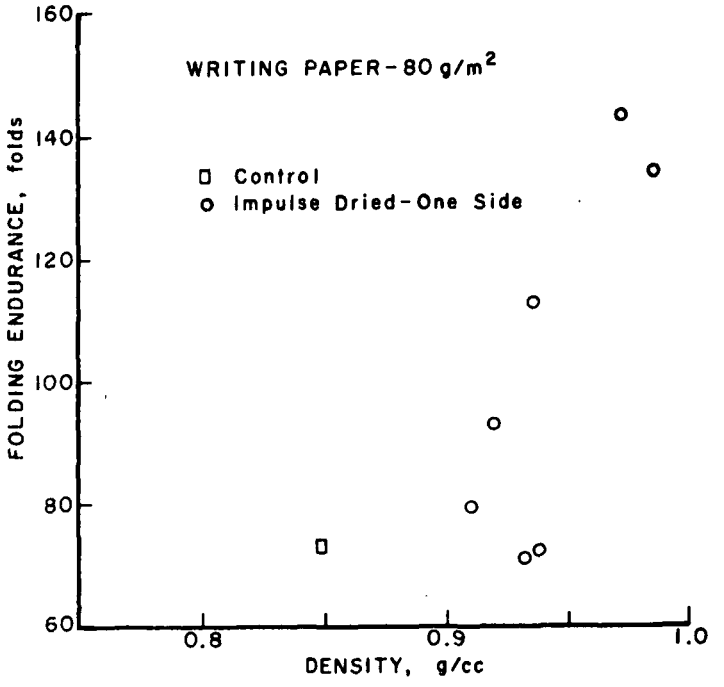

FOLD ENDURANCE VARIATIONS WITH DENSITY FOR WRITING PAPER.

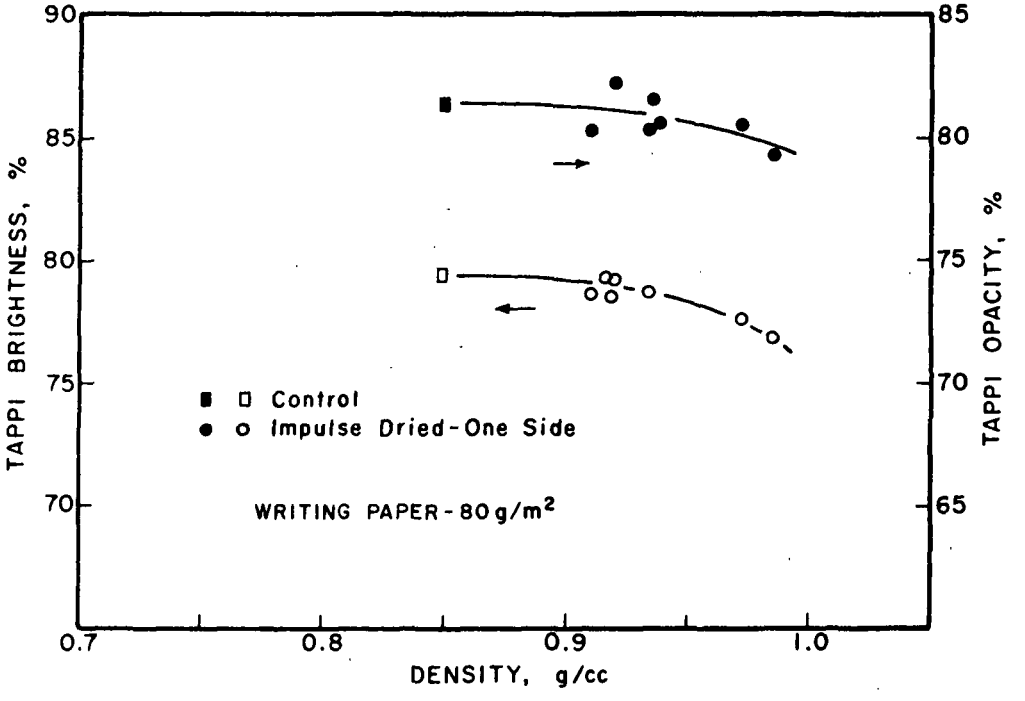

BRIGHTNESS AND OPACITY CHANGES WITH DENSITY FOR WRITING PAPER.

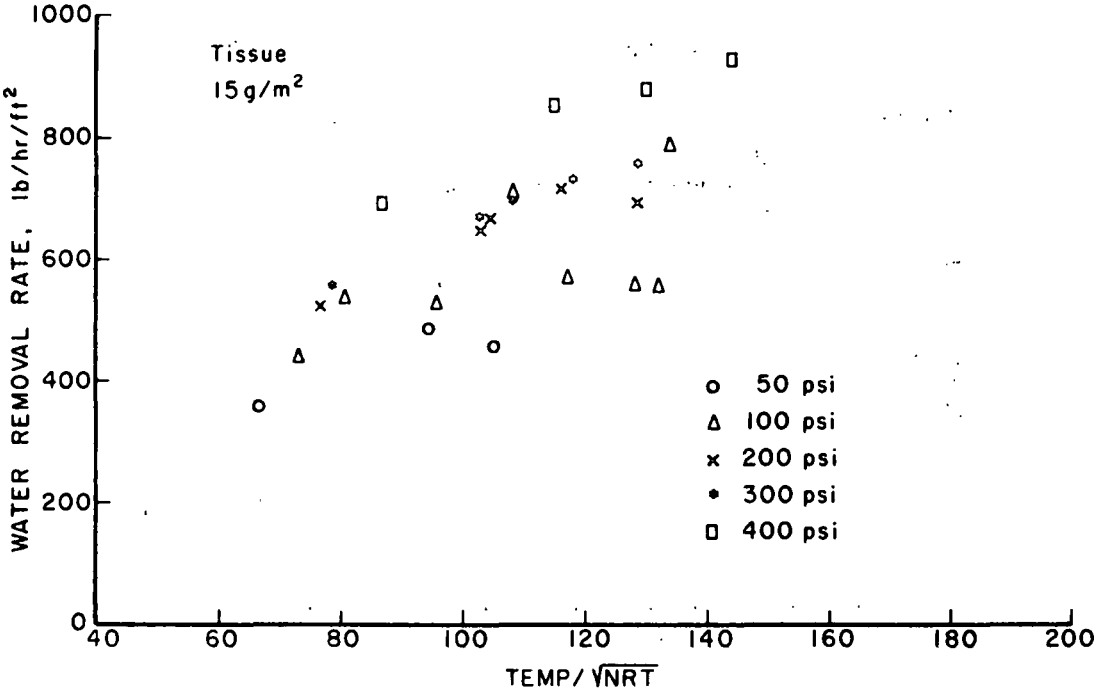

WATER REMOVAL RATES FOR TISSUE.

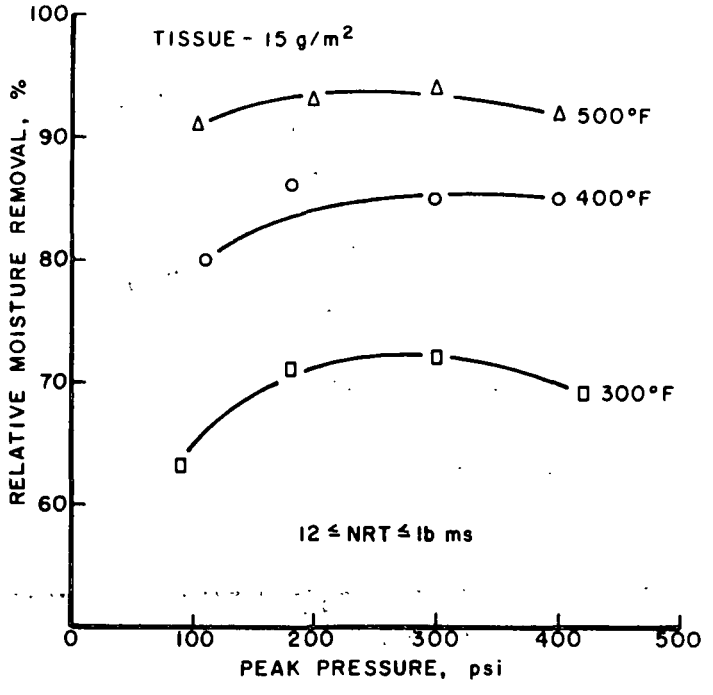

VARIATION OF RELATIVE MOISTURE REMOVAL WITH PRESSURE FOR TISSUE.

WATER REMOVAL RATE CORRELATIONS - IMPULSE DRYING

GENERAL FORM: $WRR = A + B \cdot P + C \cdot TEMP/\sqrt{NRT}$

GRADE	A	B	C	R^2	BW
VIRGIN LINER	-397	0.407	0.308	0.97	127
RECYCLED LINER	-151	0.306	0.389	0.90	127
CORRUGATING MEDIUM	290	0.314	0.115	0.32	127
WRITING PAPER	-116	0.494	0.232	0.81	80
LWC	-98.9	0.350	0.183	0.80	55
NEWSPRINT	-55.5	0.163	0.204	0.96	49

DENSITY CORRELATIONS - IMPULSE DRYING

GENERAL FORM: $\rho = D + E \cdot P + F \cdot TEMP \cdot NRT$

GRADE	D	E	F	R^2	BW
VIRGIN LINER	0.643	0.0001	0.0066	0.98	127
RECYCLED LINER	0.483	0.0003	0.0080	0.98	127
CORRUGATING MEDIUM	0.747	0.00008	0.0029	0.78	127
WRITING PAPER	0.870	0.0001	0.0019	0.78	80
LWC	0.502	0.0002	0.0088	0.93	55
NEWSPRINT	0.540	0.0001	0.0088	0.79	49

OBSERVATIONS 1

- WRR & TWR VERY HIGH TEMP NRT P
- DENSITY VERY HIGH TEMP·NRT P
- STRENGTH USUALLY INCREASES WITH DENSITY
- COMPRESSIVE STRENGTH FOLLOWS HW MODEL

OBSERVATIONS 2

- LARGE SMOOTHNESS INCREASES
- LARGE ABSORBENCY DECREASES
- LARGE AIR PERMEABILITY DECREASES
- LARGE PICK RESISTANCE INCREASES

OBSERVATIONS 3

- SMALL BRIGHTNESS DECREASES
- SMALL OPACITY DECREASES

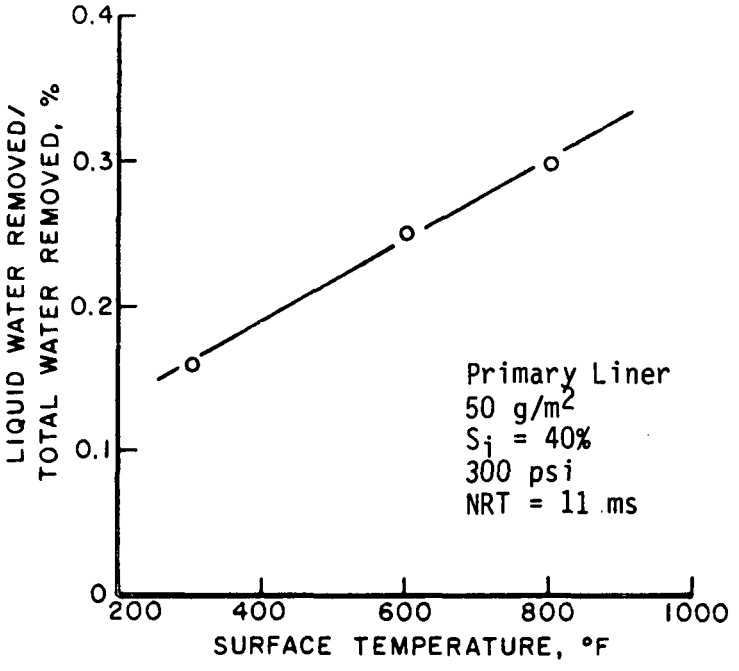

LIQUID WATER REMOVAL IN IMPULSE DRYING.

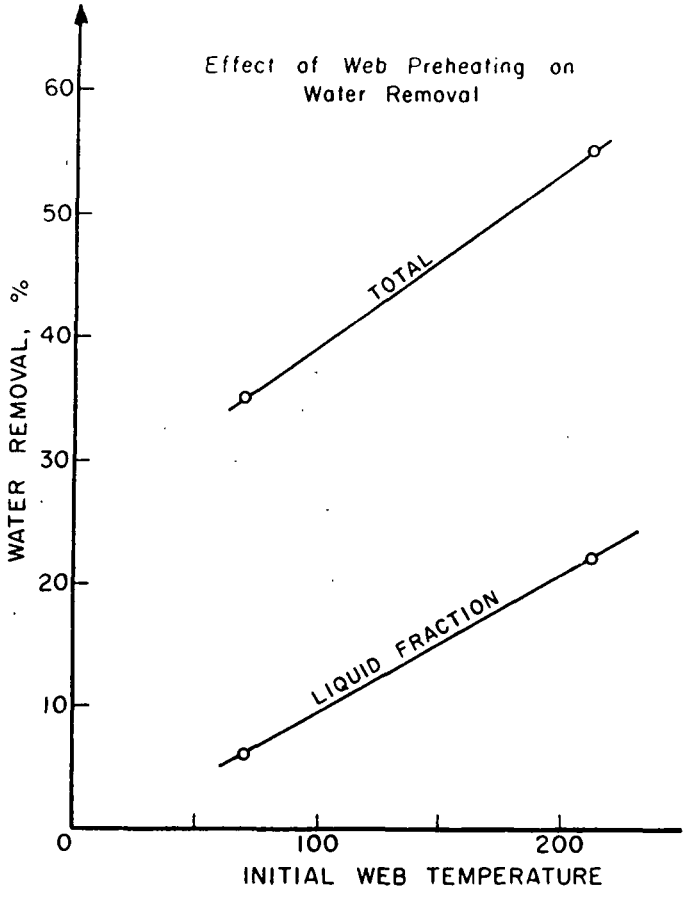

EFFECT OF WEB PREHEATING
IN LIQUID WATER REMOVAL.

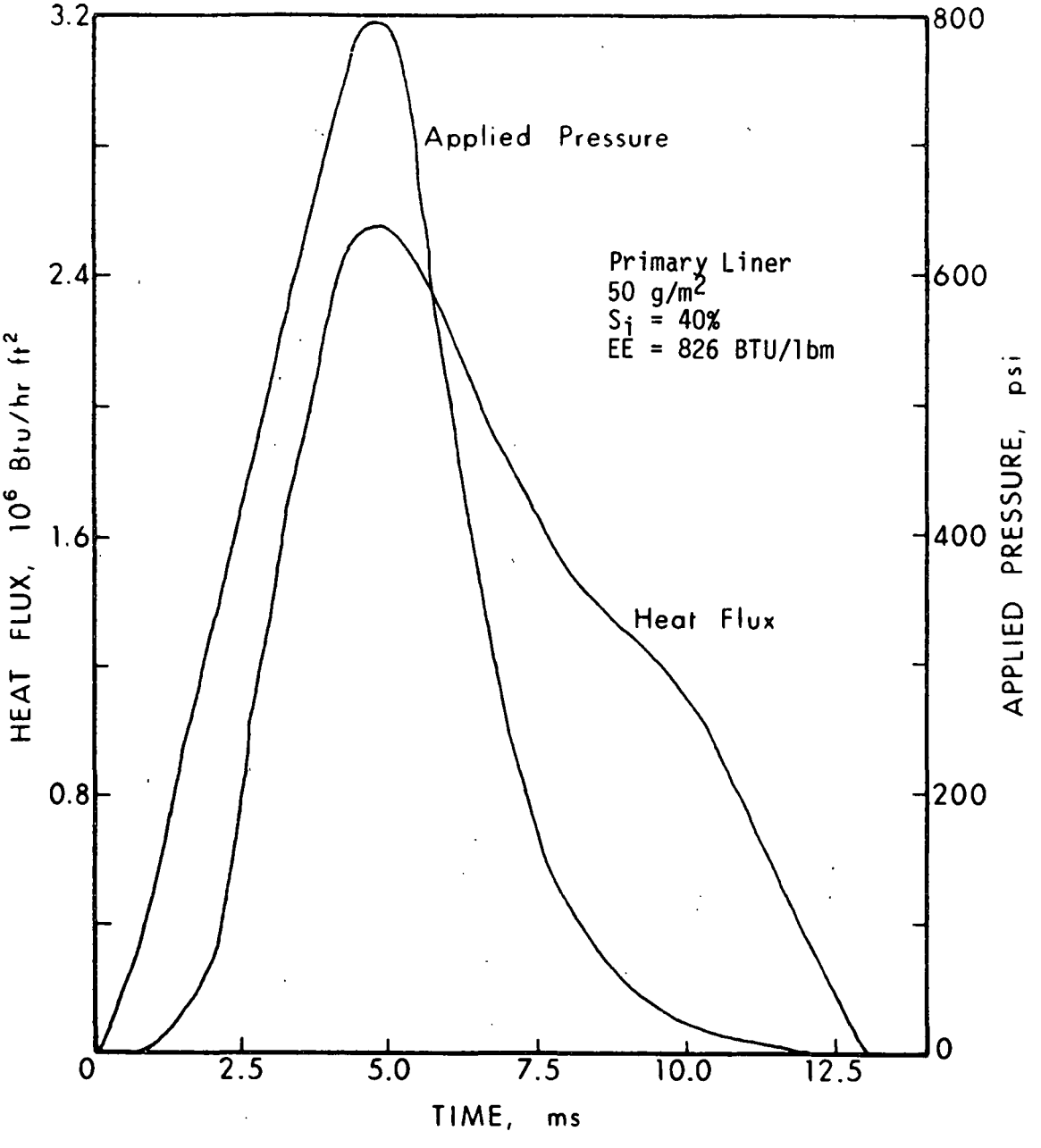

INSTANTANEOUS HEAT FLUX IN IMPULSE DRYING.
ROOM TEMPERATURE WEB.

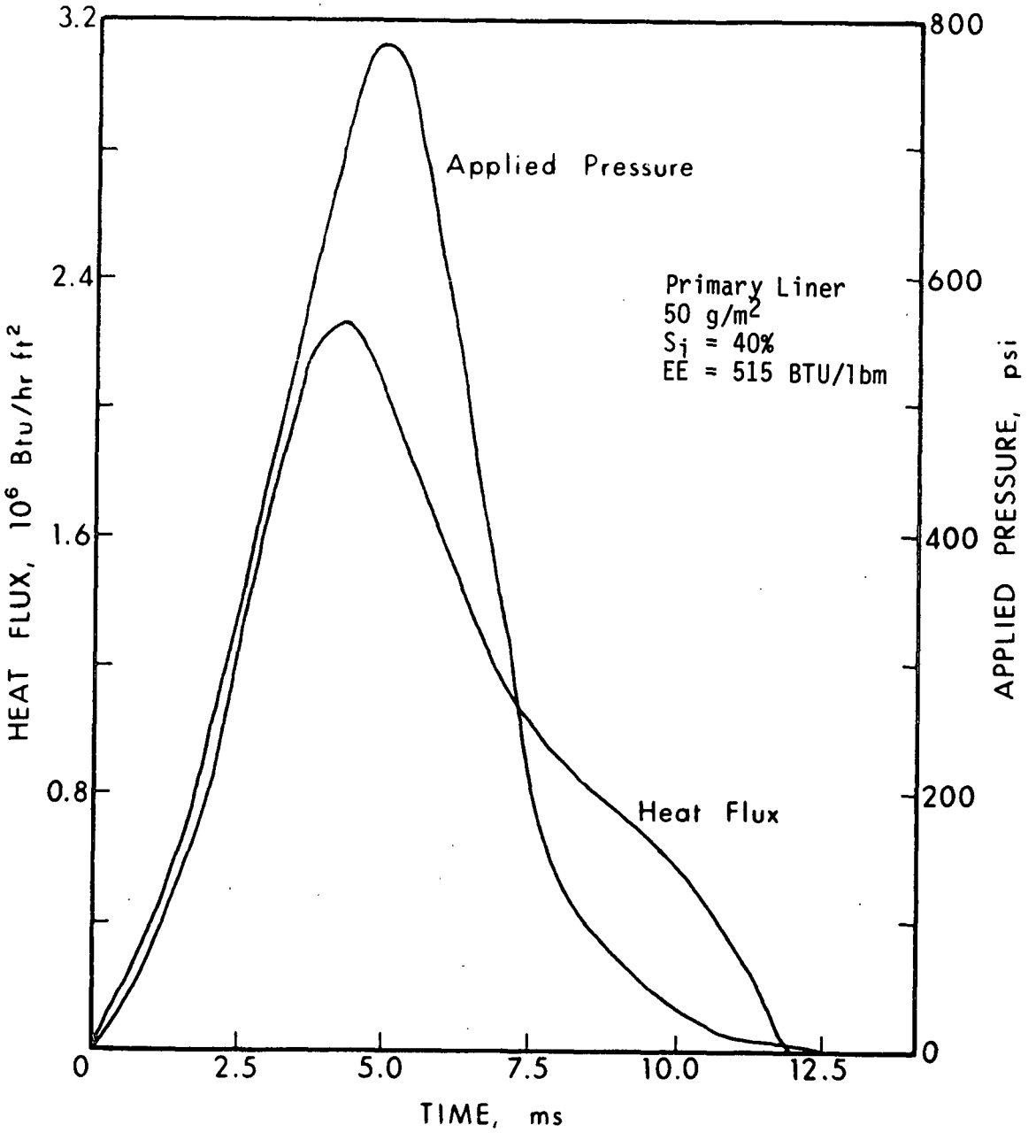

INSTANTANEOUS HEAT FLUX IN IMPULSE DRYING.
PREHEATED WEB.

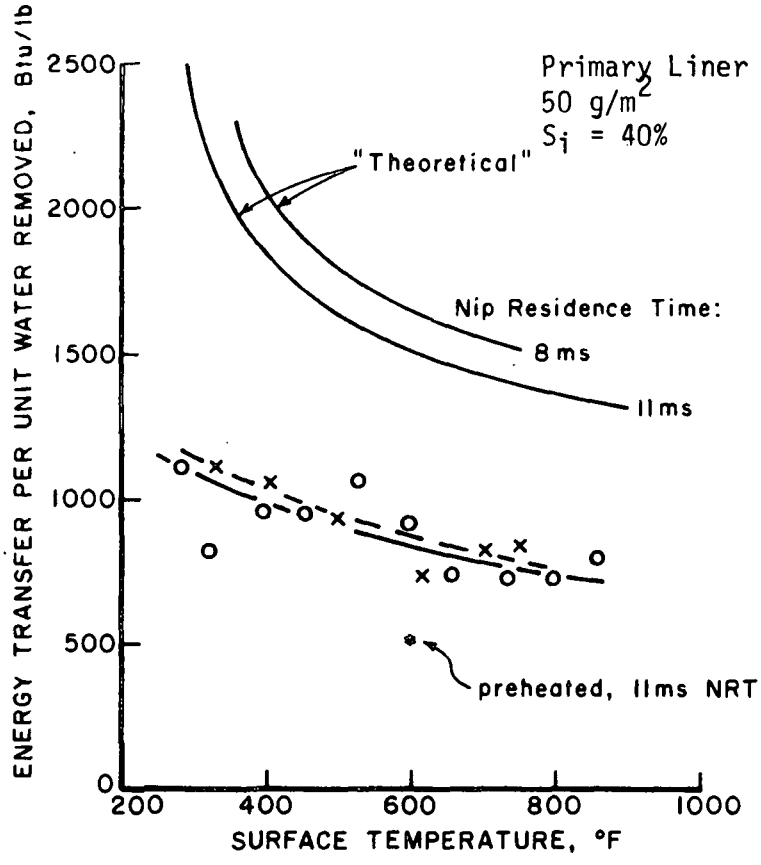

THEORETICAL HEAT INPUT FOR PURE EVAPORATION PROCESS AND ACTUAL HEAT INPUT FOR IMPULSE DRYING.

VALUE TO THE INDUSTRY

- PROPERTY DEVELOPMENT/CONTROL
- PRODUCTIVITY
- DRYER SIZE/CAPITAL COST
- MOISTURE & PROPERTY PROFILE LEVELING
- NEW PRODUCT PROPERTIES
- LESS DRYING ENERGY

IMPULSE DRYING

Plans for the coming period

Hugh P. Lavery

Topics for Discussion:

-Overview of research questions

-Priorities

-Six-month Deliverables

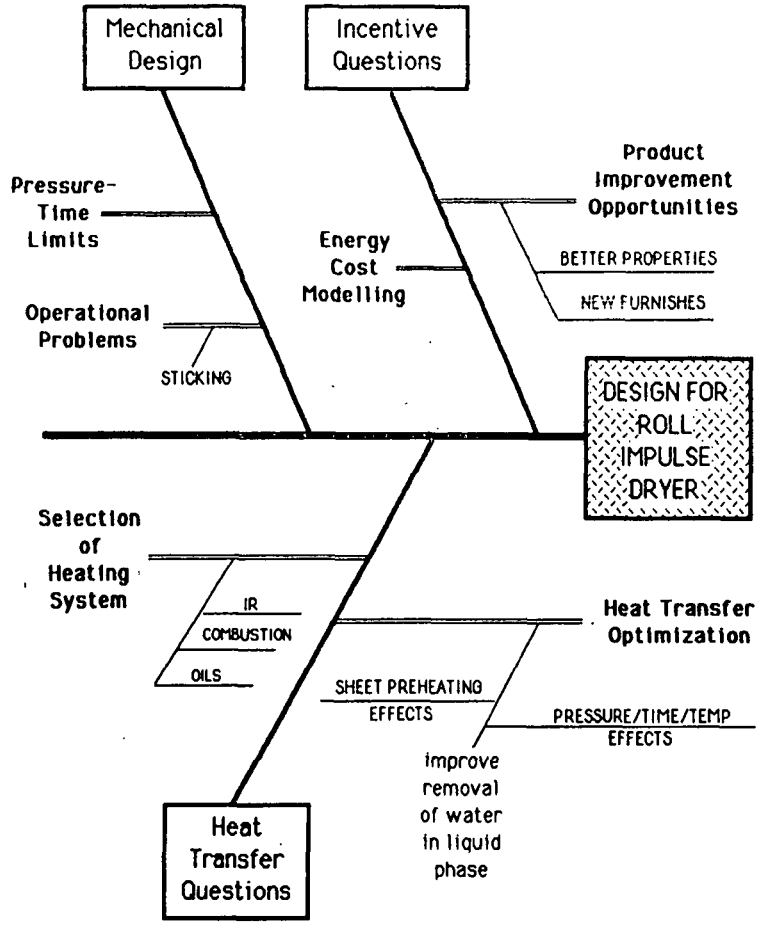

Impulse Drying

Priorities for coming period:

- To complete work to determine how to maximize liquid water removal in an impulse dryer
- To complete the heat transfer and mechanical systems designs for a pilot roll impulse dryer
- To complete the studies in progress on product improvement incentives with both conventional and alternative low-cost furnishes

Maximizing liquid water removal is essential to impulse dryer design.

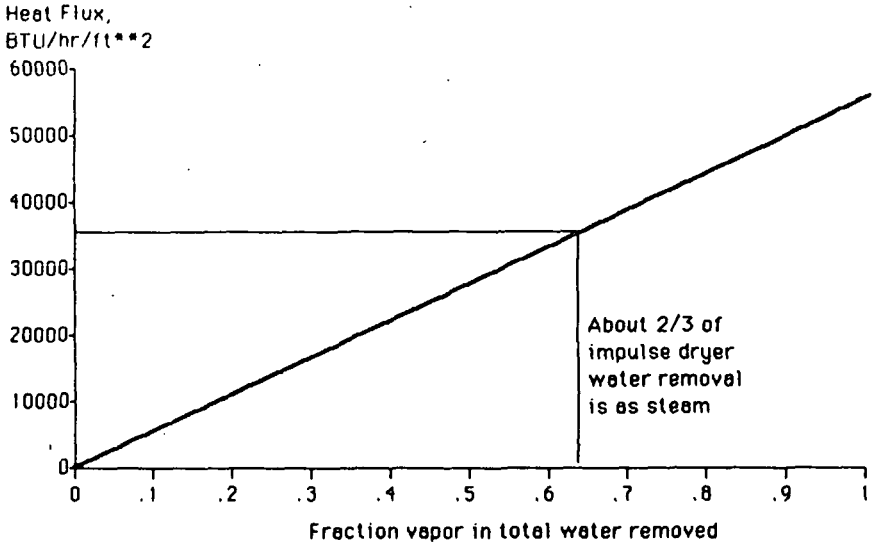

Curve was calculated assuming
a 3 foot diameter roll, and
a heater covering 3/4 of the roll surface.

Optimization of water removal in liquid phase

Plans: To complete analysis of past data and to perform additional experiments as needed.

Essential data includes heat flux through the nip and liquid water removal as measured by the LiCl tracer technique

IMPORTANT VARIABLES

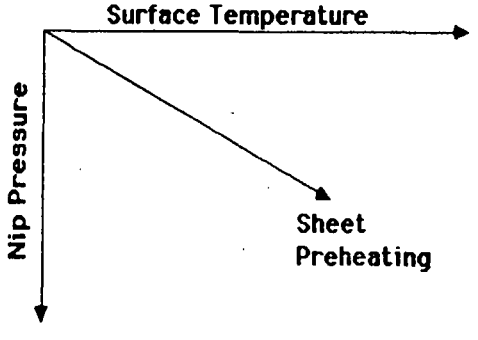

Heat fluxes correspond to reasonable heater temperatures

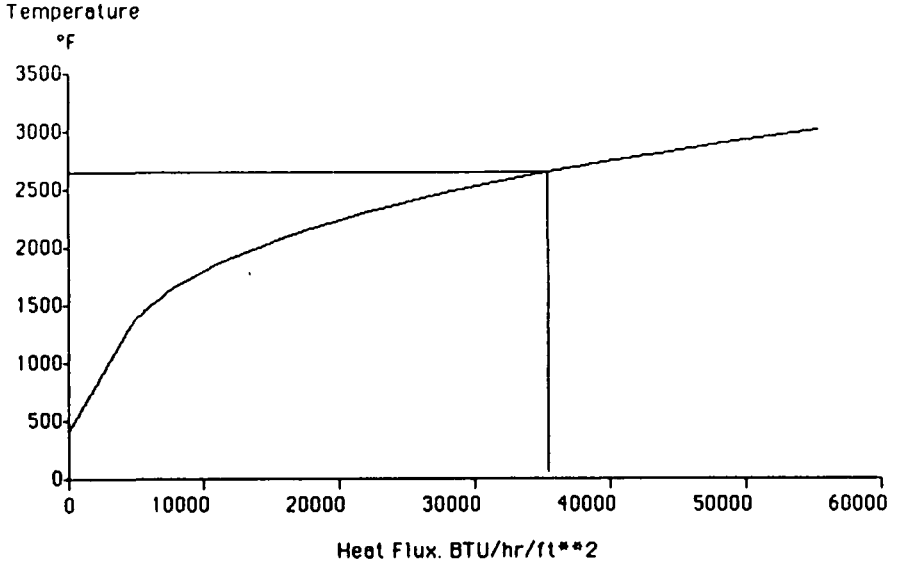

Calculated for a 400°F roll
surface temperature with
a heater emissivity of 0.8
and a roll emissivity of 0.3.
Assumed no participating gases.

Incentives:
Product improvement
and
Furnish Cost Reduction

Plans: To complete and summarize experiments on improved strength properties from conventional furnishes.

To complete the 2-level factorial experiments in P, T, and NRT on lower-cost furnishes

-TMP

-High recycle linerboard

IMPULSE DRYING

Six-Month Deliverables

- Complete design for pilot impulse dryer
- Data to optimize liquid water removal
- Data on furnish incentives
- Pilot dryer experimental plans

IMPULSE DRYING

WATER REMOVAL IN A HIGH TEMPERATURE PRESS NIP

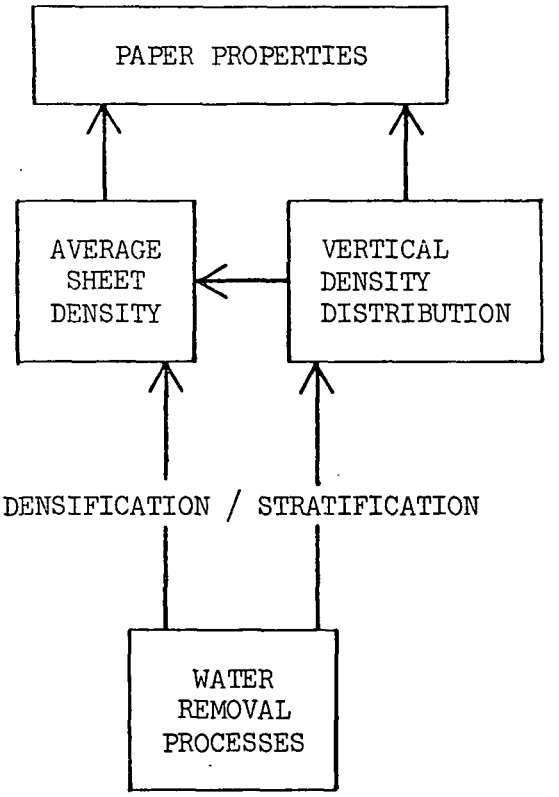

IMPULSE DRYING MECHANISMS

- ENHANCED WET PRESSING MECHANISMS
- HEAT TRANSFER/CONTACT COEFFICIENT
- THERMAL SOFTENING/INCREASED COMPRESSIBILITY
- VAPOR - INDUCED FLOW

THESIS TITLE

AN INVESTIGATION OF DYNAMIC DENSIFICATION
UNDER IMPULSE DRYING CONDITIONS

PRIMARY THESIS OBJECTIVES

TO OBTAIN A FUNDAMENTAL UNDERSTANDING, BASED ON PHYSICAL PRINCIPLES, OF THE DYNAMIC DENSIFICATION PROCESS WHICH OCCURS DURING IMPULSE DRYING AND ITS INFLUENCE ON PAPER PROPERTY DEVELOPMENT.

SPECIFIC OBJECTIVES

- TESTING OF PROPOSED HYPOTHESES
- INVESTIGATE INTERRELATIONSHIPS BETWEEN WATER REMOVAL AND DENSIFICATION MECHANISMS
- UTILIZE AND/OR EXTEND EXISTING MATHEMATICAL MODELS OF SHEET COMPRESSION

RESEARCH PLAN

- "DYNAMIC" DENSITY DISTRIBUTION STUDY
- SHEET TEMPERATURE DISTRIBUTION STUDY
- MICROSCOPIC SHEET STRUCTURE EVALUATION
- MATHEMATICAL MODELING OF PROCESS

STATUS

COMPLETED WORK:

- ° DYNAMIC DENSIFICATION STUDY
- ° TEMPERATURE DISTRIBUTION STUDY
- ° SHEET STRUCTURE EVALUATION

  VARIABLES: TEMPERATURE
  PRESSURE
  TIME
  MOISTURE
  BASIS WEIGHT
  REFINING

WORK IN PROGRESS:

- ° MATHEMATICAL MODEL

IMPULSE · DRYING SIMULATOR
"DATA COLLECTION CAPABILITIES"

- ° DISPLACEMENT MEASUREMENT SYSTEM
- ° HOT SURFACE TEMPERATURE
- ° APPLIED MECHANICAL PRESSURE
- ° HOT SURFACE VAPOR PRESSURE
- ° INTERNAL SHEET TEMPERATURES

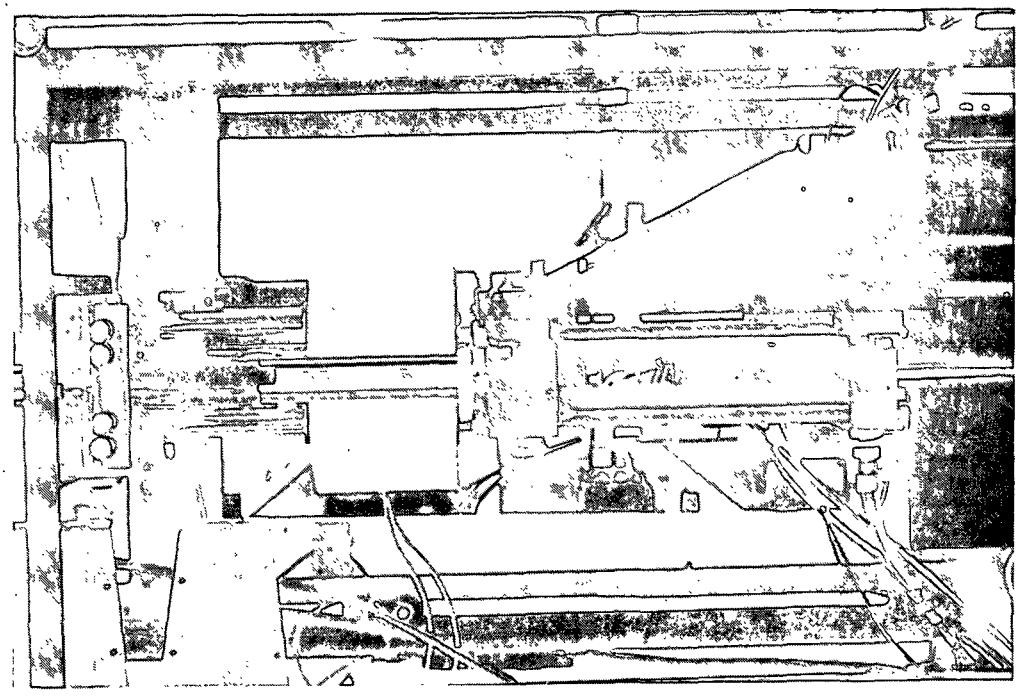

IMPULSE DRYING SIMULATOR BRAKING SYSTEM - SIDE VIEW.

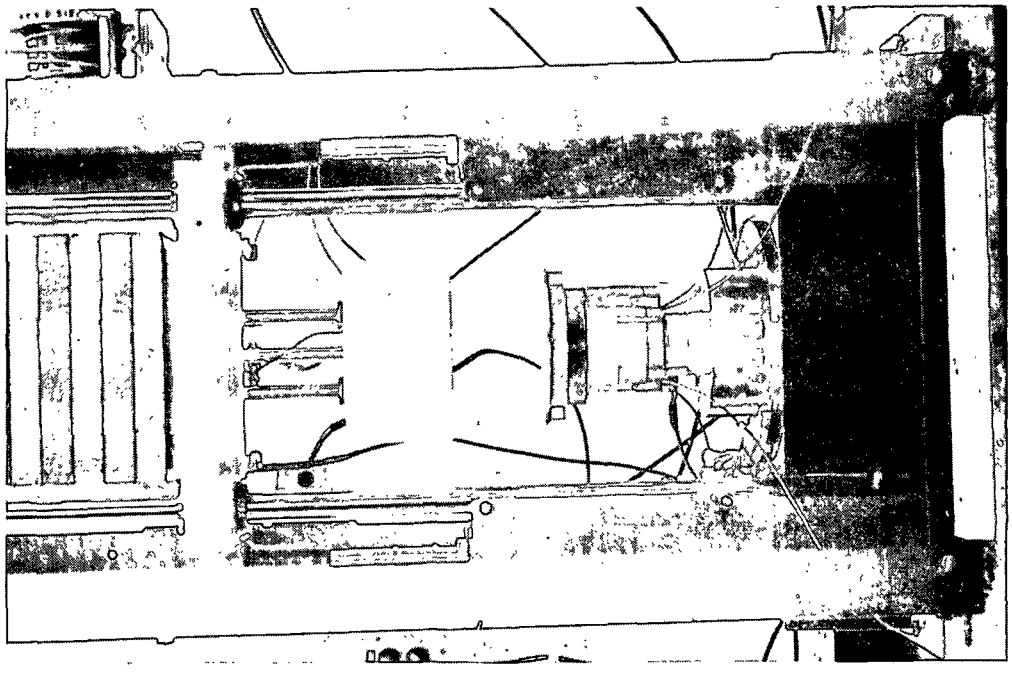

IMPULSE DRYING SIMULATOR - FRONT VIEW.

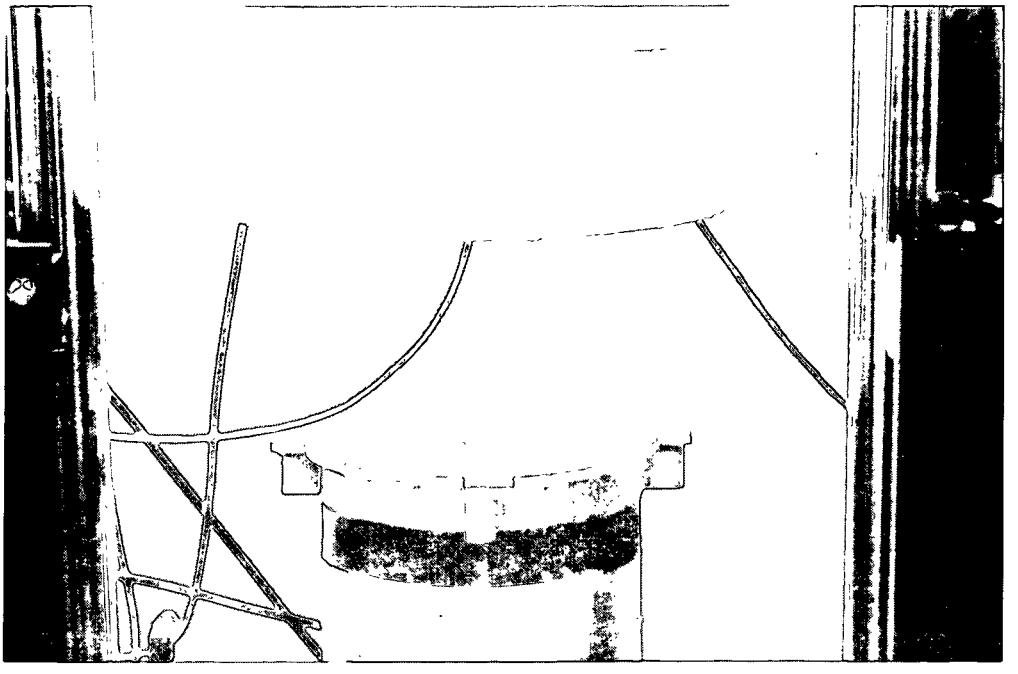

IMPULSE DRYING SIMULATOR NIP
UPPER PLATEN IS HEATED, LOWER PLATEN IS WATER RECEIVER

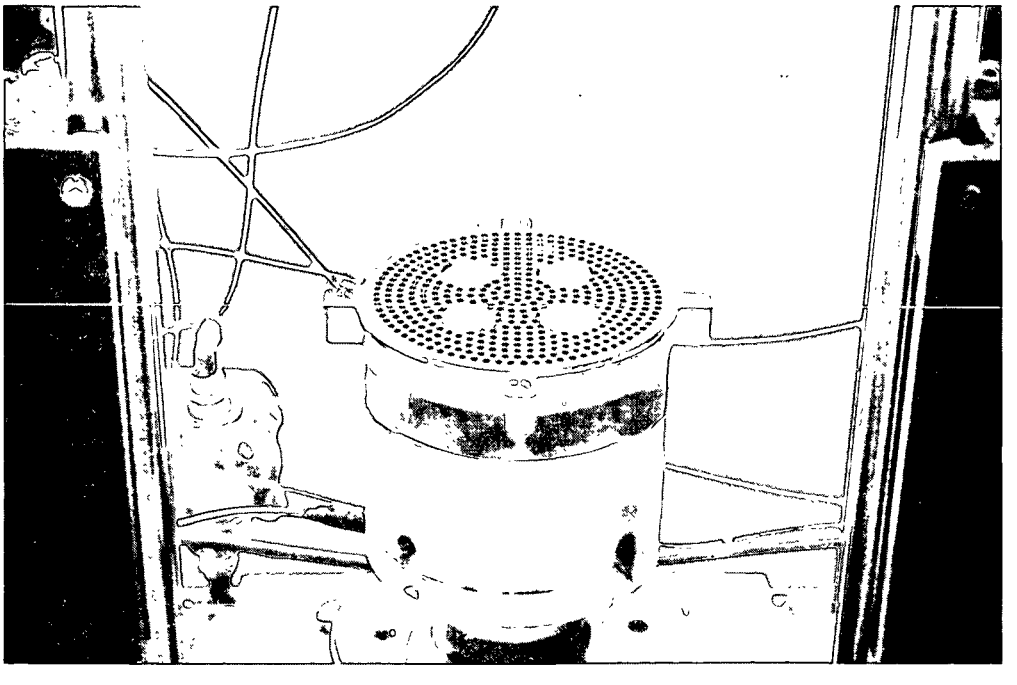

LOWER PEDESTAL OF IMPULSE DRYING SIMULATOR WITH CERAMIC REMOVED
REVEALING DISPLACEMENT TRANSDUCERS AND DRILLED PLATE

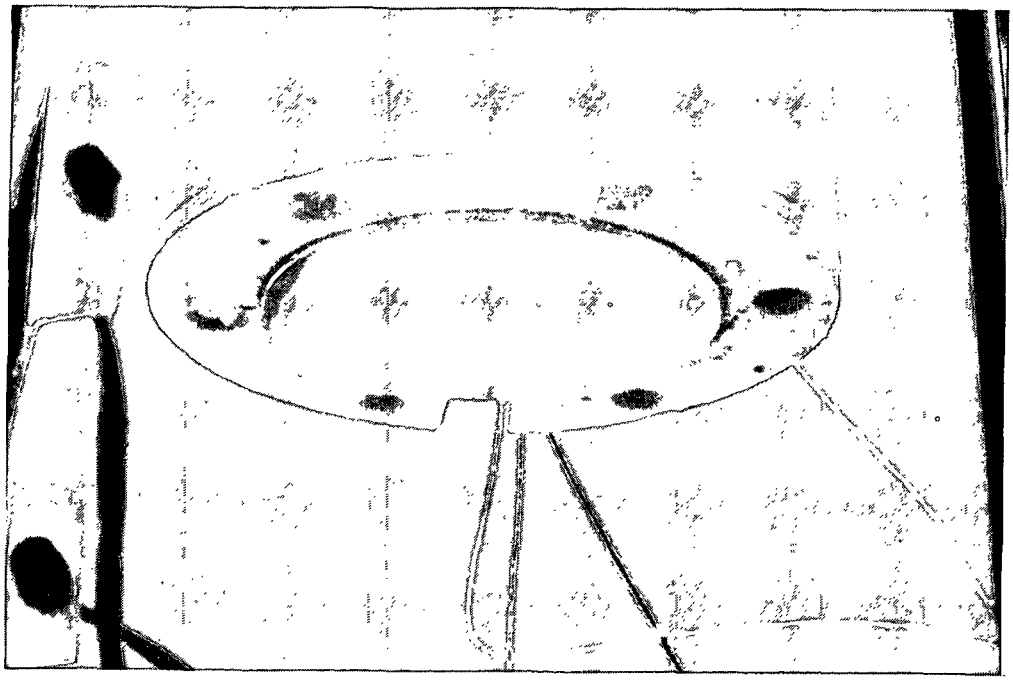

UPPER HEATED PLATEN OF IMPULSE DRYING SIMULATOR

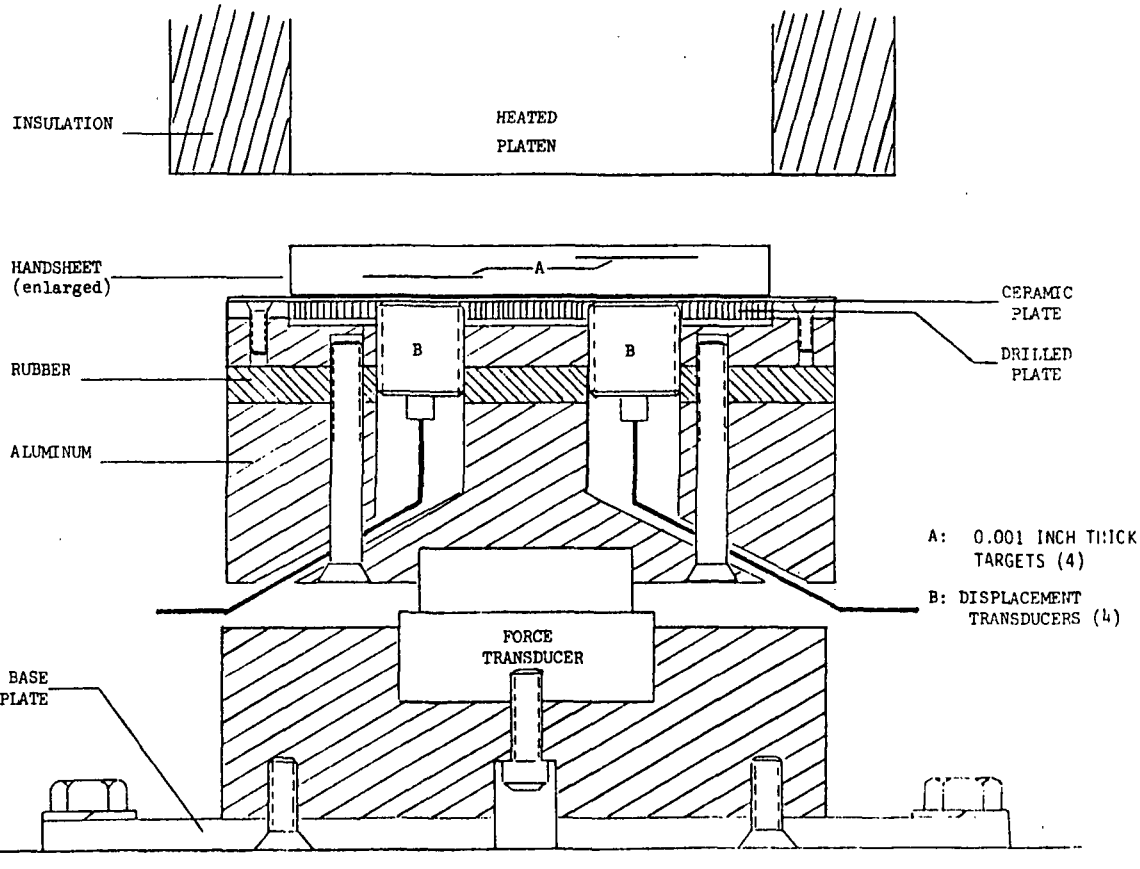

IMPULSE DRYING SIMULATOR PEDESTAL

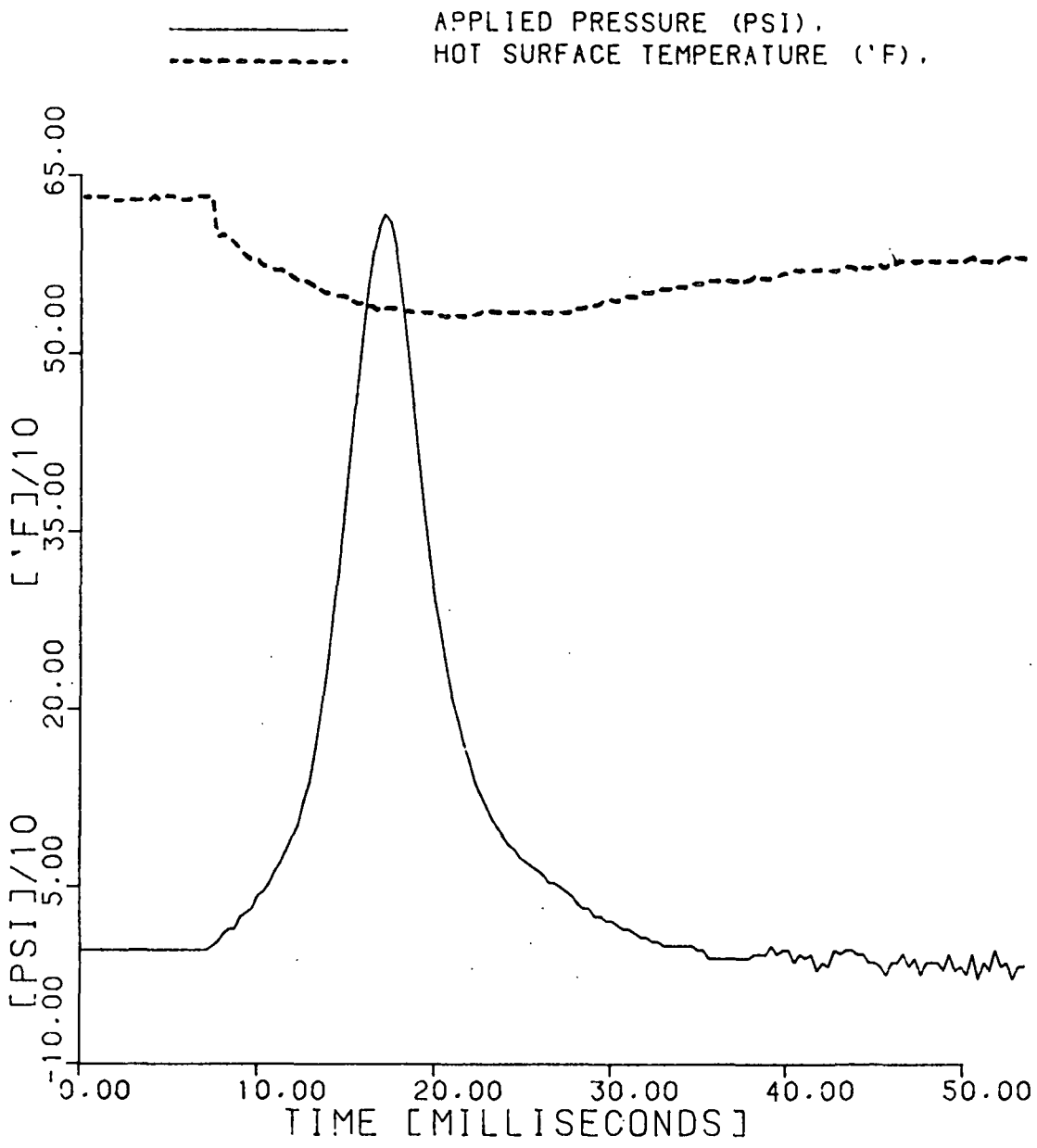

APPLIED MECHANICAL PRESSURE AND HOT SURFACE TEMPERATURE FOR AN UNBLEACHED SOFTWOOD KRAFT HANDSHEET, 166 g/m^2 BASIS WEIGHT, 2.2 INITIAL MOISTURE RATIO, 735 CSF.

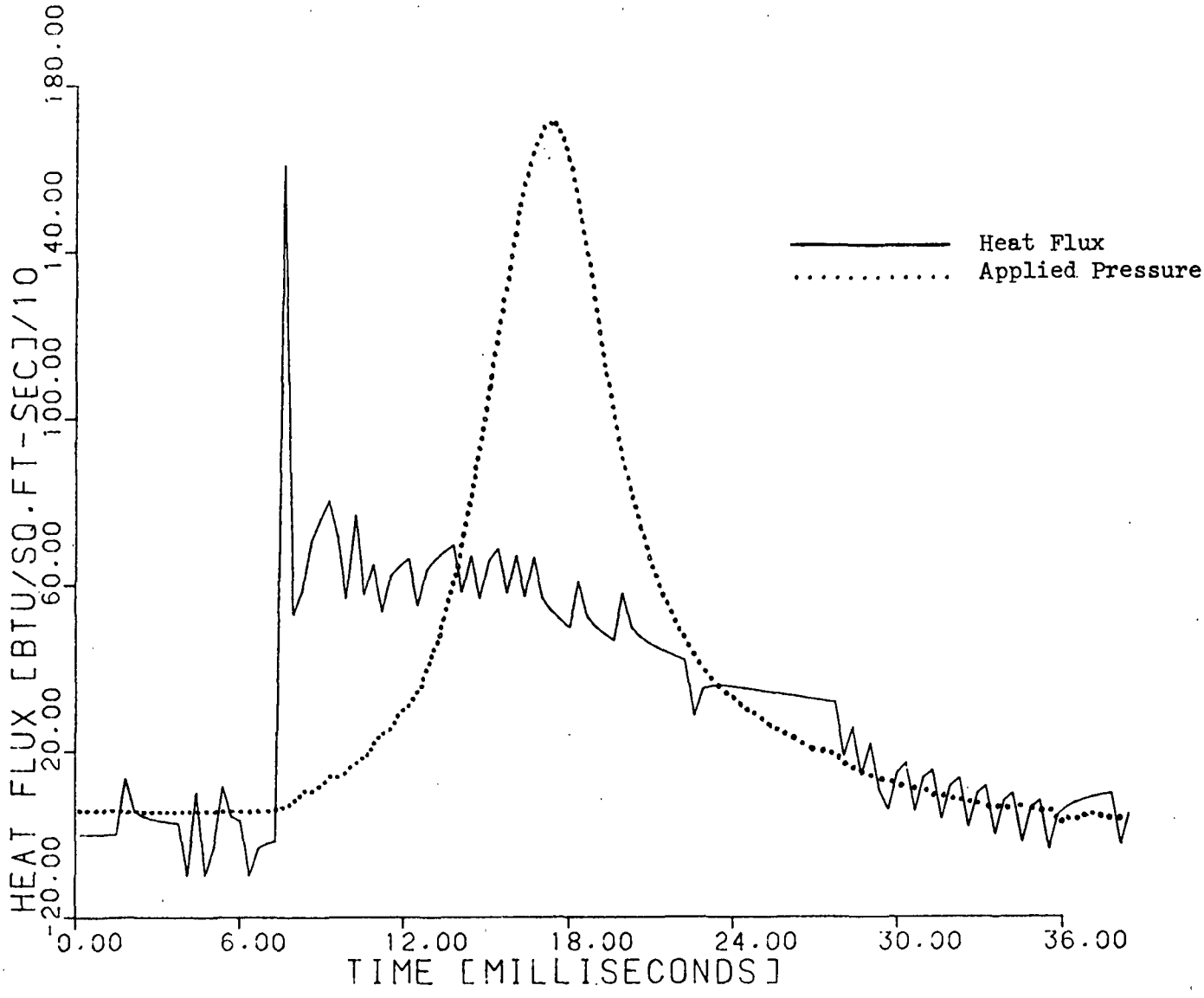

INSTANTANEOUS HEAT FLUX CALCULATED FROM THE HOT SURFACE TEMPERATURE. APPLIED MECHANICAL PRESSURE PULSE INCLUDED FOR REFERENCE.

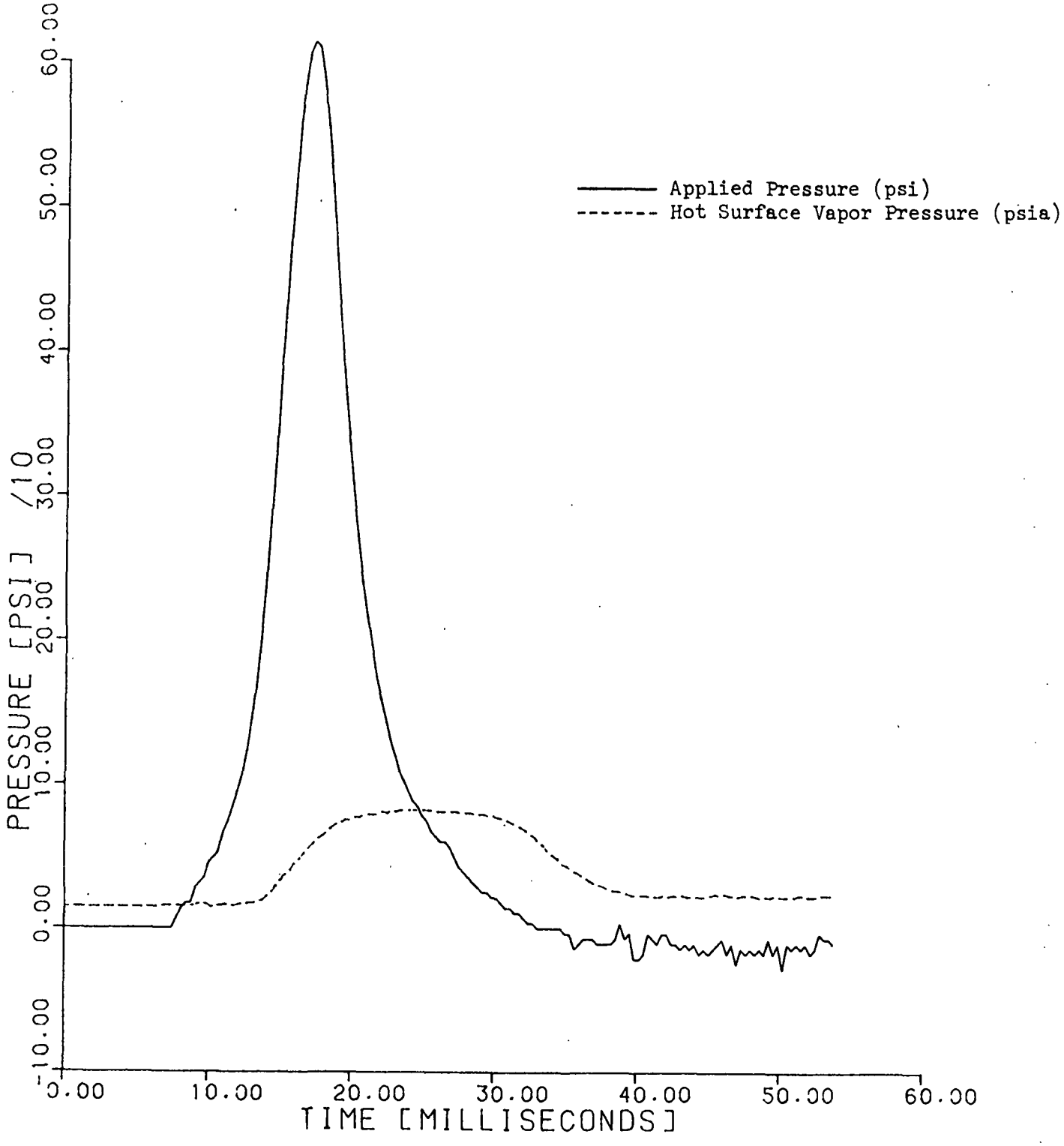

APPLIED MECHANICAL PRESSURE AND HOT SURFACE VAPOR PRESSURE FOR AN UNBLEACHED SOFTWOOD KRAFT HANDSHEET IMPULSE DRIED AT 630°F HOT SURFACE TEMPERATURE; 166 g/m^2 BASIS WEIGHT, 2.2 INITIAL MOISTURE RATIO, 735 CSF.

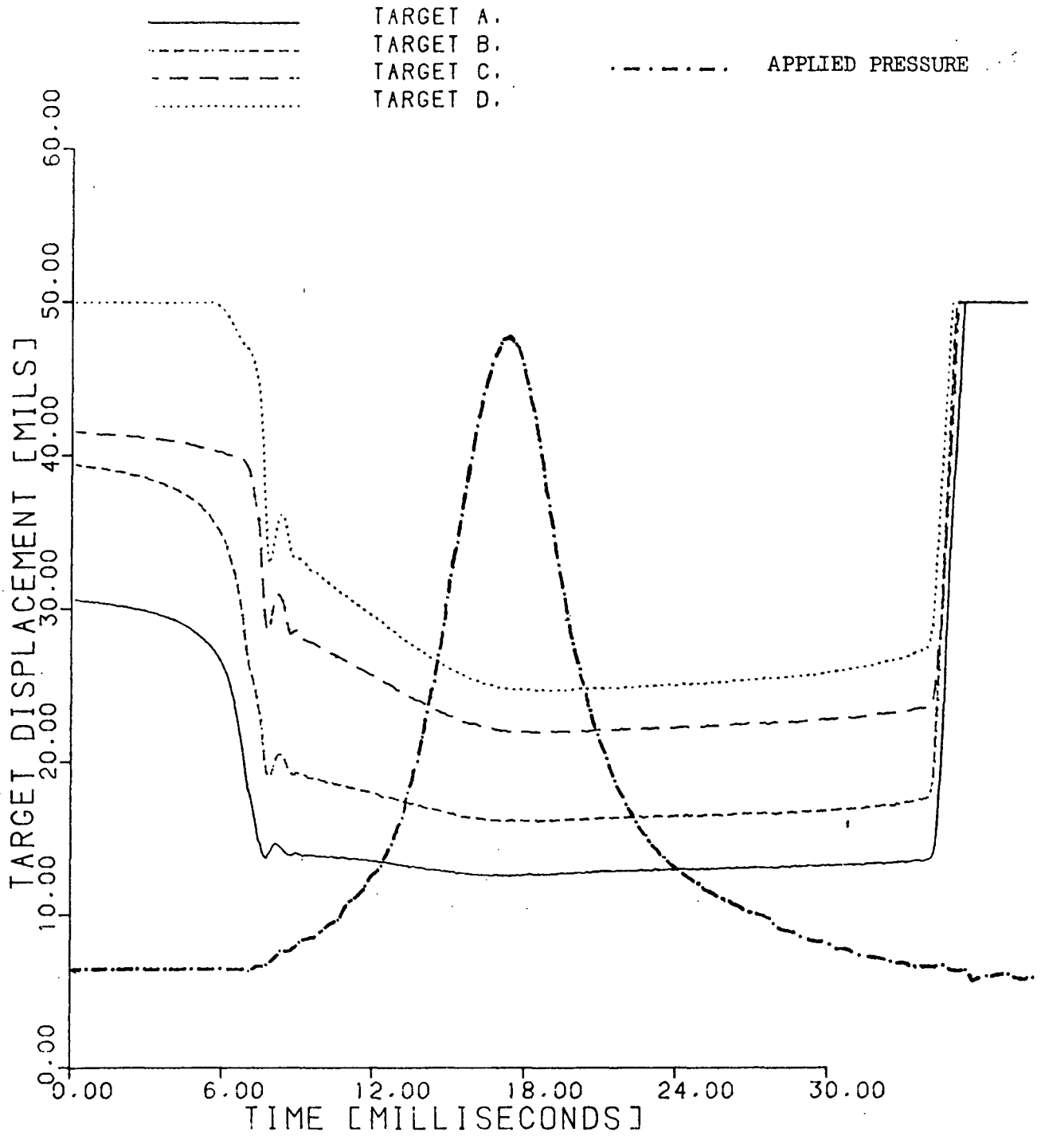

DISPLACEMENT HISTORIES OF FOUR TARGETS PLACED AT DISTINCT POSITIONS WITHIN THE FIBER MAT, WET PRESSED AT ROOM TEMPERATURE, PEAK PRESSURE OF 614 PSI AND A NIP RESIDENCE TIME OF 25 MILLISECONDS. THE HANDSHEET IS A 168 g/m^2 BASIS WEIGHT, 2.3 INITIAL MOISTURE RATIO, 735 CSF.

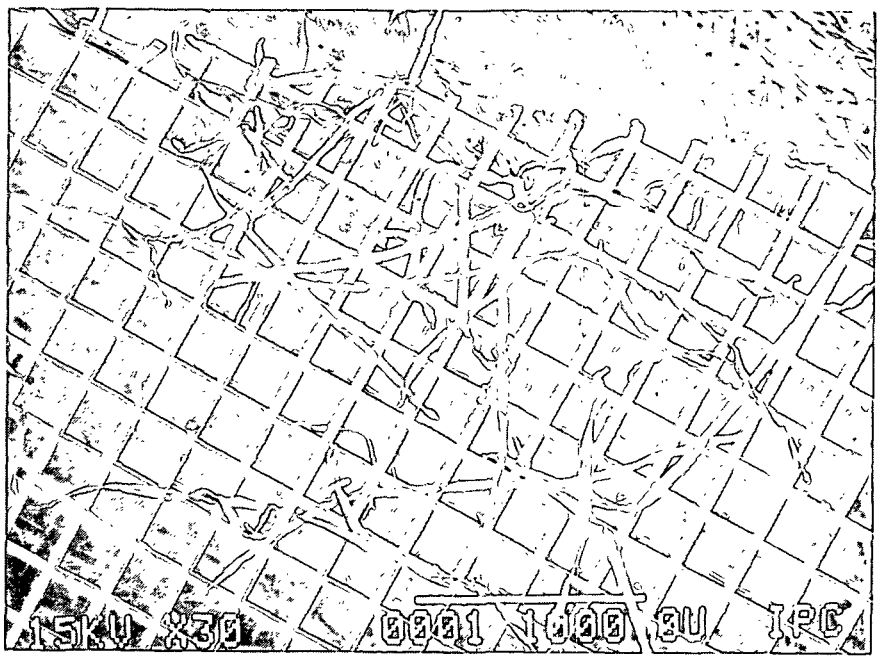

TARGET MATERIAL USED IN THICKNESS MEASUREMENT
0.001 INCH THICK COOPER MESH

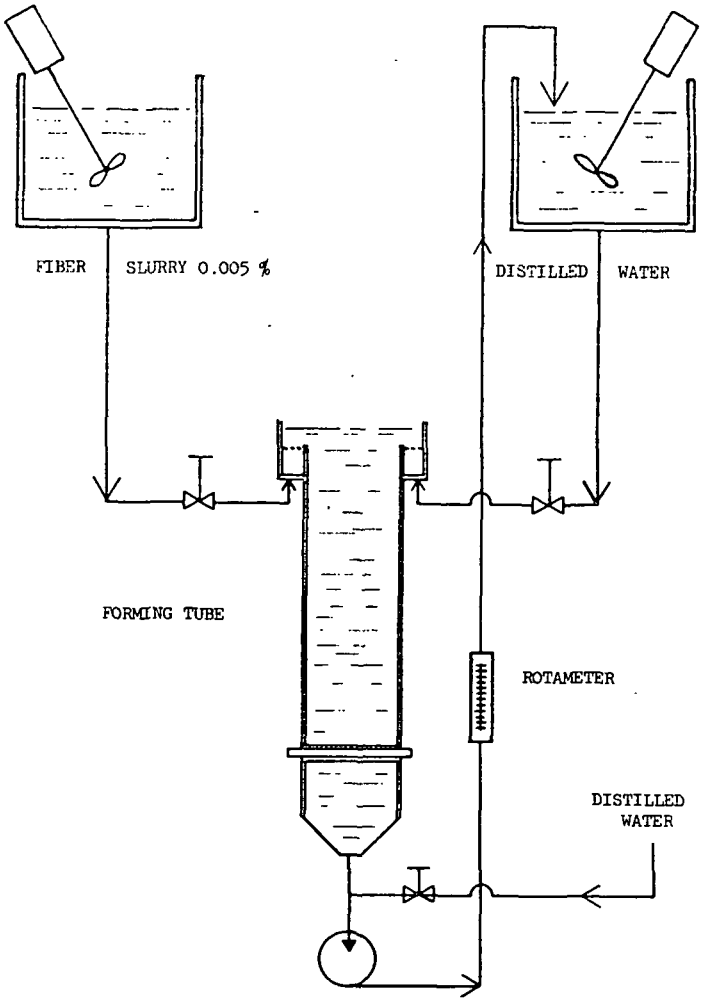

* CONSTANT RATE FORMATION
* CONTINUOUS FLOW DURING TARGET INSERTION

METHODS USED FOR DETERMINING Z-DIRECTIONAL DENSITY DISTRIBUTION

- SHEET GRINDING
- GOLD MAPPING TECHNIQUE
- DYNAMIC DENSIFICATION MEASUREMENTS

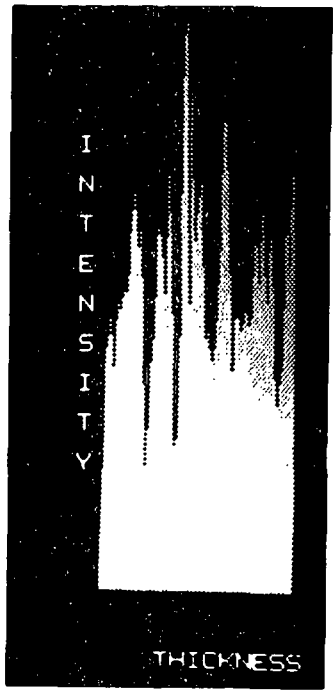

Control 70°F

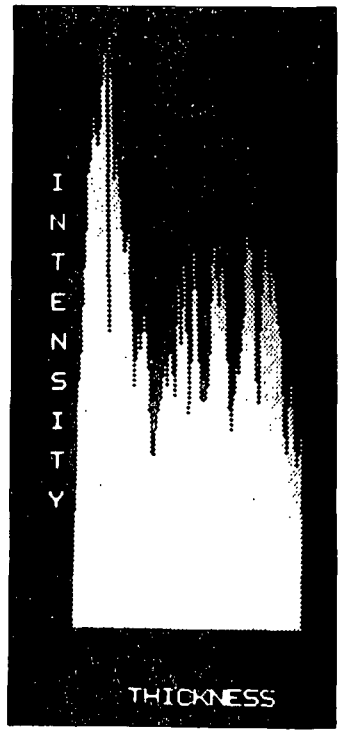

300°F

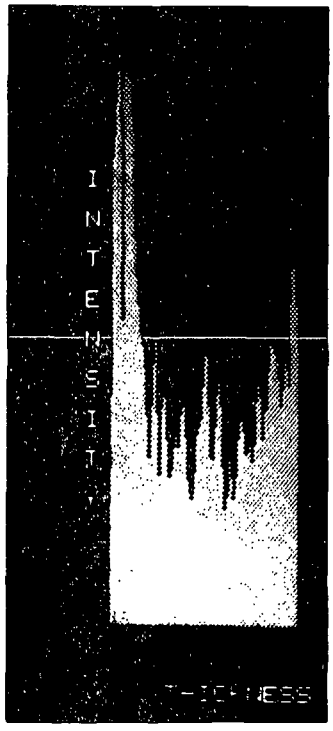

450°F

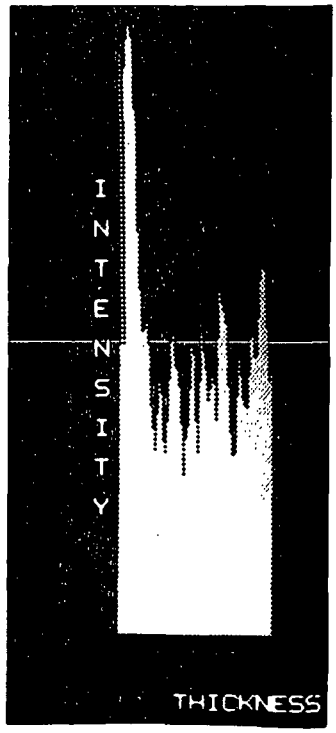

600°F

SCANNING ELECTRON MICROSCOPE MAPPINGS OF THE INTENSITY OF GOLD COUNTS (Y AXIS) VERSUS SHEET THICKNESS (X AXIS). INTENSITY IS A RELATIVE MEASURE OF THE APPARENT DENSITY OF THE WEB.

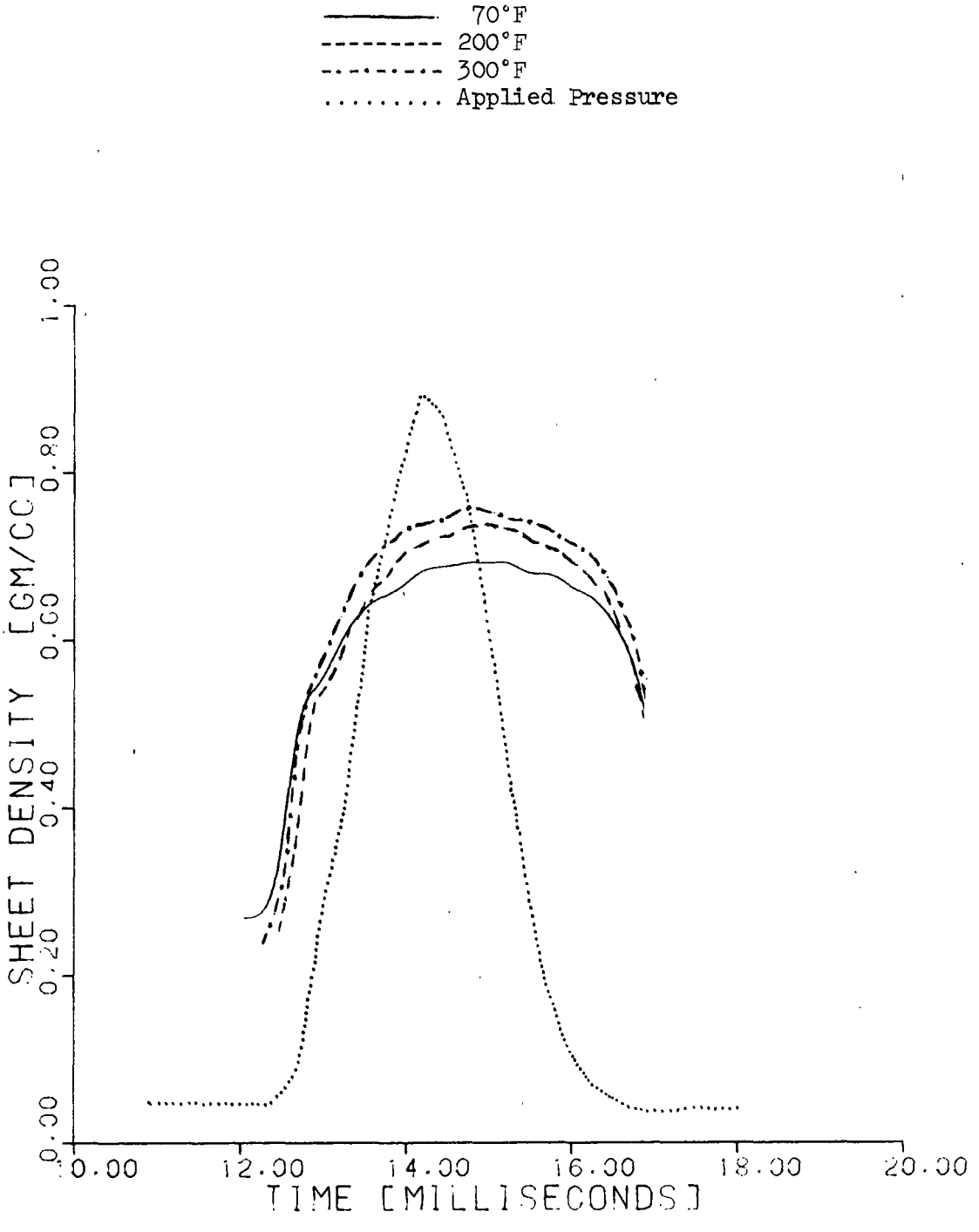

SHEET DENSITY VERSUS TIME FOR VARYING HOT SURFACE TEMPERATURES (70°F, 200°F, AND 300°F). EACH CURVE REPRESENTS A SINGLE RUN. BASIS WEIGHT 50 g/sq.m., 800 PSI PEAK APPLIED PRESSURE, 4.5 MSEC NIP RESIDENCE TIME, 735 CSF FREENESS, 1.2 INITIAL MOISTURE RATIO.

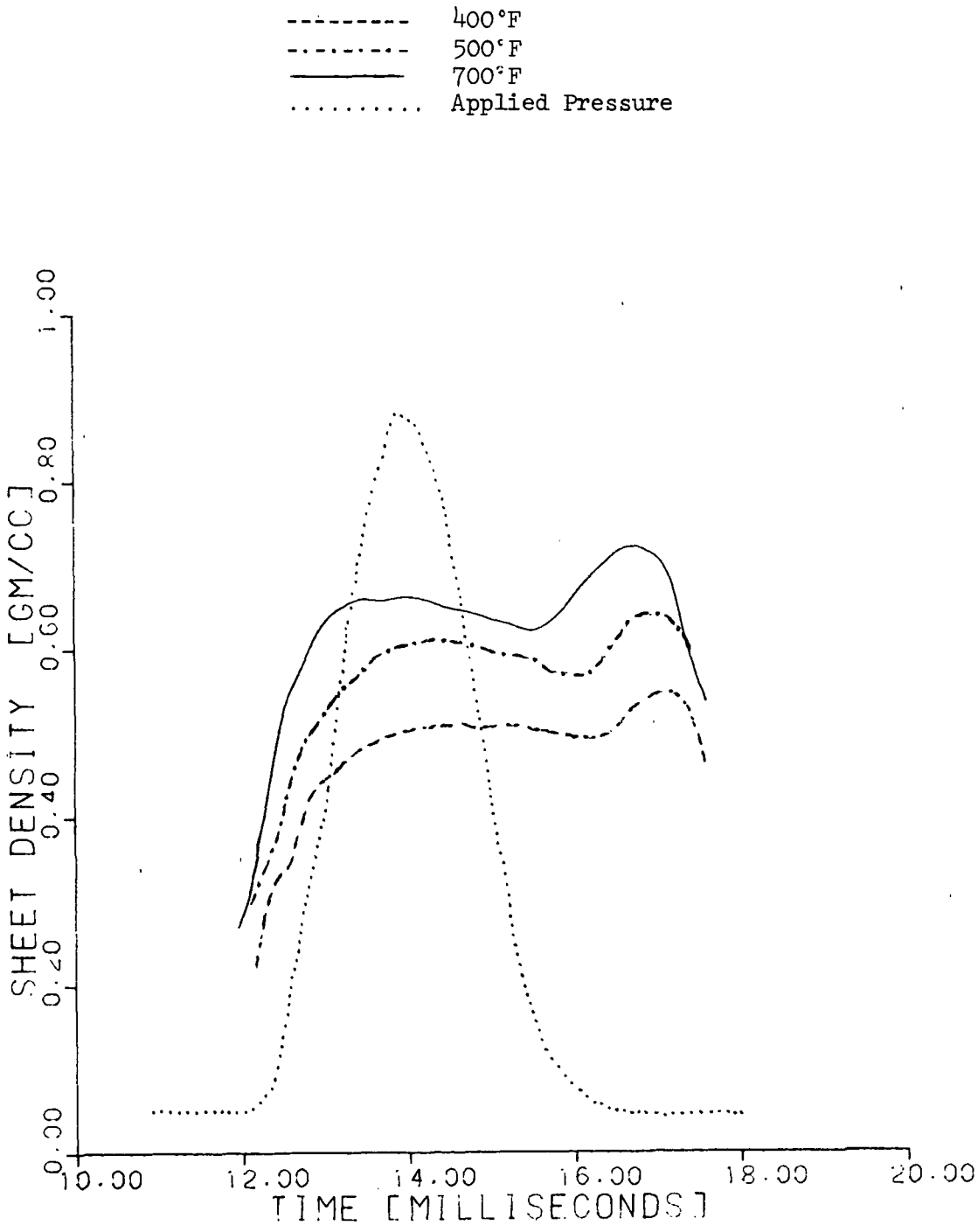

SHEET DENSITY VERSUS TIME FOR VARYING HOT SURFACE TEMPERATURES (400°F, 500°F, AND 700°F). EACH CURVE REPRESENTS A SINGLE RUN. BASIS WEIGHT 50 g/sq.m., 800 PSI PEAK APPLIED PRESSURE, 4.5 MSEC NIP RESIDENCE TIME, 420 CSF FREENESS, 1.2 INITIAL MOISTURE RATIO.

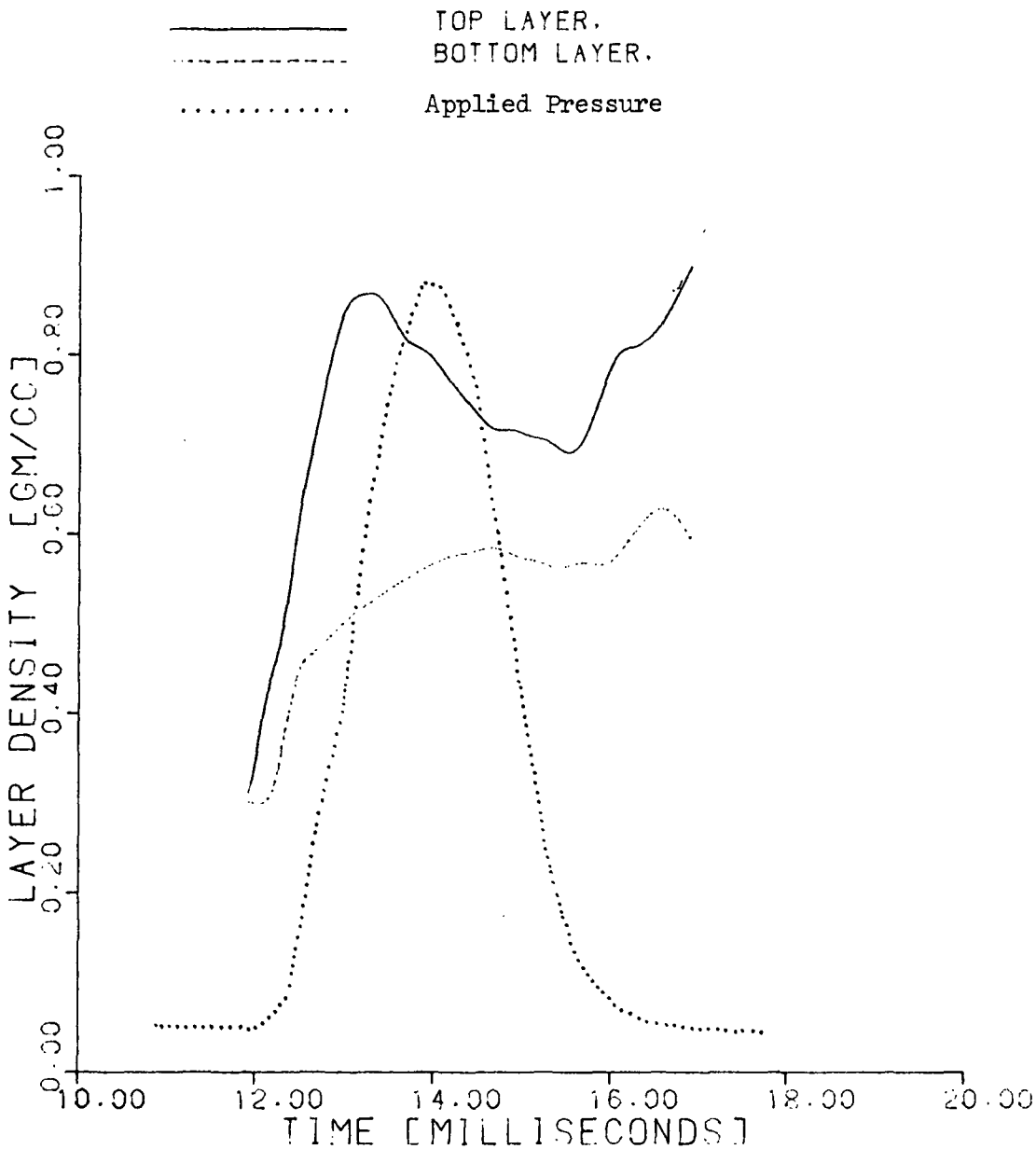

LAYER DENSITIES VERSUS TIME FOR AN IMPULSE DRIED 50 g/sq.m. BASIS WEIGHT SHEET OF 420 CSF FREENESS. 800 PSI PEAK APPLIED PRESSURE, 4.5 MSEC NIP RESIDENCE TIME, 700°F HOT SURFACE TEMPERATURE, 1.2 INITIAL MOISTURE RATIO.

EACH LAYER REPRESENTS 25 g/sq.m. BASIS WEIGHT. THE TOP LAYER IS NEXT TO THE HOT SURFACE.

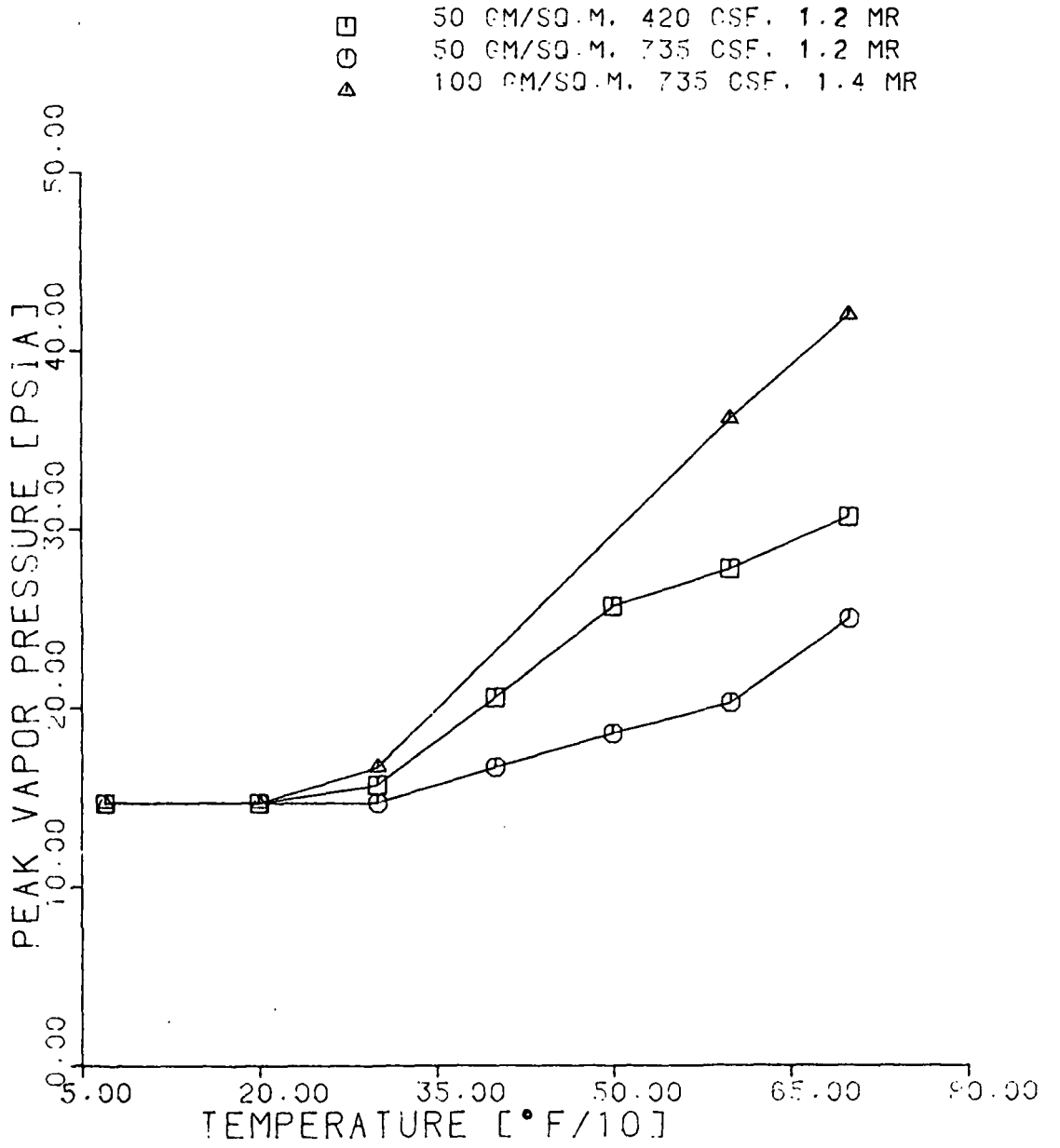

PEAK VAPOR PRESSURES AS A FUNCTION OF HOT SURFACE TEMPERATURE FOR AN 800 PSI PEAK PRESSURE, 4.5 MSEC NIP RESIDENCE TIME. BASIS WEIGHT OF 50 TO 100 g/sq.m. AND FREENESS VALUES OF 420 AND 735 CSF.

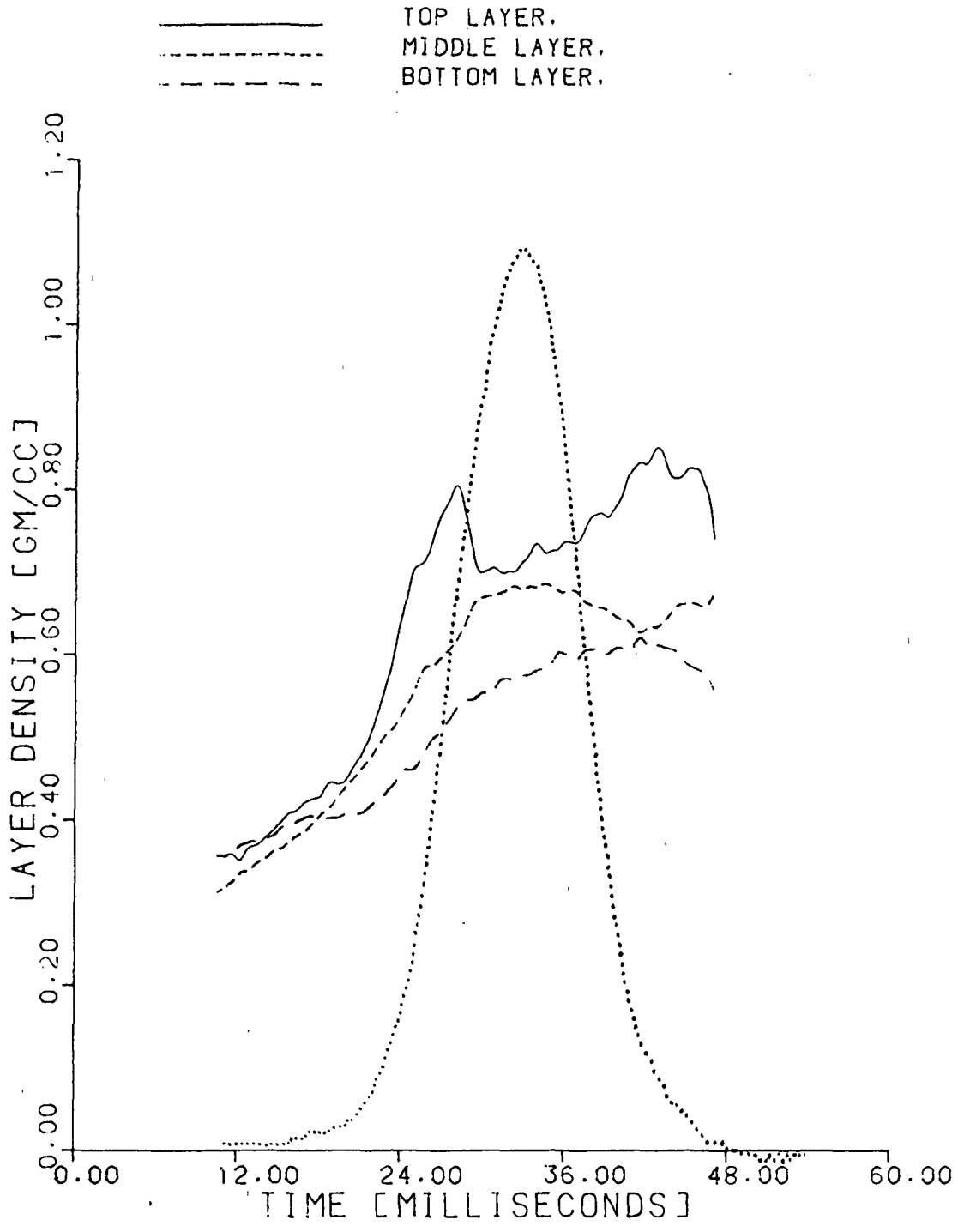

SHEET LAYER DENSITY AS A FUNCTION OF TIME FOR A 100 g/sq.m. WEB AT AN INITIAL MOISTURE RATIO OF 1.5 AND A PULP FREENESS OF 420 CSF, IMPULSE DRIED AT 600°F HOT SURFACE TEMPERATURE, 550 PSI PEAK APPLIED PRESSURE, AND A 30 MILLISECOND NIP RESIDENCE TIME. THE TOP AND BOTTOM LAYER EACH REPRESENT 25% OF THE TOTAL BASIS WEIGHT WITH THE TOP LAYER POSITIONED NEXT TO THE HEATED SURFACE. THE APPLIED PRESSURE PULSE IS INCLUDED FOR REFERENCE.

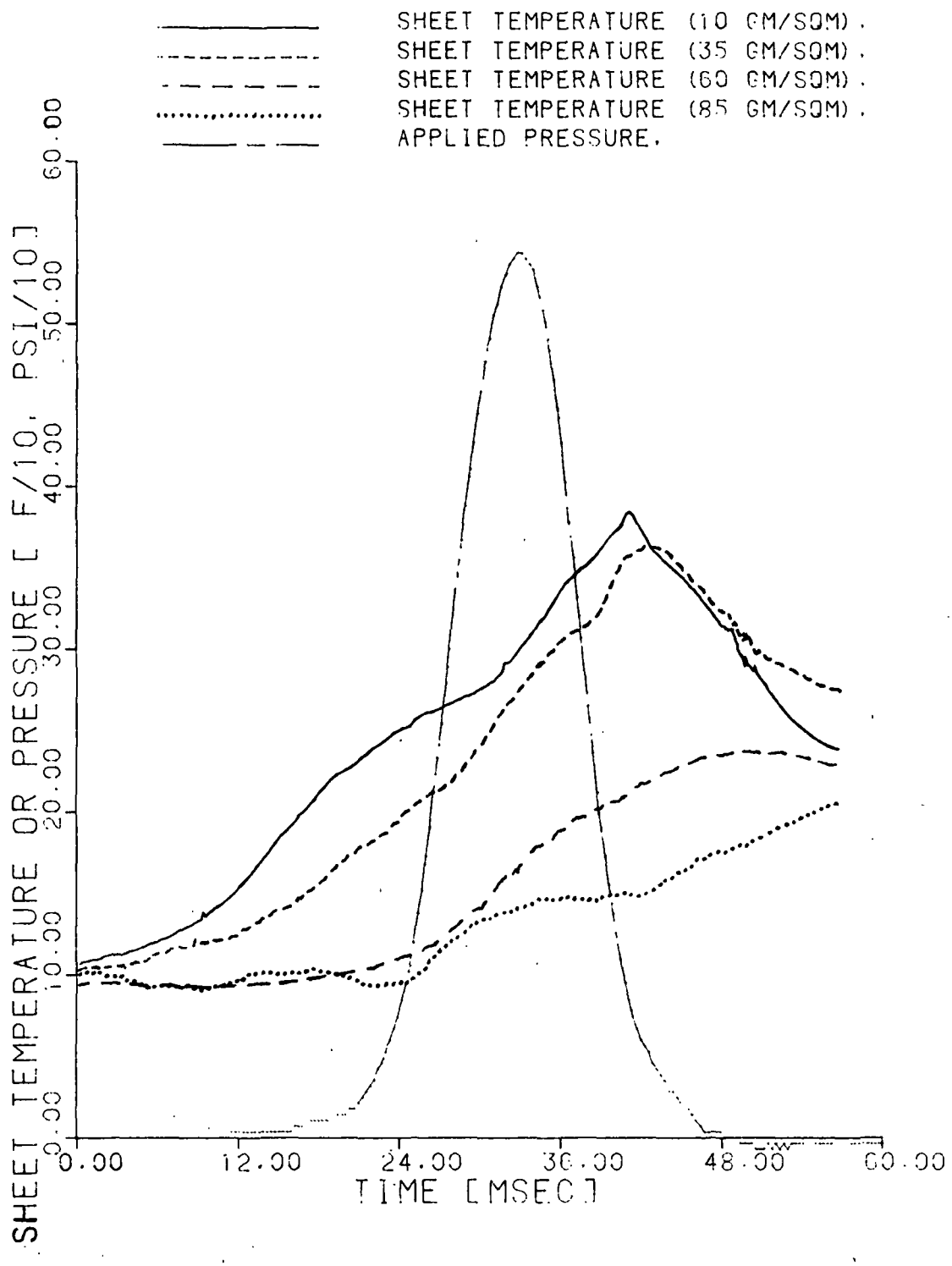

SHEET TEMPERATURE RESPONSE AS A FUNCTION OF TIME AT INCREASING DISTANCES FROM THE HOT SURFACE FOR A 100 g/sq.m. WEB AT AN INITIAL MOISTURE RATIO OF 1.5 AND A PULP FREENESS OF 420 CSF, IMPULSE DRIED AT 600°F HOT SURFACE TEMPERATURE, 550 PSI PEAK APPLIED PRESSURE, AND A 30 MILLISECOND NIP RESIDENCE TIME.

DENSIFICATION MECHANISMS

DURING IMPULSE DRYING

MOISTURE REDISTRIBUTION DUE TO EVAPORATION-CONDENSATION MECHANISM.

INTENSE DENSIFICATION OF TOP LAYER DUE TO DRYING OUT AND THERMAL SOFTENING.

ABRUPT DECREASE OR LEVELING OUT OF SHEET DENSITY NEAR THE HOT SURFACE DUE TO INTERNAL VAPOR PRESSURE GENERATION.

ENHANCED WET PRESSING MECHANISMS IN FLOW EXITING REGION OF WEB.

COLLAPSE OF SHEET STRUCTURE DUE TO RELEASE OF VAPOR AS THE APPLIED PRESSURE DECREASES BELOW VAPOR PRESSURE.

DISRUPTION OF THE INTERNAL SHEET STRUCTURE AFTER THE PRESS NIP DUE TO CONTINUED VAPOR RELEASE.